MECHANISMS OF LIPID MODULATION AND AGONIST ACTIVATION IN THE MUSCLE NICOTINIC ACETYLCHOLINE RECEPTOR

Mackenzie Thompson

Thesis submitted in partial
fulfillment of the requirements for the
Doctorate in Philosophy in Biochemistry

Department of Biochemistry, Microbiology and Immunology
Faculty of Medicine
University of Ottawa

Abstract

The muscle nicotinic acetylcholine receptor (nAChR) is a synaptic receptor that mediates neuromuscular communication by allowing cations to flow into a skeletal muscle cell in response to acetylcholine (ACh) binding. ACh binding transiently converts the nAChR from a non-conductive resting state to a conductive open state, increasing the intracellular voltage, ultimately leading to muscle contraction. The composition of the surrounding lipid environment also influences the stabilities of these, and other, conformational states to modulate nAChR function. While there is a reasonable understanding of what conformational states agonists and lipids stabilize to exert their effects, the mechanisms by which they do so remain enigmatic. In this thesis, the structural mechanisms of agonist activation and lipid modulation are explored using a combination of screening mutagenesis and electrophysiology. In manuscripts 1 and 2 extensive functional characterization of the peripheral M4 α-helices in the nAChR transmembrane domain (TMD) is used to explore different potential pathways of lipid modulation. Lipid modulation is suggested to occur through unique and independent mechanisms in each nAChR subunit that add together to account for the dramatic effects of lipids on nAChR function. In manuscript 3 new nAChR structures in apo and agonist bound states are used to guide a functional characterization of the interface between the extracellular domain (ECD) and the TMD, which is responsible for coupling agonist binding to channel gating. The new structures, which contradict previously reported mechanisms of nAChR activation, highlight conformational asymmetry at the ECD – TMD interface in α versus non-α subunits. We propose that agonist binding allows local "tension" at the ECD – TMD interfaces of the α subunits to "relax" to a conformationally symmetric active state. The results of these studies enhance our understanding of the mechanisms that underly allosteric transitions in the nAChR.

Acknowledgments

I am a product of the situations and people that have surrounded me throughout my life. I would consider myself extremely privileged to have to opportunity to pursue my passion for science at the highest level and I acknowledge that this journey has been made much easier by my demographic. With that said, I believe truly special things can happen when opportunity meets hard work, and never once did I take my privilege for granted. These past six years have been the most challenging, rewarding, and humbling of my life. This is a testament to the people that have been with me on this journey – people that I wish to acknowledge here:

I must first thank my supervisor Dr. John Baenziger, who took a chance on me and afforded me the opportunity to pursue my career in science. You have been an extraordinary mentor both in the lab and in life. I am very lucky to have had you supporting me throughout this journey.

I must acknowledge the various scientific mentors and collogues whose support and guidance have brought me through all the "waves" that come with being an experimental scientist. Dr. Corrie daCosta was integral to my development since I began by studies, both on my TAC as well as the ion channel journal club. You never took it easy on me, and for that I will be forever grateful. Dr. Hugues Nury became an important part of my scientific career during the latter part of my PhD, particularly during the eight months I spent working in his lab. Dr. Nury's passion for science and outlook on life changed my perspective and reignited my curiosity. I am undoubtable a better scientist and man because of him. Dr. Jyh-Yeuan Lee and Dr. Maria Musgaard were also integral parts of my development that deserve a huge thank you for their role in shaping this thesis.

The colleagues I have had along the way made the day-to-day grind of the PhD much more enjoyable. Dr. Camille Hénault and Jaimee Domville were responsible for teaching me, both technically and intellectually, how to be a scientist. Jacob Monast, Toka Hussein, Anna Ananchenko, Deepansh Mody, Mykhaylo Slobodyanyuk, Tatiana Labouré, and Dr. Sonja Minniberger all worked alongside me and had the unfortunate responsibility of listening to me spout my (often wrong) theories throughout the years. The fact they all still talk to me is a testament to their friendship. I also had the pleasure of working with and supervising many bright undergraduate students who were subject to similar torture. These include Annie Jiang,

Momina Ejaz, Olivier Brandts-Longtin, Yalnaz Mohasin, Janet Luttrell, Farid Monsoub Bekarkhanechi, Marshall Macduff, Stephanie Bogdan, and Rui Yan Gao.

The friends I have kept and made along the way have always kept me on track. Jordan, Andrew, Ian, Jacob, Clark, Craig, and Riley; thank you for being there and listening to me rant, despite most of the time not knowing what I was talking about. My Ottawa crew – Sam, Emma, Zoe, Cory, Nicole, Simon, Ryley, Malcolm, and Katie – you kept me sane.

My family deserves a massive thank you for staying by my side through the thick and the thin. My battles with mental health left me unsure if I could handle the stresses of a PhD but you encouraged me to pursue my passion and were there to support me when I needed it. Through success and failure your love never wavered. Without you, none of this would have been possible.

Finally, Laura. Your name should be beside mine on the title page of this thesis because without you I may not be here at all. You have been my light when all I could see is darkness. Together we have overcome the most challenging of obstacles and together we stand with this as a reminder that together we can achieve anything.

My PhD was supported financially by the following funding organizations:

-Natural Sciences and Engineering Research Council of Canada (NSERC)
-Ontario Graduate Scholarship (OGS)
-University of Ottawa Department of Biochemistry, Microbiology, and Immunology (BMI)

Preface

This thesis is presented as a collection of four manuscripts. The data is presented as described below:

Manuscript 1: Thompson, M.J., Domville, J.A., and Baenziger, J.E. (2020). The functional role of the αM4 transmembrane helix in the muscle nicotinic acetylcholine receptor probed through mutagenesis and co-evolutionary analyses. J. Biol. Chem. *295*, 11056–11067. https://doi.org/10.1074/jbc.ra120.013751.

Manuscript 2: Thompson, M.J., Domville, J.A., Edrington, C.H., Venes, A., Giguère, P.M., and Baenziger, J.E. (2022). Distinct functional roles for the M4 α-helix from each homologous subunit in the hetero-pentameric ligand-gated ion channel nAChR. J. Biol. Chem. 102104. https://doi.org/10.1016/j.jbc.2022.102104.

Manuscript 3: Thompson, M.J., Bekarkhanechi, F.M., Ananchenko, A., Nury, H., and Baenziger, J.E. (2023). Asymmetric tensed-to-relaxed subunit transitions drive gating of the heteromeric muscle nicotinic acetylcholine receptor. Accepted at Nat. Comm.

Manuscript 4: Thompson, M.J., Zarkadas, E., Nury, H., and Baenziger, J.E. (2024). Asynchronous conformational transitions during nicotinic acetylcholine receptor activation. In preparation for Neuron.

Additionally, there are two review articles included in the **Appendix**:

Thompson, M.J., and Baenziger, J.E. (2020a). Ion channels as lipid sensors: from structures to mechanisms. Nat. Chem. Biol. *16*, 1331–1342. https://doi.org/10.1038/s41589-020-00693-3.

Thompson, M.J., and Baenziger, J.E. (2020b). Structural basis for the modulation of pentameric ligand-gated ion channel function by lipids. Biochim. Biophys. Acta - Biomembr. *1862*, 183304. https://doi.org/10.1016/j.bbamem.2020.183304.

Table of Contents

List of Figures

List of Tables

List of Movies

Movies are available via figshare using the following doi: 10.6084/m9.figshare.25215806.

Movie 5.1 Motions at the intra- and inter-subunit ECD – TMD interfaces during activation. The principal α_γ (salmon) and complementary γ (light blue) subunits are shown from two orthogonal views transitioning from apo to agonist bound states. The agonist is shown in cyan sticks. (a) Loop C capping tilts the α subunit ECD moving the αβ1-β2 loop away from the complementary subunit and towards the pore while the αM2-M3 loop moves orthogonally away from the pore. (b) The capping of loop F in the complementary subunits pivots the β8-β9 loops and the β10-M1 linkers away from the channel pore. These motions are correlated with the movement of the αM2-M3 loops away from pore.

Movie 5.2 Asymmetric to symmetric transitions at the ECD – TMD interface. The top panel shows the relative movements of the Val46 and Pro265 residues in the α_γ and each of the non-α subunits when going from the apo to the agonist bound state. The bottom panel shows each of the three non-α subunits aligned to the α_γ subunit by their M2-M3 loops. The structures start in the apo state where they are asymmetric and transition into a symmetric agonist bound state.

Movie 5.3 Tripartite salt bridges undergo larger displacements during the apo to agonist bound transition in α vs non-α subunits. Side (top) and top down (bottom) views of the tripartite salt bridges transitioning from apo to agonist bound conformations are shown for each subunit. The tripartite salt bridges in the two α subunits undergo large displacements relative to the TMD during the transition while the non-α subunits do not.

Movie 5.4 Comparison of the Val – Pro motion in the *Torpedo* α subunit with other heteromeric and homomeric pLGICs. Apo to active morphs of each subunit were created once each subunit was aligned by their M2-M3 loop to view the relative motion of the Val46 equivalent. The α_γ subunit of the *Torpedo* nAChR is shown in orange and motion played in concert with three heteromeric pLGIC subunits (from left to right: the *Torpedo* nAChR β subunit, the principal agonist binding $GABA_AR$ β2 subunit, and the complementary $GABA_AR$ α1 subunit) and three homomeric pLGIC subunits (from left to right: the α7 nAChR, the $5HT_{3A}R$, and the α1 GlyR).

Movie 5.5 Top view of the Val – Pro motion in the various pLGICs. The same morphs depicted in Movie 4 are shown from a top view looking from the ECD down toward the M2-M3 loop. A principle (left) and non-principle (right) agonist binding subunit from the heteromeric *Torpedo* nAChR (top) and synaptic $GABA_AR$ (bottom) are shown in the top box. Homomeric α7 nAChR (left) and α1 GlyR (right) subunits are shown in the bottom box.

Movie 6.1 Movements of the ECD transitioning through the mono-liganded state. Motions of the ECD relative to the TMD are shown as the nAChR transitions from the un-liganded state, through the mono-liganded state to the di-liganded state. The morph is shown from a top shown view with the α subunits colored yellow, the β subunit coloured pink, the γ subunit coloured green and the δ subunit coloured blue.

Movie 6.2 Movements of the TMD/pore transitioning through the mono-liganded state. Motions of the TMD relative to the ECD are shown as the nAChR transitions from the un-

liganded state, through the mono-liganded state to the di-liganded state. The morph is shown from a top shown view with the α subunits colored yellow, the β subunit coloured pink, the γ subunit coloured green and the δ subunit coloured blue. Residues forming the hydrophobic gate (L9' and V13') are shown as tan sticks.

Movie 6.3 Motions at the principal/complementary subunit interfaces as the nAChR transitions through the mono-liganded state. Motions of the principal and complementary subunits relative to the rest of the nAChR are shown as the nAChR transitions from the un-liganded state, through the mono-liganded state to the di-liganded state. Two orthogonal views are shown for the α_γ/γ subunits (top) and the α_δ/δ subunits (bottom). The view from the left is looking at the back of the subunits toward the pore while the view on the right in rotated ~90º counterclockwise with the majority of the α subunit ECD removed for clarity. Modelled ACh in the di-liganded state are shown as red sticks.

List of Abbreviations

[^{125}I]-TID	3-trifluoromethyl-3-(*m*-[^{125}I]iodophenyl)diazirine
5-HT	5-hydroxytryptamine (serotonin)
5-HT$_3$R	Serotonin receptor
α-BTX	α-bungarotoxin
ACh	Acetylcholine
AChBP	Acetylcholine-binding protein
Ala	Alanine
AMPA	α-amino-3-hydroxy-5-methyl-4-isoxazolepropionic acid
ANOVA	Analysis of variance
Asn	Asparagine
Asp	Aspartate
ATP	Adenosine triphosphate
Arg	Arginine
C. *elegans*	Caenorhabditis elegans
Ca^{2+}	Calcium ion
cAMP	Cyclic adenosine monophosphate
Carb	Carmbamylcholine
Card	Cardiolipin
cDNA	Coding DNA
CHARMM	Chemistry at Harvard macromolecular mechanics
CHS	Cholesteryl hemisuccinate
Cl^-	Chloride ion
CMS	Congenital Myasthenic Syndrome
CNS	Central nervous system
COM	Center of mass
CRAC	Cholesterol recognition amino acid consensus
cRNA	Coding RNA
Cryo-EM	Cryo-electron microscopy
CryoSPARC	Cryo-EM single-particle *ab initio* reconstruction and classification
Cys	Cysteine
DAG	Diacylglycerol
DDM	N-dodecyl-β-D-maltoside
DeCLIC	*Desulfofustis* glycolicus Ca^{2+} activated ligand-gated ion channel
DF	Degrees of freedom
DHA	Docosahexaenoic acid
DNA	Deoxyribonucleic acid
DTT	Dithiothreitol
E. *coli*	Escherichia coli
EC_{50}	Half maximal effective concentration
ECD	Extracellular domain
ELIC	*Erwinia* ligand-gated ion channel
ER	Endoplasmic reticulum
ERAD	ER-associated degradation
EthBr	Ethidium bromide

FLIPR	Fluorescent imaging plate reader
FTIR	Fortier transform infrared spectroscopy
GABA	γ-aminobutyric acid
$GABA_AR$	GABA type A receptor
GDP	Guanosine diphosphate
GIRK	G-protein gated KIR
GLIC	*Gloeobacter* ligand-gated ion channel
Gln	Glutamine
Glu	Glutimate
GluCl	Glutimate-gated chloride channel
Gly	Glycine
GlyR	Glycine receptor
GPCR	G-protein coupled receptor
GROMACS	Groningen machine for chemical simulations
GTP	Guanosine triphosphate
GUI	Guided user interface
GUV	Giant unilamellar vesicle
HCN	Hyperpolarization-activated cyclic nucleotide-gated
HEK	Human embryotic kidney
HEPES	4-(2-hydroxyethyl)-1-piperazineethanesulfonic acid
His	Histidine
IC50	Concentration at half-maximal inhibition
ICD	Intracellular domain
Ile	Isoleucine
IPTG	Isopropyl β-d-thiogalactopyranoside
K+	Potassium ion
K_2P	two pore domain K^+
Kir	Inward rectifying K^+
KCNE	K^+ channel subfamily E member
K_v	Volatge-gate K^+
LB	Lysogeny broth
Leu	Leucine
LGIC	Ligand-gated ion channel
LINCS	Linear constraint solver
Lys	Lysine
MS	Mechanosensitive
Met	Methionine
mRNA	Messenger RNA
MS222	3-aminobenzoic acid ethyl ester methanesulfonate salt
MscL	Bacterial large conductance MS channel
mscS	Bacterial small conductance MS channel
MSP2N2	Membrane scaffold protein 2N2
mV	Millivolt
Na^+	Sodium ion
NACHO	Nicotinic cholinergic receptor regulator
nAChR	Nicotinic acetylcholine receptor

NE	No expression
NMDA	N-methyl-D-aspartate
NMJ	Neuromuscular junction
NMR	Nuclear magnetic resonance
NR	No response
ns	Nanosecond
NTD	N-terminal domain
PA	Phosphatidic acid
PAM	Positive allosteric modulator
PBS	Phosphate buffered saline
PC	Phosphatidylcholine
PCR	Polymerase chain reaction
PE	Phosphatidylethanolamine
PG	Phosphatidylglycerol
pH	Potential of hydrogen
Phe	Phenylalanine
PI	Phosphatidylinositol
PIP_2	Phosphatidylinositol-4,5-bisphosphate
pLGIC	Pentameric ligand-gated ion channel
PME	Particle mesh Ewald
PMSG	Pregnant mare serum gonadotropin
PNS	Peripheral nervous system
POPC	1-palmitoyl-2-oleoyl-sn-glycero-3-phosphocholine
POPE	1-palmitoyl-2-oleoyl-sn-glycero-3-phosphoethanolamine
Pro	Proline
PRB	Phosphate ringer buffer
PS	Phosphatidylserine
ps	Picosecond
PUFA	Polyunsaturated fatty acid
RELION	Regularized likelihood optimization
RIC-3	Resistance to Inhibitors of Cholinesterase 3
RNA	Ribonucleic acid
RTK	Receptor tyrosine kinase
SASA	Solvent accessible surface area
SE	Standard error
Ser	Serine
SH	Shimodaira-Hasegawa
SNR	Signal-to-noise ration
SOB	Super optimal broth
SUR	Sulfonylurea receptor
TEVC	Two-electrode voltage clamp
Thr	Threonine
TM	Transmembrane
TMD	Transmembrane domain
TPC	Two-pore channel
Trp	Tryptophan

TRP	Transient receptor potential
TSE	Transition state ensemble
Tyr	Tyrosine
Val	Valine
VGL	Voltage-gated like
WT	Wild-type
ZAC	Zinc-activated channel

Chapter 1. Introduction

1.1 General introduction

1.1.1 Cell membranes and the proteins tasked with their selective permeability

Cells are encapsulated by a selectively permeable membranes that compartmentalizes the materials necessary for life away from the extracellular environment. Biological membranes generally exist as bilayers of lipids. The most common lipids are glycerophospholipids, which contain two fatty acyl chains attached to a glycerol backbone and a phosphate derivatized head group (Fig. 1.1). The chemical nature and shape of these lipids cause them to spontaneously assemble into bilayers in aqueous solution with their hydrophobic tails aggregating together and their polar head groups contacting the surrounding aqueous environment. The hydrophobic interior of these membranes creates a sizable energy barrier to the crossing of polar molecules making them essentially impermeable to most soluble compounds, including small inorganic ions. This barrier is critical to life, not only for protecting cells from unwanted compounds, but also for localizing and compartmentalizing cellular machinery. This barrier also provides a challenge to the cells, however, which require the specific import and export of soluble molecules for their survival. Cells overcome this challenge by employing membrane proteins, which are tasked not only with the selective uptake and output of polar molecules, but which also play a central role in higher order processes like cell-cell communication, adenosine triphosphate (ATP) synthesis, and environment-sensing, etc. The critical roles played by these proteins, along with their ability to communicate extracellular signals into intracellular responses, have made them important drug targets with ~70% of all approved small- molecule drugs to date targeting integral membrane proteins, despite membrane proteins making up only a quarter of the genes in the human genome (Uhlén et al., 2015; Santos et al., 2017).

Figure 1.1 General lipid structure and bilayer composition

The general structure of a glycerophospholipid is shown in panel A with the two fatty acyl chains denoted R1 and R2 and the headgroup denoted X. Panel B shows different types of phospholipid headgroups commonly found in cell membranes. Panel C is a cartoon representation of membrane proteins immersed within a phospholipid bilayer. Biological membranes demonstrate heterogeneous physical properties such as asymmetric distribution of charges (denoted by negatively charged red colour head groups), membrane thickness/order (influenced by cholesterol content, which is shown as yellow ellipsoids), etc. Chemical structures were created with ChemDraw. This figure, and all the remaining figures in this thesis, were created using Affinity Designer.

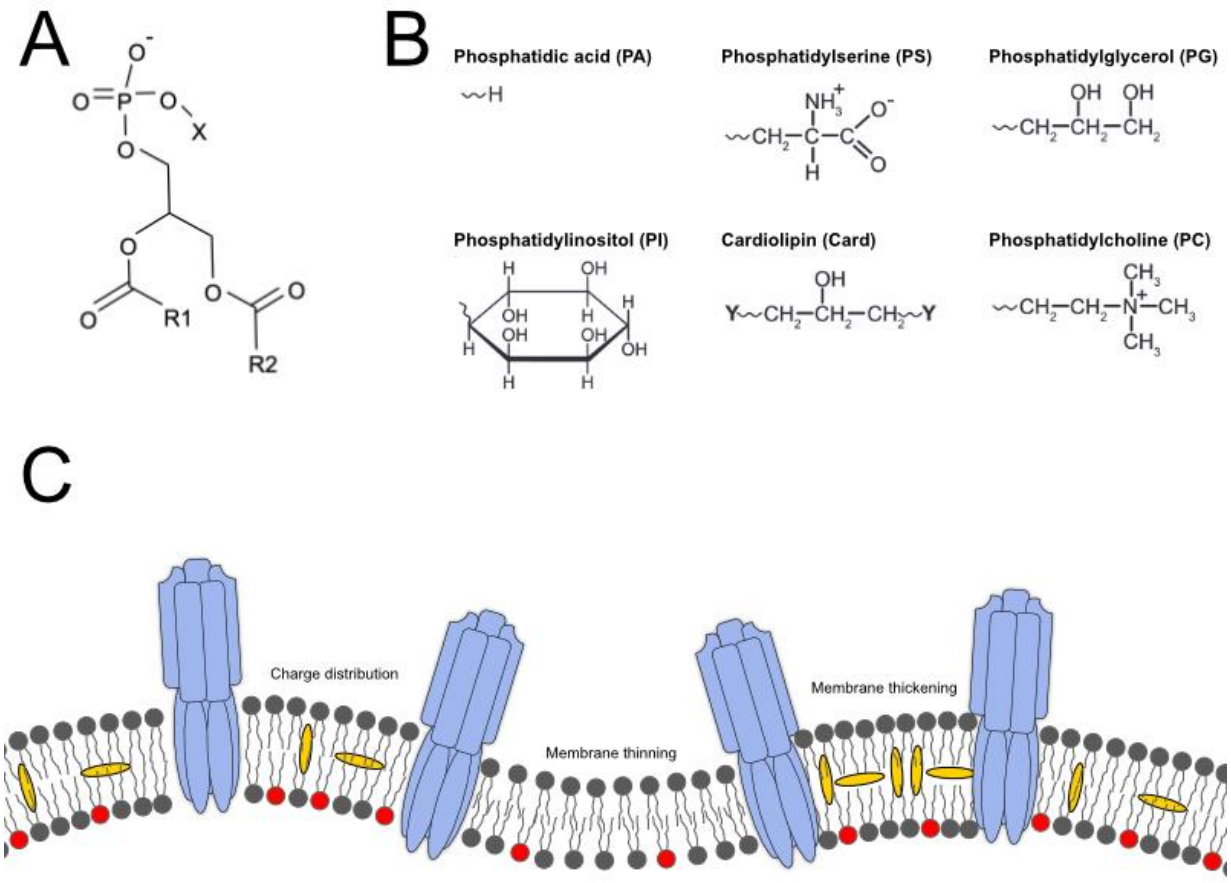
A
B
Phosphatidic acid (PA)
Phosphatidylserine (PS)
Phosphatidylglycerol (PG)
Phosphatidylinositol (PI)
Cardiolipin (Card)
Phosphatidylcholine (PC)
C
Charge distribution
Membrane thinning
Membrane thickening

Transmembrane proteins, integral membrane proteins that have at least one segment that traverses the membrane, are the primary molecules used by cells to transduce signals across the membrane. Transporters and ion channels act as catalysts for the translocation of substrates and ions across the membrane. Transporters undergo conformational changes to import/export molecules from the cell while ion channels form pore that facilitate the diffusion of ions down their electrochemical gradients. Other transmembrane proteins, named receptors, transduce signals across membranes by binding activating ligands on one side of the membrane and causing an effect on the other side of the membrane. Many types of receptors are found in humans, which include but are not limited to, receptor tyrosine kinases (RTKs) (Hubbard and Miller, 2007), G-coupled protein receptors (GPCRs) (Wootten et al., 2018), and ligand-gated ion-channels (LGICs) (Lemoine et al., 2012). Each of these receptor types communicate their signals through unique mechanisms at different time scales.

In the case of RTKs, ligand binding outside the cell induces the formation of RTK dimers. Upon dimerization, the cytoplasmic kinase domain becomes functional triggering the phosphorylation of Tyr residues on intracellular proteins to initiate signalling cascades. The covalent modifications and downstream processing of these receptors make these processes relatively slow and thus long term, occurring on the minutes to hours timescale where they are useful for process like proliferation, gene expression, and differentiation.

GPCRs also function through the binding of extracellular ligands but instead propagate the signal by undergoing a conformational change that affects the binding of the GPCR with intracellular trimeric G-proteins. This conformational change typically facilitates the exchange of the G-protein bound GDP with GTP to liberate the α subunit. These free α subunit can then bind to different targets to regulate various downstream signalling processes. GPCRs are the

most prevalent receptors in humans and are central to many physiological processes such as vision, taste, smell, behavior, cell sensing, growth, etc. Though more rapid than RTK signalling, the enzymatic nature of signal transduction through GPCRs facilitates signal propagation over the seconds to minutes timescale.

Finally, instead of inducing their signal enzymatically, LGICs do so electrically. Upon ligand binding, a LGIC opens a pore across the membrane allowing ions to rapidly diffuse down its electrochemical gradients into the cell, resulting in a change in the electrostatic potential across the membrane. The translocation of ions through these receptors approaches the diffusion limit allowing them to transduce signals on the ps to ms timescale. Many processes in human physiology require such rapid communication, the most notable being neurotransmission.

1.1.2 Neurotransmission

The human brain is composed of billions of nerve cells or neurons that are organised into vast networks that underly the brain's ability to perform complex neurological processes. Neurons are generally divided into four sections: the dendrites, soma, axon, and axon terminals (Fig. 1.2a). Dendrites receive information from other cells or neurons pass this information to the soma, the cell body that contains the nucleus and other traditional cell components. The soma transmits the received information to the axon, which then transmits the signal to the axon terminals for output to other cells. Neurons communicate with each other at synapses - the connections between the axon terminals of one neuron and the dendrites of another neuron (Fig. 1.2b). Synaptic communication is initiated by the release of chemical neurotransmitters from the axon terminals of a presynaptic neuron into the synaptic cleft. These neurotransmitters then bind to receptors on the dendrites of the post-synaptic neuron to initiate a response. Neurons can also

Figure 1.2 General structure of a neuron and simplified depiction of fast synaptic communication through LGICs

Panel A shows the general structure of a neuron with the main components labelled. A synapse is shown in the bottom right and enlarged in panel B. A simplified overview of synaptic transmission is described in panel B.

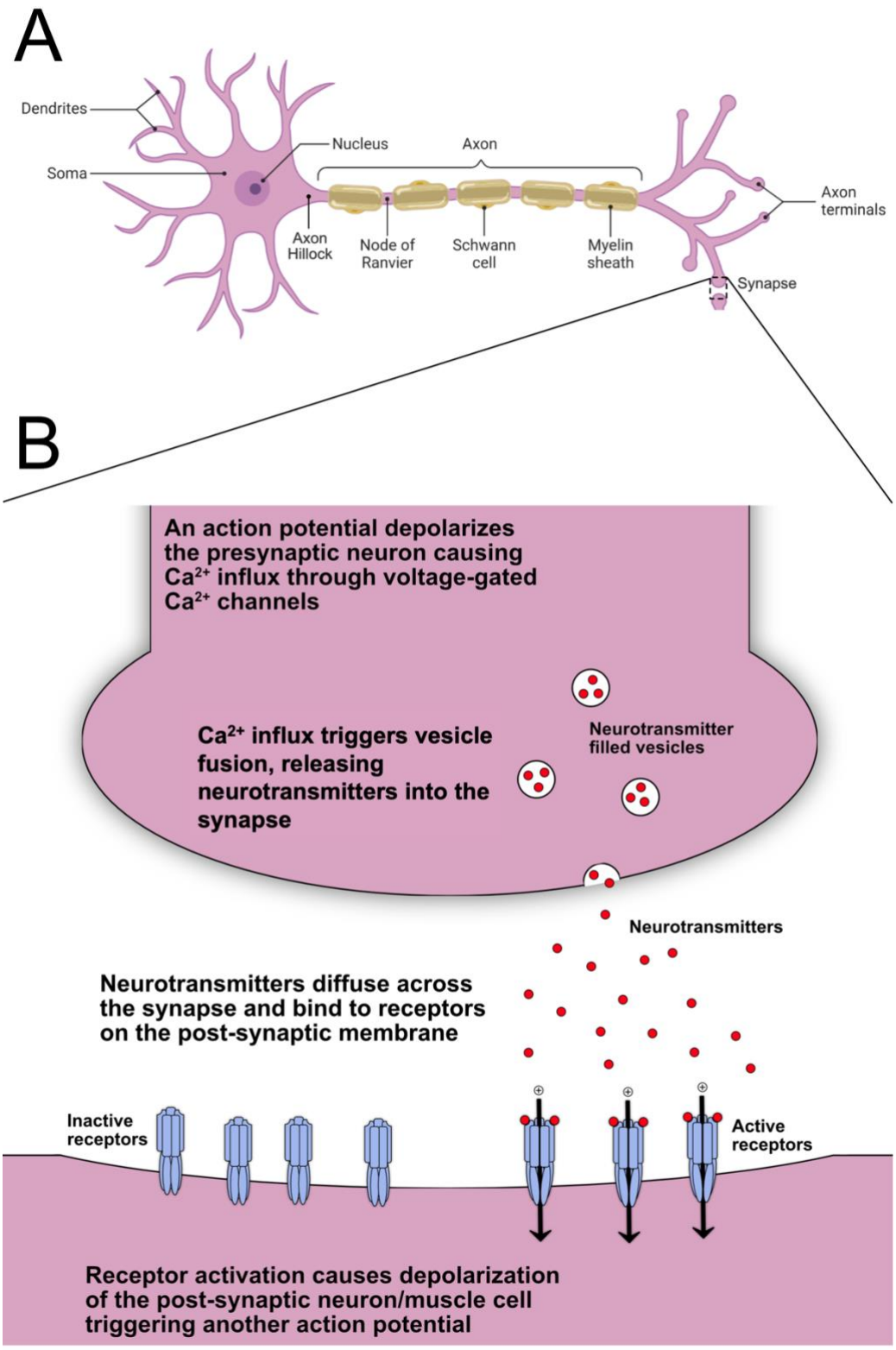
A
Dendrites
Soma
Nucleus
Axon
Axon terminals
Axon Hillock
Node of Ranvier
Schwann cell
Myelin sheath
Synapse
B
An action potential depolarizes the presynaptic neuron causing Ca^{2+} influx through voltage-gated Ca^{2+} channels
Ca^{2+} influx triggers vesicle fusion, releasing neurotransmitters into the synapse
Neurotransmitter filled vesicles
Neurotransmitters
Neurotransmitters diffuse across the synapse and bind to receptors on the post-synaptic membrane
Inactive receptors
Active receptors
Receptor activation causes depolarization of the post-synaptic neuron/muscle cell triggering another action potential

signal to other cell types such as muscle cells, immune cells, enteroendocrine cells, etc.

Information is transmitted through neurons by changes in the membrane potential. At rest, the concentrations of chloride and potassium ions are much higher inside the neuron whereas the concentration of sodium ions is much higher outside the cell, with this distribution of ions on either side of the membrane resulting in a transmembrane potential of approximately -70 mV. Excitatory neurotransmitters bind to LGICs that are selective for cations thus allowing sodium ions to flow down their electrochemical gradient into the cell leading to a depolarization of the post-synaptic membrane. This depolarization diffuses through the soma to the beginning of the axon, termed the axon hillock. If the depolarization reaching the axon hillock crosses a threshold of roughly -55 mV, voltage-gated sodium channels open to initiate an action potential that is rapidly propagated down the axon with the help of an insulating myelin sheath. Once the action potential reaches the axon terminals, voltage-gated calcium channels open to allow calcium to flow into the cell. The rise in intracellular calcium triggers the fusion of neurotransmitter filled vesicles to the presynaptic membrane, releasing the neurotransmitters into the synapse to initiate the next signalling event. The neuron then re-establishes its resting potential by opening voltage-gated potassium channels that allow potassium ions to flow out of the cell. Sodium potassium ATPase transporters then use cellular energy in the form of ATP to pump sodium ions back out of the cell, and potassium ions back into the cell, to re-establish the resting ion concentrations of the neuron for the next firing event.

Neurons receive inputs at synapses that are specialized for different signalling events depending on the types of neurotransmitters utilized for signalling. In the case of fast-synaptic communication, the receptors that are activated by neurotransmitters are LGICs. As noted, neurotransmitters that bind to cation selective LGICs are considered excitatory neurotransmitters

as their activation leads to depolarization (increase the membrane potential towards positive values). Most of the excitatory signalling in the human brain occurs through glutaminergic neurons, which release glutamate that binds to ionotropic tetrameric glutamate receptors on the post-synaptic membrane to mediate neuronal signalling. In serotoninergic and cholinergic neurons, excitatory signalling is mediated by the pentameric ligand-gated ion channels (pLGICs) gated by serotonin (5-hydroxytryptamine or 5-HT) and acetylcholine (ACh), respectively. The receptors that mediate fast serotonin signalling are referred to as 5-HT type 3 receptors (5-HT_3Rs) and are best known for their roles in mediating communications between the nervous system and the gut. The receptors mediating fast ACh signalling are referred to as nicotinic ACh receptors (nAChRs) and play a role in both neuronal and neuromuscular signalling. A third type of excitatory pLGIC that is activated by divalent cations and pH, zinc-activated channels (ZACs), also exists but is poorly characterized (Madjroh et al., 2021).

In contrast, inhibitory neurotransmitters bind anion selective pLGICs that hyperpolarize the post-synaptic neuron (decrease the membrane potential towards more negative values) thus decreasing the probability of neuronal firing. Inhibitory signalling in the brain is mediated primarily by pLGICs that respond to the neurotransmitters γ-aminobutyric acid (GABA) and glycine, termed the GABA type A receptors ($GABA_A$Rs) and glycine receptors (GlyRs), respectively.

As discussed in detail below, each of these LGIC families is further subdivided into subtypes, with each subtype formed from a different combination of the various genetically encoded subunits and each located in different regions of the nervous system (Jaiteh et al., 2016). With such diversity, neurons can employ many different LGICs to perform specific tasks, shaping neurotransmission and ultimately neurological function. This diversity also provides an

opportunity to selectively modulate channel activity in a specified way to alter neurological activity, making these channels exciting drug targets for almost all neurological disease (Bianchi and Botzolakis, 2010; Manetti et al., 2018). To capitalize on this opportunity however, there must be a detailed understanding of LGICs function.

1.2 Pentameric ligand-gated ion channels (pLGICs)

1.2.1 The pLGIC superfamily

pLGICs are found in all organisms, even predating eukaryotes and the existence of the nervous systems (Fig. 1.3). Bacterial pLGICs were first cloned almost 20 years ago, and two prokaryotic pLGICs, ELIC and GLIC, have since been used extensively as models to study pLGIC structure and function (Tasneem et al., 2004). Many more prokaryotic pLGICs have been identified, however, revealing a diverse structural and functional ensemble of pLGICs that play roles in processes like quorum sensing and cell motility (Hu et al., 2020). Non-vertebrates with fewer neurons in their nervous systems, like C. *elegans*, also have pLGICs that are not found in humans. The first anion selective pLGIC structure solved was that of the glutamate-gated chloride channel (GluCl) from C. *elegans* (Hibbs and Gouaux, 2011). Many other pLGICs in nematodes have been recently identified (Morud et al., 2021; Araujo et al., 2022). While pLGIC subtypes found in humans are those that have received the most attention, these prokaryotic/non-vertebrate pLGICs are under investigation as targets for anthelmintics and pesticides (Puinean et al., 2013; Beech and Neveu, 2015; Korona et al., 2022) and have been linked to the environmental sensing of octopus and squid (Allard et al., 2023; Kang et al., 2023).

As noted above, there are four main types of pLGICs in humans: nAChRs, 5-HT_3Rs, GlyRs, and $GABA_A$Rs. The muscle-type nAChR was the first receptor identified and serves as

Figure 1.3 Phylogenetic tree of pLGICs

Figure adapted from (Jaiteh et al., 2016). Eukaryotic pLGICs are on the left and bottom branches of the tree while prokaryotic pLGICs or shown on the right. Anion selective pLGICs in humans are amongst the red coloured branches while cation selective pLGICs in humans are amongst the dark blue branches. Circles indicate SH support above 90%.

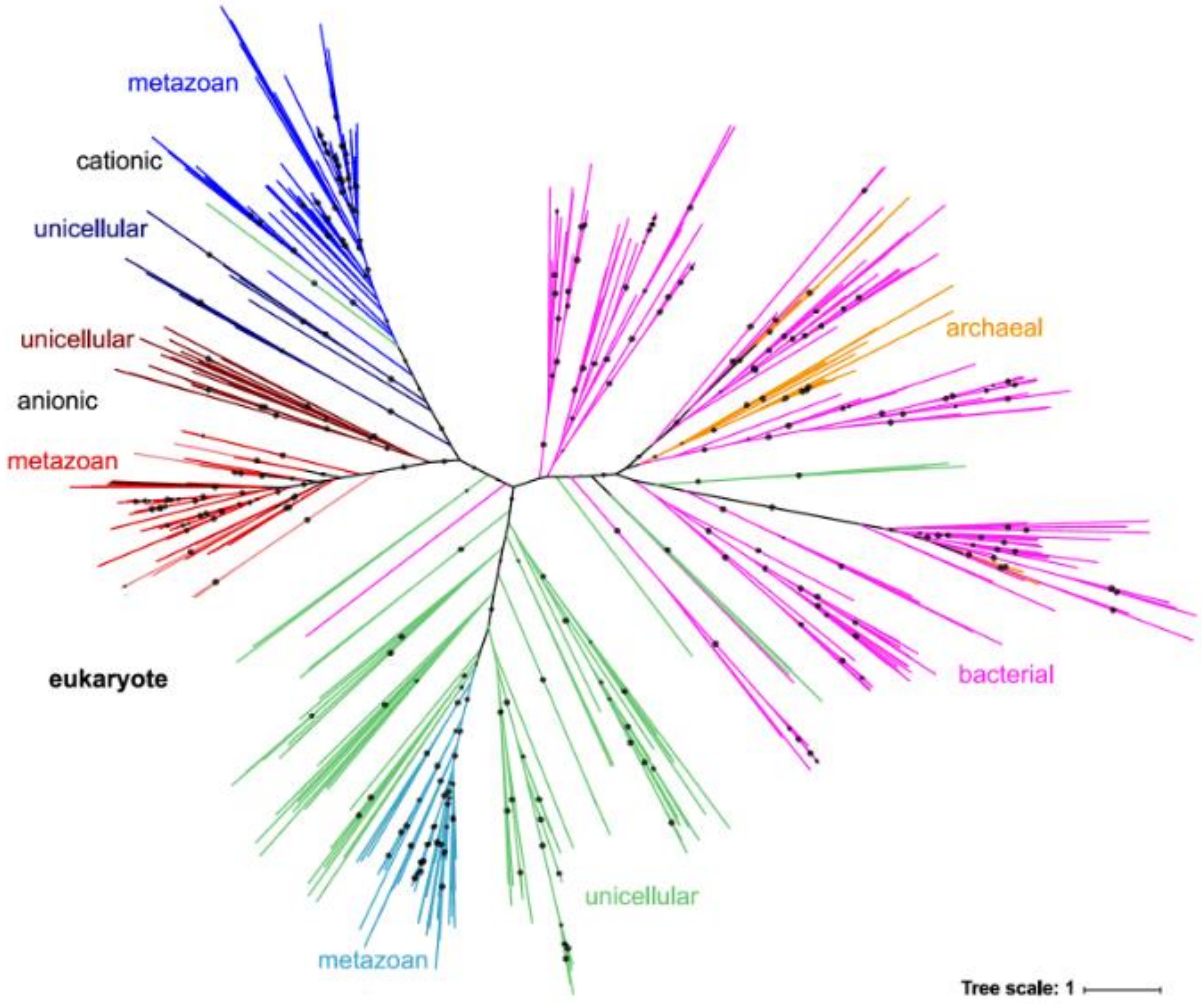
metazoan
cationic
unicellular
unicellular
anionic
metazoan
eukaryote
archaeal
bacterial
unicellular
metazoan
Tree scale: 1

the prototype for the pLGIC family (Changeux, 2012, 2020). To date, 16 nAChR subunits have been identified in humans (Albuquerque et al., 2009), including 9 α subunits (α1-α7, α9, and α10), four β subunits (β1-β4), and one δ, γ, and ε subunit. The nAChR subtype with the most strict stoichiometry is the $(\alpha1)_2\beta1\delta(\gamma/\varepsilon)$ muscle-type nAChR, which is found exclusively in post-synaptic membranes of skeletal muscle cells where it mediates muscle contraction in response to ACh binding (Bouzat and Mukhtasimova, 2018). Neonatal nAChRs contain a γ subunit that is replaced by the ε subunit in the adult form of the muscle nAChR (Hesselmans et al., 1993).

The remaining nAChR subunits are expressed almost exclusively in the brain where they assemble more promiscuously into a multitude of combinations, the most abundant of which, the α4β2, α3β4, and α7 nAChRs, will be discussed here. The α4β2 nAChR makes up ~90% of the high affinity nicotine binding sites in the brain, localizing in cholinergic synapses of the hippocampus, cerebellum, and forebrain among other brain regions (Zoli et al., 2015). These two subunits can form pentamers with the stoichiometries of $(\alpha4)_3(\beta2)_2$ and $(\alpha4)_2(\beta2)_3$ that have low and high affinity for nicotine, respectively. These receptors are typically credited with the precognitive effects of nicotine such as increased attention and memory (Lawrence et al., 2002).

The α3β4 nAChR is commonly referred to as the ganglionic nAChR due to its expression in peripheral ganglionic neurons but can be found elsewhere in the peripheral and central nervous systems. Cholinergic signals from the CNS that innervate autonomic ganglia signal through these receptors to regulate sympathetic and parasympathetic nervous systems (Wehrwein et al., 2016). The α3β4 nAChR also modulates the mesolimbic dopamine system through its expression in the habenulo-interpenducular tract associating it with several nicotine associated effects including reward, dependence, and withdrawal (Wittenberg et al., 2020).

Finally, the α7 nAChR displays unusual features in that it forms functional homopentamers, it desensitizes much faster than other nAChRs, and is more permeable to Ca^{2+} than other nAChRs. These unique properties make the α7 nAChR well suited for neuromodulation, where the rapid influx of Ca^{2+} into presynaptic neurons or interneurons initiates neurotransmitter release (Yakel, 2013). Interestingly, the α7 nAChR is expressed primarily in areas of the brain associated with memory and learning, making it the target of many therapeutics for the treatment of neurological diseases such as Parkinson's Disease (Caton et al., 2020), Alzheimer's Disease (Bertrand and Terry, 2018; Hoskin et al., 2019), and schizophrenia (Wallace and Bertrand, 2015). The α7, along with the α9 and α10, form homopentamers but can also assemble with various other nAChR subunits although the exact stoichiometries and their localization remains an active area of investigation (Elgoyhen, 2023).

5-HT_3Rs are best known for their specialized roles in gut-brain circuitry and are targeted by the well-known setron class of drugs that are used to treat irritable bowel syndrome and chemotherapy-induced vomiting (Davies, 2011). While 90% of 5-HT_3Rs are found in the gut, they also play neuromodulatory roles in the brain by opening on presynaptic glutaminergic neurons to modulate excitatory signalling and can be found in both the brainstem and hippocampus. There are five 5-HT_3R subunits, A, B, C, D, and E. The 5HT_3R A subunit is the most common and forms functional homopentamers while the remaining subunits must assemble as heteropentamers with A subunits, albeit with an unknown stoichiometry (Lummis, 2012; Miles et al., 2013). The 5-HT_{3A}R homopentamer has a relatively high permeability to calcium and has a very low unitary conductance, making them best suited for presynaptic modulation (Gill et al., 1995). 5-HT_{3AB}R heteropentamers on the other hand have a much higher unitary conductance and are not as permeable to Ca^{2+} making them better suited for postsynaptic

transmission (Hussy et al., 1994). The C, D, and E subunits are expressed in peripheral tissues where they form functional heteropentamers with the 5-HT_3R A subunit, although little is known about their physiological roles due to the lack of subunit specific antibodies (Gibbs and Chakrapani, 2021).

Fast inhibitory signalling in the human brain is primarily mediated through the anion selective $GABA_A$Rs (Fritschy and Panzanelli, 2014). There are a total of 19 $GABA_A$R subunits: six α subunits (α1-α6), three β subunits (β1-β3), three γ subunits (γ1-γ3), three ρ subunits (ρ1-ρ3) and ε, δ, π, and Θ subunits. Synaptic $GABA_A$Rs generally assemble as heteropentamers of two α subunits (α1-α3), two β subunits, and one γ2 subunit (Solomon et al., 2019). These receptors are the target of the benzodiazepine and barbiturate classes of drugs, which are used clinically to treat neurological diseases like anxiety, insomnia, and neuropathic pain. Many other $GABA_A$Rs exist extrasynaptically where they mediate low-amplitude tonic inhibitory currents when they bind ambient GABA in the plasma (Ghit et al., 2021). These receptors are instead primarily composed of α4-α6 subunits along with the δ subunit, although recent structural studies suggest many more assemblies are possible (Sente et al., 2022). The ρ subunits assemble as homopentamers and were originally classified as $GABA_C$Rs based on their low sequence homology with the other $GABA_A$R subunits (Naffaa et al., 2017). GABA is 10- to 100-fold more potent when activating $GABA_A$-ρ receptors than other $GABA_A$R subtypes and accompanying this enhanced potency are much slower rates of activation and desensitization. These properties make these channels ideal mediating tonic currents in the retina that are required for image processing in the brain. Finally, mutations to all genes encoding $GABA_A$R subunits can lead to genetic forms of epilepsy by causing hyperexcitability of the thalamocortical network (Hernandez and Macdonald, 2019). This hints that distribution of different $GABA_A$R

subtypes may be more complex than our current understanding that derives primarily from coimmunoprecipitation and mRNA screening experiments.

The final member of the pLGIC superfamily are the GlyRs. GlyRs are abundantly expressed throughout the CNS, the brainstem, and spinal cord where they regulate processes like muscle tone, motor coordination, sensory processing, respiratory rhythms, and pain (Burgos et al., 2016). There are four GlyR α subunits (α1-α4) and one β subunit, although one of the α subunits (α4) is a pseudogene in humans. GlyRs assemble as either homopentamers of α subunits or as heteropentamers of α and β subunits. The α1 subunit is expressed almost exclusively in the CNS while the α2 subunit is expressed at high levels in the brainstem and spinal cord (Burgos et al., 2016). The inclusion of the β subunit into α subunit containing pentamers not only effects how the channel is modulated by small molecule binding, but also dictates post-synaptic clustering of receptors via interactions with the intracellular clustering protein gephyrin. When glycinergic signalling is disturbed in humans, there are several health effects resulting from hyperexcitability. Mutations to genes that encode GlyR subunits cause hyperekplexia, a rare, non-epileptic, paroxysmal neurogenic disorder often referred to as human startle syndrome (Lemoine et al., 2012). In certain instances of chronic pain there is a disruption of glycinergic signalling in the spinal dorsal horn, which prevents the inhibition of pain signals to the brain (Zeilhofer et al., 2018).

1.2.2 pLGIC expression, assembly, cell surface trafficking, and localization

Various lines of evidence suggest that pLGIC subunits from the same family can assemble promiscuously in heterologous expression systems to form channels with seemingly infinite stoichiometries, thus raising the question as to how different cells in the human body

control pLGIC subtype assembly. The first way in which cells control pLGIC subunit assembly is by differential regulation of gene expression. In some cell types, such as skeletal muscle cells, the only pLGIC genes that are transcribed are those of the muscle type nAChR. In contrast, many regions of the brain transcribe many pLGIC subunits that have the potential to form diverse stoichiometries. This is exemplified by $GABA_AR$s where a combination of mRNA levels and structural compatibility have been used to predict that up to 62,847 potential receptor subtypes are possibly expressed in the brain (Sente et al., 2022). Despite the large number of potential subtypes, however, only three different α1 containing $GABA_AR$s subtypes were abundant enough to be directly purified from rat brains (Sun et al., 2023). While there may be low abundance species that avoided detection, it's clear that not all subunits that are co-expressed assemble in our brains suggesting that other factors regulate assembly and cell surface trafficking.

Following gene transcription, mRNAs encoding pLGIC subunits are translated by ribosomes on the endoplasmic reticulum (ER). During translation the subunits must undergo proper membrane insertion, maturation (i.e post-translational modifications, signal sequence cleavage, etc.), initial folding and oligomerization. While a complete understanding of these processes is lacking for most pLGICs, studies on the muscle nAChR highlight their stringency. For the muscle nAChR, assembly is both slow and inefficient, with a $t_{1/2}$ longer than 90 minutes and only ~30% of synthesized α1 subunits assembled into pentamers (Merlie and Lindstrom, 1983). The inefficiency of nAChR assembly is a product of the requirement for nAChR fidelity, that is to ensure that only fully formed, mature, nAChRs reach the cell surface to exert an ACh-induced response. To achieve this, a series of quality control systems are utilized by the cell to prevent the expression of immature nAChRs. The nAChR subunits begin by oligomerizing with

each other on the ER (Blount et al., 1990; Wanamaker et al., 2003). There is still ambiguity as to the sequence of oligomerization events that occur during receptor assembly, but we do know that there are specific ER retention motifs within certain pLGIC subunits that are only masked upon proper assembly (Wang et al., 2002; Bracamontes et al., 2014; Rudell et al., 2020; Yuan et al., 2022). This quality control step ensures that only fully formed pentamers exit the ER to the cell surface. Any subunits that are not assembled or are misfolded are targeted by the ER-associated degradation (ERAD) pathway, which utilizes ubiquitination of these subunits to target their degradation in the cytosol (Richard et al., 2013).

Once properly assembled, nAChR pentamers are trafficked from the ER to the golgi and eventually to the plasma membrane with the assistance of various chaperones. These chaperones differ depending on the cell type, and the pLGIC being trafficked, but there are several well characterized examples. The RIC-3 chaperone has little selectivity for the pLGIC, but is integral for trafficking of the α7 nAChR and the 5-HT_3R (Pirayesh et al., 2020; Loring, 2022; Do and Jansen, 2023). The α7 nAChR also needs the chaperone NACHO for expression in neurons (Gu et al., 2016). The cytoplasmic 14-3-3 chaperone is known to assist in the trafficking of the α4β2 nAChR but is selective for the stoichiometry that has a low affinity for nicotine ($(\alpha4)_3(\beta2)_2$) (Colombo et al., 2013). Nicotine also works as a chaperone for the α4β2 nAChR but instead acts by promoting assembly of the receptor on the ER, effectively increasing the trafficking of the high affinity nicotine stoichiometry ($(\alpha4)_3(\beta2)_2$) to the cell surface (Knox et al., 2022). It has also been shown that polyamines, which typically block the pore of nAChRs, enhance expression of both α7 and α4β2 nAChRs opening the possibility that many traditional pLGIC binders may influence assembly/trafficking (Dhara et al., 2020). Many other examples of chaperones are present in the literature and many others likely remain undiscovered. By expressing different

chaperones, cells can regulate not only the subtypes that are trafficked to the cell surface, but also the proportions and stoichiometries of these subtypes to adequately meet the cells requirements.

Once trafficked to the cell surface, pLGICs localize to specific regions of the plasma membrane based on the role they play within the cell. The most common example of this is on the post-synaptic membrane. The distance a neurotransmitter must diffuse across the synaptic cleft alters the time course of synaptic communication, which is typically meant to be swift and efficient. Cells have evolved to minimize the distance and variability by which this diffusion takes place by clustering pLGICs in high density adjacent to the presynaptic neuron where neurotransmitter is released (Kneussel and Betz, 2000; Zhu et al., 2006; Li et al., 2007; Barberis, 2020). This clustering is achieved by the association of pLGICs and various intracellular scaffolding proteins such as rapsyn, in the case of the muscle-type nAChR, or gephyrin in the case β subunit containing GlyRs. Some evidence also links the localization of pLGICs to lipid microdomains that are thought to assemble in synapses, namely lipid rafts (Eisensamer et al., 2005; Stetzkowski-Marden et al., 2006; Zhu et al., 2006; Allen et al., 2007; Powell et al., 2016). Together, clustering through intracellular scaffold proteins and lipid microdomain association increase the density of pLGICs in a manner that increases the efficiency of signalling through these channels. This final regulation step is critical in ensuring that the receptors that are trafficked to the cell surface are utilized effectively to perform their intended roles for the cell.

1.2.3 pLGIC structural biology

The structural biology of pLGICs began with the work of Nigel Unwin, who used electron microscopy to unveil structural information about the prototypical pLGIC, the muscle

nAChR from *Torpedo* (see below). Despite decades of efforts from many groups, the *Torpedo* nAChR was never able to form crystals that diffracted to high resolution (Hertling-Jaweed et al., 1988; Paas et al., 2003). This made electron microscopy the only available tool for obtaining high resolution information about the *Torpedo* nAChR. With the technique still in its infancy, Unwin was on the cutting edge of method development. His group discovered that native membranes obtained from *Torpedo* electroplaque tissue, which are packed densely with nAChRs, naturally form 2D helical crystalline tubes and in 1987 captured 30 Å resolution images using negative staining (Kubalek et al., 1987). Throughout the 1990's Unwin's group continued to image these tubular membranes at increasing resolutions culminating with a ~4 Å resolution structure of the extracellular domain (ECD) and the transmembrane domain (TMD) that was solved in 2003 (Unwin, 1995; Miyazawa et al., 1999, 2003). Concurrently, crystal structures of the acetylcholine binding proteins (AChBPs), water soluble homologs of the nAChR ECD, were solved to much higher resolution (Brejc et al., 2001; Celie et al., 2004; Hansen et al., 2005). Using these crystal structures and a vast catalogue of biochemical data, an improved 4 Å resolution model of essentially the entire nAChR pentamer was published in 2005 marking the first full length model of a pLGIC. While the relatively low resolution of this model resulted in several modelling errors, the structure pioneered the field of pLGIC structural biology and remained the only electron microscopy-based model of a pLGIC until 2015 (Fig. 1.4).

The next major advancement in the field of pLGIC structural biology came in the mid to late 2000's with the above noted discovery of prokaryotic pLGICs (Tasneem et al., 2004). The prokaryotic pLGICs are easier to express and purify, are stable in common detergents, and lack the intracellular domains, which is thought to complicate crystal packing. These properties made ELIC (Hilf and Dutzler, 2008) and GLIC (Bocquet et al., 2009; Hilf and Dutzler, 2009) the first

Figure 1.4 Evolution of pLGIC structural biology

Four eras of pLGIC structural biology are depicted in four rows of density maps. The top row shows the density map for the *Torpedo* nAChR TMD that was used to construct the first medium resolution of a pLGIC in 2005. The next row shows density maps from x-ray crystal structures of the prokaryotic pLGICs ELIC and GLIC. The third row shows the density maps of three non-bacterial pLGIC crystal structures, each of which being the first from their family. The final row shows four cryo-EM density maps of the four main pLGIC subtypes. The first single particle cryo-EM structure of a pLGIC is shown on the left with the increases in resolution since this map demonstrated in the maps to the right, with the highest resolution map of a pLGIC to date on the farthest right.

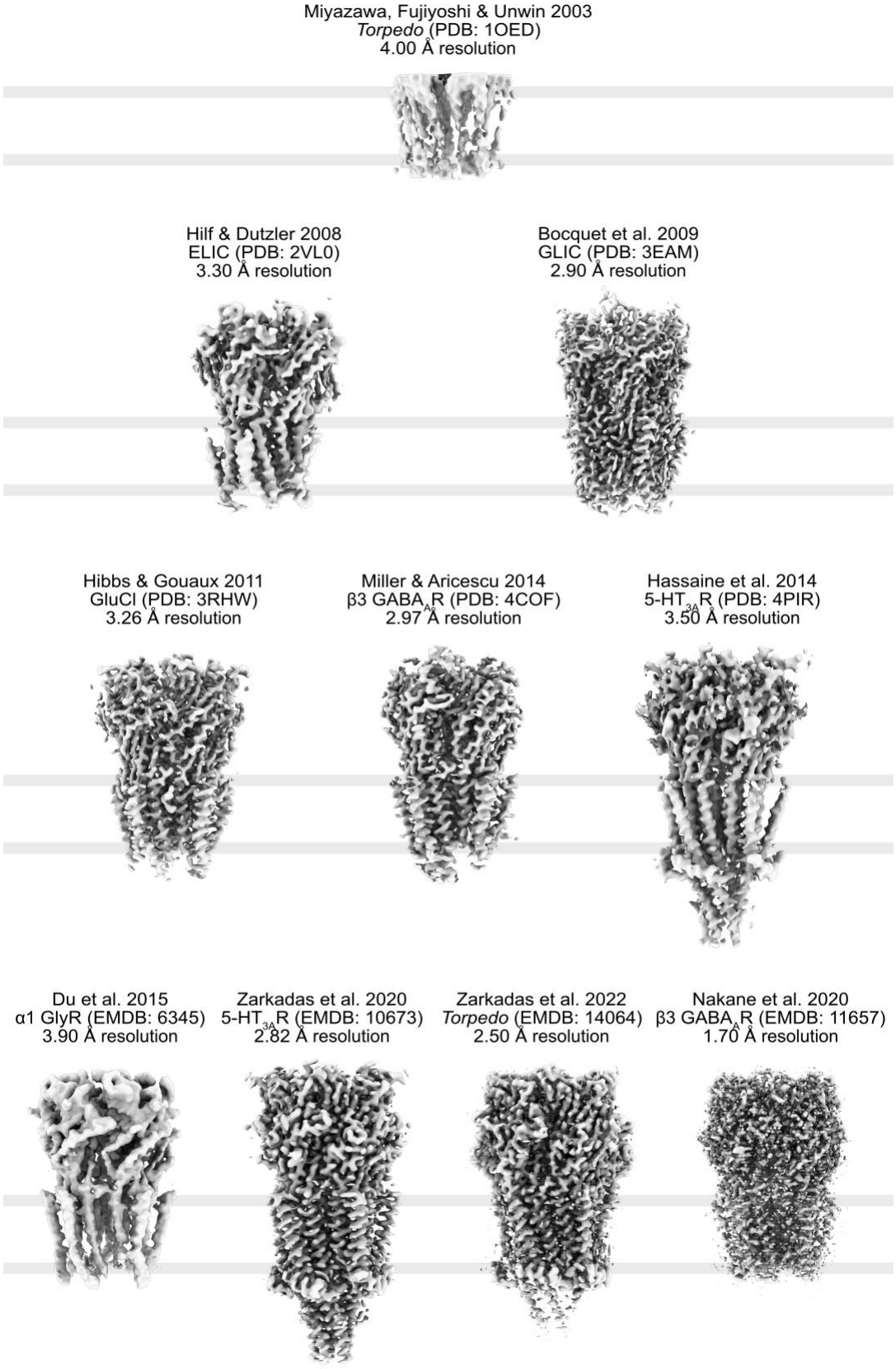
Miyazawa, Fujiyoshi & Unwin 2003
Torpedo (PDB: 1OED)
4.00 Å resolution
Hilf & Dutzler 2008
ELIC (PDB: 2VL0)
3.30 Å resolution
Bocquet et al. 2009
GLIC (PDB: 3EAM)
2.90 Å resolution
Hibbs & Gouaux 2011
GluCl (PDB: 3RHW)
3.26 Å resolution
Miller & Aricescu 2014
β3 $GABA_AR$ (PDB: 4COF)
2.97 Å resolution
Hassaine et al. 2014
5-$HT_{3A}R$ (PDB: 4PIR)
3.50 Å resolution
Du et al. 2015
α1 GlyR (EMDB: 6345)
3.90 Å resolution
Zarkadas et al. 2020
5-$HT_{3A}R$ (EMDB: 10673)
2.82 Å resolution
Zarkadas et al. 2022
Torpedo (EMDB: 14064)
2.50 Å resolution
Nakane et al. 2020
β3 $GABA_AR$ (EMDB: 11657)
1.70 Å resolution

full length pLGIC structures solved by X-ray crystallography thus facilitating the use of ELIC and GLIC as structural models to understand the mechanisms underlying the binding of drugs, ions (Hilf et al., 2010; Nury et al., 2011; Pan et al., 2012b, 2012a; Spurny et al., 2012; Sauguet et al., 2013b; Spurny et al., 2013; Nys et al., 2016; Fourati et al., 2017, 2018; Brams et al., 2020), and lipids (Basak et al., 2017; Hénault et al., 2019; Kumar et al., 2020b, 2021; Sridhar et al., 2021; Dietzen et al., 2022; Petroff et al., 2022; Bergh et al., 2023), as well as how agonist binding is coupled to gating (Prevost et al., 2012; Gonzalez-Gutierrez et al., 2013; Sauguet et al., 2013a, 2014a, 2014b; Fourati et al., 2015; Kinde et al., 2015; Bertozzi et al., 2016; Menny et al., 2017; Hu et al., 2018b; Rovšnik et al., 2021; Dalal et al., 2022). Although structures of other prokaryotic pLGICs have since been solved (Hu et al., 2018a, 2020; Lycksell et al., 2022), ELIC and GLIC remain the best structurally characterized pLGICs.

With rapid advancements in the field of X-ray crystallography along with new techniques for the expression and purification of membrane proteins, eukaryotic pLGIC structures subsequently became available, although the sequences of studied pLGIC were typically modified to enhance expression, purification and/or crystallization. The first non-prokaryotic pLGIC structure solved was that of GluCl from *C. elegans* (Hibbs and Gouaux, 2011), which paved the way for many more X-ray structures in the mid 2010's including another of GluCl, this time bound to the positive allosteric modulator (PAM) ivermectin (Althoff et al., 2014), the human β3 $GABA_AR$ homopentamer (Miller and Aricescu, 2014), the mouse $5\text{-}HT_{3A}R$ (Hassaine et al., 2014), the human α3 GlyR homopentamer in apo, glycine bound, inhibitor-bound, and ivermectin bound states (Huang et al., 2015, 2017a, 2017b), and the human α4β2 nAChR (Morales-Perez et al., 2016).

While X-ray crystallography laid the foundation for our understanding of pLGIC structural biology, it is the increased viability of solving structures by single particle cryo-electron microscopy (cryo-EM) that led to an explosion of pLGIC structures. The increased viability of single particle cryo-EM stems from advances in both the experimental apparatus and the algorithms used to process the collected data. New cameras made a significant impact by both directly detecting electrons at high quantum efficiency and recording multi-frame movies upon beam application (Doerr, 2016). Motion correction algorithms can retain high resolution information from frames throughout the beam exposure while correcting for beam induced drift and radiation damage (Cheng, 2018). Improved contrast transfer function algorithms can now process the motion corrected micrographs far more rapidly. Single particles from these micrographs still suffer from a low signal to noise ratio (SNR) but if enough particles are captured in a variety of orientations, they can be averaged to improve SNR and then reconstructed into a 3D density map. Algorithms for these processes are now widely available, user friendly programs like RELION (Scheres, 2012) and cryoSPARC (Punjani et al., 2017) now facilitate EM data processing. Data collection has also become heavily automated and run through large, specialized facilities allowing access to more researchers. The final advancement that was particularly relevant to pLGICs is the use of non-detergent membrane mimetics, such as amphipols and nanodiscs, which surround the hydrophobic transmembrane regions with a more native-like environment that improves the stability and distribution of particles in vitreous ice (Denisov and Sligar, 2016).

Since the implementation of these advances in single particle cryo-EM, structural biology of pLGICs has vastly improved leading to structures solved in environments that more closely resemble physiological conditions and at higher resolutions. The first single particle cryo-EM

structures of a pLGIC was that of the zebrafish GlyR in 2015 at resolutions near 4 Å (Du et al., 2015). Astoundingly, just five years later the human β3 $GABA_AR$ was solved to a resolution of 1.7 Å illustrating the enormous power of the technique (Nakane et al., 2020). We now have structures of various $GABA_AR$ subtypes (Liu et al., 2018; Phulera et al., 2018; Zhu et al., 2018, 2022; Kasaragod and Schindelin, 2019; Laverty et al., 2019; Masiulis et al., 2019; Kim and Hibbs, 2021; Kasaragod et al., 2022; Noviello et al., 2022; Sente et al., 2022; Cowgill et al., 2023; Legesse et al., 2023; Sun et al., 2023), homomeric and heteromeric GlyRs (Kumar et al., 2020a, 2022; Yu et al., 2021; Zhu and Gouaux, 2021; Gibbs et al., 2023; Liu and Wang, 2023), 5-HT_3Rs (Basak et al., 2018b, 2018a; Polovinkin et al., 2018; Basak et al., 2019, 2020; Zarkadas et al., 2020; Zhang et al., 2021b), and a variety of neuronal and muscle nAChRs (Walsh et al., 2018; Gharpure et al., 2019; Rahman et al., 2020b; Noviello et al., 2021; Zhao et al., 2021; Nys et al., 2022; Rahman et al., 2022; Zarkadas et al., 2022; Goswami et al., 2023).

Despite the growing number of structures, and the attempts made to solve these structures in more physiological environments, there remain many unanswered questions regarding the conformations that these receptors adopt in their native environments. The ability to solve structures of pLGICs in a lipid nanodiscs has marked an improvement over detergent solubilization, but various lines of evidence suggest that these lipid environments still do not completely replicate a native setting (Dalal et al., 2022; Real Hernandez and Levental, 2023). While some groups have begun attempting in situ structural biology of pLGICs (Kudryashev et al., 2016; Liu et al., 2020), the achievable resolution is still far too low for accurate structure determination. This, as well as the subtle conformational changes associated with different functional states, have made the assignment of solved structures to their physiological states difficult (see (Zhu et al., 2018; Cerdan and Cecchini, 2020; Zhang et al., 2021b; Zarkadas et al.,

2022)). Despite these caveats, we now have a comprehensive understanding of how pLGICs fold in three-dimensional space and a growing understanding of the motions that occur as they cycle through their conformational states.

1.2.4 pLGIC architecture

Despite having relatively low sequence homology, the general pLGIC architecture is maintained across the family. All pLGICs contain a minimum of two structural domains, an ECD and a transmembrane domain (TMD). The ECD of each subunit is composed of short N-terminal α-helix followed by ten β-strands (β1-β10). These ten β-strands fold into two β-sheets that come together to form a β-sandwich. The inner β-sheet is formed primarily by β strands 1, 2, and 6 with smaller contributions from β strands 3, 5, and 8 while the outer β-sheet is formed by three long β strands (7, 9, and 10) along with the short β4 strand. The TMD is composed of four α-helices (M1-M4) that form a diamond shaped helical bundle. M2 α-helices from each subunit come together to line the channel pore, the M1 and M3 α-helices shield the M2 α-helices from the surrounding lipid environment, and the M4 α-helices sits at the periphery of the TMD highly exposed to lipid. All eukaryotic pLGICs contain an intracellular domain (ICD) that forms from a long cytoplasmic loop connecting M3 and M4 α-helices, although the structural features of the ICD are less conserved (see below). While these three domains are classical of eukaryotic pLGICs, more and more pLGICs are being discovered that exhibit additional structural complexity. For example, a recently characterized bacterial pLGIC, DeCLIC, was shown to contain an additional extracellular N-terminal domain reminiscent of the additional extracellular domains found in ionotropic glutamate receptors (Hu et al., 2020) (Fig. 1.5).

Figure 1.5 pLGICs display a conserved core architecture with diverse auxiliary features
Side views of the prokaryote DeCLIC (PDB: 6V4S, left), the human α1β3γ2 $GABA_AR$ (PDB: 7QNE, middle), and the *Torpedo* nAChR (PDB: 7QL5, right) colored according to domains (NTD, orange; ECD, red; TMD, blue; ICD, green). Bound agonists are presented as cyan spheres at the interfaces between two subunits. Figure is adapted from (Ananchenko et al., 2022).

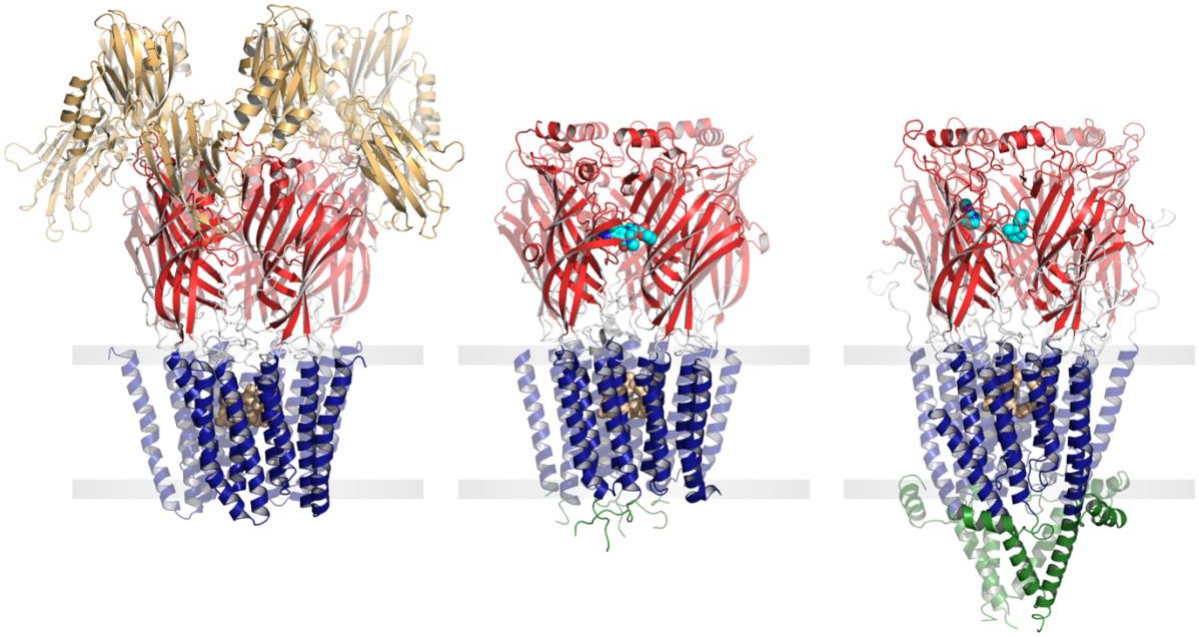

The main functional role of the ECD is to bind agonist. In essentially all pLGICs, the orthosteric binding sites exist at the interfaces between two subunits, with three loops from the principal subunit, loops A-C, and four loops from the complementary subunit, loops D-G, typically converging around the bound agonist (Sine, 2002) (Figure 1.6). Loop A is located between the β4 and β5 strands with an aromatic residue forming the bottom of the agonist site (Tyr93 in the nAChR α1 subunit). Loop B is located between the β7 and β8 strands and contributes a conserved aromatic residue that forms the back of the binding site (Trp149 in the nAChR α1 subunit). Loop C is the best studied loop in agonist binding as it undergoes a dramatic capping motion around the agonist. Structurally, loop C is located between the β9 and β10 strands and contributes two more highly conserved aromatic residues that form the front and side of the binding site (Tyr190/198 in the nAChR α1 subunit) as well as a conserved vicinal disulfide bridge at the tip of the loop in all nAChR α subunits. The other side and the top of the orthosteric site are formed by the D, E, F, and G loops, which extend from the β2 strand, the β6 strand, the β8-β9 loop, and the β1 strand from the complementary subunit, respectively. The residues within the binding site differ between pLGICs but a conserved feature is the presence of multiple aromatic residues that form the so-called aromatic box. The π electrons from these aromatic residues coordinate the region of the ligand that carry a positive or partial positive charge (ex. the choline group of ACh, the amide group of GABA, and the amine group of 5-HT/glycine).

Following the β10 strand from the ECD there is a short linker (the β10-M1 linker) that leads into the M1 α-helix from the TMD. The first turn of the M1 α-helix represents a short π-helix before becoming α-helical as it transverses the membrane (Hibbs and Gouaux, 2011; Purohit et al., 2015). Following the M1 α-helix, there is a short intracellular loop connecting M1

Figure 1.6 pLGIC ECD and agonist binding site

The ECD of the *Torpedo* nAChR Carb bound state (7QL6) is depicted in panel A with zoomed in views of the binding site shown in panels B and C. In panel A the principal α_{γ} subunit is shown in pink and the complementary γ subunit is shown in light blue. β strands in the ECD are labelled wherever possible. The agonist is shown as fat sticks and colored by residue type (C=grey, O=red, and N=blue). Panel B shows a zoomed in view of the binding site in panel A with residues important for agonist binding shown as sticks. Panel C is a top down view of the binding site rotated 90° from panel B.

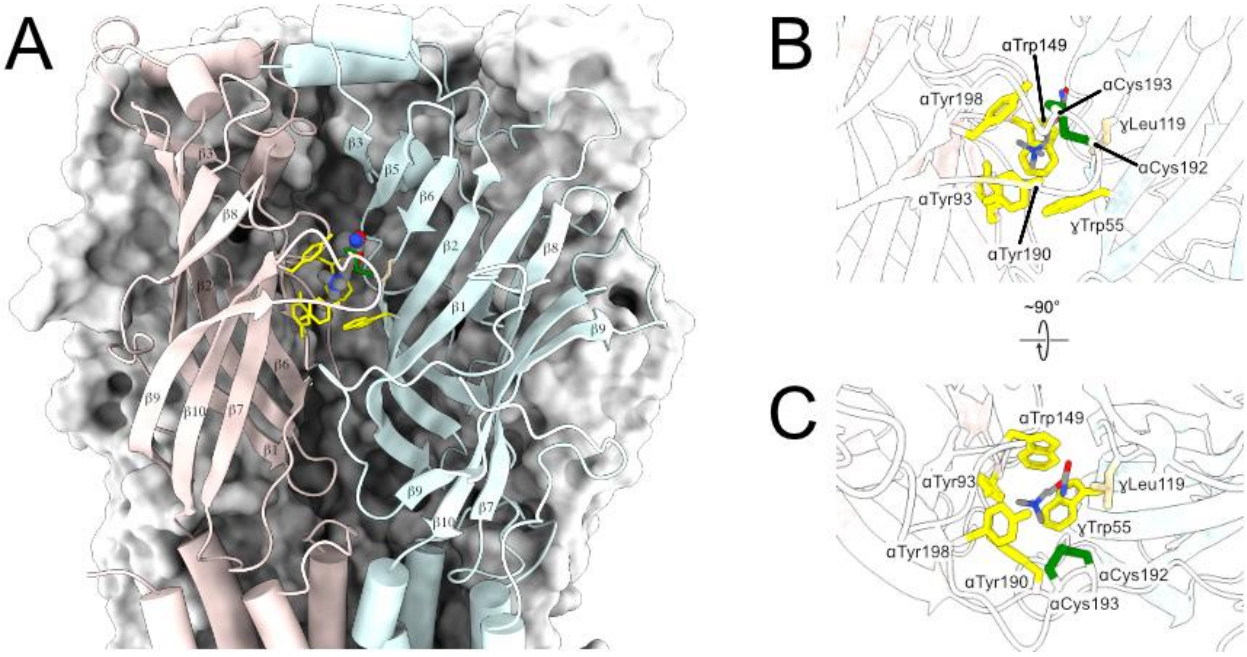
A
β3
β5
β6
β8
β2
β1
β9
β10
β7
B
αTrp149
αCys193
αTyr198
γLeu119
αCys192
αTyr93
γTrp55
αTyr190
~90°
C
αTrp149
αTyr93
γLeu119
γTrp55
αTyr198
αCys192
αTyr190
αCys193

to the pore lining M2 α-helix (the M1-M2 loop). The M2 α-helices were originally numbered via a prime scheme, with the most intracellular residue in M2 numbered 0' with each consecutive M2 residue having ascended prime numbering until the extracellular end of M2 (Miller, 1989). The most intracellular end of M2 carries conserved Glu/Gln residues in cation selective pLGICs (-1') that influence cation selectivity while a conserved Pro residues at the -2' position of anion selective pLGICs is thought to form a desensitization gate (Cymes and Grosman, 2012; Gielen and Corringer, 2018). The activation gates of these channels are formed by hydrophobic residues at the 9', 13', and 16' positions, which together create a hydrophobic barrier that prevents the passage of hydrated ions in the resting state (Beckstein and Sansom, 2006) (Fig. 1.7). The M2 α-helices are terminated by a universally conserved Pro residue (P265 in the nAChR α1 subunit), which leads into an extracellular loop connecting M2 and M3 (Jaiteh et al., 2016). The M2-M3 loop sits at the interface between the ECD and TMD where it plays a critical role in activation (see below). The M3 α-helix then transverses the membrane before the initiation of the ICD. The final and most peripheral transmembrane α-helix, M4, is positioned at the periphery of the TMD between the M1 and M3 α-helices and forms the most prominent contacts with the surrounding membrane. The end of M4 is the C-terminus of the protein in some pLGICs, while others contain C-terminal extensions that extend into the extracellular space or amphipathic α-helices that lie parallel to the membrane surface (see for example (Zarkadas et al., 2022) and (Noviello et al., 2021), respectively).

The ICDs of pLGICs are heterogeneous both in structure and sequence. While prokaryotic pLGICs have a small simple intracellular loop, eukaryotic pLGICs have long ICDs that contain a large region that is intrinsically disordered. The first structurally insight into the ICD came from low resolution cryo-EM images of the *Torpedo* nAChR, which revealed an MA

Figure 1.7 pLGIC TMD structure

A top-down view of the *Torepdo* nAChR apo state (PDB: 7QKO) TMD is shown in panel A as an illustration of the general pLGIC TMD architecture. Each subunit is coloured uniquely and their M1-M4 α-helices labelled. The pore is also labelled with residues at the 9' and 13' positions that contribute to the hydrophobic gate shown as tan sticks. Bound lipids at the periphery of the TMD are outlined. Two side views of a single subunit are shown in panel B rotated 180° from each other.

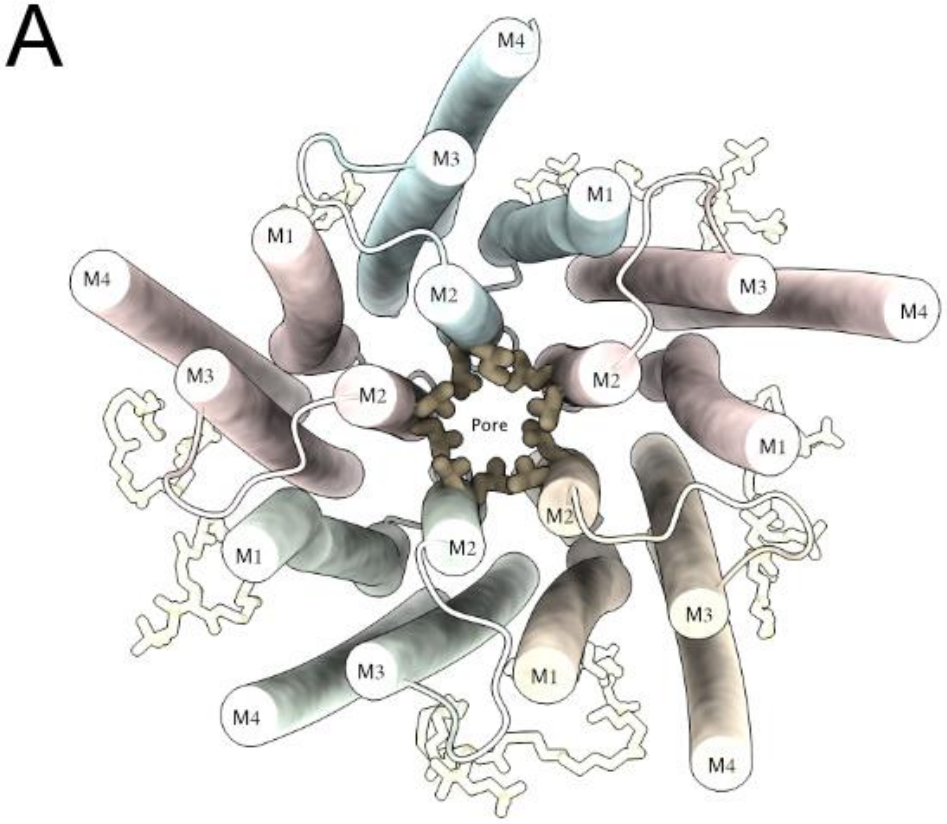
A
M4
M3
M1
M1
M4
M2
M3
M4
M3
M2
M2
Pore
M1
M2
M2
M1
M3
M3
M1
M4
M4

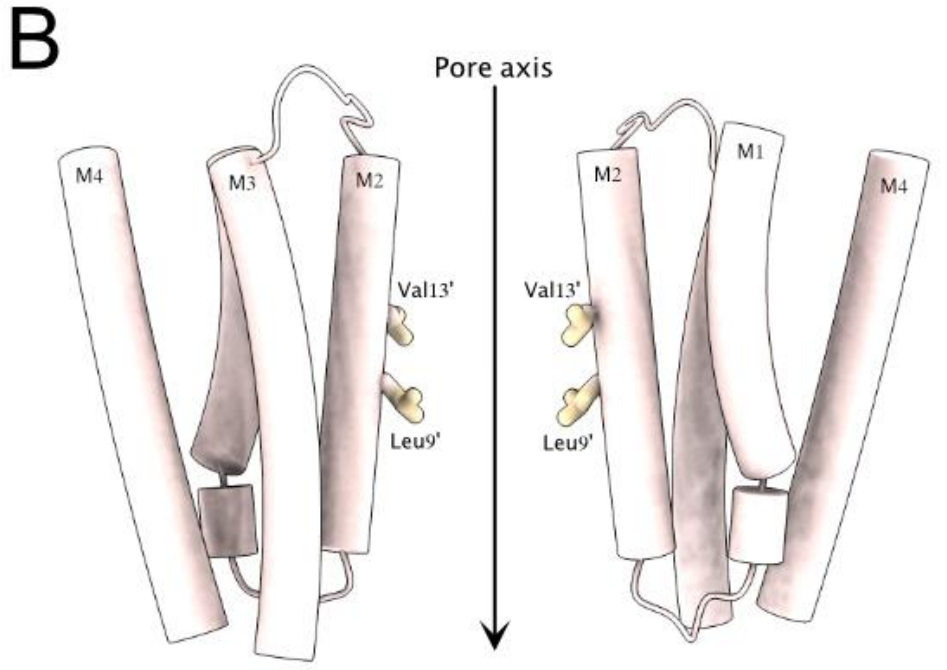
B
Pore axis
M4
M3
M2
Val13'
Leu9'
M2
M1
M4
Val13'
Leu9'

Figure 1.8 Architecture of the ICD in a cation selective pLGIC

A view of the *Torepdo* nAChR apo state (PDB: 7QKO) ICD from the cytoplasm is shown in panel A. A transparent white surface representation of the ICD is shown along with a cartoon representation where each subunit is colored uniquely. Panel B shows a view of the ICD rotated by 90° from panel A. The cartoon representation remains but the transparent surface is now coloured by its electrostatic potential with red being negative, blue being positive, and white being neutral. Lateral portals between MA α-helices of subsequent subunits are lined by negative potential contributing to charge selectivity and conductance.

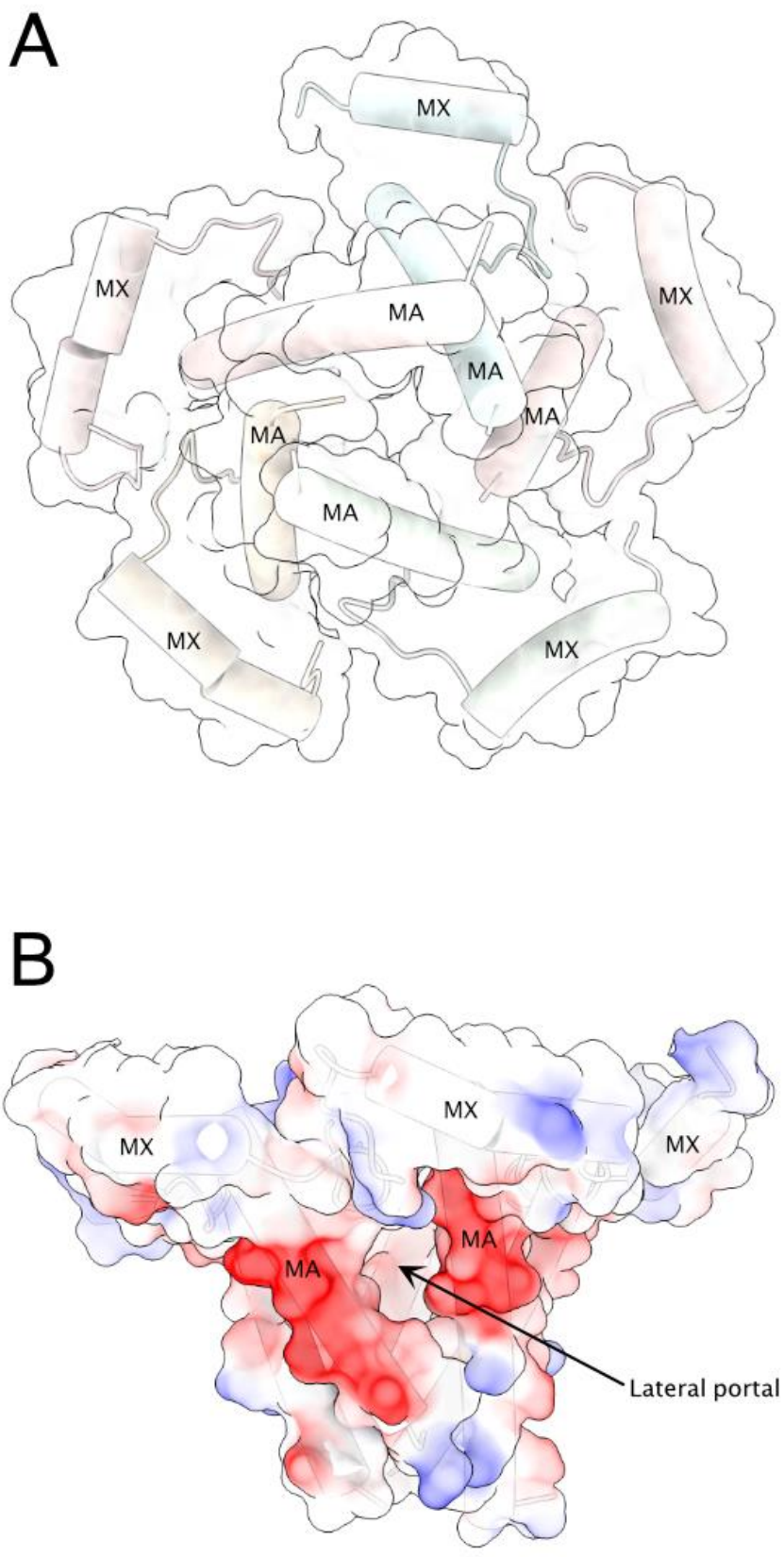
A
MX
MX
MX
MA
MA
MA
MA
MA
MX
MX
B
MX
MX
MX
MA
MA
Lateral portal

α-helix in each subunit come together to form an inverted teepee contiguous with M4 (Miyazawa et al., 2003). The only other structured region of the ICD revealed to date are the MX α-helices, which were first observed in crystal structures of the mouse 5-HT_{3A}R (Hassaine et al., 2014). The MX α-helix, which follows M3 and the M3-MX loop is an amphipathic α-helix that sits perpendicular to the bilayer with half of the α-helix contacting lipids and the other half contacting the cytoplasm. Lateral portals through the MA α-helices in cation selective pLGICs carry negative charges and have been shown to influence the unitary conductance of these channels (Kelley et al., 2003; Stuebler and Jansen, 2020). Note that the existence of these two α-helical regions in the ICD appear to be only present in cation selective pLGICs as there is little to no density present in the ICD of full-length anion selective channels (Yu et al., 2021; Cowgill et al., 2023; Gibbs et al., 2023; Sun et al., 2023). Protein prediction software, such as AlphaFold (Jumper et al., 2021), give very poor confidence scores for the disordered regions of the ICD but occasionally predict short α-helices. Indeed, solution NMR has suggested the presence of such α-helices in the disordered region of the a7 nAChR (Bondarenko et al., 2022). The ICD is thought to form complexes with various proteins including chaperones (Loring, 2022), clustering proteins (Cetin et al., 2019; Kasaragod and Schindelin, 2019), as well as G-proteins, RhoA, and the cytoskeleton (King and Kabbani, 2016) so it is likely that these binding partners are required for the ICD to adopt a 3D fold.

1.2.5 Conformational transitions underlying pLGIC function

pLGICs are allosteric proteins that function by transitioning through a series of conformational states. In the absence of agonist, synaptic pLGICs predominantly adopt a resting state that has a relatively weak agonist binding affinity and a non-conductive channel pore.

When agonists bind, receptors transiently adopt an open conformation with a conductive pore and a high agonist binding affinity. Prolonged exposure to agonist results in the formation of non-conductive, high agonist-affinity desensitized state(s). There is also growing evidence for several other conformational states of the receptor such as pre-open intermediate states (Lape et al., 2008; Mukhtasimova et al., 2009; Menny et al., 2017; Polovinkin et al., 2018; Yu et al., 2021; Cowgill et al., 2023; Shi et al., 2023), multiple open states (Zhu and Gouaux, 2021), and a lipid dependent uncoupled state (daCosta and Baenziger, 2009). The stability of these states, and the rates of interconversion between them (i.e., the stabilities of their intervening transition states), dictates the frequency and volume of ion conductance through these channels, and ultimately the physiological effect of their activation.

While the structural motions that accompany conformational transitions through these states remain speculative due to our inability to unambiguously assign pLGIC structures to defined states, several general features have been observed. In the resting state the agonist binding sites remain unoccupied with loop C from the principal subunits in an extended, uncapped conformation. The pore lining M2 α-helices come together to form a pore diameter that is larger than the radius of an un-hydrated Na^+, K^+, or Cl^- ion but smaller than the radius of hydrated ion, creating an energetic barrier to ion permeation (Rao et al., 2021). In the homomeric prokaryotic pLGICs, agonist binding is accompanied by a capping motion of loop C that causes a quaternary counterclockwise twisting and condensing of the ECD. The TMD undergoes a general "blooming" motion that twists and tilts the extracellular ends of the M2 α-helices away from the channel axis (Sauguet et al., 2014a). This motion not only expands the diameter of the pore but increases the polarity within the region of the hydrophobic gate to facilitate hydration and thus decrease the energy barrier for ion diffusion through the pore

(Beckstein and Sansom, 2006; Aryal et al., 2015; Rao et al., 2021). After prolonged exposure to agonist, the M2 α-helices tilt further to occlude the pore at the intracellular end of the channel and thus close a distinct desensitization gate (Gielen et al., 2015, 2020; Gielen and Corringer, 2018), although the process has only been observed to date in anionic pLGICs to date. Note that the described motions above are intentionally vague and general as the distinct biophysical properties displayed by different pLGICs implies that conformational transitions in each subtype are, at least partially, unique. The following articles provide a more detailed discussion into the conformational transitions of various pLGICs (Corringer et al., 2012; Calimet et al., 2013; Sauguet et al., 2014a; Taly et al., 2014; Cecchini and Changeux, 2015; Plested, 2016; Lev et al., 2017; Martin et al., 2017). The conformational transitions in the muscle nAChR, the specific pLGIC studied in this work, are discussed in more detail in the following section.

1.3 The muscle-type nAChR

1.3.1 Role of the nAChR in neuromuscular transmission and disease

The muscle type nAChR is found post-synaptically at the neuromuscular junction (NMJ), the synapse between a motor neuron and a skeletal muscle cell. NMJ formation is aided by the expression of fetal nAChRs (receptors with the stoichiometry $\alpha_2\beta\delta\gamma$ rather than $\alpha_2\beta\delta\varepsilon$ for the adult receptor) on the muscle fibers. Compared to the adult receptor, the fetal receptor has a slightly higher affinity for ACh and a slightly lower unitary conductance, allowing it to stay open longer and produce tonic currents that guide the growth of the muscle toward the motor nerve terminals (Nayak and Auerbach, 2013; Cetin et al., 2020). Postnatally, the NMJ undergoes major morphological changes that are, in part, sparked by the developmental switch in gene expression to the adult nAChR subunit stoichiometry. Each NMJ spans only ~30 μm where it

innervates a single muscle fibre. The muscle fibre organizes into junctional folds that increase the surface area of the post-synaptic membrane with the crests of these folds containing clustered nAChRs in proximity to the nerve terminal and the bottoms of these folds concentrated with voltage-gated Na^+ channels to facilitate the response (Rodriguez Cruz et al., 2018). ACh is synthesized by choline acetyltransferase in the synaptic boutons, packaged into vesicles, and released into the synapse in response to elevated Ca^{2+}. ACh then binds to the nAChR before being rapidly degraded by acetylcholine esterase in the synaptic cleft. ACh binding allows cations to flow into the muscle fibres leading to depolarization. If this depolarization reaches the threshold for an action potential, the voltage gated Na^+ channels at the base of the junctional folds open triggering an action potential. The action potential stimulates L-type Ca^{2+} channels which are mechanically coupled to ryanodine receptors in the sarcoplasmic reticulum to jointly increase the concentration of intracellular Ca^{2+}. Ca^{2+} then binds to troponin C on actin filaments to expose myosin binding sites. The binding of myosin (and subsequent liberation of bound ADP and inorganic phosphate) produces the power stroke that drives muscle contraction. Binding of ATP to myosin releases myosin from the actin filaments allowing myosin to hydrolyze ATP and repeat the process (Kuo and Ehrlich, 2015).

The muscle type nAChR has evolved to facilitate efficient neuromuscular transmission (Bouzat and Mukhtasimova, 2018), with even subtle changes in function leading to a disease call congenital myasthenic syndrome (CMS) (Engel et al., 2015). nAChR mutations that cause gain-of-function phenotypes, either by strengthening ACh binding affinity or by prolonging channel open times, result in dominant slow channel CMS while those that cause loss-of-function phenotypes, either by weakening the ACh binding affinity or by reducing channel open times, result in recessive fast channel CMS (Engel and Sine, 2005). In the former case, end-plate

potentials are lengthened causing depolarization block and postsynaptic Ca^{2+} accumulation that compromise the safety margin of neuromuscular transmission and cause myopathy. In the latter case the end-plate potential is unusually brief weakening the response and failing to generate strong muscle contractions.

It is notable that current treatment options for CMS do not directly address the cause of the disease but rather attempt to mask its effect by broadly enhancing (by inhibiting acetylcholine esterase) or inhibiting (by blocking nAChRs) neurotransmission in the case of fast-channel CMS and slow-channel CMS, respectively (Vanhaesebrouck and Beeson, 2019). As a result, these therapies are not fully effective and often come with unwanted side effects. A long-term goal would be to develop therapies that directly target the nAChR and shift the energetics of the mutated channel to match those of the wild-type (WT) nAChR, leading to more effective and less harmful treatment strategies. To achieve this goal, we must first have a better understanding of the energetics within the nAChR that regulate its transition through its conformational landscape, specifically during agonist activation.

1.3.2 The prototypic pLGIC

The muscle-type nAChR was first identified in 1905 when John Newport Langley discovered a "receptive substance" for nicotine on innervated muscle (Langley, 1905). He noted that when nicotine was applied to the muscle there was a contraction that could be inhibited by the Central American poison, curare. This fundamental discovery ultimately founded the field of "receptor biochemistry" inspiring researchers to begin the pharmacological, electrophysiological, and chemical characterization of various receptors. A major bottleneck in studying such receptors was, and still is, acquiring enough pure sample to perform biochemical

characterization. Fortunately, about 50 years after the experiments of Langley, a vast source of nAChRs was discovered in the electric organs of both the electric eel and *Torpedo* ray (Nachmansohn, 1959). These electric organs are modified neuromuscular endplates that are used to shock and even kill their prey. To create such a large current, coordinated signals are sent from the electric lobe to the heavily innervated electric organs where densely packed nAChRs are simultaneously activated (Stavrianakou et al., 2017). Serendipitously, a snake venom toxin, α-bungarotoxin (α-BTX), which was shown to specifically block neuromuscular transmission was discovered around the same time (Chang and Lee, 1963). This toxin was shown to bind the nAChR tightly (Changeux et al., 1970) and several groups used these types of toxins to create affinity columns to purify the nAChR (Miledi et al., 1971; Karlsson et al., 1972; Olsen et al., 1972). The vast abundance of nAChR from *Torpedo marmorata* and *Torpedo californica* facilitated extensive biochemical characterization. These tools, along with the vast abundance and stability of the *Torpedo* nAChR have made it the prototypical pLGIC (Changeux, 2012).

1.3.3 Proposed mechanisms of agonist activation in the nAChR

Understanding how the binding of agonist leads to channel activation has been a topic of major interest in nAChR research for decades. Following the publication of the *Torpedo* nAChR structure in 2005 (Unwin, 2005), various group used the new structural information to formulate hypotheses for how activation occurs. The β1-β2 loop from the ECD was shown in this structure to form a "pin-into-socket" interaction with the M2-M3 loop that was proposed as a potential means to couple movements in the ECD to the TMD (Miyazawa et al., 2003). Specifically, an Arg residue (Arg209) at the base of the β10 strand formed a salt bridge with a Glu residue (Glu45) on the β1-β2 loop linking the capping of loop C (the β9-β10 loop) to the gating

interface. Glu45, and the adjacent Val46, engaged tightly with Ser269 and Pro272 from the M2-M3 loop in the structure providing a means for the movement of the β1-β2 loop to directly couple to the opening of the channel pore. Mutating these residues caused large decreases in the equilibrium constant for channel gating, consistent with a role for these residues in gating (Lee and Sine, 2005). Large energetic couplings were also quantified between these residues supporting a role for interactions between these residues in coupling binding to gating. This model was later shown to extend to the Cys-loop and has remained one of the most convincing models of activation to date (Lee et al., 2008, 2009).

Another model that has received considerable attention was proposed by Auerbach and colleagues based on ϕ value analysis and energetic couplings. ϕ value analysis is used to assess the relative position of a residues along the gating transition by assessing how mutations at a specific site alter the forward vs reverse rate constants for channel gating (Grosman et al., 2000). In theory, this provides a point along the gating trajectory where the residue has transitioned from inactive to active allowing a temporal sequence of events to be visualized. Residues with similar ϕ values were bundled together to form structural blocks that transition at roughly the same time in the transition state ensemble (TSE) between the resting and open states (Gupta et al., 2017). Activation in this model initiates with a concurrent motion of the binding sites transitioning to the high affinity state along with an upward displacement of the M2-M3 loops. The ECD then twists and compacts to alter interactions at the ECD – TMD interface, making it easier for the TMD to tilt and dilate the pore. The final step is then the hydration of the pore around the hydrophobic gate to allow conduction. The results suggest that activation occurs through a sequential transition of the receptor through several pseudo stable intermediates that

move approximately as a “conformational wave” from the binding sites to the channel gate (Grosman et al., 2000).

Other models of nAChR activation have focused less on specific interactions at the ECD – TMD interface and instead suggest activation occurs through non-specific interactions. One model observed that in general, the ECD side of the ECD – TMD interface carries a net negative charge while the TMD side carries a net positive charge. Rather than direct interactions between residues at this interface dictating how the two domains communicate, this model suggest that general electrostatic attraction between these domains, and the change in charge distribution in resting vs active states allows agonist binding and channel gating to be coupled (Xiu et al., 2005). Another model concluded that specific interactions at the ECD – TMD interface were not required at all, and instead all that was required was the correct packing of interfacial loops (Cymes and Grosman, 2021). The “non-specific” bumping of these loops that occurs during activation would then allow binding to be coupled to gating.

While each of these models is intriguing, they were each proposed before high-resolution structural information of the nAChR was available in apo and agonist bound states. Now that we have this information (see the section below) none of these models appears to fully account for how activation occurs. Specifically, the first two models mentioned above cannot fully account for activation as many of the residues proposed to be critical in coupling binding to gating are no longer proximal, and the inferred motions from other pLGICs are not conserved. The structures also hint at several previously unappreciated side chain interactions at the ECD – TMD interface that could play a critical role.

Figure 1.9 High resolution *Torpedo* nAChR structures

Panel A shows side views of the three high resolution nAChR structures reported in (Zarkadas et al., 2022). The protein is colour by subunit and densities modeled as sugars, lipids, and agonists are shown in purple, yellow, and red, respectively. Panels B and C show a top-down views of the ECD and TMD in the Carb-bound structure, respectively. Agonists are shown in panel B at both binding sites and L9' residues from each subunit are shown in panel C as brown spheres.

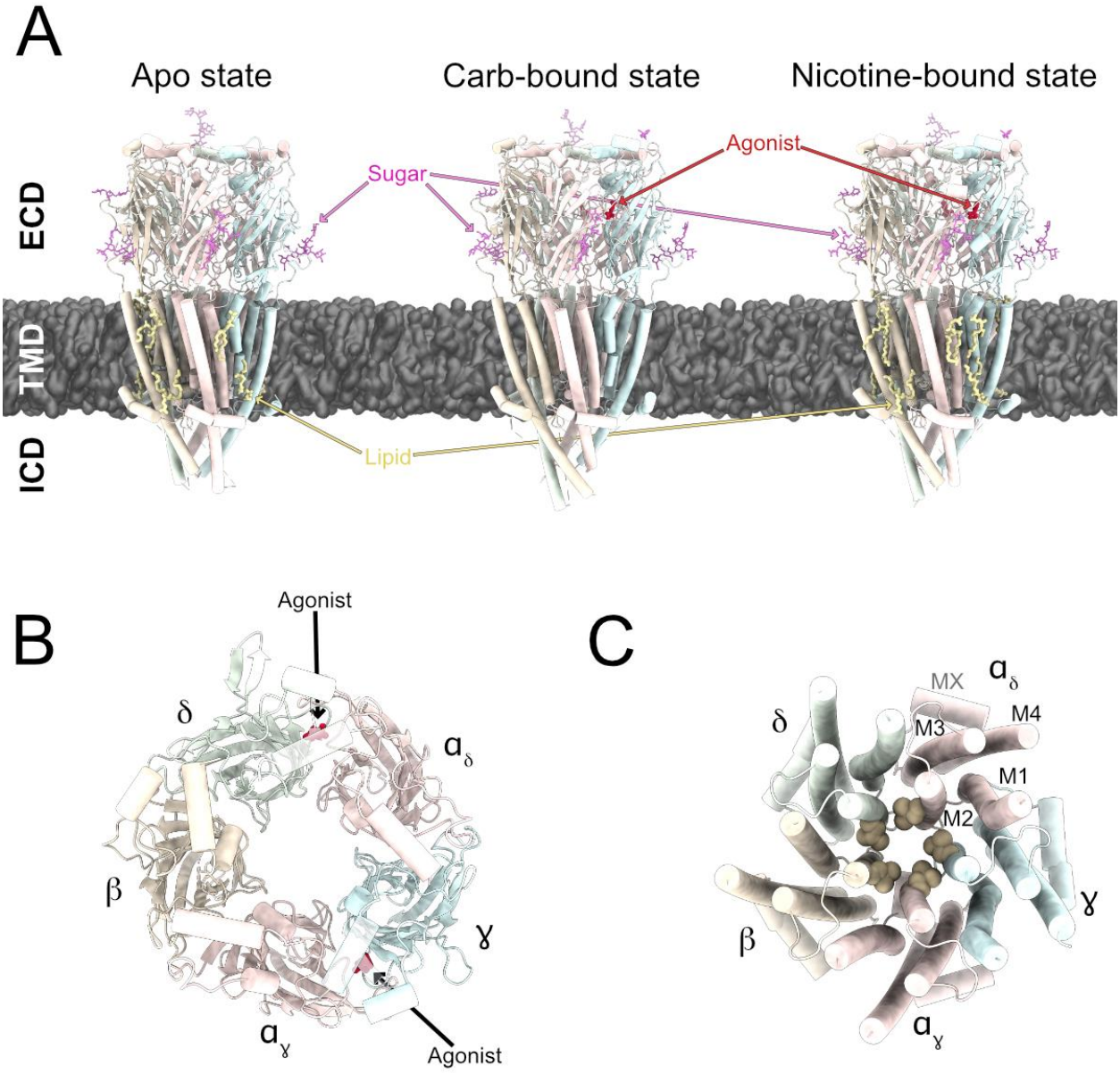
A
Apo state
Carb-bound state
Nicotine-bound state
ECD
TMD
ICD
Sugar
Agonist
Lipid
B
Agonist
δ
α δ
β
γ
α γ
Agonist
C
MX
α δ
δ
M3
M4
M1
M2
γ
β
α γ

1.3.4 Recent advances in nAChR structural biology

When I entered the field in 2017, the models of the muscle nAChR came from Uniwn's work on the *Torpedo* nAChR (Unwin, 2005; Unwin and Fujiyoshi, 2012). It was widely accepted at that time that there were several errors in the original 2005 model (see further discussion in chapters 3 and 8) limiting our ability to accurately assess the mechanistic basis of both activation and lipid modulation – two major themes of this thesis (see below). Fortunately, several high-resolution structures of the *Torepdo* nAChR are now available (Rahman et al., 2020b; Nys et al., 2022; Rahman et al., 2022; Zarkadas et al., 2022; Goswami et al., 2023). These structures have provided new insight into the conformational transitions accompanying the binding of agonists, antagonists, and toxins leading to new hypotheses to be tested with experiments. These structures of the nAChR in apo and agonist bound structures are particularly integral to this thesis and are therefore discussed in more detail below.

In 2022 three structures of the *Torpedo* nAChR were released: an apo state at 2.9 Å resolution (PDB: 7KQO), a nicotine-bound state at 2.5 Å resolution (PDB: 7QL5) and a carbamylcholine (Carb)-bound state at 3.2 Å resolution (PDB: 7QL6) (Figure 1.9). In each case, the receptor was affinity purified, reconstituted into MSP2N2 nanodiscs with soybean azolectin lipids, and incubated on ice with buffer or buffer containing a saturating concentration of the ligand of interest for 30 minutes before vitrification. The apo state contains two uncapped C loops with no agonist density in the binding sites and a de-hydrated pore incompatible with Na^+ conductance. These observations, along with biochemical evidence suggesting a large proportion of nanodisc reconstituted nAChRs adopt an activatable resting states in the absence of agonist, indicate that the structure represents a resting conformation. The full agonist Carb and the partial agonist nicotine induce similar conformational changes in the channel, albeit with

subtle rearrangements around the binding sites. In both models, loop C of both α subunits have capped around the bound agonist and the pore has expanded consistent with channel activation. As previously discussed however, assigning active conformations of pLGICs to their functional states is not trivial and the exact state occupied in these models is unclear. Based on the conditions in which they were captured, both should be in desensitized states with non-conductive pores, but molecular dynamics simulations are not compatible with this assignment. When the experimental structures are restrained to their solved conformations, the pore remains hydrated throughout simulations suggesting both bound structures are conductive. When these restraints are released, however, the pore rapidly collapses suggesting that the structure is not stable over the ns time scale and that there may be missing elements in the models. Diffuse density within the pore is present in the maps for both structures. When lipids are modelled in these densities, the unrestrained structures do not drift from their starting states over the course of the simulations. It is likely that the entry of lipids into the transiently open pore during grid preparation trap the nAChR in an intermediate conformation between open and desensitized states, but this remains speculative. It is notable that similar densities are found in all heteromeric nAChR agonist bound states solved to date, which have all been assigned as desensitized states despite some displaying pore wetting during simulations (Walsh et al., 2018; Gharpure et al., 2019; Rahman et al., 2022; Goswami et al., 2023).

While a definitive conformational assignment for the agonist bound state is lacking, conformational transitions observed when going from our apo to agonist bound states may inform us on how channel activation and/or desensitization occurs. The binding affinity for Carb and ACh is ~1,000-fold stronger in the desensitized state than the resting state (Boyd and Cohen, 1980a, 1980b), which can be rationalized structurally by the condensing of the binding site

around the bound agonist. The largest motion upon agonist binding is that of loop C where the Cα carbons of the cysteines at the tip of loop C in both binding sites move ~7-9 Å toward the bound agonist. More subtle motions of the other loops in the binding site (loops A, B, D, and E) reposition the aromatic box residues to coordinate the quaternary amide of Carb (Fig. 1.6). A unique feature of the muscle nAChR is an extended loop F from the complementary ɣ/δ subunits which have ~10 more residues than other nAChR subunits. These extended F loops also moves towards the bound agonist, stabilizing the capped conformation of loop C in a way that has only been observed for the nAChR. The effect of loop C and loop F capping extend to the ECD – TMD interface to propagate the conformational change to the TMD (Fig. 1.10). Loop C capping causes the α subunit ECDs to undergo a rocking and twisting motion pivoting the extracellular ends of the ECDs toward the complementary ɣ/δ subunits and the membrane juxtaposed ends toward the neighboring ɣ/β subunits (red arrows in Fig. 1.10). Loop F capping in the complementary ɣ/δ subunits causes the membrane juxtaposed ends loop F (the β8-β9 loops) to pivot outward (blue arrows in Fig. 1.10). The β8-β9 loops from the complementary subunits directly interact with the M2-M3 loops from the α subunits and their pivoting motions are correlated with the movement of the M2-M3 loops from the α subunits away from the pore. This causes the extracellular ends of the M2 α-helices in the TMD to twist and tilt away from the pore axis to dilate the pore. While these structures provide a crucial first step for understanding the mechanisms of nAChR activation, they do not provide understanding of how agonist binding is coupled to channel gating at the ECD – TMD interface.

Figure 1.10 Conformational transitions accompanying agonist binding in the *Torpedo* nAChR

The primary motions accompanying agonist binding are show in a schematic representation. The principal α subunit is shown on the left in orange and the γ/δ complementary subunit in blue. Red arrows denote the major movements in the α subunit, blue arrows in the γ/δ complementary subunit, and the purple arrow in the α subunit TMD. Figure adapted from (Zarkadas et al., 2022).

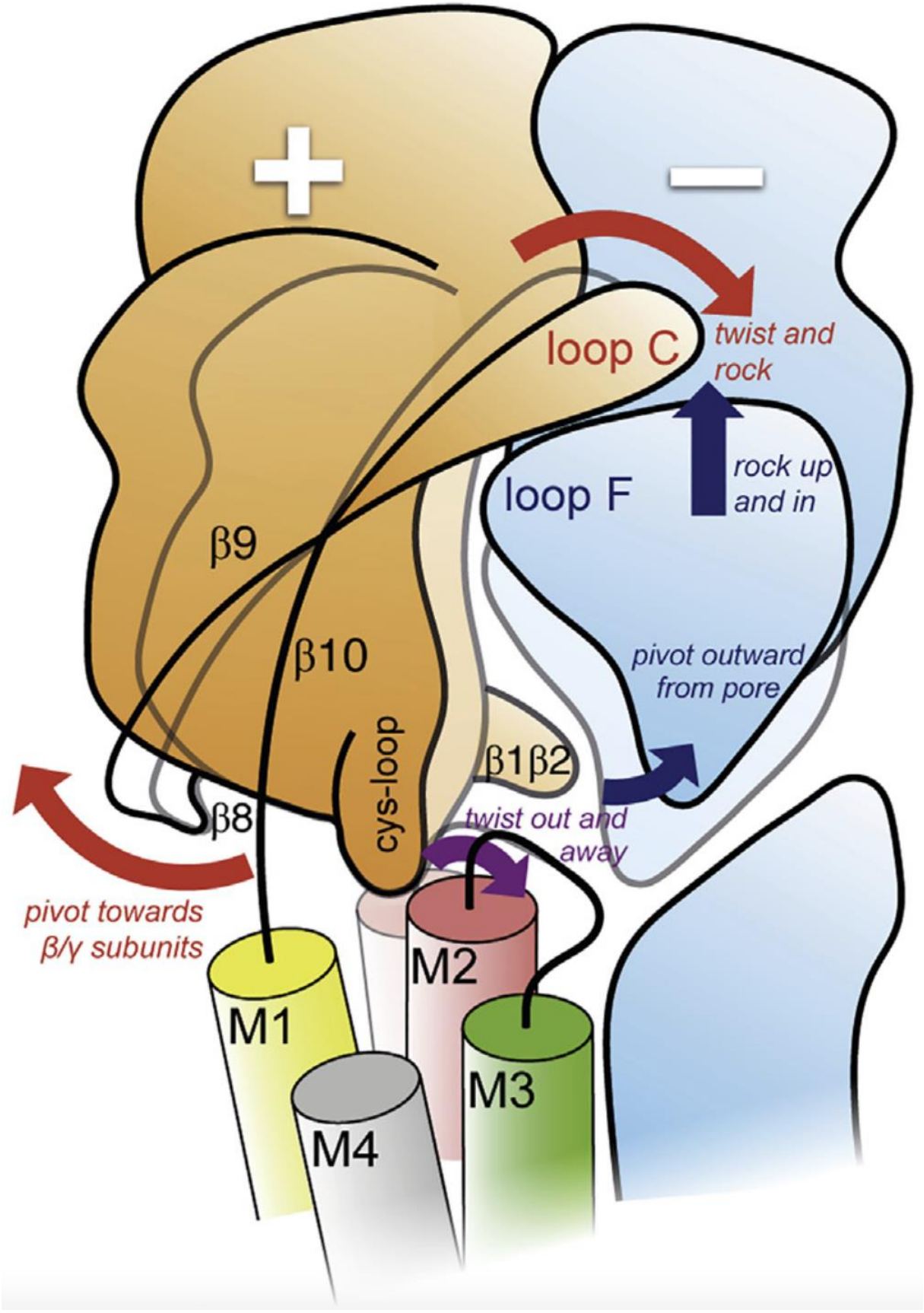
+
−
loop C
twist and rock
loop F
rock up and in
β9
β10
pivot outward from pore
β1β2
cys-loop
β8
twist out and away
pivot towards β/γ subunits
M1
M2
M3
M4

1.3.5 Modulation of nAChR function by lipids

It was evident soon after *Torpedo* nAChR was first purified that its function is highly sensitive to its surrounding membrane environment (Heidmann et al., 1980; Criado et al., 1982; Fong and McNamee, 1986). Reconstituting the receptor into a lipid bilayer can re-establish its activity, but only if the membrane contains specific lipid species that create an environment that supports agonist-activation. When reconstituted in a phosphatidylcholine (PC) membrane containing both cholesterol and anionic lipids, the nAChR is able to undergo agonist induced conformational changes leading to the initial hypothesis that cholesterol and anionic lipids are required for nAChR function (Criado et al., 1982). More detailed functional characterization, however, showed that the inclusion of increasing levels of either cholesterol or the anionic lipid phosphatidic acid (PA) in PC membranes increases the proportion of functional nAChRs (Baenziger et al., 2000; Hamouda et al., 2006a). In fact, several cholesterol analogs can also promote channel function (Sunshine and McNamee, 1992; Addona et al., 2003) suggesting that the nAChR exhibits a low functional specificity for either lipid type.

The modulation of nAChR function by lipids appears to occur predominantly by a conformational selection mechanism. When this idea was first introduced, lipids were thought to modulate the equilibrium between the agonist activatable resting and the non-activatable, desensitized state (Baenziger et al., 2000; Hamouda et al., 2006a). This model was updated in 2009 to include a conformation where agonist binding is "uncoupled" from channel gating. The existence of an uncoupled conformation arose from a comprehensive biochemical/biophysical study, which showed that the nAChR in pure PC membranes is "locked" in a conformation with resting state-like binding affinity for ligands that bind to both the ECD and TMD (daCosta et al., 2009), in contrast to the nAChR in membranes containing PC, PA, which adopts a

predominantly a resting conformation that undergoes ligand-induced conformational transitions to the open and desensitized state.

Although the influence of many different lipid compositions on the nAChR conformational equilibrium have now been documented (daCosta and Baenziger, 2009; daCosta et al., 2009, 2013; Labriola et al., 2010; Sun et al., 2017), the structural basis of how lipid combinations select different conformations remains unknown. Whether by binding to specific sites at the annulus of the nAChR or by modulating the physical properties of the bilayer (Marsh, 1996; Lee, 2004; Levental and Lyman, 2023), changes in the surrounding membrane must alter the energy landscape of the channel by some mechanism(s) (see the Appendix for a more detailed discussion of these topics). The lipid-exposed M4 α-helices in each subunit is an obvious candidate for relaying altered bilayer compositions in altered nAChR function (Barrantes, 2002; daCosta and Baenziger, 2009; Hénault et al., 2015b).

1.3.6 The M4 α-helix as a lipid-sensor

The M4 lipid-sensor model was originally based on photolabeling studies that identified the M4 α-helices as forming the primary contacts with the surrounding membrane (Blanton and Cohen, 1992) and has been supported by the identification of lipid binding sites proximal to M4 in several pLGIC structures (Hénault et al., 2015b; Thompson and Baenziger, 2020b). Mutations in the nAChR M4 α-helices have been shown to influence channel gating (Bouzat et al., 1998, 2000, 2002), and even cause CMS (Shen et al., 2006), further supporting the ability of the M4 α-helices to relay changes in lipid composition to the rest of the channel. One proposed mechanism by which M4 could influence nAChR function is by interacting the the Cys-loop, a structure extending down from the ECD towards the M2-M3 loop that has been implicated in

channel gating (daCosta and Baenziger, 2009). Alternatively, it has been suggested that enhanced interactions between side chains on M4 and the adjacent M3 α-helix can increase the stability of the open state (Domville, 2017). The putative mechanisms by which lipid-induced changes in M4 structure or orientation ultimately alter nAChR function are discussed in more detail below.

The M4-lipid sensor theory has been tested most rigorously in ELIC and GLIC. ELIC, like the nAChR, loses its ability to undergo allosteric transitions in minimal PC bilayers while GLIC remains fully functional (Labriola et al., 2013; Carswell et al., 2015a; Kumar et al., 2020b). Crystal structures of these two pLGICs showed two notable differences in their αM4 helices that could account for their distinct lipid-sensitivities: first, the interface between M4 and the adjacent M1 and M3 α-helices (the M4 – M1/M3 interface) is densely packed with aromatic residues in GLIC, but not ELIC, and second, the M4 C-termini were completely resolved in in GLIC but missing in ELIC, suggesting M4 is dynamic in ELIC (Hilf and Dutzler, 2008; Bocquet et al., 2009). Functional studies led to the conclusion that M4 – M1/M3 inter-helical aromatics interactions in GLIC lead to a tight association of M4 with the remainder of the TMD rendering the M4 – M1/M3 interface less malleable and thus less sensitive to changes in lipid composition (Carswell et al., 2015a; Therien and Baenziger, 2017). Consistent with this hypothesis, alanine mutations of aromatic residues on the M4 α-helices of GLIC to Ala, which should weaken interactions at the M4 – M1/M3 interface, almost invariably lead to losses-of-function. In contrast, the M4 – M1/M3 interface in ELIC exhibits fewer inter-helical aromatic interactions located mainly in the intracellular leaflet of the bilayer. Alanine substitutions of these aromatics typically lead to gains-of function (Hénault et al., 2015a). This led to the suggestion that the aromatic residues at the M4 – M1/M3 interface in ELIC sterically restrict tight M4 – M1/M3

interactions leading to a more malleable interface that render ELIC more sensitive to its surrounding lipid environment. Interestingly, the addition of aromatic interactions in the extracellular leaflet at the M4 – M1/M3 interface not only enhance ELIC function but render ELIC less sensitive to lipids.

A Pro residue sits near the midpoint of the M4 α-helix in ELIC, as well as all anion selective pLGICs, and creates a characteristic kink in the α-helix. When this Pro residue (Pro305) is mutated to Ala, ELIC desensitizes at a much faster rate creating a unique phenotype (Hénault et al., 2015a). Crystal structures show that when ELIC is in its closed conformation, the M4 α-helices are almost always in their kinked conformation, and a high-resolution structure of ELIC in 2019 revealed that a lipid was bound in a pocket framed by this kink in the intracellular leaflet of the bilayer (Hénault et al., 2019). The binding of either PE or PG lipids to this site was proposed to modulate ELIC activity by stabilizing a kinked conformation, a proposition supported by various lines of functional and structural data (Hénault et al., 2019; Tong et al., 2019). More recent studies also propose that the binding of lipids to the extracellular leaflet modulate ELIC desensitization (Petroff et al., 2022). Both lines of evidence suggest the binding of lipids to ELIC modulate M4 dynamics to ultimately shape how ELIC functions.

Although the above mechanisms by which lipid binding adjacent to M4 modulates ELIC function are the most compelling models of lipid-protein interactions for any pLGIC, they are not directly applicable to the nAChR as the nAChR M4 α-helices do not contain a Pro kink. Various mechanisms of lipid modulation in the nAChR have been suggested but they can be generally grouped in two broad mechanisms. It has been suggested that lipid influence function by altering interactions between M4 and either adjacent TMD α-helices or structures in the ECD (Baenziger and Corringer, 2011; Baenziger and daCosta, 2013; Baenziger et al., 2015; Domville,

2017). The latter is especially intriguing as the M4 C-termini extend toward the ECD – TMD interface, a region implicated in the coupling of agonist binding to channel gating. This, along with evidence that a region of the polypeptide backbone that is shielded from solvent in the activatable resting state, but becomes solvent exposed in the uncoupled state, have led to the hypothesis that uncoupling occurs through changes in interactions between the M4 C-termini and the ECD – TMD interface (daCosta and Baenziger, 2009; Hénault et al., 2015b). At the commencement of this thesis, the molecular underpinnings of these models of lipid action at the nAChR remained to be tested. In fact, it still remains to be determined whether lipids exert their effects by binding to specific allosteric sites or through bulk membrane effects (Thompson and Baenziger, 2020a, 2020b; Ananchenko et al., 2022; Cheng et al., 2022; Barrantes, 2023).

1.4 Summary of thesis and objectives

The thesis is presented as a series of four articles that explore how mutations in different regions of the receptor influence channel function, providing mechanistic insight into how lipids influence nAChR function and how agonist binding couples to channel gating. The first three manuscripts of this thesis use similar techniques and the methods for these papers have been presented together in Chapter 2.

When I first entered the lab, my initial goal was to perform alanine scanning mutagenesis and C-terminal deletions of the M4 α-helix in each subunit, with the aim to identify residues on M4 that form interactions with residues on either the remainder of the TMD with the ECD that are critical for channel function, and that might be modulated by lipids. Chapter 3 contains the first manuscripts in this thesis. In this paper I assess the role of the M4 α-helix from the α subunit (αM4) in channel function. I also used homology modelling and coevolutionary analysis

to identify potential interactions between M4 and the remainder of the TMD that are important to channel function, and then test these putative interactions using functional assays.

Chapter 4 contains the second manuscript in this thesis and builds upon the previous chapter. This manuscript characterizes the M4 α-helices in each of the remaining subunits of the nAChR to identify putative interactions that play a role in lipid-sensing. M4 alanine scans, C-terminal deletions, and aromatic substitutions were performed in each subunit individually, and in some cases cumulatively, to facilitate a comparison. I show that the distinct pathways that modulate nAChR function from each subunit are independent and thus likely add together to produce the exquisite lipid-sensing capability of the nAChR.

In chapter 5 the third manuscript of this thesis is presented. In this chapter, I used the new *Torpedo* nAChR structural models as templates to investigate the mechanisms by which the ECD communicates with the TMD to open the channel pore. Given the new structures, I first set out to identify previously unappreciated interactions that regulate allosteric coupling between the ECD and TMD. Despite screening close to 300 mutants, however, I failed to identify any new interactions that regulate channel gating in the context of a bevel-gear type allosteric mechanism. Instead, the data suggest that there is local subunit conformational asymmetry in the apo state at the ECD – TMD interface, with agonist binding releasing this asymmetry so that the nAChR adopts a more symmetric open conformation. I present a release of conformational asymmetry model that not only defines gating in the muscle nAChR but reconciles the extensive body of mutagenesis data pertaining to the roles of residues at the ECD – TMD domain interface. Furthermore, the same subunit transitions are observed in other pLGIC structures, albeit with subtle differences expected for homomeric versus heteromeric pLGICs.

The sixth Chapter of this thesis contains the final manuscript from my PhD with research conducted during a research stay in Hugues Nury's lab in Grenoble, France. I combine fluorescence-based assays with single particle cryo-electron microscopy (Cryo-EM) to obtain high resolution structures of the nAChR in apo, agonist bound, and intermediate conformations. The structures reveal that a singly occupied conformation of the nAChR exists as a presumptive intermediate between closed and channel open states. This mono-liganded structure is the first of its kind for any pLGIC and suggests that heterometric pLGICs may activate in a subunit sequential fashion rather than a domain sequential fashion often observed for homomeric pLGICs.

Chapter 7 presents a discussion of how the data in chapters 3-6 advance our understanding of pLGIC structure and function. I highlight the main conclusions from my work and provide context into how these results may be used as a basis to aid in the development of drugs for human disease. I also provide unpublished cryo-EM structures of the nAChR that were obtained during the final year of my thesis research while I was an exchange student in the lab of our collaborator, Dr. Hugues Nury. During this time, I developed a new data analysis framework for isolating single particles of the nAChR with only one ligand bound to the agonist site. I solved a structure of this intermediate conformation and discuss the new insight that this structure lends to our understanding of allosteric mechanisms in the nAChR.

Finally, Chapter 8 lists the references within the thesis and Chapter 9, the appendix, presents two first-author review articles that I completed during the COVID lockdown of my PhD thesis.

Chapter 2. Materials and Methods

2.1 Bacterial strains, site-directed mutagenesis, and cDNA

The following nAChR-pRBG4 cDNA clones were kindly provided by Steven Sine: Human α1, β1, γ, δ, and ε, *Torpedo* α1, β1, γ, and δ. Each nAChR subunit cDNA was transferred into the pcDNA3.1 vector as an EcoRI fragment. Site-directed mutagenesis on these constructs were performed using QuikChange Lightning kits (Agilent). Following PCR, plasmids were transformed into *E. coli* Dh5α XL1-Blue/Gold cells (Agilent) and these cells were then grown in super optimal broth (SOB: 0.5% (w/v) yeast extract, 2% (w/v) tryptone, 10 mM NaCl, 2.5 mM KCl, 20 nM $MgSO_4$) for 1 hour at 37°C. The cells were then plated on agar plates containing ampicillin for 12-18 hours at 37°C. Individual colonies from these plates were then inoculated in 5-7 mL of ampicillin containing LB and grown over night in a shaking incubator at 37°C. cDNA was then extracted and purified from the resulting cultures using a miniprep kit (Qiagen). The sequences of all constructs used were verified by Sanger sequencing (uLaval).

Once the sequences of the WT and mutant cDNA was confirmed, the plasmids were linearized using the restriction enzyme XhoI (New England Biolabs) just following the end of the coding sequence. Linearized DNA was then purified using a PCR purification kit (Qiagen). Mature cRNA was then synthesized using the mMESSAGE mMACHINE T7p *in vitro* transcription kit (Ambion). cRNA for the desired subunits were then mixed at a 2:1:1:1 ratio of α:β:δ:γ/ε at the desired concentration for oocyte injection. A total of 12.5 ng of cRNA was used for expressing the WT nAChR and up to 125 ng was injected for mutants that expressed poorly. All experiments working with RNA were performed on ice. All cDNA and cRNA was stored at -20°C.

2.2 Animal Protocols

Ovulating female *Xenopus laevis* were purchased from Nasco (Fort Atkinson, Wisconsin) and were housed in the animal care center of University of Ottawa, Faculty of Medicine. The experimental protocol involving the use of these animals has been approved by the Animal Care Committee of University of Ottawa (OHRI-2092). In some cases, donor frogs were primed with 100 IU of PMSG (500IU/kg body weight) a week ahead of oocyte retrieval. Ovulating females were anesthetized by immersing in water containing MS222 (3-aminobenzoic acid ethyl ester methanesulfonate salt, 2g per liter of water). After 20 minutes of immersion, a pinch test was performed to confirm the frog was fully anesthetized. Sacrifice was performed by guillotine, followed by pithing. An incision was then made through the skin in the lower half of the anterior abdominal wall, to both sides of the midline. The connective tissue and muscle layer under the skin are also opened using small scissors, thus making an incision into the coelomic cavity. Ovaries were then extracted using a pair of forceps and transferred to a falcon tube containing ND96- buffer (5 mM HEPES, 96 mM NaCl, 2 mM KCl, 1 mM $MgCl_2$, 2 mM pyruvate). The carcass was then stored at -20°C until disposal by incineration.

To obtain individual oocytes for electrophysiology, oocyte lobes were cut into smaller fragments using a scissors and defolliculated enzymatically using deflocculation buffer (ND96- buffer, 1 mg/mL collagenase B (Millipore Sigma), and 1 mg/mL trypsin inhibitor (ThermoFisher Scientific) for 2 hours at room temperature under constant stirring. The defolliculation buffer was then gradually removed by washing the oocytes in ND96+ buffer (5 mM HEPES, 96 mM NaCl, 2 mM KCl, 1 mM $MgCl_2$, 1 mM $CaCl_2$, 2 mM pyruvate) for several iterations. The oocytes were then allowed to stir for an additional hour at room temperature under constant

stirring with the buffer being periodically replaced until clear. Healthy oocytes were then individually selected from this collection for cRNA injection.

2.3 Electrophysiology

Defolliculated oocytes were injected with the indicated amount of mRNA and allowed to incubate for 2 to 7 days at 16°C in ND96+ buffer (5 mM HEPES, 96 mM NaCl, 2 mM KCl, 1 mM $MgCl_2$, 1 mM $CaCl_2$, 2 mM pyruvate). Injected oocytes were placed in a RC-1Z oocyte chamber (Harvard Apparatus) containing HEPES buffer (96 mM NaCl, 2 mM KCl, 1.8 mM $BaCl_2$, 1 mM $MgCl_2$, 10 mM HEPES, pH 7.3). Whole-cell currents were recorded using a two-electrode voltage-clamp apparatus (OC-725C oocyte clamp; Harvard Apparatus). The whole-cell currents were recorded while the appropriate buffer flowed through the oocyte chamber at a rate of 15-20 mL/min. Currents through the plasma membrane in response to drug concentration jumps (from 0 μM up to the indicated values) were measured with the transmembrane voltage clamped at voltages ranging from +60 mV to -120 mV. For most experiments, the drug used was acetylcholine (acetylcholine chloride, Sigma) and the transmembrane voltage was held at -60 mV. Any conditions that differed from these values are clearly indicated where the data is presented.

Dose responses for each mutant were acquired from at least two different batches of oocytes. Each individual dose-response experiment was fit with a variable slope sigmoidal dose response, and the individual EC_{50} (the concentration of ACh required to produce a half maximal peak current response) and Hill coefficients from each experiment averaged to give the values ± SD. Tables in manuscript 2 report pEC_{50} ($-\log EC_{50}$) values. A minimum of n=8 experiments were collected wherever possible. For the presented dose-response curves, the individual dose

responses for each experiment were normalized and each data point averaged. Curve fits of the averaged data are presented, with the error bars referring to the SE. Statistical significance was tested using a one-way ANOVA, followed by Dunnet's post hoc test. Degrees of freedom (DF) and F values are reported for each ANOVA test performed in manuscript 3.

2.4 Mutant cycle analysis

To determine the extent to which two or more residues contribute to channel function, the EC_{50} values obtained from the mutagenesis experiments were cast as mutant cycles:

$$\Omega = \frac{Observed\ fold\ change}{Calculated\ fold\ change}$$

where the observed fold change is the EC_{50} for a mutant where multiple residues are mutated simultaneously dived by wild-type and the calculated fold change is the expected fold change if each of the individual mutations effect function independent, i.e. the product of the fold changes for each individual mutant. In the case of a double mutant, this formula simplifies to:

$$\Omega = \frac{EC_{50}(WT) * EC_{50}(mut_{1,2})}{EC_{50}(mut_1) * EC_{50}(mut_2)}$$

where WT is wild type, mut_1 and mut_2 are the two single mutants, and $mut_{1,2}$ is the corresponding double mutant. A pair of residues that do not influence function through the same mechanism are completely independent. Their effects on the EC_{50} value will then be multiplicative yielding a value of Ω=1. The greater the deviations from independence the larger more the Ω value will deviate from unity. In the experiments conducted in this thesis, the mutations performed are generally expected to alter EC_{50} values predominately by altering the rate constants associated with channel gating rather than those associated with agonist binding making Ω a measure of how multiple mutations influence the energetics of channel gating. In

the third manuscript of this thesis, Ω values derived from our whole cell measurements are converted to energy values using the following equation:

$$\Delta G = RT ln \Omega$$

where R is the universal gas constant, T is the temperature in Kelvin, and ΔG is the free energy contribution of the mutations toward channel function. It is important to note that our ΔG values are not quantitative as the Ω values used to obtain these energies do not relate to a change in a single equilibrium constant in the kinetic scheme. These values are instead intended to facilitate the comparison of the results when the interaction of interest facilitates (negative ΔG values) or deters (positive ΔG values) channel function, respectively.

2.5 Cell culture

HEK293T cells were maintained in a humidified atmosphere at 37°C with 5% CO_2, in Dulbecco's modified Eagle's medium supplemented with 5% heat-inactivated adult bovine serum, 5% bovine calf serum, and 1% antibiotic–antimycotic (Gibco). Cells were plated in either 6-well dishes for the membrane potential assay or 12 cm dishes for the radioligand-binding assay at a density of 1.2 million cells/well. Transient transfection using polyethyleneimine proceeded with a 2:1:1:1 ratio of nAChR subunits, α1:β1:δ:ε, adding up to a total of 2 μg of DNA for the membrane potential assay or 20 μg for the radioligand-binding assay. After 24 h, the cells were washed with 1× PBS at pH 7.4 and detached using 0.05% trypsin–EDTA, before they were resuspended in Dulbecco's modified Eagle's medium containing 1% fetal bovine serum/bovine calf serum and 1% antibiotic–antimycotic. Cells destined for the membrane potential assay were then seeded in a black-walled, clear-base, poly-D-lysine–coated, 384-well plate at a density of 45,000 cells/well. Cells destined for the radioligand-binding assay were

transferred in 15 mL Falcon tubes, centrifuged at 1000 rpm for 2 min, and resuspended in 3.5 mL of phosphate ringer buffer (PRB; 140 mM KCl, 5.4 mM NaCl, 1.8 mM $CaCl_2$, 1.7 mM $MgCl_2$, 25 mM HEPES, 30 mg/L bovine serum albumin, pH = 7.4).

2.6 Membrane potential assay

Changes in membrane potential in HEK293T cells transfected with WT and mutant nAChRs were measured using the FLIPR Tetra system (Molecular Devices). A voltage-sensitive dye, DiSBAC1(3) (FIVEphoton Biochemicals), was prepared by dissolving the powder in dimethyl sulfoxide. An assay buffer containing 2.5 μM DiSBAC1(3), 200 μM Direct Blue 71 (Sigma–Aldrich), and 1× Hanks' balanced salt solution, 20 mM HEPES, pH 7.4 was freshly prepared as well. Cell medium was removed from the 384-well plate and replaced with 20 μL of the assay buffer. Cells were then incubated with the assay buffer at 37°C for 30 min before using the FLIPR Tetra system to run the experiment. Prior to any additions, baseline fluorescence levels ($\lambda_{excitation}$ = 510–545 nm, $\lambda_{emission}$ = 565–625 nm) were measured every 2 s for 20 s. At 20 s, 10 μL of each ACh concentration was added onto each well, and the emitted fluorescence was monitored every 2 s for a total of 1000 s. In each experiment, four wells for each concentration were averaged to yield the presented curves in Fig. 4.7. The change in fluorescence for each ACh concentration was taken as the difference in fluorescence at 1000 s and the fluorescence prior to ACh addition. The change in fluorescence at each ACh concentration was then normalized to the maximum change in fluorescence and fit with a variable slope sigmoidal dose–response curve. Plots were created using GraphPad Prism, and the individual pEC_{50} ($-\log EC_{50}$) values and Hill coefficients from each experiment averaged to give the presented values ± standard deviation.

2.7 Radioligand binding assays

Cell surface expression was measured where indicated on intact oocytes using [^{125}I]-α-bungarotoxin ([^{125}I]-α-BTX; PerkinElmer Life Sciences (Boston, MA)). Oocytes were injected with cRNA (125 ng) and allowed to express for 2 days. A minimum of four oocytes for each mutant were tested via TEVC to determine activity levels, then incubated with occasional shaking, for 2 h at room temperature in MOR2 buffer (82 mM NaCl, 2.5 mM KCl, 1mM Na_2HPO_4, 5 mM $MgCl_2$, 0.2 mM $CaCl_2$ and 5 mM HEPES, pH 7.4) with 2.5 nM [^{125}I]-α-BTX (143.8 Ci/mmol) and 1 mg/mL BSA. After incubation, the oocytes were washed 5 times with 2 mL of MOR2 buffer. [^{125}I]-α-BTX binding was quantified by γ-counting. Nonspecific binding was determined by the amount of toxin bound to mock-injected oocytes under the same conditions. Data presented in the tables was normalized to the number of counts for the WT nAChR. Mutants that expressed significantly more than mock injected oocytes were considered expressed. Statistical significance was tested using a one-way ANOVA, followed by Dunnet's post hoc test, with a threshold for significance of $p < 0.001$.

Cell surface in HEK293T cells was also determined using the high-affinity radiolabeled toxin, [^{125}I]-α-BTX. About 450 μL of HEK293T cells suspended in PRB were transferred into 2 mL Eppendorf tubes for each replicate of each mutant in the experiment. These cells were then rotated for 1 h at room temperature with a final concentration of 25 μM α-BTX (1:100 ratio of radiolabeled to non-radiolabeled toxin). Following incubation, cells were pelleted and excess α-BTX removed before the cells resuspended in toxin-free PRB. Using a filtration manifold, each sample was filtered through glass GF/ C filters (Whatman) for 5 s, followed by 3 × 2 mL washes with PRB. Filters were then allowed to dry under suction for an additional 15 s to remove excess

buffer. Bound [^{125}I]-α-BTX was then quantified by γ counting each filter paper, and non-specific binding was determined using the same procedure with untransfected cells.

2.8 Homology models and coevolutionary analysis

Homology models of each human adult muscle nAChR subunit presented in manuscript 1 were created based on the 4.0 Å resolution structure of the muscle nAChR from *Torpedo* (PDB: 2BG9) (Unwin, 2005), a revised 2BG9 structure with a corrected register of amino acids in the M1-M2 loop (Smelt et al., 2018), the 3.3 Å resolution structure of the α3β4 nAChR (PDB: 6PV7) (Gharpure et al., 2019), and the 2.7 Å resolution structure of the muscle nAChR from *Torpedo* (PDB: 6UWZ) (Rahman et al., 2020a) using the Swiss-Model online server (https://swissmodel.expasy.org/). Evolutionary couplings were determined using the online EVolutionary couplings server (https://evcouplings.org/).

2.9 Molecular dynamics simulations

Recently solved high resolution structures of the apo (PDB: 7QKO) and nicotine-bound (PDB: 7QL5) states of the nAChR were used as input structures for simulations (Zarkadas et al., 2022). Systems were set up using CHARMM-GUI membrane builder (Jo et al., 2008). Protein structures were embedded in a 140x140 Å pure POPC bilayer, with a box length of 190 Å, and solvated in TIP3P water and a NaCl concentration of 150 mM. Disulfide bonds were preserved as in the original structure. *In-silico* mutations were created using the CHARMM-GUI mutation tool. Simulations were performed using the GROMACS 2021 simulation engine (van der Spoel et al., 2005; Abraham et al., 2015) and the CHARMM36 forcefield (Best et al., 2012; Huang and Mackerell, 2013) was applied. Each system was energy minimized for 5000 steps using the

steepest descent algorithm or until a maximum force of 1000 $kJmol^{-1}nm^{-1}$ on any atom was reached. Equilibration was performed using the standard CHARMM-GUI protocol. Briefly, systems were equilibrated using the NPT ensemble for a total of 750 ps with a gradual lowering of protein and membrane position restraints. Temperature was held at 303.15 K using the Berendsen thermostat (Berendsen et al., 1984). For the last four steps of equilibration, pressure was held at 1 bar using the Berendsen barostat (Berendsen et al., 1984). Production runs were performed in the NPT ensemble with temperature set to 303.15 K using the Nose-Hoover thermostat (Hoover, 1985; Nosé, 2002) and pressure held at 1 bar using the Parinello-Rahman barostat (Parrinello and Rahman, 1981). Covalent bonds including hydrogen atoms were constrained using the LINCS algorithm (Hess et al., 1997). The Verlet cut-off scheme (Verlet, 1967) was used throughout all steps with a force-switch modifier starting at 10 Å and a cut-off of 12 Å. The particle mesh Ewald (PME) (Darden et al., 1993; Essmann et al., 1995) method was used for long-range electrostatics, and a cut-off of 12 Å was used for short-range electrostatics. The same simulation protocol was used for simulations of both states of the WT and mutant nAChR. Each system was simulated for 100 ns in triplicate. The MDAnalysis python package (Michaud-Agrawal et al., 2011; Gowers et al., 2016) was used to create in-house scripts for simulation analysis. The distance between backbone CA atoms of the αV255 residues in was used as a measure of pore collapse. Plots were prepared using the python package matplotlib (Hunter, 2007).

Chapter 3. Manuscript 1: The functional role of the αM4 transmembrane helix in the muscle nicotinic acetylcholine receptor probed through mutagenesis and co-evolutionary analyses

Thompson, M.J., Domville, J.A., and Baenziger, J.E. (2020). The functional role of the αM4 transmembrane helix in the muscle nicotinic acetylcholine receptor probed through mutagenesis and co-evolutionary analyses. J. Biol. Chem. *295*, 11056–11067.
Adapted as a post-print from J. Biol. Chem., https://doi.org/10.1074/jbc.ra120.013751.

3.1 Preface

This manuscript is the first of two first author publications in this thesis that are focused on elucidating the structural basis of lipid modulation in the muscle-type nAChR. Work in the lab before I started had focused on understanding lipid-sensing in the context of the prokaryotic pLGICs ELIC and GLIC. Some of the TEVC data for the M4 Ala-scans, aromatic substitutions, and C-terminal deletions were collected by Jaimee A. Domville prior to my arrival in the lab, but an interpretation of what the data was telling us was lacking. A partial reason for this was that, at the time, we were without a high-resolution structure of the nAChR making a structural interpretation of the data difficult. To overcome this, I performed a series of co-evolutionary analyses that are the foundation of protein prediction algorithms that are now commonly used (ex. AlphaFold). Using this information, I was able to hypothesize how different mutations were influencing nAChR function. To test these hypotheses, I extended and completed the characterization of all mutations, tested coevolved pairs for functional interdependence, and assessed how multiple mutations along the M4 α-helices summed together to effect nAChR function. I then critically assessed the data and framed it in the existing literature to clearly define what was learned and how it contributed to our understanding of lipid-sensing the αM4 α-helix. I the wrote the initial draft of the manuscript, work alongside Dr. Baenziger to editing and finalize the manuscript and created all the figures and tables.

3.2 Abstract

The activity of the muscle-type *Torpedo* nicotinic acetylcholine receptor (nAChR) is highly sensitive to lipids, but the underlying mechanisms remain poorly understood. The nAChR transmembrane α-helix, M4, is positioned at the perimeter of each subunit in direct contact with lipids and likely plays a central role in lipid-sensing. To gain insight into the mechanisms underlying nAChR lipid sensing, we used homology modeling, co-evolutionary analyses, site-directed mutagenesis and electrophysiology to examine the role of the α-subunit M4 (αM4) in the function of the adult muscle nAChR. Ala substitutions of most αM4 residues, including those in clusters of polar residues at both the N and C termini, and deletion of up to 11 C-terminal residues had little impact on the agonist-induced response. Even Ala substitutions of co-evolved pairs of residues at the interface between αM4 and the adjacent helices, αM1 and αM3, had little effect, although some impaired nAChR expression. On the other hand, Ala substitutions of Thr422 and Arg429 caused relatively large losses of function, suggesting functional roles for these specific residues. Ala substitutions of aromatic residues at the αM4-αM1/αM3 interface generally led to gains of function, as previously reported for the prokaryotic homolog, the *Erwinia chrysanthemi* ligand-gated ion channel (ELIC). The functional effects of individual Ala substitutions in αM4 were found to be additive, although not in a completely independent manner. Our results provide insight into the structural features of αM4 that are important. They also suggest how lipid dependent changes in αM4 structure ultimately modify nAChR function.

3.3 Introduction

Pentameric ligand-gated ion channels (pLGICs) are sensitive to a variety of allosteric modulators that act on the transmembrane domain (TMD), including lipids (Nury et al., 2011; Baenziger et al., 2015; Barrantes, 2015; Forman et al., 2015; Thompson and Baenziger, 2020b). In reconstituted membranes, the prototypic pLGIC, the *Torpedo* nicotinic acetylcholine receptor (nAChR), requires cholesterol and anionic lipids for optimal activity. These lipids promote function by stabilizing the nAChR in an agonist-activatable conformation and by enhancing transitions between conformational states (Criado et al., 1982, 1984; Fong and McNamee, 1986; Baenziger et al., 2000; daCosta et al., 2002; Hamouda et al., 2006a; daCosta et al., 2009). In the absence of both lipids, the nAChR adopts an uncoupled conformation that binds agonist, but does not normally transition to open or desensitized states (Baenziger et al., 2008; daCosta and Baenziger, 2009; daCosta et al., 2013).

Structures of the nAChR and other pLGICs place the fourth transmembrane α-helix (M4) of each subunit at the periphery of the TMD in contact with lipids, suggesting an important role for M4 in lipid-sensing (Antollini et al., 2005; Williamson et al., 2005; Xu et al., 2005; Hénault et al., 2015b). A lipid-sensing role for M4 is supported further by the observation that mutations along M4 influence channel function (Li et al., 1990; Lee et al., 1994; Lasalde et al., 1996; Bouzat et al., 1998, 2000). In addition, lipids bind to the interface between M4 and the adjacent TMD α-helices, M1 and M3, in several pLGIC structures (Bocquet et al., 2009; Gharpure et al., 2019; Hénault et al., 2019; Laverty et al., 2019; Rahman et al., 2020a; Thompson and Baenziger, 2020b).

Lipids likely influence pLGIC function by altering interactions between M4 and M1/M3 (Carswell et al., 2015a, 2015b). One model proposes that altered M4–M1/M3 interactions

modulate contact between the M4 C terminus and the β6-β7 loop (the Cys-loop in eukaryotic pLGICs), a structure at the interface between the extracellular domain (ECD) and TMD that plays an important role translating agonist binding into channel gating (Grutter et al., 2005; Lee and Sine, 2005; Lummis et al., 2005; Jha et al., 2007). This model is supported by the observation that a lipid bridges interactions between M4 and the β6-β7 loop/Cys-loop in the prokaryotic *Gloeobacter violaceus* ligand-gated ion channel, GLIC, with mutations of implicated residues impairing both function and expression (Hénault et al., 2015a). The M4 C terminus is also important in the expression and/or function of the α4β2 nAChR, the 5-HT_{3A} receptor, the ρ1 $GABA_A$ receptor and a α7/5-HT_3 receptor chimera (Pons et al., 2004; Butler et al., 2009; Alcaino et al., 2017; Cory-Wright et al., 2018), and has been implicated in neurosteroid-induced potentiation of both the neuronal α4β2 nAChR and the $GABA_A$ receptor (Paradiso et al., 2001; Hosie et al., 2006). On the other hand, specific interactions between M4 and the β6-β7loop/Cys-loop are not critical to function in the *Erwinia chrysanthemi* ligand gated ion channel, ELIC, suggesting that distinct mechanisms may underlie lipid-sensing in different pLGICs (see for example (Domville and Baenziger, 2018)).

To better understand lipid-sensing, we and others have used Ala-scanning mutagenesis to identify residues in M4 that play an important role in function (Haeger et al., 2010; Hénault et al., 2015a; Cory-Wright et al., 2018; Tang and Lummis, 2018; Mesoy et al., 2019; da Costa Couto et al., 2020). While these studies have been informative, they have all focused on homomeric pLGICs. An intriguing question that remains to be addressed is how the M4 α-helix from different subunits of a heteromeric pLGIC influences channel function and thus participates in lipid-sensing. As a first step to addressing this question, we use here a combination of mutagenesis, evolutionary couplings and two electrode voltage clamp electrophysiology to

explore the functional role of M4 from the α subunit (αM4) of the human adult muscle nAChR ($\alpha_2\beta\varepsilon\delta$). Our data reveal several unique features regarding the role of αM4 in function and provide a structural basis for understanding the lipid sensitivity of the muscle type nAChR.

3.4 Results

3.4.1 Structural models of the human muscle α subunit

To properly interpret functional data derived from mutations in αM4 of the human adult muscle nAChR, a 3D structure that accurately defines the interactions that occur between αM4 and both αM1/αM3 and lipids is required. In the absence of such a structure, we first generated homology models based on the 4 Å resolution *apo* structure of the *Torpedo* muscle-like nAChR (referred to as the 2BG9 *Torpedo* model), a revised *Torpedo* nAChR structure with a corrected sequence register in αM2/αM3 and a 3.3 Å resolution nicotine-bound structure of the neuronal α3β4 nAChR (Unwin, 2005; Newcombe et al., 2018; Gharpure et al., 2019). After the first submission of this manuscript, an α-bungarotoxin bound structure of the *Torpedo* nAChR was solved at 2.7 Å resolution (Rahman et al., 2020a). The new 6UWZ *Torpedo* structure reveals several novel features relevant here, including a corrected register in the fitting of the amino acid sequence into αM2/αM3 (Mnatsakanyan and Jansen, 2013), a short αMX helix at the periphery of the αM4 N terminus and an αM4 helix that is both contiguous with the intracellular αMA helix and rotated about its long axis to define different side chain projections towards both αM1/αM3 and lipids. The rotation of αM4 is surprising because five residues (Cys412, Met415, Cys418, Thr422 and Val425) that are labeled by the lipophilic photo-reactive probe, 3-trifluoromethyl-3-(*m*-[^{125}I]iodophenyl)diazirine ([^{125}I]-TID) and that define the αM4 – lipid interface in the *Torpedo* 2BG9 structure (Blanton and Cohen, 1992) now project towards αM1/αM3. While the positions of these residues in the new 6UWZ *Torpedo* structure are difficult to reconcile with the [^{125}I]-TID labeling, they are supported by the structures of other neuronal nAChRs (Morales-Perez et al., 2016; Walsh et al., 2018), as well as by an identified

interaction that occurs between αM1 Ser226 and αM4 Thr422 during channel function (Bouzat et al., 2000; Domville and Baenziger, 2018). The hydrogen bond donor/acceptor distances between Ser226 and Thr422 are 11.1 and 7.1 Å in the 2BG9 and 6UWZ *Torpedo* structures, respectively. The new 6UWZ *Torpedo* structure thus requires a smaller re-orientation of αM1/αM4 upon channel gating to bring Ser226 and Thr422 in close contact.

Note that the 2BG9 *Torpedo* structure was solved from cryo-electron microscopic images obtained from native *Torpedo* synaptosomes, while the 6UWZ *Torpedo* structure was solved from images obtained using nAChRs that were detergent solubilized from native *Torpedo* membranes, affinity purified and then reconstituted into lipid nanodiscs. Given the high resolution of the 6UWZ *Torpedo* structure and structures of other neuronal nAChRs, we have re-interpreted our mutagenesis data primarily in terms of a homology model based on the 6UWZ *Torpedo* structure (referred to as the 6UWZ *Torpedo* model), as shown in Figs. 3.1 and 3.2. Given the strength of the [^{125}I]-TID labeling data, however, we considered a speculative possibility that αM4 undergoes a reorientation during solubilization/affinity purification/nanodisc reconstitution, and thus have taken into account the orientation of αM4 defined in the 2BG9 *Torpedo* model.

Figure 3.1 Structure of the human αM4

A side view of the 2.7 Å cryo-electron microscopy structure of the *Torpedo* nAChR (PDB: 6UWZ) is shown on the left. A zoomed in view of the TMD of a human αM4 homology model, based on the 6UWZ structure, is shown on the right in two different orientations. Side chains are shown in ball and stick representation colored according to residue type: aromatic, yellow; polar/hydrogen bonding, green; positive, blue; negative, red; aliphatic, tan). Sequences of the M1, M3, and M4 helices from the human α1 nAChR are shown along the top with the helical regions boxed.

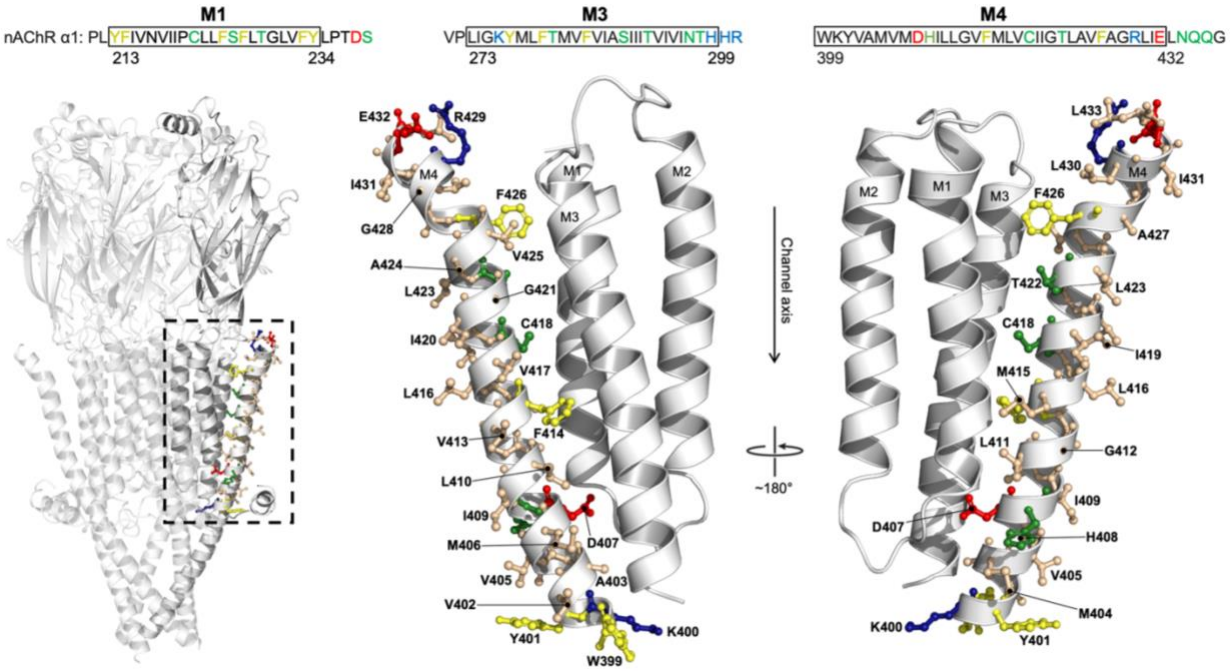
M1
nAChR α1: PLYFIVNVIIPCLLFSFLTGLVFYLPTDS
213
234
M3
VPLIGKYMLFTMVFVIASIIITVIVINTHHR
273
299
M4
WKYVAMVMDHILLGVFMLVCIIGTLAVFAGRLIELNQQG
399
432
E432
R429
I431
M4
G428
F426
M1
M3
M2
A424
V425
L423
G421
C418
I420
V417
L416
F414
V413
L410
I409
M406
D407
V405
A403
V402
Y401
K400
W399
Channel axis
~180°
L433
L430
M4
I431
M2
M1
M3
F426
A427
T422
L423
C418
I419
M415
L416
L411
G412
I409
D407
H408
V405
M404
K400
Y401

Figure 3.2 Orientation of residues on αM4 in 2BG9 *Torpedo* homology model
Cartoon representations of the TMDs of the 2BG9 *Torpedo* model shown from two transmembrane views rotated ~180° around the channel axis. Residues are shown in ball and stick representation and are colored as in Figure 3.1.

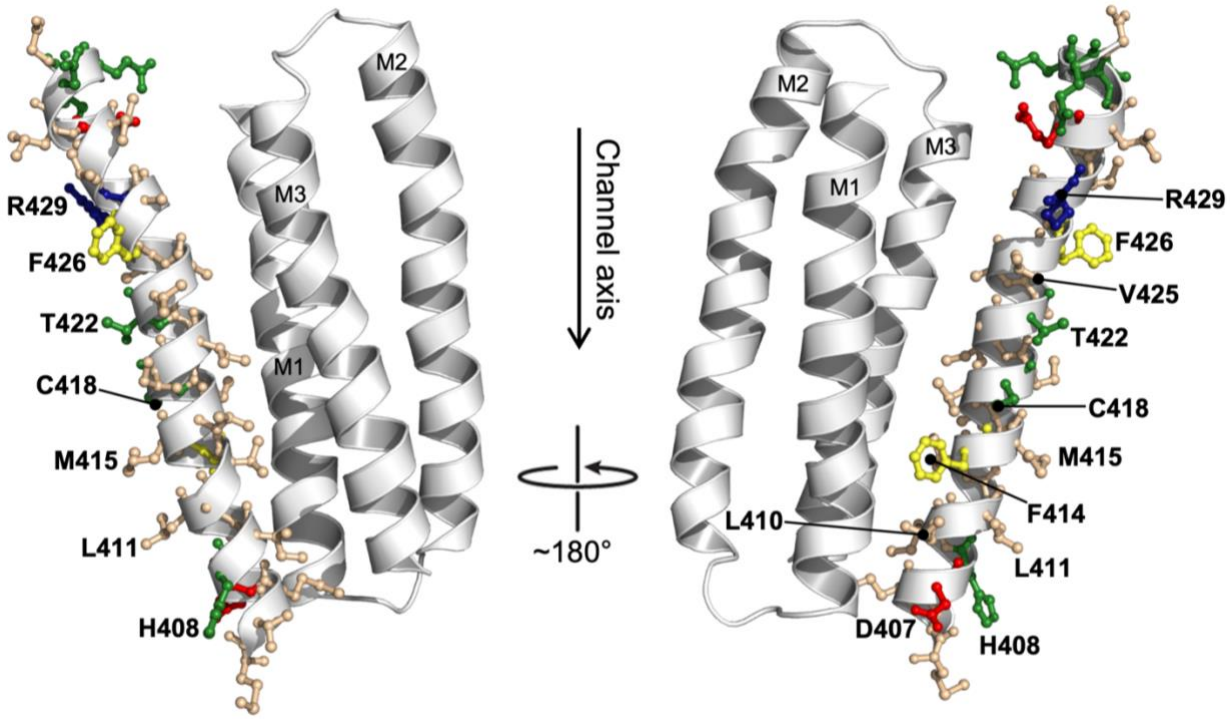
M2
M3
M1
R429
F426
T422
C418
M415
L411
H408
Channel axis
~180°
M2
M3
M1
R429
F426
V425
T422
C418
M415
F414
L410
L411
D407
H408

3.4.2 A co-evolutionary map of αM4–αM1/αM3 interactions

We used a co-evolutionary approach to test further our two homology models and to identify potential interactions at the αM4 – αM1/αM3 interface that play a role in channel function. In the co-evolutionary approach, primary amino acid sequences of related proteins from various organisms are aligned to identify pairs of residues that have co-evolved. A probability score is given to every pair of residues in the sequence, with each probability score related to the proportion of sequences in which that residue pair has evolved together through the evolutionary timeline. This approach has been shown to successfully predict residue pairs in close physical proximity in a variety of proteins (Marks et al., 2011, 2012).

Nine co-evolved pairs with probability scores of greater than 90% were identified at the αM4-αM1/αM3 interface: four pairs at the αM1 - αM4 interface (Ile219/Val425 (100%), Gly230/Leu411 (99.6%), Phe233/Phe414 (99.8%) and Tyr234/Leu411 (100%)) and five at the αM3 - αM4 interface (Tyr277/Thr422 (97.0%), Phe280/Gly421 (100%), Thr281/Cys418 (100%), Phe284/Val417 (98.5%) and Thr298/Met406 (99.5%)). Very few co-evolved pairs could be identified between αM4 and the Cys-loop, although this may reflect the extreme conservation of the Cys-loop rather than the lack of interactions between the two.

Each of the four co-evolved pairs of residues at the αM1 - αM4 interface are relatively close to each other in both homology models, although Ile219/Val425 and Phe233/Phe414 are slightly closer in the 2BG9 *Torpedo* model, while Gly230/Leu411 and Tyr234/Leu411 are closer in the 6UWZ *Torpedo* model (Fig. 3.3; Table 3.1). In contrast, the 6UWZ *Torpedo* model places four of the five co-evolved pairs of residues at the αM3-αM4 interface in much closer proximity than the 2BG9 *Torpedo* model. The large distance between co-evolved pairs of residues at the αM3 - αM4 interface in the *Torpedo* 2BG9 model provides further evidence that there is an error

in the register of the amino acid sequence in both αM2 and αM3, as confirmed in the 6UWZ *Torpedo* structure.

Figure 3.3 Co-evolved residues on αM4 and αM1 or αM3

Co-evolved residues on αM4 - αM1 (A and B) and αM4 - αM3 (C and D) are mapped onto the 2BG9 *Torpedo* (A and C) and the 6UWZ *Torpedo* (B and D) homology models of the human muscle α subunit. Each panel shows a top view of the TMD from the extracellular surface (top) and a side view from within the membrane (bottom). Residues are shown as ball and stick representation and colored according to the co-evolved residue pairs: Ile219 - Val425, brown; Gly230 - Leu411, cyan; Phe233 - Phe414, purple; Tyr234 – Leu411, cyan; Tyr277 - Thr422, dark blue; Phe280 - Gly421, red; Thr281 - Cys418; green; Phe284 - Val417, yellow; and Thr298 - Met406, black.

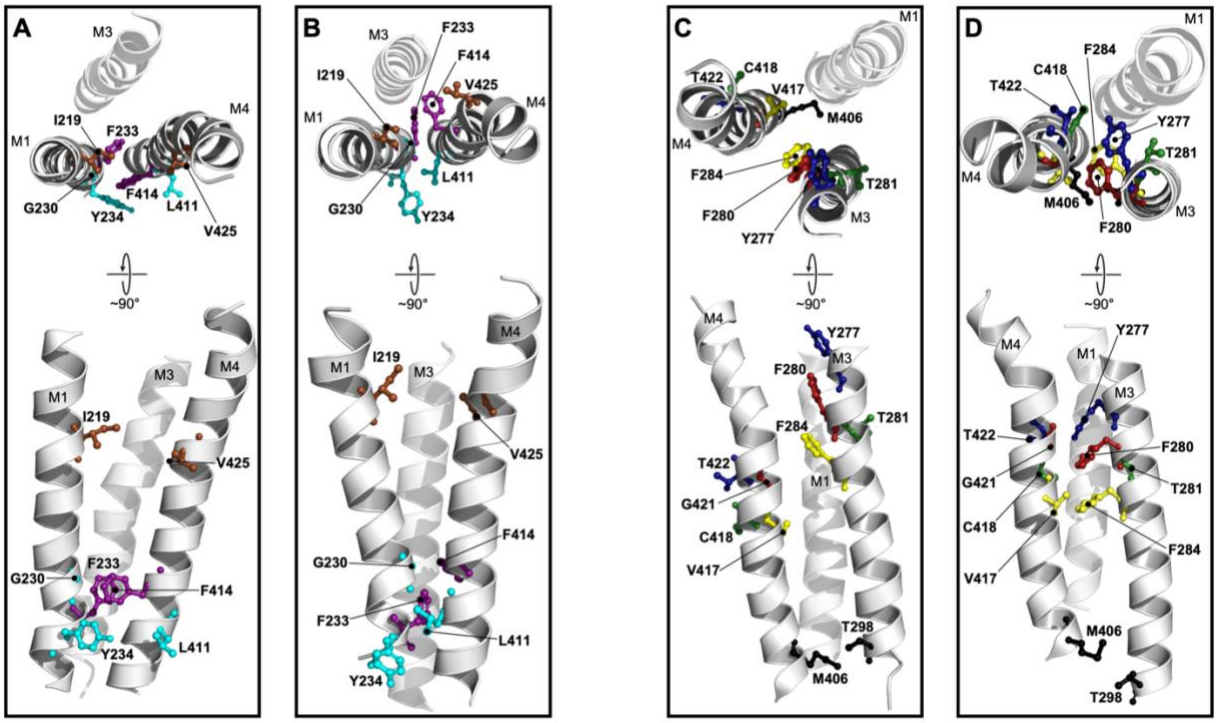
A
M3
M4
M1
I219
F233
F414
G230
Y234
L411
V425
~90°
M1
M3
M4
I219
V425
G230
F233
F414
Y234
L411
B
M3
F233
F414
I219
V425
M4
M1
L411
G230
Y234
~90°
M4
M1
I219
M3
V425
F414
G230
F233
L411
Y234
C
M1
T422
C418
V417
M406
M4
F284
T281
F280
M3
Y277
~90°
M4
Y277
M3
F280
T281
F284
T422
M1
G421
C418
V417
T298
M406
D
M1
F284
C418
T422
Y277
T281
M4
M406
F280
M3
~90°
M4
M1
Y277
M3
T422
F280
G421
T281
C418
F284
V417
M406
T298

Table 3.1 - C_α distances between co-evolved pairs of residues at the αM4-αM1/αM3 interface in the 2BG9 and 6UWZ *Torpedo* homology models.

Co-evolved pair	Probability score (%)	Distance between C_α (Å)	
		2BG9 *Torpedo*	6UWZ *Torpedo*
αM1 - αM4			
I219 - V425	100.0	10.9	11.2
G230 - L411	99.6	10.4	5.6
F233 - F414	99.8	8.5	8.6
Y234 - L411	100.0	10.0	6.4
αM3 - αM4			
Y277 - T422	97.0	16.2	7.6
F280 - G421	100.0	10.4	7.7
T281 - C418	100.0	15.8	8.2
F284 - V417	98.5	9.4	8.5
T298 - M406	99.5	8.8	9.5

3.4.3 Ala-scan of αM4

To probe the role of αM4 in nAChR function, we first generated Ala mutations at every position along αM4 and examined the functional effects of these mutations using two electrode voltage clamp electrophysiology. Given the uncertainty of our original homology models, we were generous in the choice of residues that were mutated. In total, 36 Ala mutations were generated starting at Trp399 and ending at Gly437.

The WT human adult muscle nAChR expresses robustly in *Xenopus* oocytes and responds in a concentration-dependent manner to ACh with an EC_{50} of 7.61 ± 1.25 μM (n=50) (Fig. 3.4). All 36 αM4 Ala mutants expressed, with the resulting EC_{50} values for the measured dose responses of each mutant summarized in Table 3.2. The EC_{50} values extrapolated from our measurements tell us generally about the channel function encompassing processes such as channel gating, agonist affinity, and desensitization. The mutants studied here are distant from the agonist binding site and thus observed changes in EC_{50} by these are expected to primarily alter the opening/closing rate constants (i.e. channel gating) consistent with what has been observed for other αM4 mutants (Bouzat et al., 2000; Mitra et al., 2004). Note that changes in the rates of desensitization can also influence the measured EC_{50} values; although the mutants investigated here have, at most, subtle effects on desensitization rates (Figs. 3.4 & 3.5). The reported changes or lack of reported changes in EC_{50} values do not correlate with altered rates of desensitization. Regardless, we have presented concentration-dependent whole cell trace electrophysiology recordings for a comprehensive set of mutations in Fig. 3.5.

The changes in EC_{50} value for every mutant relative to WT are heat mapped onto αM4 in Fig. 3.6, where the αM4 heat map is compared to similar heat maps generated for the prokaryotic homologs, GLIC and ELIC. Our initial discussion focuses on comparisons of the αM4 Ala-scan

with those of GLIC and ELIC because all data sets were recorded under comparable conditions (Hénault et al., 2015a). The comparisons are broadened to include other pLGICs in the Discussion.

Of the 36 Ala mutations, 13 lead to statistically significant changes in the EC_{50} values relative to WT, although two of these (Lys400, Tyr401) likely should be considered as being part of αMA and project towards the cytoplasm (Fig. 3.1). The proportion of mutations on αM4 (13 of 36) that lead to significant changes in the measured EC_{50} values is lower than in either GLIC (17 of 26) or ELIC (26 of 29), likely reflecting the fact that the α subunit, and thus each mutation, is present only twice per nAChR pentamer, whereas each mutation in both GLIC and ELIC is repeated in all five subunits. Also, a larger proportion of the generated substitutions in the human αM4 are conservative changes from a larger to a smaller aliphatic side chain (18) or from Gly to Ala (4).

On the other hand, even though fewer Ala mutations in αM4 lead to statistically significant changes in the measured EC_{50} values than in either GLIC or ELIC, three mutations, R429A, T422A and F426A, lead to changes in EC_{50} values (5.3-fold, 4.1-fold and 3.8-fold, respectively) that are similar in magnitude to the largest changes in EC_{50} values observed with M4 Ala substitutions in GLIC/ELIC, despite the fact that the αM4 mutations occur in only two of the five subunits. In fact, only a handful of Ala mutations in GLIC/ELIC lead to comparable changes in EC_{50} values. To place this observation in perspective, if the effects of the R429A mutation were independent and conserved across all five subunits, then the simultaneous Ala substitution of all five residues would lead to a 60-fold change in the measured EC_{50} value - a value greater than any functional change observed with Ala mutations in the homo-pentameric

GLIC and ELIC. This calculation highlights the functional sensitivity of the human adult muscle nAChR to mutations along αM4.

Finally, the nature and pattern of the observed changes in the EC_{50} values have both similarities and differences with those observed in GLIC and ELIC. In αM4, Ala mutations lead to a mix of both loss- (8/13) and gain-of-function (5/13) phenotypes. In contrast, the majority of the Ala mutations (15 of 17) of M4 residues in GLIC lead to *loss*-of-function phenotypes, while all 26 Ala mutations in M4 of ELIC lead to *gain*-of-function phenotypes. In addition, the vast majority of the Ala substitutions that influence GLIC function, and those with the largest gains-of-function phenotypes in ELIC, are located at the M4–M1/M3 interface. Similar to GLIC and ELIC, the 6UWZ *Torpedo* model places most (8/13) of the changes in function, including the most impactful, at the αM4 – αM1/αM3 interface. In contrast, the 2BG9 *Torpedo* model places the latter residues at the αM4 – lipid interface, with several being directly labelled by [^{125}I]-TID (Blanton and Cohen, 1992).

Figure 3.4 Functional effects of Ala substitutions to residues on αM4

Representative two electrode voltage clamp whole cell responses to different concentrations traces are shown for select mutations. Dose response relationships for select mutations are plotted on the bottom right.

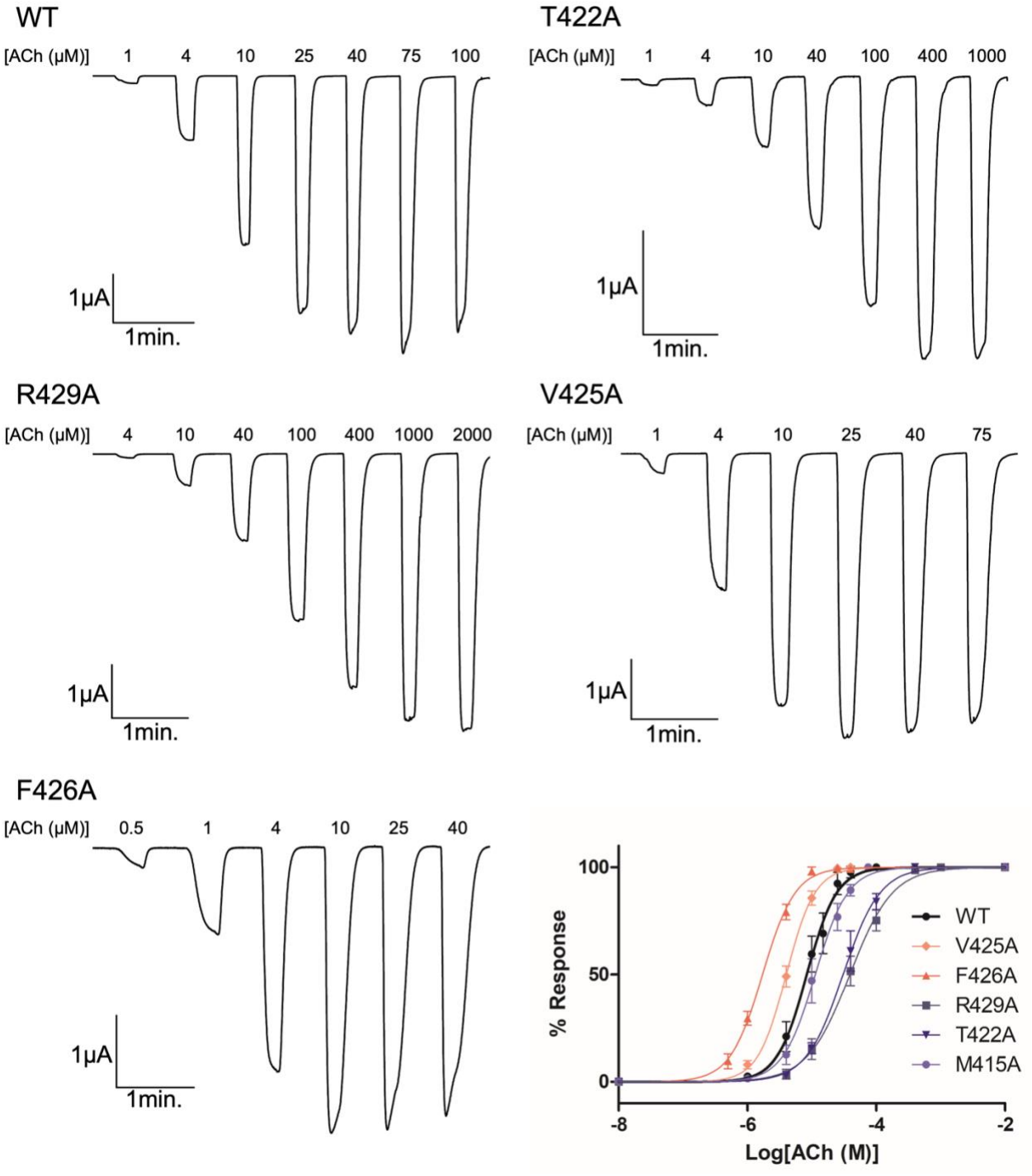
WT
[ACh (μM)] 1 4 10 25 40 75 100
1μA
1min.
T422A
[ACh (μM)] 1 4 10 40 100 400 1000
1μA
1min.
R429A
[ACh (μM)] 4 10 40 100 400 1000 2000
1μA
1min.
V425A
[ACh (μM)] 1 4 10 25 40 75
1μA
1min.
F426A
[ACh (μM)] 0.5 1 4 10 25 40
1μA
1min.
% Response
100
50
0
-8
-6
-4
-2
Log[ACh (M)]
WT
V425A
F426A
R429A
T422A
M415A

Figure 3.5 Whole-cell current traces for αM4 Ala mutants

Whole-cell agonist induced responses are shown for nAChR mutants with Ala substitutions in the membrane spanning segment of αM4. V425A and F426A mutants are shown in Fig. 3.4.

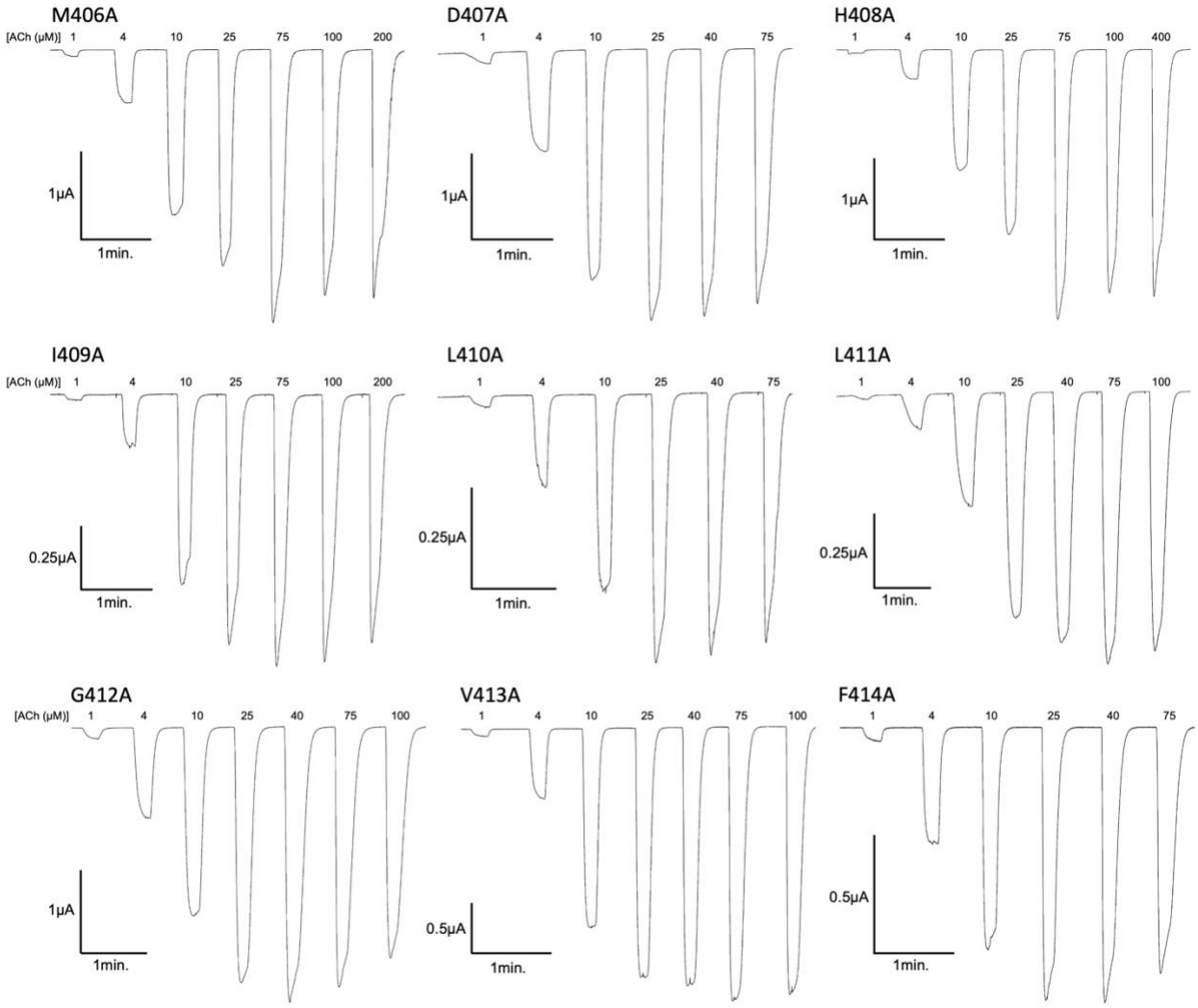
M406A
[ACh (μM)] 1 4 10 25 75 100 200
1μA
1min.
D407A
1 4 10 25 40 75
1μA
1min.
H408A
1 4 10 25 75 100 400
1μA
1min.
I409A
[ACh (μM)] 1 4 10 25 75 100 200
0.25μA
1min.
L410A
1 4 10 25 40 75
0.25μA
1min.
L411A
1 4 10 25 40 75 100
0.25μA
1min.
G412A
[ACh (μM)] 1 4 10 25 40 75 100
1μA
1min.
V413A
1 4 10 25 40 75 100
0.5μA
1min.
F414A
1 4 10 25 40 75
0.5μA
1min.

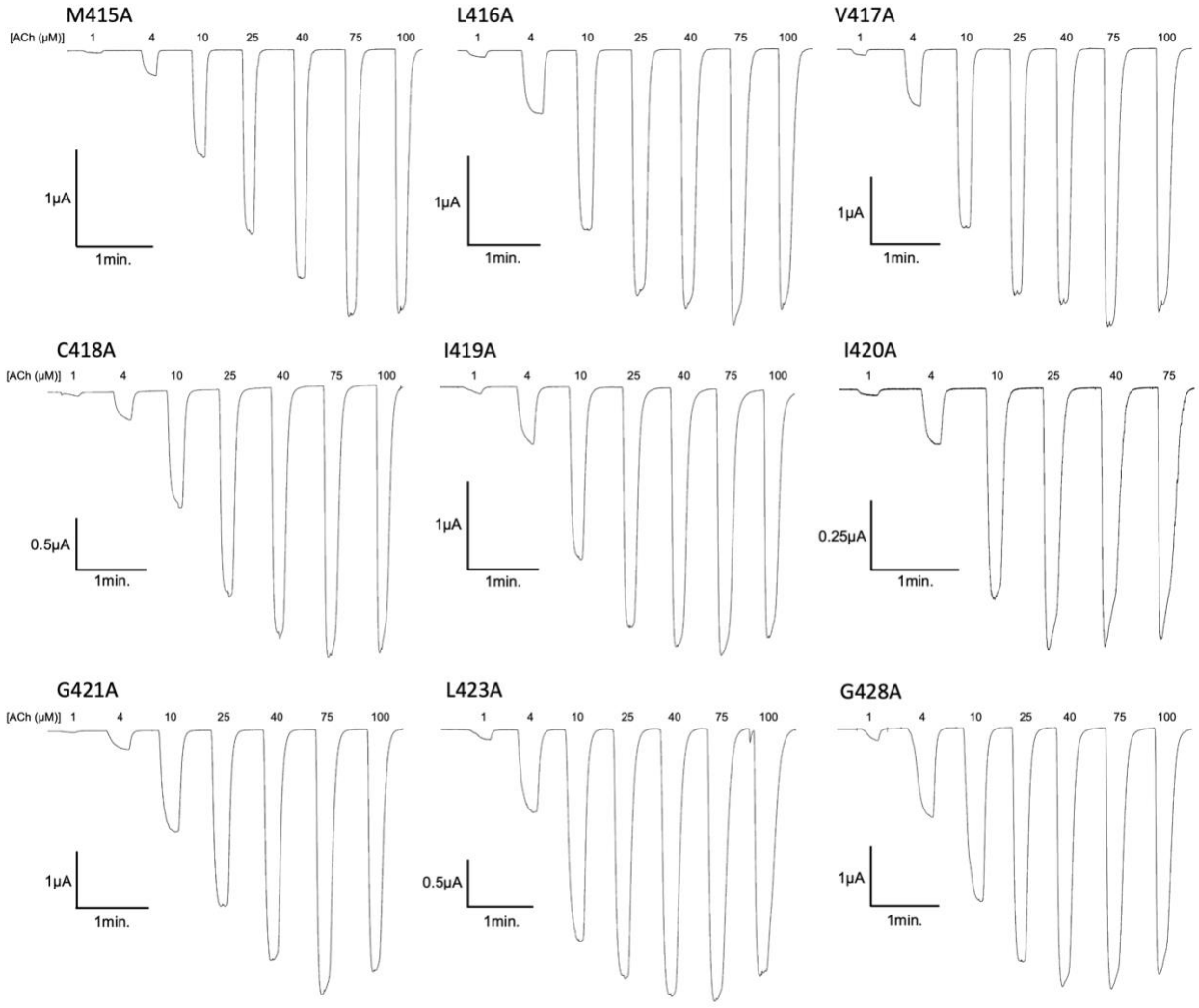
M415A
[ACh (μM)] 1 4 10 25 40 75 100
1μA
1min.
L416A
1 4 10 25 40 75 100
1μA
1min.
V417A
1 4 10 25 40 75 100
1μA
1min.
C418A
[ACh (μM)] 1 4 10 25 40 75 100
0.5μA
1min.
I419A
1 4 10 25 40 75 100
1μA
1min.
I420A
1 4 10 25 40 75
0.25μA
1min.
G421A
[ACh (μM)] 1 4 10 25 40 75 100
1μA
1min.
L423A
1 4 10 25 40 75 100
0.5μA
1min.
G428A
1 4 10 25 40 75 100
1μA
1min.

Figure 3.6 Comparison of the αM4 Ala scan heat map for the nAChR to those of GLIC and ELIC

The changes in EC_{50} values resulting from Ala mutation of each residue on M4 is heat mapped onto the structure for A) GLIC (PDB: 4HFI), B) nAChR (6UWZ *Torpedo* model), and C) ELIC (Homology model based on the GLIC structure). Residues on M4 are represented as spheres colored according to the magnitude of the change in EC_{50}. The scale runs between a 10-fold gain-of-function (red) to a 10-fold loss-of-function (blue), with no change in function shown as white. A mutant that gave no functional expression is shown in black, while a mutant that drastically altered desensitization kinetics is shown in dark grey.

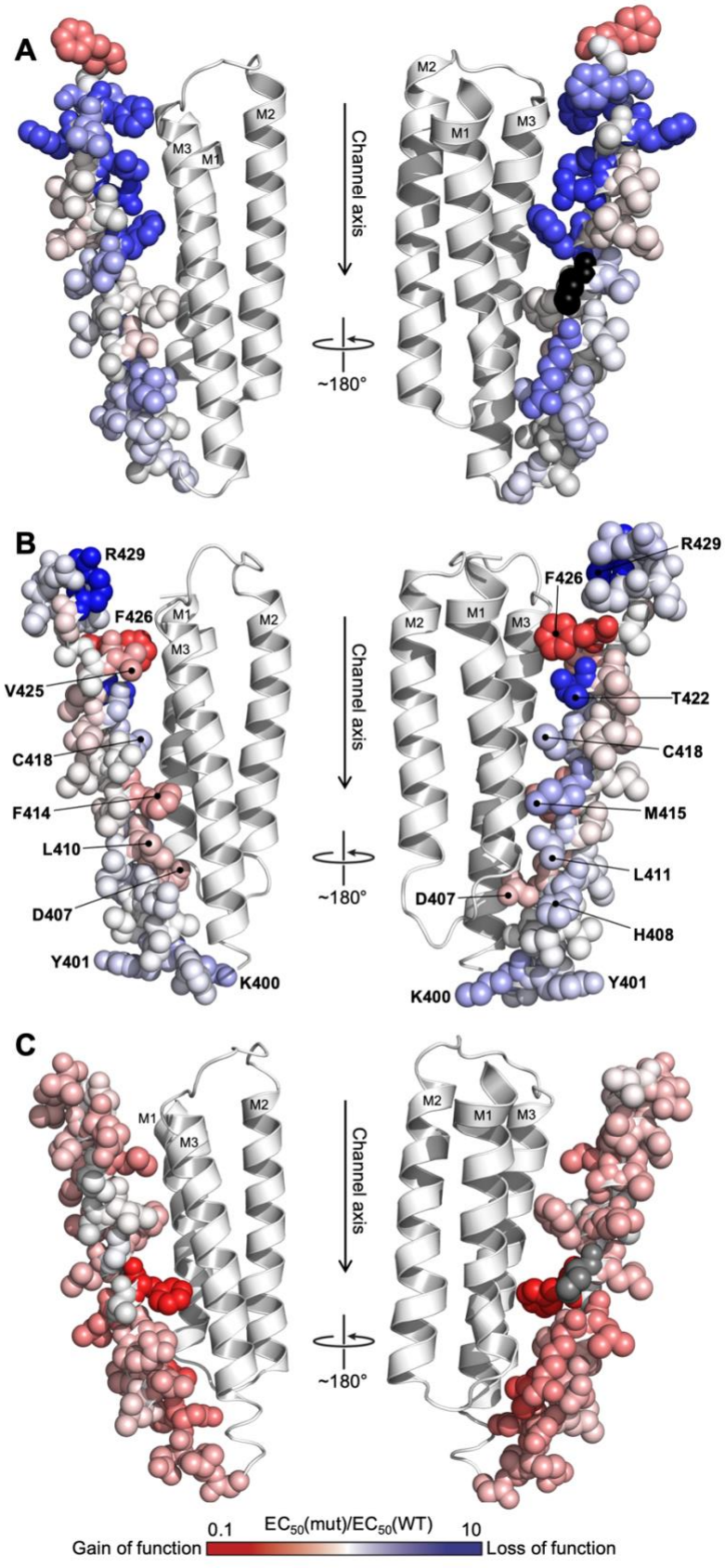
A
M2
M3
M1
Channel axis
~180°
M2
M1
M3
B
R429
F426
M1
M2
M3
V425
C418
F414
L410
D407
Y401
K400
Channel axis
~180°
R429
F426
M2
M1
M3
T422
C418
M415
L411
D407
H408
K400
Y401
C
M1
M3
M2
Channel axis
~180°
M2
M1
M3
0.1
EC50(mut)/EC50(WT)
10
Gain of function
Loss of function

Table 3.2 - Functional effects of Ala mutations on residues within αM4

Dose Response[a]			
Mutation	**EC_{50} (μM)**	**Hill slope**	**n**
WT	7.61 ± 1.25	1.70 ± 0.47	50
G437A	6.12 ± 0.87	1.58 ± 0.43	9
Q436A	8.29 ± 0.73	1.94 ± 0.14	13
Q435A	8.07 ± 0.51	2.03 ± 0.12	13
N434A	8.09 ± 0.68	1.94 ± 0.12	11
L433A	10.3 ± 1.1	1.93 ± 0.14	12
E432A	8.83 ± 0.62	1.92 ± 0.13	11
I431A	8.70 ± 0.64	1.85 ± 0.19	10
L430A	8.63 ± 1.30	1.72 ± 0.17	10
R429A	40.0 ± 9.5[b]	1.09 ± 0.12	10
G428A	6.15 ± 0.54	1.66 ± 0.28	9
A427	WT	WT	-
F426A	2.02 ± 0.64[b]	1.80 ± 0.76	11
V425A	4.30 ± 0.51[b]	1.89 ± 0.28	10
A424	WT	WT	-
L423A	5.80 ± 0.87	2.54 ± 0.66	10
T422A	31.2 ± 9.0[b]	1.40 ± 0.12	10
G421A	10.0 ± 1.2	1.96 ± 0.26	9
I420A	5.97 ± 0.94	2.71 ± 0.33	10
I419A	6.58 ± 1.08	2.15 ± 0.32	10
C418A	10.6 ± 2.85[b]	1.82 ± 0.33	9
V417A	7.71 ± 1.35	1.94 ± 0.11	10
L416A	7.11 ± 0.77	2.01 ± 0.09	10
M415A	12.5 ± 3.1[b]	1.61 ± 0.27	10
F414A	4.47 ± 0.82[b]	1.76 ± 0.34	10
V413A	7.24 ± 1.09	2.20 ± 0.26	10
G412A	6.77 ± 1.09	1.54 ± 0.31	9
L411A	9.86 ± 2.44[b]	2.35 ± 0.40	13
L410A	5.21 ± 1.08[b]	2.06 ± 0.59	21
I409A	8.22 ± 1.91	2.05 ± 0.51	10
H408A	10.1 ± 1.2[b]	1.80 ± 0.27	10
D407A	4.97 ± 0.45[b]	3.12 ± 0.78	11
M406A	8.37 ± 0.84	1.70 ± 0.21	14
V405A	7.76 ± 1.06	2.03 ± 0.39	10
M404A	8.05 ± 0.73	2.14 ± 0.40	10
A403	WT	WT	-
V402A	7.91 ± 0.38	2.05 ± 0.13	9
Y401A	9.86 ± 0.73[b]	1.75 ± 0.48	11
K400A	12.9 ± 2.6[b]	1.89 ± 0.63	15
W399A	8.90 ± 0.58	2.51 ± 0.41	10

[a]Measurements performed 1-4 days after cRNA injection (V_{hold} ranging from -20 to -80 mV).
[b]$p < 0.001$ relative to WT via one-way ANOVA followed by Dunnet's post hoc test.

3.4.4 Polar residues at the N and C termini of αM4

αM4 exhibits clusters of polar/charged residues at both its N (Asp407, His408) and C termini (Arg429, Glu432, Asn434, Gln435, and Gln436) (Fig. 3.1) that could form functionally important interactions with either lipids or adjacent residues in the TMD and/or ECD. At the αM4 N terminus, Asp407 either projects toward Lys242 on the αM1-αM2 loop (6UWZ *Torpedo* model) or towards Thr237 on M1 (2BG9 *Torpedo* model) while His408 projects toward lipids and interacts with the phosphate of a bound lipid in one α subunit of the 6UWZ *Torpedo* structure. Regardless, the Ala substitutions of either residue has little effect (1.3-fold gain- and 1.5-fold loss-of-function, respectively) on the measured EC_{50} value, suggesting that neither residue forms interactions that are critical for expression or function.

At the αM4 C terminus, the 6UWZ *Torpedo* model projects Arg429 and Glu432 towards His134 of the Cys-loop with the remaining polar residues (Asn434, Gln435 and Gln436) unresolved. In contrast, the 2BG9 *Torpedo* model projects Glu432 and Gln435 towards Phe137 of the Cys-loop, with Arg429, Asn434 and Gln436 facing the lipid. Surprisingly, Ala substitutions of Glu432, Asn434, Gln435 and Gln436 have no effect on channel function, suggesting that none of these residues form functionally significant interactions that are critical to expression or function. on the other hand, R429A leads to a relatively large 5.3-fold loss-of-function suggesting an important functional interaction between αM4 and the Cys-loop. Despite this important result, the interpretation that Arg is functionally important is clouded by the lack of an effect on the measured EC_{50} value upon deletion of this residue, as discussed below in section 3.4.6.

3.4.5 The hydrophobic core of αM4

The central core of αM4 is formed mainly by aliphatic residues, although these are interspersed with two aromatic residues, Phe414 and Phe426, and the potential hydrogen bonding residues, Cys418 and Thr422. The conservative Ala substitution of the five large aliphatic residues in the hydrophobic core of αM4, Leu410, Leu411, M415 and Val425, each leads to a statistically significant change in the EC_{50} value, although all changes are less than 2-fold. The Ala substitutions of the two aromatic residues, Phe414 and Phe426, lead to 1.7-fold and 3.8-fold gains-of-function, respectively, suggesting detrimental effects on function. The latter are of particular interest given the importance of aromatic interactions at the M4–M1/M3 interfaces in the folding and function of other pLGICs (Haeger et al., 2010; Carswell et al., 2015b). The functional roles of aromatic residues at the αM4-αM1/αM3 interface are explored in more detail below in section 3.4.7.

The Ala substitution of Thr422 leads to a relatively large 4.1-fold loss-of-function. Thr422 faces αM1 in the 6UWZ *Torpedo* model, but projects tangentially to αM1 interacting with lipid in the 2BG9 *Torpedo* model. Consistent with our data showing a loss-of-function, single channel measurements indicate that T422A in the mouse adult muscle nAChR leads to a 5-fold decrease in channel open times. In addition, a mutant cycle analysis suggests an interaction between Thr422 and the nearby αM1 Ser226 stabilizes the open state (Domville and Baenziger, 2018). Interestingly, although the adjacent C418A mutation leads to only small 1.4-fold loss-of-function, C418W leads to a relatively large 16- to 25-fold gain-of-function and a congenital myasthenic syndrome (Shen et al., 2006; Domville and Baenziger, 2018). Channel function in the adult muscle nAChR appears to be sensitive to the structure of residues in the

vicinity of Thr422. This region of αM4 may be particularly responsive to changes in the surrounding lipid environment.

3.4.6 The αM4 C terminus

Previous studies with other pLGICs have highlighted a role for the M4 C terminus in function, possibly through interactions with the Cys-loop (Butler et al., 2009; Hénault et al., 2015a; Cory-Wright et al., 2018; Tang and Lummis, 2018). In contrast, Ala mutations of most residues at the αM4 C terminus that could interact with the Cys-loop or other structures in the ECD have little effect on the measured EC_{50} values, as discussed above, suggesting that such interactions are not critical in the muscle nAChR. To further probe the functional role of αM4 – Cys-loop interactions, we generated αM4 C terminal deletions. Deleting up to four residues at the C terminus of αM4 has no effect on channel function (Table 3.3). Deleting from five to eleven residues, leads to a gradual increase in the measured EC_{50} values corresponding to a gradual loss-of-function, but the maximal loss-of-function is only three-fold despite a major disruption in the structure of αM4. Deleting twelve residues or the entire αM4 α-helix (data not shown) leads to a loss of functional expression. These data suggest that αM4 - Cys-loop interactions are not critical.

Note that the deletion of nine C terminal residues (Arg429 to Gly437) led to essentially no further change in the measured EC_{50} value than the deletion of eight C terminal residues (Leu430 to Gly437), despite the fact that the R429A mutant leads to a relatively large 5.3 fold loss-of-function. The functional importance of Arg429 may only be evident in the presence of the adjacent C terminal polar/anionic residues Glu432, Asn434, Gln435 and/or Gln436.

Table 3.3 - Functional effects of αM4 C-terminal deletions[a]

	Dose Response[b]		
Deletion(s)	**EC_{50} (μM)**	**Hill slope**	**n**
WT: …LAVFAGRLIELNQQG	7.61 ± 1.25	1.70 ± 0.47	50
Δ1: …LAVFAGRLIELNQQ	6.86 ± 0.86	2.66 ± 0.67	9
Δ2: …LAVFAGRLIELNQ	6.37 ± 0.94	2.62 ± 0.54	9
Δ3: …LAVFAGRLIELN	7.14 ± 1.09	2.36 ± 0.38	8
Δ4: …LAVFAGRLIEL	8.49 ± 1.39	2.13 ± 0.44	8
Δ5: …LAVFAGRLIE	11.8 ± 1.0[c]	1.65 ± 0.33	10
Δ6: …LAVFAGRLI	12.3 ± 1.2[c]	1.59 ± 0.25	10
Δ7: …LAVFAGRL	12.7 ± 1.7[c]	1.54 ± 0.15	10
Δ8: …LAVFAGR	14.7 ± 2.6[c]	1.46 ± 0.29	10
Δ9: …LAVFAG	14.9 ± 2.5[c]	1.77 ± 0.35	10
Δ10: …LAVFA	21.4 ± 4.2[c]	1.35 ± 0.12	10
Δ11: …LAVF	23.0 ± 5.0[c]	1.69 ± 0.36	10
Δ12: …LAV	No current[d]		8

[a]the shown sequences extend from Leu423 to Gly437

[b]Measurements performed 1-4 days after cRNA injection (V_{hold} ranging from -20 to -80 mV). Error values represented as standard deviation

[c]$p < 0.001$ relative to WT via one-way ANOVA followed by Dunnet's post hoc test

[d]No significant current observed up to 4 days after cRNA injection

3.4.7 Aromatic Residues at the αM4-αM1/αM3 interface

Given their importance in other pLGICs (Haeger et al., 2010; Carswell et al., 2015a, 2015b; Cory-Wright et al., 2018; Mesoy et al., 2019), we examined the functional role of aromatic residues at the αM4-αM1/αM3 interface in the nAChR. In the intracellular leaflet of the bilayer, αM4 Phe414 interacts with αM1 Phe233 and αM3 Phe284 in the 6UWZ *Torpedo* model, but is also close to αM1 Tyr234 in the 2BG9 *Torpedo* model (Fig. 3.7). As noted, Ala mutation of Phe414 leads to a small 1.7-fold gain-of-function, while the F233A and F284A mutations lead to 2.9-fold and 1.6-fold gains-of-function, respectively. The F414A/F233A double mutant leads to a 7-fold gain-of-function, slightly more than what would be expected if the two mutations are independent and additive (Table 3.4). These three bulky aromatic residues are detrimental to channel function and may sterically prevent optimal αM4-αM1/αM3 interactions, as is observed with aromatic residues at the M4–M1/M3 interface in ELIC.

In contrast, the Ala mutant of Tyr234 does not express, although both Y234L and Y234F give near WT EC_{50} values indicating that a bulky hydrophobic residue is required at this position for proper folding and/or function. Intriguingly, Tyr234 lies along the base of a lipid binding site in the 6UWZ structure where it interacts extensively with a bound lipid and shapes the lipid binding site. The role of this putative lipid binding aromatic residue warrants further exploration.

In the extracellular leaflet of the bilayer, αM4 Phe426 projects towards αM3 Tyr277/Phe280 in the 6UWZ *Torpedo* model. As noted, F426A mutation leads to a relatively large 3.8-fold gain-of-function. In contrast, the two αM3 aromatic mutations had minimal effects, with Y277A and F280A, leading to a 1.5-fold loss- and a 1.8-fold gain-of-function,

respectively. Even the double mutant, F280A/F284A, had little effect on the measured EC_{50} value.

We also probed the role of αM1 Phe225 on channel function, as our early models suggested that it projects towards aromatic residues located on αM3. The F225A mutant led to a relatively large 11-fold gain-of-function. Somewhat surprisingly, double aromatic mutants involving Phe225 (F225A/F280A and F225A/F284A), along with the triple αM3 aromatic mutant (Y277A/F280A/F284A) resulted in no functional expression. Note that in the new 6UWZ *Torpedo* model, Phe225 is oriented towards αM2 where it may sterically hinder movement of this gating helix as it transitions to the open state.

Figure 3.7 Aromatic residues at the αM4 – αM1/αM3 interface

Aromatic residues at the αM4 – αM1/αM3 interface are shown in ball and stick representations and are colored yellow. The TMDs from the 2BG9 *Torpedo* (left) and 6UWZ *Torpedo* (right) models are shown in both top views from the extracellular surface (top) and side views from within the membrane (bottom).

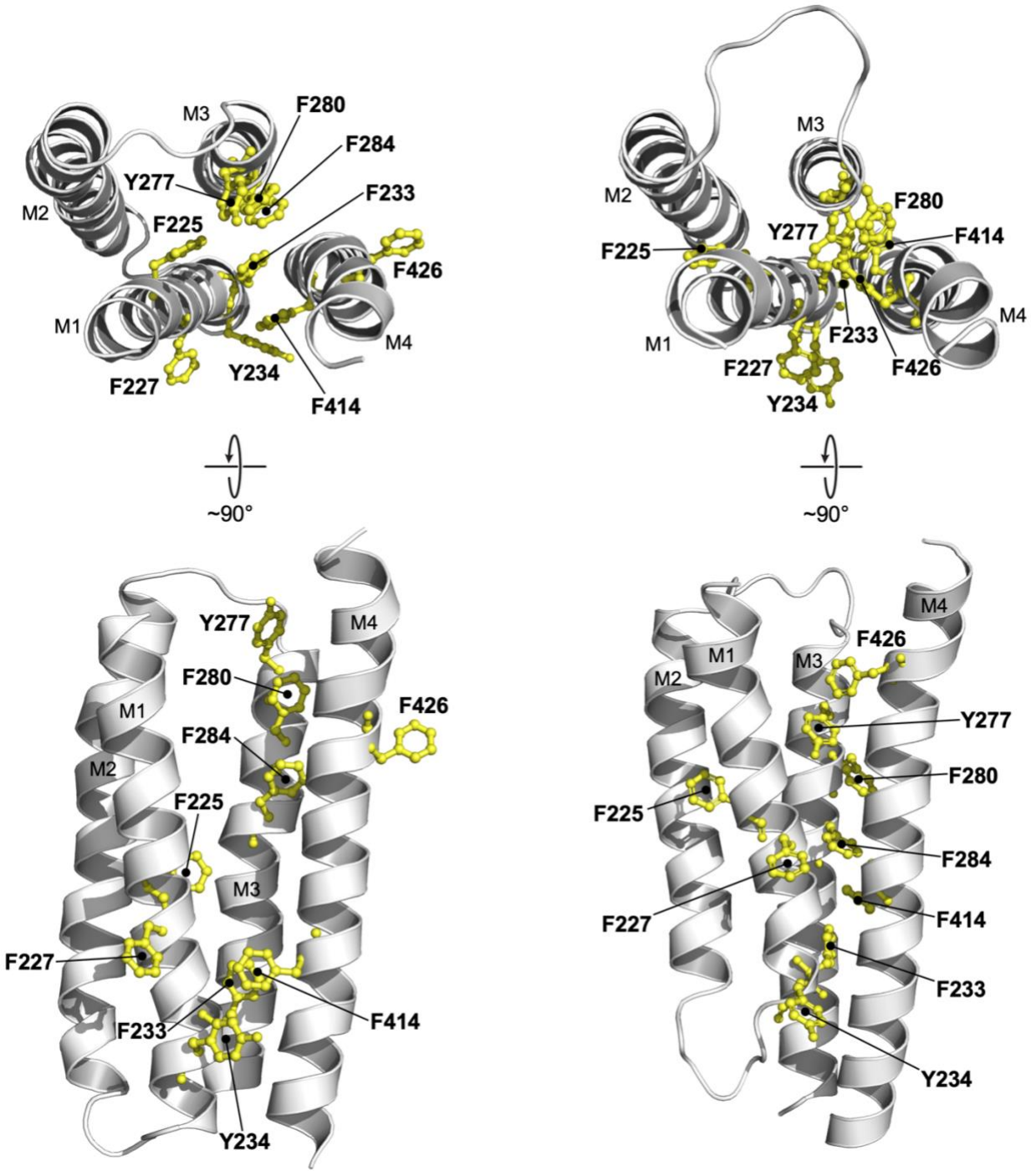
M3
F280
F284
Y277
F233
M2
F225
F426
M1
M4
F227
Y234
F414
~90°
M3
M2
F280
Y277
F414
F225
M4
M1
F233
F227
F426
Y234
~90°
Y277
M4
F280
M1
F426
F284
M2
F225
M3
F227
F414
F233
Y234
M4
F426
M1
M3
M2
Y277
F280
F225
F284
F227
F414
F233
Y234

Table 3.4 - Functional effects of mutating αM4 – αM1/αM3 interfacial aromatics

Dose Response[a]				
Mutation	**TMD α-helix**	**EC_{50} (μM)**	**Hill slope**	**n**
WT	--	7.61 ± 1.25	1.70 ± 0.47	50
F225A	αM1	0.71 ± 0.12[b]	1.57 ± 0.39	8
F227A	αM1	6.51 ± 1.47	1.43 ± 0.16	8
F233A	αM1	2.63 ± 0.31[b]	1.63 ± 0.20	9
Y234A	αM1	No current[c]		8
Y234L	αM1	5.79 ± 0.72	2.20 ± 0.33	8
Y234F	αM1	8.43 ± 2.03	1.66 ± 0.27	8
Y277A	αM3	11.2 ± 1.97[b]	1.78 ± 0.58	8
F280A	αM3	4.25 ± 1.00[b]	1.56 ± 0.29	8
F284A	αM3	4.80 ± 0.75[b]	1.33 ± 0.21	9
F414A	αM4	4.47 ± 0.82[b]	1.76 ± 0.34	10
F225A+F280A	αM1+αM3	No current[c]		8
F225A+F284A	αM1+αM3	No current[c]		8
F280A+F284A	αM3+αM3	8.42 ± 2.98	1.45 ± 0.08	9
F225A+F280A+F284A	αM1+αM3+αM3	No current[c]		8
F233A+F414A	αM1+αM4	1.08 ± 0.10[b]	2.21 ± 0.36	8

[a]Measurements performed 1-4 days after cRNA injection (V_{hold} ranging from -20 to -80 mV). Error values represented as standard deviation

[b]$p < 0.001$ relative to WT via one-way ANOVA followed by Dunnet's post hoc test

[c]No significant current observed up to 4 days after cRNA injection

3.4.8 Functional role of co-evolved residues at the αM4-αM1/αM3 interface.

We used mutant cycles to test whether interactions between co-evolved pairs of residues play a role in channel function. In a mutant cycle, the individual effects of mutating two potentially interacting residues are compared to the effect of the double mutant in order to assess whether the residues influence function independently or through a common mechanism – the latter would be the case if they were involved in a direct interaction. The independence of the functional effects is evaluated using a parameter Ω (see Experimental Methods), where an Ω value of 1 indicates that the two mutations influence channel function independently, while a Ω values of increasingly greater than or less than 1 indicate increasing degrees of mutual dependence. Although mutant cycles are ideally used when the rate constants for gating can be defined, this approach has proven informative at the whole-cell level (Daeffler et al., 2012; Domville and Baenziger, 2018). We generally consider up to ~2-fold changes in Ω values as being within the error limits of our measurements (Daeffler et al., 2012).

Both individual and double Ala mutations were created for each co-evolved pair of residues at both the αM1 - αM4 (Ile219/Val425, Gly230/Leu411, Phe233/Phe414 and Tyr234/Leu411) and αM3 - αM4 interfaces (Tyr277/Thr422, Phe280/Gly421, Thr281/Cys418, Phe284/Val417 and Thr298/Met406) (Table 3.5). At the αM1 - αM4 interface, the effects of the single and double mutations are all minimal, suggesting that these co-evolved pairs do not play a critical role in either folding or function. Similar effects are also observed with Ala mutations of co-evolved residues at the αM3 - αM4 interface, except that T281A and T298A do not functionally express. In addition, although the Ala mutations of the evolutionarily coupled residues αM3 Tyr277 and αM4 Thr422 lead to 1.5-fold and 4.1-fold losses-of-function, respectively, the Y277A/T422A double mutant does not express. Although the latter lend further

support to the hypothesis that Thr422 plays an important role in αM4 function, the collective data suggest that co-evolved residues at the αM1 - αM3/αM4 interface generally do not play a critical functional role.

Table 3.5 - Functional effects of co-evolved residues at the αM4 – αM1/αM3 interface

Dose Response[a]							
Co-evolved pair	**αM1or αM3 mutant**		**αM4 mutant**		**αM1 or αM3 + αM4 mutant**		
	EC_{50} (μM)	**n**	**EC_{50} (μM)**	**n**	**EC_{50} (μM)**	**n**	**Ω**
αM1 + αM4							
I219A + V425A	17.7 ± 10.5[b]	8	4.30 ± 0.51[b]	10	15.1 ± 4.2[b]	8	1.51
G230A + L411A	7.05 ± 1.47	8	9.86 ± 2.44[b]	13	7.26 ± 2.63	8	0.79
F233A + F414A	2.63 ± 0.31[b]	9	4.47 ± 0.82[b]	10	1.08 ± 0.10[b]	8	0.70
Y234F + L411A	5.79 ± 0.72	8	9.86 ± 2.44[b]	13	12.8 ± 4.3[b]	8	1.70
Y234L + L411A	8.43 ± 2.03	8	9.86 ± 2.44[b]	13	9.48 ± 2.97	8	0.87
αM3 + αM4							
Y277A + T422A	11.2 ± 2.0[b]	8	31.2 ± 9.0[b]	10	No current[c]	8	N/A
F280A + G421A	4.25 ± 1.00[b]	8	10.0 ± 1.2	9	4.42 ± 0.56[b]	9	0.76
T281A + C418A	No current[c]	8	10.6 ± 2.9[b]	9	1.51 ± 0.18[b]	8	N/A
F284A + V417A	4.80 ± 0.75[b]	9	7.71 ± 1.35	10	5.83 ± 0.47	9	1.22
T298A + M406A	No current[c]	8	8.37 ± 0.84	14	2.73 ± 0.37[b]	8	N/A

[a]Measurements performed 1-4 days after cRNA injection (V_{hold} ranging from -20 to -80 mV). Error values represent standard deviation.
[b]$p < 0.001$ relative to WT via one-way ANOVA followed by Dunnet's post hoc test.
[c]No significant current observed up to 4 days after cRNA injection.

3.4.9 The additivity of mutations along αM4.

Finally, we asked whether the functional effects of Ala mutations along αM4 are additive. We first created a two triple Ala mutants involving the three residues on αM4 that lead to relatively large losses-of-function (R429A (5.3-fold), T422A (4.1-fold) and L411A (1.3-fold)) and relatively large gains-of-function (F426A (3.8-fold), F414A (1.7-fold) and D407A (1.5-fold)) (Table 3.6). If each mutation impacts function via changes only to the local environment surrounding that residue, then we would expect the mutations to be independent and thus additive, leading to a 28-fold loss-of-function and a 10-fold gain-of-function, respectively. The R429A+T422A+L411A triple mutant led to only a 6-fold loss-of-function, close to 5 times less than expected. The effects of these three mutations are thus not *completely* independent. Unfortunately, the F426A+F414A+D407A triple mutant gave no functional expression.
We next created two triple Ala mutants involving residues where the individual Ala mutations led to a mix of loss- and gain-of-function phenotypes. If the mutations are independent and thus additive, we would expect the triple mutants, F426A+M415A+H408A and R429A+F414A+D407A, to lead to a 2-fold gain-of-function and a 2-fold loss-of-function, respectively. The F426A+M415A+H408A triple mutant gave a 3-fold gain of function, suggesting that these three mutants influence function independently. In contrast, the R429A+F414A+D407A triple mutant did not give functional expression.

Table 3.6 - Additive functional effects of triple αM4 Ala mutations

Dose Response[a]			
Mutation	**EC_{50} (μM)**	**Hill Slope**	**n**
WT	7.61 ± 1.25	1.70 ± 0.47	50
R429A+T422A+L411A	45.6 ± 10.0[b]	1.52 ± 0.10	8
F426A+F414A+D407A	No current[c]		8
F426A+M415A+H408A	2.30 ± 0.39[b]	2.02 ± 0.16	8
R429A+F414A+D407A	No current[c]		8

[a]Measurements performed 1-4 days after cRNA injection (V_{hold} ranging from -20 to -80 mV). Error values represent standard deviation.
[b]$p < 0.001$ relative to WT via one-way ANOVA followed by Dunnet's post hoc test.
[c]No significant current observed up to 4 days after cRNA injection.

3.5 Discussion

The long-term goal of this work is to understand the mechanisms underlying the exquisite functional sensitivity of the muscle nAChR to its surrounding membrane environment. The M4 α-helix located at the lipid exposed periphery of the transmembrane domain of each subunit plays a central role in lipid sensing. M4 likely translates changes in the surrounding membrane environment to altered channel function via its interactions with the adjacent transmembrane α-helices, M1 and M3, although the underlying pathway(s) remain unclear. An important first step in the elucidation of these pathways is to understand the functional role of the M4 α-helices in the different subunits of the $\alpha_2\beta\gamma\delta$ (fetal) or $\alpha_2\beta\varepsilon\delta$ (adult) pentamers. Here, we focused on the functional role of αM4 (i.e. M4 from the α subunit) from the human adult muscle nAChR.

We first examined the functional effects of Ala substitutions at each residue along the entire length of αM4 and found that the effects generally differ both quantitatively and qualitatively from those observed with M4 Ala mutations in other pLGICs, such as GLIC and ELIC. In the nAChR, only 13 of 36 substitutions in αM4 lead to statistically significant changes in the agonist-induced response, while a large majority of the Ala substitutions in GLIC (17 of 26) and ELIC (26 of 29) alter channel function. In the nAChR, Ala mutations in αM4 lead to a mix of both loss- and gain-of-function phenotypes, while in GLIC and ELIC the vast majority of M4 Ala mutations lead to either *loss*-of-function or *gain*-of-function phenotypes, respectively. In the nAChR and ELIC, Ala substitutions of aromatic residues at the αM4-αM1/αM3 interface generally lead to improved channel function, while similar mutations in GLIC lead to losses-of-function. Finally, although a fewer number of Ala substitutions in αM4 lead to changes in function, the magnitudes of the changes in function of the most impactful mutations are

comparable to those observed in the homomeric GLIC and ELIC, even though the mutations in αM4 are repeated in only two of the five subunits.

Collectively, these results suggest that αM4 impacts channel function in a manner that differs from the functional impact of M4 in either GLIC or ELIC. In GLIC, aromatic residues on M1, M3 and M4 interact with each other creating a tight, complementary network at the M4–M1/M3 interface. Ala substitutions to almost any of these residues lead to a reduction in or a complete loss of expression and/or function – with double aromatic substitutions being especially damaging. A tight, complementary aromatic interface between M4 and M1/M3 is not only essential for both folding and function, but leads to tighter interactions (than in ELIC) that render GLIC functionally insensitive to its surrounding membrane environment (Haeger et al., 2010; Carswell et al., 2015a). A complex network of interacting aromatic residues at the M4–M1/M3 interface is also observed in anion-selective pLGICs (Therien and Baenziger, 2017), with Ala substitutions of aromatic residues in these pLGICs generally leading to losses in function and/or expression (Haeger et al., 2010; Tang and Lummis, 2018).

In contrast, there are relatively few bulky aromatic residues at the M4-M1/M3 interface of ELIC, with Ala mutations of most residues leading to gains-in-function. Even double aromatic to Ala substitutions are tolerated and lead to enhanced channel function. It appears that the bulky aromatic side chains prevent the M4-M1/M3 interactions that are required for optimal channel function. They also likely create a more malleable M4-M1/M3 interface that renders ELIC more sensitive to its surrounding membrane environment (Carswell et al., 2015a). In fact, increased dynamics in the C terminal half of M4, which may only be possible in the absence of aromatic residues leading to strong M4–M1/M3 interactions, play a key role in lipid binding that shapes the agonist-induced response (Hénault et al., 2019).

As in ELIC, the nAChR, along with other cation selective pLGICs such as the 5-HT_3R and the neuronal α7 homo-pentameric nAChR, lacks the complex network of aromatic residues at the αM4-αM1/αM3 interface that is found in GLIC. In the α subunit of the muscle nAChR and the α7 nAChR, Ala mutations of aromatic residues at the M4–M1/M3 interface generally lead to modest gains-in-function (da Costa Couto et al., 2020). These bulky aromatic residues may prevent optimal M4–M1/M3 interactions for channel function. A more malleable αM4 - αM1/αM3 may also contribute to the exquisite lipid sensitivity of the nAChR, as has been extensively characterized for the *Torpedo* homolog (Baenziger et al., 2015). On the other hand, Ala substitutions along M4 in the 5-HT_{3A}R either have no effect or lead losses in expression and/or function (Mesoy et al., 2019).

In this context, it is important to note that the introduction of aromatic interactions at the M4–M1/M3 interface of ELIC to create the same complex network of aromatic interactions that occur in GLIC both leads to an enhancement in channel function and reduces the functional sensitivity of ELIC to lipids (Carswell et al., 2013, 2015a). While similar experiments have not been performed in the muscle nAChR, Trp residues have been introduced along αM4 in the *Torpedo* nAChR at positions originally thought, based on [^{125}I]-TID labeling, to be exposed to lipids. Although most of these Trp substitutions were detrimental to folding and/or function (Lasalde et al., 1996; Tamamizu et al., 2000), three Trp substitutions now positioned at the αM4-αM1/αM3 interface in the 6UWZ *Torpedo* nAChR structure lead to between relatively large gains-of-function. It is possible that the addition of an extra bulky aromatic residue at select positions along this interface in the *Torpedo* nAChR helps to create optimal interactions between αM4 and αM1/αM3 to enhance channel function. Further work is required to assess the effects of aromatic residues at this interface in both function and lipid sensing.

In contrast to ELIC, however, the αM4 Ala-scan suggests that two residues, Arg429 and Thr422, both play a specific role in channel function, with the R429A and T422A mutations leading to relatively large loss-of-function phenotypes. It is possible that these residues contribute to specific interactions that ultimately drive how αM4 both influences function and senses its surrounding lipid environment. Similarly, in the homopentameric 5-HT_{3A}R, three mutations along M4, D434A, Y441A and W459A, lead to losses in expression and/or function. Of particular note, the D434A mutant does not express, possibly as a result of a critical interaction with an Arg251 on the M1-M2 loop, which in turn forms a second hydrogen bond with the backbone of Leu244 on M2 (Mesoy et al., 2019). The equivalent mutation in the α7 nAChR, D446A, also does not express (da Costa Couto et al., 2020). In contrast, Ala mutation of the equivalent residue in αM4 of the muscle nAChR, Asp407, expresses robustly and produces a slight gain-of-function. It appears that the pathways by which M4 influences channel function differ in the 5-HT_{3A}R, the neuronal α7 nAChR and the α subunit of the muscle nAChR.

Finally, we assessed whether the effects of individual Ala mutations of residues located along αM4 are independent and thus additive. Although our data are limited, particularly as two of the four triple mutants do not express, they suggest that the effects of multiple mutations along M4 are additive, although not in a completely independent manner. In other words, although one of the triple mutants gives a loss-of-function larger than any of the individual mutations, the loss-of-function is less than expected if the individual effects were simply added together. These data suggest that a change in orientation of the entire αM4 could lead to changes in a number of local interactions that may add up to a significantly larger impact on channel function. Similarly, lipid dependent changes in the orientation of αM4 could alter nAChR function through the addition of multiple, subtle changes in local interactions at the αM4-αM1/αM3 interface. Further

experiments are required to both test this hypothesis and to assess how the M4 α-helix from other subunits in the heteromeric muscle nAChR contribute to channel function.

Chapter 4. Manuscript 2: Distinct functional roles for the M4 α-helix from each homologous subunit in the hetero-pentameric ligand-gated ion channel nAChR

Thompson, M.J., Domville, J.A., Edrington, C.H., Venes, A., Giguère, P.M., and Baenziger, J.E. (2022). Distinct functional roles for the M4 α-helix from each homologous subunit in the hetero-pentameric ligand-gated ion channel nAChR. J. Biol. Chem. 102104.

Adapted as a post-print from J. Biol. Chem., https://doi.org/10.1016/j.jbc.2022.102104.

4.1 Preface

This manuscript is my second first author publication and is a follow up on the first manuscript presented in this thesis. The goal of this paper was again to decipher the structural basis of lipid modulation in the muscle-type nAChR, but this time looking at each subunit rather than just the α subunits. Some data for the Ala-scans, aromatic substitutions, and C-terminal deletions were collected by Jaimee A. Domville and Claire H. Edrington alongside two undergraduate students, Anais Santos and Shobhitha Balasubramaniam, also are acknowledged in the official article. The involvement of various former lab members meant that the data needed to re-processed in a consistent manner, data that I deemed untrustworthy needed to be repeated, and any uncompleted mutants characterized. I then critically assessed the data and created new hypotheses that I felt needed to be tested to gain a deeper understanding of the difference in lipid sensing through the M4 α-helix of each subunit. To do this I tested whether a known pathway leading from M4 to altered channel function in the α subunits was conserved in the remaining subunits, I mutated M4 residues simultaneously in different subunits and assessed whether their functional contribution was independent, and orchestrated a test of M4 induced functional changes in the context of a different expression system. I performed the latter tests in the lab of Dr. Patrick M. Giguère with the help of his student, Angelica Venes. I also performed surface expression tests on HEK cells prepared in their lab using radiolabelled α-bungarotoxin. I once again wrote the initial manuscript, participated in editing alongside Dr. Baenizger, and created all the figures and tables.

4.2 Abstract

The outermost lipid-exposed α-helix (M4) in each of the homologous α, β, δ, and γ/ε subunits of the muscle nicotinic acetylcholine receptor (nAChR) has previously been proposed to act as a lipid sensor. However, the mechanism by which this sensor would function is not clear. To explore how the M4 α-helix from each subunit in human adult muscle nAChR influences function, and thus explore its putative role in lipid sensing, we functionally characterized alanine mutations at every residue in αM4, βM4, δM4, and εM4, along with both alanine and deletion mutations in the post-M4 region of each subunit. Although no critical interactions involving residues on M4 or in post-M4 were identified, we found numerous mutations at the M4 – M1/M3 interface altered the agonist-induced response. In addition, homologous mutations in M4 in different subunits were found to have different effects on channel function. The functional effects of multiple mutations either along M4 in one subunit or at homologous positions of M4 in different subunits were also found to be additive. Finally, when characterized in both *Xenopus* oocytes and HEK293T cells, select αM4 mutations displayed cell-specific phenotypes, possibly due to the different membrane lipid environments. Collectively, our data suggest different functional roles for the M4 α-helix in each heteromeric nAChR subunit and predict that lipid sensing involving M4 occurs primarily through the cumulative interactions at the M4 – M1/M3 interface, as opposed to the alteration of specific interactions that are critical to channel function.

4.3 Introduction

Although the functional sensitivity of the muscle-type ($\alpha_2\beta\gamma\delta$) nicotinic acetylcholine receptor (nAChR) from *Torpedo* to lipids has been extensively characterized (Baenziger et al., 2015; Barrantes, 2015; Thompson and Baenziger, 2020b), the mechanisms by which lipids influence function remain poorly understood. It is known that lipids alter function predominantly via a conformational selection mechanism whereby some membranes preferentially stabilize the activatable resting state while others preferentially stabilize non-activatable desensitized or uncoupled states (daCosta and Baenziger, 2009; daCosta et al., 2009, 2013; Thompson and Baenziger, 2020a). Several observations also suggest that the M4 α-helix from each of the five subunits plays a central role in lipid sensing (Hénault et al., 2015b). M4 is located at the periphery of the transmembrane domain (TMD) of each subunit where it forms extensive contacts with the lipid bilayer (Fig. 4.1). Numerous mutations in M4 influence channel function, including an αC418W potentiating mutation that leads to a congenital myasthenic syndrome (CMS) (Lasalde et al., 1996; Bouzat et al., 1998, 2000, 2002; Shen et al., 2006). Lipids are also observed bound to the interfaces between M4 and the adjacent M1 and M3 α-helices in the *Torpedo* nAChR and in other pentameric ligand-gated ion channels (pLGICs), although the functional roles of these bound lipids remain to be defined (Rahman et al., 2020a, 2022; Thompson and Baenziger, 2020b; Unwin, 2020; Zarkadas et al., 2022).

One plausible mechanism by which lipids influence nAChR function is by modulating interactions between M4 and the remainder of the transmembrane domain (TMD). More specifically, lipid induced changes in the position of M4 relative to M1 and M3 could alter inter-helical packing of the entire TMD in a manner that directly influences channel gating or desensitization, as was recently suggested for lipid binding to the M4 - M1 interface of the

prokaryotic pLGIC, ELIC (Hénault et al., 2019). Altered M4 - M1/M3 interactions could also re-position the M4 C terminus (post-M4) to interact with structures in the extracellular domain (ECD) to alter the physical coupling between the agonist binding ECD and channel gating TMD (Fig. 4.1b). The latter hypothesis is supported by the observation that post-M4 is critical to folding and function in some pLGICs (Butler et al., 2009; Haeger et al., 2010; Carswell et al., 2015b; Alcaino et al., 2017; Cory-Wright et al., 2018; Noviello et al., 2021), albeit not in others (Hénault et al., 2015a; Thompson et al., 2020).

As a first step towards understanding the mechanisms by which the nAChR senses its lipid environment, we set out to characterize the functional role of the M4 α-helix from each subunit in a hetero-pentameric muscle-type nAChR. In a previous publication, we probed the functional role of M4 from the α subunit (αM4) of the human adult muscle nAChR (Thompson et al., 2020). Here we extend this study to include M4 from each of the remaining β (βM4), δ (δM4), and ε (εM4) subunits. Through mutagenesis and electrophysiological recordings, we identify interactions between M4 and M1/M3 in each subunit that influence channel function and that could thus participate in lipid sensing, although no critical functional interactions were identified. In addition, we show that the functional effects of point mutations along each M4 or at homologous positions in M4 from different subunits are additive so that multiple simultaneous mutations add together leading to substantial functional effects. Finally, we show that the functional consequences of some M4 mutations are dependent upon the cellular context. Our data predict that lipid sensing in the muscle nAChR via M4 is governed by cumulative changes in multiple interactions at the M4 – M1/M3 interface that add up to substantive functional effects, as opposed to the alteration of specific interactions that play a critical role in channel function.

Figure 4.1 The M4 lipid sensors from each subunit of the nAChR are the most lipid exposed TMD α-helices

Homology model of the human adult muscle nAChR based on the 2.7 Å resolution *Torpedo* nAChR structure (PDB: 6UWZ). (A) Side view of the full model coloured by domain with agonist binding sites residues (αTrp149) and channel gate residues (9' and 13') are shown as spheres colored cyan and tan, respectively. (B) Zoomed in view of a single subunit with the MA α-helix removed for clarity. The M4 α-helix, post-M4, and the Cys-loop are shown in red, blue, and green, respectively. (C) Top-down view of the TMD with M4 helices from each subunit coloured red.

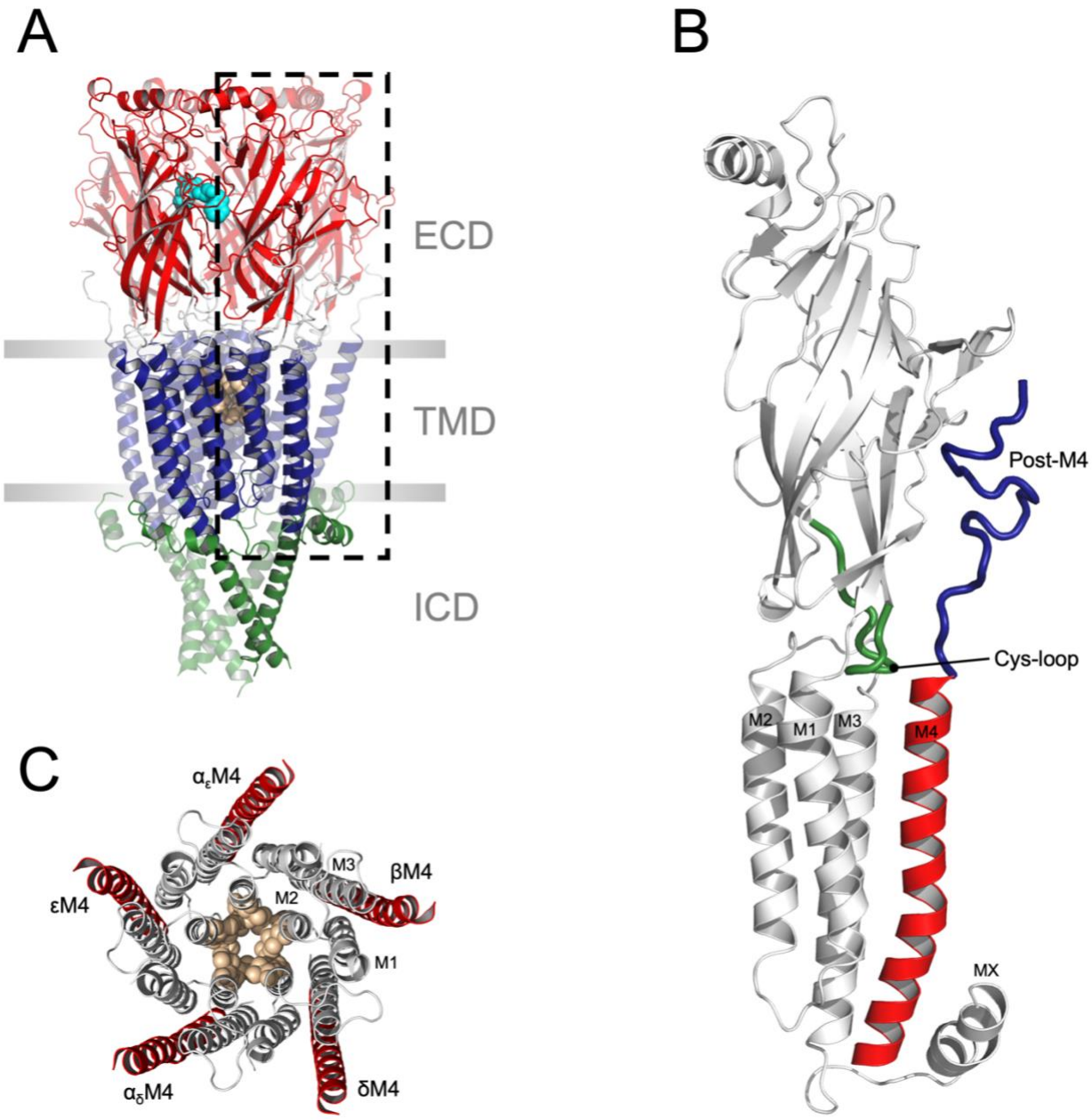
A
ECD
TMD
ICD
B
Post-M4
Cys-loop
M2
M1
M3
M4
MX
C
αεM4
βM4
εM4
M3
M2
M1
αδM4
δM4

4.4 Results

4.4.1 Alanine scan of αM4, βM4, δM4, and εM4.

The M4 α-helix from each of the four nAChR subunits is composed predominantly of aliphatic residues interspersed with neutral hydrogen bonding, charged and aromatic residues that could each form interactions with side chains on M1/M3 or with lipids that are essential to channel function and that could thus play a role in lipid sensing. To identify functionally important interactions, we generated an alanine mutation of each residue on M4 from the α, β, δ, and ε subunits. We were generous in our definition of M4 and included several residues in flanking regions, including many in post-M4. We examined the functional consequences by expressing each M4-mutated subunit along with non-mutated subunits in *Xenopus* oocytes. The concentration response of each to acetylcholine (ACh) was measured using two electrode voltage clamp electrophysiology.

Of the 155 generated alanine mutants (36 in α, 40 in β, 37 in δ and 42 in ε), all but one (εM430A) functionally expressed, with each of the functional mutants leading to robust inward currents whose peak amplitudes increase in an ACh concentration-dependent manner (Fig. 4.2). Derived EC_{50}/pEC_{50} values for those mutations that led to statistically significant changes in function are summarized in Table 4.1, with the EC_{50}/pEC_{50} values for all mutations presented in Tables 4.2-4.5. Note that each EC_{50}/pEC_{50} value reflects a weighted ensemble of all the rate constants associated with both agonist binding/dissociation and channel opening/closing, although the measured values can be influenced by the rates of desensitization. We assume that the changes in the measured EC_{50}/pEC_{50} values reflect primarily changes in the channel opening/closing rate constants as 1) the studied mutations are distant from the agonist binding site and thus unlikely to directly alter agonist binding/dissociation

Figure 4.2 Functional effects of alanine mutations to residues within each M4 α-helix of the nAChR

Representative whole-cell two-electrode voltage clamp traces are shown for WT and the largest function altering mutants Ala mutants in the M4 α-helices of each subunit. Normalized concentration response curves for the selected mutants are shown in the bottom right.

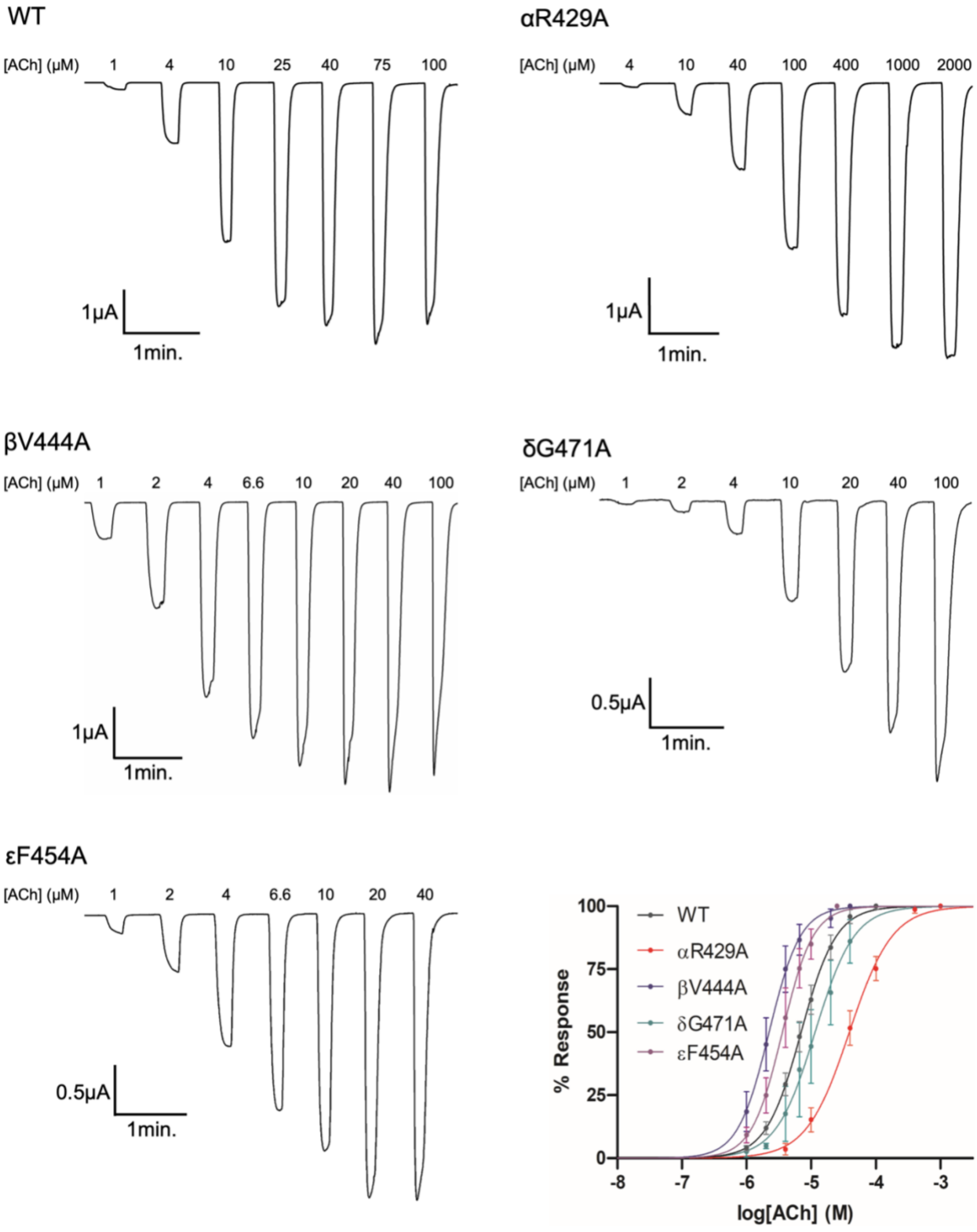
WT
[ACh] (μM) 1 4 10 25 40 75 100
1μA
1min.
αR429A
[ACh] (μM) 4 10 40 100 400 1000 2000
1μA
1min.
βV444A
[ACh] (μM) 1 2 4 6.6 10 20 40 100
1μA
1min.
δG471A
[ACh] (μM) 1 2 4 10 20 40 100
0.5μA
1min.
εF454A
[ACh] (μM) 1 2 4 6.6 10 20 40
0.5μA
1min.
% Response
100
75
50
25
0
-8 -7 -6 -5 -4 -3
log[ACh] (M)
WT
αR429A
βV444A
δG471A
εF454A

Table 4.1 - Alanine mutations in M4 of each subunit that led to statistically significant changes in pEC_{50}

Mutant	Dose response[a,b] EC_{50} (μM)	pEC_{50} (M)	Hill slope	n	Fold change $\frac{EC_{50}(Mut)}{EC_{50}(WT)}$
WT	7.61	5.12 ± 0.07	1.70 ± 0.47	50	-
		α subunit			
αL433A	10.3	4.99 ± 0.04	1.93 ± 0.14	12	1.35
αR429A	40.0	4.41 ± 0.11	1.09 ± 0.12	10	5.25
αF426A	2.02	5.71 ± 0.14	1.80 ± 0.76	11	0.27
αV425A	4.30	5.37 ± 0.05	1.89 ± 0.28	10	0.57
αL423A	5.80	5.24 ± 0.07	2.54 ± 0.66	10	0.76
αT422A	31.2	4.52 ± 0.13	1.40 ± 0.12	10	4.10
αG421A	10.0	5.00 ± 0.05	1.96 ± 0.26	9	1.32
αI420A	5.97	5.23 ± 0.07	2.71 ± 0.33	10	0.78
αC418A	10.6	4.99 ± 0.13	1.82 ± 0.33	9	1.40
αM415A	12.5	4.92 ± 0.13	1.61 ± 0.27	10	1.65
αF414A	4.47	5.36 ± 0.09	1.76 ± 0.34	10	0.59
αL411A	9.86	5.02 ± 0.10	2.35 ± 0.40	13	1.30
αL410A	5.21	5.27 ± 0.06	2.06 ± 0.59	21	0.68
αH408A	10.1	5.00 ± 0.05	1.80 ± 0.27	10	1.33
αD407A	4.97	5.31 ± 0.04	3.12 ± 0.78	11	0.65
αY401A	9.86	5.01 ± 0.03	1.75 ± 0.48	11	1.30
αK400A	12.9	4.90 ± 0.09	1.89 ± 0.63	15	1.70
		β subunit			
βP476A	4.98	5.33 ± 0.20	1.49 ± 0.34	13	0.65
βD475A	4.15	5.39 ± 0.11	1.27 ± 0.31	8	0.54
βH470A	13.0	4.90 ± 0.11	1.24 ± 0.19	13	1.71
βD466A	5.08	5.31 ± 0.14	1.57 ± 0.48	11	0.67
βI463A	3.67	5.44 ± 0.16[b]	1.78 ± 0.11	8	0.48
βG459A	14.4	4.90 ± 0.28	1.12 ± 0.30	10	1.89
βS457A	13.2	4.93 ± 0.22	1.10 ± 0.24	11	1.74
βI453A	4.57	5.36 ± 0.12	1.46 ± 0.24	8	0.60
βW450A	12.7	4.94 ± 0.19	1.27 ± 0.20	14	1.66
βL449A	15.9	4.82 ± 0.15	1.45 ± 0.19	8	2.09
βF448A	4.36	5.38 ± 0.15	1.63 ± 0.48	8	0.57
βV444A	2.22	5.66 ± 0.07	1.89 ± 0.30	11	0.29
		δ subunit			
δP478A	4.72	5.34 ± 0.11[b]	1.43 ± 0.56	7	0.62
δP477A	11.7	4.94 ± 0.09[b]	1.26 ± 0.14	8	1.51
δG471A	14.1	4.86 ± 0.11[b]	1.57 ± 0.25	4	1.85
δL469A	5.13	5.30 ± 0.09[b]	1.71 ± 0.38	9	0.67
δI467A	4.63	5.34 ± 0.07[b]	1.91 ± 0.79	7	0.61
δW466A	5.49	5.28 ± 0.14[b]	1.57 ± 0.27	8	0.72
δG463A	4.88	5.32 ± 0.10[b]	1.71 ± 0.38	8	0.64
δP458A	4.08	5.40 ± 0.09[b]	2.06 ± 0.75	7	0.54
δV456A	5.06	5.33 ± 0.19[b]	1.58 ± 0.41	8	0.66
δC452A	4.86	5.32 ± 0.07[b]	1.56 ± 0.16	11	0.64
δR450A	5.15	5.29 ± 0.04[b]	1.72 ± 0.17	7	0.68
δD449A	5.03	5.34 ± 0.20[b]	2.00 ± 0.19	8	0.66
δV444A	4.35	5.36 ± 0.03[b]	2.02 ± 0.17	8	0.57
		ε subunit			
εI471A	15.5	4.81 ± 0.07[b]	1.61 ± 0.24	10	2.04

εC470A	13.4	4.88 ± 0.05[b]	1.54 ± 0.08	12	1.76
εP463A	12.1	4.93 ± 0.08[b]	1.77 ± 0.10	9	1.59
εY458A	5.10	5.30 ± 0.07[b]	1.43 ± 0.20	8	0.67
εF454A	3.90	5.42 ± 0.10[b]	1.80 ± 0.25	8	0.51
εI453A	4.50	5.35 ± 0.06[b]	1.83 ± 0.27	8	0.59
εG449A	5.62	5.26 ± 0.12[b]	1.54 ± 0.52	9	0.74
εC438A	10.1	5.00 ± 0.06[b]	1.67 ± 0.20	9	1.33
εN436A	12.9	4.90 ± 0.09[b]	1.76 ± 0.22	11	1.70
εG431A	10.6	4.99 ± 0.11[b]	1.60 ± 0.17	8	1.40
εM430A	No current[c]	-	-	8	-
εV428A	5.62	5.25 ± 0.06[b]	1.56 ± 0.19	8	0.74
εW427A	5.85	5.25 ± 0.14[b]	1.37 ± 0.39	9	0.77

[a]Measurements performed 1-4 days after cRNA injection (V_{hold} ranging from -20 to -80 mV). Error values represented as standard deviation

[b]$p < 0.001$ relative to WT via one-way ANOVA followed by Dunnet's post hoc test

[c]No significant current observed up to 4 day after cRNA injection

Table 4.2 - Effects of Ala mutations in αM4 on nAChR function

	Dose response[a]			
Mutant	EC_{50} (μM)	pEC_{50} (M)	Hill slope	n
WT	7.61	5.12 ± 0.07	1.70 ± 0.47	50
G437A	6.12	5.22 ± 0.06	1.58 ± 0.43	9
Q436A	8.29	5.08 ± 0.04	1.94 ± 0.14	13
Q435A	8.07	5.09 ± 0.03	2.03 ± 0.12	13
N434A	8.09	5.09 ± 0.04	1.94 ± 0.12	11
L433A	10.3	4.99 ± 0.04[b]	1.93 ± 0.14	12
E432A	8.83	5.05 ± 0.03	1.92 ± 0.13	11
I431A	8.70	5.06 ± 0.03	1.85 ± 0.19	10
L430A	8.63	5.07 ± 0.07	1.72 ± 0.17	10
R429A	40.0	4.41 ± 0.11[b]	1.09 ± 0.12	10
G428A	6.15	5.21 ± 0.04	1.66 ± 0.28	9
F426A	2.02	5.71 ± 0.14[b]	1.80 ± 0.76	11
V425A	4.30	5.37 ± 0.05[b]	1.89 ± 0.28	10
L423A	5.80	5.24 ± 0.07[b]	2.54 ± 0.66	10
T422A	31.2	4.52 ± 0.13[b]	1.40 ± 0.12	10
G421A	10.0	5.00 ± 0.05[b]	1.96 ± 0.26	9
I420A	5.97	5.23 ± 0.07[b]	2.71 ± 0.33	10
I419A	6.58	5.19 ± 0.07	2.15 ± 0.32	10
C418A	10.6	4.99 ± 0.13[b]	1.82 ± 0.33	9
V417A	7.71	5.12 ± 0.08	1.94 ± 0.11	10
L416A	7.11	5.15 ± 0.05	2.01 ± 0.09	10
M415A	12.5	4.92 ± 0.13[b]	1.61 ± 0.27	10
F414A	4.47	5.36 ± 0.09[b]	1.76 ± 0.34	10
V413A	7.24	5.14 ± 0.07	2.20 ± 0.26	10
G412A	6.77	5.17 ± 0.07	1.54 ± 0.31	9
L411A	9.86	5.02 ± 0.10[b]	2.35 ± 0.40	13
L410A	5.21	5.27 ± 0.06[b]	2.06 ± 0.59	21
I409A	8.22	5.10 ± 0.10	2.05 ± 0.51	10
H408A	10.1	5.00 ± 0.05[b]	1.80 ± 0.27	10
D407A	4.97	5.31 ± 0.04[b]	3.12 ± 0.78	11
M406A	8.37	5.08 ± 0.04	1.70 ± 0.21	14
V405A	7.76	5.11 ± 0.06	2.03 ± 0.39	10
M404A	8.05	5.10 ± 0.04	2.14 ± 0.40	10
V402A	7.91	5.10 ± 0.02	2.05 ± 0.13	9
Y401A	9.86	5.01 ± 0.03[b]	1.75 ± 0.48	11
K400A	12.9	4.90 ± 0.09[b]	1.89 ± 0.63	15
W399A	8.90	5.05 ± 0.03	2.51 ± 0.41	10

[a]Measurements performed 1-4 days after cRNA injection (V_{hold} ranging from -20 to -80 mV). Error values represented as standard deviation

[b]$p < 0.001$ relative to WT via one-way ANOVA followed by Dunnet's post hoc test

[c]No significant current observed up to 4 day after cRNA injection

Table 4.3 - Effects of Ala mutations in βM4 on nAChR function

	Dose response[a]			
Mutant	EC_{50} (μM)	pEC_{50} (M)	Hill slope	n
WT	7.61	5.12 ± 0.07	1.70 ± 0.47	50
P478A	5.29	5.29 ± 0.11	1.59 ± 0.20	10
F477A	6.27	5.21 ± 0.10	1.59 ± 0.13	8
P476A	4.98	5.33 ± 0.20[b]	1.49 ± 0.34	13
D475A	4.15	5.39 ± 0.11[b]	1.27 ± 0.31	8
P474A	6.20	5.22 ± 0.13	1.27 ± 0.24	12
P273A	8.04	5.11 ± 0.11	1.29 ± 0.29	11
P472A	7.91	5.11 ± 0.10	1.21 ± 0.20	9
L471A	7.44	5.14 ± 0.10	1.63 ± 0.71	11
H470A	13.0	4.90 ± 0.11[b]	1.24 ± 0.19	13
Y469A	7.76	5.12 ± 0.10	1.20 ± 0.10	9
T468A	7.54	5.13 ± 0.07	1.34 ± 0.15	11
D466A	5.08	5.31 ± 0.14[b]	1.57 ± 0.48	11
L465A	9.71	5.03 ± 0.11	1.20 ± 0.22	11
F464A	8.55	5.08 ± 0.11	1.38 ± 0.19	10
I463A	3.67	5.44 ± 0.16[b]	1.78 ± 0.11	8
V462A	7.79	5.12 ± 0.10	1.57 ± 0.79	11
L461A	6.78	5.17 ± 0.05	1.57 ± 0.38	9
T460A	8.84	5.06 ± 0.09	1.56 ± 0.15	11
G459A	14.4	4.90 ± 0.28[b]	1.12 ± 0.30	10
V458A	7.03	5.16 ± 0.11	1.73 ± 0.45	8
S457A	13.2	4.93 ± 0.22[b]	1.10 ± 0.24	11
T456A	8.26	5.12 ± 0.18	1.24 ± 0.18	8
F455A	6.72	5.18 ± 0.09	1.73 ± 0.66	10
I454A	6.07	5.25 ± 0.20	1.46 ± 0.45	11
I453A	4.57	5.36 ± 0.12[b]	1.46 ± 0.24	8
F452A	10.5	4.98 ± 0.07	1.69 ± 0.11	8
T451A	10.4	5.00 ± 0.11	1.25 ± 0.24	11
W450A	12.7	4.94 ± 0.19[b]	1.27 ± 0.20	14
L449A	15.9	4.82 ± 0.15[b]	1.45 ± 0.19	8
F448A	4.36	5.38 ± 0.15[b]	1.63 ± 0.48	8
L447A	9.14	5.06 ± 0.16	1.24 ± 0.23	8
R446A	12.6	4.92 ± 0.14	1.18 ± 0.23	9
D445A	11.9	4.99 ± 0.30	1.46 ± 0.13	9
V444A	2.22	5.66 ± 0.07[b]	1.89 ± 0.30	11
V443A	9.98	5.02 ± 0.14	1.16 ± 0.21	11
M442A	11.3	4.96 ± 0.13	1.45 ± 0.29	12
V440A	7.28	5.14 ± 0.08	1.49 ± 0.30	12
F439A	7.11	5.15 ± 0.07	1.80 ± 0.08	9
Q438A	7.92	5.10 ± 0.02	1.33 ± 0.22	9
W437A	8.88	5.07 ± 0.12	1.56 ± 0.26	9

[a]Measurements performed 1-4 days after cRNA injection (V_{hold} ranging from -20 to -80 mV). Error values represented as standard deviation

[b]$p < 0.001$ relative to WT via one-way ANOVA followed by Dunnet's post hoc test

[c]No significant current observed up to 4 day after cRNA injection

Table 4.4 - Effects of Ala mutations in δM4 on nAChR function

	Dose response[a]			
Mutant	EC_{50} (μM)	pEC_{50} (M)	Hill slope	n
WT	7.61	5.12 ± 0.07	1.70 ± 0.47	50
Q479A	5.96	5.24 ± 0.12	1.70 ± 0.11	8
P478A	4.72	5.34 ± 0.11[b]	1.43 ± 0.56	7
P477A	11.5	4.94 ± 0.09[b]	1.26 ± 0.14	8
P476A	8.28	5.08 ± 0.04	1.63 ± 0.15	8
Q475A	6.60	5.19 ± 0.10	1.14 ± 0.32	8
N474A	7.50	5.13 ± 0.09	1.74 ± 0.17	8
Y473A	6.84	5.17 ± 0.09	1.49 ± 0.26	8
V472A	8.78	5.08 ± 0.15	1.22 ± 0.26	7
G471A	14.1	4.86 ± 0.11[b]	1.57 ± 0.25	4
Q470A	7.36	5.15 ± 0.14	1.43 ± 0.29	7
L469A	5.13	5.30 ± 0.09[b]	1.71 ± 0.38	9
F468A	5.83	5.25 ± 0.10	1.60 ± 0.27	7
I467A	4.63	5.34 ± 0.07[b]	1.91 ± 0.79	7
W466A	5.49	5.28 ± 0.14[b]	1.57 ± 0.27	8
T464A	8.24	5.09 ± 0.08	1.28 ± 0.14	7
G463A	4.88	5.32 ± 0.10[b]	1.71 ± 0.38	8
V462A	7.41	5.15 ± 0.12	1.45 ± 0.27	8
V461A	7.13	5.15 ± 0.07	1.60 ± 0.27	9
M460A	7.23	5.15 ± 0.07	1.52 ± 0.22	8
V459A	10.2	5.00 ± 0.12	1.31 ± 0.19	8
P458A	4.08	5.40 ± 0.09[b]	2.06 ± 0.75	7
T457A	7.84	5.12 ± 0.13	1.38 ± 0.15	7
V456A	5.06	5.33 ± 0.19[b]	1.58 ± 0.41	8
V455A	5.77	5.26 ± 0.16	1.78 ± 0.50	8
F454A	7.67	5.12 ± 0.05	1.64 ± 0.17	8
L453A	7.66	5.12 ± 0.08	1.39 ± 0.24	8
C452A	4.86	5.32 ± 0.07[b]	1.56 ± 0.16	11
L451A	7.46	5.14 ± 0.11	1.60 ± 0.22	9
R450A	5.15	5.29 ± 0.04[b]	1.72 ± 0.17	7
D449A	5.03	5.34 ± 0.20[b]	2.00 ± 0.19	8
V448A	8.53	5.07 ± 0.05	1.63 ± 0.07	8
T447A	6.57	5.19 ± 0.07	1.85 ± 0.15	8
R446A	7.87	5.11 ± 0.09	1.54 ± 0.17	8
V444A	4.35	5.36 ± 0.03[b]	2.02 ± 0.17	8
R443A	9.66	5.03 ± 0.13	1.34 ± 0.22	7
N442A	7.82	5.11 ± 0.08	1.34 ± 0.18	7
W441A	5.71	5.24 ± 0.01	1.80 ± 0.07	3

[a]Measurements performed 1-4 days after cRNA injection (V_{hold} ranging from -20 to -80 mV). Error values represented as standard deviation

[b]$p < 0.001$ relative to WT via one-way ANOVA followed by Dunnet's post hoc test

[c]No significant current observed up to 4 day after cRNA injection

Table 4.5 - Effects of Ala mutations in εM4 on nAChR function

	Dose response[a]			
Mutant	EC_{50} (μM)	pEC_{50} (M)	Hill slope	n
WT	7.61	5.12 ± 0.07	1.70 ± 0.47	50
P473A	8.76	5.07 ± 0.09	1.79 ± 0.11	8
Q472A	6.02	5.22 ± 0.04	1.71 ± 0.13	8
I471A	15.5	4.81 ± 0.07[b]	1.61 ± 0.24	10
C470A	13.4	4.88 ± 0.05[b]	1.54 ± 0.08	12
P469A	6.68	5.18 ± 0.03	1.92 ± 0.36	10
Y467A	7.51	5.14 ± 0.10	1.58 ± 0.16	8
P466A	7.90	5.11 ± 0.09	1.54 ± 0.08	8
L465A	7.72	5.12 ± 0.07	1.73 ± 0.24	9
D464A	8.06	5.10 ± 0.06	1.96 ± 0.59	8
P463A	12.1	4.93 ± 0.08[b]	1.77 ± 0.10	9
V462A	6.88	5.17 ± 0.06	1.52 ± 0.15	8
R461A	7.42	5.13 ± 0.05	1.73 ± 0.07	8
N460A	7.63	5.13 ± 0.11	1.66 ± 0.13	8
F459A	6.35	5.20 ± 0.07	1.63 ± 0.11	8
Y458A	5.10	5.30 ± 0.07[b]	1.43 ± 0.20	8
G456A	7.95	5.11 ± 0.09	1.51 ± 0.07	8
L455A	7.46	5.13 ± 0.04	1.72 ± 0.12	8
F454A	3.90	5.42 ± 0.10[b]	1.80 ± 0.25	8
I453A	4.50	5.35 ± 0.06[b]	1.83 ± 0.27	8
L452A	7.96	5.10 ± 0.05	1.64 ± 0.12	8
S451A	8.70	5.06 ± 0.06	1.77 ± 0.10	9
S450A	8.05	5.09 ± 0.02	1.89 ± 0.25	8
G449A	5.62	5.26 ± 0.12[b]	1.54 ± 0.52	9
V448A	7.52	5.13 ± 0.05	1.69 ± 0.15	8
S447A	9.33	5.03 ± 0.05	1.66 ± 0.18	8
F446A	8.89	5.06 ± 0.07	1.51 ± 0.18	9
L445A	8.04	5.11 ± 0.10	1.53 ± 0.28	8
V444A	7.40	5.14 ± 0.08	1.48 ± 0.13	8
L443A	8.08	5.10 ± 0.08	1.69 ± 0.13	11
W440A	7.48	5.13 ± 0.04	1.57 ± 0.15	8
F439A	8.59	5.07 ± 0.07	1.81 ± 0.08	8
C438A	10.1	5.00 ± 0.06[b]	1.67 ± 0.20	9
I437A	7.58	5.13 ± 0.08	1.83 ± 0.22	8
N436A	12.9	4.90 ± 0.09[b]	1.76 ± 0.22	11
D435A	8.03	5.10 ± 0.05	1.73 ± 0.18	8
L434A	8.07	5.10 ± 0.08	1.89 ± 0.21	8
N432A	8.66	5.07 ± 0.06	1.69 ± 0.11	8
G431A	10.6	4.99 ± 0.11[b]	1.60 ± 0.17	8
M430A	No current[c]			8
R429A	7.29	5.14 ± 0.04	1.54 ± 0.21	8
V428A	5.63	5.25 ± 0.06[b]	1.56 ± 0.19	8
W427A	5.85	5.25 ± 0.14[b]	1.37 ± 0.39	9

Same legend as previous three tables

(Bouzat et al., 2000; Mitra et al., 2004), and 2) only minor changes in the rates of desensitization are observed making very little impact on the reported EC_{50} values (Fig. 4.2). A left shift in the concentration response leading to a decrease in EC_{50} reflects a gain-of-function while a right shift leading to an increase in EC_{50} reflects a loss-of-function.

As was observed previously with alanine substitutions in αM4 (Thompson et al., 2020), alanine substitutions in βM4, δM4, and εM4 led to a mix of gain- and loss-of-function phenotypes, with most of the function altering mutations located along the M4 – M1/M3 interface (Fig. 4.3). The proportion of mutations leading to statistically significant changes in function is slightly lower in β, δ or ε than in α, which is present twice per pentamer (17 of 36 in α (47%); 12 of 40 in β (30%); 13 of 37 in δ (35%); and 12 of 42 (29%) in ε). Furthermore, only four of the 119 mutations in β, δ and ε combined led to more than a two-fold change in function (βV444A, βL449A, βI463A, εI471A) with the largest being a 3.4-fold gain-of-function with βV444A. In contrast, three out of 36 mutants do so in the α subunit, with these three mutants leading to larger 4.1-fold, 3.8-fold and 5.3-fold changes in function (αT422A, αF426A and αR429A, respectively). The detected changes in EC_{50} values show that there are interactions at both the M4 – M1/M3 and M4 - lipid interface that influence channel function. On the other hand, the absence of dramatic changes in the EC_{50} values (except for εM430A, see below) suggests that there are no specific interactions at either interface that are critical for channel function.

The data also exhibit several intriguing trends that allow us to glean some insight into the functional roles played by the M4 α-helix from each of the different subunits:

Figure 4.3 Functional effects of every M4 alanine mutant on nAChR function

Changes in EC_{50} relative to WT for M4 alanine mutant are heat mapped onto each subunit. Residues coloured red correspond to gain-of-function mutants, those coloured blue loss-of-function mutants, and those coloured white cause no change in EC_{50}.

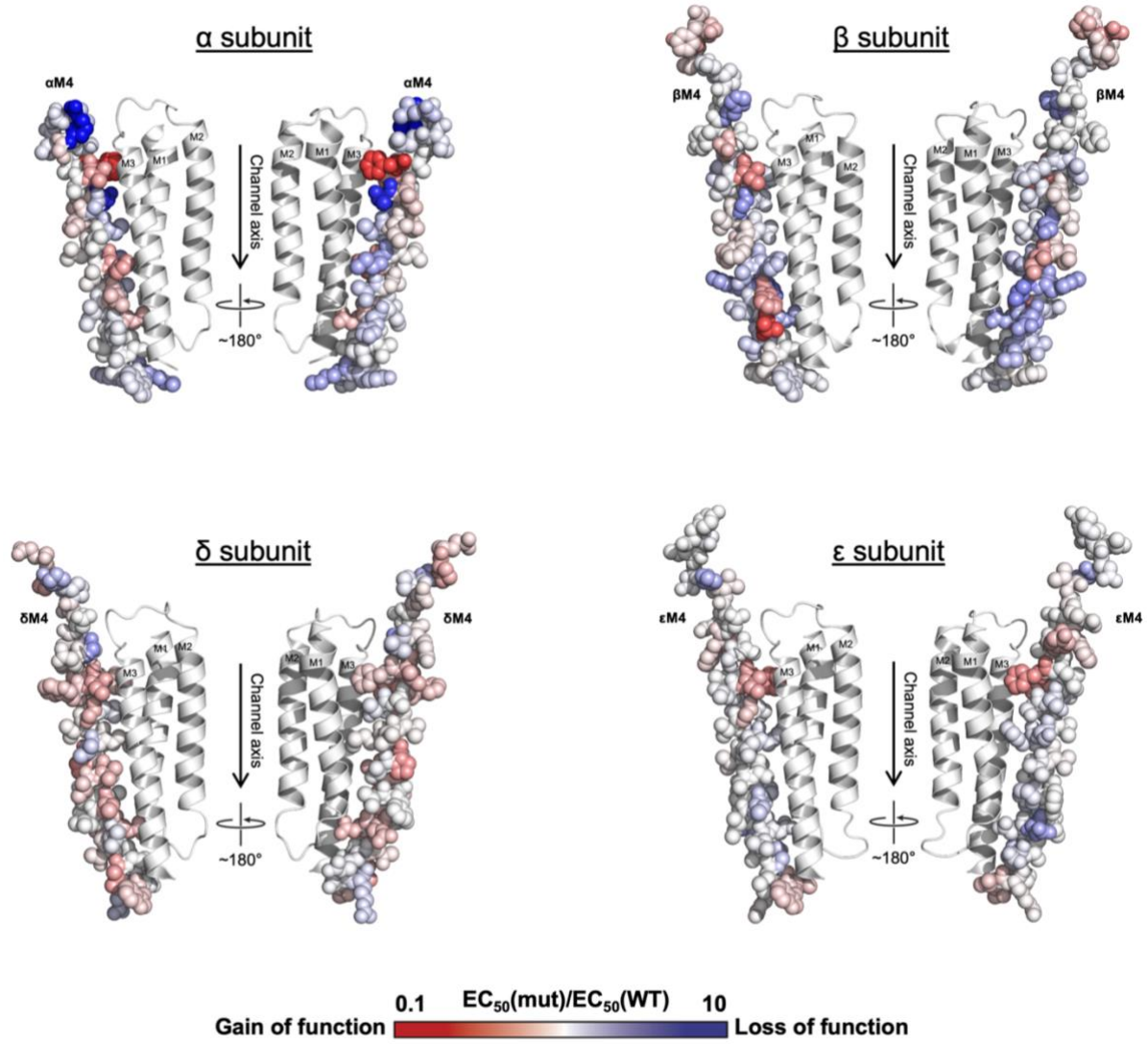
α subunit
αM4
αM4
M2
M3
M1
M2
M1
M3
Channel axis
~180°
β subunit
βM4
βM4
M1
M3
M2
M2
M1
M3
Channel axis
~180°
δ subunit
δM4
δM4
M1
M2
M3
M2
M1
M3
Channel axis
~180°
ε subunit
εM4
εM4
M1
M2
M3
M2
M1
M3
Channel axis
~180°
0.1
EC50(mut)/EC50(WT)
10
Gain of function
Loss of function

First, of the four alanine mutations in β/δ/ε that altered function by more than two-fold, three of these are in βM4 (βV444A, βL449A, and βI463A) (Fig 4.4). In contrast, although δM4 has a higher proportion of statistically significant function altering alanine mutants than βM4, none produced more than a two-fold change of function. Furthermore, alanine mutations in εM4 led to relatively few statistically significant changes in function, although εI471A, which is in post-M4, alters the EC_{50} ~2-fold. The relatively large changes in function observed with the three alanine mutations in βM4 suggests that specific regions along the βM4 - βM1/βM3 interface are functionally important. This finding was unexpected given that β is a structural subunit that is not directly involved in agonist binding. In addition, the four TMD α-helices in the β subunit undergo the lowest amplitude motions upon agonist binding (Rahman et al., 2022; Zarkadas et al., 2022).

Second, none of the alanine mutations of residues in β, δ and ε that align with those residues in αM4, whose mutation to alanine led to relatively large changes in function, have substantial effects on the measured EC_{50} values. Specifically, αT422A, αF426A and αR429A led to 4.1-fold, 3.8-fold and 5.3-fold changes in the recorded EC_{50} values, as noted above. The equivalent residues in the other three subunits are βT460, βF464 and βA467; δT464, δF468 and δG471; and εS450, εF454 and εA457. Of the alanine mutations generated for these equivalent residues, only εF454A and δG471A led to statistically significant changes in the EC_{50} values, although the effects on function in both cases are less than 2-fold. These data show that identical changes in the structure of the M4 α-helix from different subunits lead to different effects on function. The M4 α-helix from the α, β, δ and ε subunits thus each plays a subtly different role in channel function.

Third, εM430A is the only mutant that did not functionally express (Fig. 4.4). εMet430 extends toward εMX into a hydrophobic pocket formed by residues on εM3, εM4 and εMX. εMX is implicated in the assembly/cell surface trafficking of the muscle nAChR, with mutations in εMX reducing cell surface expression leading to CMS (Rudell et al., 2020). Residues in M4 that project towards MX may play a particularly important role in nAChR expression.

Finally, we were surprised to see that the εC470A mutant led to robust ACh-induced currents that are comparable in magnitude to those observed with the WT nAChR. In contrast, εC470A, εC470S and a deletion mutation at εC470 each inhibits cell surface expression of the nAChR in HEK293T cells, with low expression of the latter in humans leading to CMS (Ealing et al., 2002). It has been suggested that the sulfhydryl side chain of εCys470 is critical for folding and expression. Our data show that the side chain of εC470 is not intrinsically required for folding. The differential effects of the mutant in different expression systems can be may be a product of unique cellular quality control machinery, but it is also possible that the lipid environment of an oocyte supports folding of the εC470A mutant while the lipid environments of HEK293T cells and muscle cells do not (see section 4.5).

Figure 4.4 Position of residues that cause significant changes in function when mutated to Ala

Zoomed in views of each subunit's TMD with residues from M4 that significantly altered the EC_{50} when mutated to Ala shown as sticks and coloured according to residues type: aliphatic, *tan*; aromatic, yellow; polar/hydrogen bonding, *green*; negative, *red*; positive, *blue*. A sequence alignment of M4 α-helices from each subunits of the human adult nAChR is shown at the bottom with residues coloured according to residue type (aliphatic, *black*; aromatic, yellow; polar/hydrogen bonding, *green*; negative, *red*; positive, *blue*) with post-M4 highlighted in grey.

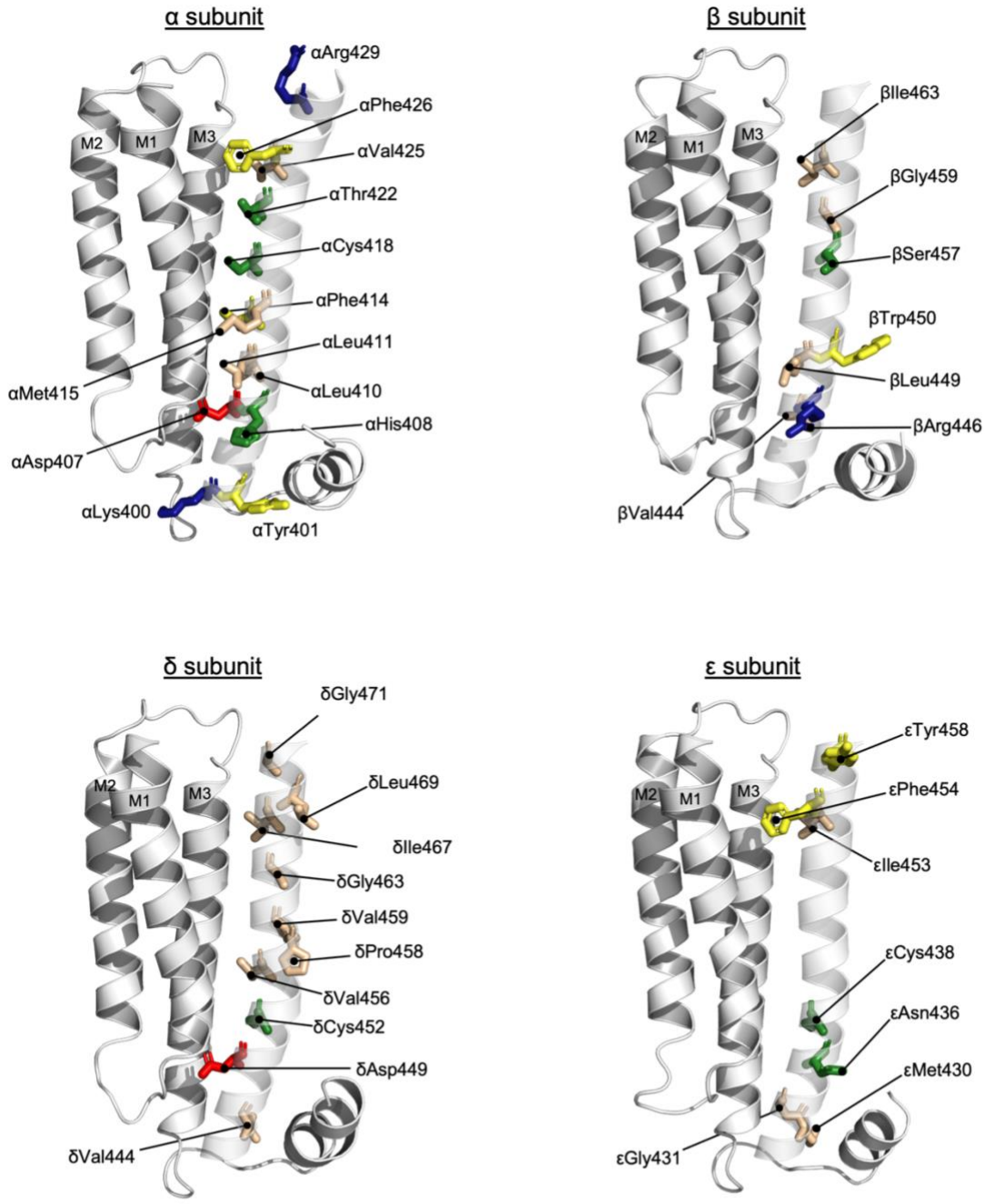

αM4	399	WKYVAMVMDHILLGVFMLVCIIGTLAVFAGRLIELNQQG
βM4	437	WQFVAMVVDRLFLWTFIIFTSVGTLVIFLDATYHLPPPDPFP
δM4	441	WNRVARTVDRLCLFVVTPVMVVGTAWIFLQGVYNQPPPQPFPGDPYSYNVQDKRFI
εM4	427	WVRMGNALDNICFWAALVLFSVGSSLIFLGAYFNRVPDLPYAPCIQP

4.4.2 Role of post-M4 in channel function

Post-M4 is required for optimal expression/function in some pLGICs but not in others (Butler et al., 2009; Haeger et al., 2010; Carswell et al., 2015b; Alcaino et al., 2017; Cory-Wright et al., 2018; Noviello et al., 2021). In our alanine scans, we observed that only nine out of 51 mutations in post-M4 led to statistically significant changes in function (αL433A, βH470A, βD475A, βP476A, δP477A, δP478A, εP463A, εC470A, and εI471A), but none of these altered function by more than ~2-fold.

Although the subtle effects of the single alanine mutants imply that interactions between post-M4 and the remainder of the nAChR are not critical for folding/function, we explored this possibility further by generating a series of C-terminal deletions in each subunit. In the α-subunit, deletion of up to nine residues (αΔ9) led to only a two-fold or less loss-of-function, with the deletion of additional residues extending into the M4 α-helix (αΔ12) eventually leading to a loss of functional expression (Thompson et al., 2020) (Fig. 4.5; Table 4.6). Similarly, deleting up to 8 residues in βM4 and εM4, or 12 residues in δM4 had little to no effect, with further deletions of up to 13 residues in βM4 and 24 residues in either δM4 or εM4 leading to subtle losses- (β and δ) or gains-of-function (ε). Surprisingly, the 24-residue deletion in δ restored WT activity, while the 15- and 24-residue deletions in β and ε, respectively, led to gains-of-function (εΔ24 led to a relatively large 6.3-fold gain-of-function). These results show that the post-M4 region is not important in the folding or function of the adult muscle nAChR.

Figure 4.4 Location of C-terminal deletions in each subunit

Side views of each subunit are shown with M4 helices and post-M4 semi-transparent. Black spheres denote α-carbons for each deletion mutation.

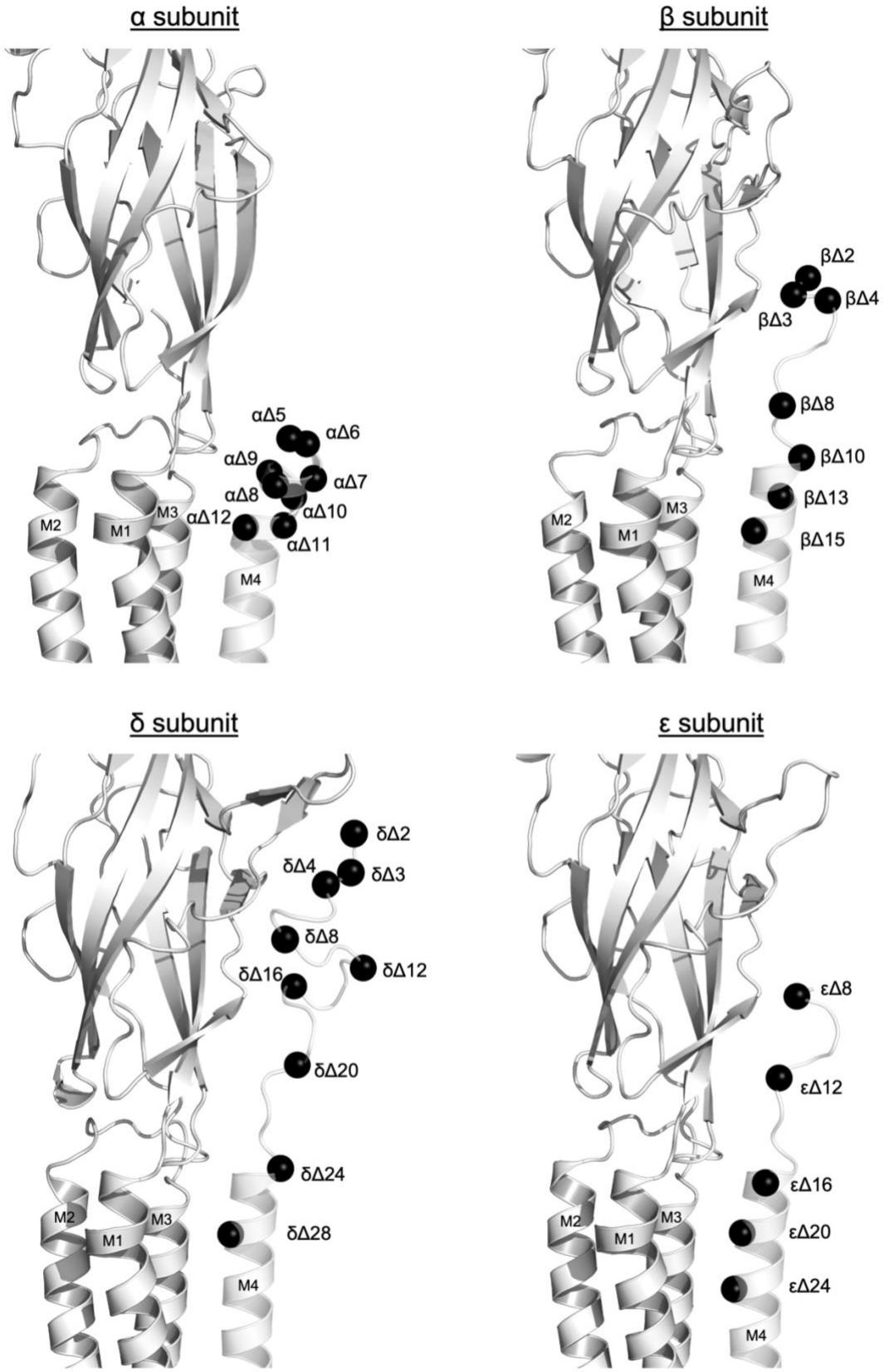
α subunit
αΔ5
αΔ6
αΔ9
αΔ7
αΔ8
αΔ10
αΔ12
αΔ11
M2
M1
M3
M4
β subunit
βΔ2
βΔ4
βΔ3
βΔ8
βΔ10
βΔ13
βΔ15
M2
M1
M3
M4
δ subunit
δΔ2
δΔ4
δΔ3
δΔ8
δΔ12
δΔ16
δΔ20
δΔ24
δΔ28
M2
M1
M3
M4
ε subunit
εΔ8
εΔ12
εΔ16
εΔ20
εΔ24
M2
M1
M3
M4

Table 4.6 - Effects of M4 C-terminal deletions on nAChR function and expression

	Dose response[a]			
Deletion(s)	EC_{50} (μM)	pEC_{50} (M)	Hill slope	n
<u>α subunit</u>				
WT: …LAVFAGRLIELNQQG	7.61	5.12 ± 0.07	1.70 ± 0.47	50
Δ1: …LAVFAGRLIELNQQ	6.86	5.17 ± 0.06	2.66 ± 0.67	9
Δ2: …LAVFAGRLIELNQ	6.37	5.20 ± 0.07	2.62 ± 0.54	9
Δ3: …LAVFAGRLIELN	7.14	5.15 ± 0.07	2.36 ± 0.38	8
Δ4: …LAVFAGRLIEL	8.49	5.08 ± 0.07	2.13 ± 0.44	8
Δ5: …LAVFAGRLIE	11.8	4.93 ± 0.04[b]	1.65 ± 0.33	10
Δ6: …LAVFAGRLI	12.3	4.91 ± 0.04[b]	1.59 ± 0.25	10
Δ7: …LAVFAGRL	12.7	4.90 ± 0.06[b]	1.54 ± 0.15	10
Δ8: …LAVFAGR	14.7	4.84 ± 0.07[b]	1.46 ± 0.29	10
Δ9: …LAVFAG	14.9	4.83 ± 0.08[b]	1.77 ± 0.35	10
Δ10: …LAVFA	21.4	4.68 ± 0.08[b]	1.35 ± 0.12	10
Δ11: …LAVF	23.0	4.65 ± 0.09[b]	1.69 ± 0.36	10
Δ12: …LAV	No current[c]	-	-	8
<u>β subunit</u>				
WT: …LVIFLDATYHLPPPDPFP	7.61	5.12 ± 0.07	1.70 ± 0.47	50
Δ1: …LVIFLDATYHLPPPDPF	9.77	5.02 ± 0.09	1.59 ± 0.08	13
Δ2: …LVIFLDATYHLPPPDP	9.65	5.02 ± 0.05	1.61 ± 0.11	11
Δ3: …LVIFLDATYHLPPPD	9.04	5.05 ± 0.08	1.46 ± 0.19	12
Δ4: …LVIFLDATYHLPPP	7.00	5.13 ± 0.15	1.75 ± 0.13	10
Δ8: …LVIFLDATYH	8.36	5.10 ± 0.16	1.79 ± 0.20	7
Δ10: …LVIFLDAT	11.6	4.94 ± 0.08[b]	1.45 ± 0.21	9
Δ13: …LVIFL	15.0	4.84 ± 0.14[b]	1.32 ± 0.30	11
Δ15: …LVI	4.25	5.33 ± 0.15[b]	1.87 ± 0.20	9
<u>δ subunit</u>				
WT: …WIFLQGVYNQPPPQPFPGDPYSYNVQDKRFI	7.61	5.12 ± 0.07	1.70 ± 0.47	50
Δ1: …WIFLQGVYNQPPPQPFPGDPYSYNVQDKRF	9.20	5.04 ± 0.07	1.46 ± 0.20	8
Δ2: …WIFLQGVYNQPPPQPFPGDPYSYNVQDKR	7.72	5.13 ± 0.13	1.71 ± 0.13	8
Δ3: …WIFLQGVYNQPPPQPFPGDPYSYNVQDK	5.95	5.24 ± 0.14	1.55 ± 0.10	8
Δ4: …WIFLQGVYNQPPPQPFPGDPYSYNVQD	8.11	5.10 ± 0.07	1.60 ± 0.21	8
Δ8: …WIFLQGVYNQPPPQPFPGDPYSY	8.88	5.06 ± 0.07	1.50 ± 0.33	9
Δ12: …WIFLQGVYNQPPPQPFPGD	9.90	5.01 ± 0.06	1.32 ± 0.18	8
Δ16: …WIFLQGVYNQPPPQP	14.2	4.85 ± 0.07[b]	1.68 ± 0.24	8
Δ20: …WIFLQGVYNQP	15.1	4.84 ± 0.12[b]	1.51 ± 0.20	8
Δ24: …WIFLQGV	7.59	5.12 ± 0.01	1.55 ± 0.13	3
Δ28: …WIF	No current[c]	-	-	8
<u>ε subunit</u>				
WT: …SVGSSLIFLGAYFNRVPDLPYAPCIQP	7.61	5.12 ± 0.07	1.70 ± 0.47	50
Δ1: …SVGSSLIFLGAYFNRVPDLPYAPCIQ	7.86	5.11 ± 0.05	1.62 ± 0.10	8
Δ2: …SVGSSLIFLGAYFNRVPDLPYAPCI	6.40	5.20 ± 0.05	1.72 ± 0.08	8
Δ3: …SVGSSLIFLGAYFNRVPDLPYAPC	8.44	5.08 ± 0.07	1.67 ± 0.11	9
Δ4: …SVGSSLIFLGAYFNRVPDLPYAP	9.26	5.04 ± 0.06	1.47 ± 0.17	8
Δ8: …SVGSSLIFLGAYFNRVPDL	6.20	5.22 ± 0.10	1.75 ± 0.25	8
Δ13: …SVGSSLIFLGAYFN	3.47	5.46 ± 0.05[b]	1.87 ± 0.24	8
Δ16: …SVGSSLIFLGA	4.22	5.38 ± 0.06[b]	1.87 ± 0.22	8
Δ18: …SVGSSLIFL	1.89	5.74 ± 0.13[b]	1.99 ± 0.16	9
Δ20: …SVGSSLI	1.21	5.92 ± 0.09[b]	1.87 ± 0.37	4
Δ24: …SVG	No current[c]	-	-	8

[a]Measurements performed 1-4 days after cRNA injection (V_{hold} ranging from -20 to -80 mV). Error values represented as standard deviation
[b]$p < 0.001$ relative to WT via one-way ANOVA followed by Dunnet's post hoc test
[c]No significant current observed up to 4 day after cRNA injection

4.4.3 Aromatic Residues at the M4 - M1/M3 interface

Aromatic residues play a critical role at the M4 – M1/M3 interface in many pLGICs. Some pLGICs, such as the 5-HT_3A R, the α1 GlyR, the α7 nAChR, the ρ1 $GABA_A$R and the prokaryote GLIC, exhibit an extensive network of interacting aromatic residues that drives M4 - M1/M3 interactions to facilitate folding and possibly function (Haeger et al., 2010; Therien and Baenziger, 2017; Cory-Wright et al., 2018; Tang and Lummis, 2018; Mesoy et al., 2019; da Costa Couto et al., 2020). In contrast, fewer aromatic residues at this interface in ELIC are thought to sterically prevent tight interactions between M4 and M1/M3 thus creating a more malleable M4 - M1/M3 interface that is potentially more sensitive to modulation by factors, such as the surrounding lipid environment (Carswell et al., 2015a). As in ELIC, the muscle nAChR exhibits relatively few aromatic residues likely leading to a malleable M4 - M1/M3 interface that might underlie its exquisite lipid sensitivity (Therien and Baenziger, 2017).

We mutated every aromatic residue at this interface in each subunit of the nAChR to alanine and tested the effects of each on channel function (Fig. 4.6; Table 4.7). In general, we found that aromatic to alanine substitutions in the α, β, δ, and ε subunits led to either no effect or subtle gains-in-function. These data suggest that bulky aromatic side chains sterically prevent optimal M4 – M1/M3 interactions, with the reduction in size possibly promoting tighter interactions to enhance channel function.

Figure 4.6 Aromatic residues along the M4 – M1/M3 interface in each subunit
Top-down (top) and side (bottom) views of each subunit's TMD with aromatic residues at the M4 – M1/M3 interface shown as yellow sticks.

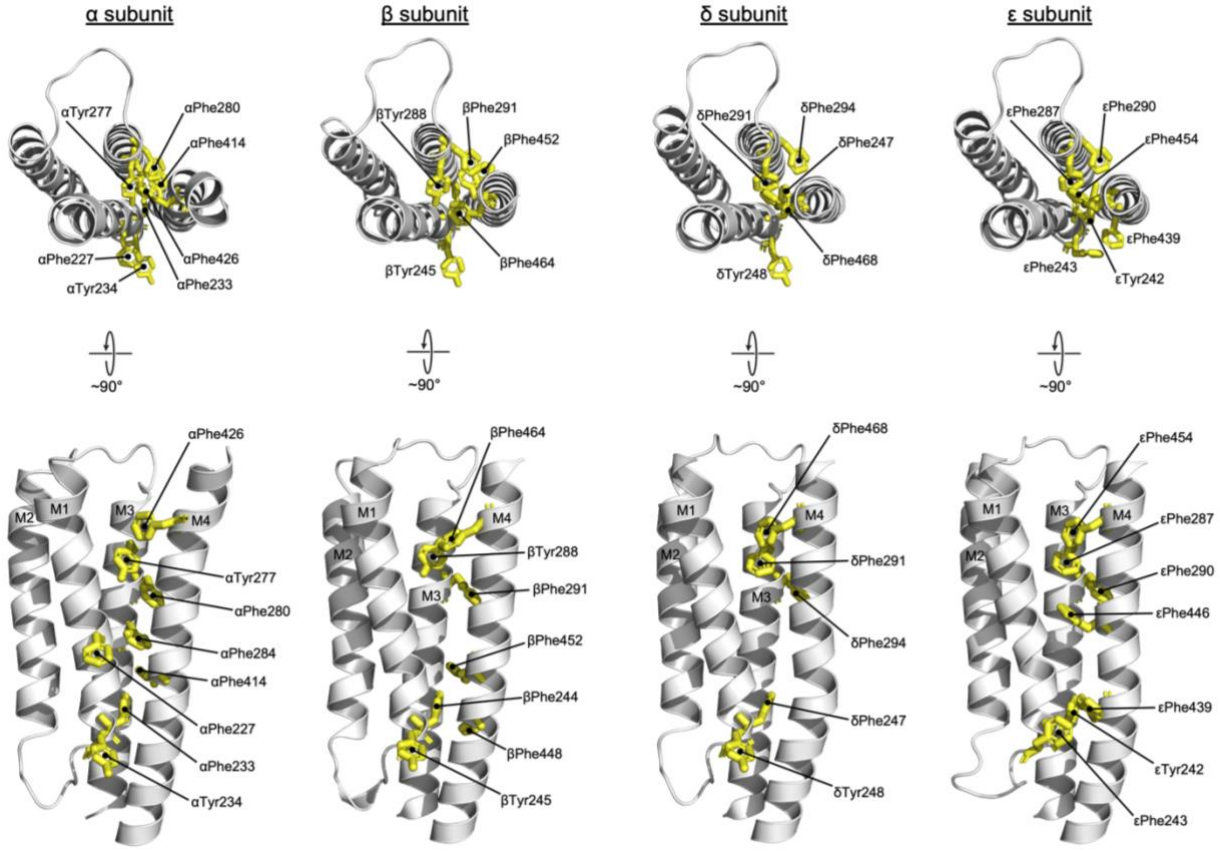
α subunit
β subunit
δ subunit
ε subunit
αTyr277
αPhe280
αPhe414
αPhe227
αPhe426
αTyr234
αPhe233
βTyr288
βPhe291
βPhe452
βTyr245
βPhe464
δPhe291
δPhe294
δPhe247
δPhe468
δTyr248
εPhe287
εPhe290
εPhe454
εPhe439
εPhe243
εTyr242
~90°
~90°
~90°
~90°
αPhe426
M1
M2
M3
M4
αTyr277
αPhe280
αPhe284
αPhe414
αPhe227
αPhe233
αTyr234
βPhe464
βTyr288
βPhe291
βPhe452
βPhe244
βPhe448
βTyr245
δPhe468
δPhe291
δPhe294
δPhe247
δTyr248
εPhe454
εPhe287
εPhe290
εPhe446
εPhe439
εTyr242
εPhe243

Table 4.7 - Effects of mutating aromatic residues at the M4 – M1/M3 interface on nAChR function

Dose response[a]					
Mutation	TMD α-helix	EC_{50} (μM)	pEC_{50} (M)	Hill slope	n
WT		7.61	5.12 ± 0.07	1.70 ± 0.47	50
		α subunit			
αF227A	M1	6.51	5.20 ± 0.09	1.43 ± 0.16	8
αF233A	M1	2.63	5.58 ± 0.05[b]	1.63 ± 0.20	9
αY234A	M1	No current[c]	-	-	8
αY277A	M3	11.2	4.96 ± 0.08[b]	1.78 ± 0.58	8
αF280A	M3	4.25	5.38 ± 0.11[b]	1.56 ± 0.29	8
αF284A	M3	4.80	5.32 ± 0.07[b]	1.33 ± 0.21	9
αF414A	M4	4.47	5.36 ± 0.09[b]	1.76 ± 0.34	10
αF426A	M4	2.02	5.71 ± 0.14[b]	1.80 ± 0.76	11
		β subunit			
βF244A	M1	4.46	5.35 ± 0.14[b]	2.23 ± 0.77	9
βY245A	M1	7.44	5.13 ± 0.10	1.56 ± 0.16	7
βY288A	M3	5.43	5.27 ± 0.10[b]	1.77 ± 0.30	8
βF291A	M3	10.5	4.98 ± 0.09[b]	1.66 ± 0.35	9
βF448A	M4	4.36	5.38 ± 0.15[b]	1.63 ± 0.48	8
βF452A	M4	10.5	4.98 ± 0.07	1.69 ± 0.11	8
βF464A	M4	8.55	5.08 ± 0.11	1.38 ± 0.19	10
		δ subunit			
δF247A	M1	11.2	4.95 ± 0.10[b]	1.45 ± 0.12	9
δY248A	M1	3.67	5.44 ± 0.12[b]	1.57 ± 0.22	9
δF291A	M3	6.18	5.21 ± 0.08	1.62 ± 0.16	9
δF294A	M3	3.86	5.41 ± 0.07[b]	1.72 ± 0.13	8
δF468A	M4	5.83	5.25 ± 0.10	1.60 ± 0.27	7
		ε subunit			
εY242A	M1	8.12	5.09 ± 0.04	1.67 ± 0.11	10
εF243A	M1	8.02	5.10 ± 0.10	1.78 ± 0.19	9
εF287A	M3	12.7	4.90 ± 0.06[b]	1.51 ± 0.13	9
εF290A	M3	6.14	5.21 ± 0.12	2.06 ± 0.36	7
εF439A	M4	8.59	5.07 ± 0.07	1.81 ± 0.08	8
εF446A	M4	8.89	5.06 ± 0.07	1.51 ± 0.18	9
εF454A	M4	3.90	5.42 ± 0.10[b]	1.80 ± 0.25	8

[a]Measurements performed 1-4 days after cRNA injection (V_{hold} ranging from -20 to -80 mV). Error values represented as standard deviation

[b]$p < 0.001$ relative to WT via one-way ANOVA followed by Dunnet's post hoc test

[c]No significant current observed up to 4 day after cRNA injection

4.4.4 αC418W-induced potentiation of channel function

To compare further how similar changes in the structure of the M4 α-helix from different subunits influences channel function, we focused on a site where the introduction of a tryptophan in the α-subunit, αC418W, potentiates channel function 16 to 25-fold leading to a slow channel CMS (Shen et al., 2006) (Table 4.8). Mutant cycles show that the αC418W-induced potentiation is driven primarily by a new interaction that forms between the introduced tryptophan, αTrp418, and an adjacent residue on αM1, αSer226, with this interaction likely stabilizing the open state (Domville and Baenziger, 2018). The importance of this interaction in αC418W-induced potentiation is demonstrated by the fact that αC418W only potentiates channel function 3.4-fold when the tryptophan is introduced onto the αS226A background.

Given that β, δ and ε each contains a homologous residue to αSer226 (βThr237, δSer240 and εSer235) on M1, we expected a similar degree of potentiation upon mutation of the αCys418 equivalent residue in each subunit (βThr456, δMet460 and εPhe446) to tryptophan. In contrast, tryptophan substitutions in β, δ and ε, (βT456W, δM460W and εF446W) led to only a 1.7-fold gain, a 1.6-fold loss and a 1.8-fold gain-of-function, respectively, consistent with what is observed in the *Torpedo* nAChR (Lee et al., 1994; Ortiz-Acevedo et al., 2004; Kloda et al., 2007). Furthermore, the βT237A mutation on M1 had no effect on the magnitude of the βT456W-induced response implying that the introduced tryptophan, βT456W, does not interact with βT237 to potentiate channel function. In the δ subunit, the δS240A mutant on M1 did not functionally express. In contrast, the εS235A mutation in M1 of the ε subunit enhances εF446W-induced potentiation suggesting that an interaction between F446W and εS235 is detrimental to εF446W-induced potentiation. These data illustrate how even analogous changes in the structure of M4 from different subunits can lead to different effects on channel function.

Table 4.8 - Interactions between the αC418W mutant and its equivalents and adjacent residues from M1

	Dose response[a]								Fold change
	WT				αC418W				
Background	EC_{50}(μM)	pEC_{50}(M)	Hill slope	n	EC_{50}(μM)	pEC_{50}(M)	Hill slope	n	$\frac{EC_{50}(WT)}{EC_{50}(mut)}$
WT	7.61	5.12 ± 0.07	1.70 ± 0.47	50	0.47	6.33 ± 0.13[b]	1.54 ± 0.23	50	16.2
αS226A	12.3	4.92 ± 0.11[b]	1.70 ± 0.47	8	3.66	5.45 ± 0.11[b]	1.26 ± 0.12	8	3.4
	WT				βT456W				
WT	7.61	5.12 ± 0.07	1.70 ± 0.47	50	4.50	5.36 ± 0.10[b]	1.73 ± 0.17	10	1.7
βT237A	6.28	5.22 ± 0.16	1.77 ± 0.10	8	4.26	5.38 ± 0.07[b]	1.59 ± 0.11	8	1.5
	WT				δM460W				
WT	7.61	5.12 ± 0.07	1.70 ± 0.47	50	12.1	4.93 ± 0.12[b]	1.41 ± 0.16	9	0.6
δS240A	No current[c]	-	-	8	5.89	5.23 ± 0.07	1.83 ± 0.17	4	-
	WT				εF446W				
WT	7.61	5.12 ± 0.07	1.70 ± 0.47	50	4.26	5.39 ± 0.14[b]	1.75 ± 0.13	9	1.8
εS235A	1.39	5.86 ± 0.06[b]	1.78 ± 0.43	4	0.38	6.43 ± 0.11[b]	1.74 ± 0.47	8	3.7

[a]Measurements performed 1-4 days after cRNA injection (V_{hold} ranging from -20 to -80 mV). Error values represented as standard deviation

[b]$p < 0.001$ relative to WT via one-way ANOVA followed by Dunnet's post hoc test

[c]No significant current observed up to 4 day after cRNA injection

4.4.5 M4 mutations in different subunits are additive

We previously observed with that the subtle functional effects of individual alanine mutations along αM4 are additive and thus can cumulatively lead to much larger changes in channel function. This implies that a reorientation of M4 could modulate many interactions at the M4 – M1/M3 interface with functional effects of the individual alterations in structure adding up to a more substantial effect. Here we tested whether mutations on different M4 α-helices are additive. Specifically, we focused on three positions where individual mutations in αM4 (αF426A, αV425A, and αC418W) lead to relatively large changes in function. We produced the equivalent mutations in the remaining β, δ and ε subunits and then assessed the effect on function when all mutated subunits were expressed at the same time.

A phenylalanine at equivalent positions near the C-terminus of M4 in all four subunits, αPhe426, βPhe464, δPhe468 and εPhe454, projects towards αM1 and αM3. The alanine mutation of each residue individually led to a 3.8-fold gain-, a 1.1-fold loss-, a 1.3-fold gain- and a 2.0-fold gain-of-function, respectively. The simultaneous quadruple mutant, αF426A+βF464A+δF468A+εF454A, led to an 11.4-fold gain-of-function (Table 4.9), which is close to the 8.6-fold gain-of-function predicted if the functional effects of the mutations are independent and thus additive. Similarly, the adjacent αV426A, βI464A, δI468A and εI454A mutants individually led to a 1.8-fold, a 2.1-fold, a 1.6-fold and a 1.7-fold gain-of-function, respectively, with the quadruple αV426A+βI464A+δI468A+εI454A mutant leading to a 12.1-fold gain-of-function, again a value close to the 10.2-fold gain-of-function expected for independent, additive mutations. Finally, the αC418W, βT456W, δM460W and εF446W mutants noted above led to a 16-fold gain, a 1.7-fold gain, a 1.6-fold loss, and a 1.8-fold gain-of-function, respectively. The quadruple αC418W+βT456W+δM460W+εF446W mutant led to a

30.0-fold gain-of-function, virtually the same as that predicted (30.7-fold) for independent additive mutations.

Table 4.9 - Mutations to aligned residues in each M4 α-helix have independent effects on function

	Dose response[a]					
Mutation(s)	EC_{50} (μM)	pEC_{50} (M)	Hill slope	n	Fold change	
WT	7.61	5.12 ± 0.07	1.70 ± 0.47	50	Observed	Predicted[b]
αF426A	2.02	5.71 ± 0.14[b]	1.80 ± 0.76	11	3.76	-
βF464A	8.55	5.08 ± 0.11	1.38 ± 0.19	10	0.89	-
δF468A	5.83	5.25 ± 0.10	1.60 ± 0.27	7	1.31	-
εF454A	3.90	5.42 ± 0.10[b]	1.80 ± 0.25	8	1.95	-
αF426A+ βF464A+ δF468A+ εF454A	0.67	6.17 ± 0.17[b]	2.04 ± 0.15	8	11.4	8.54
αV425A	4.30	5.37 ± 0.05[b]	1.89 ± 0.28	10	1.77	-
βI463A	3.67	5.44 ± 0.16[b]	1.78 ± 0.11	8	2.07	-
δI467A	4.63	5.34 ± 0.07[b]	1.91 ± 0.79	7	1.65	-
εI453A	4.50	5.35 ± 0.06[b]	1.83 ± 0.27	8	1.69	-
αV425A+ βI463A+ δI467A+ εI453A	0.63	6.20 ± 0.17[b]	2.11 ± 0.28	7	12.1	10.2
αC418W	0.47	6.33 ± 0.13[b]	1.54 ± 0.23	50	16.2	-
βT456W	4.50	5.36 ± 0.10[b]	1.73 ± 0.17	10	1.69	-
δM460W	12.2	4.93 ± 0.12[b]	1.41 ± 0.16	9	0.63	-
εF446W	4.26	5.39 ± 0.14[b]	1.75 ± 0.13	9	1.79	-
αC418W+ βT456W+ δM460W+ εF446W	0.25	6.60 ± 0.08[b]	1.90 ± 0.58	9	30.0	30.7

[a]Measurements performed 1-4 days after cRNA injection (V_{hold} ranging from -20 to -80 mV). Error values represented as standard deviation

[b]Predicted fold change if individual mutations affect function independently

[c]$p < 0.001$ relative to WT via one-way ANOVA followed by Dunnet's post hoc test

4.4.6 M4 mutations have different effects on nAChR function in different membrane environments

Recent studies have shown that mutations in the M4 α-helix of the homo-pentameric 5-HT3$_A$ receptor have different effects on function when the receptor is expressed in HEK293T cells versus *Xenopus* oocytes, with the different phenotypes attributed to the different lipid compositions of the plasma membranes (Crnjar et al., 2021). To determine if the functional effects of M4 mutations in the muscle nAChR are also dependent on their cellular context, we characterized six αM4 mutants in HEK293T cells using a membrane potential sensitive fluorescent dye (Fig. 4.7). Although the measured EC_{50} values obtained using the fluorescent dye differ from those measured using two-electrode voltage clamp electrophysiology in oocytes, we observed that two single αM4 Ala mutants, αF414A and αF426A, gave rise to a similar fold changes in EC_{50} values relative to the wild type nAChR in both heterologous expression systems (Table 4.10). In contrast, both αD407A and αR429A did not give rise to an agonist induced response. [^{125}I]-α-bungarotoxin (α-BTX) binding showed that while αR429A did not express, αD407A expressed well above background levels (Table 4.10). The αD407A mutant receptors that do reach the cell surface are thus unable to produce an agonist induced response. Even though αD407A leads to a slight gain-of function when expressed in *Xenopus* oocytes, the same αD407A mutation renders the nAChR inactive in HEK293T cells.

We also examined the functional effects of two triple M4 mutants. The first triple mutant, αL411A+αT422A+αR429A, led to a similar loss in function in both cell types (8-fold and 6-fold loss of function in HEK293T cells versus oocytes, respectively). In contrast, the second triple mutant, αD407A+αF414A+αF426A, led to a complete loss of a response in HEK293T cells despite expressing at levels consistent with the αD407A mutant. Overall, the

data show that the functional effects of select mutations within αM4 in the human muscle nAChR are different in HEK293T cells and oocytes.

Figure 4.7 Effect of αM4 mutations on the function and expression of the nAChR in HEK293T cells

A) Exemplary fluorescence traces for WT and untrasfected cells (top), αM4 mutants that were functionally expressed (middle), and non-expressing/non-functional αM4 mutants (bottom) from the membrane potential assay. Each coloured line corresponds to a different ACh concentration (0, *black*; 1 nM, *red*; 10 nM, *blue*; 100 nM, *green*; 1 μM, *pink*; 10 μM, *gold*; 100 μM, *navy*; 1 mM, *burgundy*). B) For mutants that responded to agonist, changes in fluorescence for each ACh concentration were normalized and plotted as dose-response curves. C) Normalized surface expression for each mutant that did not respond to agonist are compared to WT and untransfected cells. *Denotes mutants that expressed significantly less than WT but significantly more than untransfected controls.

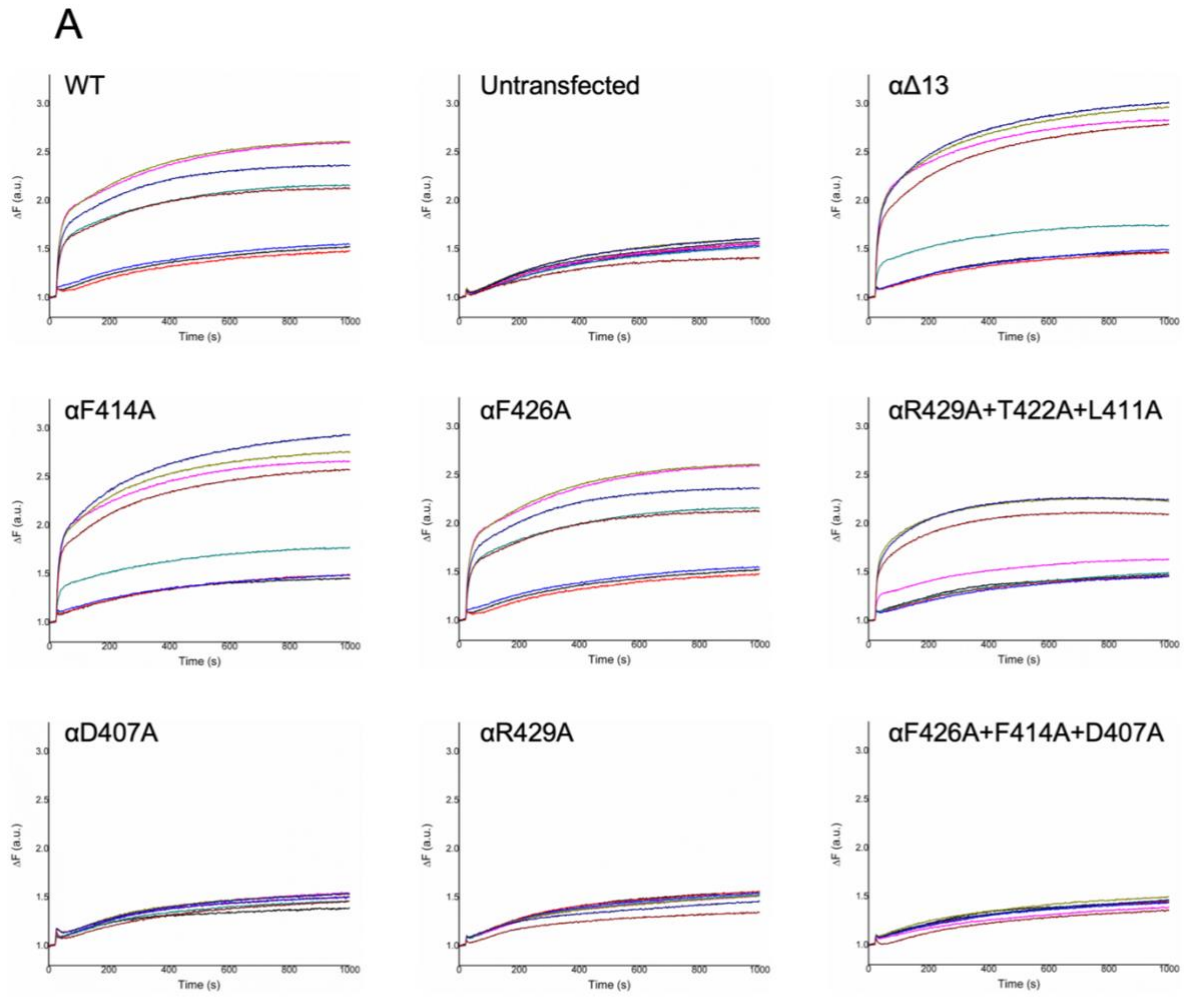
A
WT
Untransfected
αΔ13
αF414A
αF426A
αR429A+T422A+L411A
αD407A
αR429A
αF426A+F414A+D407A
ΔF (a.u.)
Time (s)

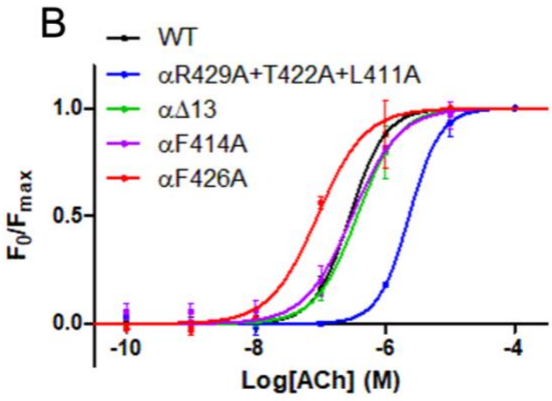
B
WT
αR429A+T422A+L411A
αΔ13
αF414A
αF426A
F0/Fmax
Log[ACh] (M)

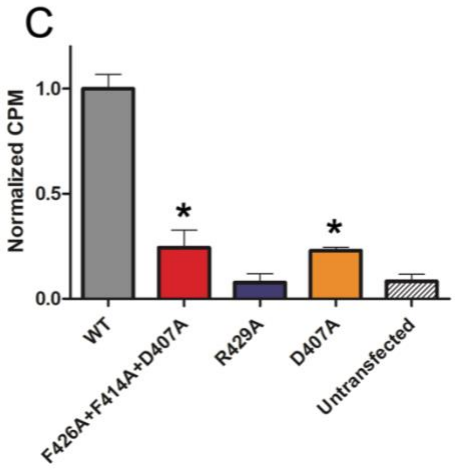
C
Normalized CPM
WT
F426A+F414A+D407A
R429A
D407A
Untransfected

Table 4.10 - Effects of M4 mutations on nAChR function and expression in HEK293T cells

	Dose response[a]					[^{125}I]-α-BTX[b]
Mutation(s)	EC_{50} (μM)	pEC_{50} (M)	Hill slope	n	Fold change	CPM_{mutant}/CPM_{WT}
WT	0.30	6.54 ± 0.13	1.58 ± 0.32	9	-	1.00 ± 0.07
αD407A	-	-	-	3	-	0.23 ± 0.01[c,d]
αF414A	0.33	6.48 ± 0.06	1.41 ± 0.22	4	1.10	-
αF426A	0.09	7.04 ± 0.09[c]	1.12 ± 0.22	3	0.31	-
αR429A	-	-	-	3	-	0.08 ± 0.04[c]
αF426A+F414A+D407A	-	-	-	3	-	0.24 ± 0.08[c,d]
αR429A+T422A+L411A	2.31	5.64 ± 0.12[b]	1.87 ± 0.40	3	7.68	-
Untransfected	-	-	-	9	-	0.08 ± 0.03[c]

[a]Measurements performed 2 days post-transfection. Error values represented as standard deviation.
[b]Measurements performed 2 days post transfection in triplicate. Error values represented as standard deviation.
[c]No agonist induced response observed
[d]$p < 0.001$ relative to WT via one-way ANOVA followed by Dunnet's post hoc test
[e]$p < 0.001$ relative to untransfected cells via one-way ANOVA followed by Dunnet's post hoc test

4.5 Discussion

The goal of this work was to probe how the structure of the M4 α-helix from each of the four distinct nAChR subunits influences channel function as a foundation for understanding the role played by each as a lipid sensor. In particular, we hoped to identify putative interactions involving residues on each M4 that are essential to channel function and that could be modulated by lipids to stabilize the non-activatable uncoupled state that forms in phosphatidylcholine membranes lacking cholesterol and anionic lipids. To identify interactions that are essential to channel function, we generated alanine mutations of every M4 residue in each subunit. Surprisingly, all of the generated mutants expressed robustly in frog oocytes except for one, εM430A, which extends towards a structure, εMX, that has been implicated in assembly/cell surface trafficking (Rudell et al., 2020). Of those that expressed, 54 of 155 mutations led to statistically significant changes in the measured EC_{50} values and thus in channel function. Of these, only eight, however, led to shifts in EC_{50} values greater than ~2-fold, with αT422A and αR429A leading to 4.1-fold and 5.3-fold losses-of-function, respectively, and αF426A and βV444A leading to 3.8-fold and 3.4-fold gains-in-function, respectively. Although the detected changes in EC_{50} values confirm that interactions involving residues on M4 from each subunit influence channel function, no single interaction appears capable of fully uncoupling the nAChR.

We also examined whether the post-M4 sequence in each subunit, which extends above the lipid bilayer, forms interactions with the ECD that are important to channel gating. We created a total of 51 Ala mutations in the post-M4 segments of the α, β, δ and ε subunits, but all 51 of these mutants led to functional nAChRs with none altering the measured EC_{50} values by more than ~2-fold. Furthermore, deleting various regions or the entire post-M4 segment from any subunit (αΔ5, βΔ10, δΔ24, and εΔ16) had minimal detrimental effects on the measured EC_{50}

values. In fact, some deletions, such as εΔ24, led to relatively large (6.3-fold) gains-of-function. These results suggest that there are no functionally essential interactions involving residues in post-M4 from any subunit.

The lack of essential interactions involving residues on M4 or post-M4 contrasts what has been observed in other pLGICs (Cory-Wright et al., 2018; Tang and Lummis, 2018; Mesoy et al., 2019; da Costa Couto et al., 2020; Mesoy and Lummis, 2021) and leads to a question as to how some lipid environments stabilize a non-activatable uncoupled state. One possibility is that lipid-dependent uncoupling results from the cumulative effects of many changes in interactions involving residues on M4 that individually have only subtle impacts on channel function. This possibility is supported by two observations. First, the functional effects of multiple alanine substitutions on a single M4 α-helix are additive with simultaneous mutations leading to more pronounced effects on channel function, in some cases actually preventing functional expression altogether (Thompson et al., 2020). Second, the functional effects of mutations of residues on the M4 α-helices from different subunits are also additive with multiple simultaneous mutations leading to large cumulative effects. For example, simultaneous mutations of residues in each subunit equivalent to αV425A, αF426A or αC418W led to 12.1-, 11.4- and 30.4-fold changes in the recorded EC_{50} values, each close to the 10.2-, 8.6- and 30.6-fold change in function predicted if the effect of each mutation is independent. Further work will be required to understand how cumulative changes to many subtle interactions involving M4 ultimately influence channel function.

On the other hand, it is intriguing to note that of the 173 alanine mutations characterized in this report, two led to nAChRs that did not functionally express in oocytes. One of the mutants, εM430A (εM4), likely impacts on nAChR assembly/cell surface trafficking. On the

other hand, both εM430A and the other non-functional expressing mutant, αY234A (αM1) are located near the cytoplasmic surface of the bilayer close to newly identified phospholipid binding sites on the *Torpedo* nAChR and cholesterol binding sites on the α4β2 and α3β4 nAChRs (Walsh et al., 2018; Gharpure et al., 2019; Rahman et al., 2020a, 2022; Zarkadas et al., 2022). In fact, αY234 is thought to form part of a phospholipid binding motif. The lack of functional expression of both these mutants may suggest that impaired lipid binding influences nAChR folding. Such lipid binding sites could also play a role in lipid-sensing. Further studies are currently aimed towards defining the roles of these lipid binding sites in nAChR function.

Our mutational studies reveal additional features that impact on our understanding of potential mechanisms of lipid sensing via M4. First, our data reveal a common theme that a mutation in M4 from one subunit can have a different effect on function than the analogous mutation in a different subunit. For example, alanine substitutions of αR429, αF426 and αT422A lead to a 5.3-fold loss-, a 3.8-fold gain- and a 4.1-fold loss-of-function, respectively. In contrast, alanine substitutions at equivalent sites in βM4 (βT460, βF464 and βA467), δM4 (δT464, δF468 and δG471) and εM4 (εS450, εF454 and εA457) have virtually no effect. Even more striking, while the CMS-causing mutation on αM4, αC418W, potentiates channel function 15 – 25-fold primarily through a stabilizing interaction with an adjacent serine residue, αSer226, on αM1, the analogous tryptophan substitutions in other subunits have little effect on function despite the presence of a homologous serine or threonine residue at the same position on M1 in each of the β (βThr237), δ (δerS240), and ε (εSer235) subunits. The lack of conservation of function despite a conserved structural motif suggests that the TMD α-helices from each subunit undergo different motions upon channel activation thus leading to different poses of the M4 α-helix from different subunits relative to their adjacent M1 and M3 α-helices. In agreement,

recent cryo-EM structures of the *Torpedo* nAChR solved in the presence and absence of agonist reveal subunit specific tertiary deformations in each TMD (Rahman et al., 2022; Zarkadas et al., 2022). These findings suggest that the same lipid induced change in M4 structure in one subunit could have a strikingly different effect on channel function in another subunit.

Second, we found that alanine substitutions of bulky aromatic residues at the M4 – M1/M3 interface typically led to subtle and more variable effects on nAChR function (11 of 27 significantly potentiate function) than in some pLGICs. For example, the glycine receptor and the prokaryotic homolog, GLIC, exhibit a complex network of interacting aromatic residues at this interface that is essential to folding and function. In these pLGICs, alanine substitutions of M4 - M1/M3 interfacial aromatic residues invariably lead to losses-of-function, with multiple substitutions typically leading to a complete loss of functional expression (Cory-Wright et al., 2018; Tang and Lummis, 2018). Other pLGICs, such as the prokaryotic pLGIC ELIC, however, have relatively few aromatic residues. In the latter, aromatic to alanine substitutions invariably lead to gains-in-function suggesting that the bulky aromatic side chains sterically block the formation of M4 – M1/M3 interactions that are optimal for channel function (Therien and Baenziger, 2017). Furthermore, the introduction of aromatic residues at the M4 – M1/M3 interface in ELIC to mimic the complex aromatic network observed in GLIC not only enhanced ELIC function but renders ELIC less functionally sensitive to its membrane environment (Carswell et al., 2015a). While the trends observed with GLIC and ELIC are not adhered to strictly in all pLGICs (Cory-Wright et al., 2018; Tang and Lummis, 2018; Mesoy et al., 2019; da Costa Couto et al., 2020; Mesoy and Lummis, 2021), they have led to the suggestion that a more malleable M4 – M1/M3 interface due to a lack of aromatic residues may lead to a more lipid-sensitive pLGIC. Our data show that as in ELIC, aromatic-to-alanine substitutions are well

tolerated in the nAChR, consistent with a more malleable M4 – M1/M3 interface that may contribute to a higher sensitivity to its surrounding lipid environment.

Finally, we characterized the effects of select αM4 mutations on nAChR function and expression in HEK293T cells to determine if these mutations have different effects when in membranes that differ in their lipid composition. Previous studies have shown that the effects of M4 mutations in the 5-HT_{3A}R are different when expressed in HEK293T cells versus oocytes (Crnjar et al., 2021). Specifically, certain mutations that cause large shifts in EC_{50} or lead to non-functional receptors in HEK293T cells often have little to no influence on function in oocytes. In agreement, we find that mutations in αM4 that have little effect on nAChR function in oocytes, such as the αD407A and αR429A, cause a dramatic reduction in function in HEK293T cells. Similar trends have also been observed with other mutations, such as εC470A and βD445A, δD449A and εD435A, both here and in other studies (Ealing et al., 2002; Strikwerda and Sine, 2021). While more robust studies in model membranes are required to determine whether these changes are in fact caused by changes in lipid environment or by other differences between cell types, these observations hit at a potential role for these residues in lipid-sensing.

The observed difference in the functional effects of M4 mutations in HEK293T cells vs oocytes can be attributed to several factors, including different intracellular chaperones, proximal membrane proteins, post-translational modifications, or the lipid composition of the surrounding membrane. While speculative, we favor the latter hypothesis given that the mutations we have investigated here are within the lipid exposed αM4 helix. In addition, previous studies have shown that the biophysical properties of the WT receptor are very similar between the two systems (Zhang et al., 1995). The lipid composition of oocytes appear to be quite similar to that

of a neuronal membrane, although the defined lipid profile in both sets of membranes does vary depending on the methods used for quantifying the different lipids (Stith et al., 2000; Santiago et al., 2001; Opekarová and Tanner, 2003; Hill et al., 2005). On the other hand, the lipid composition of cultured HEK293T cells clearly lacks polyunsaturated fatty acids (PUFAs) (Else, 2020). PUFAs make up between 40 and 50% of fatty acids in neuronal membranes but less than 20% in cultured HEK293T cells (Ingólfsson et al., 2017; Symons et al., 2021). This change in lipid composition is likely to have a dominant effect on both the fluidity of the bilayer and the formation of lipid nanodomains. Given that lipid composition has a dramatic effect the coupling of binding and gating in the *Torpedo* muscle-like nAChR function, it may be that the effects of mutations studied here are more dramatic when the nAChR is imbedded in an unfavorable membrane environment.

Chapter 5. Manuscript 3: A release of local subunit conformational heterogeneity underlies gating in a muscle nicotinic acetylcholine receptor.

Thompson, M.J., Bekarkhanechi, F.M., Ananchenko, A., Nury, H., and Baenziger, J.E. (2023). A release of local subunit conformational heterogeneity underlies gating in a muscle nicotinic acetylcholine receptor.

Accepted at Nat. Comm.

5.1 Preface

In 2021, we had the first ever structures of the *Torpedo* nAChR in apo and agonist bound states. Because the structures weren't published until 2022, I was given the opportunity to investigate an alternative gating mechanism that had received little attention. Throughout 2021 and 2022 I used these new structures to guide a functional characterization of the ECD – TMD interface. During this time, I supervised an undergraduate student, Farid Mansoub Bekarkhanechi, who worked under me to characterize a subset of the mutants. He also finished up loose ends of the project while I was working in France during the 2022-2023 winter term. Anna Ananchenko also participated in the project by performing and analyzing the molecular dynamics simulations. I performed all other experimental work, processed the vast majority of the electrophysiological data, wrote the initial draft of the manuscript, participated in editing (along with John E. Baenziger and Hugues Nury), and created all the tables, figures, and movies.

5.2 Abstract

Synaptic receptors respond to neurotransmitters by opening an ion channel across the post-synaptic membrane to elicit a cellular response. Here we use recent *Torpedo* acetylcholine receptor structures and functional measurements to delineate a key feature underlying allosteric communication between the agonist-binding extracellular and channel-gating transmembrane domains. Extensive mutagenesis at this inter-domain interface re-affirms a critical energetically coupled role for the principal α subunit β1-β2 and M2-M3 loops, with agonist binding re-positioning a key β1-β2 glutamate/valine so that a conserved M2-M3 proline translates outward to open the channel gate. Notably, the analogous structures in non-α subunits adopt a locally *active-like* conformation in the apo state even though each L9' hydrophobic gate residue in each pore-lining M2 α-helix is closed. Agonist binding releases local conformational heterogeneity transitioning all five subunits into a conformationally symmetric open state. A release of conformational heterogeneity provides a new framework for understanding allosteric communication in pentameric ligand-gated ion channels.

5.3 Introduction

A central unanswered question in pentameric ligand-gated ion channel (pLGIC) biology is how the binding of a neurotransmitter to its receptor leads to the opening of a transmembrane gate to allow the flow of ions down their electrochemical gradient into the cell. In the prototypic pLGIC, the muscle *Torpedo* nicotinic acetylcholine receptor (nAChR), two binding sites for acetylcholine (ACh) are located at the interfaces between each of the two principal α (α_γ and α_δ) and the complementary γ or δ subunits in the extracellular domain (ECD), while the ion channel gate is located ~60 Å away along the central pore axis in the transmembrane domain (TMD) (Fig. 5.1). Coupling of an ACh-induced conformational change in the ECD with the motions of the pore-lining M2 α-helices in the TMD that open the channel gate is facilitated by both the covalent linkage between β-strand 10 (β10) and the first transmembrane α-helix, M1, and the noncovalent interactions between the β1-β2, β6-β7, and β8-β9 loops from the ECD and a key TMD M2-M3 loop. How changes to these inter-domain structures propagate a conformational change from the ECD to the TMD, and vice versa, to facilitate channel gating, however, remains unclear.

Increasing structural data highlight the tertiary/quaternary motions that occur upon agonist binding to pLGICs (Fig. 5.1 and Movie 1) (Taly et al., 2014; Cecchini and Changeux, 2015; Gupta et al., 2017; Noviello et al., 2021; Yu et al., 2021). These motions are typically interpreted in terms of a gating mechanism whereby the closing of loop C around the agonist translates into a conformational change in the β1-β2 and β6-β7 loops along with the covalent link between β10 and M1, that couples with movements of the M2-M3 loop to open the pore-lining M2 α-helix. It has been suggested that this coupling is mediated by alterations in the overall distribution of charges across the ECD–TMD interface or by nonspecific bumping of

Figure 5.1 Residues at the ECD – TMD interface allosterically communicate agonist binding into channel gating.

(a) A top-down view of the *Torpedo* nAChR ECD (PDB: 7QL5) is shown on the top and coloured by subunit. A side view of the full receptor is shown on the bottom with the α_γ (left) and γ (right) subunits shown as cartoons and coloured according to domain (ECD, salmon; TMD, light blue; ICD, pale green). Bound nicotine shown as cyan spheres. (b) Zoomed in views of the intra-subunit ECD – TMD interface are shown in apo (pink, PDB:7QKO) and agonist-bound (green, PDB:7QL5) states from two orthogonal views. Arrows depict the roughly orthogonal motions of the loops. (c) Zoomed in views of the inter-subunit ECD – TMD interface are shown in the same orientations as panel b. Arrows depict the concerted motions of the αM2-M3 loop with the β8-β9 loop and the $\gamma\beta$10-M1 loops from the complementary subunits. These motions can be visualized in Movie 1.

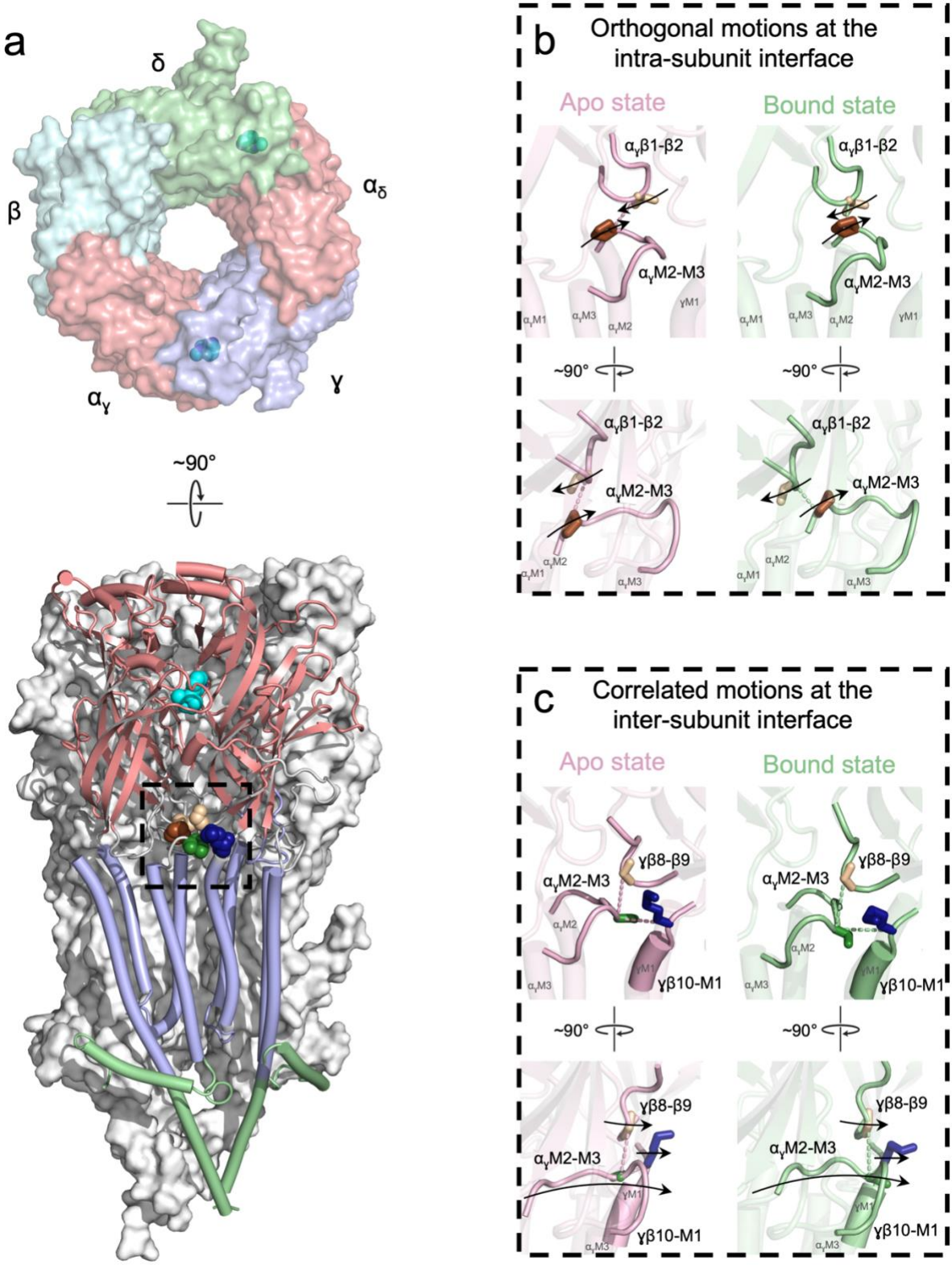
a
δ
β
αδ
αγ
γ
~90°
b
Orthogonal motions at the intra-subunit interface
Apo state
Bound state
αγβ1-β2
αγM2-M3
αγM1
αγM3
αγM2
γM1
~90°
αγβ1-β2
αγM2-M3
αγM2
αγM1
αγM3
c
Correlated motions at the inter-subunit interface
Apo state
Bound state
γβ8-β9
αγM2-M3
αγM2
γM1
αγM3
γβ10-M1
~90°
γβ8-β9
αγM2-M3
γM1
γβ10-M1
αγM3

closely apposed domains (Xiu et al., 2005; Cymes and Grosman, 2021). On the other hand, the pioneering 4 Å resolution cryo-electron microscopy reconstruction of the muscle-type *Torpedo* nAChR (PDB code 2BG9) (Unwin, 2005) identified a molecular continuum in the principal $\alpha_\gamma/\alpha_\delta$ subunits leading from each agonist binding site to a critical salt bridge between αArg209 at the base of β10 and αGlu45 at the tip of the β1-β2 loop, with αGlu45 and the adjacent αVal46 straddling αPro272 on the M2-M3 loop (Fig. 5.2a) (Unwin, 2005). Compelling functional data show that these and other residues at the ECD-TMD interface of each muscle α subunit are not only essential for, but couple energetically with each other during channel gating (Lee and Sine, 2005; Lee et al., 2008, 2009).

Higher resolution *Torpedo* structures, however, now position αPro272, and other implicated side chains, four residues further along the M2-M3 loop, where they are distant from β1-β2. The structures also show that the tip of β1-β2 not only does not engage tightly with, but moves roughly orthogonal to M2-M3 upon agonist binding (Fig. 5.2b) (Rahman et al., 2022; Zarkadas et al., 2022). Both observations suggest that coupling at the intra-α subunit ECD-TMD interface does not drive channel gating. On the other hand, unique to the muscle nAChR, the extended F loops from the complementary γ/δ subunits rock in upon agonist binding, which causes their membrane juxtaposed β8-β9 loops/β10-M1 linkers to pivot outward (Fig. 5.1c). Significantly, both β8-β9 loops/β10-M1 linkers from γ and δ sandwich the M2-M3 loops from the adjacent α_γ and α_δ subunits, with these structures moving in concert to open the L9' gate. Both the tight interactions and the concerted motions at these inter-subunit ECD-TMD domain interfaces raise the possibility that it is the γ/δ β8-β9 loops/β10-M1 linkers, not the $\alpha_\gamma/\alpha_\delta$ β1-β2 loops, that primarily couple the movements of the ECD to those of M2-M3 (Movie 1 compares

Figure 5.2 New models reposition key residues at the ECD – TMD interface and show their movements during gating are not coupled.

(a) A zoomed in view comparing the α subunit ECD – TMD interfaces of the 4.0 Å resolution 2005 (left, PDB: 2BG9) and 2.9 Å resolution 2022 (two orthogonal views on the right, PDB: 7QKO) *Torpedo* nAChR models. Residues in the α subunit β1-β2 and M2-M3 loops that are implicated in channel gating are shown as sticks with transparent surfaces. (b) The movements of the α subunit β1-β2 and M2-M3 loops upon agonist binding are highlighted in the apo (pink, PDB: 7QKO) and nicotine bound (green, PDB: 7QL5) states, with the structures superimposed on their complementary subunits. Arrows on the side chains of αVal46 and αPro265 depict the roughly orthogonal motions of the loops. (c) Violin plots of the measured EC_{50} values for mutations at the intra-α subunit ECD – TMD interfaces of human adult and *Torpedo* nAChRs. Grey crossed boxes indicate mutants that did not produce currents. Exact values can be found in table 5.2.

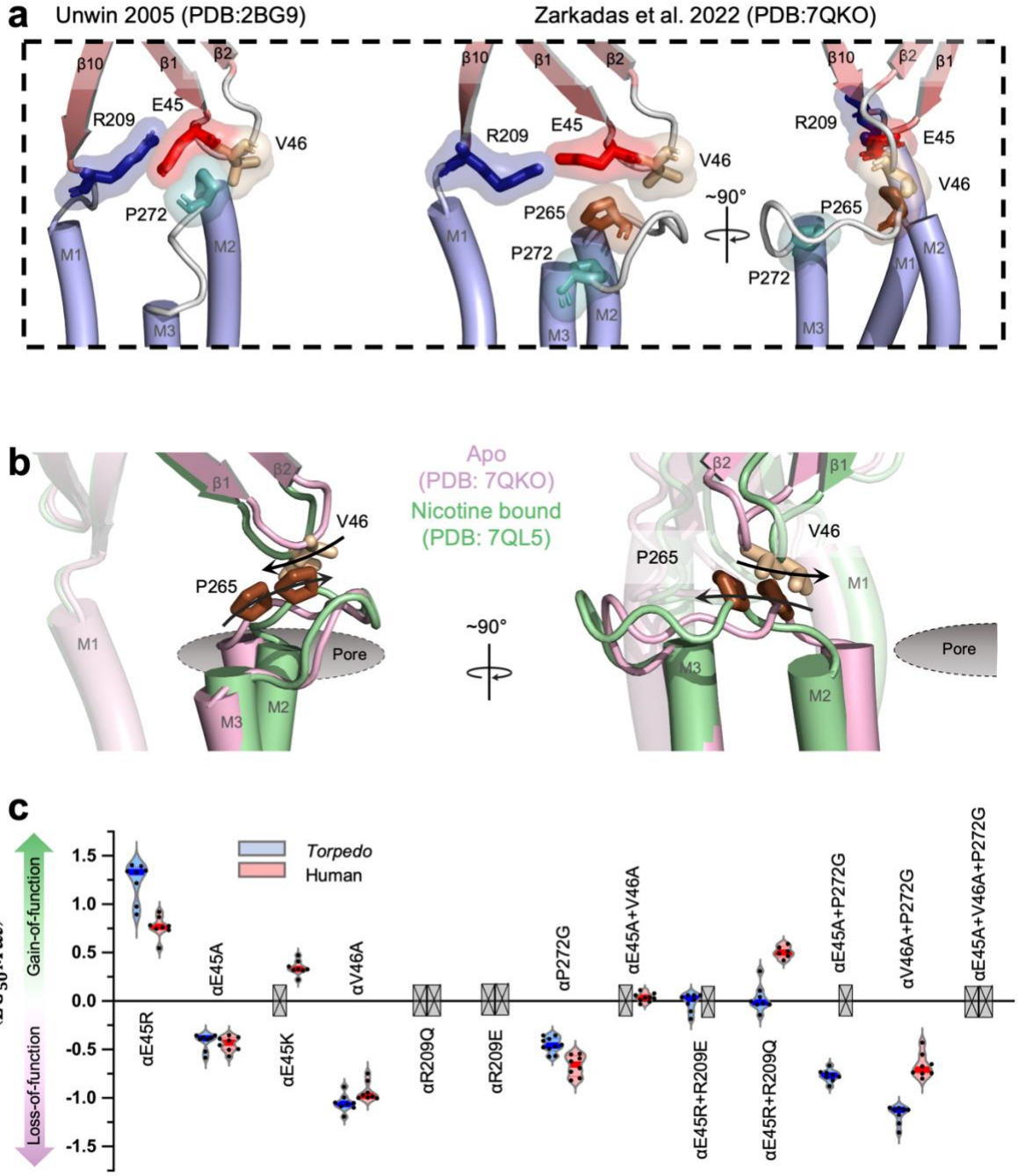
a
Unwin 2005 (PDB:2BG9)
Zarkadas et al. 2022 (PDB:7QKO)
β10
β1
β2
R209
E45
V46
P272
P265
M1
M2
M3
~90°
b
Apo
(PDB: 7QKO)
Nicotine bound
(PDB: 7QL5)
Pore
c
Torpedo
Human
Gain-of-function
Loss-of-function
log(EC50WT/EC50Mut)
αE45R
αE45A
αE45K
αV46A
αR209Q
αR209E
αP272G
αE45A+V46A
αE45R+R209E
αE45R+R209Q
αE45A+P272G
αV46A+P272G
αE45A+V46A+P272G

the agonist-induced motions at both the intra- and inter-subunit interfaces of α_γ and α_γ-γ, respectively).

With recent higher resolution structures repositioning many key residues at the ECD-TMD interfaces in the muscle nAChR (Rahman et al., 2020b, 2022; Zarkadas et al., 2022), we set out to identify previously unappreciated interactions that regulate allosteric coupling between the ECD and TMD, focusing on both the intra-α subunit and the inter-$\alpha_\gamma/\alpha_\delta$ - γ/δ subunit interfaces. To explore the large number of potential interacting side chains, mitigate the complications arising from integrating mutagenesis data obtained using whole cell versus single channel recordings of muscle nAChRs from different species and with different subunit compositions (fetal versus adult) expressed in different heterologous systems, and to ensure that our functional data is directly relatable to the *Torpedo* structures, we used a screening mutagenesis approach with each mutation functionally characterized in the *Torpedo* nAChR expressed in *Xenopus* oocytes using two electrode voltage clamp electrophysiology. Despite screening close to 300 mutations, we failed to identify any new interactions that clearly define channel gating. Instead, our integrated structural and functional approach identified local subunit conformational asymmetry in the apo state at the ECD – TMD interface, with agonist binding releasing this asymmetry so that the nAChR adopts a more symmetric open conformation. We propose that this release of conformational asymmetry is a key feature underlying allosteric communication at the ECD-TMD interface in the muscle nAChR. Furthermore, the same subunit transitions are observed in other pLGIC structures, albeit with subtle differences expected for homomeric versus heteromeric pLGICs.

5.4 Results

The intra-α subunit ECD-TMD domain interface is important to channel function in both human adult and Torpedo nAChRs. We first explored the functional role of the intra-α subunit ECD-TMD interfaces in the context that the compelling functional data suggesting a mechanism involving αArg209, αGlu45, and αVal46 from the ECD (referred to as the ECD triad) interacting with αPro272 and other residues of M2-M3 were obtained from single channel recordings of the *human adult muscle* nAChR (Lee and Sine, 2005), while the structural data revealing roughly orthogonal agonist-induced motions of β1-β2 and M2-M3 were obtained using the *Torpedo* nAChR (Zarkadas et al., 2022). To definitively rule out the possibility that these *apparent* discrepancies arise from subtle mechanistic differences between the human adult and *Torpedo* forms, we compared the functional consequences of key mutations in both receptors expressed in frog oocytes (Figs. 5.2c & 5.3, Tables 5.1 & 5.2; representative whole cell traces are presented in Fig. 5.4). We observed essentially identical functional consequences when each of these residues was mutated suggesting that each residue contributes similarly to channel function in both the adult muscle and *Torpedo* nAChRs. Both data sets highlight an important role for the salt bridge between αArg209 and αGlu45 in that charge reversal or neutralizing mutations of αArg209 lead to no expression while side chain substitutions of αGlu45 lead to large changes in function. On the other hand, the double charge reversal mutations, αE45R+αR209Q and αE45R+αR209E yield close to WT EC_{50} values. Both data sets also show that αVal46 and αPro272 play an important functional role as changing the residues to alanine and glycine, respectively, leads to loss-of-function phenotypes, with αV46A leading to the largest loss-of-function (12-fold) for any single mutation generated in this study. Finally, the αV46A+αP272G and the αE45A+αP272G double mutants have less of an effect on the measured EC_{50} values than

Figure 5.3 Relative sensitivities of EC50 versus θ to changes in channel function.

Measured changes in EC_{50} values relative to wild type for mutations in the muscle nAChR are typically of lesser magnitude than the changes observed in the di-liganded gating equilibrium constant, θ, for the same mutation. Measurements of EC_{50} are thus less sensitive to changes in channel gating. Such differences are expected, however, because EC_{50} values, which reflect both agonist binding (K_d) and channel gating (θ), are mathematically weighted towards the K_d, as illustrated by the following equation (Cecchini and Changeux, 2022):

$$EC_{50} = \frac{K_{d,R} * (1 + \sqrt{\theta + 2})}{\theta + 1}$$

which assumes that gating only occurs from the di-liganded state:

$$R + 2L \overset{K_{d,R}}{\rightleftarrows} RL_2 \overset{\theta}{\rightleftarrows} OL_2$$

where R corresponds to the closed resting state, O the activated open state, and $K_{d,R}$ the resting state agonist (acetylcholine) affinity assuming both agonist sites are equivalent.

To explore the relationship between EC_{50} and θ, we first *estimated* the $K_{d,R}$ for both *Torpedo* (64.6 μM) and the human adult muscle (54.6 μM) nAChR using our measured EC_{50} values and a common θ value of 60, which was determined elsewhere for the human adult muscle nAChR (Mukhtasimova et al., 2016). A) Assuming a constant $K_{d,R}$, we illustrate the non-linearity of the relationship between EC_{50} and θ by plotting the expected change in θ as a function of a change in EC_{50} value. The black dot represents WT values for the *Torpedo* nAChR. The non-linearity of the relationship is further illustrated in B), which compares how the fold change in θ relative to WT (red curve) manifests as a fold change in EC_{50} relative to WT (blue curve) as θ deviates from WT (black dot).

The two curves illustrate that the greater the functional effect of the mutant on channel gating (i.e., the greater the change in θ), the larger the discrepancy between the measured fold change in EC_{50} versus θ. For example, using these approximations, 2-, 5- and 10-fold changes in EC_{50} in the Torpedo nAChR should correspond to roughly 3, 15 and 70-fold changes in θ, respectively.

C) The table compares the experimentally measured EC_{50} values for select mutants in both the *Torpedo* and the adult human muscle nAChR, along with the fold change in each EC_{50} relative to WT (this study), to the changes in the di-liganded gating equilibrium constant, θ, calculated for each mutation in the adult human muscle nAChR from kinetic fitting of single channel measurements (Lee and Sine, 2005). Considering the expected differences in the sensitivities of EC_{50} versus θ values to changes in channel function, the functional data obtained using both whole cell and single channel electrophysiological recordings present a consistent picture regarding the importance of residues at the intra-α subunit ECD-TMD domain interface. Despite structures showing that β1-β2 moves roughly orthogonally to M2-M3 upon agonist binding (Fig. 5.1b and Movie 1, panel a), the mutagenesis data reaffirms that the ECD triad plays an important role in channel gating.

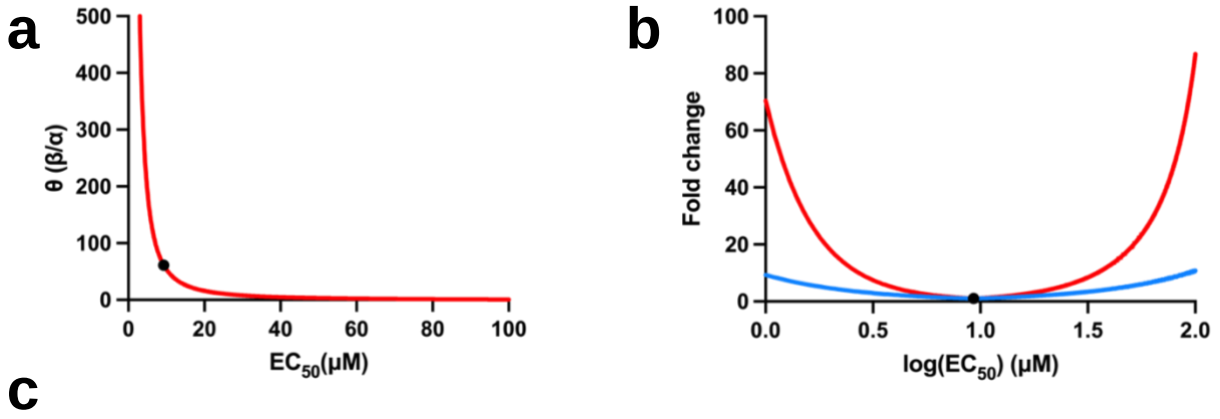

	Torpedo nAChR		Human adult nAChR			
Mutant	EC_{50} (μM)	Fold change (EC_{50})	EC_{50} (μM)	Fold change (EC_{50})	θ (lit)[b]	Fold change (θ) (lit)[b]
WT	9.40	-	7.98	-	27.0	-
αE45R	0.600	0.063	1.40	0.176	4.10	6.59
αE45A	24.4	2.67	22.3	2.79	2.10	12.9
αE45K	NR[a]		3.63	0.457	0.224	121
αV46A	108	11.5	69.4	8.74	0.057	474
αP272G	27.1	2.88	37.9	4.77	0.170	159
αE45R+αR209Q	9.16	0.974	2.50	3.19	19.0	1.42
αE45R+αR209E	9.80	1.04	NR[a]			1.35
αE45A+αV46A	NR[a]		7.32	1.08	0.005	5,870
αE45A+αP272G	55.8	5.93	NR[a]		0.042	643
αV46A+αP272G	142	15.1	38.0	4.76	0.006	4,820
αE45A+V46A+αP272G	NR[a]		NR[a]		0.005	5,000

[a]No response (NR). No significant agonist induced current observed up to 4 day after cRNA injection.

[b]θ values from (Lee and Sine, 2005).

Table 5.1 - Functional effects of mutations to residues at the intra- and inter-subunit ECD-TMD interfaces.

Mutant[a]	EC_{50} (μM)	Hill slope	n	Fold change
WT	9.40 ± 1.82	1.78 ± 0.35	87	
Intra-subunit gating interface				
αE45R	0.600 ± 0.316[b]	1.39 ± 0.21	8	15.7 gain
αE45A	25.1 ± 5.5[b]	1.83 ± 0.31	8	2.67 loss
αE45K	NR[c]			
αV46A	108 ± 21[b]	2.00 ± 0.41	8	11.5 loss
αR209Q	NE[d]			
αR209E	NE[d]			
αI264A	28.5 ± 6.3[d]	1.45 ± 0.19	10	3.03 loss
αP265A	2.10 ± 0.65[b]	1.58 ± 0.35	9	4.47 gain
αP265G	19.8 ± 5.5[b]	1.85 ± 0.54	8	2.11 loss
αP272G	27.1 ± 4.9[b]	1.63 ± 0.15	10	2.88 loss
Inter-subunit gating interface				
αS266A	41.6 ± 7.3[b]	1.58 ± 0.20	8	4.42 loss
αT267A	27.4 ± 3.1[b]	1.57 ± 0.17	8	2.91 loss
αS268A	2.21 ± 0.33[b]	1.77 ± 0.28	8	4.26 gain
αS269A	3.83 ± 0.30	1.97 ± 0.47	8	2.45 gain
αS266A+αT267A+αS268A+αS269A	4.32 ± 1.42	2.12 ± 0.26	8	2.16 gain
αS266G+αT267G+αS268G+αS269G	14.3 ± 2.2	1.79 ± 0.13	8	1.53 loss
βE272G+βT273G+βS274G+βL275G	14.0 ± 1.5	1.85 ± 0.18	14	1.35 loss
δE280G+δT281G+δA282G+δL283G	21.5 ± 3.2[b]	1.63 ± 0.15	7	2.28 loss
γE275G+γT276G+γS277G+γL278G	19.7 ± 2.6[b]	1.51 ± 0.18	8	2.10 loss
αβδγ(STSS → GGGG)	16.2 ± 3.4[b]	2.14 ± 0.47	7	1.73 loss
δG188A	19.3 ± 3.5[b]	1.59 ± 0.20	8	2.06 loss
γG182A + δG188A	31.0 ± 2.1[b]	1.68 ± 0.30	9	3.33 loss
γE183A	15.9 ± 3.3	1.69 ± 0.15	8	1.69 loss
δE189A	10.2 ± 1.1	1.80 ± 0.21	8	1.09 loss
γE183A+δE189A	16.3 ± 4.0	1.50 ± 0.51	8	1.73 loss
γK218A	2.39 ± 0.66	1.91 ± 0.25	8	3.94 gain
δK224A	4.24 ± 0.98	1.84 ± 0.26	9	2.20 gain
γK218A+δK224A	0.956 ± 0.434[b]	2.14 ± 0.57	9	9.76 gain
γP219A	11.8 ± 1.5	2.07 ± 0.56	8	1.26 loss
δP225A	12.0 ± 1.5	1.93 ± 0.59	8	1.28 loss
γP219A+δP225A	12.0 ± 1.4	1.67 ± 0.59	8	1.28 loss
γL220A	8.83 ± 2.14	1.81 ± 0.11	8	1.06 gain
δL226A	4.48 ± 0.70	2.20 ± 0.35	8	2.08 gain
γL220A+δL226A	6.42 ± 0.81	1.87 ± 0.33	8	1.46 gain
γF221A	17.6 ± 3.0[b]	1.72 ± 0.28	8	1.87 loss
δF227A	5.67 ± 0.78	2.10 ± 0.71	8	1.64 gain
γF221A+δF227A	18.0 ± 7.2[b]	2.04 ± 0.25	8	1.92 loss

[a]Measurements performed 2-4 days after cRNA injection (V_{hold} = -60 mV). Error values represented as standard deviation
[b]$p < 0.001$ relative to WT via one-way ANOVA followed by Dunnet's post hoc test. DF=283. F_{EC50}=176.3. F_{Hill}=3.357.
[c]No response (NR). No significant agonist induced current observed up to 4 day after cRNA injection
[d]No expression (NE). No significant expression or agonist induced current observed up to 4 day after cRNA injection

Table 5.2 - Functional effects of mutations to the ECD triad and residues in the M2-M3 loop of the *Torpedo* versus human adult muscle nAChR.

	Torpedo nAChR[a]				Human adult nAChR[a]			
Mutant	EC_{50} (μM)	Hill slope	n	Fold change	EC_{50} (μM)	Hill slope	N	Fold change
WT	9.40 ± 1.82	1.78 ± 0.35	87	-	7.98 ± 1.75	1.87 ± 0.32	53	-
αE45R	0.600 ± 0.316[b]	1.39 ± 0.21	8	15.7 gain	1.40 ± 0.39	1.43 ± 0.31	8	5.71 gain
αE45A	25.1 ± 5.5[b]	1.83 ± 0.31	8	2.67 loss	22.3 ± 4.0[b]	1.85 ± 0.31	8	2.79 loss
αE45K	NR[c]				3.63 ± 0.61	1.77 ± 0.45	8	2.20 gain
αV46A	108 ± 21[b]	2.00 ± 0.41	8	11.5 loss	69.4 ± 13.5[b]	1.38 ± 0.35	8	8.70 loss
αR209Q	NE[d]				NR[c]			
αR209E	NE[d]				NR[c]			
αP272G	27.1 ± 4.9[b]	1.63 ± 0.15	10	2.88 loss	37.9 ± 9.4[b]	1.82 ± 0.37	8	4.75 loss
αE45R+αR209Q	9.16 ± 2.47	1.92 ± 0.40	8	1.03 gain	2.50 ± 0.35	2.18 ± 0.22	6	3.19 gain
αE45R+αR209E	9.80 ± 2.23	1.72 ± 0.09	8	1.04 loss	NR[c]			
αE45A+αV46A	NR[c]				7.32 ± 0.73	2.26 ± 0.20	9	1.10 gain
αE45A+αP272G	55.8 ± 8.2[b]	1.49 ± 0.18	8	5.93 loss	NR[c]			
αV46A+αP272G	142 ± 33[b]	2.29 ± 0.50	8	15.1 loss	38.0 ± 9.4[b]	1.56 ± 0.50	8	4.76 loss
αE45A+αV46A+ αP272G	NR[c]				NR[c]			

[a]Measurements performed 2-4 days after cRNA injection (V_{hold} = -60 mV). Error values represented as standard deviation
[b]$p < 0.001$ relative to WT via one-way ANOVA followed by Dunnet's post hoc test. *Torpedo* DF=144. *Torpedo* F_{EC50}=294.9. *Torpedo* F_{Hill}=5.657. Human adult DF=107. Human adult F_{EC50}=185.8. Human adult F_{Hill}=6.736.
[c]No response (NR). No significant agonist induced current observed up to 4 day after cRNA injection
[d]No expression (NE). No significant expression or agonist induced current observed up to 4 day after cRNA injection

Figure 5.4 Raw TEVC traces used to plot dose-response curves.

Representative traces from select mutants are presented in the pages below as a change in current over time in response to increasing concentrations of ACh. Horizontal bars above each trace represent the time the indicated concentration of ACh was exposed to the oocyte.

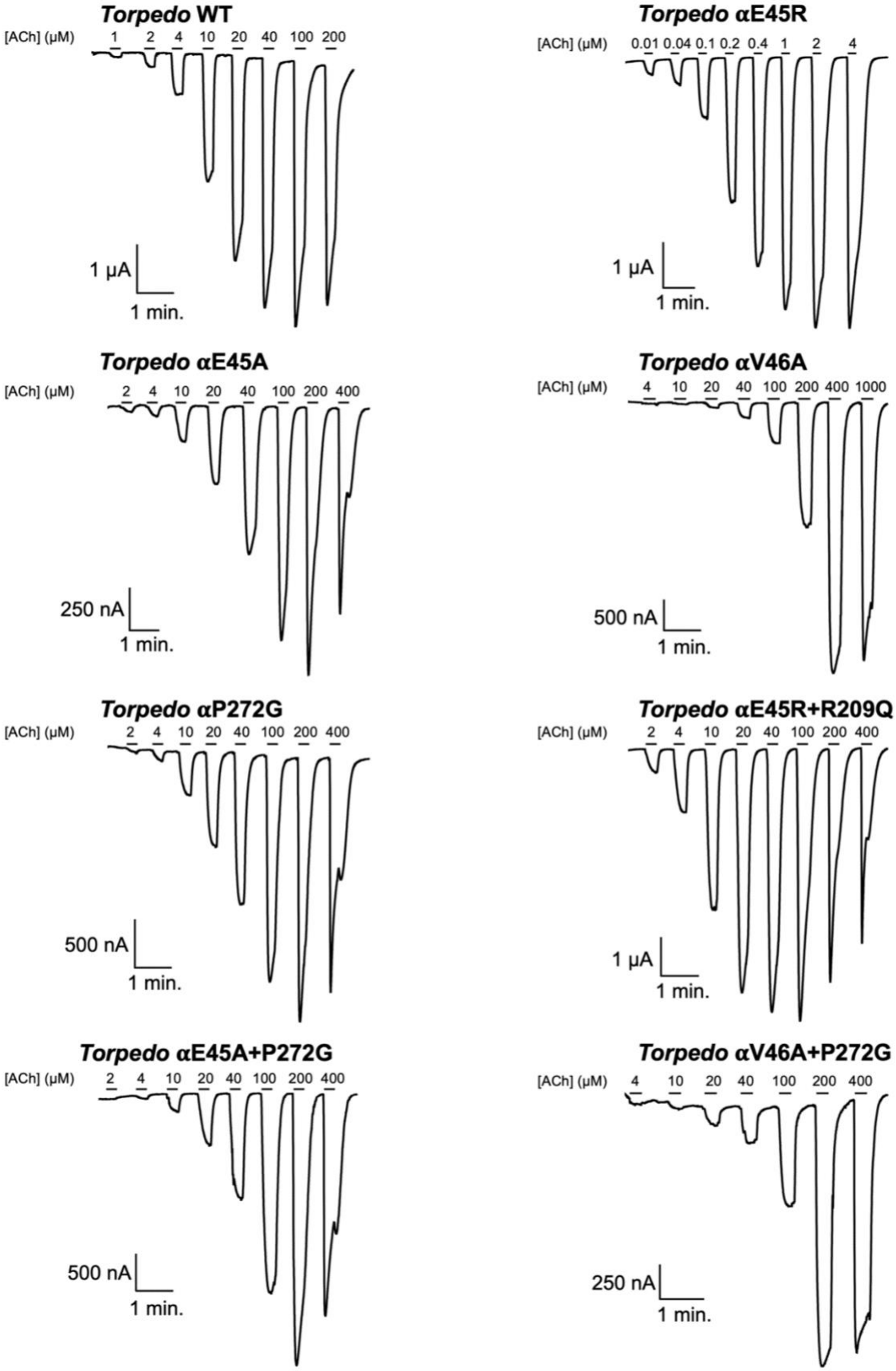
Torpedo WT
[ACh] (μM)
1 2 4 10 20 40 100 200
1 μA
1 min.
Torpedo αE45R
[ACh] (μM)
0.01 0.04 0.1 0.2 0.4 1 2 4
1 μA
1 min.
Torpedo αE45A
[ACh] (μM)
2 4 10 20 40 100 200 400
250 nA
1 min.
Torpedo αV46A
[ACh] (μM)
4 10 20 40 100 200 400 1000
500 nA
1 min.
Torpedo αP272G
[ACh] (μM)
2 4 10 20 40 100 200 400
500 nA
1 min.
Torpedo αE45R+R209Q
[ACh] (μM)
2 4 10 20 40 100 200 400
1 μA
1 min.
Torpedo αE45A+P272G
[ACh] (μM)
2 4 10 20 40 100 200 400
500 nA
1 min.
Torpedo αV46A+P272G
[ACh] (μM)
4 10 20 40 100 200 400
250 nA
1 min.

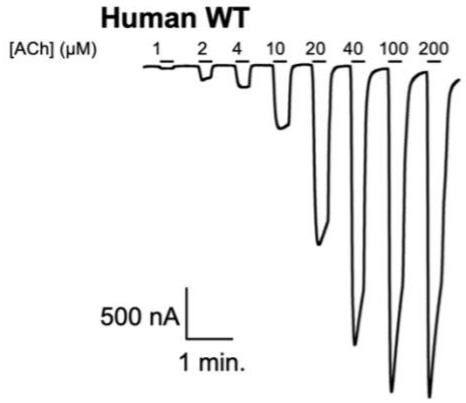
Human WT
[ACh] (μM)
1 2 4 10 20 40 100 200
500 nA
1 min.

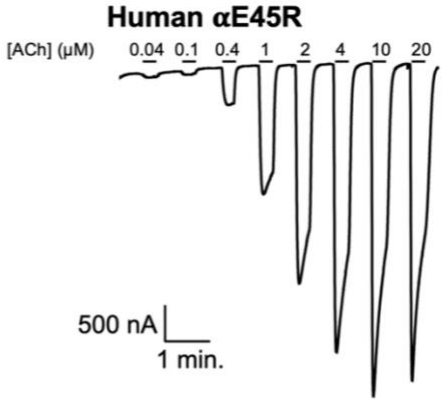
Human αE45R
[ACh] (μM)
0.04 0.1 0.4 1 2 4 10 20
500 nA
1 min.

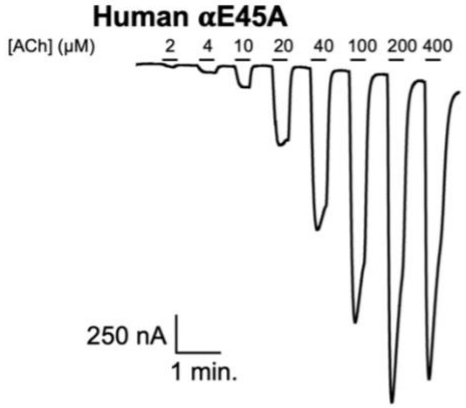
Human αE45A
[ACh] (μM)
2 4 10 20 40 100 200 400
250 nA
1 min.

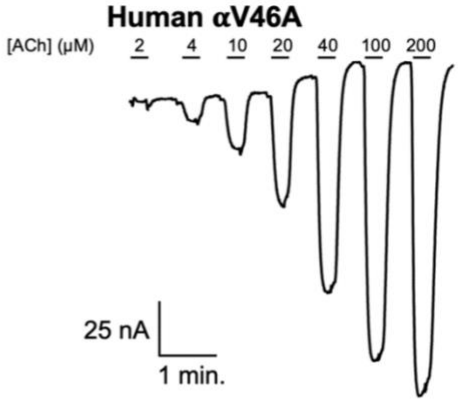
Human αV46A
[ACh] (μM)
2 4 10 20 40 100 200
25 nA
1 min.

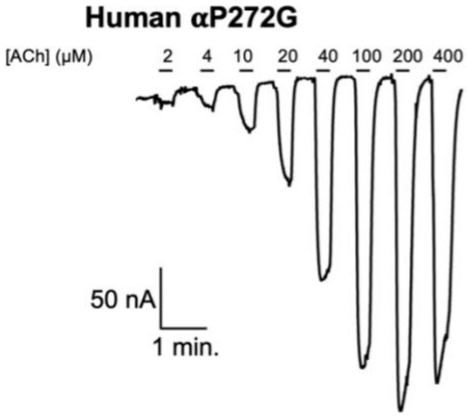
Human αP272G
[ACh] (μM)
2 4 10 20 40 100 200 400
50 nA
1 min.

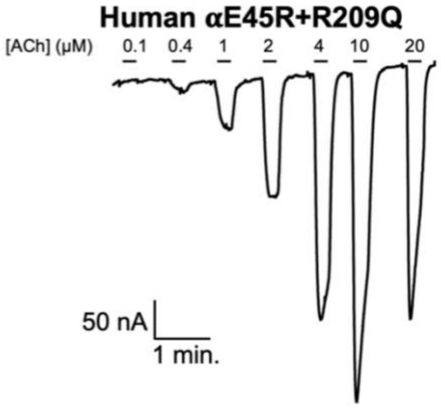
Human αE45R+R209Q
[ACh] (μM)
0.1 0.4 1 2 4 10 20
50 nA
1 min.

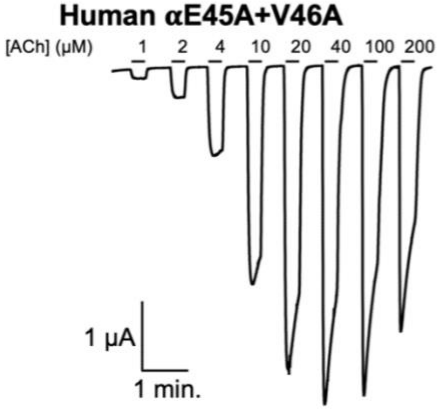
Human αE45A+V46A
[ACh] (μM)
1 2 4 10 20 40 100 200
1 μA
1 min.

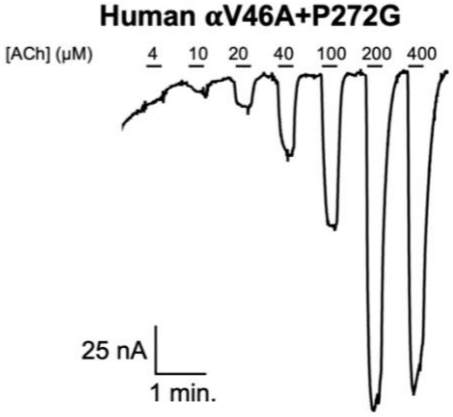
Human αV46A+P272G
[ACh] (μM)
4 10 20 40 100 200 400
25 nA
1 min.

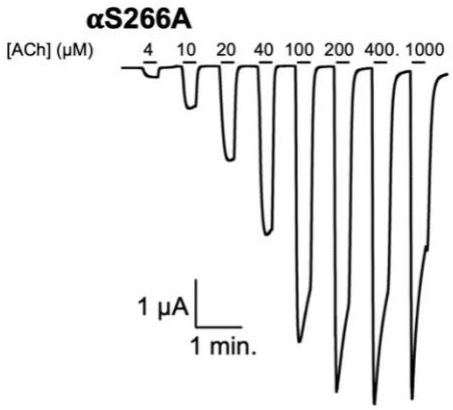
αS266A
[ACh] (μM)
4 10 20 40 100 200 400. 1000
1 μA
1 min.

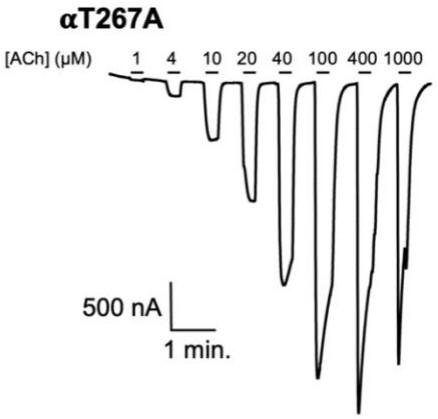
αT267A
[ACh] (μM)
1 4 10 20 40 100 400 1000
500 nA
1 min.

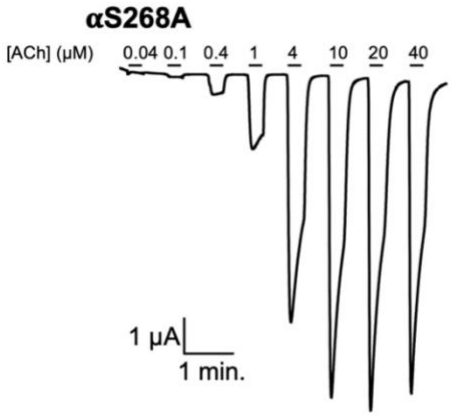
αS268A
[ACh] (μM)
0.04 0.1 0.4 1 4 10 20 40
1 μA
1 min.

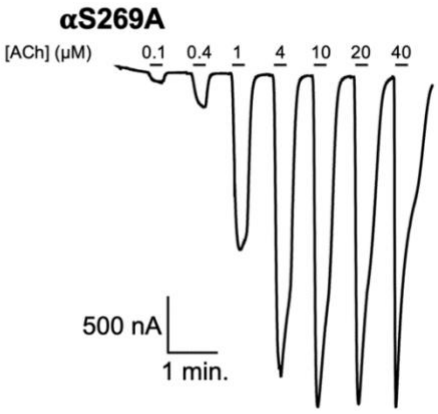
αS269A
[ACh] (μM)
0.1 0.4 1 4 10 20 40
500 nA
1 min.

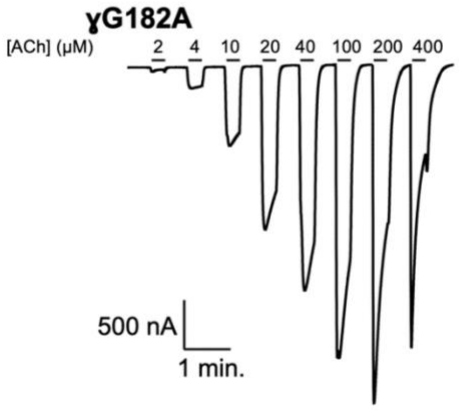
γG182A
[ACh] (μM)
2 4 10 20 40 100 200 400
500 nA
1 min.

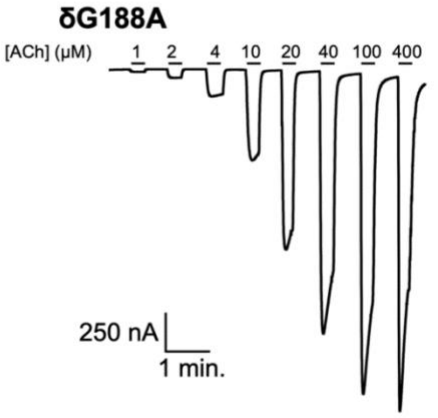
δG188A
[ACh] (μM)
1 2 4 10 20 40 100 400
250 nA
1 min.

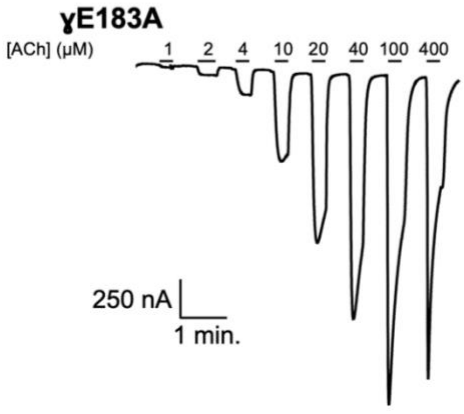
γE183A
[ACh] (μM)
1 2 4 10 20 40 100 400
250 nA
1 min.

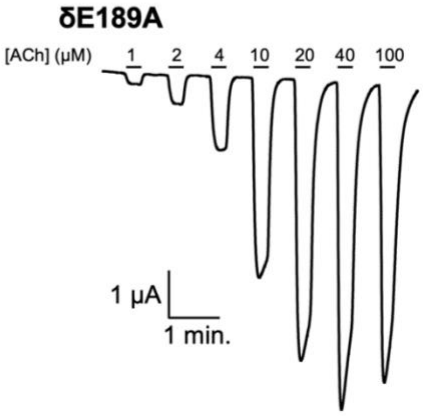
δE189A
[ACh] (μM)
1 2 4 10 20 40 100
1 μA
1 min.

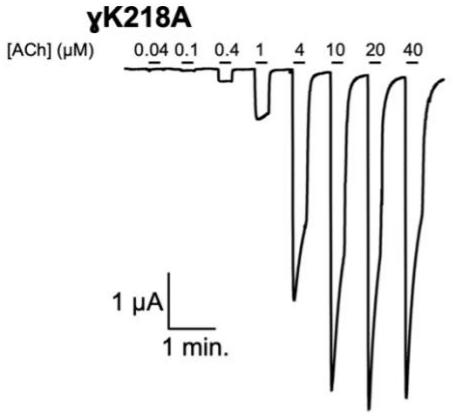
γK218A
[ACh] (μM)
0.04 0.1 0.4 1 4 10 20 40
1 μA
1 min.

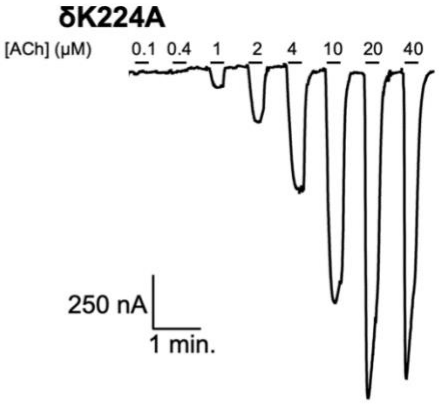
δK224A
[ACh] (μM)
0.1 0.4 1 2 4 10 20 40
250 nA
1 min.

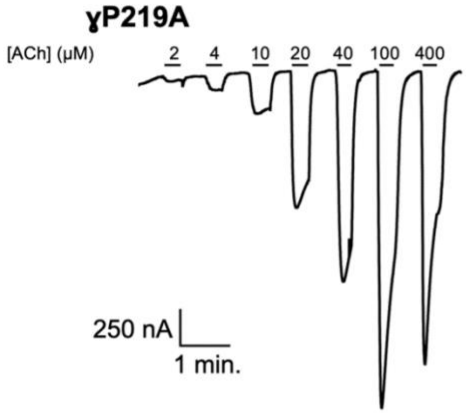
γP219A
[ACh] (μM)
2 4 10 20 40 100 400
250 nA
1 min.

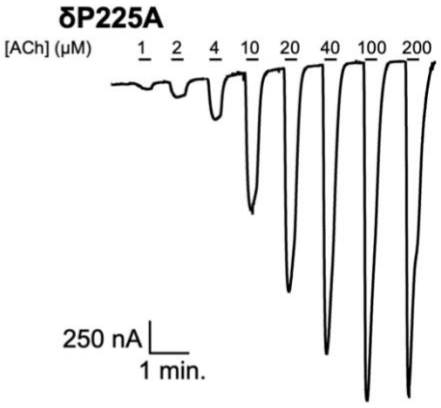
δP225A
[ACh] (μM)
1 2 4 10 20 40 100 200
250 nA
1 min.

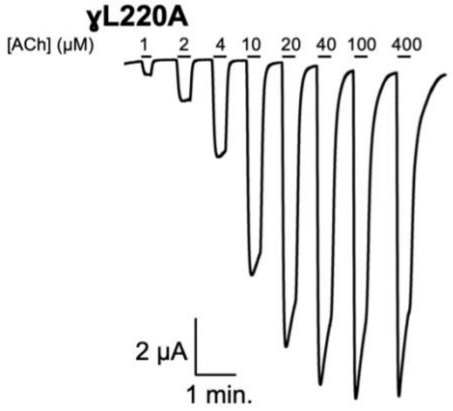
γL220A
[ACh] (μM)
1 2 4 10 20 40 100 400
2 μA
1 min.

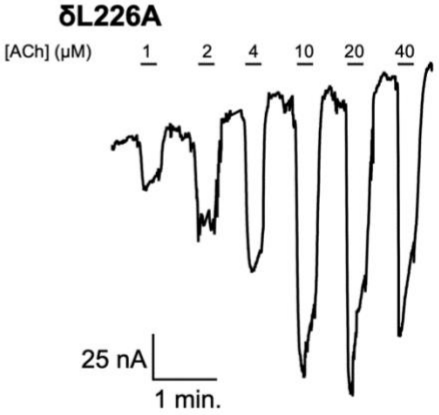
δL226A
[ACh] (μM)
1 2 4 10 20 40
25 nA
1 min.

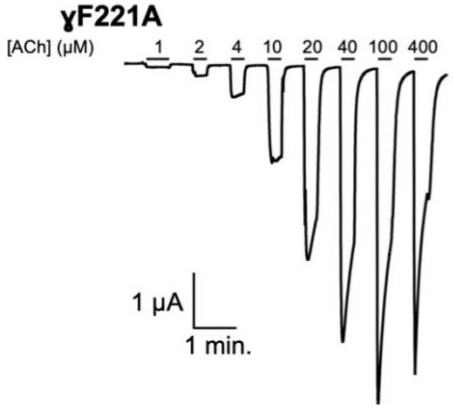
γF221A
[ACh] (μM)
1 2 4 10 20 40 100 400
1 μA
1 min.

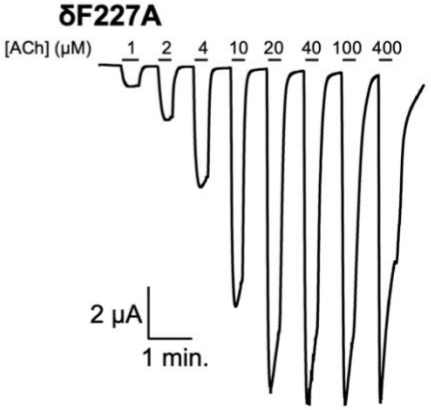
δF227A
[ACh] (μM)
1 2 4 10 20 40 100 400
2 μA
1 min.

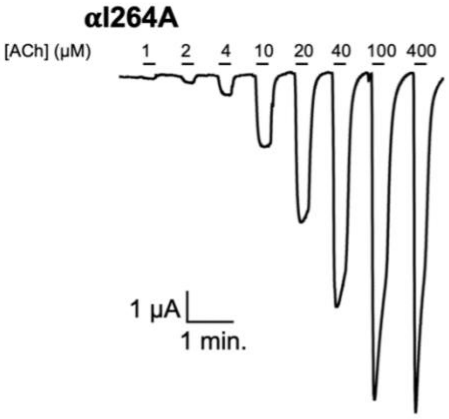
αI264A
[ACh] (μM)
1 2 4 10 20 40 100 400
1 μA
1 min.

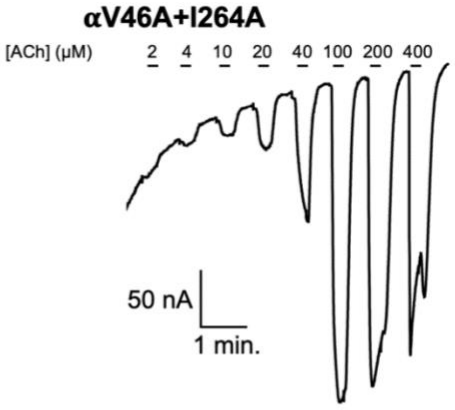
αV46A+I264A
[ACh] (μM)
2 4 10 20 40 100 200 400
50 nA
1 min.

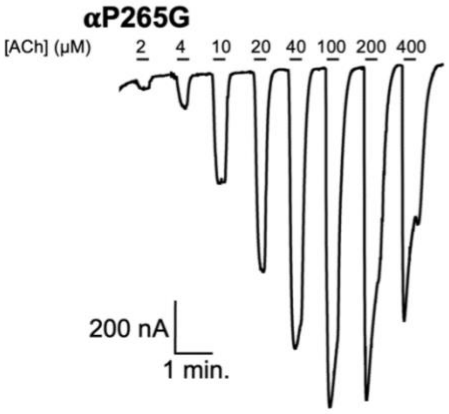
αP265G
[ACh] (μM)
2 4 10 20 40 100 200 400
200 nA
1 min.

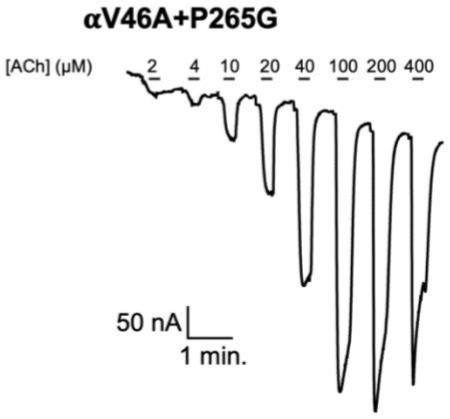
αV46A+P265G
[ACh] (μM)
2 4 10 20 40 100 200 400
50 nA
1 min.

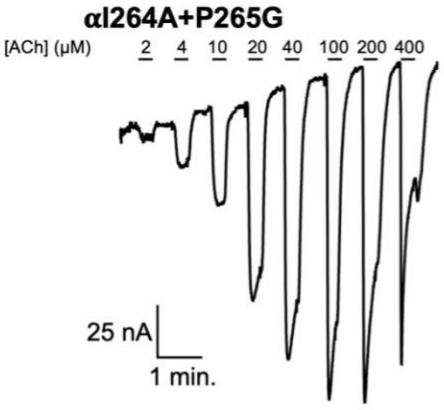
αI264A+P265G
[ACh] (μM)
2 4 10 20 40 100 200 400
25 nA
1 min.

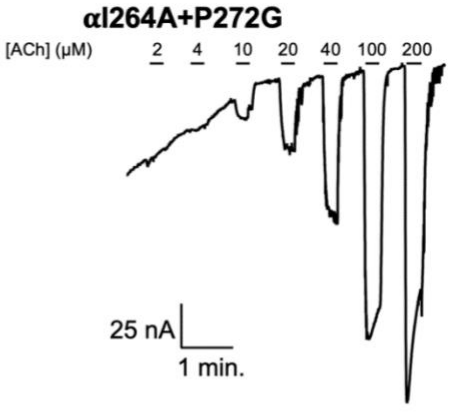
αI264A+P272G
[ACh] (μM)
2 4 10 20 40 100 200
25 nA
1 min.

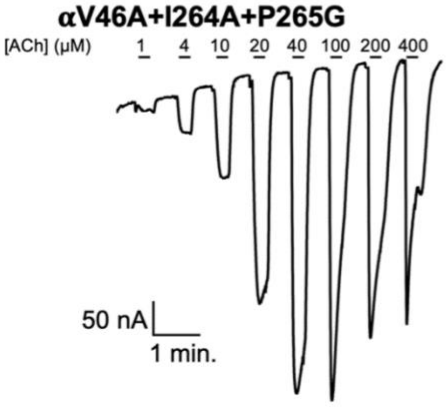
αV46A+I264A+P265G
[ACh] (μM)
1 4 10 20 40 100 200 400
50 nA
1 min.

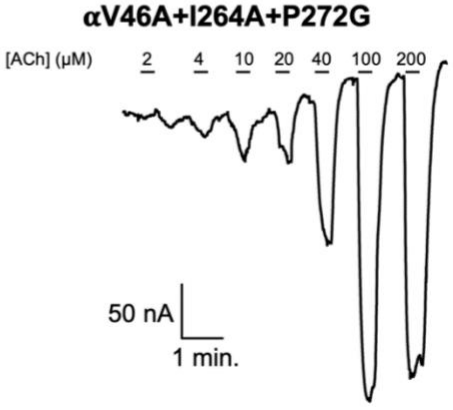
αV46A+I264A+P272G
[ACh] (μM)
2 4 10 20 40 100 200
50 nA
1 min.

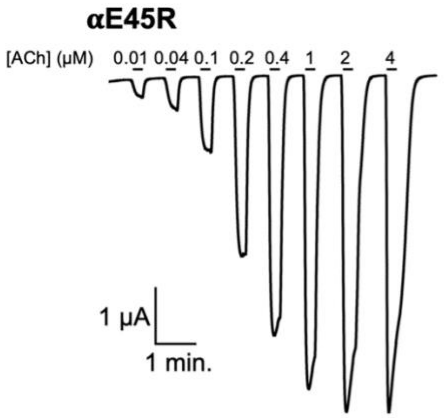
αE45R
[ACh] (μM) 0.01 0.04 0.1 0.2 0.4 1 2 4
1 μA
1 min.

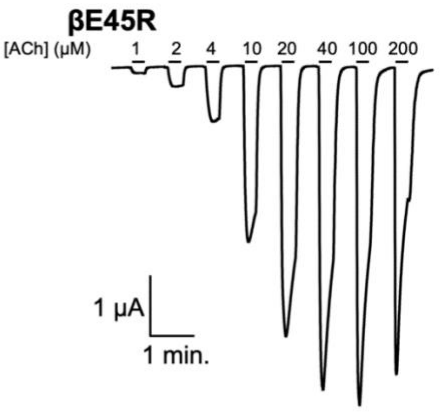
βE45R
[ACh] (μM) 1 2 4 10 20 40 100 200
1 μA
1 min.

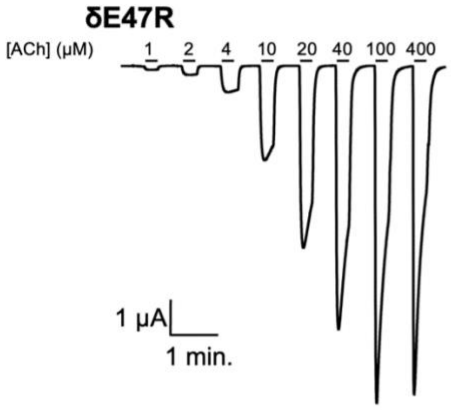
δE47R
[ACh] (μM) 1 2 4 10 20 40 100 400
1 μA
1 min.

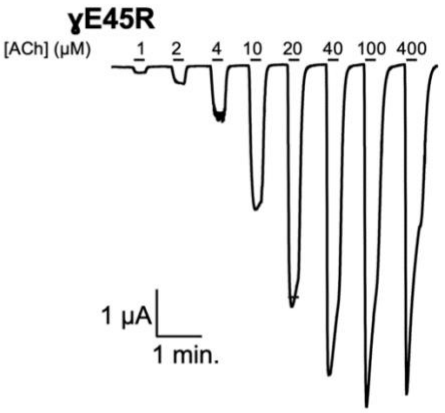
γE45R
[ACh] (μM) 1 2 4 10 20 40 100 400
1 μA
1 min.

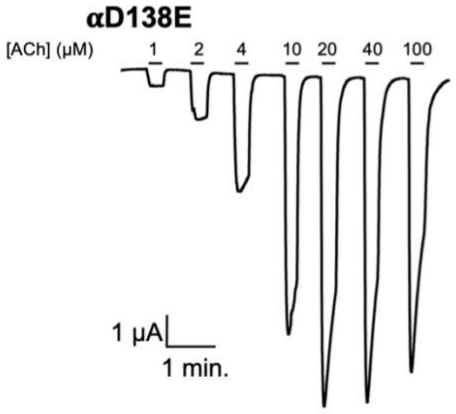
αD138E
[ACh] (μM) 1 2 4 10 20 40 100
1 μA
1 min.

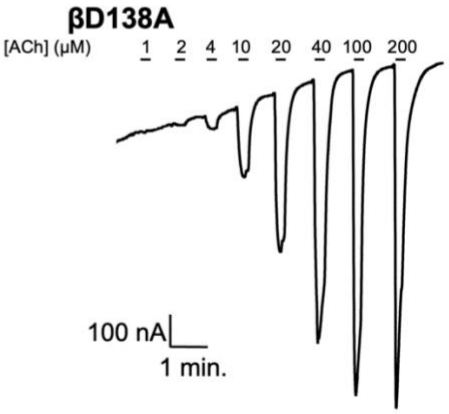
βD138A
[ACh] (μM) 1 2 4 10 20 40 100 200
100 nA
1 min.

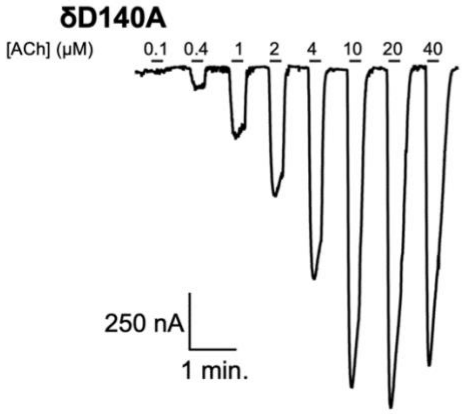
δD140A
[ACh] (μM) 0.1 0.4 1 2 4 10 20 40
250 nA
1 min.

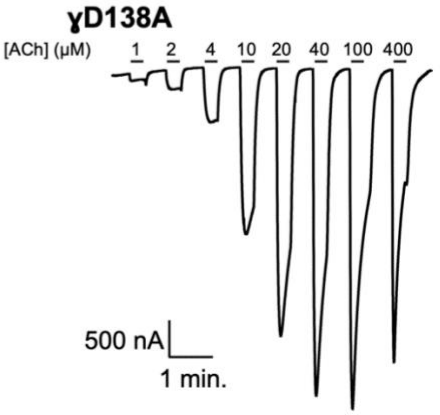
γD138A
[ACh] (μM) 1 2 4 10 20 40 100 400
500 nA
1 min.

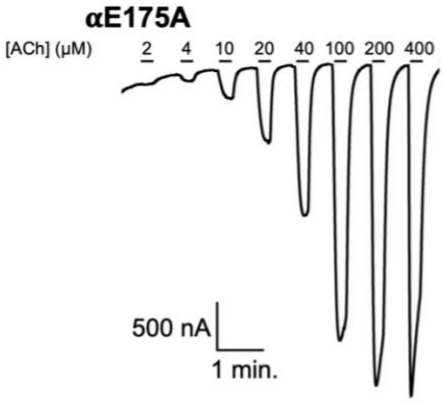
αE175A
[ACh] (μM)
2 4 10 20 40 100 200 400
500 nA
1 min.

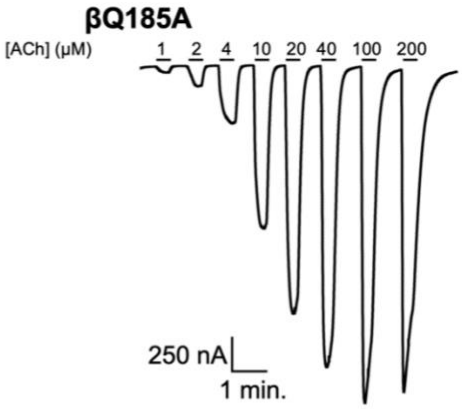
βQ185A
[ACh] (μM)
1 2 4 10 20 40 100 200
250 nA
1 min.

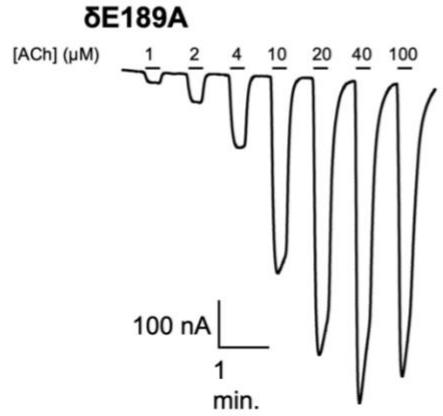
δE189A
[ACh] (μM)
1 2 4 10 20 40 100
100 nA
1
min.

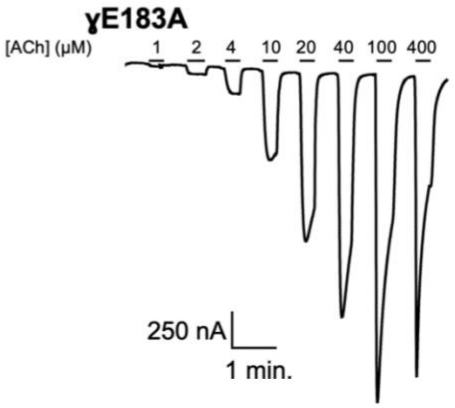
γE183A
[ACh] (μM)
1 2 4 10 20 40 100 400
250 nA
1 min.

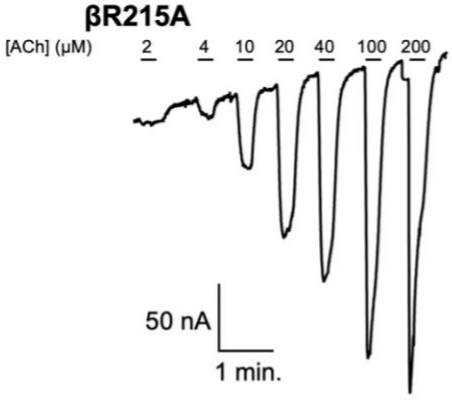
βR215A
[ACh] (μM)
2 4 10 20 40 100 200
50 nA
1 min.

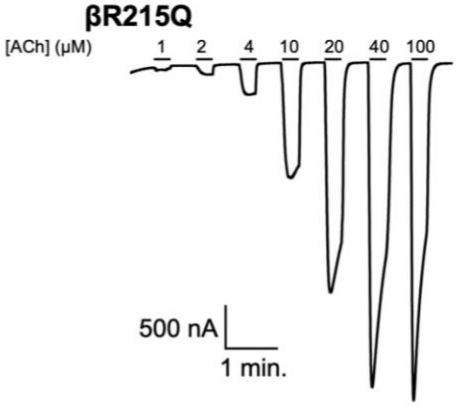
βR215Q
[ACh] (μM)
1 2 4 10 20 40 100
500 nA
1 min.

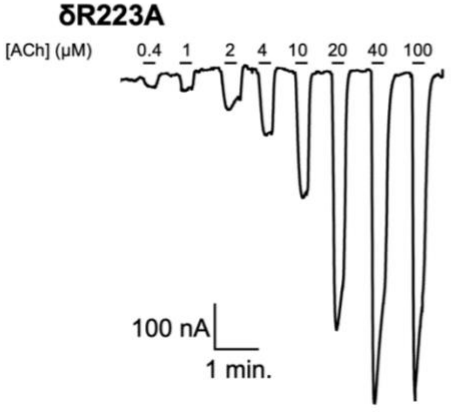
δR223A
[ACh] (μM)
0.4 1 2 4 10 20 40 100
100 nA
1 min.

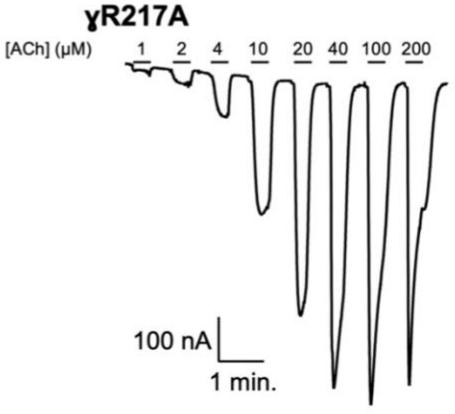
γR217A
[ACh] (μM)
1 2 4 10 20 40 100 200
100 nA
1 min.

would be expected if each individual mutation influenced function independently, consistent with the previously reported energetic couplings across this intra-subunit ECD-TMD domain interface (Table 5.3). Despite structures showing that β1-β2 moves roughly orthogonally to M2-M3 upon agonist binding (Fig. 5.1b and Movie 1, panel a), our mutagenesis data reaffirm that the ECD triad plays an important role in channel gating (see Fig. 5.3) and does so, at least in part, by energetically coupling with the M2-M3 loop.

Side chain interactions at the inter-subunit ECD-TMD interface are not critical for driving allosteric communication. We next considered the possibility that agonist-induced motions of γ/δ β8-β9 loops/β10-M1 linkers play a key role energetic role driving the gating motions of the $\alpha_\gamma/\alpha_\delta$ M2-M3 loops. As noted, the apo and agonist bound structures of the *Torpedo* nAChR show that the extended F loops from the complementary γ/δ subunits rock in towards the bound agonist causing their membrane juxtaposed regions, the β8-β9 loops/β10-M1 linkers, to pivot outward, with these outward motions occuring in concert with the outward motions of the $\alpha_\gamma/\alpha_\delta$ M2-M3 loops that open the L9' gate (Fig. 5.5a and Movie 1, panel b). We first probed the functional importance of the γ/δ F loops, which cap around the agonist so that γAsp174/δAsp180 and γGlu176/δGlu182 form hydrogen bonds with the backbone nitrogen of αThr191 (loop C) and the backbone carbonyl of αTyr189 (β9), respectively (Fig. 5.5b). Capping of loop F is *not* observed in the homomeric α7 nAChR, likely because loop F is too short to close around the bound agonist (Noviello et al., 2021). We therefore substituted the ^{172}HI**D**P**E**D^{177}(γ)/^{178}II**D**P**E**A^{183}(δ) sequences with the corresponding "DI**S**G--" sequence from the α7 loop F to eliminate the noted contacts and thus prevent or minimize this capping motion. The individual substitutions at the α-γ and α-δ sites led to 5- and 2-fold losses of function, respectively, while the simultaneous mutation in both subunits led to a 10-fold loss of function

Table 5.3 - Energetic couplings across the intra- and inter-subunit ECD-TMD interfaces.

Mutant[a]	EC_{50} (μM)	Hill slope	n	Fold change	Predicted[b]	Ω[c]	ΔΔG (kJ/mol)[d]
Intra-subunit ECD-TMD domain interface							
αE45R+αR209Q	9.16 ± 2.47	1.92 ± 0.40	8	1.03 gain			
αE45R+αR209E	9.80 ± 2.23	1.72 ± 0.09	8	1.04 loss			
αE45A+αV46A	NR[f]				30.6 loss		
αE45A+αP272G	55.8 ± 8.2[e]	1.49 ± 0.18	8	5.93 loss	7.69 loss	0.77	-0.64 ± 0.24
αV46A+αI264A	143 ± 27[e]	1.69 ± 0.28	8	15.2 loss	34.7 loss	0.44	-2.04 ± 0.82
αV46A+αP265A	32.2 ± 6.0[e]	2.01 ± 0.26	8	3.43 loss	2.56 loss	1.34	+0.72 ± 0.33
αV46A+αP265G	34.2 ± 3.6[e]	1.99 ± 0.22	7	3.63 loss	24.2 loss	0.15	-4.69 ± 1.90
αV46A+αP272G	142 ± 33[e]	2.29 ± 0.50	8	15.1 loss	33.0 loss	0.46	-1.94 ± 0.79
αI264A+αP265G	6.52 ± 1.32	1.42 ± 0.33	8	1.44 gain	6.38 loss	0.11	-5.50 ± 2.48
αI264A+αP272G	54.5 ± 9.8[e]	1.59 ± 0.38	9	5.80 loss	8.72 loss	0.66	-1.01 ± 0.39
αE45A+αV46A+αP272G	NR[f]				88.1 loss		
αV46A+αI264A+αP265G	7.80 ± 1.20	1.66 ± 0.26	8	1.21 gain	73.1 loss	0.01	-11.1 ± 5.7
αV46A+αI264A+αP272G	105 ± 14[e]	2.11 ± 0.52	8	11.2 loss	99.9 loss	0.11	-5.43 ± 2.51
Inter-subunit ECD-TMD domain interface							
αS266A+γG182A/δG188A	46.3 ± 6.7[e]	2.15 ± 0.23	8	4.93 loss	22.6 loss	0.22	-3.77 ± 1.57
αS266A+ γE183A/δE189A	28.7 ± 4.8[e]	1.87 ± 0.37	8	3.06 loss	8.11 loss	0.38	-2.42 ± 1.05
αT267A+γG182A/δG188A	33.2 ± 3.5[e]	2.25 ± 0.54	8	3.53 loss	14.9 loss	0.24	-3.56 ± 1.40
αT267A+γF221A/ δF227A	NR[f]				3.29 loss		
αS268A+ γG182A/δG188A	11.0 ± 3.1	1.82 ± 0.49	8	1.17 loss	1.20 loss	0.98	-0.05 ± 0.02
αS268A+γK218A/δK224A	0.486 ± 0.126	2.22 ± 0.45	8	19.4 gain	37.3 gain	1.93	+1.62 ± 0.88
αS268P+ γG182A/δG188A	6.50 ± 2.47	1.63 ± 0.55	8	1.45 gain	5.24 loss	0.13	-5.02 ± 2.09
αS269A+γG182A/δG188A	NR[f]				2.08 loss		
αS269A+γK218A/δK224A	0.439 ± 0.126	2.03 ± 0.73	4	21.4 gain	21.5 gain	1.00	0.00 ± 0.00
αS269A+ γL220A/δL226A	NR[f]				5.49 gain		
αS266A/αT267A+γG182A/δG188A	31.5 ± 4.6[e]	2.13 ± 0.32	9	3.35 loss	65.7 loss	0.05	-7.37 ± 3.49
αS266A/αT267A+ γE183A/δE189A	27.3 ± 9.2[e]	2.30 ± 0.69	8	2.90 loss	23.6 loss	0.12	-5.20 ± 2.95
αS268A/αS269A+γG182A/δG188A	5.05 ± 0.97	1.96 ± 0.72	8	1.86 gain	2.05 gain	1.10	+0.24 ± 0.11
αS268A/αS269A+γK218A/δK224A	0.176 ± 0.064	2.99 ± 0.92[e]	5	53.4 gain	91.5 gain	1.71	+1.33 ± 0.96
αS266G/αT267G/S268G/S269G+γG182A	20.6 ± 8.2	1.65 ± 0.22	8	2.19 loss	3.80 loss	0.58	-1.36 ± 0.66
αS266G/αT267G/S268G/S269G+δG188A	22.1 ± 2.4	1.87 ± 0.21	8	2.35 loss	3.12 loss	0.75	-0.70 ± 0.23
αS266G/αT267G/S268G/S269G+γG182A/δG188A	30.1 ± 5.9[e]	1.81 ± 0.54	8	3.20 loss	7.77 loss	0.41	-2.20 ± 0.95
αS266G/αT267G/S268G/S269G+γG182I	8.16 ± 1.17	2.06 ± 0.15	8	1.15 gain	2.17 gain	1.88	+1.57 ± 0.50
αS266G/αT267G/S268G/S269G+ δG188I	9.49 ± 1.07	1.78 ± 0.30	8	1.01 loss	1.78 gain	1.80	+1.45 ± 0.75
αS266G/αT267G/S268G/S269G+γG182I/δG188I	NR[f]				5.89 gain		

[a]Measurements performed 2-4 days after cRNA injection (V_{hold} = -60 mV). Error values represented as standard deviation.
[b]Predicted fold change if the mutants influenced function independently.
[c]Ω value quantifies the variance from independence (see methods).
[d]An energetic coupling is calculated from EC_{50} values to facilitate comparisons. Energy values provided are not quantitative (see methods and Figure S1).
[e]$p < 0.001$ relative to WT via one-way ANOVA followed by Dunnet's post hoc test. DF=270. F_{EC50}=186.7. F_{Hill}=4.207.
[f]No response (NR). No significant agonist induced current observed up to 4 day after cRNA injection

Figure 5.5 Agonist-induced motions of the complementary γ/δ subunits correlate with the movement of the $\alpha_\gamma/\alpha_\delta$ M2-M3 loops.

(a) The α_γ-γ interface of the *Torpedo* nAChR apo (pink, PDB: 7QKO) and nicotine-bound (green, PDB: 7QL5) states are viewed through the α_γ subunit with the α_γ ECD hidden for clarity. The capping motions of γloop F around the bound agonist (cyan) and the motions of the γβ8-β9, γβ10-M1 and the α_γM2-M3 loops away from the channel pore are depicted by black arrows. (b) Zoomed-in views of the α_γ (left) and α_δ (right) agonist binding sites in the nicotine-bound model, rotated ~90° from the image on the left. The α subunits are both coloured salmon and the δ/γ subunit coloured light blue. Residues extending from loop F to interact with loop C are shown as sticks with their hydrogen bonds depicted as dashed lines. (c) Residues in the α_γM2-M3 loop, the γβ8-β9 loop, and the γβ10-M1 loop at the ECD – TMD interface are shown as sticks with transparent surfaces highlighting the tight association. (d) Violin plots showing the effects of mutations to residues shown in panel C on channel function are subtle. Exact values can be found in table 5.1.

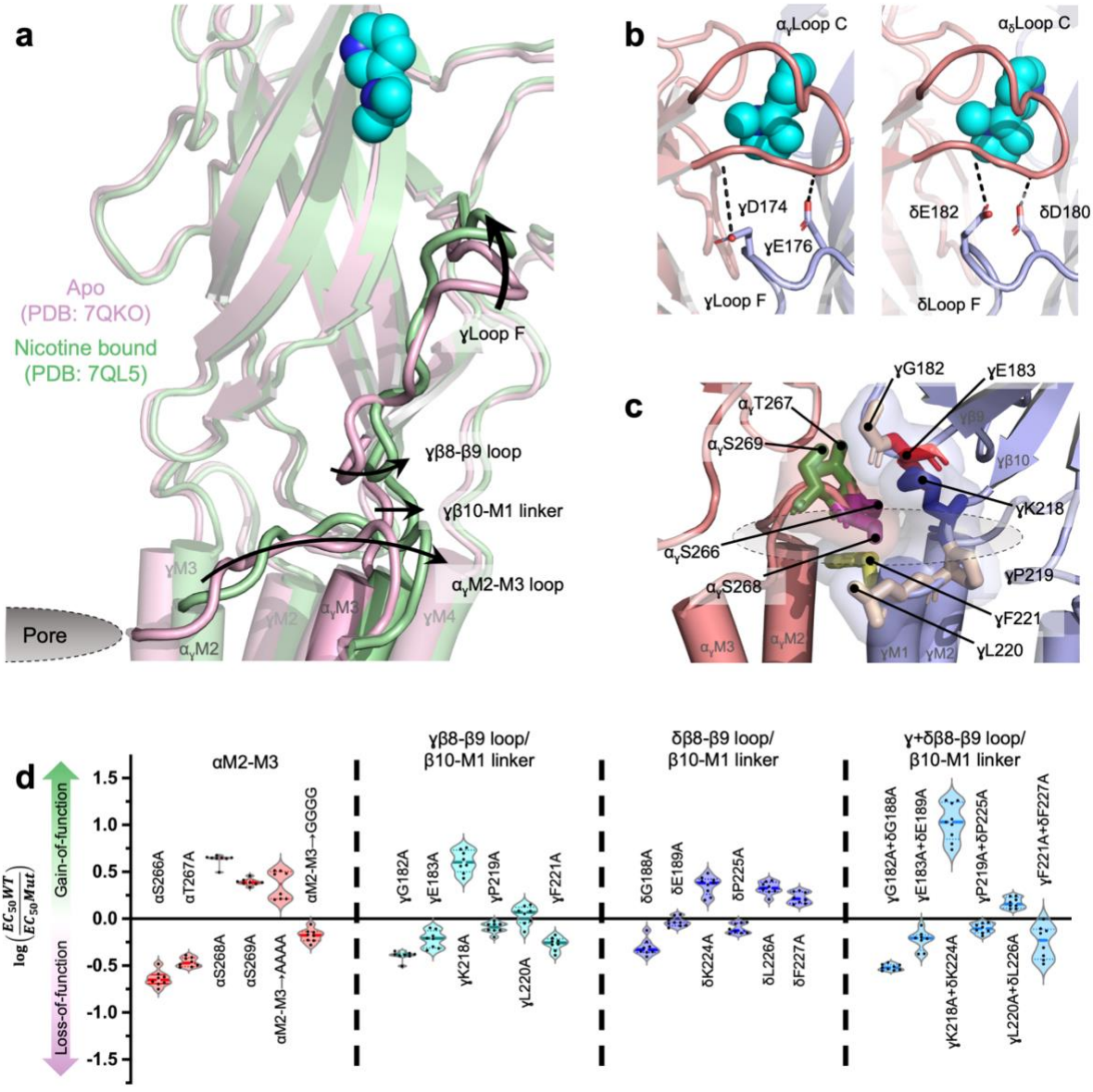
a
Apo
(PDB: 7QKO)
Nicotine bound
(PDB: 7QL5)
γLoop F
γβ8-β9 loop
γβ10-M1 linker
αγM2-M3 loop
γM3
αγM3
γM2
γM4
Pore
αγM2
b
αγLoop C
αδLoop C
γD174
γE176
γLoop F
δE182
δD180
δLoop F
c
γG182
γE183
αγT267
αγS269
γβ9
γβ10
γK218
αγS266
αγS268
γP219
γF221
γL220
αγM3
αγM2
γM1
γM2
d
αM2-M3
γβ8-β9 loop/
β10-M1 linker
δβ8-β9 loop/
β10-M1 linker
γ+δβ8-β9 loop/
β10-M1 linker
Gain-of-function
Loss-of-function
log(EC50WT/EC50Mut)
1.5
1.0
0.5
0.0
-0.5
-1.0
-1.5
αS266A
αT267A
αS268A
αS269A
αM2-M3→AAAA
αM2-M3→GGGG
γG182A
γE183A
γK218A
γP219A
γL220A
γF221A
δG188A
δE189A
δK224A
δP225A
δL226A
δF227A
γG182A+δG188A
γE183A+δE189A
γK218A+δK224A
γP219A+δP225A
γL220A+δL226A
γF221A+δF227A

(Table 5.4). Consistent with the *Torpedo* structures, our functional data suggest that the agonist-induced motions of the two F loops are functionally important.

We next explored whether the closing of the F loops contributes to channel gating via interactions between the γ/δ β8-β9 loop/β10-M1 linker and the $\alpha_\gamma/\alpha_\delta$ M2-M3 loop. αSer266, αThr267, αSer268, and αSer269 from the $\alpha_\gamma/\alpha_\delta$ M2-M3 loop are tightly sandwiched between γGly182/δGly188 and γGlu183/δGlu189 from the complementary γ/δ subunit β8-β9 loop and γLys218/δLys224 from the β10-M1 linker on one side, and γLeu220/δLeu226 and γPhe221/δPhe227 from β10-M1 on the other side (Fig. 5.5c). We first changed each of the serine/threonine residues in the M2-M3 loop individually to Ala, with αS266A and αT267A leading to 4- and 3-fold losses-in-function, respectively, while αS268A and αS269A led to 4- and 2-fold gains-of-function, respectively (Fig. 5.5d, Table 5.1). Remarkably, changing all four residues simultaneously to either Ala or Gly had almost no impact on the measured EC_{50} values (Table 5.1). For comparison, we repeated the Gly mutations at the aligned positions in the remaining β, γ and δ subunits where M2-M3 does not translate outwards upon agonist binding and observed the same results. Even when quadruple glycine mutations were generated simultaneously in all five subunits, functional channels with near WT EC_{50} values were observed. The side chains of the four Ser/Thr residues in $\alpha_\gamma/\alpha_\delta$ M2-M3 are not critical to channel function.

Subtle effects on channel function were also observed when mutations were generated to potentially interacting residues on the complementary γ/δ subunits. The γG182A/δG188A and γK218A/δK224A mutations each led to a ~3-fold loss or a ~4-fold gain of function, respectively, while γE183A/δE189A, γL220A/δL226A and γF221A/δF227A each led to less than two-fold changes in the measured EC_{50} values (Fig. 5.5d, Table 5.1). The γK218A+δK224A double

Table 5.4 - Functional effects of mutations to β8-β9/β10-M1 and M2-M3 of the *Torpedo* nAChR.

Mutant[a]	EC_{50} (μM)	Hill slope	n	Fold change
WT	9.40 ± 1.8	1.78 ± 0.35	87	
α7 Loop F transplants				
δ(^{178}IIDPEA^{183} → ^{178}DISG--^{181})	16.7 ± 9.8[b]	0.72 ± 0.19[b]	8	1.78 loss
γ(^{173}HIDPED^{178} → ^{173}DISG--^{176})	54.4 ± 3.7[b]	1.41 ± 0.13	8	5.78 loss
δ+γ(loop F → ^{173}DISG--^{176})	98.3 ± 22.7[b]	1.71 ± 0.40	5	10.5 loss
M2-M3 of α subunit				
αS268P	9.67 ± 1.69	1.81 ± 0.41	8	1.03 loss
αS266A+αT267A	31.4 ± 3.3[b]	1.99 ± 0.12	8	3.34 loss
αS268A+αS269A	0.857 ± 0.342[b]	1.55 ± 0.32	8	11.0 gain
β8-β9 and β10-M1 of γ and δ subunit				
γN181A	7.49 ± 1.23	1.95 ± 0.16	8	1.26 gain
γN181D	1.65 ± 0.56[b]	1.91 ± 0.50	8	5.69 gain
γN181Y	9.29 ± 2.08	2.00 ± 0.31	10	1.01 gain
δN187D	5.82 ± 0.60	1.84 ± 0.27	9	1.62 gain
γW184A	10.4 ± 1.6	2.07 ± 0.34	8	1.10 loss
γT185A	7.64 ± 2.06	1.92 ± 0.35	8	1.23 gain
γT185D	4.60 ± 1.16[b]	1.64 ± 0.24	8	2.04 gain
δE191A	11.6 ± 2.1	1.83 ± 0.22	9	1.23 loss
δE191K	17.6 ± 4.8[b]	2.09 ± 0.27	9	1.87 loss
γI215A	22.6 ± 4.5[b]	1.58 ± 0.19	8	2.41 loss
γR217A	10.5 ± 1.5	2.05 ± 0.34	8	1.11 loss
γR217W	NE[c]			
γR217E	NE[c]			
γR217K	NE[c]			
δR223A	7.02 ± 1.37	1.60 ± 0.26	8	1.33 gain
δR223W	5.73 ± 1.06	1.82 ± 0.59	8	1.63 gain
δR223E	5.95 ± 2.09	1.99 ± 0.42	9	1.57 gain
δR223K	16.8 ± 13.3[b]	1.41 ± 0.57	7	1.78 loss
γY222A	13.9 ± 1.3	1.83 ± 0.32	8	1.48 loss
δY228A	18.6 ± 3.3[b]	1.64 ± 0.22	8	2.00 loss
γK272A	12.4 ± 2.4	1.80 ± 0.32	8	1.32 loss
δR277A	10.8 ± 1.5	1.67 ± 0.23	8	1.15 loss

[a]Measurements performed 2-4 days after cRNA injection (V_{hold} = -60 mV). Error values represented as standard deviation
[b]$p < 0.001$ relative to WT via one-way ANOVA followed by Dunnet's post hoc test. DF=309. F_{EC50}=120.8. F_{Hill}=4.907.

mutant did lead to a relatively large ~10-fold *gain-of-function*, but this appears to be due to the release of a developed steric clash with both αSer268 and αSer269 on M2-M3 (see below). γN181/δN187, γW184, γT185/δE191, γI215, γR217/δR223, γP219, γY222/δY228, γK272 were also changed to non-interacting side chains but these substitutions had minimal functional consequences (Table 5.4). Although mutations to some of the side chains at the inter-subunit interface are detrimental suggesting important functional roles, the relatively small functional consequences for most of the mutations (see Fig. 5.2 for a discussion of how relative changes in EC_{50} correlate with changes in channel gating) suggest that the interacting side chains are not critical to channel gating.

To further test the functional importance of the inter-subunit ECD-TMD domain interface, we cast paired mutations of potentially interacting residues as mutant cycles and found that only two positions in the complementary subunits, γLys218/δLys224 and γGly182/δGly188, couple energetically with residues on $\alpha_\gamma/\alpha_\delta$ M2-M3 (Tables 5.3 and 5.5). Mutating both lysine (γLys218 and δLys224) and adjacent serine (αSer268 plus αSer269) residues simultaneously to alanine led to a 30-fold gain of function, 3-fold *less* than would be expected if the mutations influence function independently, consistent with a developing steric clash between the side chains that is detrimental to channel activation. Also, changing both γGly182/δGly188 and αSer266/αThr267 residues to alanine led to only a 3.4-fold loss of function despite an expected 66-fold loss of function if the individual mutants influenced function independently. This energetic coupling could be due to the disruption of a hydrogen bond that forms between the backbone carbonyl of γGly182/δGly188 and the backbone amide group of αSer268 that contributes energetically to the activated state (agonist binding decreases the hydrogen bond donor - acceptor distance from 3.4 Å to 2.9 Å; Fig. 5.6) as the losses of function observed for the

Table 5.5 - Energetic couplings between individual residues at the β8-β9/β10-M1 - M2-M3 interfaces.

Mutant	EC_{50} (μM)	Hill slope	n	Fold change	Predicted[b]	Ω	ΔΔG (kJ/mol)[d]
αS266A+γG182A	44.5 ± 4.9[b]	2.47 ± 0.56	8	4.74 loss	11.0 loss	0.43	-2.09 ± 0.64
αS266A+γG182I	7.91 ± 3.21	1.98 ± 0.29	9	1.19 gain	1.34 loss	0.63	-1.15 ± 0.58
αS266A+γG182S	32.0 ± 2.9[b]	1.85 ± 0.16	9	3.41 loss	6.87 loss	0.50	-1.74 ± 0.51
αS266A+δG188A	46.2 ± 6.2[b]	2.18 ± 0.32	9	4.91 loss	9.06 loss	0.54	-1.52 ± 0.52
αS266A+γE183A	36.7 ± 5.84[b]	1.87 ± 0.27	10	3.90 loss	7.47 loss	0.52	-1.61 ± 0.59
αS266A+γK218A	15.7 ± 4.5[b]	1.76 ± 0.42	8	1.67 loss	1.12 loss	1.48	+0.98 ± 0.47
αS266A+γK272A	37.4 ± 14.4[b]	1.81 ± 0.42	9	3.98 loss	5.83 loss	0.68	-0.95 ± 0.48
αT267A+γG182A	32.5 ± 3.4[b]	2.16 ± 0.46	8	3.45 loss	7.25 loss	0.48	-1.83 ± 0.50
αT267A+γG182I	16.2 ± 2.2[b]	1.69 ± 0.19	8	1.73 loss	1.13 gain	1.96	+1.67 ± 0.49
αT267A+γG182S	28.1 ± 4.7[b]	1.85 ± 0.15	8	2.99 loss	4.52 loss	0.66	-1.03 ± 0.30
αT267A+δG188A	33.2 ± 2.8[b]	1.93 ± 0.23	9	3.53 loss	5.96 loss	0.59	-1.30 ± 0.39
αT267A+γK218A	10.1 ± 4.4	2.07 ± 0.46	8	1.07 loss	1.35 gain	1.45	+0.92 ± 0.52
αS268A+γE183A	4.54 ± 1.12[b]	1.60 ± 0.32	8	2.07 gain	2.52 gain	1.22	+0.49 ± 0.20
αS268A+γK218A	0.911 ± 0.134[b]	1.89 ± 0.53	8	10.3 gain	16.8 gain	1.63	+1.21 ± 0.48
αS268A+γK218E	0.524 ± 0.079 [b]	2.24 ± 0.38	8	17.9 gain	17.2 gain	0.96	-0.11 ± 0.04
αS268A+δK224A	0.864 ± 0.168[b]	1.79 ± 0.40	12	10.9 gain	9.46 gain	0.87	-0.35 ± 0.13
αS268A+γL220A	1.57 ± 0.33[b]	1.80 ± 0.19	9	5.98 gain	4.54 gain	0.76	-0.69 ± 0.28
αS269A+γK218A	1.02 ± 0.12[b]	1.99 ± 0.33	8	9.19 gain	9.67 gain	1.05	+0.13 ± 0.05
αS269A+γK218E	0.652 ± 0.168[b]	2.51 ± 0.93[b]	8	14.4 gain	9.88 gain	0.68	-0.94 ± 0.37
αS269A+δK224A	1.49 ± 0.44[b]	1.59 ± 0.33	8	6.29 gain	5.44 gain	0.87	-0.36 ± 0.15

[a]Measurements performed 2-4 days after cRNA injection (V_{hold} = -60 mV). Error values represented as standard deviation
[b]Predicted fold change if both individual mutants influence function independently
[c]$p < 0.001$ relative to WT via one-way ANOVA followed by Dunnet's post hoc test. DF=238. F_{EC50}=172.3. F_{Hill}=3.562.

Figure 5.6 The interdependence between γGly182/δGly188 and the αγ/αδ M2-M3 loops is mediated by a backbone hydrogen bond with αSer268.

Apo (pink) and agonist-bound (green) states of the nAChR are shown in panel a with a dashed line highlighting the backbone hydrogen bond between γGly182 and αSer268. The αS268P mutant has almost no effect on channel function alone but eliminates the effect of the γG182A/δG188A double mutant.

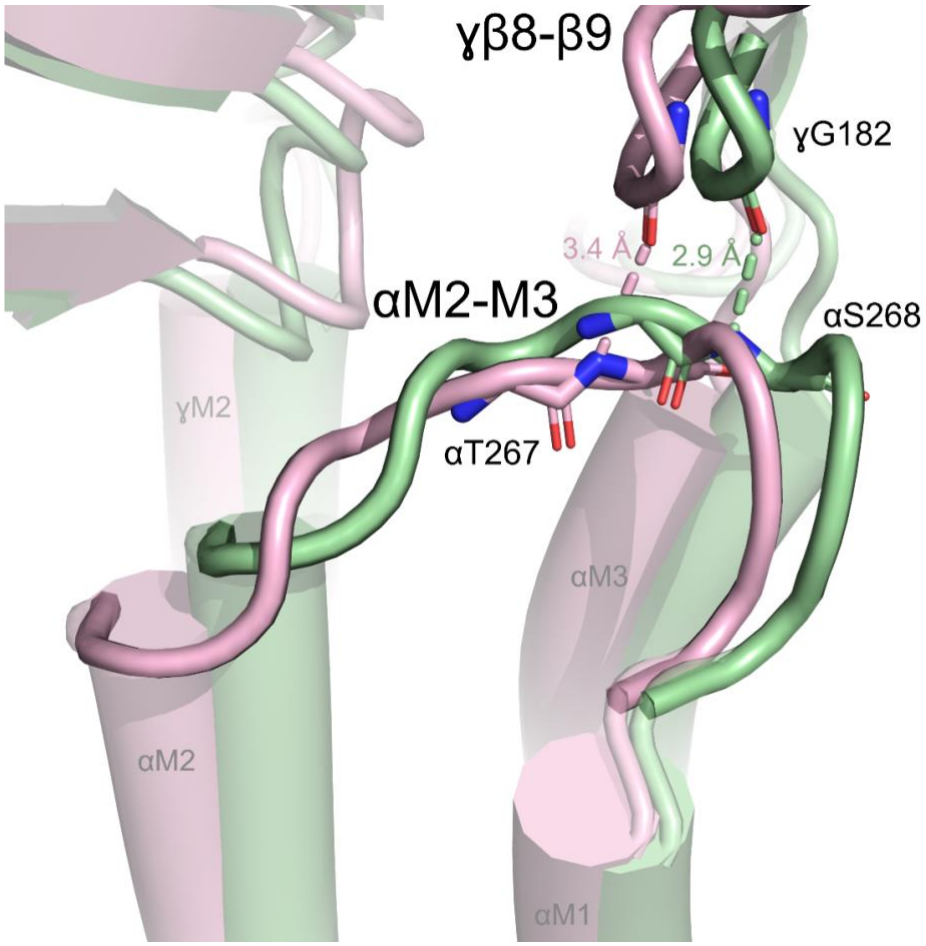

	Dose-response[a]						Fold-change
	WT			αS268P			EC_{50}(WT)
Mutant	EC_{50} (μM)	Hill slope	n	EC_{50} (μM)	Hill slope	n	EC_{50}(S268P)
WT	9.40 ± 1.82	1.78 ± 0.35	87	9.67 ± 1.69	1.81 ± 0.41	8	0.97
γG182A	23.4 ± 2.8[b]	1.53 ± 0.26	8	7.81 ± 1.71	1.67 ± 0.18	9	3.00
δG188A	19.3 ± 3.5[b]	1.59 ± 0.20	8	11.5 ± 0.7	1.62 ± 0.13	8	1.68
γG182A+δG188A	31.0 ± 2.1[b]	1.68 ± 0.30	9	6.50 ± 2.47	1.63 ± 0.55	8	4.77
αS266A+αT267A	31.4 ± 3.3[b]	1.99 ± 0.12	8	13.9 ± 1.3	1.65 ± 0.19	10	2.26
αS266A+αT267A+γG182A	33.0 ± 5.6[b]	1.87 ± 0.26	9	8.43 ± 2.67	2.14 ± 1.0	8	3.91
αS266A+αT267A+δG188A	37.2 ± 1.8[b]	1.82 ± 0.31	9	16.1 ± 1.9[c]	1.66 ± 0.45	8	2.31
αS266A+αT267A+γG182A+δG188A	31.5 ± 4.6[b]	2.13 ± 0.32	9	NR[d]			-

[a]Measurements performed 2-4 days after cRNA injection (V_{hold} = -60 mV). Error values represented as standard deviation
[b]$p < 0.001$ relative to WT via one-way ANOVA followed by Dunnet's post hoc test. DF=139. F_{EC50}=332.7. F_{Hill}=3.011.
[c]$p < 0.001$ relative to αS268P via one-way ANOVA followed by Dunnet's post hoc test. DF=52. F_{EC50}=20.84. F_{Hill}=1.194.
[d]No response (NR). No significant agonist induced current observed up to 4 day after cRNA injection

γG182A/δG188A mutations no longer affect function on the αS268P background (Fig. 5.6). Both the γG182A and αS266A+αT267A and the δG188A and αS266A+αT267A triple mutants affect function to a lesser extent than expected given the individual mutations. The triple mutations are also independent on the S268P background. On the other hand, the αS268P alone had no effect on the measured EC_{50} value. These observations are consistent with single channel recordings, which show that mutations to residues in the β8-β9 loop of the human adult muscle nAChR ε subunit typically have minimal effects on the di-liganded gating equilibrium contast (Jha et al., 2012). The only detected energetic coupling across the inter-subunit interface was between εGly183 (the γGly182 equivalent in the *Torpedo* nAChR) and Pro265. Although the structural and functional findings suggest that a backbone hydrogen bond between carbonyl of γGly182/δGly188 and the amide of αSer268 at the inter-subunit interface is important to activation, both the relatively small functional consequences of individual mutations and the relatively few energetic couplings between side chains across this interface suggest that side chain interactions at the inter-subunit interface do not play a major role role energetically driving the conformational changes that open the channel gate.

We also considered the possibility that non-specific steric interactions couple the motions of γ/δ β8-β9/β10-M1 to those of $\alpha_\gamma/\alpha_\delta$ M2-M3 (Cymes and Grosman, 2021). As noted above, replacing all four serine/threonine side chains in $\alpha_\gamma/\alpha_\delta$ M2-M3 with four glycine residues to reduce the side chain bulk had essentially no effect on the measured EC_{50} values suggesting that tight steric interactions between $\alpha_\gamma/\alpha_\delta$ M2-M3 and γ/δ β8-β9/β10-M1 are not critical. On the other hand, increasing the bulk and/or charge of residues on the $\alpha_\gamma/\alpha_\delta$ M2-M3 loop by replacing all four simultaneously with Asp or Trp led to a complete loss of expression. The quadruple Asn mutant expressed to even higher levels than WT but did not yield agonist-induced currents

(Table 5.6), although molecular dynamics simulations suggest that the loss-of-function results because the mutations energetically stabilize the resting state (Fig. 5.7). We also noted that the small side chain of γGly182/δGly188 is present in almost all nAChR subtypes and allows the β8-β9 loop to pack tightly against the neighbouring M2-M3 loop. When γGly182 is changed to Ala, Ser or Met there is a subtle loss of function (Table 5.6). In contrast, the larger branched amino acids Ile, Trp, Glu, Arg, and Val all lead to gains-of-function. To test whether these gains-of-function reflect enhanced steric interactions between γ/δ β8-β9 and $\alpha_\gamma/\alpha_\delta$ M2-M3, γG182I/δG188I was superimposed onto the quadruple $\alpha_\gamma/\alpha_\delta$ M2-M3 glycine mutant, but this led to a similar gain-of-function to that observed when the mutation was superimposed on the WT background, suggesting that steric interactions between γ/δ β8-β9/β10-M1 and $\alpha_\gamma/\alpha_\delta$ M2-M3 do not underlie these functional effects (Table 5.3).

Channel opening is accompanied by subunit asymmetric local structural rearrangements at the intra-α subunit ECD-TMD domain interface. Perplexed by the absence of critical side chains/side chain interactions at the inter-subunit ECD-TMD domain interface that facilitate channel gating, we refocused our attention on the ECD triad of $\alpha_\gamma/\alpha_\delta$. We were intrigued by the αV46A mutation, which leads to the largest loss-of-function of any single mutation reported in this study. The relatively large negative impact of the αV46A mutation is surprising given that it involves only a reduction in the volume of the side chain. Furthermore, kinetic fitting of single channel measurements suggests the αV46A mutation in the adult muscle nAChR leads to a large ~500-fold decrease in the di-liganded gating equilibrium constant while the αE45A+αV46A double mutation leads to a ~6,000-fold reduction in channel gating that almost abolishes the agonist-induced response (Lee and Sine, 2005). The αV46A loss-of-function is driven mainly by a reduction in the channel opening rate constant suggesting that its main effect is to enhance

Table 5.6 - Non-specific bumping of residues at the $\alpha_\gamma/\alpha_\delta$ M2-αM3 - γ/δ β8-β9 loops on nAChR.

Dose-response[a]					[^{125}I]-α-BTX[b]
Mutant	EC_{50} (μM)	Hill slope	n	Fold change	Normalized CPM
WT	9.40 ± 1.82	1.78 ± 0.35	87	-	1.00 ± 0.11
αM2-M3 bulky substitutions					
αS266N+T267N+S268N+S269N	NR[c]				1.38 ± 0.50[e]
αS266D+T267D+S268D+S269D	NE[d]				0.06 ± 0.03[f]
αS266W+T267W+S268W+S269W	NE[d]				0.05 ± 0.02[f]
Mock	-				0.07 ± 0.03
γG182/δG188 substitutions					
Mutant	EC_{50} (μM)	Hill slope	n	Fold change	Residue Volume (Å^3)
γG182A	23.4 ± 2.8[f]	1.53 ± 0.26	8	2.49 loss	90.1
γG182S	14.6 ± 1.4[f]	1.81 ± 0.33	8	1.56 loss	94.2
γG182V	3.70 ± 0.52[f]	1.93 ± 0.36	8	2.54 gain	139.1
γG182E	4.99 ± 0.94[f]	1.81 ± 0.23	9	1.89 gain	140.8
γG182Q	5.71 ± 1.4[f]	2.01 ± 0.37	8	1.65 gain	149.4
γG182I	2.84 ± 0.39[f]	1.70 ± 0.03	8	3.31 gain	164.9
γG182M	13.3 ± 1.7[f]	1.70 ± 0.22	10	1.42 loss	167.7
γG182R	2.82 ± 0.52[f]	1.90 ± 0.31	9	3.33 gain	192.8
γG182W	3.47 ± 0.47[f]	1.76 ± 0.17	9	2.71 gain	231.7
δG188A	19.3 ± 3.5[f]	1.59 ± 0.20	8	2.05 loss	90.1
δG188S	16.3 ± 3.0[f]	1.60 ± 0.11	8	1.73 loss	94.2
δG188I	3.46 ± 1.53[f]	1.43 ± 0.28	8	2.72 gain	164.9
γG182A+δG188A	31.0 ± 2.1[f]	1.68 ± 0.30	8	3.30 loss	
γG182I+δG188I	NE[c]				

[a]Measurements performed 2-4 days after cRNA injection (V_{hold} = -60 mV). Error values represented as standard deviation
[b]Measurements performed 2 days after cRNA injection on a minimum of 10 oocyes. Error values represented as standard deviation
[c]No response (NR). No significant agonist induced current observed up to 4 day after cRNA injection
[d]No response (NE). No significant agonist induced current observed up to 4 day after cRNA injection
[e]$p < 0.001$ relative to mock injected oocytes via one-way ANOVA followed by Dunnet's post hoc test
[f]$p < 0.001$ relative to WT via one-way ANOVA followed by Dunnet's post hoc test. DF=309. F_{EC50}=120.8. F_{Hill}=4.907.

Figure 5.7 The quadruple Asn αM2-M3 mutant stabilizes the resting state.
The M2 α-helices and M2-M3 loops of both α subunits are shown on the left for the WT apo state after 100 ns of simulation (pink) and the WT nicotine state after minimization but prior to the simulation (green). Residues in the M2-M3 loop are shown as sticks and the α carbons of αVal255 (V13') are shown as spheres with the distance between the two depicted by dashed lines to highlight the difference in pore diameter. Three repeat all atom simulations of the apo nAChR (top right, green traces) show that the pore is stably closed. In contrast, unless the diffuse density observed in the pore is modeled with bound lipids (see (Zarkadas et al., 2022)), the open pore of the nicotine bound structure closes within ~40 ns to a conformation with a diameter slightly larger than the apo state (top right, orange traces). On the bottom right, the pore diameter of the quadruple Asn mutant (orange) after 100 ns simulation is compared to the apo WT (green) after 100 ns simulation. The average distance between αV13' residues from the three repeats show that the quadruple Asn mutation in M2-M3 accelerates the collapse of the pore all the way back to the apo WT state.

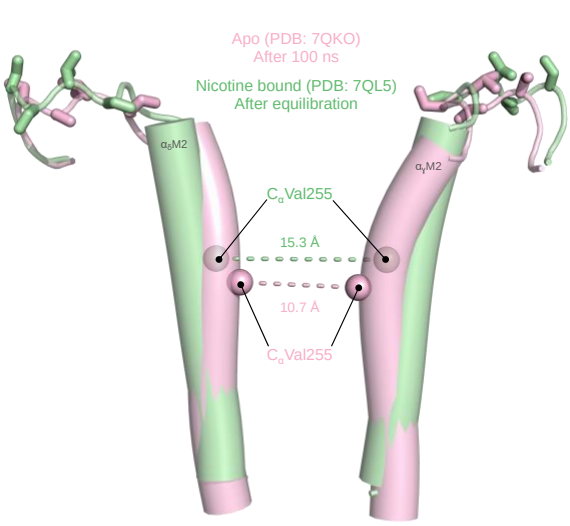
Apo (PDB: 7QKO)
After 100 ns
Nicotine bound (PDB: 7QL5)
After equilibration
αδM2
αγM2
CαVal255
15.3 Å
10.7 Å
CαVal255

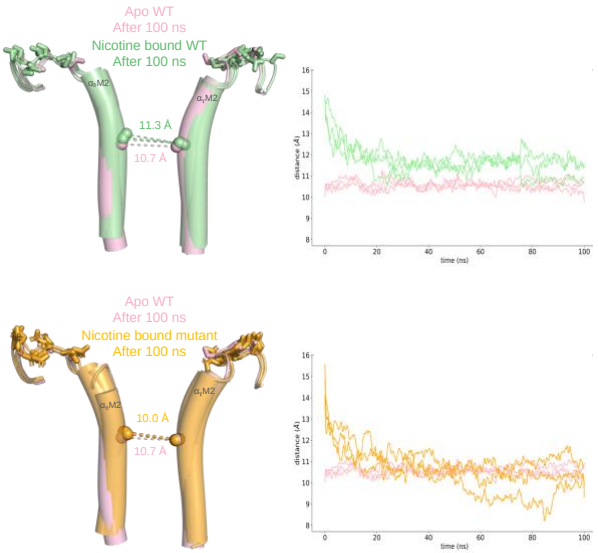
Apo WT
After 100 ns
Nicotine bound WT
After 100 ns
αδM2
αγM2
11.3 Å
10.7 Å
distance (Å)
time (ns)
Apo WT
After 100 ns
Nicotine bound mutant
After 100 ns
αδM2
αγM2
10.0 Å
10.7 Å
distance (Å)
time (ns)

the energetic stability of the resting or another pre-open closed state. As the reduction in the bulk of the side chain should reduce, not enhance, local interactions, the large enhancement of the resting state stability must arise because the bulkier valine side chain locally destabilizes the ECD-TMD domain interface in the closed state, with the smaller alanine/glycine side chains reducing this destabilization.

To account for the single channel data, we hypothesized that the energetic coupling between αVal46 and αPro272 established here and elsewhere underlies the local instability created by the bulky valine side chain (Lee and Sine, 2005). Although the original 4 Å resolution 2BG9 structure modeled αGlu45 and αVal46 of β1-β2 straddling αPro272 of M2-M3, higher resolution structures now place αPro272 distant from αVal46 and αGlu45, with the latter two residues now projecting towards αPro265 (Zarkadas et al., 2022). We changed αPro265 to Gly to reduce its steric bulk and this led a subtle ~2-fold loss of function. When the αV46A mutation was generated on the αP265G background, however, the observed loss of function was reduced from 12-fold to less than 2-fold indicating that there is an energetic connection between these two residues (Table 5.3). We also hypothesized that the adjacent αIle264, which orients toward M3 and directly contacts αPro272 (Fig. 5.8a), is a structural link that underlies the energetic coupling between αVal46 and αPro272. Consistent with this hypothesis, the 12-fold loss of function observed for the αV46A mutation was reduced slightly to 5-fold on both the αI264A and the αP272G backgrounds and then reduced further to 2-fold on the αI264A+αP272G background showing that the coupling between αVal46 and αPro272 is dependent upon the intervening αIle264. The available data show that αVal46 couples

Figure 5.8 Agonist binding transitions the five intra-subunit ECD – TMD interfaces from a locally asymmetric to a symmetric conformation.

(a) The ECD – TMD interface of the α_γ subunit is shown in two orthogonal views in apo (pink, PDB: 7QKO,) and nicotine bound (green, PDB: 7QL5) states. The roughly orthogonal motions of the β1-β2 and M2-M3 loops create a functional interdependence between αVal46 (tan) and αPro265 (brown) in the apo state with that is propagated to αPro272 (deep teal) via the intervening αIle264 (magenta). (b) The position of αVal46 relative to αPro265, along with their equivalents in the remaining subunits (βLys46, blue; βPro271, brown; δThr48, green; δP279, brown; γLys46, blue; γPro274, brown), are shown for each in both the apo and nicotine bound states. The αVal46 equivalents in the non-α subunits sit on the pore proximal side of the conserved Pro in both states while αVal46 are on the pore distill side in the apo state (asymmetric) and transition to the pore proximal side in the agonist bound state (symmetric). (c) A side view of the pore lining M2 helices are shown on the left for both apo and nicotine bound states with the hydrophobic gate forming V13' and L9' residues shown as sticks. Top-down views of the V13' (top) and L9' (bottom) residues are shown on the right to highlight the more symmetric conformational changes within the channel pore.

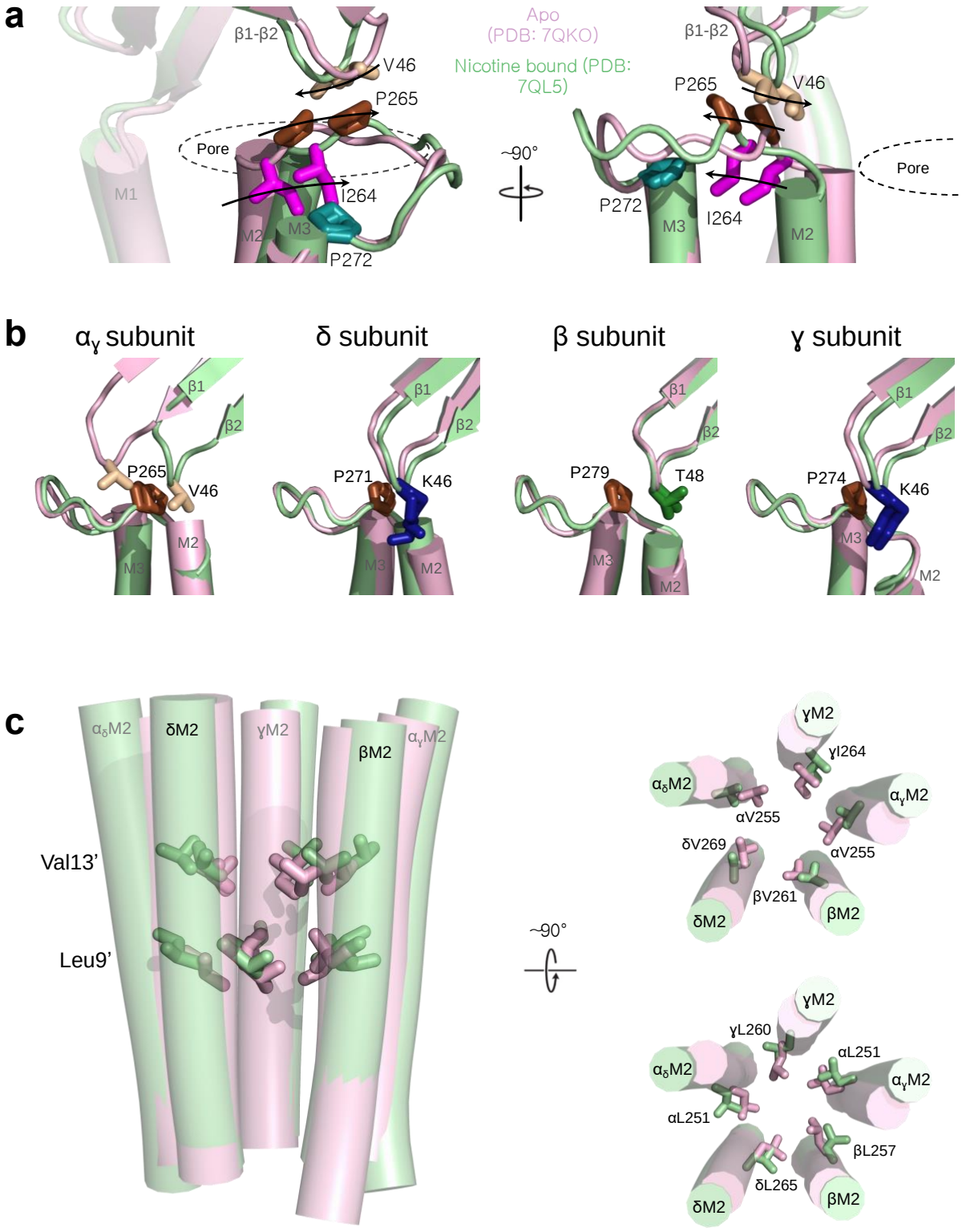
a
β1-β2
V46
P265
Pore
M1
I264
M2
M3
P272
Apo
(PDB: 7QKO)
Nicotine bound (PDB:
7QL5)
~90°
β1-β2
P265
V46
Pore
P272
M3
I264
M2
b
αγ subunit
δ subunit
β subunit
γ subunit
β1
β2
P265
V46
M2
M3
β1
β2
P271
K46
M3
M2
β1
β2
P279
T48
M3
M2
β1
β2
P274
K46
M3
M2
c
αδM2
δM2
γM2
βM2
αγM2
Val13'
Leu9'
~90°
γM2
γI264
αδM2
αγM2
αV255
δV269
αV255
βV261
δM2
βM2
γM2
γL260
αL251
αδM2
αγM2
αL251
βL257
δL265
δM2
βM2

energetically with αPro265, αIle264, and αPro272, along with other residues in the M2-M3 loop (Lee and Sine, 2005; Lee et al., 2008, 2009), with the main point of contact being αPro265.

To better understand how αVal46 couples energetically with αPro265, we re-examined the apo and agonist bound structures and noted that the positions of αGlu45/αVal46 relative to αPro265 change upon agonist binding (Fig. 5.8b and Movie 2). In the apo state, αGlu45/αVal46 are positioned on the pore distal (i.e., further from the pore axis) side of αPro265, while in the agonist-bound state they are positioned on the pore proximal side (i.e., closer to the pore axis). Agonist binding thus transitions αGlu45/αVal46 essentially from one side of the bulky αPro265 side chain to the other. This transition likely accounts for the energetic coupling between these residues during channel gating. The transition also suggests an unappreciated role for these three residues in allosteric communication. Specifically, the position of αGlu45/Val46 on the pore-distal side of αPro265 in the apo state may sterically hinder the outward motions of αPro265 that are required to open the channel gate and may thus help restrain M2-M3 in a closed conformation. Agonist-induced motions of β1-β2, and thus αGlu45/Val46, may release the constraints holding the M2-M3 loop in a closed conformation thus allowing it to move outward to open the channel pore.

In this context, we examined the interface between β1-β2 and M2-M3 in each of the non-α subunits, β, γ, and δ, and noted, surprisingly, that each αGlu45/αVal46-equivalent residue is positioned on the *pore proximal side* of each αPro265-equivalent residue *in both apo and agonist-bound states* (Fig. 5.8b). All three non-α subunits thus occupy a locally active-like conformation in the apo state akin to the agonist-bound conformation at this interface in both α subunits. The local subunit conformational heterogeneity rationalizes previous functional data,

which highlight an important functional role for residues at the intra-subunit ECD-TMD interface of α, but not non-α subunits (Lee and Sine, 2005). Note, however, that this local conformational heterogeneity does not extend to the remainder of either the ECD or TMD. Although the ECD of each non-α subunit undergoes only subtle movements upon agonist binding, both conformations for each subunit are distinct from the apo and agonist-bound α subunit ECD conformations (see section 5.7) (Lev et al., 2017). In contrast, at the hydrophobic gate level, all five M2 a-helices adopt a relatively symmetric configuration with both the 9' leucine and 13' valine residues projecting towards the channel pore forming the well-described constriction that prevents cation flux (Fig. 5.8c). Agonist binding releases the local conformational heterogeneity at the ECD – TMD interface allowing all five subunits to adopt a more symmetric open state where all five sets of αGlu45/αVal46 equivalent residues are positioned on the pore-proximal side of the corresponding αPro265 equivalent residues and all five 9' and 13' side chains at the transmembrane gate have rotated sideways or tilted away from the pore lumen, respectively.

These data suggest an alternative gating mechanism as discussed in more detail below. Instead of driving the allosteric communication between the ECD and TMD, interactions between the two domains, primarily between β1-β2 and M2-M3 of $\alpha_\gamma/\alpha_\delta$, may help restrain the channel pore in a closed conformation that exhibits local conformational asymmetry, with agonist binding allowing the five subunits to relax into a more symmetric open state. Significantly, essentially the same release of conformational asymmetry is observed in the heteromeric $\alpha1_2\beta2_2\gamma2$ $GABA_AR$ suggesting that this is a defining feature of gating in all heteromeric pLGICs (see Discussion and Fig. 5.9). Similar motions of β1-β2 relative to M2-M3

Figure 5.9 Agonist-induced motions of the β1-β2 and M2-M3 loops at the ECD – TMD interface are a conserved feature of pLGICs.

Resting and agonist-bound conformations (pink and green, respectively) are shown in (a) for heteromeric pLGICs, the *Torpedo* nAChR (top) (Zarkadas et al., 2022) and the human synaptic α1β2γ2 $GABA_AR$ (bottom) (Kim and Hibbs, 2021), and in (b) for homomeric pLGICs, the human α7 nAChR (Noviello et al., 2021), mouse 5-$HT_{3A}R$ (Polovinkin et al., 2018), and zebrafish α1 GlyR (Yu et al., 2021)). All structures are aligned by their M2-M3 loop to emphasize the relative motion of the β1-β2 loop.

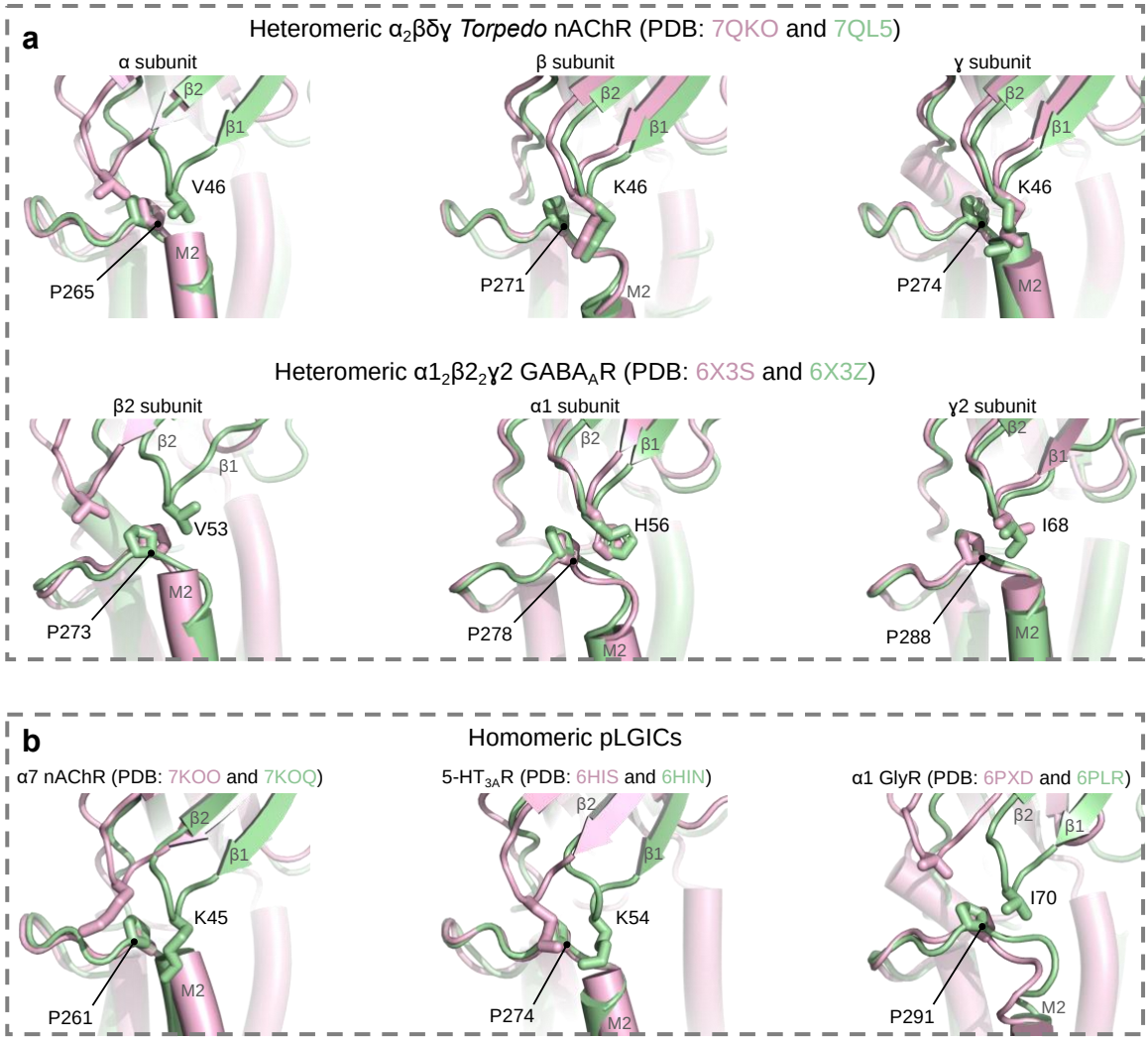
a
Heteromeric α2βδγ Torpedo nAChR (PDB: 7QKO and 7QL5)
α subunit
β subunit
γ subunit
β2
β1
V46
K46
K46
M2
P265
P271
P274
Heteromeric α1β2γ2 GABAAR (PDB: 6X3S and 6X3Z)
β2 subunit
α1 subunit
γ2 subunit
V53
H56
I68
P273
P278
P288
b
Homomeric pLGICs
α7 nAChR (PDB: 7KOO and 7KOQ)
5-HT3AR (PDB: 6HIS and 6HIN)
α1 GlyR (PDB: 6PXD and 6PLR)
K45
K54
I70
P261
P274
P291

have also been suggested to underlie gating in the glutamate activated chloride channel, GluCl (Calimet et al., 2013).

A tripartite salt bridge is required for whole body motions of the principal α subunit ECD. An agonist-induced whole-body pivoting of each principal α subunit ECD is allosterically linked to the structural changes at the ECD-TMD domain interface that open the channel pore. These concerted movements are likely facilitated by interactions within the ECD β sandwich including a conserved tripartite salt bridge between the αArg209 and the anionic residues αGlu45 (β1-β2), αAsp138 (β6-β7), and αGlu175 (β8-β9). As noted, previous studies have highlighted a critical functional role for the salt bridge between αArg209 and the anionic residues αGlu45 (β1-β2) (Chakrapani et al., 2004; Lee and Sine, 2005; Xiu et al., 2005; Bruhova and Auerbach, 2010; Jha et al., 2012; Mukhtasimova and Sine, 2013; Shen et al., 2016, 2018). In the *Torpedo* nAChR, both charge neutralization and reversal mutants of αArg209 did not express (Fig. 5.10c, Table 5.7). Mutations to the coordinated anionic residues were better tolerated than those of αArg209, presumably because they can partially compensate for the loss of each other, but still lead to relatively large changes in EC_{50} values (Table 5.7). Considerable functional data show that the tripartite salt bridge at the base of the principal subunit ECD is critical to channel function (Chakrapani et al., 2004; Lee and Sine, 2005; Xiu et al., 2005; Jha et al., 2012; Mukhtasimova and Sine, 2013; Shen et al., 2016).

In contrast, other than the movements of loop F in γ and δ, the tertiary structures of each non-α subunit ECD is maintained throughout the transition so that each subunit moves essentially as a single rigid body (Movie 3). Given the lack of whole-body pivoting motions of each non-α subunit ECD, we hypothesized that the tripartite salt bridge in β, γ, and δ would not play a critical role in channel function. Consistent with this hypothesis and in agreement with

Figure 5.10 Agonist-induced movements of a tripartite salt bridge at the ECD – TMD interface of each subunit.

(a) Side views of the ECD - TMD interface of the α_γ subunit are shown from two angles with the residues forming the tripartite salt bridges shown as sticks. (b) Top-down views of the apo (pink) and nicotine bound (green) models of the nAChR, aligned by their ECDs, are shown for an α and each non-α subunit with residues composing the tripartite salt bridges shown as sticks. The movements in the α subunit are depicted by arrows while the non-α subunits remain essentially static. (c) Violin plots of the fold changes in EC_{50} values for mutations to each residue in the tripartite salt bridges of each subunit in the *Torpedo* nAChR. Grey crossed boxes indicate mutants that did not produce currents. Exact values can be found in table 5.7.

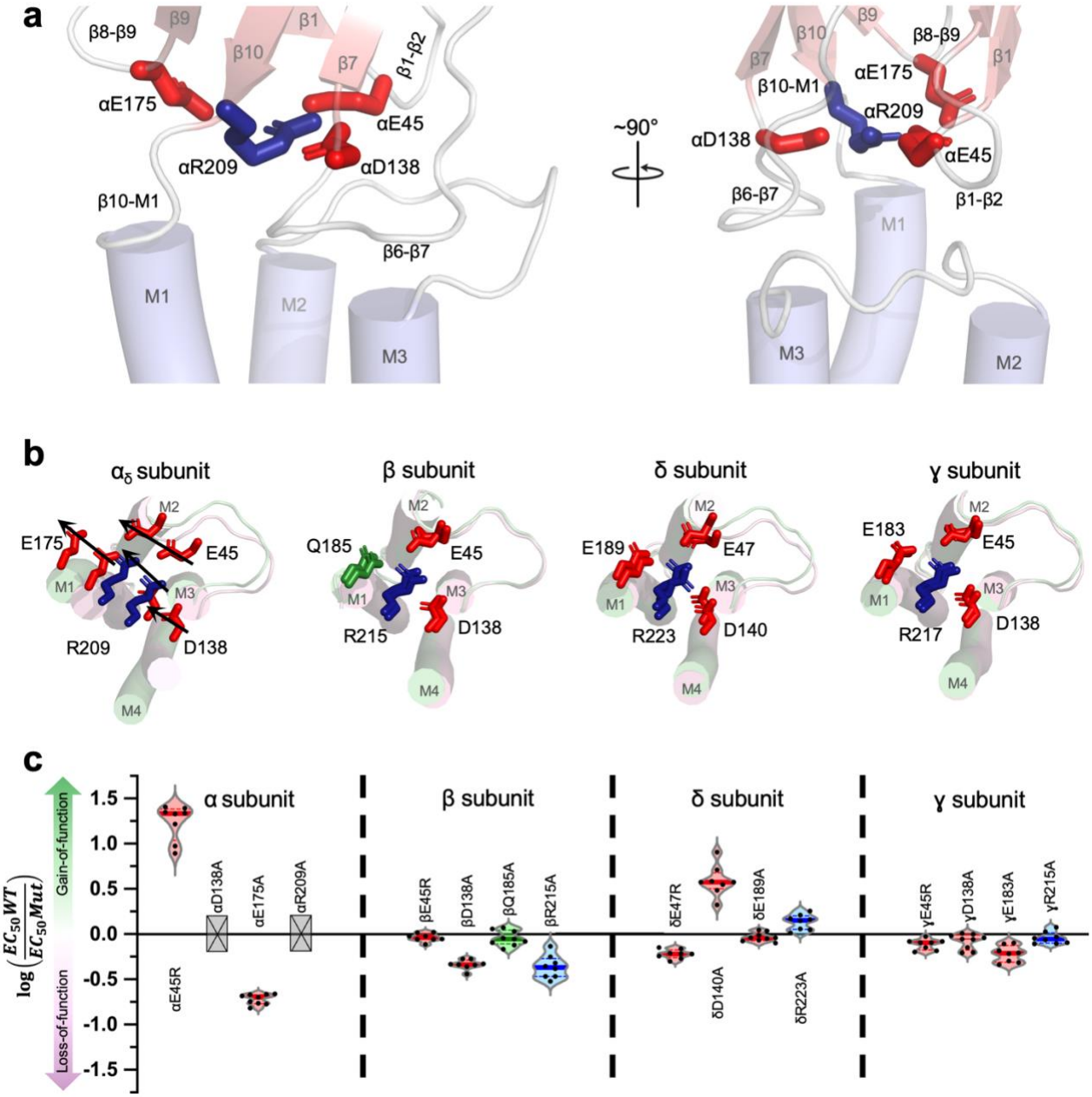
a
β8-β9
β9
β10
β1
β7
β1-β2
αE175
αE45
αR209
αD138
β10-M1
β6-β7
M1
M2
M3
~90°
β10
β9
β8-β9
β7
β1
αE175
β10-M1
αR209
αD138
αE45
β6-β7
β1-β2
M1
M3
M2
b
αδ subunit
β subunit
δ subunit
ɣ subunit
E175
E45
R209
D138
Q185
R215
E189
E47
R223
D140
E183
R217
M1
M2
M3
M4
c
α subunit
β subunit
δ subunit
ɣ subunit
Gain-of-function
Loss-of-function
log(EC50WT/EC50Mut)
1.5
1.0
0.5
0.0
-0.5
-1.0
-1.5
αE45R
αD138A
αE175A
αR209A
βE45R
βD138A
βQ185A
βR215A
δE47R
δD140A
δE189A
δR223A
ɣE45R
ɣD138A
ɣE183A
ɣR215A

Table 5.7 - Subunit specific effects of mutating residues contributing to conserved tripartite salt bridges at the ECD – TMD interfaces.

	Dose-response[a]				[^{125}I]-α-BTX[b,d]
Mutant	EC_{50} (μM)	Hill slope	n	Fold change	CPM_{mutant}/CPM_{WT}
WT	9.40 ± 1.82	1.78 ± 0.35	87	-	1.00 ± 0.24
α subunit					
αE45A	24.4 ± 6.1[e]	1.55 ± 0.10	8	2.62 loss	
αE45R	0.600 ± 0.316	1.39 ± 0.21	8	15.6 gain	
αD138A	NE[c]			-	0.15 ± 0.05
αD138E	6.14 ± 0.69	1.93 ± 0.17	8	1.53 gain	
αD138R	NE[c]			-	0.10 ± 0.04
αE175A	49.7 ± 6.7[e]	1.69 ± 0.13	9	5.29 loss	
αE175R	17.3 ± 4.2[e]	1.58 ± 0.10	9	1.84 loss	
αR209A	NE[c]			-	0.04 ± 0.02
αR209Q	NE[c]			-	0.05 ± 0.03
αR209E	NE[c]			-	0.02 ± 0.02
β subunit					
βE45A	10.0 ± 1.4	1.68 ± 0.21	8	1.07 loss	
βE45R	10.3 ± 1.0	1.64 ± 0.16	8	1.09 loss	
βD138A	20.5 ± 2.6[e]	1.79 ± 0.16	8	2.18 gain	
βD138E	8.63 ± 1.74	1.66 ± 0.22	8	1.09 gain	
βD138R	9.98 ± 4.25	2.02 ± 0.75	8	1.06 gain	
βQ185A	10.6 ± 2.0	1.79 ± 0.23	9	1.12 loss	
βQ185R	13.2 ± 2.6[e]	1.38 ± 0.23	9	1.41 loss	
βR215A	22.4 ± 6.1[e]	1.56 ± 0.58	8	2.39 loss	
βR215Q	16.0 ± 1.8[e]	1.63 ± 0.21	8	1.70 loss	
βR215E	18.2 ± 2.3[e]	1.70 ± 0.24	9	1.94 loss	
δ subunit					
δE47A	13.0 ± 2.1[e]	2.32 ± 0.61	9	1.38 loss	
δE47R	15.7 ± 1.8[e]	1.90 ± 0.27	8	1.69 loss	
δD140A	2.58 ± 0.96[e]	1.66 ± 0.26	8	3.65 gain	
δD140E	9.55 ± 0.83[e]	2.21 ± 0.29	8	1.02 gain	
δD140R	4.64 ± 1.12[e]	1.80 ± 0.66	8	2.20 gain	
δE189A	10.2 ± 1.1[e]	1.80 ± 0.21	9	1.09 loss	
δE189R	34.5 ± 5.1[e]	1.86 ± 0.25	9	3.67 loss	
δR223A	7.02 ± 1.37[e]	1.60 ± 0.26	8	1.33 gain	
δR223Q	7.36 ± 2.50[e]	1.32 ± 0.48	8	1.28 gain	
δR223E	5.95 ± 2.09[e]	1.99 ± 0.42	9	1.57 gain	
γ subunit					
γE45A	5.98 ± 0.74	1.95 ± 0.23	8	1.57 gain	
γE45R	12.3 ± 1.7	1.92 ± 0.26	8	1.31 loss	
γD138A	11.5 ± 2.3	1.90 ± 0.23	9	1.22 loss	
γD138E	12.0 ± 2.8	1.96 ± 0.40	8	1.27 loss	
γD138R	NE[c]		-		0.13 ± 0.02
γE183A	15.9 ± 3.3	1.69 ± 0.15	8	1.69 loss	
γE183R	NE[c]		-	-	0.09 ± 0.03
γR217A	10.5 ± 1.5	2.05 ± 0.34	8	1.11 loss	
γR217Q	NE[c]		-	-	0.17 ± 0.05
γR217E	NE[c]		-	-	0.07 ± 0.03
Mock					0.07 ± 0.03

[a]Measurements performed 2-4 days after cRNA injection (V_{hold} = -60 mV). Error values represented as standard deviation
[b]Measurements performed 2 days after cRNA injection on a minimum of 10 oocyes. Error values represented as standard deviation
[c]No response (NE). No significant agonist induced current observed up to 4 day after cRNA injection
[d]None of the mutants tested were significantly ($p < 0.001$) more expressed than mock injected oocytes via one-way ANOVA followed by Dunnet's post hoc test
[e]$p < 0.001$ relative to WT via one-way ANOVA followed by Dunnet's post hoc test. DF=292. F_{EC50}=123.7. F_{Hill}=3.311.

previously published data (Lee and Sine, 2005; Xiu et al., 2005), mutations to the analogous charged residues in these non-α subunits are well tolerated, expressing robustly and with EC_{50} values close to WT (Table 5.7). For example, charge neutralization of the central arginine of the tripartite salt bridge was tolerated in each of the β, γ, and δ subunits with little effect on channel gating. Furthermore, while the charge reversal R217E mutation in the γ subunit did not express, the charge reversals at this position had no effect on channel function in the β and δ subunits. These findings highlight the importance of electrostatic bridging interactions in the ECD of $\alpha_\gamma/\alpha_\delta$, while suggesting that whole body ECD motions in the β, δ, and γ do not contribute to channel function.

5.5 Discussion

We set out to identify new interactions that facilitate allosteric communication between the agonist site and the channel gate in the dual context of new *Torpedo* structures that reposition many key residues at the ECD-TMD domain interface and a body of contradictory mutagenesis data obtained from different labs using muscle nAChRs from different species and with different subunit compositions expressed in different heterologous systems. To mitigate the complications arising from the latter, we used a screening mutagenesis approach with each mutant functionally characterized in *Xenopus* oocytes using two electrode voltage clamp electrophysiology and focused on mutations in the *Torpedo* nAChR, which are unambiguously relatable to the *Torpedo* structures. A key finding of our data, bolstered by single channel measurements (Lee and Sine, 2005; Jha et al., 2012), is that larger loss-of-function mutations and more extensive energetic couplings occur at the intra-α subunit ECD-TMD interface than at the inter-subunit ECD-TMD interface despite the fact that the interacting residues at the intra-α subunit interface do not engage tightly with each other and move roughly orthogonally to each other while interacting residues at the inter-subunit interface engage tightly and move in concert upon agonist binding. Even changing all four Ser/Thr residues on $\alpha_\gamma/\alpha_\delta$ M2-M3, which engage with the β8-β9 loops/β10-M1 linkers from γ/δ, to Ala or Gly has little effect on channel function. These contradictory structural and functional observations are not easily reconciled in the context of the mechanisms that are typically used to frame agonist-induced channel gating. In such models, agonist binding is assumed to lead to movements of the ECD that result in the formation of new or enhanced interactions across the ECD-TMD domain that energetically stabilize the open pore. Although such interactions do occur, such as the formation of a backbone hydrogen bond between the carbonyl of γGly182/δGly188 and the amide group of αSer268, the inability to

identify consensus interactions across the ECD-TMD interface that define the open state, despite the extensive mutagenesis studies performed here and elsewhere (Xiu et al., 2005; Cymes and Grosman, 2021), suggests that such *open state defining interactions* do not exist. Instead, we propose that allosteric communication is governed by conformational restraints imposed primarily at the α subunit ECD-TMD interface, with agonist-binding releasing these restraints allowing the nAChR pentamer to relax from a locally asymmetric to a more symmetric open state. We base this model on the several sets of observations.

First, our and other mutagenesis data highlight the enormous functional importance of residues at the interface between the β1-β2 and M2-M3 loops of the α subunit, notably αGlu45 and αVal46 from β1-β2 and αPro265 from M2-M3, but not the analogous residues in non-α subunits (Lee and Sine, 2005). In fact, it has been suggested that αPro265 plays key role orchestrating the agonist-induced response (Gupta et al., 2017). Our data also highlight an energetic link between αGlu45/αVal46 and αPro265 that likely stems from the structural rearrangements of these residues upon agonist binding. Specifically, αGlu45/αVal46 are positioned in the apo state on the pore distal of αPro265 where they may sterically prevent the outward motions of M2-M3 that are required to open the channel gate and thus constrain M2-M3 in a closed conformation. The β8-β9 loop/β10-M1 linker from γ/δ also interact extensively with M2-M3 $\alpha_\gamma/\alpha_\delta$ in a manner that may restrain M2-M3 from transitioning outward into an open state, although side chain interactions at this interface appear less critical to channel function. Agonist-induced motions of the $\alpha_\gamma/\alpha_\delta$ ECD that move its membrane juxtaposed regions upward and sideways toward the adjacent β/γ subunits, along with motions of the γ/δ β8-β9 loop/β10-M1 linker, may simply release $\alpha_\gamma/\alpha_\delta$ M2-M3 allowing it to translate outward to open the pore, with

wetting and de-wetting of the pore possibly playing a significant role establishing the energetics between closed and open states (Aryal et al., 2015; Gupta et al., 2017). Note that there are conflicting reports as to whether the isolated TMD exhibits an energetic preference for closed or open states (Zhu and Hummer, 2010). Although such measurements are ultimately required, the hypothesis that the ECD restrains the pore in a closed conformation is consistent with the fact that isolated TMDs of the nAChR and the glycine receptor both form pentamers that not only undergo spontaneous opening/closing transitions, but that also have a greater propensity to adopt an open conformation than the intact receptors (Bondarenko et al., 2012, 2013; Mowrey et al., 2013b). Biophysical studies of ion flux through these isolated TMDs led to a similar hypothesis that the ECD restrains the pore in a closed conformation with agonist-binding releasing the restraints so that the TMD rapidly relaxes into its preferred open conformation (Mowrey et al., 2015). This hypothesis is further supported by studies of ancestral nicotinic subunits (Tessier et al., 2022), as discussed below.

Second, our data highlight the importance of concerted whole-body motions of the principal α subunit ECD, which appear to be essential to release potential conformational restraints at the α subunit interface between β1-β2 and M2-M3. Concerted whole-body motions of the α subunit ECD are likely facilitated by a conserved tripartite salt bridge involving a central αArg209 at the base of β10 and anionic residues in the β1-β2 loop (αGlu45), the β6-β7 loop (αAsp138), and the β8-β9 loop (αGlu175). Consistent with this hypothesis, mutations to any of these charged residues in the *Torpedo* nAChR lead to large changes in channel function, with mutations to the salt bridge between αArg209 and αGlu45 having a particularly detrimental effect (Lee and Sine, 2005; Xiu et al., 2005; Jha et al., 2012; Mukhtasimova and Sine, 2013; Shen et al., 2016). In contrast, mutations to analogous charged residues in non-α subunits,

which do not undergo such agonist-induced whole body ECD motions, are remarkably well tolerated.

Third, unlike both α subunits, each non-α subunit adopts a locally active-like conformation at its intra-subunit ECD-TMD domain interface even prior to agonist binding. The subunit conformational asymmetry, however, is *not* maintained at the hydrophobic gate, with all five pore-lining M2 α-helices adopting a closed conformation that blocks cation flux. One interpretation is that the principal α subunits *impose* a global closed phenotype onto the entire TMD. This interpretation is strongly supported by a recent study showing that a non-agonist binding muscle type ancestral β subunit (β_{Anc}) forms homo-pentamers that undergo spontaneous bursts of channel openings (Tessier et al., 2022), while the incorporation of a muscle α subunit represses these spontaneous channel openings leading to a closed, yet agonist activatable channel (Tessier et al., 2023). The repression of spontaneous openings by the α subunit in the β_{Anc} hetero-pentamers is consistent with our suggestion that the α subunit in the *Torpedo* nAChR imposes a closed conformation onto each non-α subunit TMD. We suggest that this internal local conformational asymmetry leads to local tension within the nAChR pentamer that is released upon agonist binding, and that this release of tension contributes to the relative energies of the closed and open states. The proposed release of local conformational tension may mimic the allosteric transitions that occur in hemoglobin, where oxygen binding relieves local tension in the porphyrin ring to shift hemoglobin from a low affinity oxygen binding "tensed" to a high affinity oxygen binding "relaxed" conformation (Monod et al., 1965).

Notably, the same release of conformational asymmetry is observed upon agonist binding to another heteromeric pLGIC (Fig. 6). In the $\alpha1_2\beta2_2\gamma2$ $GABA_AR$, the αVal46 equivalent residue in the β1-β2 loop of the principal agonist binding β2 subunits, β2Val53, transitions from

the pore distal to the pore proximal side of β2Pro273 of M2-M3 upon agonist binding, while the equivalent residues in the non-principal agonist binding subunits, α1His56/γIle68, are located on the pore proximal side of α1Pro278/γPro288 both prior to and after agonist binding (Masiulis et al., 2019; Kim et al., 2020). As in the nAChR, this subunit conformational heterogeneity, however, is not maintained in the TMD with the pore lining hydrophobic residues adopting a relatively symmetric girdle that does not conduct anions. Agonist binding, however, releases the conformational restraints so that the pentamer relaxes into a more symmetric open state. Note also that mutagenesis data from the $\alpha1_2\beta2_2\gamma2$ $GABA_AR$ further support our gating model in that they show the functional importance of the αVal46 and αPro265 equivalent residues in principal agonist binding, but not in non-principal subunits. Specifically, β2V53A severely impairs channel gating, almost exclusively by slowing channel opening, while α1H55A has almost no effect (Kaczor et al., 2021; Kłopotowski et al., 2023). Mutations to β2Pro273 also have much larger effects on channel function than similar mutations to α1P277A (Brodzki and Mozrzymas, 2022; Kaczor et al., 2022).

The homomeric α7 nAChR, $5\text{-}HT_{3A}R$, α1 GlyR, ELIC, and GLIC also undergo similar structural rearrangements at each intra-subunit ECD-TMD domain interface (Bocquet et al., 2009; Sauguet et al., 2014a; Polovinkin et al., 2018; Noviello et al., 2021; Rovšnik et al., 2021; Yu et al., 2021; Petroff et al., 2022) suggesting that a release of conformational restraints model applies to homomeric pLGICs, although such receptors do not exhibit local conformational asymmetry (Fig. 6). In the homomeric pLGICs, similar whole-body motions of the ECD may release each M2-M3 loop to relax outwards into an open conformation, with the resulting conformational transitions energetically governed by the energetics of wetting/de-wetting. Considerable data suggest that the αVal46 and αPro265 equivalent residues in these homomeric

pLGICs play an important role in the channel function, although the effects of mutations to these residues are nuanced. For example, changing the αVal46 equivalent residue, Lys46, in the α7 nAChR to Cys or Glu (Sala et al., 2005) leads to a complete loss of function, as does the equivalent αP265G mutation in both the 5-HT_{3A}R and the α7 nAChR (Deane and Lummis, 2001; Mosesso et al., 2019). In contrast, mutations to the αVal46 equivalent in the α1 GlyR have less of an effect (Kash et al., 2004). Of particular interest, changing the αPro265 equivalent residue in (Pro246) GLIC to Gly leads to a large loss-of-function. Crystal structures grown under activating conditions (pH=4.0) show that the P246G mutant adopts a conformation where the ECD remains in an active state but the pore collapses to a closed conformation with Lys32 now adopting a position on the pore distal side of Gly246 (Prevost et al., 2012). This structure not only highlights the importance of Pro246 in GLIC gating but suggests that P246G may alter the structure of M2-M3 so that the TMD can easily transition between open and closed conformations, with crystallization capturing the TMD in a locally closed conformation. It remains to be determined whether subunit conformational asymmetry contributes to gating in homomeric pLGICs.

Finally, the concerted whole-body motions of the principal subunit ECD observed in the *Torpedo* nAChR are conserved in all pLGIC structures solved to date (see Movie S5 in ref. 10) As noted, charged residues in the *Torpedo* nAChR appear to facilitate these whole-body motions, with the salt bridge between αArg209 and αGlu45 playing a particularly important role. Mutations to the two analogous residues in the homomeric α1GlyR, ρ1$GABA_AR$, 5-HT_{3A}R, and α7 nAChR, have profound effects on channel function/expression, in many cases completely abolishing agonist-activation (Absalom et al., 2003; Sala et al., 2005; Price et al., 2007; Wang et al., 2007; Pless et al., 2011). To our knowledge, the only heteromeric pLGICs where mutations

to these residues have been characterized are the synaptic α1β2γ2 $GABA_AR$ and the ganglionic α3β4 nAChR, where alanine/charge reversal mutations surprisingly have almost no effect (Kash et al., 2004; Keramidas et al., 2006; Aldea et al., 2010). The latter, however, may indicate that the concerted movements of the ECD in these heteromeric pLGICs are facilitated by other interactions. In the prokaryote, GLIC, this salt bridge is conserved (Arg192 and Asp31) and is critical to channel function, with the D31A mutant expressing robustly but failing to exhibit agonist-induced currents. In the prokaryote, ELIC, the αGlu45 equivalent residue is Thr28. Interestingly, the T28D mutation, which re-instates a salt bridge with Arg199 on the β10-M1 linker, leads to a 50-fold gain-of-function without any effect on agonist binding affinity (Bertozzi et al., 2016).

5.6 Conclusions

We have elucidated a key feature underlying allosteric communication at the ECD – TMD interface in the heteromeric muscle nAChR. In the apo state, the β1-β2 loop extending down from the ECD of the principal agonist binding α subunit is positioned where it likely restrains the α subunit M2-M3 loop in a closed conformation while the same structures in non-α subunits already adopt a locally active conformation. Agonist binding leads to whole body movements of the principal subunit ECD that reposition the β1-β2 loop to release this local conformational heterogeneity and allow the α subunit M2-M3 loop to transition outward into a conformationally symmetric open state. Our data are consistent with early cryo-EM reconstructions of the *Torpedo* nAChR (Unwin et al., 2002), reconcile an extensive body of mutagenesis data pertaining to the functional roles of residues at the ECD-TMD interface, and provide a new framework for understanding allosteric communication at the ECD-TMD interface in other pLGICs.

5.7 Discussion of the conformation adopted by the ECD of each subunit in apo and agonist bound forms of the *Torpedo* nAChR.

To assess whether the local conformational asymmetry observed at the interface between the β1-β2 and M2-M3 loops in different subunits extends to the entire ECD of each subunit, as originally proposed by (Unwin et al., 2002), we used several parameters including those developed by (Lev et al., 2017) and (Calimet et al., 2013).

To assess the capping of loop C, we first analyzed the apparent counterclockwise rotation of each subunit's ECD that occurs during activation. To capture these changes, we aligned the TMDs of apo and bound states and calculated the ECD twist angle using the metric documented in ref 5. Although GLIC undergoes an ~2° decrease in twist angle between the closed and open states, there is essentially no change in twist angle for the α subunits of the nAChR (Figure 5.11, panel B). The non-α subunits also have little change in twist angle but appear to increase rather than decrease during gating. It appears that there are differences in the twisting motions between homomeric and heteromeric pLGICs.

We quantified the ECD motions by measuring both the solvent accessible surface area (SASA) at the different ECD-ECD interfaces and the binding site contraction(Calimet et al., 2013). The SASA of the subunit-subunit interfaces in the ECD decreased in all subunits (Figure 5.11, panel C), but the largest decreases occurred in both α subunits primarily due to a larger binding site contraction (Figure 5.11, panel D). Neither metric seem to provide any evidence for pre-activation elsewhere in the ECD of the non-α subunits. The loop C capping of the non-α subunits, which should be captured in the binding site contraction metric, did not provide evidence for pre-existence in either apo or bound states. This is likely because the non-α subunit

C loops adopt unique conformations that are morphologically dissimilar to the α subunits (Figure 5.11, panel A) and are therefor difficult to directly compare.

We next used three previously defined metrics of activation, upper and lower ECD spreading and β-expansion, to assess whether the non-α subunits adopt a pre-active conformation. ECD spreading was calculated as the distance between the center of mass (COM) of the entire ECD at both the extracellular (upper) and TMD adjacent (lower) ends, to the COM of each subunit at the upper and lower ends. To find the COMs at the upper and lower ends of the entire ECD and the individual subunit ECD, an ellipsoid around the targets were created using the "measure inertia" command on ChimeraX using just the Cα's of conserved β-strands in each subunit. The COM of the ellipsoid, along with the vector of the longest principal axis (corresponding to the height axis of the domain), were used to find COMs at two z positions at the top and bottom of each ECD (see panel A of Fig. 5.12). The distance between the full ECD COM and the subunit COM in both apo and bound states is defined as the ECD spread (ref. 5) and is plotted on the right section of panel A of Figure 5.12. We found that there is a small inward motion of the upper ECD from each subunit, with no obvious change between a and non-a subunits. At the lower ECD, there does seem to be a subtle difference in spreading in a versus non-a subunits with a larger spreading occurring in the non-a subunits. This is a product of the scissor-like motion that occurs during activation in the α subunits that is described in (Zarkadas et al., 2022). The magnitudes of the ECD spreads do not provide evidence for a pre-active ECD conformation of the non-α subunits.

We also used β-expansion, a parameter used for both GLIC (Lev et al., 2017) and the homomeric ρ1 $GABA_AR$ (Cowgill et al., 2023) to measure activation. We used the same protocol as previously described taking the COM of the Cα's from two five residues stretches

(one in the β1-β2 loop and one in the β10-M1 linker) and measuring the distance in both apo and agonist bound state for each subunit (see panel B of the Fig. 5.12). The expansion was originally described from the open to closed state of GLIC and thus is a contraction in the activation transition. We also see a subtle contraction in the α subunits, but the non-α subunits instead expand. It is notable however that for both homomeric receptors, the magnitude of the contraction are ~2Å , while here the magnitudes of the α subunit contractions are <0.2Å and the non-α subunit expansions are <0.8Å. Furthermore, neither the contractions in the α subunits nor the expansions in non-α subunits suggest a pre-activate like conformation of the non-α subunits in the apo state.

Finally, we examined the changes in tilt angles that occur in each subunit ECD upon agonist binding. This was done in two ways: first by assessing how much each ECD changes its tilt angle along the z plane (relative to the pore) during activation and second by determining the relative change in tilt angle between the ECD and TMD in each subunit during activation. The former was measured by calculating the change in angle between the vector derived from longest principal axis used to create the ellipsoids around each ECD and the z-axis (or pore axis). During activation, each subunit (other than the δ subunit) undergoes a straightening motion that decreases the angle relative to the pore axis (panels A and B in Fig. 5.13)). This motion is conserved, and of a similar magnitude, in α and non-α subunits leaving no evidence for pre-activation of non-α subunits. It is notable however that while the non-α subunits seem to pivot with their membrane juxtaposed ends staying in the same position, the α subunits seem to translate toward the pore axis while also tilting (Fig. 5.13 panel A). Because each subunit was aligned by their TMD, the relative translation of the α subunit ECD suggests the angle between ECD and TMD in the α subunits would differ from the non-α subunits. To measure this, we

calculated the change in angle between the vectors of the longest principal axis of ellipsoids around the ECD and TMD of the same subunit for both apo and bound states. Panel C shows that the interdomain tilt angle in the non-α subunits increase during activation but decreases in the α subunits due to their scissor like interdomain motions.

Altogether, we were not able to identify any evidence for the pre-active like conformation of the ECD – TMD interfaces of the non-α subunit extending more globally to the remainder of the ECD.

Figure 5.11 ECD twist does not provide evidence for pre-activation.
Panel A shows top-down views of each subunit in the nAChR aligned by their TMDs in apo (pink) and agonist bound (green) states to show the relative motion of the ECD. Panel B shows change in ECD twist angle as defined in (Lev et al., 2017). Panel C shows changes in solvent accessible surface area at each ECD – ECD interface. Panel D shows binding site contraction at each subunit interface as defined in (Calimet et al., 2013).

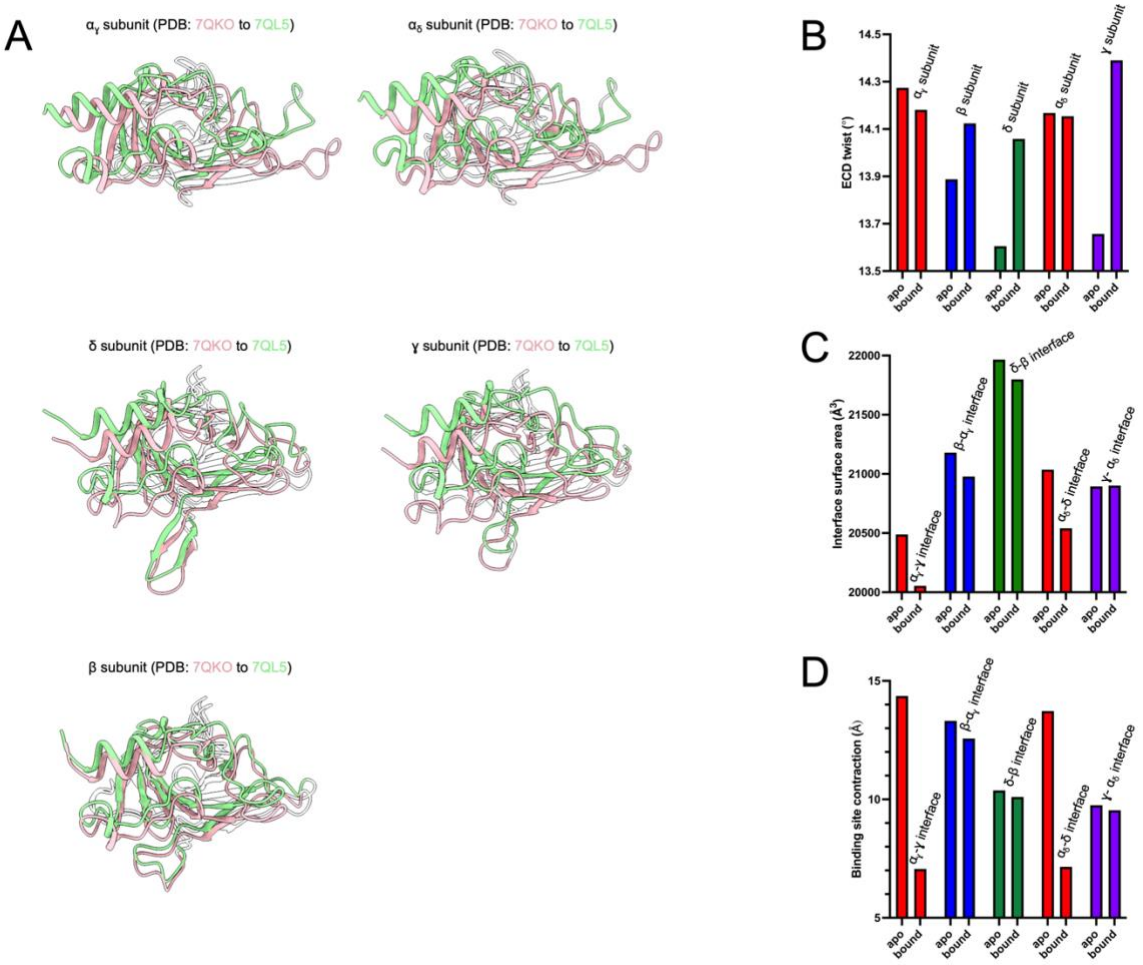
A
αγ subunit (PDB: 7QKO to 7QL5)
αδ subunit (PDB: 7QKO to 7QL5)
δ subunit (PDB: 7QKO to 7QL5)
γ subunit (PDB: 7QKO to 7QL5)
β subunit (PDB: 7QKO to 7QL5)
B
ECD twist (°)
14.5
14.3
14.1
13.9
13.7
13.5
αγ subunit
β subunit
δ subunit
αδ subunit
γ subunit
apo
bound
C
Interface surface area (Å²)
22000
21500
21000
20500
20000
αγ-γ interface
β-αγ interface
δ-β interface
αδ-δ interface
γ- αδ interface
D
Binding site contraction (Å)
15
10
5

Figure 5.12 ECD spreading and β-expansion.

Upper and lower ECD spreading (Lev et al., 2017) is quantified for each subunit in panel A. The left shows the ECD of the apo (pink) and agonist bound (green) states aligned by their entire TMDs. Center of mass (COM) for the ECD of each subunit as well as the COM for the entire ECD are shown as spheres and the distances are depicted as dashed lines and plotted in the graph on the right. Panel B shows β-expansion in each subunit (Lev et al., 2017) with the minimal changes shown in both the models (left) and the graph (right).

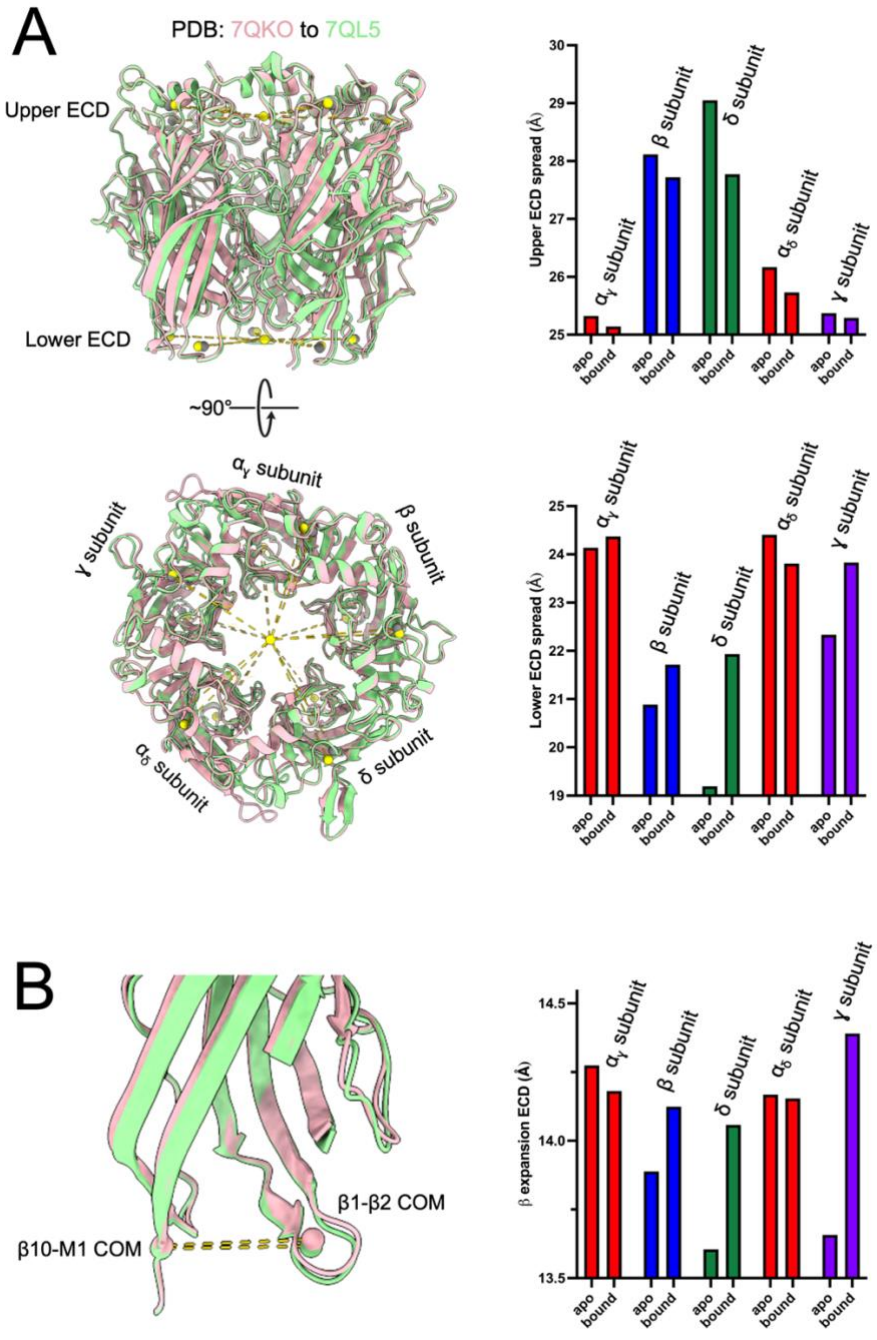
A
PDB: 7QKO to 7QL5
Upper ECD
Lower ECD
~90°
αγ subunit
β subunit
γ subunit
αδ subunit
δ subunit
Upper ECD spread (Å)
Lower ECD spread (Å)
apo
bound
B
β1-β2 COM
β10-M1 COM
β expansion ECD (Å)

Figure 5.13 ECD-tilt angles.

A COM and vector corresponding to the principal axis through the COM were defined for each subunit ECD using only the Cα carbons from the conserved β stands in each subunit. The ECD tilt was defined as the angle between the principal ECD axis and the pore axis for each subunit. A COM and vector corresponding to the principal axis for each TMD was then defined and the angle between the vectors for the principal ECD and TMD axis was defined as the ECD-TMD tilt.

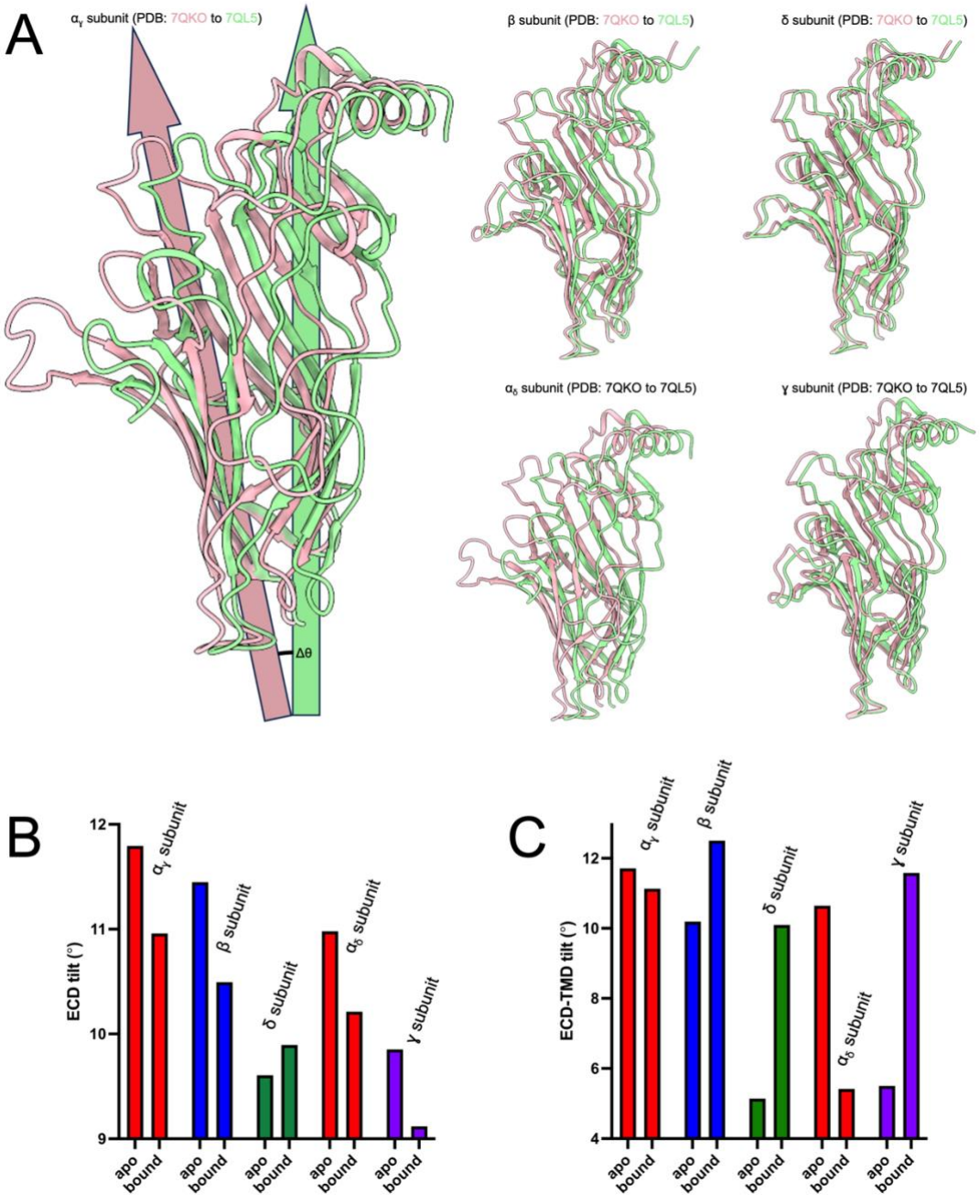
A
αγ subunit (PDB: 7QKO to 7QL5)
β subunit (PDB: 7QKO to 7QL5)
δ subunit (PDB: 7QKO to 7QL5)
αδ subunit (PDB: 7QKO to 7QL5)
γ subunit (PDB: 7QKO to 7QL5)
Δθ
B
ECD tilt (°)
12
11
10
9
αγ subunit
β subunit
δ subunit
αδ subunit
γ subunit
apo
bound
C
ECD-TMD tilt (°)
12
10
8
6
4
αγ subunit
β subunit
δ subunit
αδ subunit
γ subunit
apo
bound

Chapter 6. Manuscript 4: Asynchronous conformational transitions during nicotinic acetylcholine receptor activation

Manuscript in preperation.

6.1 Preface

The research performed in the manuscript was obtained while I was working in Hugues Nury's lab at the Institut de Biologie Structurale in Grenoble, France. We had established a pipeline for imaging the *Torpedo* nAChR using single particle cryo-EM and hypothesized that intermediate conformations of the receptor could be captured at high-resolution using this technique. I performed all the biochemical experiments on the nanodisc reconstituted nAChR that was kindly prepared by Dr. Camille Henault. Anna Ananchenko performed the molecular dynamics simulations. Dr. Eleftherios Zarkadas, Dr. Baenziger, and I prepared grids and imaged the nAChR in the presence of several concentrations of ACh. I performed all the image analysis, data processing, and model building. I created all the figures and movies and wrote the manuscript alongside Dr. Nury and Dr. Baenziger.

6.2 Abstract

The nicotinic acetylcholine receptor (nAChR) has been a model for studying protein allostery for more than half a century. Recent cryo-electron microscopy (cryo-EM) structures of the nAChR in un-liganded/pore-closed and di-liganded/pore-open states have provided novel insights into the conformational transitions that accompany nAChR activation, but the sequence of these transitions remains unknown due to the lack of intermediate conformations along the activation trajectory. Here I use a fluorescence-based assay to guide a series of cryo-EM data collections at sub-saturating concentrations of the native agonist acetylcholine (ACh). Using advanced particle sorting algorithms, a small subset of particles adopting a mono-liganded state were isolated and resolved to high resolution. The mono-liganded state reveals a subunit sequential activation mechanism whereby binding of ACh to the α_γ-γ site causes the α_γ subunit to adopt an active like conformation while the α_δ subunit remains inactive but appears primed for full activation. The results provide insight into the series of allosteric conformational transitions that underly nAChR activation.

6.3 Introduction

The nicotinic acetylcholine receptor (nAChR) from *Torpedo* has been a prototype for studying protein allostery for more than 50 years thanks to its abundance in native tissue, affinity for venomous toxins, and biochemical stability (Changeux, 2012). Like all allosteric proteins, the nAChR exists in several conformational states with both the relative stabilities of these states and the rates of interconversion between them determining the time course of channel activation and thus the temporal nature of the post-synaptic response. In the absence of agonist, the nAChR exists predominantly in a resting conformation that has a relatively low affinity for agonist and a closed, non-conductive ion channel pore. Energy derived from the binding of the endogenous agonist, acetylcholine (ACh), to each of the two orthosteric sites stabilizes an open, conductive conformation allowing cations to flow down their electrochemical gradient into the cell, while prolonged exposure to agonist leads to the formation of a desensitized conformation that maintains a high agonist binding affinity but is non-conductive.

At relatively high concentrations of ACh (10-1000 uM), single channel measurements show that the nAChR undergoes bursts or clusters of channel openings separated by salient periods of desensitization. Within each activation cluster, the probability of the nAChR being in an open state increases with increasing concentration of ACh, with this increased open probability arising from an increasing frequency of long versus short channel open times attributed to di- versus mono-/un-liganded channel openings, respectively. Kinetic fittings of single channel recordings further show that opening only occurs after the resting state has transitioned to a pre-open closed state termed flipped or primed (Lape et al., 2008; Mukhtasimova et al., 2009). A minimum of nine conformational states must therefore be included in any kinetic scheme describing channel activation (Fig. 6.1).

Figure 6.1 Kinetic scheme of nAChR activation

A kinetic scheme of nAChR activation derived from single channel measurements (Mukhtasimova et al., 2016). The scheme depicts an apo resting (R) receptor that can bind one or two agonist molecules ('A'). The un-, mono-, and di-liganded R receptor transitions through a primed (R') state prior to channel opening (O), although un-liganded priming and opening are infrequent in the WT nAChR and are typically ignored. At high concentrations of agonist, the O state can also be blocked (B) by agonist binding to the pore, although blocking in the singly liganded open state is not appreciable and is thus omitted from the scheme. The rate constants for binding and unbinding (k_+ and k_-), priming and unpriming (p_+ and p_-), opening and closing (β and α), and blocking and unblocking (k_{+B} and k_{-B}) are shown for each step in the kinetic scheme.

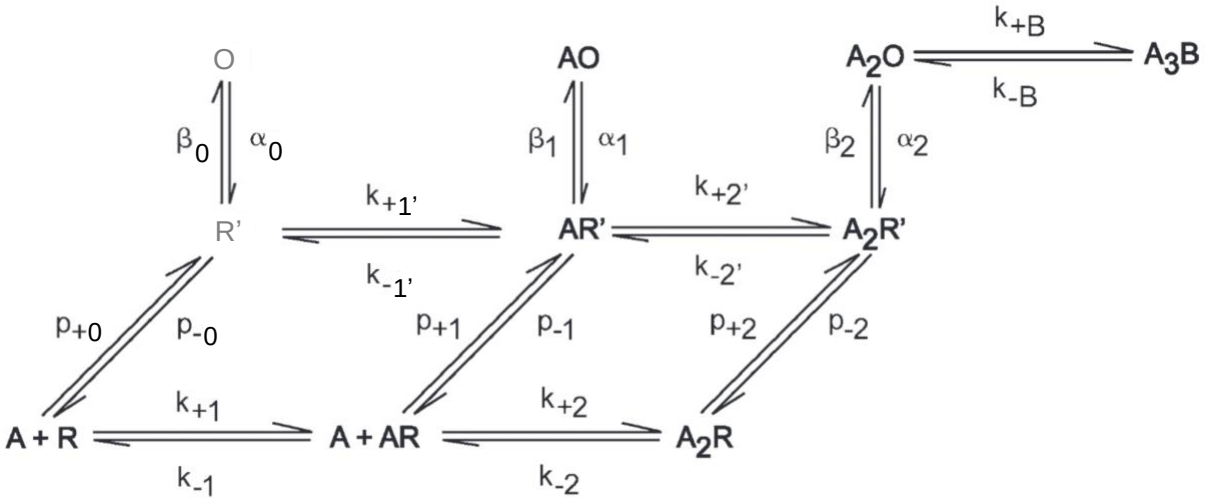
O
AO
A2O
k+B
A3B
k-B
β0
α0
β1
α1
β2
α2
k+1'
k+2'
R'
AR'
A2R'
k-1'
k-2'
p+0
p-0
p+1
p-1
p+2
p-2
k+1
k+2
A + R
A + AR
A2R
k-1
k-2

High resolution structures of the apo resting and agonist-bound pore open states have been determined for many pLGICs, including the nAChR, thus providing insight into the conformational transition that culminates in channel activation. In contrast, only limited structures along the trajectory between apo and activated states have been solved, with these intermediate conformations restricted to homomeric, as opposed to heteromeric, pLGICs (Prevost et al., 2012; Polovinkin et al., 2018; Yu et al., 2021; Petroff et al., 2022; Cowgill et al., 2023). A common feature of these intermediate structures is that they all exhibit an extracellular domain (ECD) that has transitioned to an active or active-like state while the transmembrane domain (TMD) remains predominantly inactive. This implies a concerted domain sequential activation mechanism moving from the ECD to the TMD, a model further supported by both biochemical experiments (Peverini et al., 2023; Shi et al., 2023) and molecular dynamics simulations (Calimet et al., 2013; Lev et al., 2017; Martin et al., 2017). As heteromeric nAChR structures have only been captured in un-liganded and di-liganded states, however, it remains unclear whether this concerted domain sequential activation can be extended to subunit asymmetric pLGICs, such as the nAChR. It is also unclear such a domain sequential activation mechanism could correlate with flipped or primed intermediate states.

A major roadblock to solving structures along the trajectory between apo and di-liganded channel open states is the rapid timescales of these transitions. Even though there have been advancements in time-resolved cryo-electron microscopy (cryo-EM), it remains a challenge to capture such rapid conformational transitions, which are on the order of nanoseconds (Frank, 2017; Yoder et al., 2020; Bhattacharjee et al., 2023). An alternative approach to capturing intermediate structures is to image the pLGICs at sub-saturating agonist concentrations. This method has been used to capture a variety of conformations in other ion channels and complexes

(Hite and MacKinnon, 2017; Haselbach et al., 2018; Kwon et al., 2022; Papasergi-Scott et al., 2023), but has not yet been applied to pLGICs.

Here I use a fluorescence-based ethidium bromide binding assay to establish an acetylcholine (ACh) concentration-response curve for the nAChR reconstituted into lipid nanodiscs and to thus guide the collection of cryo-EM datasets at both saturating and sub-saturating concentrations of ACh. Using advanced particle sorting algorithms, I isolate a population of particles that exist in a mono-liganded conformation where ACh is bound at the α_γ-γ but not the α_δ-δ orthosteric site. I then refine a 3.1 Å resolution density map and built a structural model of the mono-liganded state, which is compared to structures of the un-liganded (3.2 Å resolution) and di-liganded (2.8 Å) nAChR. The structures suggest that the nAChR undergoes a subunit asymmetric channel activation mechanism whereby agonist binding to the α_γ-γ interface essentially leads to activation of the α_γ and γ subunits, while the α_δ and other subunits adopt an inactivated conformation that appears to be primed for full activation. These new structures suggest that activation occurs through an asynchronous subunit transition mechanism as opposed to the domain sequential activation mechanism proposed for homomeric pLGICs.

6.4 Experimental Methods and Data Processing

6.4.1 nAChR purification and nanodisc reconstitution.

The nAChR was purified on a bromoacetylcholine bromide (BAC)-derivatized Affi-Gel 102 column (Bio-Rad) as previously described (Zarkadas et al., 2022), but with the following modifications. After the nAChR was eluted from the column, it was incubated with 15 mM DTT prior to purification on a Superose6 size-exclusion column. The purified monomeric form of the nAChR pentamers was incubated with soybean azolectin and MSP2N2 (Grinkova et al., 2010) and then dialyzed (12-14 kDa cut-off) five times against 2 L of tris dialysis buffer (TDB), with buffer changed every 12 h. The MSP2N2 nanodisc-reconstituted nAChR was further purified by size-exclusion chromatography, with the appropriate fractions pooled, concentrated, aliquoted, snap frozen in liquid nitrogen and stored at -80°C.

To ensure any residual Carb used in the nAChR elution was removed from the sample, aliquots of the MSP2N2 reconstituted nAChR were diluted 75-fold in TDB, incubated for 30 minutes on ice with occasional stirring, and concentrated back to the original volume, with this dilution/concentration cycle repeated five times. The buffer exchanged nAChR was injected once again on the size-exclusion column and the monomeric nAChR peak pooled. The pooled fractions were concentrated to 0.65 mg/mL, aliquoted, snap frozen in liquid nitrogen and stored at -80 C for characterization by the EthBr assay or for cryo-EM grid preparation.

6.4.2 Fluorescence measurements of ACh-activation.

Fluorescence experiments were performed essentially as described previously (daCosta and Baenziger, 2009) on a Cary Eclipse fluorescence spectrophotometer (Varian Inc.) with the ethidium fluorescence excited at 500 nm (±5 nm slits) and the fluorescence emission intensity

measured at 590 nm (±20 nm slits). ~60 μg of nanodisc reconstituted nAChR was first incubated with 0.1 μM EthBr in a cuvette at room temperature for ~15 minutes under constant stirring. Increasing concentrations of ACh were then added every 2 minutes, with the resulting changes in fluorescence measured at each concentration of ACh. A plot of the increase in fluorescence versus concentration of ACh was fit with a variable slope sigmoidal dose-response curve and the individual EC_{50} and Hill coefficients averaged and reported as the mean ± standard deviation.

6.4.3 Electron microscopy and image analysis.

The nAChR in asolectin-MSP2N2 nanodiscs was mixed with the megabody Mbc7HopQNbF3 (Uchański et al., 2021), which binds MSP2N2 not the nAChR, at a molar ratio 1:3 to overcome orientation bias of the nAChR on the cryo-EM grids. After incubating with the desired concentration of ACh for 30 min on ice, 3.5 mls of each sample were deposited onto glow-discharged (30 mA, 50 s) Quantifoil Au/C R 1.2/1.3 grids. Each grid was blotted for 6 s with force 0 at 8 ◦C and 100% humidity and then plunge-frozen in liquid ethane using a Mark IV Vitrobot (Thermo Fisher Scientific).

All cryo-EM datasets were recorded on a Glacios electron microscope at the Institut de Biologie Structural in Grenoble, France. Movies (40 frames) were recorded at a nominal magnification of 36,000 with SerialEM and a Gatan K2 Summit camera. The raw movies were imported to Cryosparc (Punjani et al., 2017), aligned, and summed. CTF estimation was calculated for the non-dose-weighted sums. Particles were autopicked with crYOLO 1.7.6 (Wagner et al., 2019) using the general model for low-pass filtered images. Particle coordinates were imported into Cryosparc where all subsequent data processing was performed. Raw particle stacks were extracted at 256 pixel box sizes.

The initial workflow was the same for each individual dataset. Two rounds of 2D classifications were performed with particles from all classes exhibiting both clear pLGIC features and a monomeric form selected and submitted to *ab initio* reconstruction & heterogeneous refinement with 3 classes. After the first round of *ab initio* and heterogeneous refinement, the particles in classes that showed density for all three domains were subject to another round of ab initio and heterogeneous refinement. The one class showing the best nAChR features, map integrity and best isotropic viewing angle distributions, was selected and refined using non-uniform & local refinements (Punjani et al., 2020) to yield a "consensus refinement" for each of the datasets.

Each of the datasets was then subjected to three types of analyses to reveal conformational heterogeneity: 3D classification (10 classes), and both 3D variability analysis (3DVA) intermediates (30 frames) and clusters (8 clusters) (Punjani and Fleet, 2021). For each analysis, a single focused mask that encompasses the regions of the nAChR that change most between apo and agonist bound states was used to identify particles in different conformations. This mask included the two binding sites and loop C, the pore line M2 α-helices, and the α_8 M4 α-helix. In the case of the apo dataset and the saturating ACh dataset, I was unable to identify substantial conformational heterogeneity (see results). In the datasets collected at sub-saturating agonist concentrations, substantial conformational heterogeneity was identified thus leading to further data processing.

The 2,461,091 particles from the consensus refinements of each of the five datasets at sub-saturating concentrations were combined and subjected to the same three types of analyses used to detect conformational heterogeneity in each individual data set, as described above. Particles sorted into each of the 8 clusters and 10 classes from the 3DVA and 3D

classification, respectively, were refined and manually inspected. Particles in clusters/classes that did not clearly resemble un-liganded apo or di-liganded pore open states were subjected to another round of analysis. 30 frame volume series from 3DVA were also manually inspected with the principal component of variability revealing a trajectory from un-liganded apo to di-liganded pore open states. Particles in frames that did not clearly resemble un-liganded apo or di-liganded pore open states were subjected to another round of analysis. 1,494,365 particles in non-end state from the first round of analysis were again combined and subjected to the same analysis a second time. After the second round of analysis 772,485 particles remained in non-end states, but refining these particles revealed that heterogeneity remained in the variable regions of the nAChR. Three states were consistently observed in the 3D classification and 3DVA cluster analysis: un-liganded resting states, di-liganded pore-open states, and states that contained a capped α_{γ} loop C with density for agonist and an uncapped α_{δ} loop C with no density for agonist (mono-liganded state). To remove remaining conformational heterogeneity, reference maps from the 3D classification for each of these states were selected and used as inputs for 3D classification and heterogeneous refinements. 379,957 particles were sorted into the mono-liganded state, and these particles were refined. The corresponding density map revealed a mono-liganded state with some remaining heterogeneity around α_{γ} loop C. To ensure all particles in the reconstruction corresponded to the mono-liganded state, a second round of 3D classification with input maps was performed and 129,828 particles were sorted to the mono-liganded state. These particles were refined to obtain a well-defined 3.13 Å resolution reconstruction of the mono-liganded state.

6.4.4 Model refinement and structure analysis.

Preliminary model building was performed in Isolde (Croll, 2018). Cycles of real-space refinement were then performed in Phenix (Liebschner et al., 2019), alternating with manual rebuilding in Coot (Emsley et al., 2010) using the maps from Cryosparc and, occasionally, maps post-processed with DeepEMhancer (Sanchez-Garcia et al., 2021). Validation was performed with Molprobity (Williams et al., 2018) (Table 6.1).

For the un-liganded state, the model contains chains A (α_γ): 1-331, 368-434; B (β): 1-334, 400-469: C (δ): 1-341, 418-500; D (α_δ): 1-331, 376-435; and E (γ): 2-331,416-489. Elongated density surrounding the TMD was attributed to lipids and modeled as 8 POPC molecules (POV). The model also comprises 14 N-acetylglucosamine (NAG), 19 α-D-mannose (MAN) and 7 β-D-mannose (BMA) residues of N-linked glycosylation attributed to densities protruding from N141 of both α subunits (chains A and D), N141 of β (chain B), N70, N143 and N208 of δ (chain C), and N68 of γ (chain E).

For the mono-liganded state, the model contains chains: A (α_γ): 1-329, 368-434; B (β): 1-334, 400-469; C (δ): 1-341, 418-500; D (α_δ): 1-323, 376-435; and E (γ): 2-331, 416-489. One ACh (ACH) molecule is present at in the α_γ-γ orthosteric site. The model also comprises elongated density surrounding the TMD that was attributed to lipids and modeled as 5 POPC molecules (POV) as well as 14 N-acetylglucosamine (NAG), 17 α-D-mannose (MAN) and 6 β-D-mannose (BMA) residues of N-linked glycosylation attributed to densities protruding from N141 of both α subunits (chains A and D), N141 of β (chain B), N70, N143 and N208 of δ (chain C), and N68 of γ (chain E).

For the di-liganded state, the model contains chains: A (α_γ): 1-331, 370-432; B (β): 1-335, 399-469; C (δ): 1-342, 417-501; D (α_δ): 1-323, 370-426; and E (γ): 2-335, 410-489. One ACh

(ACH) molecule was placed at each orthosteric site. The model also comprises 14 N-acetylglucosamine (NAG), 16 α-D-mannose (MAN) and 6 β-D-mannose (BMA) residues of N-linked glycosylation attributed to densities protruding from N141 of both α subunits (chains A and D), N141 of β (chain B), N70, N143 and N208 of δ (chain C), and N68 of γ (chain E).

Table 6.1 - Cryo-EM data collection, refinement and validation statistics.

	Un-liganded	Mono-liganded	Di-liganded
Data collection & processing			
Microscope	Glacios-IBS	Glacios-IBS	Glacios-IBS
Magnification	36,000	36,000	36,000
Voltage (kV)	200	200	200
Frames (Exposure time in s)	40 (4)	40 (4)	40 (4)
Total movies (no.)	1,843	38,674	9,810
Electron dose (e/A^2)	42	42	42
Collection mode	Counting	Counting	Counting
Effective pixel size (A)	1.145	1.145	1.1
Initial particle images (no.)	664,005	15,064,889*	4,133,568
Final particle images (no.)	169,980	129,828	552,159
Symmetry imposed	C1	C1	C1
Map resolution (A)	3.20	3.13	2.80
Model refinement			
Initial model used (PDB code)	7QKO	7QL5	7QL5
Model composition			
Non-hydrogen atoms	17,181	16,980	16,853
Protein residues	2,201	2,013	2,021
Carbohydrates	40	37	36
Lipids	8	5	0
B-factors (min/max/mean A^2)			
Protein	-1.00/262.75/143.24	52.55/338.74/125.00	95.12/335.62/150.97
Ligand	97.47/332.05/178.23	92.07/326.51/155.95	71.74/241.54/155.99
R.M.S. Deviations			
Bond length (A)	0.005 (0)	0.003 (0)	0.004 (0)
Bond angles (0)	0.806 (3)	0.619 (0)	0.670 (5)
Validation			
MolProbity score	1.51	1.54	1.52
Clashscore	9.67	10.58	9.88
Rotamer outliers (%)	0.75	0.81	0.32
Ramachandran plot (%)			
Favored	98.00	98.04	98.25
Allowed	1.95	1.96	1.75
Outliers	0.05	0.00	0.00
Model Resolution	3.8	3.6	3.4

*A total of 2,461,091 particles were used for the consensus refinements in each dataset at sub-saturating ACh and used for down-stream variability analyses.

6.5 Results

6.5.1 ACh potency of the nanodisc reconstituted nAChR.

The conformationally sensitive fluorescent probe, ethidium bromide (EthBr), was used to determine the concentration of ACh required to activate the nAChR reconstituted into the soybean azolectin MSP2N2 nanodiscs used for cryo-EM imaging. Previous studies have shown that in both native and reconstituted liposomes, EthBr binds with a higher affinity to the pore of the open (K_D not determined) and agonist-bound desensitized (K_D = 0.3 – 0.9 μM) states than to the apo resting state (K_D ~1mM) (Herz et al., 1987; daCosta and Baenziger, 2009; Sun et al., 2017), with its fluorescence emission intensity increasing ~15-fold upon pore binding. In MSP2N2 nanodiscs, EthBr binds in the presence of 100 μM Carb to the desensitized state with a similar affinity (K_D = 0.44 ± 0.05 μM, n=3). In the absence of Carb, EthBr binding shifts the nAChR conformational equilibrium towards the desensitized state at lower concentrations (K_{EQ} = 1.7 ± 0.5 μM, n=6) than in reconstituted or native liposomes (K_{EQ} of 4-7 μM) (Fig. 6.2). To minimize the effect of EthBr on nAChR conformational equilibria, ACh titrations were performed in the presence of only 0.1 μM EthBr.

ACh titrations of the MSP2N2 reconstituted nAChR in the presence of 0.1 μM EthBr show that measurable transitions of the MSP2N2-reconstituted nAChR to the open then desensitized states occur at concentrations of ACh as low as 2 nM, with the response essentially saturating at concentrations of ~10 μM. The measured EC_{50} for the ACh-induced response is 133 ± 55 nM (Fig. 6.3a).

Figure 6.2 EthBr titrations performed on the nanodisc reconstituted nAChR

EthBr titrations performed on the MSP2N2 nanodisc reconstituted nAChR in the absence (A) or presence (B) of a saturating concentration of the agonist Carb. The difference in fluorescence emission intensity between cuvettes with and without the nAChR were recorded at each EthBr concentration and was then normalized to the maximum fluorescence intensity. Individual values from each assay are averaged and the standard deviation shown as error bars.

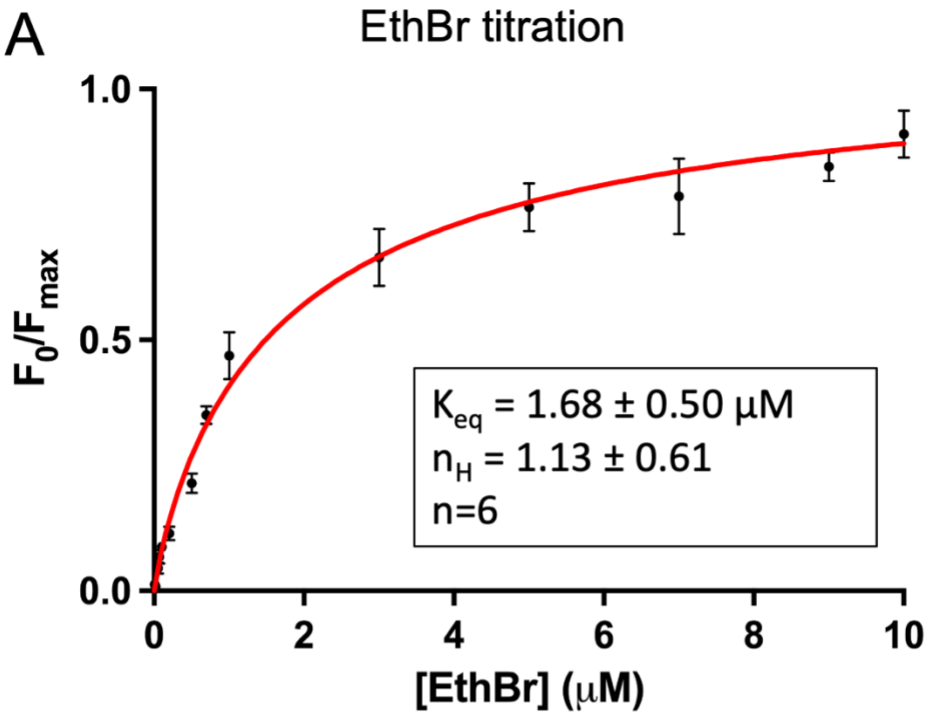
A
EthBr titration
1.0
0.5
0.0
F_0/F_{max}
K_{eq} = 1.68 ± 0.50 µM
n_H = 1.13 ± 0.61
n=6
0
2
4
6
8
10
[EthBr] (µM)

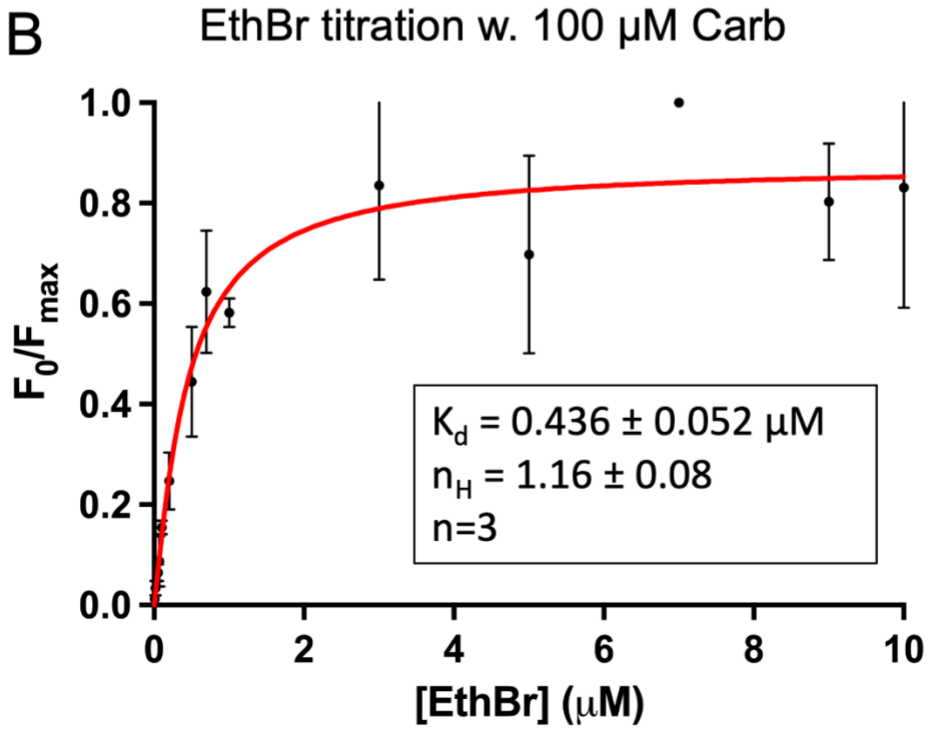
B
EthBr titration w. 100 µM Carb
1.0
0.8
0.6
0.4
0.2
0.0
F_0/F_{max}
K_d = 0.436 ± 0.052 µM
n_H = 1.16 ± 0.08
n=3
0
2
4
6
8
10
[EthBr] (µM)

Figure 6.3 Imaging the nAChR with different concentrations of ACh

Panel A shows the ACh dose-response curve derived from the EthBr assays for the MSP2N2 reconstituted nAChR. The red X's on the curve highlight the concentrations of ACh used in the seven recorded cryo-EM datasets. The bottom and tops of the curve are the concentrations used to solve the structures of the apo (un-liganded) and di-liganded ACh-bound states, and the middle five concentrations were used to solve the structure of the intermediate mono-liganded state. Panel B shows the density maps for each of the three solved structures from both side (top) and top-down (bottom) views. The density is colored by subunit (α, light pink; β, light orange; γ, light blue; δ, light green) with non-protein shown in transparent white.

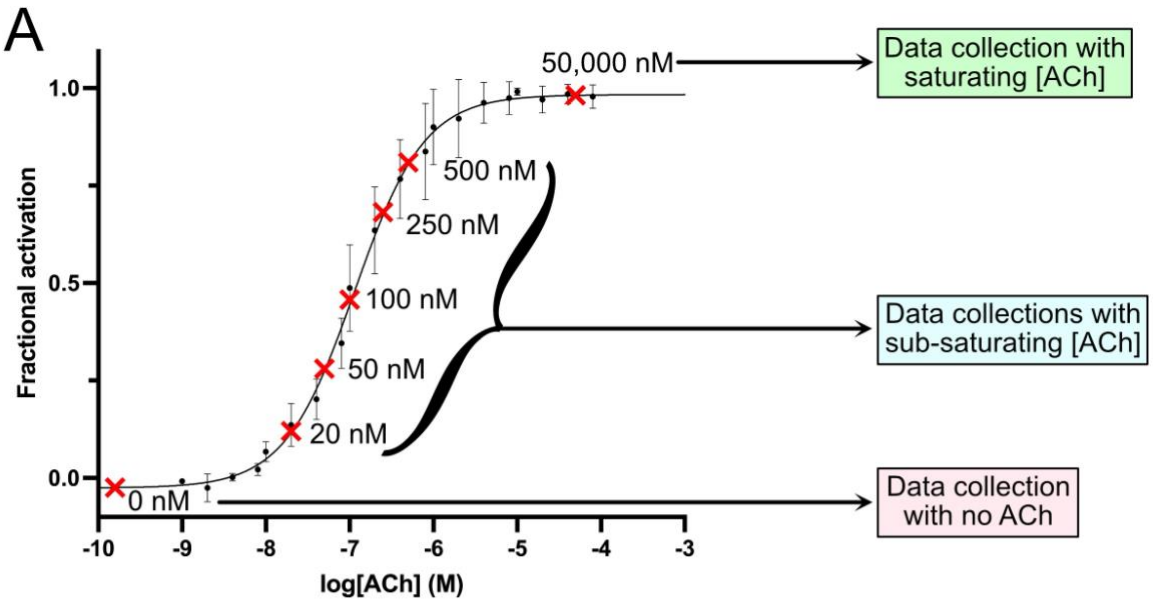
A
Fractional activation
1.0
0.5
0.0
-10
-9
-8
-7
-6
-5
-4
-3
log[ACh] (M)
50,000 nM
500 nM
250 nM
100 nM
50 nM
20 nM
0 nM
Data collection with saturating [ACh]
Data collections with sub-saturating [ACh]
Data collection with no ACh

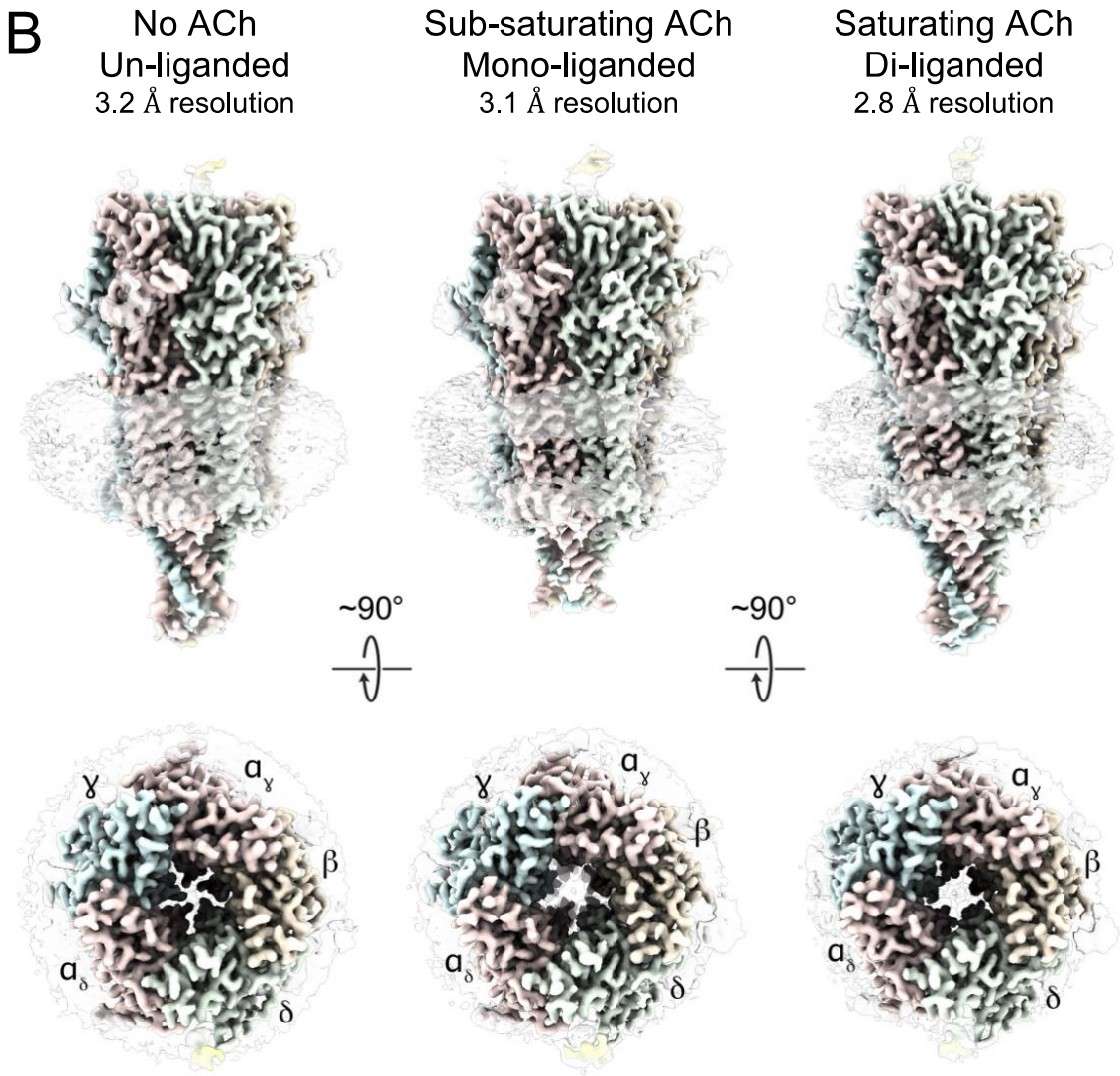
B
No ACh
Un-liganded
3.2 Å resolution
Sub-saturating ACh
Mono-liganded
3.1 Å resolution
Saturating ACh
Di-liganded
2.8 Å resolution
~90°
~90°
γ
αγ
β
αδ
δ

6.5.2 Cryo-EM datasets for un- and di-liganded states.

Cryo-EM datasets were first collected in the absence of ACh and at saturating 50 μM ACh concentrations. The two datasets were processed using standard protocols (see Methods) to yield consensus reconstructions of 3.2 Å and 2.8 Å resolution for the un- and di-liganded states, respectively (Fig. 6.4). The un-liganded reconstruction closely resembles *Torpedo* nAChR structures previously solved in the absence of agonist (PDB:7QKO RMSD=0.40 Å; PDB:7SMM RMSD=0.54 Å) (Rahman et al., 2022; Zarkadas et al., 2022) with uncapped C loops in both α subunits (α_γ and α_δ), a closed channel pore, and an untilted M4 α-helix in α_δ. Similarly, the di-liganded ACh bound state resembles other agonist bound structures (nicotine bound PDB:7QL5 RMSD=0.44 Å; Carb bound PDB:7QL6 and 7SMR with RMSDs of 0.44 Å and 0.55 Å, respectively) (Rahman et al., 2022; Zarkadas et al., 2022) with capped C loops in both α subunits, a dilated channel pore, and a tilted/dynamic M4 α-helix in the α_δ subunit.

To search for potential conformational heterogeneity in these two datasets, a focused mask was created around the regions that undergo the largest changes in conformation upon agonist binding (the C loops, pore lining α-helices, and C-termini of α_δM4) and the datasets were subjected to both 3D classifications and 3D variability analysis (3DVA) in CryoSparc (Punjani et al., 2017; Punjani and Fleet, 2021). Neither method was able to detect meaningful conformational heterogeneity in either dataset (data not shown). The lack of conformational heterogeneity is emphasized further when the particles were separated into 30 frames along a principal component of variability and then visualized as a trajectory of density maps. The apo dataset reveals only a subtle capping motion of the C loops near the end of the trajectory, suggesting that only a very small number of particles adopt non-apo states. The di-liganded ACh-bound state remains in a uniform bound state throughout the trajectory (data not shown).

Figure 6.4 Data processing for un- and di-liganded states

Data processing for the un- (panels A-F) and the di- (panels G-L) liganded datasets. Motion and CTF corrected micrographs are shown in panels A and G. 2D projections are shown in panels B and H. Sharpened maps coloured by local resolution are shown in panels C and I. Schematics of the image analysis workflow are shown in panels D and J. Heat maps of the angular distribution of particle projections are shown in panels E and K. Gold-standard Fourier shell correlation (FSC) curves are shown in panels F and L.

A

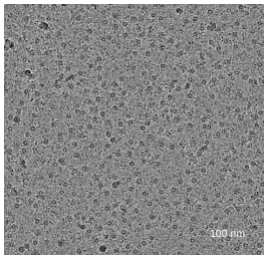

B

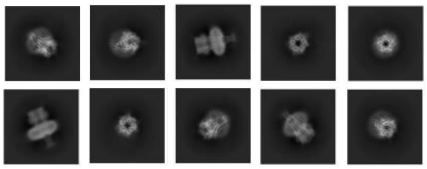

C

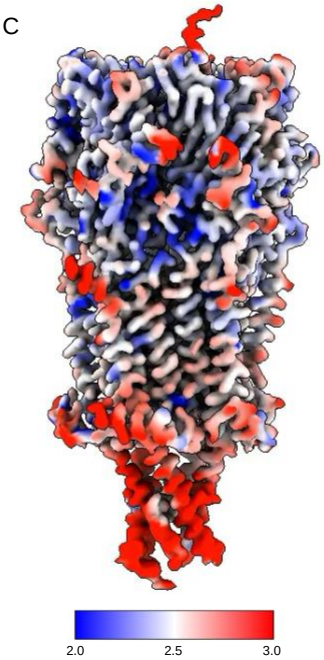

D

1,843 micrographs
664,005 raw particles

2D classification (2 rounds)
430,592 selected particles

Ab initio reconstruction &
heterogeneous refinement (2 rounds)
(1 out of 3 classes selected)
169,980 particles

Non-Uniform & local refinement

E

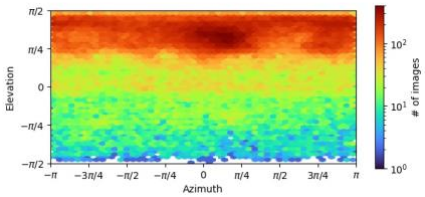

F

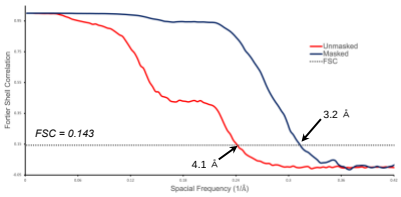

G

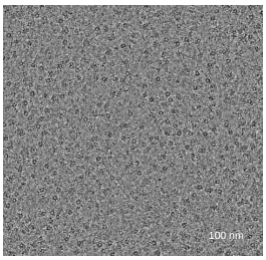

H

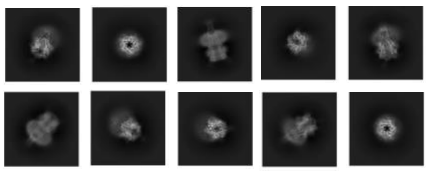

I

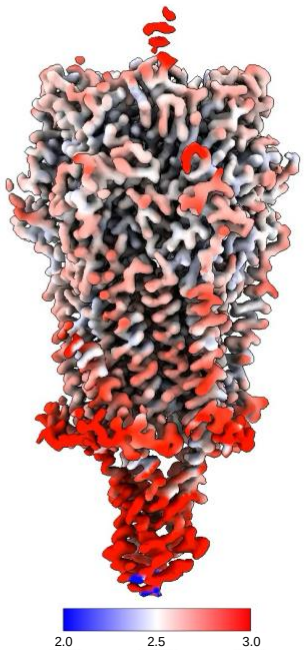

J

9,810 micrographs
4,133,568 raw particles

2D classification (2 rounds)
2,498,697 selected particles

Ab initio reconstruction &
heterogeneous refinement (2 rounds)
(1 out of 3 classes selected)
552,159 particles

Non-Uniform & local refinement

K

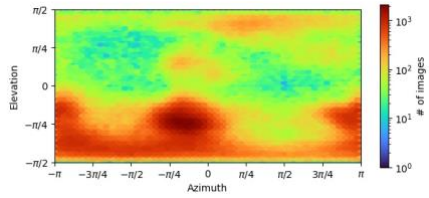

L

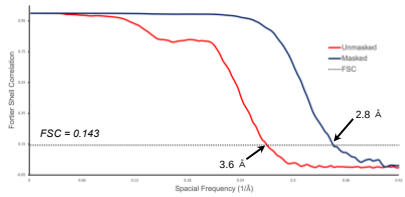

6.5.3 Cryo-EM data sets at sub-saturating concentrations of ACh.

Two datasets were next collected at sub-saturating concentrations of ACh near the bottom of the dose-response curve (20 nM and 50 nM). The same protocols used to process the un- and di-liganded datasets were performed on both datasets yielding consensus refinements with features that resemble the un-liganded apo state (Fig. 6.5), but with poorly defined density in the noted variable regions (the C loops, pore lining α-helices, and C-termini of α_δM4) suggesting conformational heterogeneity. When subjected to 3DVA, both datasets captured transitions from the un-liganded to the di-liganded state along their principal components of variability, confirming that multiple conformations exist in each dataset (data not shown). When the particles were separated along three components of variability and grouped into clusters or subjected to focused 3D classifications (see Methods), the resulting reconstructions were predominantly in un-liganded apo states with uncapped C loops and closed channel pores. Some conformations resembled the di-liganded state, with capped C loops and open pores. Notably, other conformations suggested a potential intermediate state(s). The *only* resolved maps for these potential intermediate states were in a state where loop C in the α_γ subunit is capped appreciably around the agonist density while loop C in the α_δ subunit is uncapped and agonist density is absent. This state is referred to as the "mono-liganded state". None of the maps generated from these analyses revealed a mono-liganded state with the α_δ subunit capped and the α_γ subunit uncapped. Taken together, the data show that cryo-EM images recorded at sub-saturating concentrations of ACh capture a mono-liganded conformation with ACh bound to the α_γ-γ orthosteric site but not the α_δ-δ orthosteric site. In the *Torpedo* nAChR, it can thus be concluded that the α_γ-γ orthosteric site exhibits a higher affinity for ACh than α_δ-δ. Density maps of this mono-liganded state, however, could only be refined to ~4 Å resolution as only a

Figure 6.5 Data processing of datasets collected under sub-saturating concentrations of ACh

(A) Data processing for the five datasets collected at sub-saturating ACh are presented. For each datasets a motion and CTF corrected micrograph, 2D projections, heat maps of the angular distribution of particle projections, and schematics of the image analysis workflow are shown. Particles in the consensus refinement for each dataset were combined and subjected to further processing that is depicted in panel B. (B) Image analysis workflow used to isolate intermediate particles from each sub-saturating dataset into the final mono-liganded state reconstruction. (C) Distribution of particles that adopt un- (orange), mono- (yellow), and di- (grey) liganded states in the sub-saturating datasets both individually and combined. Several poorly defined particles (blue) were also distinguished during the data processing. These particles resulted in reconstructions with poor/missing density in variable regions (for example the binding sites or pore line M2 α-helices) making them impossible to classify.

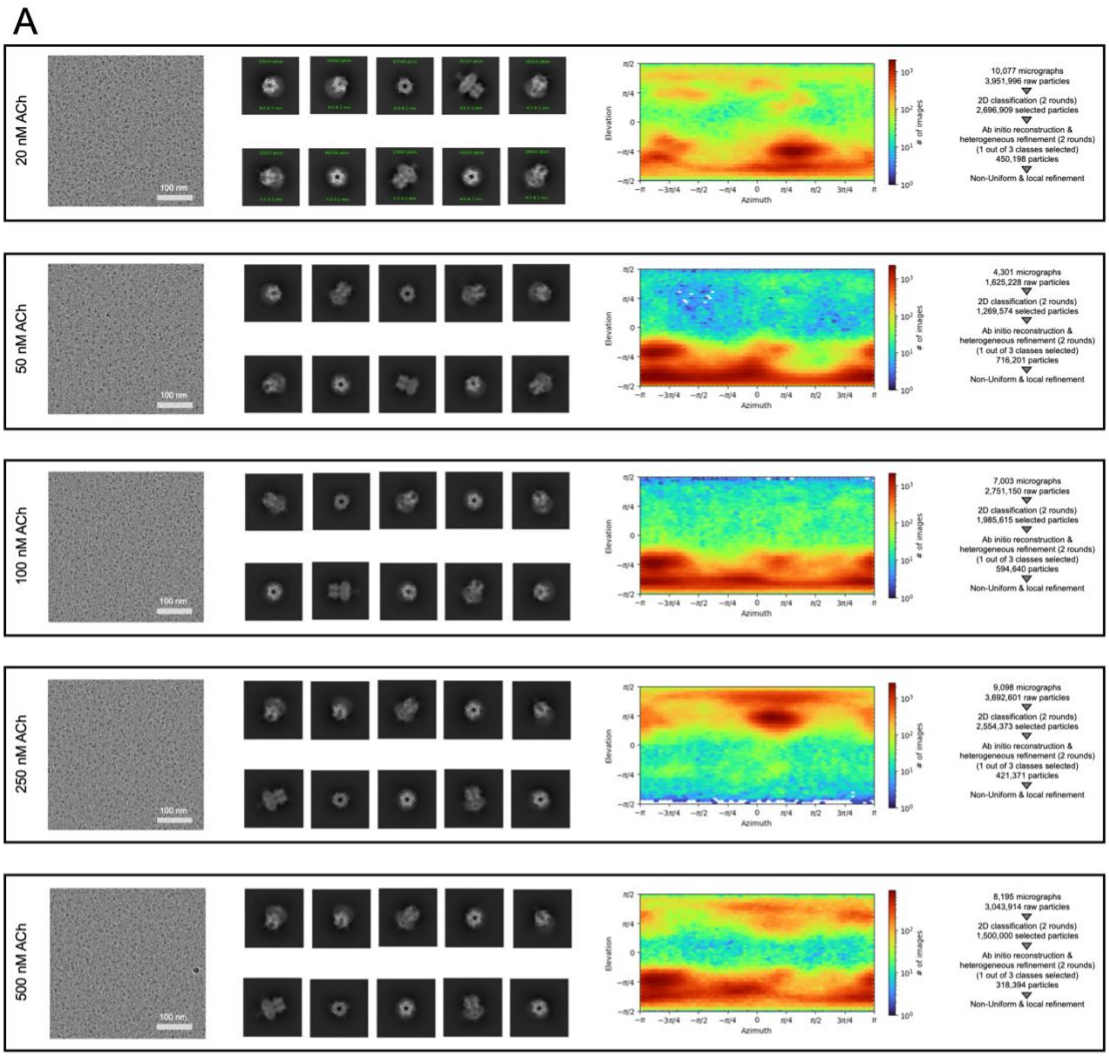

B

2,461,091 particles from consensus refinements

3DVA clusters (8 clusters), 3DVA intermediates (30 frames), 3D classification (10 classes) on each dataset individually

2,461,091 particles

Combine non-apo particles and subject to 3D classification (30 classes)

1,494,365 particles

Heterogeneous refinement and 3D classification with reference maps (un-, mono-, and di-liganded reference maps)

772,485 particles

Overlap, Non-Uniform & local refinement

379,957 particles

Heterogeneous refinement and 3D classification with reference maps (un-, mono-, and di-liganded reference maps)

379,957 particles

Overlap, Non-Uniform & local refinement

129,828 particles

C

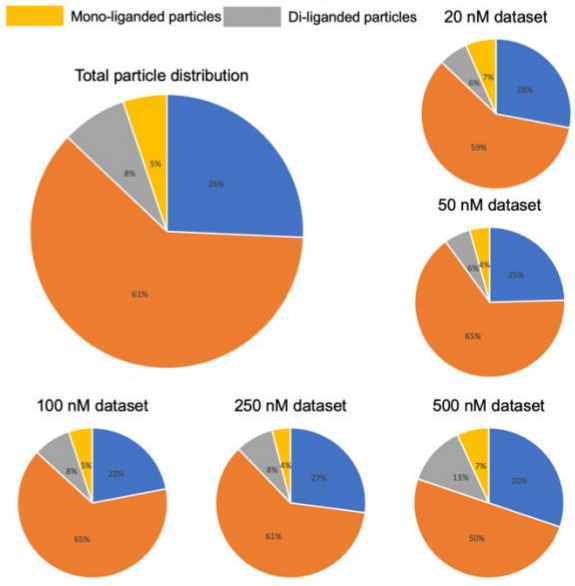

small subset of particles in the two datasets adopted the mono-liganded conformation.

To increase the number of particles in the mono-liganded conformation and thus increase the resolution of the mono-liganded density maps, additional datasets were recorded in the presence of 100 nM, 250 nM, and 500 nM ACh. Each data set was processed individually using the same strategy described above leading to consensus refinements at increasing ACh concentrations with increasing agonist density in both binding sites (Fig. 6.6). Once again, 3DVA revealed substantial conformational heterogeneity in each dataset and captured transitions from the un-liganded to the di-liganded state along the principal components of variability, although increasing ACh led to larger proportions of particles adopting the di-liganded state. Significantly, the same mono-liganded conformation was identified in each of these datasets further confirming that α_{γ}-γ is the high affinity site for ACh. The proportion of particles that adopt this mono-liganded state was similar at each concentration of ACh (20 nM: ~8%, 50 nM: ~5%, 100 nM: ~6%, 250 nM: ~4%, 500 nM: ~8%) – consistent with the expected proportions of flipped or primed conformations at each of these ACh concentrations (see below). The five datasets gave five mono-liganded maps that were qualitatively similar, but each still exhibited relatively low resolution.

To increase the number of particles used for mono-liganded state reconstruction, particles that were included in the mono-liganded consensus refinements of each of the five datasets at sub-saturating concentrations were combined and collectively subject to further processing (see Figures 6.4 and 6.5 for a summary of the data processing protocol) yielding a density map at 3.13 Å resolution. In this map, the density for the agonist binding sites, the channel pore and the agonist bound to the α_{γ}-γ orthosteric site was of sufficient quality for model building.

Figure 6.6 Agonist density in datasets recorded at sub-saturating ACh concentrations
A) Full view of the nAChR with boxed region depicting the view shown in panels B and C. Density at the α_{γ}-γ site (panel B) and α_{δ}-δ site (panel C) is shown for the consensus refinements of each sub-saturating ACh dataset. A cartoon representation of the bound state model is shown and coloured according to subunit (α subunits, yellow; β subunit, pink; δ subunit, blue; γ subunit, green) with the bound ACh molecules shown as red sticks. Density maps are shown as transparency surfaces with the red patches of density corresponding to the ACh density in each map.

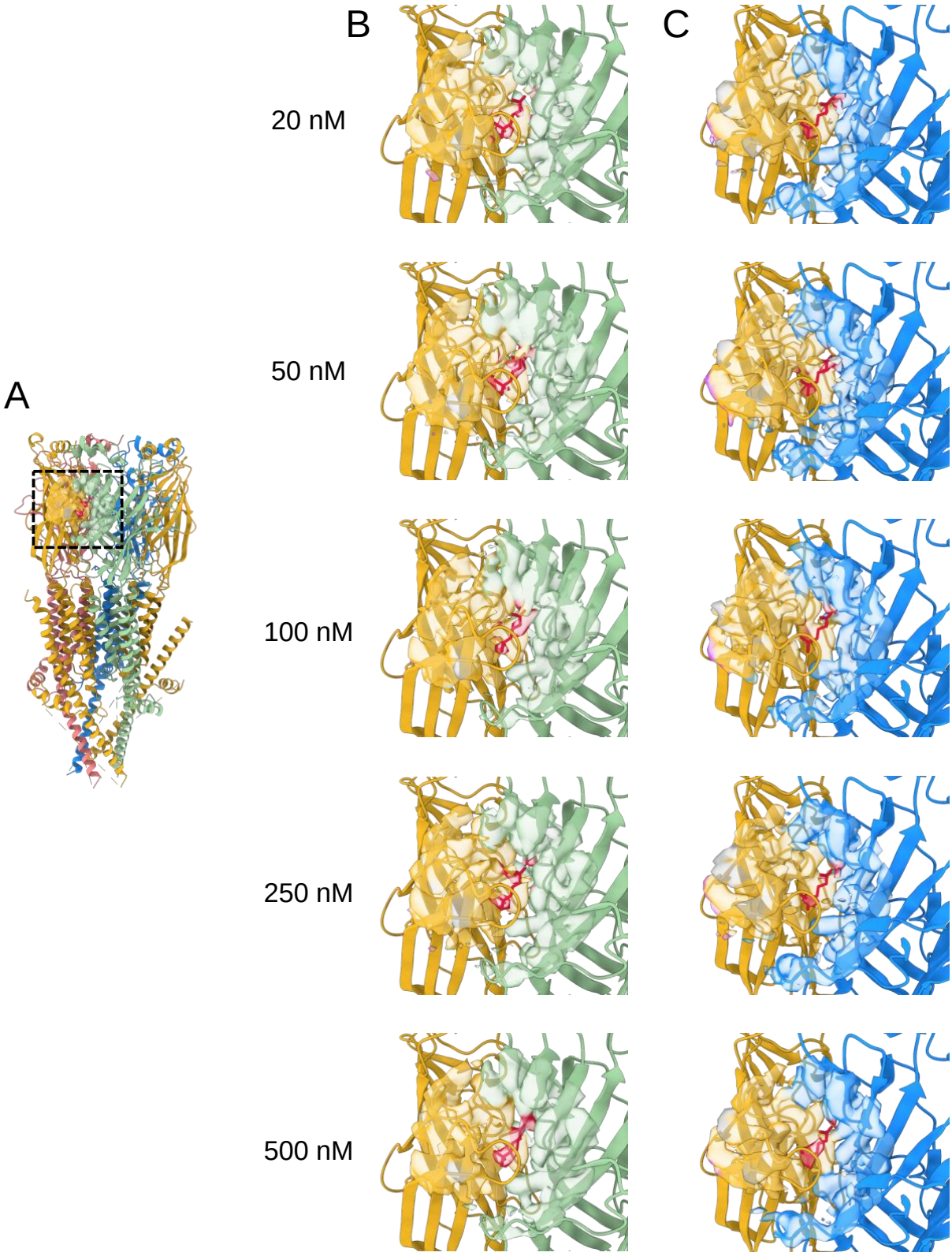
A
B
C
20 nM
50 nM
100 nM
250 nM
500 nM

6.5.4 Structures of un-, mono-, and di-liganded states.

Models of the nAChR in un-, mono-, and di-liganded states were built to compare the mono-liganded to the two end states. In the mono-liganded state, the α_γ subunit, where ACh is bound, adopts an active-like conformation similar to that observed in the di-liganded state, while the α_δ subunit remaining in an inactive-like conformation similar to that observed in the un-liganded state. Notably, this conformational asymmetry is not only observed at the orthosteric sites but extends throughout each entire subunit. A more detailed comparison of the mono-liganded state to the two end states will be made below, starting at the agonist binding sites and ending in the channel pore.

The binding of ACh to the α_γ-γ site leads to the capping of loop C from the principal α_γ subunit and loop F from the complementary γ subunit (Fig. 6.7, Movie 6.1) leading to a contraction of the binding site. This contraction can be quantified by measuring the distance between the Cα of α_γTyr190 on loop C and γGlu176 (Lev et al., 2017), which decreases from 14.7 Å in the apo state to 8.0 Å in the mono-liganded state and 6.9 Å in the di-liganded state. The capping of loop C also leads to a collapse of the aromatic box around the quaternary amine of ACh, which can be quantified by measuring the area of the quadrilateral formed by the Cα carbons of four aromatic box residues: αTrp149, αTyr190, αTyr198, and γTrp55. The area of this quadrilateral decreases from 109 $Å^2$ in the un-liganded state to 79 $Å^2$ in the mono-liganded state and 73 $Å^2$ in the di-liganded state (Fig. 6.8). Even though the α_γ-γ binding site has not contracted in the mono-liganded state to the same extent as the di-liganded state, the remainder of the subunit appears to have transitioned to an active state suggesting that a complete binding site contraction is not required to promote allosteric transitions (see below).

Figure 6.7 Loop C capping at the α_{γ}-γ and α_{δ}-δ sites in un-, mono-, and di-liganded states
Agonist binding sites in the un- (pink), mono- (blue), and di- (green) liganded state models are shown from top-down views. The left column shows the α_{γ}-γ binding site and the right column shows the α_{δ}-δ binding site with loop C from the α subunits labelled and modelled ACh shown in red.

Un-liganded State

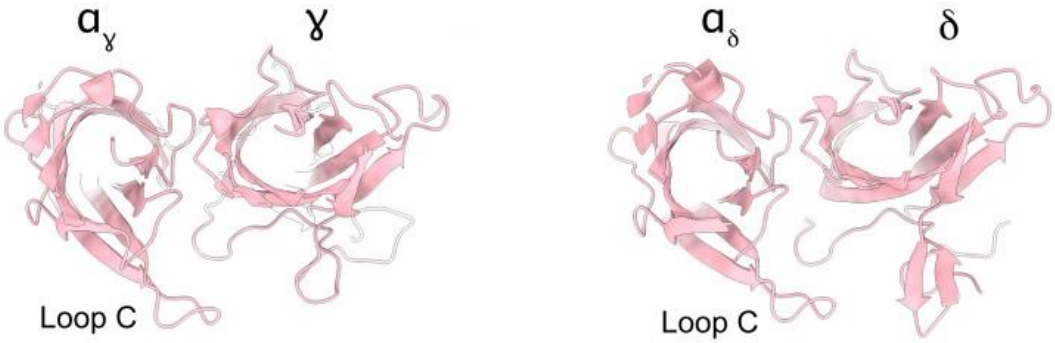

Mono-liganded State

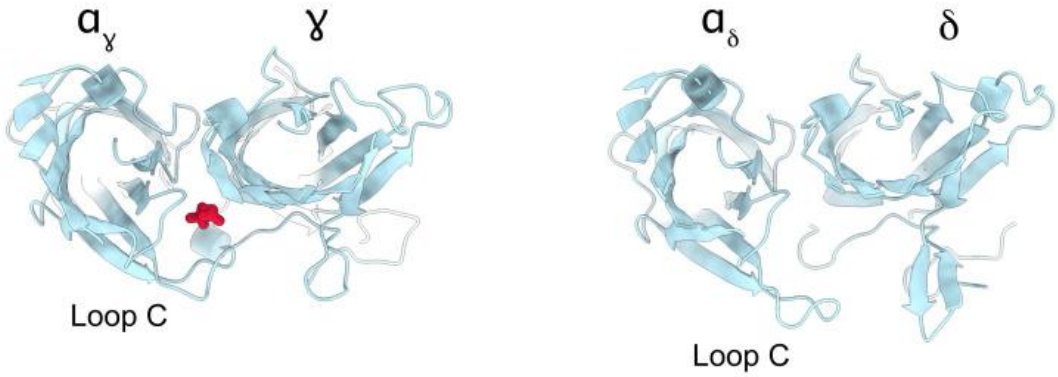

Di-liganded State

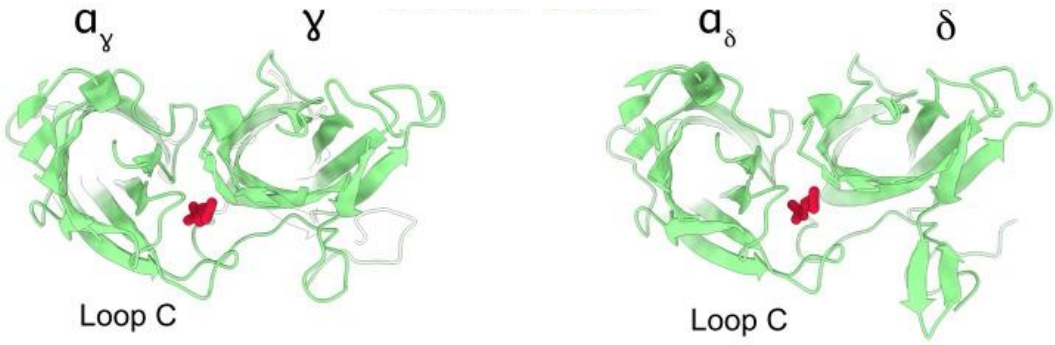

Figure 6.8 Evolution of the agonist site aromatic box in un-, mono-, and di-liganded states
A top-down view of four aromatic residues that contribute to the aromatic box, which coordinates the quaternary amine of ACh, in un-liganded (pink), mono-liganded (blue) di-liganded (green) states at the (A) α_{γ}-γ and (B) α_{δ}-δ sites. The Cα carbon of each aromatic box residue is shown as a ball, with the side chain shown as transparent sticks projecting away from the viewer. Imaginary lines connecting the Cα carbons highlight the contraction of the aromatic upon ACh binding. The distance measurements between residues were made between the Cα carbons after alignment with the complementary subunit ECD. Modelled ACh in the di-liganded state is shown as sticks coloured by atom (grey, carbon; blue, nitrogen; red, oxygen).

A

α_{γ}-γ binding site

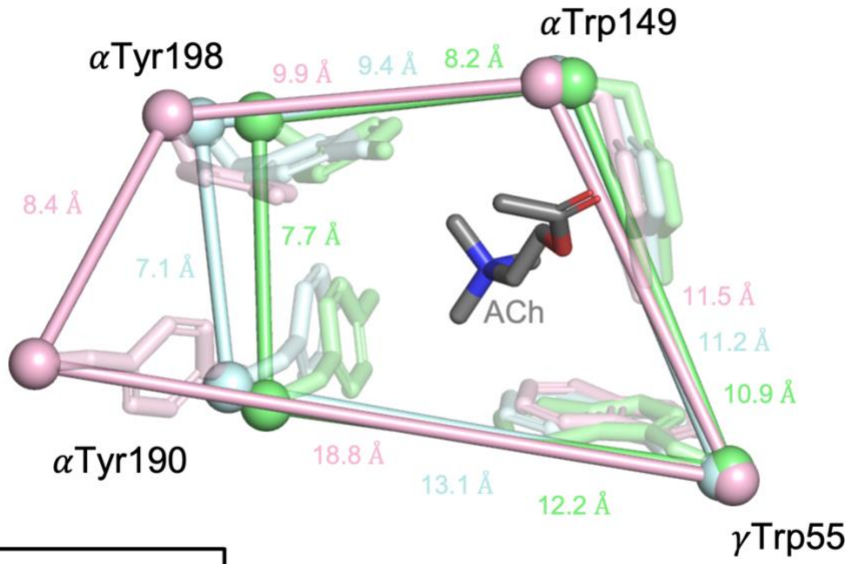

Un-liganded state
Mono-liganded state
Di-liganded state

B

α_{δ}-δ binding site

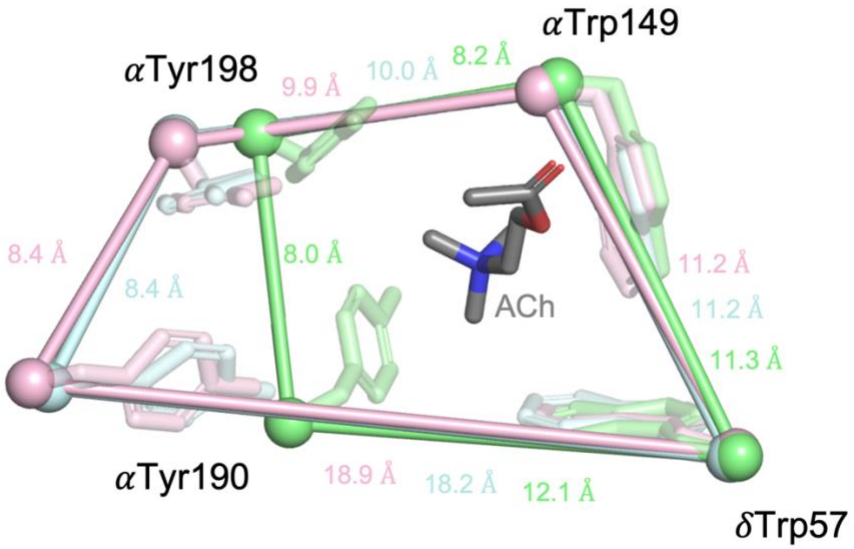

In contrast, the α_δ-δ site in the mono-liganded state remains unoccupied. Although both α_δ loop C and δ loop F remain mostly uncapped (Fig. 6.7), both loops move slightly toward their positions in the di-liganded state creating a subtle contraction and thus potentially a priming of the binding site. In particular, the distance between the Cα of α_δTyr190 on loop C and δGlu176 on loop F decreases from 13.7 Å in the un-liganded state to 12.6 Å in the mono-liganded state. This contraction of the α_δ loop C, however, is too small to condense the aromatic box of α_δ-δ around the bound agonist, with the quadrilateral formed by the Cα carbons of αTrp149, αTyr190, αTyr198, and δTrp57 only decreasing from 107 $Å^2$ in the un-liganded state to 106 $Å^2$ in the mono-liganded state. The same quadrilateral in the di-liganded state has an area of 75 $Å^2$ (Fig. 6.8).

The binding of agonist at the α_γ-γ site triggers a conformational change that manifests itself throughout the ECD leading to altered packing at the ECD-TMD interface. In fact, the α_γ and γ subunits undergo essentially the same motions upon transitioning from the in the un- to mono-liganded states that are observed upon transitioning from the un- to the di-liganded states. The ECD of the α_γ subunit undergoes a counterclockwise twisting and rocking motion along with a radial tilting that shifts the extracellular end of the ECD toward the γ subunit and the membrane juxtaposed end toward the β subunit. Notably, α_γVal46 (β1-β2 loop) moves from the pore proximal side of α_γPro265 (M2-M3 loop) in the un-liganded state to the pore distal side in the mono-liganded state (Fig. 6.9). The relative positions of α_γVal46 and α_γPro265 closely resemble that of the di-liganded active state indicating the subunit has adopted an "active-like" conformation (Chapter 5 and Calimet et al., 2013). Surprisingly, despite the α_δ-δ orthosteric site being empty and adopting a conformation similar to the un-liganded state, the ECD-TMD interface in the α_δ and δ subunits in the mono-liganded state adopts a conformation intermediate

Figure 6.9 α subunit ECD – TMD interface in the un-, mono-, and di-liganded states
α subunits of the un- (pink), mono- (blue), and di- (green) liganded states aligned by their M2-M3 loops to highlight the relative position of the β1-β2 loops. In the un-liganded state, αVal46 from both α subunits are positioned on the pore distal side of αPro265. In the di-liganded state, αVal46 from both α subunits are positioned on the pore proximal side of αPro265. In the mono-liganded state, Val46 from α_γ has transitioned to the pore proximal side of α_γPro265 while α_δVal46 remains on the pore distal side of α_δPro265.

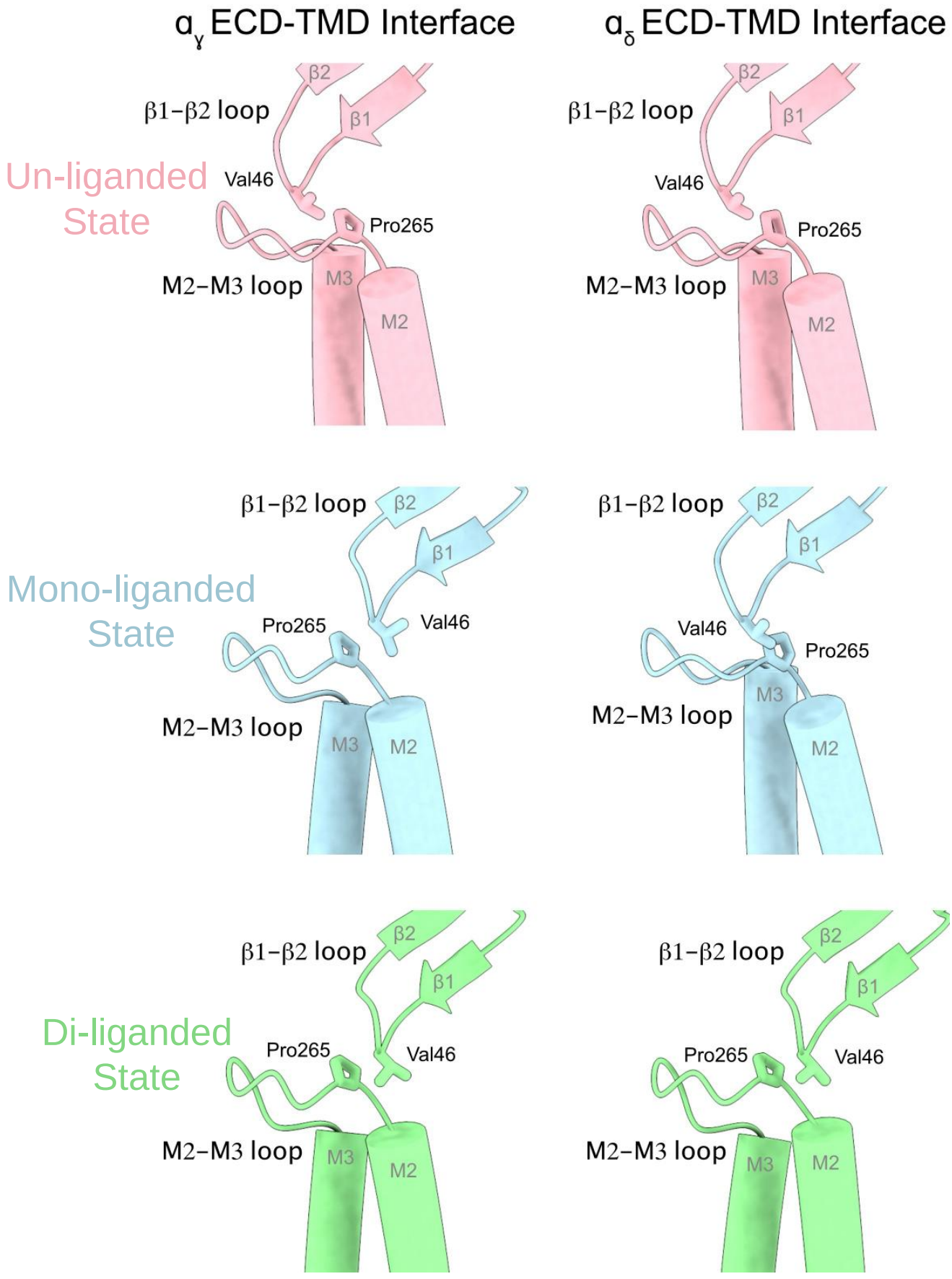
αγ ECD-TMD Interface
αδ ECD-TMD Interface
Un-liganded State
Mono-liganded State
Di-liganded State
β1−β2 loop
β2
β1
Val46
Pro265
M2−M3 loop
M3
M2

between inactive and active. Specifically, the β1-β2 loop of α_δ shifts slightly towards the pore while the M2-M3 loop of α_δ moves slightly away from the pore. Rather than sitting clearly on the pore distal side of α_δPro265 (M2-M3 loop), however, α_δVal46 is now positioned immediately adjacent to α_δPro265 in the mono-liganded state (Fig. 6.9).

Finally, the ACh-induced changes at the ECD-TMD ultimately lead to a conformational transition at the level of the ion channel pore. The movements of α_γVal46 (β1-β2 loop) from the pore proximal side of α_γPro265 (M2-M3 loop) in the un-liganded state to the pore distal side in the mono-liganded state allows the α_γM2 α-helix to twist clockwise and tilt away from the pore axis to the position it adopts in the di-liganded state (Fig. 6.10, Movie 6.2). Notably, the extracellular ends of the remaining M2 α-helices, including the α_δM2 α-helix, also tilt away from the pore axis, although to a lesser extent than in the di-liganded state. These other M2 helices, especially α_δM2, do not undergo as large of a twisting motion as in the di-liganded state leaving the channel gate forming residues near their position in the un-liganded, closed, conformation. Although adopting a conformation similar to that observed in the un-liganded resting conformation, these pore lining α-helices appear poised to transition to the open state.

To test the functional pore conformation of the mono-liganded state, unbiased molecular dynamics simulations were performed. These preliminary MD simulations suggest the pore of the mono-liganded state is not hydrated and is thus non-conductive (Fig. 6.11).

Figure 6.10 Activation in the α_γ subunit may prime the α_δ subunit for activation

M2 α-helices in the un- (pink), mono- (blue), and di- (green) liganded states are overlayed and shown from a top-down view. The top of the M2 α-helix in the α_γ subunit and the Leu9' residue (shown as sticks), overlap in both the mono-liganded and di-liganded state indicating M2 fully transitions to an active state upon ACh binding to the α_γ-γ. In the α_δ subunit of the mono-liganded state, the top of the M2 α-helix has partially transitioned to the active state while the Leu9' residue remains in the inactive state.

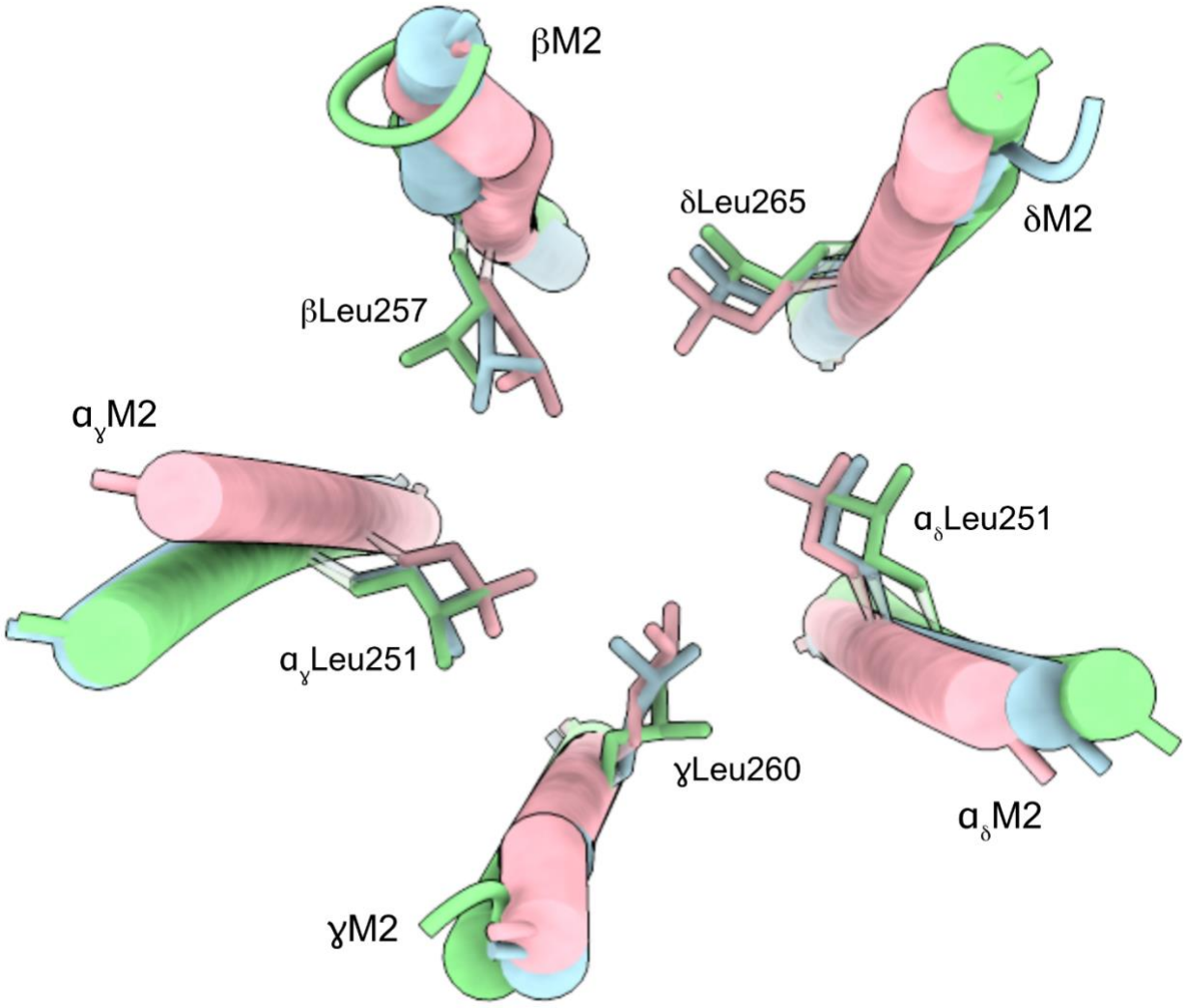
βM2
βLeu257
δLeu265
δM2
αγM2
αγLeu251
αδLeu251
γLeu260
αδM2
γM2

Figure 6.11 Pore hydration of mono- and di-liganded states

Plots of pore hydration over time are shown for the mono- (top) and di- (bottom) liganded states. Taken from preliminary MD simulations. Cα restraints were applied for the first 50 ns of the simulations before being released for the final 50 ns of simulation time. Tan areas are dehydrated, with increasing hydration depicted as darker blue. Simulations were performed by Anna Ananchenko.

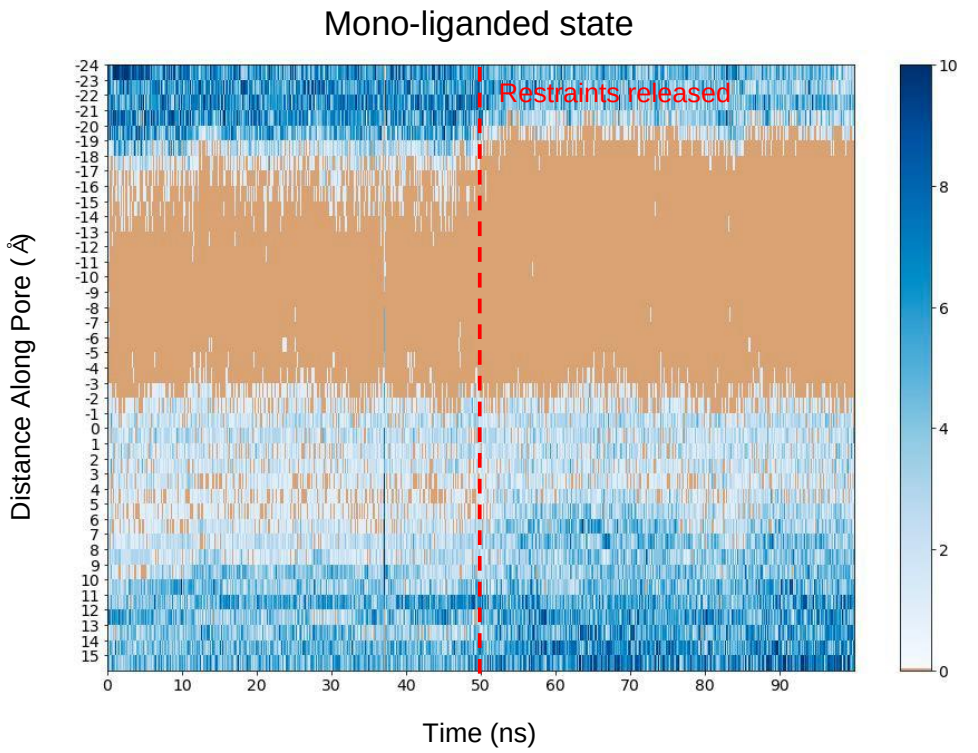
Mono-liganded state
Restraints released
Distance Along Pore (Å)
Time (ns)

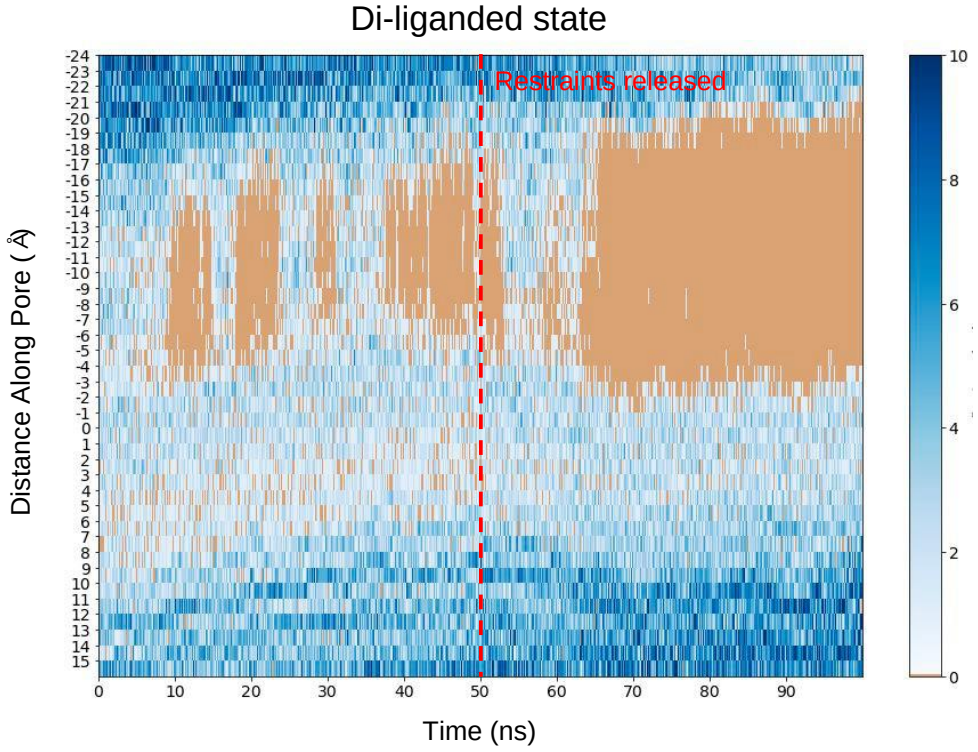
Di-liganded state
Restraints released
Distance Along Pore (Å)
Time (ns)

6.6 Discussion

Electrophysiology recordings describing nAChR activation were initially interpreted in terms of a two-step mechanism whereby agonist binds to an inactive resting state receptor that then isomerizes into an active open state, implying the nAChR exists in two conformations that differ in terms of their agonist binding affinity (del Castillo and Katz, 1957). Subsequent single channel recordings, however, revealed gating behaviour suggestive of more complex gating. In particular, the nAChR exhibits three distinct open channel lifetimes with two short and one long channel openings that predominate at low and high agonist concentrations, respectively. Stochastic fitting of single channel data suggested that the two orthosteric sites on the nAChR exhibit distinct ACh binding affinities, with the shorter channel openings attributed to un- and mono-liganded openings and the longer channel openings attributed to di-liganded channel openings (Colquhoun and Hawkes, 1981). It has also been noted that less efficacious or partial agonists, which exhibit low open probabilities at saturating ligand concentrations, exhibit the same channel opening profile (i.e., three open channel lifetimes) as that observed with the full agonist, ACh thus implying similar un-, mono-, and di-liganded opening events. To account for the low open probability of partial agonists, it was proposed that a primed state exists in the reaction coordinate just prior to the channel opening events, with the low efficacy of partial agonists attributed to a reduced ability to stabilize the primed nAChR (Lape et al., 2008; Mukhtasimova et al., 2009). The nAChR thus adopts a minimum of three conformational states along the activation trajectory, resting to primed to open, which each bind zero, one, or two agonists (Mukhtasimova et al., 2016). The stability of the resting, primed, and open states are such that they are appreciably occupied during the gating transition.

The cryo-EM structural studies presented in this chapter elucidate two key features regarding the structural transitions that occur along the trajectory from unliganded to the di-liganded channel open state. First, at sub-saturating concentrations of ACh, particles with strong agonist density at the α_γ-γ site but no density at the α_δ-δ site were consistently observed. These particles could be used to capture a mono-liganded state with agonist bound to α_γ-γ. In contrast, particles with strong agonist density at the α_δ-δ site but not at the α_γ-γ site could not be identified and a mono-liganded structure with ACh bound to α_δ-δ but not the α_γ-γ site could thus not be captured. The cryo-EM data show that at sub-saturating agonist concentrations, ACh binds to the α_γ-γ orthosteric site of the *Torpedo* nAChR prior to binding to the α_δ-δ site and thus that the α_γ-γ site is the higher affinity orthosteric site. This conclusion is consistent with observations from a recent cryo-EM study of the nAChR, which noted an ensemble of interactions at α_γ-γ orthosteric site that are absent at α_δ-δ, with the absence of these interactions at α_δ-δ possibly leading to increased fluctuations between capped and uncapped conformations of loop C and thus faster agonist dissociation (Zarkadas et al., 2022). Both sets of structural observations, however, contradict [^{125}I]-α-bungarotoxin competition binding experiments performed on either intracellularly assembled dimeric α plus complementary subunit pairs (α_γ-γ or α_δ-δ) or assembled $\alpha_2\beta\delta_2/\alpha_2\beta\gamma_2$ pentamers, which suggest that the α_δ-δ site is the high affinity orthosteric site (Blount and Merlie, 1989; Sine and Claudio, 1991; Prince and Sine, 1996). It is possible that the hetero-pentameric structure of the *Torpedo* nAChR ($\alpha_2\beta\gamma\delta$) imposes structural restraints on the orthosteric sites that lead to enhanced agonist affinity at α_γ-γ.

It is clear that the observed affinity differences between the two orthosteric sites in the *Torpedo* nAChR do not correlate with the affinity differences between the two sites in the mammalian adult and fetal forms. In the mouse and human adult nAChR, which contain an ε

subunit instead of γ, the two agonist binding sites are essentially equivalent (Jha and Auerbach, 2010), while in the fetal nAChR, which contains a γ subunit instead of ε, the affinity for ACh at the α_{γ}-γ site is much higher. In fact, the relatively high ACh affinity at the α_{γ}-γ site in the open (K_D=0.15 nM) versus the resting (K_D=8 uM) state contributes -6.9 kcal/mol of energy toward channel activation (Nayak and Auerbach, 2013). Notably, the structural correlates of affinity in the mammalian nAChR are thought to arise mainly from sequence variations in the β4-β5 hairpin (PDGC in ε, EGGY in γ, and DSGY in δ in the mouse nAChR) (Nayak et al., 2016). Although some phylogenetic analyses suggest the *Torpedo* nAChR γ subunit more closely resembles the mammalian adult ε subunit, the corresponding β4-β5 hairpin in the *Torpedo* nAChR exhibits a sequence (NDGS) distinct from that of all three mammalian subunits thus possibly accounting for observed differences in affinity between the various nAChRs.

A second key finding from this study is that agonist binding to the α_{γ}-γ site leads to a capping of both the α_{γ} subunit C loop and the γ subunit F loop around the bound agonist, with these local conformational transitions in α_{γ} extending to both the ECD-TMD interface and the channel pore (Movie 6.3). In contrast, α_{δ} remains predominantly in a non-activated conformation. The muscle nAChR thus undergoes a subunit sequential, as opposed to the domain sequential gating mechanism postulated for homomeric pLGICs. These structural observations highlight the complexity underlying allosteric transition in the muscle nAChR relative to other allosteric proteins, such as hemoglobin. While allosteric transitions in the heteromeric muscle nAChR clearly deviate from an all or none fashion with asymmetric subunit structural transitions along the trajectory between un-liganded resting and di-liganded active or open states, allosteric transitions in hemoglobin are an all or none phenomenon with ligand

binding facilitating subunit symmetric transitions between two distinct conformations, tense and relaxed.

One intriguing feature of the mono-liganded structure is that although agonist binding to the α_γ-γ site leads to activation of both the α_γ subunit, subtle movements also occur in the ECD, at the ECD-TMD interface, and in pore of the α_δ subunit as if agonist binding to α_γ-γ primes the α_δ subunit for activation (Movie 6.3). I propose that the mono-liganded structure corresponds to the kinetically observed primed state based on the following observations:

First, each of the sub-saturating datasets was recorded at concentrations near the midpoint of the dose-response curve where primed states are expected to be their most prevalent. To demonstrate this, I calculated the probability of the nAChR adopting a given state at a given concentration of ACh based on equilibrium constants determined for the human adult nAChR (Fig. 6.12). In the absence of ACh the probability of the receptor being in the un-liganded/resting state is ~100%, while the probability of the nAChR being in a pore-open state (AO, A_2O, and A_3B) at 50 uM ACh is close to 100%. These results echo what is observed in the cryo-EM experiments, although slight variability is observed for the un-liganded state. The probability of the nAChR adopting a primed state (AR' or A_2R') at the sub-saturating concentrations of ACh used in our experiment would be 1.35%, 1.42%, 1.38%, 1.23%, and 1.03%, for the 20, 50, 100, 250, and 500 nM ACh datasets, respectively (Fig. 12b). While this is slightly less than the 4-8% of particles observed in the mono-liganded state in each sub-saturating dataset, the relative distributions of these states between 20-500 nM ACh closely resembles that observed in the cryo-EM data, particularly when one considers that the calculations do not take into account time-dependent desensitization.

Figure 6.12 Probability of state occupancy with increasing ACh concentration

(A) The probability of the nAChR adopting conformational states from the kinetic scheme shown in Fig. 6.1 at different ACh concentrations were calculated using experimentally derived equilibrium constants for the human adult nAChR. Each state in the kinetic scheme is represented as a different colour line indicated in the legend. Dashed lines indicate concentrations of ACh where sub-saturating datasets were collected. (B) A zoomed in view of the grey box in panel A to allow visualization of less populated states. Note that these calculations do not account for time-dependent transitions to the desensitized state.

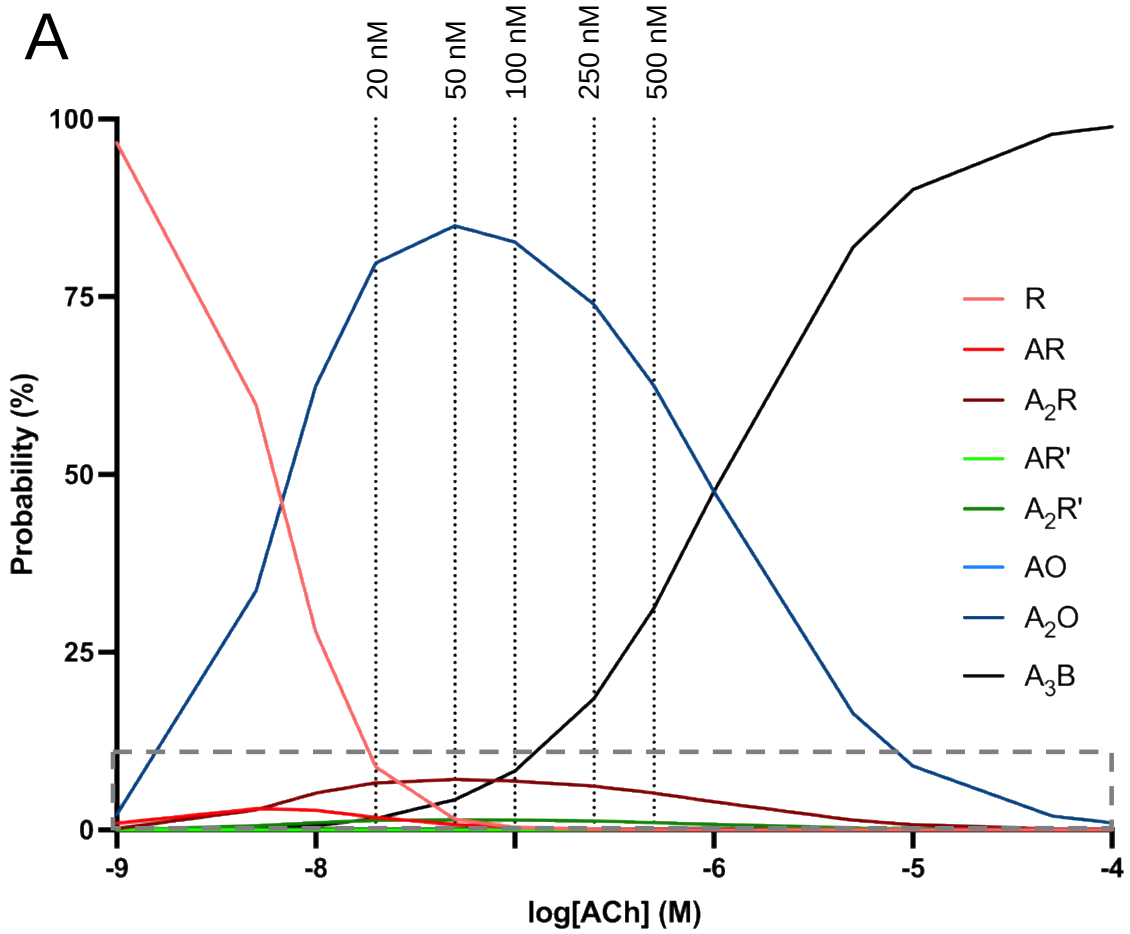
A
20 nM
50 nM
100 nM
250 nM
500 nM
100
75
50
25
0
Probability (%)
-9
-8
-6
-5
-4
log[ACh] (M)
R
AR
A2R
AR'
A2R'
AO
A2O
A3B

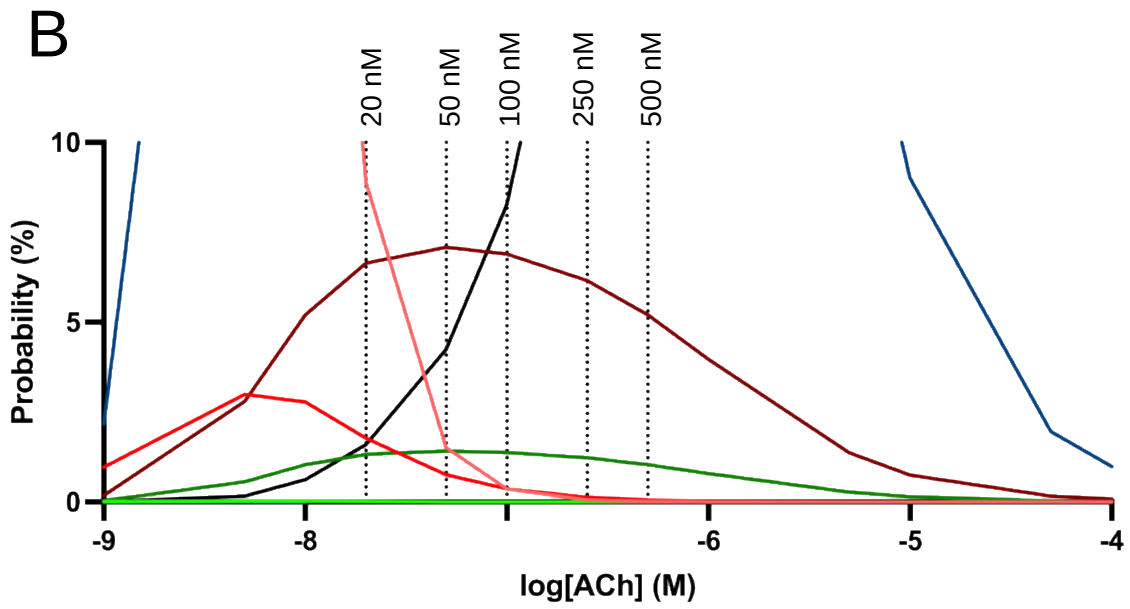
B
20 nM
50 nM
100 nM
250 nM
500 nM
10
5
0
Probability (%)
-9
-8
-6
-5
-4
log[ACh] (M)

Second, the mono-liganded state displays several structural features expected for an intermediate between the un-liganded apo/closed state and the di-liganded agonist-bound/pore-open state. The primed state is expected to exhibit a closed channel pore. Consistent with this expectation, MD simulations suggest that the pore of the mono-liganded state is dehydrated. Despite being dehydrated, the pore of the mono-liganded state is dilated slightly compared to the un-liganded state and thus requires smaller movements to ultimately open the channel pore. Although the pore remains closed, it appears primed for activation.

Priming has also been associated with loop C capping. When pore mutations are engineered in the human adult nAChR, the channel opens spontaneously, with almost all these opening events being brief (Mukhtasimova et al., 2009). When disulfide bonds are engineered between loop C and the complementary subunits, openings are predominantly long duration, leading to the hypothesis that loop C capping promotes a doubly primed state. When the same disulfide bridges were engineered at a single site, however, there was no change in the frequency of short vs long openings making it unclear whether a single capped loop C is enough to promote a singly primed state. More intriguing still, in the absence of pore mutations, oxidizing agents no longer induce long opening events meaning there is gate-site communication that allows the C loops to get trapped in their capped conformations only when the channel spontaneously opens. This is consistent with what observe in the mono-liganded state, where pore dilation has partially transitioned the α_s subunit to an active-like state at the ECD – TMD interface, slightly priming the α_s-δ site for the second binding event.

Finally, I recently proposed that nAChR activation occurs through the relaxation of conformational restraints in the two α subunits (Chapter 5). It is possible that the two distinct open times observed in single channel experiments are a product of these restraints being

released asynchronously, where the binding of one agonist releases restraints at one α subunit while the binding of two agonists releases restraints in both α subunits. Energy provided by the release of restraints in one α subunit could stabilize the open state just enough that its mean lifetime is short, whereas the release of restraints in both α subunits would stabilize longer duration openings. This hypothesis would rationalize how changes in ligand occupancy correlate with changes in channel open probability.

In this work I have solved the first mono-liganded state of a pLGIC. The mono-liganded state challenges current paradigms of protein allostery, showing that agonist binding to one site activates nAChR subunits sequentially rather than by globally stabilizing an active state. While such asynchronous transitions have been suggested (Mitra et al., 2005), this is the first structural evidence of this phenomenon and opens avenues for the functional interrogation of such transitions to better understand nAChR function.

Chapter 7. General Discussion and Conclusions

The overarching goal of this thesis was to better understand the structural basis for how nAChR activity is modulated by the binding of lipids (manuscripts 1 & 2) and agonists (manuscript 3 & 4). These two types of binders may appear superficially distinct, but under the lens of pharmacology the lines between the two can become blurred. An agonist in pharmacology refers to a molecule that activates an allosteric protein by binding with higher affinity for the active (open) vs the inactive (closed) conformation (Monod et al., 1965). The additional binding energy helps to stabilize and thus promote transitions to the active state with the ratio of how much stronger an agonist binds to the active vs resting state dictating its efficacy (Auerbach, 2016). When no agonist is present, the muscle-type nAChR has an estimated open probability of ~10^{-6} as the resting state is estimated to be 8.3 kcal/mol more stable than the unliganded open state (Purohit et al., 2008; Nayak et al., 2012). The full agonist ACh binds ~10,000 times stronger to the open state than the resting state stabilizing the open state by 10.2 kcal/mol and increasing the open probability to 0.96 (Nayak and Auerbach, 2017). The ratio of binding affinity for the open vs resting state is lower for less efficacious agonists, such as choline, which therefor have a lesser ability to stabilize the open state. The same exact principals exist for lipids and can be easily illustrated for the lipid-gated channel Kir2. The open conformation of Kir2 has a much higher affinity for PIP_2 than the resting state, so PIP_2 acts as an agonist to directly gate open the channel (Hansen et al., 2011) (see appendix for further discussion).

In the case of the nAChR, lipids do not directly activate the channel and are thus not considered agonists. Instead, they can be considered as allosteric modulators as they appear to exert their effects through conformational selection mechanisms without directly activating the

nAChR. This is evident for the anionic lipids PS and PA, which when included in PC membranes (that alone stabilize an uncoupled state) preferentially stabilize desensitized and resting conformations, respectively. While it is much more difficult experimentally to characterize the influence of a lipids as allosteric modulators than soluble compounds (see for example (Smelt et al., 2018; Arias et al., 2022)), attempts to test such allosteric modulation kinetically support this type of model (Dietzen et al., 2022; Petroff et al., 2022).

Be it an agonist or a lipid, these compounds exert their functional effects through some sort of allosteric mechanism that influences the stability of the nAChR in its various conformational states. While it is relatively well established which states these molecules stabilize, the mechanisms by which they stabilize these states remain unclear. This is the principal goal of each of the chapters in this thesis, to either define or shed light on the underlying mechanisms by which agonists or lipids exert their functional effects.

7.1 Attempts to uncover mechanisms of lipid modulation in the nAChR

7.1.1 What we've learned about how lipids may influence nAChR function

Lipid modulation of the nAChR can occur through binding of lipids to specific sites (direct mechanisms), changes in bilayer physical properties (indirect mechanisms), and most likely, through a combination of both. Lipid binding sites can be non-annular or annular. While non-annular sites were originally suggested (Jones and McNamee, 1988; Brannigan et al., 2008), more recent cryo-EM structures and simulations seem to indicate that only annular sites exist on the nAChR (Sharp and Brannigan, 2021; Rahman et al., 2022; Unwin, 2022; Zarkadas et al., 2022). Each subunit of the nAChR shows appreciable lipid binding, and while the occupancy and specificity of each site is expected to differ, there aren't any binding sites that appear to have

evolved to tightly coordinate a specific lipid (see examples of PIP_2 binding sites in Kir2 channels and $GABA_A$Rs in the Appendix). Each of the M4 α-helices, despite their limited sequence homology, fold in similar ways and have similar interaction patterns with their neighboring M1 and M3 α-helices and so bulk membrane effects like hydrophobic mismatch, curvature, or lateral pressure are expected to influence each subunit similarly. It is thus unsurprising that no single residue in any of the peripheral M4 α-helices is critical to nAChR function (at least in the context of an oocyte membrane) and no single interaction can fully explain how lipids modulate nAChR function. Instead, we favor a model similar to that proposed for voltage-gated K^+ channels (Jiang, 2018) where the summation of energetic contributions, from both direct and indirect mechanisms of lipid modulation, through each M4 α-helix cumulate to dictate the effect of lipid composition on nAChR function.

While our data suggest each subunit plays an independent role in lipid modulation, this does not imply that their contributions are equal. In fact, lipid binding is expected to differ depending on the subunit. Anionic lipids, which primarily exist in the inner leaflet of the membrane, play a major role in nAChR function and their binding should be influenced by the charge distribution of the various binding sites. While the majority of lipid facing residues in the TMD are non-polar, pockets rich in positively charged residues form at the intracellular end of the TMD on the M3, M4 and MX α-helices (Fig. 7.1). The pockets have less electro-positivity when the complementary face of the pocket is formed by an α subunit, as the conserved cationic residue in M4 in the non-α subunits (βArg437, δArg455, and γLys449, *Torpedo* numbering) is replaced by a His (αHis408) (Fig. 7.1 top row). Unpublished course-grained simulations of the nAChR in membranes containing anionic lipids are consistent with an enrichment of anionic

Figure 7.1 Electrostatic potential of lipid binding sites at different subunit interfaces
Each of the five subunit interfaces in the *Torpedo* nAChR apo state (PDB: 7QKO) are shown, with each view rotated by 72°. A slightly transparent surface representation is coloured according to the coulombic electrostatic potential of the molecule, with a scale bar shown in the bottom right. The two interfaces with an α subunit on the complementary face are shown in the top row, the two with α subunits at the principal face are shown in the middle row, and the one interface without an α subunit is shown in the bottom left. Bound lipids in the cryo-EM structure are shown as sticks and coloured yellow.

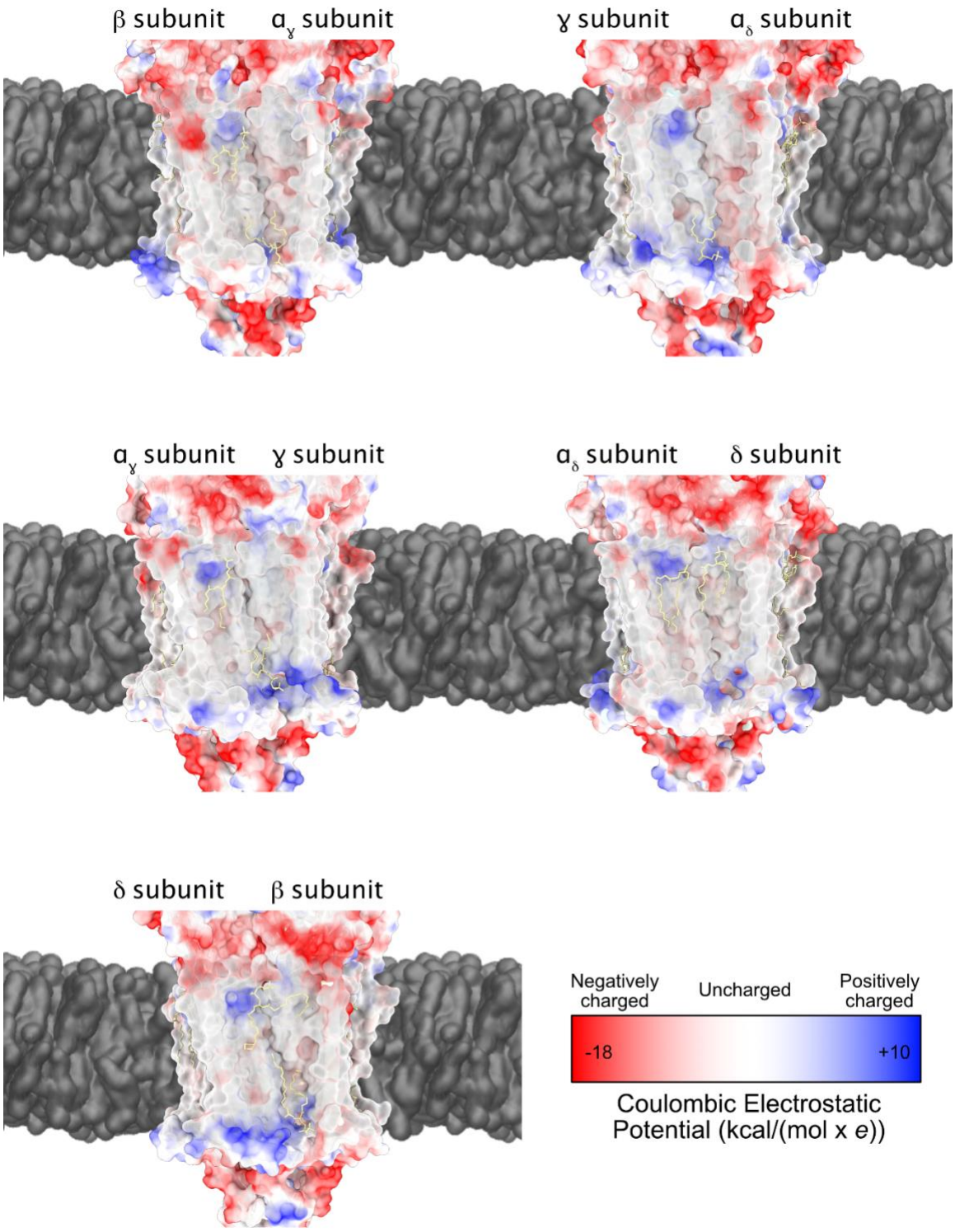
β subunit
αγ subunit
γ subunit
αδ subunit
αγ subunit
γ subunit
αδ subunit
δ subunit
δ subunit
β subunit
Negatively charged
Uncharged
Positively charged
-18
+10
Coulombic Electrostatic Potential (kcal/(mol x e))

lipids at interfaces where the complementary face of the pocket is not formed by an α subunit (Ananchenko et al. unpublished). Along with unique lipid binding pockets, I showed that the mechanisms of lipid modulation likely differ between subunits, as, for example, a known M4 – M1 pathway in the α subunits that influences function is not conserved in the non-α subunits. Other studies have provided a potential subunits specific link between the M4 and M2 α-helices of the β and δ subunits via a conserved intracellular salt bridge (Strikwerda and Sine, 2021; Strikwerda et al., 2023), but these results are inconsistent with our data and may arise from differences in expression systems (see below). Other mechanisms of lipid induced modulation have remained elusive in our study and may require other techniques to decipher.

The most intriguing influence of lipids on the nAChR is their ability to influence the proportion of receptors in an activatable conformation where agonist binding couples to gating. The hypothesis that interactions between the M4 C-termini and the ECD – TMD interface regulate coupling was based on two observations: first, the M4 C-termini directly interact at the ECD – TMD interface, and second, a buried region in coupled receptors becomes solvent exposed in the uncoupled state (daCosta and Baenziger, 2009). My data show, however, that deletions of the M4 C-termini are without consequence in any subunits of the muscle nAChR. It may be that all C-terminal deletions must be performed simultaneously to see an effect, but the third manuscript of this thesis shows that coupling of binding and gating is primarily mediated through the α subunits so M4 C-terminal deletions in α alone should be sufficient to test such interactions in channel function. Furthermore, high resolution structures solved after the publication of manuscript 1 and 2 show that the resting to active transition is accompanied by a separation of the M4 C-terminus in the α_δ subunit from the ECD – TMD interface (Fig. 7.2). In fact, the general anesthetic etomidate appears to desensitize the channel, at least partially, by

Figure 7.2 αM4 tilting is correlated with nAChR activation

Resting (left; PDB: 7QKO) and active (right; PDB:7QL5) conformations of the *Torpedo* nAChR α_δ subunit are shown in pink and green, respectively. The M4 C-terminus interacts with the conserved FPF motif of the Cys-loop in the resting state but tilts away from the remainder of the subunit and becomes disordered in the active state.

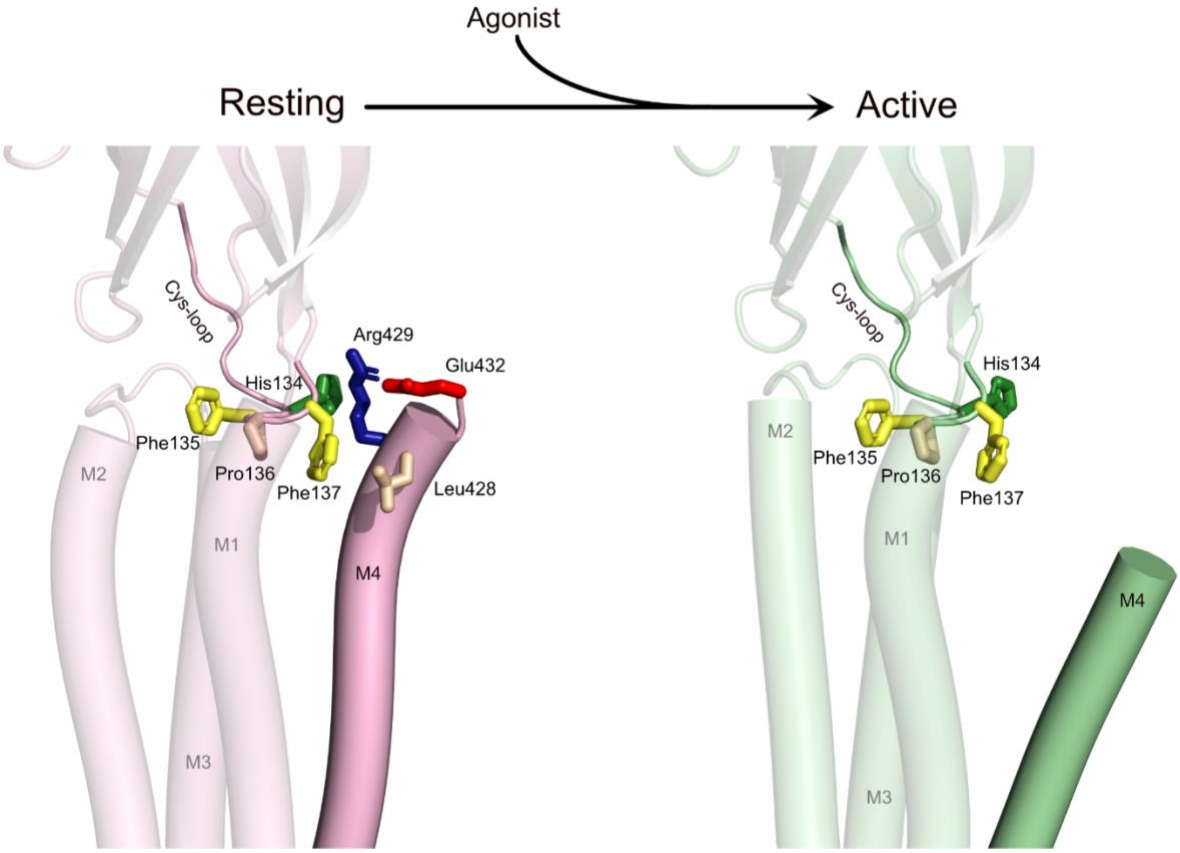
Agonist
Resting
Active
Cys-loop
Arg429
Glu432
His134
Phe135
Pro136
Phe137
Leu428
M2
M1
M4
M3
Cys-loop
His134
M2
Phe135
Pro136
Phe137
M1
M4
M3

binding between the M4 C-termini of both α subunits and ECD – TMD interface. Functional measurements also support a role for this M4 dissociation in desensitization rather than in coupling binding to gating (Rahman et al., 2022; Goswami et al., 2023). While it remains unclear what portion of the nAChR becomes solvent exposed in the uncoupled state, we now have the tools to solve structures of the nAChR in its uncoupled conformation by reconstituting it in pure POPC nanodiscs. Acquiring such a structure would significantly aide in our understanding of how lipids stabilize an uncoupled state.

7.2.2 The future of nAChR-lipid research

It is intriguing, but perhaps not surprising, that mutations to residues in the M4 α-helices have varying effects depending on their expression system. Cultured cell lines are the backbone of biochemical and biophysical research – the use of native cells like oocytes or native tissue like *Torpedo* electroplax tissue is simply not feasible for the study of most proteins. Given their importance, it is surprising that more hasn't been done to ensure a more native like membrane environment in cultured cell lines (Else, 2020). This is especially worrisome for receptors like the nAChR, which display high sensitivity to their lipid environment. I and others have collected indirect evidence for a crucial role of expression system dependent effects on M4 mutations. Specifically, M4 mutations to the muscle nAChR, the α4β2 nAChR, and the 5-HT_{3A}R that have little to no effect in oocytes, can render the receptors non-functional in HEK cells (Crnjar et al., 2021; Mesoy et al., 2022; Thompson et al., 2022). The techniques used to characterize function also change between expression systems, however, and while it is unlikely, they may also contribute to the observed discrepancies. As highlighted in manuscript 3, there are substantial differences in the literature regarding the effects of different mutations on channel function. This

is caused by differences in the type of technologies used to assess these differences (ex. single channel electrophysiology, whole cell patch clamp, TEVC, membrane potential sensitive dyes), different expression systems, (ex. HEK293T cells, BOSC cells, CHO cells, oocytes), different activating agonists (ex. ACh, Carb, choline), and different ways of analyzing the data (ex. Bind-bind-gate scheme vs primed scheme, different t_{crit} thresholds). To rule out methodological changes as the root of the observed differences, the same technique should be performed on the same M4 mutant expressed in both oocytes and HEK cells. Future studies could characterize the function of these mutants in excised patches from both types of cells to facilitate a more direct comparison.

As described above, the complexity of living cells can cloud the conclusions of mechanistic studies of lipid-protein interactions. Instead, it may be more useful to study these proteins in the context of more controlled systems. One way to do so is the use of planar bilayer systems (Maher and Allen, 2018). In this technique, a lipid concoction of a specific composition is painted into an electrophysiology chamber along 2D plane. When protein in detergent, liposomes, or nanodiscs are added to the apparatus, spontaneous insertion of the protein into the planar bilayer occurs. By monitoring the trans-bilayer voltage in response to agonist exposure, activity in a defined lipid environment can be measured. It would then be possible to measure changes in nAChR function in defined lipid compositions for different mutants allowing for much clearer understanding of the mechanisms underlying lipid modulation. This technique is of course not without its caveats. The protein would still need to be expressed in cells, the membranes of these cells collected, and then either the raw membrane pellets or detergent/liposome/nanodisc solubilized protein applied. Applying raw membranes would ensure the native like lipids are included, but the protein would likely be poorly concentrated and

other membrane proteins would also be inserted into the membrane. Purified protein reconstituted into the same lipid composition of the planar bilayer would be the best option, but obtaining enough protein through this method would be challenging. Poor control of bilayer thickness has also been reported for this technique, limiting the types of lipids that can be included (Pfeffermann et al., 2021).

Another method of characterizing nAChR function in a controlled lipid composition would be to patch giant unilameller vesicles (GUVs) with the nAChR and mutants reconstituted within them, as has been performed previously with GLIC and ELIC (Velisetty and Chakrapani, 2012; Velisetty et al., 2012, 2014; Hénault et al., 2019). In this case, receptor would need to be solubilized in detergent, purified and then incorporated into GUVs using either dialysis or Bio-Beads® (Van Den Bogaart et al., 2011). Once again, this technique should allow one to control the lipid composition of the bilayer in a native like setting but without the hydrophobic thickness requirements of the planar bilayer technique. The major drawback of this is our current inability to purify muscle type nAChRs expressed in cell lines in sufficient quantities. The sensitivity of electrophysiology requires only very small quantities of the nAChR be present for successful recordings, but even obtaining this level of purified protein is absent in the literature. Even if enough pure protein could be acquired, patching GUVs is extremely difficult, and their sizes are heterogeneous (Levental and Lyman, 2023). While this technique may hold the most promise in theory, better expression and purification protocols may be required for it to provide utility.

The study of lipid-protein interactions is challenging but technological advances are expanding the toolbox that can be used. Along with some of the functional technologies noted above, improved membrane mimetics combined with single particle cryo-EM give unprecedented structural correlates for lipid binding and the effect of lipid composition on

membrane protein structure. Combining better structures with higher powered molecular dynamics simulations that can simulate complex membrane environments (Enkavi et al., 2019; Manna et al., 2019) and be analyzed with a growing number of tools (Corey et al., 2019; Ansell et al., 2022) should drastically improve our ability to define the mechanisms of lipid modulation in the nAChR.

7.2 New insight into the mechanisms underlying nAChR activation

For several decades the mechanism(s) of nAChR activation have remained enigmatic, primarily due to the lack of high resolution structures in resting and active states. Several mechanisms of activation were proposed for the nAChR prior to the availability of these structures (Lee and Sine, 2005; Xiu et al., 2005; Gupta et al., 2017) and several others have been proposed for pLGICs in general (Miyazawa et al., 2003; Lummis et al., 2005; Calimet et al., 2013; Althoff et al., 2014; Sauguet et al., 2014a; Lev et al., 2017; Polovinkin et al., 2018; Masiulis et al., 2019; Oliveira et al., 2019; Kumar et al., 2020a; Cymes and Grosman, 2021; Noviello et al., 2021; Yu et al., 2021; Kasaragod et al., 2022). None of these models, however, are consistent with the ensemble of functional data and/or the new nAChR structures. In manuscript 3 a mechanism is proposed that is consistent with both the functional and structural data. Rather than activation occurring through the formation of new interactions that stabilize the active state of the nAChR, this model postulates that activation may instead occur primarily through the release of local conformational restraints in the resting state. The tenets of the model are established in manuscript 3 and discussed in section 5.5. Rather than reiterating what has been discussed in those sections, the discussion will focus on how the model effects our current understanding of the nAChR (and pLGICs in general).

Through the lenses of a sequential vs a global model of protein allostery the proposed mechanism can be viewed quite differently. Sequentially, agonist binding induces loop C capping, which leads to a twisting and tilting of the α subunit ECDs, releasing conformational restraints at the α subunit ECD – TMD interfaces, allowing the TMD to "relax" to an open state. While this is still speculative, the model appears consistent with the conformational wave theory proposed by Auerbach and collogues based on ϕ value analysis (Grosman et al., 2000). The conformational wave encompasses a TSE that is quantified for residues throughout the protein. In general, residues in the binding sites move early in the TSE, followed by the ECD – TMD interface, the TMD, and then the pore (Gupta et al., 2017). The nAChR can be divided into "blocks" of residues with similar ϕ values that move sequentially through the TSE in the gating mechanism.

The other lens through which the model can be viewed is a global (or MWC) model, which postulates that during a conformational change the entire protein moves synchronously through two stable conformational states. This model was first considered in the context of hemoglobin undergoing a transition between tensed and relaxed conformations with the binding of oxygen stabilizing the relaxed state (Monod et al., 1965). While our model does not necessarily include a temporal sequence of events, it is difficult to rationalize in a simple two state scheme (i.e. resting to active) that seems to depend on new interactions forming to stabilize an active state. It is widely accepted, however, that the receptor must transition through at least one pre-active intermediate conformation (termed "flipped" or "primed") before transitioning to its open state (Lape et al., 2008; Mukhtasimova et al., 2009; Jadey and Auerbach, 2012). In fact, one could imagine a continuum of intermediate conformations along the resting to active state trajectory with infinite zoom whose stabilities may be such that their existence is extremely

transient. In such a case, these pseudo intermediates could be viewed as the blocks of sequential changes described in the previous paragraphs.

In some ways the discrepancies between the models are semantic, but they do have a subtle impact on how a potential drugs would be designed. To create a positive allosteric modulator, the molecule of interest would need to preferentially stabilize an active state of the receptor without activating the nAChR directly, while a negative allosteric modulator would need to preferentially stabilize an inactive state. The success of such a design would depend on knowing how the site of interest changes along the activation trajectory. While we are still far from having a full ensemble of structures along this trajectory, our mono-liganded structure hints at how the conformation of the nAChR changes during activation. Our data suggests that the mono-liganded openings of the nAChR are primarily mediated through ACh binding to the α-ɣ interface making drugs that target this interface potentially more impactful for briefer, mono-liganded opening events that predominate at low concentrations of ACh while those at the α-δ interface could be more impactful for longer, di-liganded opening events that occur at high ACh concentrations, like the NMJ.

Along with structural information, functional annotation of drug binding sites is key for successful design. Many drugs that target pLGICs bind to sites within the ECD – TMD interface near the M2-M3 loops including anesthetics (Nury et al., 2011; Pan et al., 2012b; Sauguet et al., 2013b; Forman et al., 2015; Forman and Miller, 2016; Fourati et al., 2018; Kim et al., 2020), hypnotics (Zhu et al., 2022), benzodiazepines (Masiulis et al., 2019; Kim et al., 2020; Zhu et al., 2022), barbiturates (Forman and Miller, 2016; Yu and Cohen, 2017), and ethanol (Sauguet et al., 2013b). Our model of activation pinpoints a specific interaction within the ECD – TMD

interface that may be critical in understanding how drugs that bind to these sites exert their functional effects.

7.4 Overall conclusions

The studies described in this thesis have built upon years of nAChR research to further our understanding of the allosteric mechanisms that dictate nAChR function. While manuscripts 1 and 2 did not provide a detailed mechanism for how lipids modulate nAChR function, they provide valuable insight into how the lipid exposed M4 α-helices may propagate changes in lipid composition to the function of the channel. With growing structural information and more sophisticated methods for analyzing lipid – protein interactions, future studies will be able to build upon the vast mutagenesis data presented here to elucidate the mechanisms of lipid modulation in more detail. Manuscript 3 & 4 on the other hand uses new structures of the nAChR to revise the currently described mechanisms of nAChR activation. Through extensive electrophysiological characterization we believe we have uncovered a new mechanism of activation that changes the previous paradigms in the field. Further validation will be required to conclusively establish this mechanism, but for now we believe that 100 years after the nAChR was identified as the first receptor ever, we have figured out – at least in part – how it activates.

Chapter 8. References

Abraham, M. J.; Murtola, T.; Schulz, R.; Páll, S.; Smith, J. C.; Hess, B.; Lindahl, E. Gromacs: High Performance Molecular Simulations through Multi-Level Parallelism from Laptops to Supercomputers. *SoftwareX* **2015**, *1–2*, 19–25.

Absalom, N. L.; Lewis, T. M.; Kaplan, W.; Pierce, K. D.; Schofield, P. R. Role of Charged Residues in Coupling Ligand Binding and Channel Activation in the Extracellular Domain of the Glycine Receptor. *J. Biol. Chem.* **2003**, *278* (50), 50151–50157.

Addona, G. H.; Sandermann, H.; Kloczewiak, M. A.; Husain, S. S.; Miller, K. W. Where Does Cholesterol Act during Activation of the Nicotinic Acetylcholine Receptor? *Biochimica et Biophysica Acta - Biomembranes* **1998**, *1370* (2), 299–309.

Addona, G. H.; Sandermann, H.; Kloczewiak, M. A.; Miller, K. W. Low Chemical Specificity of the Nicotinic Acetylcholine Receptor Sterol Activation Site. *Biochimica et Biophysica Acta - Biomembranes* **2003**, *1609* (2), 177–182.

Albuquerque, E. X.; Pereira, E. F. R.; Alkondon, M.; Rogers, S. W. Mammalian Nicotinic Acetylcholine Receptors: From Structure to Function. *Physiol. Rev.* **2009**, *89* (1), 73–120.

Alcaino, C.; Musgaard, M.; Minguez, T.; Mazzaferro, S.; Faundez, M.; Iturriaga-Vasquez, P.; Biggin, P. C.; Bermudez, I. Role of the Cys Loop and Transmembrane Domain in the Allosteric Modulation of A4β2 Nicotinic Acetylcholine Receptors. *J. Biol. Chem.* **2017**, *292* (2), 551–562.

Aldea, M.; Castillo, M.; Mulet, J.; Sala, S.; Criado, M.; Sala, F. Role of the Extracellular Transmembrane Domain Interface in Gating and Pharmacology of a Heteromeric Neuronal Nicotinic Receptor. *J. Neurochem.* **2010**, *113* (4), 1036–1045.

Allard, C. A. H.; Kang, G.; Kim, J. J.; Valencia-Montoya, W. A.; Hibbs, R. E.; Bellono, N. W. Structural Basis of Sensory Receptor Evolution in Octopus. *Nature* **2023**, *616* (7956), 373–377.

Allen, J. A.; Halverson-Tamboli, R. A.; Rasenick, M. M. Lipid Raft Microdomains and Neurotransmitter Signalling. *Nature Reviews Neuroscience* **2007**, *8* (2), 128–140.

Almarza, G.; Sánchez, F.; Barrantes, F. J. Transient Cholesterol Effects on Nicotinic Acetylcholine Receptor Cell-Surface Mobility. *PLoS One* **2014**, *9* (6), e100346.

Althoff, T.; Hibbs, R. E.; Banerjee, S.; Gouaux, E. X-Ray Structures of GluCl in Apo States Reveal a Gating Mechanism of Cys-Loop Receptors. *Nature* **2014**, *512* (7514), 333–337.

Ananchenko, A.; Hussein, T. O. K.; Mody, D.; Thompson, M. J.; Baenziger, J. E. Recent Insight into Lipid Binding and Lipid Modulation of Pentameric Ligand-Gated Ion Channels. *Biomolecules* **2022**, *12* (6), 814.

Ansell, T. B.; Song, W.; Coupland, C. E.; Carrique, L.; Robin, A.; Ward, A. B.; Siebold, C.; Stansfeld, P. J.; Mark, S. P. LipIDens : Simulation Assisted Interpretation of Lipid Densities in Cryo-EM Structures of Membrane Proteins. *bioRxiv* **2022**.

Antollini, S. S.; Barrantes, F. J. Disclosure of Discrete Sites for Phospholipid and Sterols at the Protein-Lipid Interface in Native Acetylcholine Receptor-Rich Membrane. *Biochemistry* **1998**, *37* (47), 16653–16662.

Antollini, S. S.; Xu, Y.; Jiang, H.; Barrantes, F. J. Fluorescence and Molecular Dynamics Studies of the Acetylcholine Receptor ΓM4 Transmembrane Peptide in Reconstituted Systems. *Mol. Membr. Biol.* **2005**, *22* (6), 471–484.

Araujo, N. R.; Hernando, G.; Corradi, J.; Bouzat, C. The Nematode Serotonin-Gated Chloride Channel MOD-1: A Novel Target for Anthelmintic Therapy. *J. Biol. Chem.* **2022**, *298* (9).

Arias, H. R.; Germann, A. L.; Pierce, S. R.; Sakamoto, S.; Ortells, M. O.; Hamachi, I.; Akk, G. Modulation of the Mammalian GABAA Receptor by Type I and Type II Positive Allosteric Modulators of the A7 Nicotinic Acetylcholine Receptor. *Br. J. Pharmacol.* **2022**, *179* (24), 5323–5337.

Aryal, P.; Sansom, M. S. P.; Tucker, S. J. Hydrophobic Gating in Ion Channels. *J. Mol. Biol.* **2015**, *427* (1), 121–130.

Auerbach, A. Dose-Response Analysis When There Is a Correlation between Affinity and Efficacy. *Mol. Pharmacol.* **2016**, *89* (2), 297–302.

Baenziger, J. E.; Corringer, P.-J. 3D Structure and Allosteric Modulation of the Transmembrane Domain of Pentameric Ligand-Gated Ion Channels. *Neuropharmacology* **2011**, *60* (1), 116–125.

Baenziger, J. E.; daCosta, C. J. B. Molecular Mechanisms of Acetylcholine Receptor–Lipid Interactions: From Model Membranes to Human Biology. *Biophys. Rev.* **2013**, *5* (1), 1–9.

Baenziger, J. E.; Darsaut, T. E.; Morris, M. L. Internal Dynamics of the Nicotinic Acetylcholine Receptor in Reconstituted Membranes. *Biochemistry* **1999**, *38* (16), 4905–4911.

Baenziger, J. E.; Morris, M. L.; Darsaut, T. E.; Ryan, S. E. Effect of Membrane Lipid Composition on the Conformational Equilibria of the Nicotinic Acetylcholine Receptor. *J. Biol. Chem.* **2000**, *275* (2), 777–784.

Baenziger, J. E.; Ryan, S. E.; Goodreid, M. M.; Vuong, N. Q.; Sturgeon, R. M.; daCosta, C. J. B. Lipid Composition Alters Drug Action at the Nicotinic Acetylcholine Receptor. *Mol. Pharmacol.* **2008**, *73* (3), 880–890.

Baenziger, J. E.; Hénault, C. M.; Therien, J. P. D.; Sun, J. Nicotinic Acetylcholine Receptor–Lipid Interactions: Mechanistic Insight and Biological Function. *Biochimica et Biophysica Acta (BBA) - Biomembranes* **2015**, *1848* (9), 1806–1817.

Baenziger, J. E.; Domville, J. A.; Therien, J. P. D. The Role of Cholesterol in the Activation of Nicotinic Acetylcholine Receptors. In *Current Topics in Membranes*; Levitan, I., Ed.; Academic Press, 2017; Vol. 80, pp 95–137.

Báez-Pagán, C. A.; Del Hoyo-Rivera, N.; Quesada, O.; Otero-Cruz, J. D.; Lasalde-Dominicci, J. A. Heterogeneous Inhibition in Macroscopic Current Responses of Four Nicotinic Acetylcholine Receptor Subtypes by Cholesterol Enrichment. *J. Membr. Biol.* **2016**, *249* (4), 539–549.

Bai, Y.; Yu, X.; Chen, H.; Horne, D.; White, R.; Wu, X.; Lee, P.; Gu, Y.; Ghimire-Rijal, S.; Lin, D. C.-H.; et al. Structural Basis for Pharmacological Modulation of the TRPC6 Channel. *Elife* **2020**, *9*.

Baier, C. J.; Fantini, J.; Barrantes, F. J. Disclosure of Cholesterol Recognition Motifs in Transmembrane Domains of the Human Nicotinic Acetylcholine Receptor. *Sci. Rep.* **2011**, *1* (1), 1–7.

Barbera, N.; Ayee, M. A. A.; Akpa, B. S.; Levitan, I. Molecular Dynamics Simulations of Kir2.2 Interactions with an Ensemble of Cholesterol Molecules. *Biophys. J.* **2018**, *115* (7), 1264–1280.

Barbera, N. A.; Minke, B.; Levitan, I. Comparative Docking Analysis of Cholesterol Analogs to Ion Channels to Discriminate between Stereospecific Binding vs. Stereospecific Response. *Channels* **2019**, *13* (1), 136–146.

Barberis, A. Postsynaptic Plasticity of GABAergic Synapses. *Neuropharmacology* **2020**, *169* (May 2019), 107643.

Barrantes, F. J. Lipid Matters: Nicotinic Acetylcholine Receptor-Lipid Interactions (Review). *Molecular Membrane Biology* **2002**, *19* (4), 277–284.

Barrantes, F. J. Modulation of Nicotinic Acetylcholine Receptor Function through the Outer and Middle Rings of Transmembrane Domains. *Curr. Opin. Drug Discov. Devel.* **2003**, *6* (5), 620–632.

Barrantes, F. J. Phylogenetic Conservation of Protein–Lipid Motifs in Pentameric Ligand-Gated Ion Channels. *Biochimica et Biophysica Acta (BBA) - Biomembranes* **2015**, *1848* (9), 1796–1805.

Barrantes, F. J. Structure and Function Meet at the Nicotinic Acetylcholine Receptor-Lipid Interface. *Pharmacological Research* **2023**, *190*, 106729.

Basak, S.; Chatterjee, S.; Chakrapani, S. Site Directed Spin Labeling and EPR Spectroscopic Studies of Pentameric Ligand-Gated Ion Channels. *J. Vis. Exp.* **2016**, No. 113.

Basak, S.; Schmandt, N.; Gicheru, Y.; Chakrapani, S. Crystal Structure and Dynamics of a Lipid-Induced Potential Desensitized-State of a Pentameric Ligand-Gated Channel. *Elife* **2017**, *6*, e23886.

Basak, S.; Gicheru, Y.; Rao, S.; Sansom, M. S. P.; Chakrapani, S. Cryo-EM Reveals Two Distinct Serotonin-Bound Conformations of Full-Length 5-HT3A Receptor. *Nature* **2018a**, *563* (7730), 270–274.

Basak, S.; Gicheru, Y.; Samanta, A.; Molugu, S. K.; Huang, W.; Fuente, M. la de; Hughes, T.; Taylor, D. J.; Nieman, M. T.; Moiseenkova-Bell, V.; et al. Cryo-EM Structure of 5-HT3A Receptor in Its Resting Conformation. *Nat. Commun.* **2018b**, *9* (1), 514.

Basak, S.; Gicheru, Y.; Kapoor, A.; Mayer, M. L.; Filizola, M.; Chakrapani, S. Molecular Mechanism of Setron-Mediated Inhibition of Full-Length 5-HT3A Receptor. *Nat. Commun.* **2019**, *10* (1), 3225.

Basak, S.; Kumar, A.; Ramsey, S.; Gibbs, E.; Kapoor, A.; Filizola, M.; Chakrapani, S. High-Resolution Structures of Multiple 5-HT3AR-Setron Complexes Reveal a Novel Mechanism of Competitive Inhibition. *Elife* **2020**, *9*.

Bass, R. B.; Strop, P.; Barclay, M.; Rees, D. C. Crystal Structure of Escherichia Coli MscS, a Voltage-Modulated and Mechanosensitive Channel. *Science* **2002**, *298* (5598), 1582–1587.

Bavi, N.; Cortes, D. M.; Cox, C. D.; Rohde, P. R.; Liu, W.; Deitmer, J. W.; Bavi, O.; Strop, P.; Hill, A. P.; Rees, D.; et al. The Role of MscL Amphipathic N Terminus Indicates a Blueprint for Bilayer-Mediated Gating of Mechanosensitive Channels. *Nat. Commun.* **2016**, *7*, 11984.

Beckstein, O.; Sansom, M. S. P. A Hydrophobic Gate in an Ion Channel: The Closed State of the Nicotinic Acetylcholine Receptor. *Phys. Biol.* **2006**, *3* (2), 147–159.

Beech, R. N.; Neveu, C. The Evolution of Pentameric Ligand-Gated Ion-Channels and the Changing Family of Anthelmintic Drug Targets. *Parasitology* **2015**, *142* (2), 303–317.

Berendsen, H. J. C.; Postma, J. P. M.; van Gunsteren, W. F.; DiNola, A.; Haak, J. R. Molecular Dynamics with Coupling to an External Bath. *J. Chem. Phys.* **1984**, *81* (8), 3684–3690.

Bergh, C.; Rovšnik, U.; Howard, R. J.; Lindahl, E. Discovery of Lipid Binding Sites in a Ligand-Gated Ion Channel by Integrating Simulations and Cryo-EM. *bioRxiv*, 2023, 2023.01.06.523006.

Bertozzi, C.; Zimmermann, I.; Engeler, S.; Hilf, R. J. C.; Dutzler, R. Signal Transduction at the Domain Interface of Prokaryotic Pentameric Ligand-Gated Ion Channels. *PLoS Biol.* **2016**, *14* (3), e1002393.

Bertrand, D.; Terry, A. V. The Wonderland of Neuronal Nicotinic Acetylcholine Receptors. *Biochem. Pharmacol.* **2018**, *151*, 214–225.

Best, R. B.; Zhu, X.; Shim, J.; Lopes, P. E. M.; Mittal, J.; Feig, M.; MacKerell, A. D., Jr. Optimization of the Additive CHARMM All-Atom Protein Force Field Targeting Improved Sampling of the Backbone φ, ψ and Side-Chain χ(1) and χ(2) Dihedral Angles. *J. Chem. Theory Comput.* **2012**, *8* (9), 3257–3273.

Bhattacharjee, B.; Rahman, M. M.; Hibbs, R. E.; Stowell, M. H. B. A Simple Flash and Freeze System for Cryogenic Time-Resolved Electron Microscopy. *Front Mol Biosci* **2023**, *10*, 1129225.

Bianchi, M. T.; Botzolakis, E. J. Targeting Ligand-Gated Ion Channels in Neurology and Psychiatry: Is Pharmacological Promiscuity an Obstacle or an Opportunity? *BMC Pharmacol.* **2010**, *10* (3), 1–8.

Blanton, M. P.; Cohen, J. B. Mapping the Lipid-Exposed Regions in the Torpedo Californica Nicotinic Acetylcholine Receptor. *Biochemistry* **1992**, *31* (15), 3738–3750.

Blount, P.; Merlie, J. P. Molecular Basis of the Two Nonequivalent Ligand Binding Sites of the Muscle Nicotinic Acetylcholine Receptor. *Neuron* **1989**, *3* (3), 349–357.

Blount, P.; Smith, M. M.; Merlie, J. P. Assembly Intermediates of the Mouse Muscle Nicotinic Acetylcholine Receptor in Stably Transfected Fibroblasts. *The Journal of Cell Biology* **1990**, *111* (6), 2601–2611.

Bocquet, N.; Nury, H.; Baaden, M.; Le Poupon, C.; Changeux, J.-P.; Delarue, M.; Corringer, P.-J. X-Ray Structure of a Pentameric Ligand-Gated Ion Channel in an Apparently Open Conformation. *Nature* **2009**, *457* (7225), 111–114.

Bondarenko, V.; Mowrey, D. D.; Tillman, T. S.; Cui, T.; Liu, L. T.; Xu, Y.; Tang, P. NMR Structures of the Transmembrane Domains of the A4β2 NAChR. *Biochimica et Biophysica Acta - Biomembranes* **2012**, *1818* (5), 1261–1268.

Bondarenko, V.; Mowrey, D. D.; Liu, L. T.; Xu, Y.; Tang, P. NMR Resolved Multiple Anesthetic Binding Sites in the TM Domains of the A4β2 NAChR. *Biochimica et Biophysica Acta - Biomembranes* **2013**, *1828* (2), 398–404.

Bondarenko, V.; Wells, M. M.; Chen, Q.; Tillman, T. S.; Singewald, K.; Lawless, M. J.; Caporoso, J.; Brandon, N.; Coleman, J. A.; Saxena, S.; et al. Structures of Highly Flexible Intracellular Domain of Human A7 Nicotinic Acetylcholine Receptor. *Nat. Commun.* **2022**, *13* (1), 793.

Borroni, V.; Barrantes, F. J. Cholesterol Modulates the Rate and Mechanism of Acetylcholine Receptor Internalization. *J. Biol. Chem.* **2011**, *286* (19), 17122–17132.

Borroni, V.; Baier, C. J.; Lang, T.; Bonini, I.; White, M. M.; Garbus, I.; Barrantes, F. J. Cholesterol Depletion Activates Rapid Internalization of Submicron-Sized Acetylcholine Receptor Domains at the Cell Membrane. *Mol. Membr. Biol.* **2007**, *24* (1), 1–15.

Bouzat, C.; Mukhtasimova, N. The Nicotinic Acetylcholine Receptor as a Molecular Machine for Neuromuscular Transmission. *Current Opinion in Physiology* **2018**, *4*, 40–48.

Bouzat, C.; Roccamo, A. M.; Garbus, I.; Barrantes, F. J. Mutations at Lipid-Exposed Residues of the Acetylcholine Receptor Affect Its Gating Kinetics. *Mol. Pharmacol.* **1998**, *54* (1), 146–153.

Bouzat, C.; Barrantes, F.; Sine, S. Nicotinic Receptor Fourth Transmembrane Domain: Hydrogen Bonding by Conserved Threonine Contributes to Channel Gating Kinetics. *J. Gen. Physiol.* **2000**, *115* (5), 663–672.

Bouzat, C.; Gumilar, F.; del Carmen Esandi, M.; Sine, S. M. Subunit-Selective Contribution to Channel Gating of the M4 Domain of the Nicotinic Receptor. *Biophys. J.* **2002**, *82* (4), 1920–1929.

Bouzat, C.; Bartos, M.; Corradi, J.; Sine, S. M. The Interface between Extracellular and Transmembrane Domains of Homomeric Cys-Loop Receptors Governs Open-Channel Lifetime and Rate of Desensitization. *J. Neurosci.* **2008**, *28* (31), 7808–7819.

Boyd, N. D.; Cohen, J. B. Kinetics of Binding of [3H]Acetylcholine and [3H]Carbamoylcholine to Torpedo Postsynaptic Membranes: Slow Conformational Transitions of the Cholinergic Receptor. *Biochemistry* **1980a**, *19* (23), 5344–5353.

Boyd, N. D.; Cohen, J. B. Kinetics of Binding of [3H]Acetylcholine to Torpedo Postsynaptic Membranes: Association and Dissociation Rate Constants by Rapid Mixing and Ultrafiltration. *Biochemistry* **1980b**, *19* (23), 5353–5358.

Bracamontes, J. R.; Li, P.; Akk, G.; Steinbach, J. H. Mutations in the Main Cytoplasmic Loop of the GABA(A) Receptor A4 and δ Subunits Have Opposite Effects on Surface Expression. *Mol. Pharmacol.* **2014**, *86* (1), 20–27.

Brams, M.; Govaerts, C.; Kambara, K.; Price, K. L.; Spurny, R.; Gharpure, A.; Pardon, E.; Evans, G. L.; Bertrand, D.; Lummis, S. C. R.; et al. Modulation of the Erwinia Ligand-Gated Ion Channel (ELIC) and the 5-HT3 Receptor via a Common Vestibule Site. *Elife* **2020**, *9*, 1–19.

Brannigan, G.; Hénin, J.; Law, R.; Eckenhoff, R.; Klein, M. L. Embedded Cholesterol in the Nicotinic Acetylcholine Receptor. *Proc. Natl. Acad. Sci. U. S. A.* **2008**, *105* (38), 14418–14423.

Brejc, K.; Van Dijk, W. J.; Klaassen, R. V.; Schuurmans, M.; Van Der Oost, J.; Smit, A. B.; Sixma, T. K. Crystal Structure of an ACh-Binding Protein Reveals the Ligand-Binding Domain of Nicotinic Receptors. *Nature* **2001**, *411* (6835), 269–276.

Brodzki, M.; Mozrzymas, J. W. GABAA Receptor Proline 273 at the Interdomain Interface of the B2 Subunit Regulates Entry into Desensitization and Opening/Closing Transitions. *Life Sci.* **2022**, *308*, 120943.

Brohawn, S. G. How Ion Channels Sense Mechanical Force: Insights from Mechanosensitive K2P Channels TRAAK, TREK1, and TREK2. *Ann. N. Y. Acad. Sci.* **2015**, *1352*, 20–32.

Brohawn, S. G.; del Mármol, J.; MacKinnon, R. Crystal Structure of the Human K2P TRAAK, a Lipid- and Mechano-Sensitive K+ Ion Channel. *Science* **2012**, *335* (6067), 436–441.

Brohawn, S. G.; Campbell, E. B.; MacKinnon, R. Physical Mechanism for Gating and Mechanosensitivity of the Human TRAAK K+ Channel. *Nature* **2014**, *516* (7529), 126–130.

Bruhova, I.; Auerbach, A. Subunit Symmetry at the Extracellular Domain-Transmembrane Domain Interface in Acetylcholine Receptor Channel Gating. *J. Biol. Chem.* **2010**, *285* (50), 38898–38904.

Budelier, M. M.; Cheng, W. W. L.; Chen, Z.-W.; Bracamontes, J. R.; Sugasawa, Y.; Krishnan, K.; Mydock-McGrane, L.; Covey, D. F.; Evers, A. S. Common Binding Sites for Cholesterol and Neurosteroids on a Pentameric Ligand-Gated Ion Channel. *Biochim. Biophys. Acta Mol. Cell Biol. Lipids* **2019**, *1864* (2), 128–136.

Burgos, C. F.; Yévenes, G. E.; Aguayo, L. G. Structure and Pharmacologic Modulation of Inhibitory Glycine Receptors. *Mol. Pharmacol.* **2016**, *90* (3), 318–325.

Butler, A. S.; Lindesay, S. A.; Dover, T. J.; Kennedy, M. D.; Patchell, V. B.; Levine, B. A.; Hope, A. G.; Barnes, N. M. Importance of the C-Terminus of the Human 5-HT3A Receptor Subunit. *Neuropharmacology* **2009**, *56* (1), 292–302.

Calimet, N.; Simoes, M.; Changeux, J.-P.; Karplus, M.; Taly, A.; Cecchini, M. A Gating Mechanism of Pentameric Ligand-Gated Ion Channels. *Proc. Natl. Acad. Sci. U. S. A.* **2013**, *110* (42), E3987-96.

Carswell, C. L.; Labriola, J. M.; Baenziger, J. E. Effects of Lipids on the Structure and Function of GLIC and ELIC. *Biophys. J.* **2013**, *104* (2), 219a.

Carswell, C. L.; Sun, J.; Baenziger, J. E. Intramembrane Aromatic Interactions Influence the Lipid Sensitivities of Pentameric Ligand-Gated Ion Channels. *J. Biol. Chem.* **2015a**, *290* (4), 2496–2507.

Carswell, C. L.; Hénault, C. M.; Murlidaran, S.; Therien, J. P. D.; Juranka, P. F.; Surujballi, J. A.; Brannigan, G.; Baenziger, J. E. Role of the Fourth Transmembrane α Helix in the Allosteric Modulation of Pentameric Ligand-Gated Ion Channels. *Structure* **2015b**, *23* (9), 1655–1664.

del Castillo, J.; Katz, B. Interaction at End-Plate Receptors between Different Choline Derivatives. *Proc. R. Soc. Lond. B Biol. Sci.* **1957**, *924* (146), 369–381.

Caton, M.; Ochoa, E. L. M.; Barrantes, F. J. The Role of Nicotinic Cholinergic Neurotransmission in Delusional Thinking. *npj Schizophrenia* **2020**, *6* (1), 16.

Cecchini, M.; Changeux, J.-P. The Nicotinic Acetylcholine Receptor and Its Prokaryotic Homologues: Structure, Conformational Transitions & Allosteric Modulation. *Neuropharmacology* **2015**, *96* (Pt B), 137–149.

Cecchini, M.; Changeux, J.-P. Nicotinic Receptors: From Protein Allostery to Computational Neuropharmacology. *Mol. Aspects Med.* **2022**, *84*, 101044.

Celie, P. H. N.; van Rossum-Fikkert, S. E.; van Dijk, W. J.; Brejc, K.; Smit, A. B.; Sixma, T. K. Nicotine and Carbamylcholine Binding to Nicotinic Acetylcholine Receptors as Studied in AChBP Crystal Structures. *Neuron* **2004**, *41* (6), 907–914.

Cerdan, A. H.; Cecchini, M. On the Functional Annotation of Open-Channel Structures in the Glycine Receptor. *Structure* **2020**, *28* (6), 690-693.e3.

Cerdan, A. H.; Martin, N. É.; Cecchini, M. An Ion-Permeable State of the Glycine Receptor Captured by Molecular Dynamics. *Structure* **2018**, *26* (11), 1555-1562.e4.

Cetin, H.; Liu, W.-W.; Cheung, J.; Cossins, J.; Vanhaesebrouck, A. E.; Maxwell, S.; Vincent, A.; Beeson, D.; Webster, R. Rapsyn Facilitates Recovery from Desensitization in Fetal and Adult Acetylcholine Receptors Expressed in a Muscle Cell Line. *J. Physiol.* **2019**, *597* (14), 3713–3725.

Cetin, H.; Beeson, D.; Vincent, A.; Webster, R. The Structure, Function, and Physiology of the Fetal and Adult Acetylcholine Receptor in Muscle. *Front. Mol. Neurosci.* **2020**, *13* (September), 581097.

Chakrapani, S.; Bailey, T. D.; Auerbach, A. Gating Dynamics of the Acetylcholine Receptor Extracellular Domain. *J. Gen. Physiol.* **2004**, *123* (4), 341–356.

Chang, C. C.; Lee, C. Y. Isolation of Neurotoxins from the Venom of Bungarus Multicinctus and Their Modes of Neuromuscular Blocking Action. *Arch. Int. Pharmacodyn. Ther.* **1963**, *144* (Jul 1), 241–257.

Chang, G.; Spencer, R. H.; Lee, A. T.; Barclay, M. T.; Rees, D. C. Structure of the MscL Homolog from Mycobacterium Tuberculosis: A Gated Mechanosensitive Ion Channel. *Science* **1998**, *282* (5397), 2220–2226.

Changeux, J.-P. The Nicotinic Acetylcholine Receptor: The Founding Father of the Pentameric Ligand-Gated Ion Channel Superfamily. *J. Biol. Chem.* **2012**, *287* (48), 40207–40215.

Changeux, J.-P. 50 Years of Allosteric Interactions: The Twists and Turns of the Models. *Nat. Rev. Mol. Cell Biol.* **2013**, *14* (12), 819–829.

Changeux, J.-P. Discovery of the First Neurotransmitter Receptor: The Acetylcholine Nicotinic Receptor. *Biomolecules* **2020**, *10* (4).

Changeux, J.-P.; Kasai, M.; Lee, C.-Y. Use of a Snake Venom Toxin to Characterize the Cholinergic Receptor Protein. *Proceedings of the National Academy of Sciences* **1970**, *67* (3), 1241–1247.

Chemin, J.; Patel, A. J.; Duprat, F.; Lauritzen, I.; Lazdunski, M.; Honoré, E. A Phospholipid Sensor Controls Mechanogating of the K+ Channel TREK-1. *EMBO J.* **2005**, *24* (1), 44–53.

Chen, Q.; Wells, M. M.; Arjunan, P.; Tillman, T. S.; Cohen, A. E.; Xu, Y.; Tang, P. Structural Basis of Neurosteroid Anesthetic Action on GABAA Receptors. *Nat. Commun.* **2018**, *9* (1), 3972.

Chen, X.; Webb, T. I.; Lynch, J. W. The M4 Transmembrane Segment Contributes to Agonist Efficacy Differences between α 1 and α 3 Glycine Receptors. *Mol. Membr. Biol.* **2009**, *26* (5–7), 321–332.

Chen, Z.-W.; Bracamontes, J. R.; Budelier, M. M.; Germann, A. L.; Shin, D. J.; Kathiresan, K.; Qian, M.-X.; Manion, B.; Cheng, W. W. L.; Reichert, D. E.; et al. Multiple Functional Neurosteroid Binding Sites on GABAA Receptors. *PLoS Biol.* **2019**, *17* (3), e3000157.

Cheng, W. W. L.; D'Avanzo, N.; Doyle, D. A.; Nichols, C. G. Dual-Mode Phospholipid Regulation of Human Inward Rectifying Potassium Channels. *Biophys. J.* **2011**, *100* (3), 620–628.

Cheng, W. W. L.; Chen, Z.-W.; Bracamontes, J. R.; Budelier, M. M.; Krishnan, K.; Shin, D. J.; Wang, C.; Jiang, X.; Covey, D. F.; Akk, G.; et al. Mapping Two Neurosteroid-Modulatory Sites in the Prototypic Pentameric Ligand-Gated Ion Channel GLIC. *J. Biol. Chem.* **2018**, *293* (8), 3013–3027.

Cheng, W. W. L.; Arcario, M. J.; Petroff, J. T., II. Druggable Lipid Binding Sites in Pentameric Ligand-Gated Ion Channels and Transient Receptor Potential Channels. *Front. Physiol.* **2022**, *12*, 798102.

Cheng, Y. Single-Particle Cryo-EM-How Did It Get Here and Where Will It Go. *Science* **2018**, *361* (6405), 876–880.

Clark, M. D.; Contreras, G. F.; Shen, R.; Perozo, E. Electromechanical Coupling in the Hyperpolarization-Activated K+ Channel KAT1. *Nature* **2020**, *583* (7814), 145–149.

Colombo, S. F.; Mazzo, F.; Pistillo, F.; Gotti, C. Biogenesis, Trafficking and up-Regulation of Nicotinic ACh Receptors. *Biochem. Pharmacol.* **2013**, *86* (8), 1063–1073.

Colón-Sáez, J. O.; Yakel, J. L. The A7 Nicotinic Acetylcholine Receptor Function in Hippocampal Neurons Is Regulated by the Lipid Composition of the Plasma Membrane. *J. Physiol.* **2011**, *589* (Pt 13), 3163–3174.

Colquhoun, D.; Hawkes, A. G. On the Stochastic Properties of Single Ion Channels. *Proceedings of the Royal Society of London. Series B, Biological Sciences* **1981**, *211* (1183), 205–235.

Comoglio, Y.; Levitz, J.; Kienzler, M. A.; Lesage, F.; Isacoff, E. Y.; Sandoz, G. Phospholipase D2 Specifically Regulates TREK Potassium Channels via Direct Interaction and Local Production of Phosphatidic Acid. *Proc. Natl. Acad. Sci. U. S. A.* **2014**, *111* (37), 13547–13552.

Corey, R. A.; Vickery, O. N.; Sansom, M. S. P.; Stansfeld, P. J. Insights into Membrane Protein-Lipid Interactions from Free Energy Calculations. *J. Chem. Theory Comput.* **2019**, *15* (10), 5727–5736.

Corradi, V.; Sejdiu, B. I.; Mesa-Galloso, H.; Abdizadeh, H.; Noskov, S. Y.; Marrink, S. J.; Tieleman, D. P. Emerging Diversity in Lipid-Protein Interactions. *Chem. Rev.* **2019**, *119* (9), 5775–5848.

Corringer, P.-J.; Poitevin, F.; Prevost, M. S.; Sauguet, L.; Delarue, M.; Changeux, J.-P. Structure and Pharmacology of Pentameric Receptor Channels: From Bacteria to Brain. *Structure* **2012**, *20* (6), 941–956.

Cory-Wright, J.; Alqazzaz, M.; Wroe, F.; Jeffreys, J.; Zhou, L.; Lummis, S. C. R. Aromatic Residues in the Fourth Transmembrane-Spanning Helix M4 Are Important for GABAρ Receptor Function. *ACS Chem. Neurosci.* **2018**, *9* (2), 284–290.

da Costa Couto, A. R. G. M.; Price, K. L.; Mesoy, S.; Capes, E.; Lummis, S. C. R. The M4 Helix Is Involved in A7 NACh Receptor Function. *ACS Chem. Neurosci.* **2020**, *11* (10), 1406–1412.

Cowgill, J.; Fan, C.; Haloi, N.; Tobiasson, V.; Zhuang, Y.; Howard, R. J.; Lindahl, E. Structure and Dynamics of Differential Ligand Binding in the Human ρ-Type GABAA Receptor. *bioRxiv*, 2023, 2023.06.16.545288.

Cox, C. D.; Bavi, N.; Martinac, B. Bacterial Mechanosensors. *Annu. Rev. Physiol.* **2018**, *80*, 71–93.

Cox, C. D.; Bavi, N.; Martinac, B. Biophysical Principles of Ion-Channel-Mediated Mechanosensory Transduction. *Cell Rep.* **2019**, *29* (1), 1–12.

Criado, M.; Eibl, H.; Barrantes, F. J. Effects of Lipids on Acetylcholine Receptor. Essential Need of Cholesterol for Maintenance of Agonist-Induced State Transitions in Lipid Vesicles. *Biochemistry* **1982**, *21*, 3622–3629.

Criado, M.; Eibl, H.; Barrantes, F. J. Functional Properties of the Acetylcholine Receptor Incorporateidn Model Lipid Membranes. *The Journal of biological chemistry* **1984**, *259* (14), 9188–9198.

Crnjar, A.; Mesoy, S. M.; Lummis, S. C. R.; Molteni, C. A Single Mutation in the Outer Lipid-Facing Helix of a Pentameric Ligand-Gated Ion Channel Affects Channel Function Through a Radially-Propagating Mechanism. *Frontiers in Molecular Biosciences* **2021**, *8*.

Croll, T. I. ISOLDE: A Physically Realistic Environment for Model Building into Low-Resolution Electron-Density Maps. *Acta Crystallogr D Struct Biol* **2018**, *74* (Pt 6), 519–530.

Cymes, G. D.; Grosman, C. The Unanticipated Complexity of the Selectivity-Filter Glutamates of Nicotinic Receptors. *Nat. Chem. Biol.* **2012**, *8* (12), 975–981.

Cymes, G. D.; Grosman, C. Signal Transduction through Cys-Loop Receptors Is Mediated by the Nonspecific Bumping of Closely Apposed Domains. *Proc. Natl. Acad. Sci. U. S. A.* **2021**, *118* (14), e2021016118.

daCosta, C. J. B.; Baenziger, J. E. A Lipid-Dependent Uncoupled Conformation of the Acetylcholine Receptor. *J. Biol. Chem.* **2009**, *284* (26), 17819–17825.

daCosta, C. J. B.; Ogrel, A. A.; McCardy, E. A.; Blanton, M. P.; Baenziger, J. E. Lipid-Protein Interactions at the Nicotinic Acetylcholine Receptor. A Functional Coupling between Nicotinic Receptors and Phosphatidic Acid-Containing Lipid Bilayers. *J. Biol. Chem.* **2002**, *277* (1), 201–208.

daCosta, C. J. B.; Wagg, I. D.; McKay, M. E.; Baenziger, J. E. Phosphatidic Acid and Phosphatidylserine Have Distinct Structural and Functional Interactions with the Nicotinic Acetylcholine Receptor. *J. Biol. Chem.* **2004**, *279* (15), 14967–14974.

daCosta, C. J. B.; Medaglia, S. A.; Lavigne, N.; Wang, S.; Carswell, C. L.; Baenziger, J. E. Anionic Lipids Allosterically Modulate Multiple Nicotinic Acetylcholine Receptor Conformational Equilibria. *J. Biol. Chem.* **2009**, *284* (49), 33841–33849.

daCosta, C. J. B.; Dey, L.; Therien, J. P. D.; Baenziger, J. E. A Distinct Mechanism for Activating Uncoupled Nicotinic Acetylcholine Receptors. *Nat. Chem. Biol.* **2013**, *9* (11), 701–707.

Daeffler, K. N.-M.; Lester, H. A.; Dougherty, D. A. Functionally Important Aromatic–Aromatic and Sulfur−π Interactions in the D2 Dopamine Receptor. *J. Am. Chem. Soc.* **2012**, *134* (36), 14890–14896.

Dalal, V.; Arcario, M. J.; Petroff, J. T., II; Dietzen, N. M.; Rau, M. J.; Fitzpatrick, J. A. J.; Brannigan, G.; Cheng, W. W. L. Lipid Nanodisc Scaffold and Size Alters the Structure of a Pentameric Ligand-Gated Ion Channel. *bioRxiv*, 2022, 2022.11.20.517256.

Dämgen, M. A.; Biggin, P. C. A Refined Open State of the Glycine Receptor Obtained Via Molecular Dynamics Simulations. *Structure* **2020**, *28*, 130–139.

Darden, T.; York, D.; Pedersen, L. Particle Mesh Ewald: An*N*·log(*N*) Method for Ewald Sums in Large Systems. *J. Chem. Phys.* **1993**, *98* (12), 10089–10092.

Dart, C. Lipid Microdomains and the Regulation of Ion Channel Function. *J. Physiol.* **2010**, *588* (Pt 17), 3169–3178.

Dascal, N. Signalling via the G Protein-Activated K+ Channels. *Cell. Signal.* **1997**, *9* (8), 551–573.

Davies, P. A. Allosteric Modulation of the 5-HT(3) Receptor. *Current Opinion in Pharmacology* **2011**, *11* (1), 75–80.

Deane, C. M.; Lummis, S. C. R. The Role and Predicted Propensity of Conserved Proline Residues in the 5-HT3 Receptor. *J. Biol. Chem.* **2001**, *276* (41), 37962–37966.

Denisov, I. G.; Sligar, S. G. Nanodiscs for Structural and Functional Studies of Membrane Proteins. *Nat. Struct. Mol. Biol.* **2016**, *23* (6), 481–486.

Dhara, M.; Matta, J. A.; Lei, M.; Knowland, D.; Yu, H.; Gu, S.; Bredt, D. S. Polyamine Regulation of Ion Channel Assembly and Implications for Nicotinic Acetylcholine Receptor Pharmacology. *Nat. Commun.* **2020**, *11* (1), 2799.

Di Scala, C.; Baier, C. J.; Evans, L. S.; Williamson, P. T. F.; Fantini, J.; Barrantes, F. J. Relevance of CARC and CRAC Cholesterol-Recognition Motifs in the Nicotinic Acetylcholine Receptor and Other Membrane-Bound Receptors. In *Current Topics in Membranes*; Academic Press Inc., 2017; Vol. 80, pp 3–23.

Dietzen, N. M.; Arcario, M. J.; Chen, L. J.; Petroff, J. T., II; Moreland, K. T.; Krishnan, K.; Brannigan, G.; Covey, D. F.; Cheng, W. W. L. Polyunsaturated Fatty Acids Inhibit a Pentameric Ligand-Gated Ion Channel through One of Two Binding Sites. *eLife* **2022**, *11*, e74306.

Dineley, K. T.; Pandya, A. A.; Yakel, J. L. Nicotinic ACh Receptors as Therapeutic Targets in CNS Disorders. *Trends Pharmacol. Sci.* **2015**, *36* (2), 96–108.

Do, H. Q.; Jansen, M. Binding Motif for RIC-3 Chaperon Protein in Serotonin Type 3A Receptors. *J. Gen. Physiol.* **2023**, *155* (6).

Doerr, A. Single-Particle Cryo-Electron Microscopy. *Nat. Methods* **2016**, *13* (1), 23–23.

Domville, J. A. Mapping the Allosteric Pathway Leading from a Mutation in the Nicotinic Acetylcholine Receptor to a Congenital Myasthenic Syndrome. Biochemistry, University of Ottawa, 2017.

Domville, J. A.; Baenziger, J. E. An Allosteric Link Connecting the Lipid-Protein Interface to the Gating of the Nicotinic Acetylcholine Receptor. *Sci. Rep.* **2018**, *8*, 3898.

Dong, Y. Y.; Pike, A. C. W.; Mackenzie, A.; McClenaghan, C.; Aryal, P.; Dong, L.; Quigley, A.; Grieben, M.; Goubin, S.; Mukhopadhyay, S.; et al. K2P Channel Gating Mechanisms Revealed by Structures of TREK-2 and a Complex with Prozac. *Science* **2015**, *347* (6227), 1256–1259.

Douguet, D.; Honoré, E. Mammalian Mechanoelectrical Transduction: Structure and Function of Force-Gated Ion Channels. *Cell* **2019**, *179* (2), 340–354.

Doyle, D. A.; Cabral, J. M.; Pfuetzner, R. A.; Kuo, A.; Gulbis, J. M.; Cohen, S. L.; Chait, B. T.; MacKinnon, R. The Structure of the Potassium Channel: Molecular Basis of K+ Conduction and Selectivity. *Science* **1998**, *280* (5360), 69–77.

Du, J.; Lü, W.; Wu, S.; Cheng, Y.; Gouaux, E. Glycine Receptor Mechanism Elucidated by Electron Cryo-Microscopy. *Nature* **2015**, *526* (7572), 224–229.

Duncan, A. L.; Corey, R. A.; Sansom, M. S. P. Defining How Multiple Lipid Species Interact with Inward Rectifier Potassium (Kir2) Channels. *Proc. Natl. Acad. Sci. U. S. A.* **2020a**, *117* (14), 7803–7813.

Duncan, A. L.; Song, W.; Sansom, M. S. P. Lipid-Dependent Regulation of Ion Channels and G Protein–Coupled Receptors: Insights from Structures and Simulations. *Annu. Rev. Pharmacol. Toxicol.* **2020b**, *60* (1), 31–50.

Dunn, S. M.; Shelman, R. A.; Agey, M. W. Fluorescence Measurements of Anion Transport by the GABAA Receptor in Reconstituted Membrane Preparations. *Biochemistry* **1989**, *28* (6), 2551–2557.

Dutzler, R.; Campbell, E. B.; Cadene, M.; Chait, B. T.; MacKinnon, R. X-Ray Structure of a CIC Chloride Channel at 3.0 Å Reveals the Molecular Basis of Anion Selectivity. *Nature* **2002**, *415* (6869), 287–294.

Ealing, J.; Webster, R.; Brownlow, S.; Abdelgany, A.; Oosterhuis, H.; Muntoni, F.; Vaux, D. J.; Vincent, A.; Beeson, D. Mutations in Congenital Myasthenic Syndromes Reveal an ε Subunit C-Terminal Cysteine, C470, Crucial for Maturation and Surface Expression of Adult AChR. *Hum. Mol. Genet.* **2002**, *11* (24), 3087–3096.

Eisensamer, B.; Uhr, M.; Meyr, S.; Gimpl, G.; Deiml, T.; Rammes, G.; Lambert, J. J.; Zieglgänsberger, W.; Holsboer, F.; Rupprecht, R. Antidepressants and Antipsychotic Drugs Colocalize with 5-HT3 Receptors in Raft-like Domains. *Journal of Neuroscience* **2005**, *25* (44), 10198–10206.

Elgoyhen, A. B. The A9α10 Acetylcholine Receptor: A Non-Neuronal Nicotinic Receptor. *Pharmacol. Res.* **2023**, *190*, 106735.

Ellena, J. F.; Blazing, M. A.; McNamee, M. G. Lipid-Protein Interactions in Reconstituted Membranes Containing Acetylcholine Receptor. *Biochemistry* **1983**, *22* (24), 5523–5535.

Else, P. L. The Highly Unnatural Fatty Acid Profile of Cells in Culture. *Prog. Lipid Res.* **2020**, *77*, 101017.

Emsley, P.; Lohkamp, B.; Scott, W. G.; Cowtan, K. Features and Development of Coot. *Acta Crystallogr. D Biol. Crystallogr.* **2010**, *66* (Pt 4), 486–501.

Engel, A. G.; Sine, S. M. Current Understanding of Congenital Myasthenic Syndromes. *Curr. Opin. Pharmacol.* **2005**, *5* (3), 308–321.

Engel, A. G.; Shen, X.-M.; Selcen, D.; Sine, S. M. Congenital Myasthenic Syndromes: Pathogenesis, Diagnosis, and Treatment. *Lancet Neurol.* **2015**, *14* (4), 420–434.

Enkavi, G.; Javanainen, M.; Kulig, W.; Róg, T.; Vattulainen, I. Multiscale Simulations of Biological Membranes: The Challenge To Understand Biological Phenomena in a Living Substance. *Chem. Rev.* **2019**, *119* (9), 5607–5774.

Essmann, U.; Perera, L.; Berkowitz, M. L.; Darden, T.; Lee, H.; Pedersen, L. G. A Smooth Particle Mesh Ewald Method. *J. Chem. Phys.* **1995**, *103* (19), 8577–8593.

Fan, C.; Choi, W.; Sun, W.; Du, J.; Lü, W. Structure of the Human Lipid-Gated Cation Channel TRPC3. *Elife* **2018**, *7*.

Fantini, J.; Di Scala, C.; Evans, L. S.; Williamson, P. T. F.; Barrantes, F. J. A Mirror Code for Protein-Cholesterol Interactions in the Two Leaflets of Biological Membranes. *Sci. Rep.* **2016**, *6*, 21907.

Fantini, J.; Epand, R. M.; Barrantes, F. J. Cholesterol-Recognition Motifs in Membrane Proteins. In *Advances in Experimental Medicine and Biology*; Springer New York LLC, 2019; Vol. 1135, pp 3–25.

Fernández-Nievas, G. A.; Barrantes, F. J.; Antollini, S. S. Modulation of Nicotinic Acetylcholine Receptor Conformational State by Free Fatty Acids and Steroids. *J. Biol. Chem.* **2008**, *283* (31), 21478–21486.

Ferraro, N. A.; Cascio, M. Cross-Linking-Mass Spectrometry Studies of Cholesterol Interactions with Human A1 Glycine Receptor. *Anal. Chem.* **2018**, *90* (4), 2508–2516.

Fong, T. M.; McNamee, M. G. Correlation between Acetylcholine Receptor Function and Structural Properties of Membranes. *Biochemistry* **1986**, *25* (4), 830–840.

Forman, S. A.; Miller, K. W. Mapping General Anesthetic Sites in Heteromeric γ-Aminobutyric Acid Type A Receptors Reveals a Potential for Targeting Receptor Subtypes. *Anesth. Analg.* **2016**, *123* (5), 1263–1273.

Forman, S. A.; Chiara, D. C.; Miller, K. W. Anesthetics Target Interfacial Transmembrane Sites in Nicotinic Acetylcholine Receptors. *Neuropharmacology* **2015**, *96* (Pt B), 169–177.

Fourati, Z.; Sauguet, L.; Delarue, M. Genuine Open Form of the Pentameric Ligand-Gated Ion Channel GLIC. *Acta Crystallogr. D Biol. Crystallogr.* **2015**, *71* (Pt 3), 454–460.

Fourati, Z.; Ruza, R. R.; Laverty, D.; Drège, E.; Delarue-Cochin, S.; Joseph, D.; Koehl, P.; Smart, T. G.; Delarue, M. Barbiturates Bind in the GLIC Ion Channel Pore and Cause Inhibition by Stabilizing a Closed State. *J. Biol. Chem.* **2017**, *292* (5), 1550–1558.

Fourati, Z.; Howard, R. J.; Heusser, S. A.; Hu, H.; Ruza, R. R.; Sauguet, L.; Lindahl, E.; Delarue, M. Structural Basis for a Bimodal Allosteric Mechanism of General Anesthetic Modulation in Pentameric Ligand-Gated Ion Channels. *Cell Rep.* **2018**, *23* (4), 993–1004.

Frank, J. Time-Resolved Cryo-Electron Microscopy: Recent Progress. *J. Struct. Biol.* **2017**, *200* (3), 303–306.

Fritschy, J. M.; Panzanelli, P. GABAA Receptors and Plasticity of Inhibitory Neurotransmission in the Central Nervous System. *Eur. J. Neurosci.* **2014**, *39* (11), 1845–1865.

Gamal El-Din, T. M.; Lenaeus, M. J.; Zheng, N.; Catterall, W. A. Fenestrations Control Resting-State Block of a Voltage-Gated Sodium Channel. *Proc. Natl. Acad. Sci. U. S. A.* **2018**, *115* (51), 13111–13116.

Gao, Y.; Cao, E.; Julius, D.; Cheng, Y. TRPV1 Structures in Nanodiscs Reveal Mechanisms of Ligand and Lipid Action. *Nature* **2016**, *534* (7607), 347–351.

Gharpure, A.; Teng, J.; Zhuang, Y.; Noviello, C. M.; Walsh, R. M.; Cabuco, R.; Howard, R. J.; Zaveri, N. T.; Lindahl, E.; Hibbs, R. E. Agonist Selectivity and Ion Permeation in the A3β4 Ganglionic Nicotinic Receptor. *Neuron* **2019**, *104* (3), 501-511.e6.

Ghit, A.; Assal, D.; Al-shami, A. S.; Hussein, D. E. E. GABAA Receptors: Structure, Function, Pharmacology, and Related Disorders. *Journal of Genetic Engineering and Biotechnology* **2021**, *19* (1), 123.

Gibbs, E.; Chakrapani, S. Structure, Function and Physiology of 5-Hydroxytryptamine Receptors Subtype 3. In *Macromolecular Protein Complexes III: Structure and Function. Subcellular Biochemistry*; Harris, J. R., Marles-Wright, J., Eds.; Springer International Publishing, 2021; Vol. 96, pp 373–408.

Gibbs, E.; Klemm, E.; Seiferth, D.; Kumar, A.; Ilca, S. L.; Biggin, P. C.; Chakrapani, S. Conformational Transitions and Allosteric Modulation in a Heteromeric Glycine Receptor. *Nat. Commun.* **2023**, *14* (1), 1363.

Gielen, M.; Corringer, P.-J. The Dual-Gate Model for Pentameric Ligand-Gated Ion Channels Activation and Desensitization. *J. Physiol.* **2018**, *596* (10), 1873–1902.

Gielen, M.; Thomas, P.; Smart, T. G. The Desensitization Gate of Inhibitory Cys-Loop Receptors. *Nat. Commun.* **2015**, *6* (1), 6829.

Gielen, M.; Barilone, N.; Corringer, P. J. The Desensitization Pathway of GABAA Receptors, One Subunit at a Time. *Nat. Commun.* **2020**, *11* (1), 5369.

Gill, C. H.; Peters, J. A.; Lambert, J. J. An Electrophysiological Investigation of the Properties of a Murine Recombinant 5-HT3 Receptor Stably Expressed in HEK 293 Cells. *Br. J. Pharmacol.* **1995**, *114* (6), 1211–1221.

Gonzalez-Gutierrez, G.; Cuello, L. G.; Nair, S. K.; Grosman, C. Gating of the Proton-Gated Ion Channel from Gloeobacter Violaceus at PH 4 as Revealed by X-Ray Crystallography. *Proc. Natl. Acad. Sci. U. S. A.* **2013**, *110* (46), 18716–18721.

Goswami, U.; Rahman, M. M.; Teng, J.; Hibbs, R. E. Structural Interplay of Anesthetics and Paralytics on Muscle Nicotinic Receptors. *Nat. Commun.* **2023**, *14* (1), 3169.

Gowers, R. J.; Linke, M.; Barnoud, J.; Reddy, T. J. E.; Melo, M. N.; Seyler, S. L.; Domański, J.; Dotson, D. L.; Buchoux, S.; Kenney, I. M.; et al. MDAnalysis: A Python Package for the Rapid Analysis of Molecular Dynamics Simulations. In *Proceedings of the 15th Python in Science Conference*; Benthall, S., Rostrup, S., Eds.; 2016; pp 98–105.

Grinkova, Y. V.; Denisov, I. G.; Sligar, S. G. Engineering Extended Membrane Scaffold Proteins for Self-Assembly of Soluble Nanoscale Lipid Bilayers. *Protein Eng. Des. Sel.* **2010**, *23* (11), 843–848.

Grosman, C.; Zhou, M.; Auerbach, A. Mapping the Conformational Wave of Acetylcholine Receptor Channel Gating. *Nature* **2000**, *403* (6771), 773.

Grutter, T.; de Carvalho, L. P.; Dufresne, V.; Taly, A.; Edelstein, S. J.; Changeux, J.-P. Molecular Tuning of Fast Gating in Pentameric Ligand-Gated Ion Channels. *Proc. Natl. Acad. Sci. U. S. A.* **2005**, *102* (50), 18207–18212.

Gu, S.; Matta, J. A.; Lord, B.; Harrington, A. W.; Sutton, S. W.; Davini, W. B.; Bredt, D. S. Brain A7 Nicotinic Acetylcholine Receptor Assembly Requires NACHO. *Neuron* **2016**, *89* (5), 948–955.

Guo, Y. R.; MacKinnon, R. Structure-Based Membrane Dome Mechanism for Piezo Mechanosensitivity. *Elife* **2017**, *6*.

Gupta, S.; Chakraborty, S.; Vij, R.; Auerbach, A. A Mechanism for Acetylcholine Receptor Gating Based on Structure, Coupling, Phi, and Flip. *J. Gen. Physiol.* **2017**, *149* (1), 85–103.

Guzmán, G. R.; Ortiz-Acevedo, A.; Ricardo, A.; Rojas, L. V.; Lasalde-Dominicci, J. A. The Polarity of Lipid-Exposed Residues Contributes to the Functional Differences between Torpedo and Muscle-Type Nicotinic Receptors. *J. Membr. Biol.* **2006**, *214* (3), 131–138.

Haeger, S.; Kuzmin, D.; Detro-Dassen, S.; Lang, N.; Kilb, M.; Tsetlin, V.; Betz, H.; Laube, B.; Schmalzing, G. An Intramembrane Aromatic Network Determines Pentameric Assembly of Cys-Loop Receptors. *Nat. Struct. Mol. Biol.* **2010**, *17* (1), 90–98.

Hammond, J. R.; Martin, I. L. Solubilization of the Benzodiazepine/γ-Aminobutyric Acid Receptor Complex: Comparison of the Detergents Octylglucopyranoside and 3-[(3-cholamidopropyl)-dimethylammonio] 1-propanesulfonate (CHAPS). *J. Neurochem.* **1986**, *47* (4), 1161–1171.

Hammond, J. R.; Martin, I. L. Modulation of [3H]Flunitrazepam Binding to Rat Cerebellar Benzodiazepine Receptors by Phosphatidylserine. *Eur. J. Pharmacol.* **1987**, *137*, 49–58.

Hamouda, A. K.; Sanghvi, M.; Sauls, D.; Machu, T. K.; Blanton, M. P. Assessing the Lipid Requirements of the Torpedo Californica Nicotinic Acetylcholine Receptor. *Biochemistry* **2006a**, *45* (13), 4327–4337.

Hamouda, A. K.; Chiara, D. C.; Sauls, D.; Cohen, J. B.; Blanton, M. P. Cholesterol Interacts with Transmembrane α-Helices M1, M3, and M4 of the Torpedo Nicotinic Acetylcholine Receptor: Photolabeling Studies Using [3H]Azichoiesterol. *Biochemistry* **2006b**, *45* (3), 976–986.

Hansen, S. B.; Sulzenbacher, G.; Huxford, T.; Marchot, P.; Taylor, P.; Bourne, Y. Structures of Aplysia AChBP Complexes with Nicotinic Agonists and Antagonists Reveal Distinctive Binding Interfaces and Conformations. *EMBO J.* **2005**, *24* (20), 3635–3646.

Hansen, S. B.; Tao, X.; MacKinnon, R. Structural Basis of PIP2 Activation of the Classical Inward Rectifier K+ Channel Kir2.2. *Nature* **2011**, *477* (7365), 495–498.

Haselbach, D.; Komarov, I.; Agafonov, D. E.; Hartmuth, K.; Graf, B.; Dybkov, O.; Urlaub, H.; Kastner, B.; Lührmann, R.; Stark, H. Structure and Conformational Dynamics of the Human Spliceosomal Bact Complex. *Cell* **2018**, *172* (3), 454-464.e11.

Haselwandter, C. A.; Mackinnon, R. Piezo's Membrane Footprint and Its Contribution to Mechanosensitivity. *Elife* **2018**, *7*, e41968.

Hassaine, G.; Deluz, C.; Grasso, L.; Wyss, R.; Tol, M. B.; Hovius, R.; Graff, A.; Stahlberg, H.; Tomizaki, T.; Desmyter, A.; et al. X-Ray Structure of the Mouse Serotonin 5-HT3 Receptor. *Nature* **2014**, *512* (7514), 276–281.

Hedger, G.; Sansom, M. S. P. Lipid Interaction Sites on Channels, Transporters and Receptors: Recent Insights from Molecular Dynamics Simulations. *Biochim. Biophys. Acta* **2016**, *1858* (10), 2390–2400.

Heidmann, T.; Sobel, A.; Changeux, J.-P. Recovery of Allosteric Interactions between a Fluorescent Cholinergenic Agonist and Local Anesthetics after Removal of the Detergent from Cholate-Solubilized Membrane Fragments Rich in Acetylcholine Receptor. *FEBS Lett.* **1978**, *94* (2), 397–404.

Heidmann, T.; Sobel, A.; Popot, J.-L.; Changeux, J.-P. Reconstitution of a Functional Acetylcholine Receptor. Conservation of the Conformational and Allosteric Transitions and Recovery of the Permeability Response; Role of Lipids. *Eur. J. Biochem.* **1980**, *110*, 35–55.

Hénault, C. M.; Juranka, P. F.; Baenziger, J. E. The M4 Transmembrane α-Helix Contributes Differently to Both the Maturation and Function of Two Prokaryotic Pentameric Ligand-Gated Ion Channels. *J. Biol. Chem.* **2015a**, *290* (41), 25118–25128.

Hénault, C. M.; Sun, J.; Therien, J. P. D.; daCosta, C. J. B.; Carswell, C. L.; Labriola, J. M.; Juranka, P. F.; Baenziger, J. E. The Role of the M4 Lipid-Sensor in the Folding, Trafficking, and Allosteric Modulation of Nicotinic Acetylcholine Receptors. *Neuropharmacology* **2015b**, *96*, 157–168.

Hénault, C. M.; Govaerts, C.; Spurny, R.; Brams, M.; Estrada-Mondragon, A.; Lynch, J. W.; Bertrand, D.; Pardon, E.; Evans, G. L.; Woods, K.; et al. A Lipid Site Shapes the Agonist Response of a Pentameric Ligand-Gated Ion Channel. *Nat. Chem. Biol.* **2019**, *15* (12), 1156–1164.

Hernandez, C. C.; Macdonald, R. L. A Structural Look at GABAA Receptor Mutations Linked to Epilepsy Syndromes. *Brain Res.* **2019**, *1714* (February), 234–247.

Hertling-Jaweed, S.; Bandini, G.; Müller-Fahrnow, A.; Dommes, V.; Hucho, F. Rapid Preparation of the Nicotinic Acetylcholine Receptor for Crystallization in Detergent Solution. *FEBS Lett.* **1988**, *241* (1–2), 29–32.

Herz, J. M.; Johnson, D. A.; Taylor, P. Interaction of Noncompetitive Inhibitors with the Acetylcholine Receptor. The Site Specificity and Spectroscopic Properties of Ethidium Binding. *J. Biol. Chem.* **1987**, *262* (15), 7238–7247.

Hesketh, T. R.; Smith, G. A.; Houslay, M. D.; McGill, K. A.; Birdsall, N. J.; Metcalfe, J. C.; Warren, G. B. Annular Lipids Determine the ATPase Activity of a Calcium Transport Protein Complexed with Dipalmitoyllecithin. *Biochemistry* **1976**, *15* (19), 4145–4151.

Hess, B.; Bekker, H.; Berendsen, H. J. C.; Fraaije, J. G. E. M. LINCS: A Linear Constraint Solver for Molecular Simulations. *J. Comput. Chem.* **1997**, *18* (12), 1463–1472.

Hesselmans, L. F. G. M.; Jennekens, F. G. I.; Van denOord, C. J. M.; Veldman, H.; Vincent, A. Development of Innervation of Skeletal Muscle Fibers in Man: Relation to Acetylcholine Receptors. *Anat. Rec.* **1993**, *236* (3), 553–562.

Hibbs, R. E.; Gouaux, E. Principles of Activation and Permeation in an Anion-Selective Cys-Loop Receptor. *Nature* **2011**, *474* (7349), 54–60.

Hibino, H.; Inanobe, A.; Furutani, K.; Murakami, S.; Findlay, I.; Kurachi, Y. Inwardly Rectifying Potassium Channels: Their Structure, Function, and Physiological Roles. *Physiol. Rev.* **2010**, *90* (1), 291–366.

Hilf, R. J. C.; Dutzler, R. X-Ray Structure of a Prokaryotic Pentameric Ligand-Gated Ion Channel. *Nature* **2008**, *452* (7185), 375–379.

Hilf, R. J. C.; Dutzler, R. Structure of a Potentially Open State of a Proton-Activated Pentameric Ligand-Gated Ion Channel. *Nature* **2009**, *457* (7225), 115–118.

Hilf, R. J. C.; Bertozzi, C.; Zimmermann, I.; Reiter, A.; Trauner, D.; Dutzler, R. Structural Basis of Open Channel Block in a Prokaryotic Pentameric Ligand-Gated Ion Channel. *Nat. Struct. Mol. Biol.* **2010**, *17* (11), 1330–1336.

Hilgemann, D. W.; Ball, R. Regulation of Cardiac Na+, Ca2+ Exchange and KATP Potassium Channels by PIP2. *Science* **1996**, *273* (5277), 956–959.

Hill, W. G.; Southern, N. M.; MacIver, B.; Potter, E.; Apodaca, G.; Smith, C. P.; Zeidel, M. L. Isolation and Characterization of the Xenopus Oocyte Plasma Membrane: A New Method for Studying Activity of Water and Solute Transporters. *Am. J. Physiol. Renal Physiol.* **2005**, *289* (1), F217-24.

Hite, R. K.; MacKinnon, R. Structural Titration of Slo2.2, a Na+-Dependent K+ Channel. *Cell* **2017**, *168* (3), 390-399.e11.

Hite, R. K.; Butterwick, J. A.; MacKinnon, R. Phosphatidic Acid Modulation of Kv Channel Voltage Sensor Function. *Elife* **2014**, *3*.

Honoré, E.; Patel, A. J.; Chemin, J.; Suchyna, T.; Sachs, F. Desensitization of Mechano-Gated K2P Channels. *Proc. Natl. Acad. Sci. U. S. A.* **2006**, *103* (18), 6859–6864.

Hoover, W. G. Canonical Dynamics: Equilibrium Phase-Space Distributions. *Phys. Rev. A Gen. Phys.* **1985**, *31* (3), 1695–1697.

Hosie, A. M.; Wilkins, M. E.; da Silva, H. M. A.; Smart, T. G. Endogenous Neurosteroids Regulate GABAA Receptors through Two Discrete Transmembrane Sites. *Nature* **2006**, *444* (7118), 486–489.

Hoskin, J. L.; Al-Hasan, Y.; Sabbagh, M. N. Nicotinic Acetylcholine Receptor Agonists for the Treatment of Alzheimer's Dementia: An Update. *Nicotine Tob. Res.* **2019**, *21* (3), 370–376.

Hu, H.; Nemecz, Á.; Van Renterghem, C.; Fourati, Z.; Sauguet, L.; Corringer, P.-J.; Delarue, M. Crystal Structures of a Pentameric Ion Channel Gated by Alkaline PH Show a Widely Open Pore and Identify a Cavity for Modulation. *Proc. Natl. Acad. Sci. U. S. A.* **2018a**, *115* (17), E3959–E3968.

Hu, H.; Ataka, K.; Menny, A.; Fourati, Z.; Sauguet, L.; Corringer, P.-J.; Koehl, P.; Heberle, J.; Delarue, M. Electrostatics, Proton Sensor, and Networks Governing the Gating Transition in

GLIC, a Proton-Gated Pentameric Ion Channel. *Proceedings of the National Academy of Sciences* **2018b**, *115* (52), E12172–E12181.

Hu, H.; Howard, R. J.; Bastolla, U.; Lindahl, E.; Delarue, M. Structural Basis for Allosteric Transitions of a Multidomain Pentameric Ligand-Gated Ion Channel. *Proc. Natl. Acad. Sci. U. S. A.* **2020**, *117* (24), 13437–13446.

Huang, C. L.; Feng, S.; Hilgemann, D. W. Direct Activation of Inward Rectifier Potassium Channels by PIP2 and Its Stabilization by Gβγ. *Nature* **1998**, *391* (6669), 803–806.

Huang, J.; Mackerell, A. D., Jr. CHARMM36 All-Atom Additive Protein Force Field: Validation Based on Comparison to NMR Data. *J. Comput. Chem.* **2013**, *34* (25), 2135–2145.

Huang, X.; Chen, H.; Michelsen, K.; Schneider, S.; Shaffer, P. L. Crystal Structure of Human Glycine Receptor-A3 Bound to Antagonist Strychnine. *Nature* **2015**, *526* (7572), 277–280.

Huang, X.; Shaffer, P. L.; Ayube, S.; Bregman, H.; Chen, H.; Lehto, S. G.; Luther, J. A.; Matson, D. J.; McDonough, S. I.; Michelsen, K.; et al. Crystal Structures of Human Glycine Receptor A3 Bound to a Novel Class of Analgesic Potentiators. *Nat. Struct. Mol. Biol.* **2017a**, *24* (2), 108–113.

Huang, X.; Chen, H.; Shaffer, P. L. Crystal Structures of Human GlyRα3 Bound to Ivermectin. *Structure* **2017b**, *25* (6), 945-950.e2.

Hubbard, S. R.; Miller, W. T. Receptor Tyrosine Kinases: Mechanisms of Activation and Signaling. *Curr. Opin. Cell Biol.* **2007**, *19* (2), 117–123.

Hughes, T. E. T.; Pumroy, R. A.; Yazici, A. T.; Kasimova, M. A.; Fluck, E. C.; Huynh, K. W.; Samanta, A.; Molugu, S. K.; Zhou, Z. H.; Carnevale, V.; et al. Structural Insights on TRPV5 Gating by Endogenous Modulators. *Nat. Commun.* **2018**, *9* (1), 4198.

Hunter, J. D. Matplotlib: A 2D Graphics Environment. *Computing in Science & Engineering* **2007**, *9* (3), 90–65.

Hussy, N.; Lukas, W.; Jones, K. A. Functional Properties of a Cloned 5-Hydroxytryptamine Ionotropic Receptor Subunit: Comparison with Native Mouse Receptors. *J. Physiol.* **1994**, *481 (Pt 2)*, 311–323.

Ingólfsson, H. I.; Carpenter, T. S.; Bhatia, H.; Bremer, P.-T.; Marrink, S. J.; Lightstone, F. C. Computational Lipidomics of the Neuronal Plasma Membrane. *Biophys. J.* **2017**, *113* (10), 2271–2280.

Jadey, S.; Auerbach, A. An Integrated Catch-and-Hold Mechanism Activates Nicotinic Acetylcholine Receptors. *J. Gen. Physiol.* **2012**, *140* (1), 17–28.

Jaiteh, M.; Taly, A.; Hénin, J. Evolution of Pentameric Ligand-Gated Ion Channels: Pro-Loop Receptors. *PLoS One* **2016**, *11* (3), e0151934.

Jayakar, S. S.; Dailey, W. P.; Eckenhoff, R. G.; Cohen, J. B. Identification of Propofol Binding Sites in a Nicotinic Acetylcholine Receptor with a Photoreactive Propofol Analog. *J. Biol. Chem.* **2013**, *288* (9), 6178–6189.

Jha, A.; Auerbach, A. Acetylcholine Receptor Channels Activated by a Single Agonist Molecule. *Biophys. J.* **2010**, *98* (9), 1840–1846.

Jha, A.; Cadugan, D. J.; Purohit, P. G.; Auerbach, A. Acetylcholine Receptor Gating at Extracellular Transmembrane Domain Interface: The Cys-Loop and M2-M3 Linker. *J. Gen. Physiol.* **2007**, *130* (6), 547–558.

Jha, A.; Gupta, S.; Zucker, S. N.; Auerbach, A. The Energetic Consequences of Loop 9 Gating Motions in Acetylcholine Receptor-Channels. *J. Physiol.* **2012**, *590* (1), 119–129.

Jiang, Q.-X. Lipid-Dependent Gating of Ion Channels. In *Protein-Lipid Interactions: Perspectives, Techniques and Challenges*; 2018; pp 160–163.

Jiang, Y.; Lee, A.; Chen, J.; Ruta, V.; Cadene, M.; Chait, B. T.; MacKinnon, R. X-Ray Structure of a Voltage-Dependent K+ Channel. *Nature* **2003**, *423* (6935), 33–41.

Jin, P.; Bulkley, D.; Guo, Y.; Zhang, W.; Guo, Z.; Huynh, W.; Wu, S.; Meltzer, S.; Cheng, T.; Jan, L. Y.; et al. Electron Cryo-Microscopy Structure of the Mechanotransduction Channel NOMPC. *Nature* **2017**, *547* (7661), 118–122.

Jo, S.; Kim, T.; Iyer, V. G.; Im, W. CHARMM-GUI: A Web-Based Graphical User Interface for CHARMM. *J. Comput. Chem.* **2008**, *29* (11), 1859–1865.

Jones, O. T.; McNamee, M. G. Annular and Nonannular Binding Sites for Cholesterol Associated with the Nicotinic Acetylcholine Receptor. *Biochemistry* **1988**, *27* (7), 2364–2374.

Jost, P. C.; Griffith, O. H.; Capaldi, R. A.; Vanderkooi, G. Evidence for Boundary Lipid in Membranes. *Proc. Natl. Acad. Sci. U. S. A.* **1973**, *70* (2), 480–484.

Jumper, J.; Evans, R.; Pritzel, A.; Green, T.; Figurnov, M.; Ronneberger, O.; Tunyasuvunakool, K.; Bates, R.; Žídek, A.; Potapenko, A.; et al. Highly Accurate Protein Structure Prediction with AlphaFold. *Nature* **2021**, *596* (7873), 583–589.

Kaczor, P. T.; Wolska, A. D.; Mozrzymas, J. W. A1 Subunit Histidine 55 at the Interface between Extracellular and Transmembrane Domains Affects Preactivation and Desensitization of the GABAA Receptor. *ACS Chem. Neurosci.* **2021**, *12* (3), 562–572.

Kaczor, P. T.; Michalowski, M. A.; Mozrzymas, J. W. A1 Proline 277 Residues Regulate GABAAR Gating through M2-M3 Loop Interaction in the Interface Region. *ACS Chem. Neurosci.* **2022**, *13* (21), 3044–3056.

Kang, G.; Allard, C. A. H.; Valencia-Montoya, W. A.; van Giesen, L.; Kim, J. J.; Kilian, P. B.; Bai, X.; Bellono, N. W.; Hibbs, R. E. Sensory Specializations Drive Octopus and Squid Behaviour. *Nature* **2023**, *616* (7956), 378–383.

Karlsson, E.; Heilbronn, E.; Widlund, L. Isolation of the Nicotinic Acetylcholine Receptor by Biospecific Chromatography on Insolubilized Naja Naja Neurotoxin. *FEBS Lett.* **1972**, *28* (1), 107–111.

Kasaragod, V. B.; Schindelin, H. Structure of Heteropentameric GABAA Receptors and Receptor-Anchoring Properties of Gephyrin. *Front. Mol. Neurosci.* **2019**, *12* (August), 1–9.

Kasaragod, V. B.; Mortensen, M.; Hardwick, S. W.; Wahid, A. A.; Dorovykh, V.; Chirgadze, D. Y.; Smart, T. G.; Miller, P. S. Mechanisms of Inhibition and Activation of Extrasynaptic Aβ GABAA Receptors. *Nature* **2022**, *602* (7897), 529–533.

Kash, T. L.; Dizon, M.-J. F.; Trudell, J. R.; Harrison, N. L. Charged Residues in the B2 Subunit Involved in GABAA Receptor Activation. *J. Biol. Chem.* **2004**, *279* (6), 4887–4893.

Kawate, T.; Michel, J. C.; Birdsong, W. T.; Gouaux, E. Crystal Structure of the ATP-Gated P2X(4) Ion Channel in the Closed State. *Nature* **2009**, *460* (7255), 592–598.

Kelley, S. P.; Dunlop, J. I.; Kirkness, E. F.; Lambert, J. J.; Peters, J. A. A Cytoplasmic Region Determines Single-Channel Conductance in 5-HT3 Receptors. *Nature* **2003**, *424* (6946), 321–324.

Keramidas, A.; Kash, T. L.; Harrison, N. L. The Pre-M1 Segment of the Alpha1 Subunit Is a Transduction Element in the Activation of the GABAA Receptor. *J. Physiol.* **2006**, *575* (Pt 1), 11–22.

Kim, J. J.; Hibbs, R. E. Direct Structural Insights into GABAA Receptor Pharmacology. *Trends Biochem. Sci.* **2021**, *46* (6), 502–517.

Kim, J. J.; Gharpure, A.; Teng, J.; Zhuang, Y.; Howard, R. J.; Zhu, S.; Noviello, C. M.; Jr, R. M. W.; Lindahl, E.; Hibbs, R. E. Shared Structural Mechanisms of General Anaesthetics and Benzodiazepines. *Nature* **2020**, *585* (7824), 303–308.

Kinde, M. N.; Chen, Q.; Lawless, M. J.; Mowrey, D. D.; Xu, J.; Saxena, S.; Xu, Y.; Tang, P. Conformational Changes Underlying Desensitization of the Pentameric Ligand-Gated Ion Channel ELIC. *Structure* **2015**, *23* (6), 995–1004.

King, J. R.; Kabbani, N. Alpha 7 Nicotinic Receptor Coupling to Heterotrimeric G Proteins Modulates RhoA Activation, Cytoskeletal Motility, and Structural Growth. *J. Neurochem.* **2016**, *138* (4), 532–545.

Kloda, A.; Martinac, B.; Adams, D. J. Polymodal Regulation of NMDA Receptor Channels. *Channels* **2007**, *1* (5), 334–343.

Kłopotowski, K.; Michałowski, M. A.; Gos, M.; Mosiądz, D.; Czyżewska, M. M.; Mozrzymas, J. W. Mutation of Valine 53 at the Interface between Extracellular and Transmembrane Domains of the B2 Principal Subunit Affects the GABAA Receptor Gating. *Eur. J. Pharmacol.* **2023**, *947*, 175664.

Kneussel, M.; Betz, H. Clustering of Inhibitory Neurotransmitter Receptors at Developing Postsynaptic Sites: The Membrane Activation Model. *Trends in Neurosciences* **2000**, *23* (9), 429–435.

Knox, H. J.; Rego Campello, H.; Lester, H. A.; Gallagher, T.; Dougherty, D. A. Characterization of Binding Site Interactions and Selectivity Principles in the A3β4 Nicotinic Acetylcholine Receptor. *J. Am. Chem. Soc.* **2022**, *144* (35), 16101–16117.

Korona, D.; Dirnberger, B.; Giachello, C. N. G.; Queiroz, R. M. L.; Popovic, R.; Müller, K. H.; Minde, D. P.; Deery, M. J.; Johnson, G.; Firth, L. C.; et al. Drosophila Nicotinic Acetylcholine Receptor Subunits and Their Native Interactions with Insecticidal Peptide Toxins. *Elife* **2022**, *11*.

Kubalek, E.; Ralston, S.; Lindstrom, J.; Unwin, N. Location of Subunits within the Acetylcholine Receptor by Electron Image Analysis of Tubular Crystals from Torpedo Marmorata. *J. Cell Biol.* **1987**, *105* (July 1987), 9–18.

Kudryashev, M.; Castaño-Díez, D.; Deluz, C.; Hassaine, G.; Grasso, L.; Graf-Meyer, A.; Vogel, H.; Stahlberg, H. The Structure of the Mouse Serotonin 5-HT3 Receptor in Lipid Vesicles. *Structure* **2016**, *24* (1), 165–170.

Kumar, A.; Basak, S.; Rao, S.; Gicheru, Y.; Mayer, M. L.; Sansom, M. S. P.; Chakrapani, S. Mechanisms of Activation and Desensitization of Full-Length Glycine Receptor in Lipid Nanodiscs. *Nat. Commun.* **2020a**, *11* (1), 3752.

Kumar, A.; Kindig, K.; Rao, S.; Zaki, A.-M.; Basak, S.; Sansom, M. S. P.; Biggin, P. C.; Chakrapani, S. Structural Basis for Cannabinoid-Induced Potentiation of Alpha1-Glycine Receptors in Lipid Nanodiscs. *Nat. Commun.* **2022**, *13* (1), 4862.

Kumar, P.; Wang, Y.; Zhang, Z.; Zhao, Z.; Cymes, G. D.; Tajkhorshid, E.; Grosman, C. Cryo-EM Structures of a Lipid-Sensitive Pentameric Ligand-Gated Ion Channel Embedded in a Phosphatidylcholine-Only Bilayer. *Proceedings of the National Academy of Sciences* **2020b**, *117* (3), 1788–1798.

Kumar, P.; Cymes, G. D.; Grosman, C. Structure and Function at the Lipid – Protein Interface of a Pentameric Ligand-Gated Ion Channel. *Proc. Natl. Acad. Sci. U. S. A.* **2021**, *118* (23), e2100164118.

Kuo, A.; Gulbis, J. M.; Antcliff, J. F.; Rahman, T.; Lowe, E. D.; Zimmer, J.; Cuthbertson, J.; Ashcroft, F. M.; Ezaki, T.; Doyle, D. A. Crystal Structure of the Potassium Channel KirBac1.1 in the Closed State. *Science* **2003**, *300* (5627), 1922–1926.

Kuo, I. Y.; Ehrlich, B. E. Signaling in Muscle Contraction. *Cold Spring Harb. Perspect. Biol.* **2015**, *7* (2), a006023.

Kwon, D. H.; Zhang, F.; Fedor, J. G.; Suo, Y.; Lee, S.-Y. Vanilloid-Dependent TRPV1 Opening Trajectory from CryoEM Ensemble Analysis. *Nat. Commun.* **2022**, *13* (1), 2874.

Labriola, J. M.; daCosta, C. J. B.; Wang, S.; Figeys, D.; Smith, J. C.; Sturgeon, R. M.; Baenziger, J. E. Phospholipase C Activity Affinity Purifies with the Torpedo Nicotinic Acetylcholine Receptor. *J. Biol. Chem.* **2010**, *285* (14), 10337–10343.

Labriola, J. M.; Pandhare, A.; Jansen, M.; Blanton, M. P.; Corringer, P.-J.; Baenziger, J. E. Structural Sensitivity of a Prokaryotic Pentameric Ligand-Gated Ion Channel to Its Membrane Environment. *J. Biol. Chem.* **2013**, *288* (16), 11294–11303.

Langley, J. N. On the Reaction of Cells and of Nerve-Endings to Certain Poisons, Chiefly as Regards the Reaction of Striated Muscle to Nicotine and to Curari. *J. Physiol.* **1905**, *33* (4–5), 374–413.

Lape, R.; Colquhoun, D.; Sivilotti, L. G. On the Nature of Partial Agonism in the Nicotinic Receptor Superfamily. *Nature* **2008**, *454* (7205), 722–727.

Lasalde, J. A.; Tamamizu, S.; Butler, D. H.; Vibat, C. R.; Hung, B.; McNamee, M. G. Tryptophan Substitutions at the Lipid-Exposed Transmembrane Segment M4 of Torpedo Californica Acetylcholine Receptor Govern Channel Gating. *Biochemistry* **1996**, *35* (45), 14139–14148.

Laverty, D.; Thomas, P.; Field, M.; Andersen, O. J.; Gold, M. G.; Biggin, P. C.; Gielen, M.; Smart, T. G. Crystal Structures of a GABAA-Receptor Chimera Reveal New Endogenous Neurosteroid-Binding Sites. *Nat. Struct. Mol. Biol.* **2017**, *24* (11), 977–985.

Laverty, D.; Desai, R.; Uchański, T.; Masiulis, S.; Stec, W. J.; Malinauskas, T.; Zivanov, J.; Pardon, E.; Steyaert, J.; Miller, K. W.; et al. Cryo-EM Structure of the Human A1β3γ2 GABAA Receptor in a Lipid Bilayer. *Nature* **2019**, *565* (7740), 516–520.

Lawrence, N. S.; Ross, T. J.; Stein, E. A. Cognitive Mechanisms of Nicotine on Visual Attention. *Neuron* **2002**, *36* (3), 539–548.

Lee, A. G. How Lipids Affect the Activities of Integral Membrane Proteins. *Biochim. Biophys. Acta* **2004**, *1666* (1–2), 62–87.

Lee, C.-H.; MacKinnon, R. Structures of the Human HCN1 Hyperpolarization-Activated Channel. *Cell* **2017**, *168* (1–2), 111-120.e11.

Lee, K. P. K.; Chen, J.; MacKinnon, R. Molecular Structure of Human KATP in Complex with ATP and ADP. *Elife* **2017**, *6*.

Lee, S.-J.; Ren, F.; Zangerl-Plessl, E.-M.; Heyman, S.; Stary-Weinzinger, A.; Yuan, P.; Nichols, C. G. Structural Basis of Control of Inward Rectifier Kir2 Channel Gating by Bulk Anionic Phospholipids. *J. Gen. Physiol.* **2016**, *148* (3), 227–237.

Lee, W. Y.; Sine, S. M. Principal Pathway Coupling Agonist Binding to Channel Gating in Nicotinic Receptors. *Nature* **2005**, *438* (7065), 243–247.

Lee, W. Y.; Free, C. R.; Sine, S. M. Nicotinic Receptor Interloop Proline Anchors B1-B2 and Cys Loops in Coupling Agonist Binding to Channel Gating. *J. Gen. Physiol.* **2008**, *132* (2), 265–278.

Lee, W. Y.; Free, C. R.; Sine, S. M. Binding to Gating Transduction in Nicotinic Receptors: Cys-Loop Energetically Couples to Pre-M1 and M2-M3 Regions. *Journal of Neuroscience* **2009**, *29* (10), 3189–3199.

Lee, Y. H.; Li, L.; Lasalde-Dominicci, J. A.; Rojas, L. V.; McNamee, M. G.; Ortiz-Miranda, S. I.; Pappone, P. Mutations in the M4 Domain of Torpedo Californica Acetylcholine Receptor Dramatically Alter Ion Channel Function. *Biophys. J.* **1994**, *66* (3), 646–653.

Legesse, D. H.; Fan, C.; Teng, J.; Zhuang, Y.; Howard, R. J.; Noviello, C. M.; Lindahl, E.; Hibbs, R. E. Structural Insights into Opposing Actions of Neurosteroids on GABAA Receptors. *Nat. Commun.* **2023**, *14* (1), 5091.

Leibel, W. S.; Firestone, L. L.; Legler, D. C.; Braswell, L. M.; Miller, K. W. Two Pools of Cholesterol in Acetylcholine Receptor-Rich Membranes from Torpedo. *Biochim. Biophys. Acta* **1987**, *897* (2), 249–260.

Lemoine, D.; Jiang, R.; Taly, A.; Chataigneau, T.; Specht, A.; Grutter, T. Ligand-Gated Ion Channels: New Insights into Neurological Disorders and Ligand Recognition. *Chemical Reviews* **2012**, *112* (12), 6285–6318.

Lev, B.; Murail, S.; Poitevin, F.; Cromer, B. A.; Baaden, M.; Delarue, M.; Allen, T. W. String Method Solution of the Gating Pathways for a Pentameric Ligand-Gated Ion Channel. *Proc. Natl. Acad. Sci. U. S. A.* **2017**, *114* (21), E4158–E4167.

Levental, I.; Lyman, E. Regulation of Membrane Protein Structure and Function by Their Lipid Nano-Environment. *Nat. Rev. Mol. Cell Biol.* **2023**, *0123456789* (2), 107–122.

Levina, N.; Totemeyer, S.; Stokes, N. R.; Louis, P.; Jones, M. A.; Booth, I. R. Protection of Escherichia Coli Cells against Extreme Turgor by Activation of MscS and MscL Mechanosensitive Channels: Identification of Genes Required for MscS Activity. *EMBO J.* **1999**, *18* (7), 1730–1737.

Levitan, I.; Singh, D. K.; Rosenhouse-Dantsker, A. Cholesterol Binding to Ion Channels. *Front. Physiol.* **2014**, *5*, 65.

Li, H.; Papadopoulos, V. Peripheral-Type Benzodiazepine Receptor Function in Cholesterol Transport. Identification of a Putative Cholesterol Recognition/Interaction Amino Acid Sequence and Consensus Pattern. *Endocrinology* **1998**, *139* (12), 4991–4997.

Li, L.; Schuchard, M.; Palma, A.; Pradier, L.; McNamee, M. G. Functional Role of the Cysteine 451 Thiol Group in the M4 Helix of the γ Subunit of Torpedo Californica Acetylcholine Receptor. *Biochemistry* **1990**, *29* (23), 5428–5436.

Li, L.; Lee, Y.-H.; Pappone, P.; Palma, A.; McNamee, M. G. Site-Specific Mutations of Nicotinic Acetylcholine Receptor at the Lipid-Protein Interface Dramatically Alter Ion Channel Gating. *Biophysical Journal* **1992**, *62*, 61–63.

Li, X.; Serwanski, D. R.; Miralles, C. P.; Bahr, B. A.; De Blas, A. L. Two Pools of Triton X-100-Insoluble GABA(A) Receptors Are Present in the Brain, One Associated to Lipid Rafts and Another One to the Post-Synaptic GABAergic Complex. *J. Neurochem.* **2007**, *102* (4), 1329–1345.

Liang, X.; Howard, J. Structural Biology: Piezo Senses Tension through Curvature. *Curr. Biol.* **2018**, *28* (8), R357–R359.

Lichtenegger, M.; Tiapko, O.; Svobodova, B.; Stockner, T.; Glasnov, T. N.; Schreibmayer, W.; Platzer, D.; De La Cruz, G. G.; Krenn, S.; Schober, R.; et al. An Optically Controlled Probe Identifies Lipid-Gating Fenestrations within the TRPC3 Channel Article. *Nat. Chem. Biol.* **2018**, *14* (4), 396–404.

Liebschner, D.; Afonine, P. V.; Baker, M. L.; Bunkóczi, G.; Chen, V. B.; Croll, T. I.; Hintze, B.; Hung, L. W.; Jain, S.; McCoy, A. J.; et al. Macromolecular Structure Determination Using X-Rays, Neutrons and Electrons: Recent Developments in Phenix. *Acta Crystallogr D Struct Biol* **2019**, *75* (Pt 10), 861–877.

Liu, K.; Li, L.; Luan, S. An Essential Function of Phosphatidylinositol Phosphates in Activation of Plant Shaker-Type K+ Channels. *Plant J.* **2005**, *42* (3), 433–443.

Liu, S.; Xu, L.; Guan, F.; Liu, Y. T.; Cui, Y.; Zhang, Q.; Zheng, X.; Bi, G. Q.; Zhou, Z. H.; Zhang, X.; et al. Cryo-EM Structure of the Human A5β3 GABAA Receptor. *Cell Res.* **2018**, *28* (9), 958–961.

Liu, X.; Wang, W. Asymmetric Gating of a Human Hetero-Pentameric Glycine Receptor. *Res Sq* **2023**.

Liu, Y. T.; Tao, C. L.; Zhang, X.; Xia, W.; Shi, D. Q.; Qi, L.; Xu, C.; Sun, R.; Li, X. W.; Lau, P. M.; et al. Mesophasic Organization of GABAA Receptors in Hippocampal Inhibitory Synapses. *Nat. Neurosci.* **2020**, *23* (12), 1589–1596.

Long, S. B.; Campbell, E. B.; Mackinnon, R. Voltage Sensor of Kv1.2: Structural Basis of Electromechanical Coupling. *Science* **2005**, *309* (5736), 903–908.

Loring, R. H. Speculation on How RIC-3 and Other Chaperones Facilitate A7 Nicotinic Receptor Folding and Assembly. *Molecules* **2022**, *27* (14), 4527.

Lummis, S. C. R. 5-HT(3) Receptors. *J. Biol. Chem.* **2012**, *287* (48), 40239–40245.

Lummis, S. C. R.; Beene, D. L.; Lee, L. W.; Lester, H. A.; Broadhurst, R. W.; Dougherty, D. A. Cis–Trans Isomerization at a Proline Opens the Pore of a Neurotransmitter-Gated Ion Channel. *Nature* **2005**, *438* (7065), 248–252.

Lycksell, M.; Rovšnik, U.; Hanke, A.; Martel, A.; Howard, R. J.; Lindahl, E. Biophysical Characterization of Calcium-Binding and Modulatory-Domain Dynamics in a Pentameric Ligand-Gated Ion Channel. *PNAS* **2022**, *119* (50), e2210669119.

Madjroh, N.; Mellou, E.; Davies, P. A.; Söderhielm, P. C.; Jensen, A. A. Discovery and Functional Characterization of N-(Thiazol-2-Yl)-Benzamide Analogs as the First Class of Selective Antagonists of the Zinc-Activated Channel (ZAC). *Biochem. Pharmacol.* **2021**, *193* (September), 114782.

Maher, J.; Allen, M. Planar Lipid Bilayers in Recombinant Ion Channel Research. *Methods* **2018**, *147*, 206–212.

Manetti, D.; Bellucci, C.; Chiaramonte, N.; Dei, S.; Teodori, E.; Romanelli, M. N. Designing Selective Modulators for the Nicotinic Receptor Subtypes: Challenges and Opportunities. *Future Med. Chem.* **2018**, *10* (4), 433–459.

Manna, M.; Nieminen, T.; Vattulainen, I. Understanding the Role of Lipids in Signaling Through Atomistic and Multiscale Simulations of Cell Membranes. *Annu. Rev. Biophys.* **2019**, *48*, 421–439.

Marks, D. S.; Colwell, L. J.; Sheridan, R.; Hopf, T. A.; Pagnani, A.; Zecchina, R.; Sander, C. Protein 3D Structure Computed from Evolutionary Sequence Variation. *PLoS One* **2011**, *6* (12), e28766.

Marks, D. S.; Hopf, T. A.; Sander, C. Protein Structure Prediction from Sequence Variation. *Nat. Biotechnol.* **2012**, *30* (11), 1072–1080.

Marsh, D. Lateral Pressure in Membranes. *Biochimica et Biophysica Acta - Reviews on Biomembranes* **1996**, *1286* (3), 183–223.

Marsh, D. Electron Spin Resonance in Membrane Research: Protein-Lipid Interactions from Challenging Beginnings to State of the Art. *Eur. Biophys. J.* **2010**, *39* (4), 513–525.

Marsh, D.; Barrantes, F. J. Immobilized Lipid in Acetylcholine Receptor-Rich Membranes from Torpedo Marmorata. *Proc. Natl. Acad. Sci. U. S. A.* **1978**, *75* (9), 4329–4333.

Martin, N. É.; Malik, S.; Calimet, N.; Changeux, J.-P.; Cecchini, M. Un-Gating and Allosteric Modulation of a Pentameric Ligand-Gated Ion Channel Captured by Molecular Dynamics. *PLoS Comput. Biol.* **2017**, *13* (10), e1005784.

Masiulis, S.; Desai, R.; Uchański, T.; Serna Martin, I.; Laverty, D.; Karia, D.; Malinauskas, T.; Zivanov, J.; Pardon, E.; Kotecha, A.; et al. GABAA Receptor Signalling Mechanisms Revealed by Structural Pharmacology. *Nature* **2019**, *565* (7740), 454–459.

Mathiharan, Y. K.; Glaaser, I. W.; Zhao, Y.; Robertson, M. J.; Skiniotis, G.; Slesinger, P. A. Structural Basis of GIRK2 Channel Modulation by Cholesterol and PIP2. *bioRxiv*, 2020, 2020.06.04.134544.

McCarthy, M. P.; Moore, M. A. Effects of Lipids and Detergents on the Conformation of the Nicotinic Acetylcholine Receptor from Torpedo Californica. *J. Biol. Chem.* **1992**, *267* (11), 7655–7663.

McGoldrick, L. L.; Singh, A. K.; Saotome, K.; Yelshanskaya, M. V.; Twomey, E. C.; Grassucci, R. A.; Sobolevsky, A. I. Opening of the Human Epithelial Calcium Channel TRPV6. *Nature* **2018**, *553* (7687), 233–237.

Menny, A.; Lefebvre, S. N.; Schmidpeter, P. A. M.; Drège, E.; Fourati, Z.; Delarue, M.; Edelstein, S. J.; Nimigean, C. M.; Joseph, D.; Corringer, P.-J. Identification of a Pre-Active Conformation of a Pentameric Channel Receptor. *Elife* **2017**, *6*, 1–28.

Merlie, J. P.; Lindstrom, J. Assembly in Vivo of Mouse Muscle Acetylcholine Receptor: Identification of an α Subunit Species That May Be an Assembly Intermediate. *Cell* **1983**, *34* (3), 747–757.

Mesoy, S.; Jeffreys, J.; Lummis, S. C. R. Characterization of Residues in the 5-HT3 Receptor M4 Region That Contribute to Function. *ACS Chem. Neurosci.* **2019**, *10* (7), 3167–3172.

Mesoy, S. M.; Lummis, S. C. R. M4, the Outermost Helix, Is Extensively Involved in Opening of the A4β2 NACh Receptor. *ACS Chem. Neurosci.* **2021**, *12* (1), 133–139.

Mesoy, S. M.; Bridgland-taylor, M.; Lummis, S. C. R. Mutations of the NACh Receptor M4 Helix Reveal Different Phenotypes in Different Expression Systems : Could Lipids Be Responsible ? *Front. Physiol.* **2022**, *13* (May), 850782.

Méthot, N.; Demers, C. N.; Baenziger, J. E. Structure of Both the Ligand- and Lipid-Dependent Channel-Inactive States of the Nicotinic Acetylcholine Receptor Probed by FTIR Spectroscopy and Hydrogen Exchange. *Biochemistry* **1995**, *34* (46), 15142–15149.

Michaud-Agrawal, N.; Denning, E. J.; Woolf, T. B.; Beckstein, O. MDAnalysis: A Toolkit for the Analysis of Molecular Dynamics Simulations. *J. Comput. Chem.* **2011**, *32* (10), 2319–2327.

Miledi, R.; Molinoff, P.; Potter, L. T. Isolation of the Cholinergic Receptor Protein of Torpedo Electric Tissue. *Aust. J. Sci. Res. B* **1971**, *229* (February 19), 554–557.

Miles, T. F.; Dougherty, D. A.; Lester, H. A. The 5-HT3AB Receptor Shows an A3B2 Stoichiometry at the Plasma Membrane. *Biophys. J.* **2013**, *105* (4), 887–898.

Miller, C. Genetic Manipulation of Ion Channels: A New Approach to Structure and Mechanism. *Nueron* **1989**, *2*, 1195–1205.

Miller, P. S.; Aricescu, A. R. Crystal Structure of a Human GABAA Receptor. *Nature* **2014**, *512* (7514), 270–275.

Miller, P. S.; Scott, S.; Masiulis, S.; De Colibus, L.; Pardon, E.; Steyaert, J.; Aricescu, A. R. Structural Basis for GABAA Receptor Potentiation by Neurosteroids. *Nat. Struct. Mol. Biol.* **2017**, *24* (11), 986–992.

Mitra, A.; Bailey, T. D.; Auerbach, A. L. Structural Dynamics of the M4 Transmembrane Segment during Acetylcholine Receptor Gating. *Structure* **2004**, *12* (10), 1909–1918.

Mitra, A.; Cymes, G. D.; Auerbach, A. Dynamics of the Acetylcholine Receptor Pore at the Gating Transition State. *Proc. Natl. Acad. Sci. U. S. A.* **2005**, *102* (42), 15069–15074.

Miyazawa, A.; Fujiyoshi, Y.; Stowell, M.; Unwin, N. Nicotinic Acetylcholine Receptor at 4.6 Å Resolution: Transverse Tunnels in the Channel Wall. *J. Mol. Biol.* **1999**, *288* (4), 765–786.

Miyazawa, A.; Fujiyoshi, Y.; Unwin, N. Structure and Gating Mechanism of the Acetylcholine Receptor Pore. *Nature* **2003**, *423* (6943), 949–955.

Mnatsakanyan, N.; Jansen, M. Experimental Determination of the Vertical Alignment between the Second and Third Transmembrane Segments of Muscle Nicotinic Acetylcholine Receptors. *J. Neurochem.* **2013**, *125* (6), 843–854.

Monod, J.; Wyman, J.; Changeux, J.-P. On the Nature of Allosteric Transitions: A Plausible Model. *J. Mol. Biol.* **1965**, *12* (1), 88–118.

Morales-Perez, C. L.; Noviello, C. M.; Hibbs, R. E. X-Ray Structure of the Human 42 Nicotinic Receptor. *Nature* **2016**, *538* (7625), 411.

Morud, J.; Hardege, I.; Liu, H.; Wu, T.; Choi, M. K.; Basu, S.; Zhang, Y.; Schafer, W. R. Deorphanization of Novel Biogenic Amine-Gated Ion Channels Identifies a New Serotonin Receptor for Learning. *Curr. Biol.* **2021**, *31* (19), 4282-4292.e6.

Mosesso, R.; Dougherty, D. A.; Lummis, S. C. R. Proline Residues in the Transmembrane/Extracellular Domain Interface Loops Have Different Behaviors in 5-HT3 and NACh Receptors. *ACS Chem. Neurosci.* **2019**, *10* (7), 3327–3333.

Mowrey, D. D.; Liu, Q.; Bondarenko, V.; Chen, Q.; Seyoum, E.; Xu, Y.; Wu, J.; Tang, P. Insights into Distinct Modulation of A7 and A7β2 Nicotinic Acetylcholine Receptors by the Volatile Anesthetic. *J. Biol. Chem.* **2013a**, *288* (50), 35793–35800.

Mowrey, D. D.; Cui, T.; Jia, Y.; Ma, D.; Makhov, A. M.; Zhang, P.; Tang, P.; Xu, Y. Open-Channel Structures of the Human Glycine Receptor A1 Full-Length Transmembrane Domain. *Structure* **2013b**, *21* (10), 1897–1904.

Mowrey, D. D.; Kinde, M. N.; Xu, Y.; Tang, P. Atomistic Insights into Human Cys-Loop Receptors by Solution NMR. *Biochimica et Biophysica Acta (BBA) - Biomembranes* **2015**, *1848* (1), 307–314.

Mukhtasimova, N.; Sine, S. M. Nicotinic Receptor Transduction Zone: Invariant Arginine Couples to Multiple Electron-Rich Residues. *Biophys. J.* **2013**, *104* (2), 355–367.

Mukhtasimova, N.; Lee, W. Y.; Wang, H.-L.; Sine, S. M. Detection and Trapping of Intermediate States Priming Nicotinic Receptor Channel Opening. *Nature* **2009**, *459* (7245), 451–454.

Mukhtasimova, N.; daCosta, C. J. B.; Sine, S. M. Improved Resolution of Single Channel Dwell Times Reveals Mechanisms of Binding, Priming, and Gating in Muscle AChR. *J. Gen. Physiol.* **2016**, *148* (1), 43–63.

Nachmansohn, D. *The Chemical and Molecular Basis of Nerve Activity*; Academic Press: New York, 1959.

Naffaa, M. M.; Hung, S.; Chebib, M.; Johnston, G. A. R.; Hanrahan, J. R. GABA-ρ Receptors: Distinctive Functions and Molecular Pharmacology. *Br. J. Pharmacol.* **2017**, *174* (13), 1881–1894.

Nakane, T.; Kotecha, A.; Sente, A.; McMullan, G.; Masiulis, S.; Brown, P. M. G. E.; Grigoras, I. T.; Malinauskaite, L.; Malinauskas, T.; Miehling, J.; et al. Single-Particle Cryo-EM at Atomic Resolution. *Nature* **2020**, *587* (7832), 152–156.

Narayanaswami, V.; McNamee, M. G. Protein-Lipid Interactions and Torpedo Californica Nicotinic Acetylcholine Receptor Function. 2. Membrane Fluidity and Ligand-Mediated Alteration in the Accessibility of γ Subunit Cysteine Residues to Cholesterol. *Biochemistry* **1993**, *32* (46), 12420–12427.

Nayak, T. K.; Auerbach, A. Asymmetric Transmitter Binding Sites of Fetal Muscle Acetylcholine Receptors Shape Their Synaptic Response. *Proceedings of the National Academy of Sciences of the United States of America*. National Academy of Sciences 2013, pp 13654–11365.

Nayak, T. K.; Auerbach, A. Cyclic Activation of Endplate Acetylcholine Receptors. *Proc. Natl. Acad. Sci. U. S. A.* **2017**, *114* (45), 11914–11919.

Nayak, T. K.; Purohit, P. G.; Auerbach, A. The Intrinsic Energy of the Gating Isomerization of a Neuromuscular Acetylcholine Receptor Channel. *J. Gen. Physiol.* **2012**, *139* (5), 349–358.

Nayak, T. K.; Chakraborty, S.; Zheng, W.; Auerbach, A. Structural Correlates of Affinity in Fetal versus Adult Endplate Nicotinic Receptors. *Nat. Commun.* **2016**, *7*, 11352.

Nemecz, Á.; Prevost, M. S.; Menny, A.; Corringer, P.-J. Emerging Molecular Mechanisms of Signal Transduction in Pentameric Ligand-Gated Ion Channels. *Neuron* **2016**, *90* (3), 452–470.

Newcombe, J.; Chatzidaki, A.; Sheppard, T. D.; Topf, M.; Millar, N. S. Diversity of Nicotinic Acetylcholine Receptor Positive Allosteric Modulators Revealed by Mutagenesis and a Revised Structural Model. *Mol. Pharmacol.* **2018**, *93* (2), 128–140.

Nosé, S. A Molecular Dynamics Method for Simulations in the Canonical Ensemble. *Mol. Phys.* **2002**, *100* (1), 191–198.

Nothdurfter, C.; Tanasic, S.; Di Benedetto, B.; Rammes, G.; Wagner, E. M.; Kirmeier, T.; Ganal, V.; Kessler, J. S.; Rein, T.; Holsboer, F.; et al. Impact of Lipid Raft Integrity on 5-HT 3 Receptor Function and Its Modulation by Antidepressants. *Neuropsychopharmacology* **2010**, *35* (7), 1510–1519.

Noviello, C. M.; Gharpure, A.; Mukhtasimova, N.; Borek, D.; Sine, S. M.; Hibbs, R. E.; Cabuco, R.; Baxter, L. Structure and Gating Mechanism of the A7 Nicotinic Acetylcholine Receptor. *Cell* **2021**, *184* (8), 2121-2134.e13.

Noviello, C. M.; Kreye, J.; Teng, J.; Prüss, H.; Hibbs, R. E. Structural Mechanisms of GABAA Receptor Autoimmune Encephalitis. *Cell* **2022**, *185* (14), 2469-2477.e13.

Nury, H.; Van Renterghem, C.; Weng, Y.; Tran, A.; Baaden, M.; Dufresne, V.; Changeux, J.-P.; Sonner, J. M.; Delarue, M.; Corringer, P.-J. X-Ray Structures of General Anaesthetics Bound to a Pentameric Ligand-Gated Ion Channel. *Nature* **2011**, *469* (7330), 428–431.

Nys, M.; Wijckmans, E.; Farinha, A.; Yoluk, Ö.; Andersson, M.; Brams, M.; Spurny, R.; Peigneur, S.; Tytgat, J.; Lindahl, E.; et al. Allosteric Binding Site in a Cys-Loop Receptor Ligand-Binding Domain Unveiled in the Crystal Structure of ELIC in Complex with Chlorpromazine. *Proc. Natl. Acad. Sci. U. S. A.* **2016**, *113* (43), E6696–E6703.

Nys, M.; Zarkadas, E.; Brams, M.; Mehregan, A.; Kambara, K.; Kool, J.; Casewell, N. R.; Bertrand, D.; Baenziger, J. E.; Nury, H.; et al. The Molecular Mechanism of Snake Short-Chain Alpha-Neurotoxin Binding to Muscle-Type Nicotinic Acetylcholine Receptors. *Nat. Commun.* **2022**, *13* (1), 4543.

Oliveira, A. S. F.; Edsall, C. J.; Woods, C. J.; Bates, P.; Nunez, G. V.; Wonnacott, S.; Bermudez, I.; Ciccotti, G.; Gallagher, T.; Sessions, R. B.; et al. A General Mechanism for Signal Propagation in the Nicotinic Acetylcholine Receptor Family. *J. Am. Chem. Soc.* **2019**, *141* (51), 19953–19958.

Olsen, R. W.; Meunier, J. C.; Changeux, J. P. Progress in the Purification of the Cholinergic Receptor Protein from Electrophorus Electricus by Affinity Chromatography. *FEBS Lett.* **1972**, *28* (1), 96–100.

Opekarová, M.; Tanner, W. Specific Lipid Requirements of Membrane Proteins - A Putative Bottleneck in Heterologous Expression. *Biochimica et Biophysica Acta - Biomembranes* **2003**, *1610* (1), 11–22.

Ortiz-Acevedo, A.; Melendez, M.; Asseo, A. M.; Biaggi, N.; Rojas, L. V.; Lasalde-Dominicci, J. A. Tryptophan Scanning Mutagenesis of the ΓM4 Transmembrane Domain of the Acetylcholine Receptor from Torpedo Californica. *J. Biol. Chem.* **2004**, *279* (40), 42250–42257.

Overington, J. P.; Al-Lazikani, B.; Hopkins, A. L. How Many Drug Targets Are There? *Nat. Rev. Drug Discov.* **2006**, *5* (12), 993–996.

Oyola-Cintrón, J.; Caballero-Rivera, D.; Ballester, L.; Baéz-Pagán, C. A.; Martínez, H. L.; Vélez-Arroyo, K. P.; Quesada, O.; Lasalde-Dominicci, J. A. Lateral Diffusion, Function, and Expression of the Slow Channel Congenital Myasthenia Syndrome AC418W Nicotinic Receptor Mutation with Changes in Lipid Raft Components. *J. Biol. Chem.* **2015**, *290* (44), 26790–26800.

Paas, Y.; Cartaud, J.; Recouvreur, M.; Grailhe, R.; Dufresne, V.; Pebay-Peyroula, E.; Landau, E. M.; Changeux, J.-P. Electron Microscopic Evidence for Nucleation and Growth of 3D Acetylcholine Receptor Microcrystals in Structured Lipid-Detergent Matrices. *Proc. Natl. Acad. Sci. U. S. A.* **2003**, *100* (20), 11309–11314.

Pan, J.; Chen, Q.; Willenbring, D.; Yoshida, K.; Tillman, T. S.; Kashlan, O. B.; Cohen, A. E.; Kong, X.-P.; Xu, Y.; Tang, P. Structure of the Pentameric Ligand-Gated Ion Channel ELIC Cocrystallized with Its Competitive Antagonist Acetylcholine. *Nat. Commun.* **2012a**, *3* (1), 714.

Pan, J.; Chen, Q.; Willenbring, D.; Mowrey, D.; Kong, X.-P.; Cohen, A.; Divito, C. B.; Xu, Y.; Tang, P. Structure of the Pentameric Ligand-Gated Ion Channel GLIC Bound with Anesthetic Ketamine. *Structure* **2012b**, *20* (9), 1463–1469.

Papasergi-Scott, M. M.; Pérez-Hernández, G.; Batebi, H.; Gao, Y.; Eskici, G.; Seven, A. B.; Panova, O.; Hilger, D.; Casiraghi, M.; He, F.; et al. Time-Resolved Cryo-EM of G Protein Activation by a GPCR. *bioBxiv* **2023**.

Paradiso, K.; Zhang, J.; Steinbach, J. H. The C Terminus of the Human Nicotinic A4β2 Receptor Forms a Binding Site Required for Potentiation by an Estrogenic Steroid. *Journal of Neuroscience* **2001**, *21* (17), 6561–6568.

Parrinello, M.; Rahman, A. Polymorphic Transitions in Single Crystals: A New Molecular Dynamics Method. *J. Appl. Phys.* **1981**, *52* (12), 7182–7190.

Payandeh, J.; Scheuer, T.; Zheng, N.; Catterall, W. A. The Crystal Structure of a Voltage-Gated Sodium Channel. *Nature* **2011**, *475* (7356), 353–358.

Perozo, E.; Cortes, D. M.; Sompornpisut, P.; Kloda, A.; Martinac, B. Open Channel Structure of MscL and the Gating Mechanism of Mechanosensitive Channels. *Nature* **2002**, *418* (6901), 942–948.

Petroff, J. T.; Dietzen, N. M.; Santiago-McRae, E.; Deng, B.; Washington, M. S.; Chen, L. J.; Trent Moreland, K.; Deng, Z.; Rau, M.; Fitzpatrick, J. A. J.; et al. Open-Channel Structure of a Pentameric Ligand-Gated Ion Channel Reveals a Mechanism of Leaflet-Specific Phospholipid Modulation. *Nat. Commun.* **2022**, *13* (1), 7017.

Pettersen, E. F.; Goddard, T. D.; Huang, C. C.; Meng, E. C.; Couch, G. S.; Croll, T. I.; Morris, J. H.; Ferrin, T. E. UCSF ChimeraX: Structure Visualization for Researchers, Educators, and Developers. *Protein Sci.* **2021**, *30* (1), 70–82.

Peverini, L.; Shi, S.; Medjebeur, K.; Corringer, P.-J. Mapping the Molecular Motions of 5-HT3 Serotonin-Gated Channel by Voltage-Clamp Fluorometry. *bioRxiv*, 2023, 2023.09.28.559960.

Pfeffermann, J.; Eicher, B.; Boytsov, D.; Hannesschlaeger, C.; Galimzyanov, T. R.; Glasnov, T. N.; Pabst, G.; Akimov, S. A.; Pohl, P. Photoswitching of Model Ion Channels in Lipid Bilayers. *J. Photochem. Photobiol. B* **2021**, *224*, 112320.

Phulera, S.; Zhu, H.; Yu, J.; Claxton, D. P.; Yoder, N.; Yoshioka, C.; Gouaux, E. Cryo-EM Structure of the Benzodiazepine-Sensitive A1β1γ2S Tri-Heteromeric GABAA Receptor in Complex with GABA. *Elife* **2018**, *7*.

Pirayesh, E.; Stuebler, A. G.; Pandhare, A.; Jansen, M. Delineating the Site of Interaction of the 5-HT3A Receptor with the Chaperone Protein RIC-3. *Biophys. J.* **2020**, *118* (4), 934–943.

Pless, S. A.; Leung, A. W. Y.; Galpin, J. D.; Ahern, C. A. Contributions of Conserved Residues at the Gating Interface of Glycine Receptors. *J. Biol. Chem.* **2011**, *286* (40), 35129–35136.

Plested, A. J. R. Structural Mechanisms of Activation and Desensitization in Neurotransmitter-Gated Ion Channels. *Nat. Struct. Mol. Biol.* **2016**, *23* (6), 494–502.

Polovinkin, L.; Hassaine, G.; Perot, J.; Neumann, E.; Jensen, A. A.; Lefebvre, S. N.; Corringer, P.-J.; Neyton, J.; Chipot, C.; Dehez, F.; et al. Conformational Transitions of the Serotonin 5-HT3 Receptor. *Nature* **2018**, *563* (7730), 275–279.

Pons, S.; Sallette, J.; Bourgeois, J. P.; Taly, A.; Changeux, J.-P.; Devillers-Thiéry, A. Critical Role of the C-Terminal Segment in the Maturation and Export to the Cell Surface of the Homopentameric A7-5HT3A Receptor. *Eur. J. Neurosci.* **2004**, *20* (8), 2022–2030.

Poveda, J. A.; Marcela Giudici, A.; Lourdes Renart, M.; Morales, A.; González-Ros, J. M. Towards Understanding the Molecular Basis of Ion Channel Modulation by Lipids: Mechanistic Models and Current Paradigms. *Biochim. Biophys. Acta Biomembr.* **2017**, *1859* (9 Pt B), 1507–1516.

Powell, A. D.; Grafton, G.; Roberts, A.; Larkin, S.; O'Neill, N.; Palandri, J.; Otvos, R.; Cooper, A. J.; Ulens, C.; Barnes, N. M. Novel Mechanism of Modulation at a Ligand-Gated Ion Channel; Action of 5-Cl-Indole at the 5-HT3 A Receptor. *Br. J. Pharmacol.* **2016**, *173* (24), 3467–3479.

Prevost, M. S.; Sauguet, L.; Nury, H.; Van Renterghem, C.; Huon, C.; Poitevin, F.; Baaden, M.; Delarue, M.; Corringer, P.-J. A Locally Closed Conformation of a Bacterial Pentameric Proton-Gated Ion Channel. *Nat. Struct. Mol. Biol.* **2012**, *19* (6), 642–649.

Price, K. L.; Millen, K. S.; Lummis, S. C. R. Transducing Agonist Binding to Channel Gating Involves Different Interactions in 5-HT3 and GABAC Receptors. *J. Biol. Chem.* **2007**, *282* (35), 25623–25630.

Prince, R. J.; Sine, S. M. Molecular Dissection of Subunit Interfaces in the Acetylcholine Receptor. Identification of Residues That Determine Agonist Selectivity. *J. Biol. Chem.* **1996**, *271* (42), 25770–25777.

Puinean, A. M.; Lansdell, S. J.; Collins, T.; Bielza, P.; Millar, N. S. A Nicotinic Acetylcholine Receptor Transmembrane Point Mutation (G275E) Associated with Resistance to Spinosad in Frankliniella Occidentalis. *Journal of Neurochemistry* **2013**, *124* (5), 590–601.

Punjani, A.; Fleet, D. J. 3D Variability Analysis: Resolving Continuous Flexibility and Discrete Heterogeneity from Single Particle Cryo-EM. *J. Struct. Biol.* **2021**, *213* (2), 107702.

Punjani, A.; Rubinstein, J. L.; Fleet, D. J.; Brubaker, M. A. CryoSPARC: Algorithms for Rapid Unsupervised Cryo-EM Structure Determination. *Nat. Methods* **2017**, *14* (3), 290–296.

Punjani, A.; Zhang, H.; Fleet, D. J. Non-Uniform Refinement: Adaptive Regularization Improves Single-Particle Cryo-EM Reconstruction. *Nat. Methods* **2020**, *17* (12), 1214–1221.

Purohit, P. G.; Auerbach, A.; Aldrich, R. W. Unliganded Gating of Acetylcholine Receptor Channels. *Proc. Natl. Acad. Sci. U. S. A.* **2008**, *106*, 115–120.

Purohit, P. G.; Chakraborty, S.; Auerbach, A. Function of the M1 π-Helix in Endplate Receptor Activation and Desensitization. *J. Physiol.* **2015**, *593* (13), 2851–2866.

Rahman, M.; Teng, J.; Worrell, B. T.; Karlin, A.; Stowell, M. H. B.; Hibbs, R. E.; Noviello, C. M.; Lee, M. Structure of the Native Muscle-Type Nicotinic Receptor and Inhibition by Snake Venom Toxins Article Structure of the Native Muscle-Type Nicotinic Receptor and Inhibition by Snake Venom Toxins. *Neuron* **2020a**, *106*, 1–11.

Rahman, M. M.; Teng, J.; Worrell, B. T.; Noviello, C. M.; Lee, M.; Karlin, A.; Stowell, M. H. B.; Hibbs, R. E. Structure of the Native Muscle-Type Nicotinic Receptor and Inhibition by Snake Venom Toxins. *Neuron* **2020b**, *106* (6), 952-962.e5.

Rahman, M. M.; Basta, T.; Teng, J.; Lee, M.; Worrell, B. T.; Stowell, M. H. B.; Hibbs, R. E. Structural Mechanism of Muscle Nicotinic Receptor Desensitization and Block by Curare. *Nat. Struct. Mol. Biol.* **2022**, *29* (4), 386–394.

Rao, S.; Klesse, G.; Lynch, C. I.; Tucker, S. J.; Sansom, M. S. P. Molecular Simulations of Hydrophobic Gating of Pentameric Ligand Gated Ion Channels: Insights into Water and Ions. *J. Phys. Chem. B* **2021**, *125* (4), 981–994.

Rasmussen, T.; Flegler, V. J.; Rasmussen, A.; Böttcher, B. Structure of the Mechanosensitive Channel MscS Embedded in the Membrane Bilayer. *J. Mol. Biol.* **2019**, *431* (17), 3081–3090.

Real Hernandez, L. M.; Levental, I. Lipid Packing Is Disrupted in Copolymeric Nanodiscs Compared with Intact Membranes. *Biophys. J.* **2023**, *122* (11), 2256–2266.

Reddy, B.; Bavi, N.; Lu, A.; Park, Y.; Perozo, E. Molecular Basis of Force-from-Lipids Gating in the Mechanosensitive Channel MscS. *Elife* **2019**, *8*.

Richard, M.; Boulin, T.; Robert, V. J. P.; Richmond, J. E.; Bessereau, J. L. Biosynthesis of Ionotropic Acetylcholine Receptors Requires the Evolutionarily Conserved ER Membrane Complex. *Proc. Natl. Acad. Sci. U. S. A.* **2013**, *110* (11), E1055–E1063.

Riquelme, G.; Morato, E.; López, E.; Ruiz-Gómez, A.; Ferragut, J. A.; González Ros, J. M.; Mayor, F. Agonist Binding to Purified Glycine Receptor Reconstituted into Giant Liposomes Elicits Two Types of Chloride Currents. *FEBS Lett.* **1990**, *276* (1–2), 54–58.

Rodriguez Cruz, P. M.; Palace, J.; Beeson, D. The Neuromuscular Junction and Wide Heterogeneity of Congenital Myasthenic Syndromes. *Int. J. Mol. Sci.* **2018**, *19* (6), 1677.

Rohács, T. Phosphoinositide Regulation of TRP Channels. In *Mammalian Transient Receptor Potential (TRP) Cation Channels: Volume II*; Nilius, B., Flockerzi, V., Eds.; Springer International Publishing: Cham, 2014; pp 1143–1176.

Romanenko, V. G.; Fang, Y.; Byfield, F.; Travis, A. J.; Vandenberg, C. A.; Rothblat, G. H.; Levitan, I. Cholesterol Sensitivity and Lipid Raft Targeting of Kir2.1 Channels. *Biophys. J.* **2004**, *87* (6), 3850–3861.

Rovšnik, U.; Zhuang, Y.; Forsberg, B. O.; Carroni, M.; Yvonnesdotter, L.; Howard, R. J.; Lindahl, E. Dynamic Closed States of a Ligand-Gated Ion Channel Captured by Cryo-EM and Simulations. *Life Sci Alliance* **2021**, *4* (8).

Rudell, J. C.; Borges, L. S.; Yarov-Yarovoy, V.; Ferns, M. The MX-Helix of Muscle NAChR Subunits Regulates Receptor Assembly and Surface Trafficking. *Front. Mol. Neurosci.* **2020**, *13*, 48.

Ryan, S. E.; Demers, C. N.; Chew, J. P.; Baenziger, J. E. Structural Effects of Neutral and Anionic Lipids on the Nicotinic Acetylcholine Receptor. An Infrared Difference Spectroscopy Study. *J. Biol. Chem.* **1996**, *271* (40), 24590–24597.

Sala, F.; Mulet, J.; Sala, S.; Gerber, S.; Criado, M. Charged Amino Acids of the N-Terminal Domain Are Involved in Coupling Binding and Gating in A7 Nicotinic Receptors. *J. Biol. Chem.* **2005**, *280* (8), 6642–6647.

Sanchez-Garcia, R.; Gomez-Blanco, J.; Cuervo, A.; Carazo, J. M.; Sorzano, C. O. S.; Vargas, J. DeepEMhancer: A Deep Learning Solution for Cryo-EM Volume Post-Processing. *Communications Biology* **2021**, *4* (1), 874.

Santiago, J.; Guzmán, G. R.; Rojas, L. V.; Marti, R.; Asmar-Rovira, G. A.; Santana, L. F.; McNamee, M. G.; Lasalde-Dominicci, J. A. Probing the Effects of Membrane Cholesterol in the Torpedo Californica Acetylcholine Receptor and the Novel Lipid-Exposed Mutation AC418W in Xenopus Oocytes. *J. Biol. Chem.* **2001**, *276* (49), 46523–46532.

Santos, R.; Ursu, O.; Gaulton, A.; Bento, A. P.; Donadi, R. S.; Bologa, C. G.; Karlsson, A.; Al-Lazikani, B.; Hersey, A.; Oprea, T. I.; et al. A Comprehensive Map of Molecular Drug Targets. *Nat. Rev. Drug Discov.* **2017**, *16* (1), 19–34.

Saotome, K.; Murthy, S. E.; Kefauver, J. M.; Whitwam, T.; Patapoutian, A.; Ward, A. B. Structure of the Mechanically Activated Ion Channel Piezo1. *Nature* **2018**, *554* (7693), 481–486.

Sauguet, L.; Poitevin, F.; Murail, S.; Van Renterghem, C.; Moraga-Cid, G.; Malherbe, L.; Thompson, A. W.; Koehl, P.; Corringer, P.-J.; Baaden, M.; et al. Structural Basis for Ion Permeation Mechanism in Pentameric Ligand-Gated Ion Channels. *EMBO J.* **2013a**, *32* (5), 728–741.

Sauguet, L.; Howard, R. J.; Malherbe, L.; Lee, U. S.; Corringer, P.-J.; Adron Harris, R.; Delarue, M. Structural Basis for Potentiation by Alcohols and Anaesthetics in a Ligand-Gated Ion Channel. *Nat. Commun.* **2013b**, *4* (1), 1697.

Sauguet, L.; Shahsavar, A.; Poitevin, F.; Huon, C.; Menny, A.; Nemecz, Á.; Haouz, A.; Changeux, J.-P.; Corringer, P.-J.; Delarue, M. Crystal Structures of a Pentameric Ligand-Gated Ion Channel Provide a Mechanism for Activation. *Proc. Natl. Acad. Sci. U. S. A.* **2014a**, *111* (3), 966–971.

Sauguet, L.; Shahsavar, A.; Poitevin, F.; Huon, C.; Menny, A.; Nemecz, Á.; Haouz, A.; Changeux, J.-P.; Corringer, P.-J.; Delarue, M. Structural Basis for Allosteric Transitions in the GLIC Pentameric Proton-Gated Ion Channel. *Biophys. J.* **2014b**, *106* (2), 343a.

Scheres, S. H. W. RELION: Implementation of a Bayesian Approach to Cryo-EM Structure Determination. *J. Struct. Biol.* **2012**, *180* (3), 519–530.

Sente, A.; Desai, R.; Naydenova, K.; Malinauskas, T.; Jounaidi, Y.; Miehling, J.; Zhou, X.; Masiulis, S.; Hardwick, S. W.; Chirgadze, D. Y.; et al. Differential Assembly Diversifies GABA A Receptor Structures and Signalling. *Nature* **2022**, *604* (7904), 190–194.

Sharp, L.; Brannigan, G. Spontaneous Lipid Binding to the Nicotinic Acetylcholine Receptor in a Native Membrane. *J. Chem. Phys.* **2021**, *154* (18), 185102.

She, J.; Guo, J.; Chen, Q.; Zeng, W.; Jiang, Y.; Bai, X.-C. Structural Insights into the Voltage and Phospholipid Activation of the Mammalian TPC1 Channel. *Nature* **2018**, *556* (7699), 130–134.

She, J.; Zeng, W.; Guo, J.; Chen, Q.; Bai, X.-C.; Jiang, Y. Structural Mechanisms of Phospholipid Activation of the Human TPC2 Channel. *Elife* **2019**, *8*.

Shen, X. M.; Brengman, J.; Neubauer, D.; Sine, S. M.; Engel, A. G. Investigation of Congenital Myasthenia Reveals Functional Asymmetry of Invariant Acetylcholine Receptor (AChR) Cys-Loop Aspartates. *J. Biol. Chem.* **2016**, *291* (7), 3291–3301.

Shen, X.-M.; Deymeer, F.; Sine, S. M.; Engel, A. G. Slow-Channel Mutation in Acetylcholine Receptor AM4 Domain and Its Efficient Knockdown. *Ann. Neurol.* **2006**, *60* (1), 128–136.

Shen, X.-M.; Brengman, J. M.; Shen, S.; Durmus, H.; Preethish-Kumar, V.; Yuceyar, N.; Vengalil, S.; Nalini, A.; Deymeer, F.; Sine, S. M.; et al. Mutations Causing Congenital Myasthenia Reveal Principal Coupling Pathway in the Acetylcholine Receptor ε-Subunit. *JCI Insight* **2018**, *3* (2), e97826.

Shi, S.; Lefebvre, S. N.; Peverini, L.; Cerdan, A.; Rodríguez, P. M.; Gielen, M.; Changeux, J.-P.; Cecchini, M.; Corringer, P.-J. Illumination of a Progressive Allosteric Mechanism Mediating the Glycine Receptor Activation. *Nat. Commun.* **2023**, *14*, 795.

Sine, S. M. The Nicotinic Receptor Ligand Binding Domain. *J. Neurobiol.* **2002**, *53* (4), 431–446.

Sine, S. M.; Claudio, T. G- and b-Subunits Regulate the Affinity and the Cooperativity of Ligand Binding to the Acetylcholine Receptor. *J. Biol. Chem.* **1991**, *266* (29), 19369–19377.

Smelt, C. L. C.; Sanders, V. R.; Newcombe, J.; Burt, R. P.; Sheppard, T. D.; Topf, M.; Millar, N. S. Identification by Virtual Screening and Functional Characterisation of Novel Positive and Negative Allosteric Modulators of the A7 Nicotinic Acetylcholine Receptor. *Neuropharmacology* **2018**, *139*, 194–204.

Sobolevsky, A. I.; Rosconi, M. P.; Gouaux, E. X-Ray Structure, Symmetry and Mechanism of an AMPA-Subtype Glutamate Receptor. *Nature* **2009**, *462* (7274), 745–756.

Solomon, V. R.; Tallapragada, V. J.; Chebib, M.; Johnston, G. A. R.; Hanrahan, J. R. GABA Allosteric Modulators: An Overview of Recent Developments in Non-Benzodiazepine Modulators. *Eur. J. Med. Chem.* **2019**, *171*, 434–461.

Sooksawate, T.; Simmonds, M. A. Effects of Membrane Cholesterol on the Sensitivity of the GABA(A) Receptor to GABA in Acutely Dissociated Rat Hippocampal Neurones. *Neuropharmacology* **2001a**, *40* (2), 178–184.

Sooksawate, T.; Simmonds, M. A. Influence of Membrane Cholesterol on Modulation of the GABA(A) Receptor by Neuroactive Steroids and Other Potentiators. *Br. J. Pharmacol.* **2001b**, *134* (6), 1303–1311.

Soussia, I. B.; Choveau, F. S.; Blin, S.; Kim, E. J.; Feliciangeli, S.; Chatelain, F. C.; Kang, D.; Bichet, D.; Lesage, F. Antagonistic Effect of a Cytoplasmic Domain on the Basal Activity of Polymodal Potassium Channels. *Front. Mol. Neurosci.* **2018**, *11* (September), 301.

Sparling, B. A.; DiMauro, E. F. Progress in the Discovery of Small Molecule Modulators of the Cys-Loop Superfamily Receptors. *Bioorg. Med. Chem. Lett.* **2017**, *27* (15), 3207–3218.

van der Spoel, D.; Lindahl, E.; Hess, B.; Groenhof, G.; Mark, A. E.; Berendsen, H. J. C. GROMACS: Fast, Flexible, and Free. *Journal of Computational Chemistry* **2005**, *26* (16), 1701–1718.

Spurny, R.; Ramerstorfer, J.; Price, K. L.; Brams, M.; Ernst, M.; Nury, H.; Verheij, M.; Legrand, P.; Bertrand, D.; Bertrand, S.; et al. Pentameric Ligand-Gated Ion Channel ELIC Is Activated by GABA and Modulated by Benzodiazepines. *Proc. Natl. Acad. Sci. U. S. A.* **2012**, *109* (44), E3028-34.

Spurny, R.; Billen, B.; Howard, R. J.; Brams, M.; Debaveye, S.; Price, K. L.; Weston, D. A.; Strelkov, S. V.; Tytgat, J.; Bertrand, S.; et al. Multisite Binding of a General Anesthetic to the Prokaryotic Pentameric Erwinia Chrysanthemi Ligand-Gated Ion Channel (ELIC). *J. Biol. Chem.* **2013**, *288* (12), 8355–8364.

Sridhar, A.; Lummis, S. C. R.; Pasini, D.; Mehregan, A.; Brams, M.; Kambara, K.; Bertrand, D.; Lindahl, E.; Howard, R. J.; Ulens, C. Regulation of a Pentameric Ligand-Gated Ion Channel by a Semiconserved Cationic Lipid-Binding Site. *Journal of Biological Chemistry* **2021**, *297* (2), 100899.

Stavrianakou, M.; Perez, R.; Wu, C.; Sachs, M. S.; Aramayo, R.; Harlow, M. Draft de Novo Transcriptome Assembly and Proteome Characterization of the Electric Lobe of Tetronarce Californica: A Molecular Tool for the Study of Cholinergic Neurotransmission in the Electric Organ. *BMC Genomics* **2017**, *18* (1), 611.

Stetzkowski-Marden, F.; Recouvreur, M.; Camus, G.; Cartaud, A.; Marchand, S.; Cartaud, J. Rafts Are Required for Acetylcholine Receptor Clustering. *Journal of Molecular Neuroscience* **2006**, *30*, 37–38.

Stith, B. J.; Hall, J.; Ayres, P.; Waggoner, L.; Moore, J. D.; Shaw, W. A. Quantification of Major Classes of Xenopus Phospholipids by High Performance Liquid Chromatography with Evaporative Light Scattering Detection. *J. Lipid Res.* **2000**, *41* (9), 1448–1454.

Strikwerda, J. R.; Sine, S. M. Unmasking Coupling between Channel Gating and Ion Permeation in the Muscle Nicotinic Receptor. *Elife* **2021**, *10*, e66225.

Strikwerda, J. R.; Natarajan, K.; Sine, S. M. Impact on AChR Open Channel Noise by Pore-Peripheral Salt Bridge Depends on Voltage and Divalent Cations. *Biophys. J.* **2023**.

Stuebler, A. G.; Jansen, M. Mobility of Lower MA-Helices for Ion Conduction through Lateral Portals in 5-HT 3A Receptors. *Biophys. J.* **2020**, *119*, 2593–2603.

Sturgeon, R. M.; Baenziger, J. E. Cations Mediate Interactions between the Nicotinic Acetylcholine Receptor and Anionic Lipids. *Biophys. J.* **2010**, *98* (6), 989–998.

Sugasawa, Y.; Bracamontes, J. R.; Krishnan, K.; Covey, D. F.; Reichert, D. E.; Akk, G.; Chen, Q.; Tang, P.; Evers, A. S.; Cheng, W. W. L. The Molecular Determinants of Neurosteroid Binding in the GABA(A) Receptor. *J. Steroid Biochem. Mol. Biol.* **2019**, *192*, 105383.

Sun, C.; Zhu, H.; Clark, S.; Gouaux, E. Cryo-EM Structures Reveal Native GABA A Receptor Assemblies and Pharmacology. *Nature* **2023**.

Sun, J.; MacKinnon, R. Cryo-EM Structure of a KCNQ1/CaM Complex Reveals Insights into Congenital Long QT Syndrome. *Cell* **2017**, *169* (6), 1042-1050.e9.

Sun, J.; MacKinnon, R. Structural Basis of Human KCNQ1 Modulation and Gating. *Cell* **2020**, *180* (2), 340-347.e9.

Sun, J.; Comeau, J. F.; Baenziger, J. E. Probing the Structure of the Uncoupled Nicotinic Acetylcholine Receptor. *BBA - Biomembranes* **2017**, *1859* (2), 146–154.

Sunshine, C.; McNamee, M. G. Lipid Modulation of Nicotinic Acetylcholine Receptor Function: The Role of Neutral and Negatively Charged Lipids. *BBA - Biomembranes* **1992**, *1108* (2), 240–246.

Symons, J. L.; Cho, K.-J.; Chang, J. T.; Du, G.; Waxham, M. N.; Hancock, J. F.; Levental, I.; Levental, K. R. Lipidomic Atlas of Mammalian Cell Membranes Reveals Hierarchical Variation Induced by Culture Conditions, Subcellular Membranes, and Cell Lineages. *Soft Matter* **2021**, *17* (2), 288–297.

Taly, A.; Hénin, J.; Changeux, J.-P.; Cecchini, M. Allosteric Regulation of Pentameric Ligand-Gated Ion Channels: An Emerging Mechanistic Perspective. *Channels* **2014**, *8* (4), 350–360.

Tamamizu, S.; Guzmán, G. R.; Santiago, J.; Rojas, L. V.; McNamee, M. G.; Lasalde-Dominicci, J. A. Functional Effects of Periodic Tryptophan Substitutions in the AM4 Transmembrane Domain of the Torpedo Californica Nicotinic Acetylcholine Receptor. *Biochemistry* **2000**, *39* (16), 4666–4673.

Tang, B.; Lummis, S. C. R. The Roles of Aromatic Residues in the Glycine Receptor Transmembrane Domain. *BMC Neurosci.* **2018**, *19* (1), 53.

Tasneem, A.; Iyer, L. M.; Jakobsson, E.; Aravind, L. Identification of the Prokaryotic Ligand-Gated Ion Channels and Their Implications for the Mechanisms and Origins of Animal Cys-Loop Ion Channels. *Genome Biol.* **2004**, *6* (1), R4.

Tessier, C. J. G.; Sturgeon, R. M.; Emlaw, J. R.; McCluskey, G. D.; Pérez-Areales, F. J.; daCosta, C. J. B. Ancestral Acetylcholine Receptor β-Subunit Forms Homopentamers That Prime before Opening Spontaneously. *Elife* **2022**, *11*, e76504.

Tessier, C. J. G.; Emlaw, J. R.; Sturgeon, R. M.; daCosta, C. J. B. Derepression May Masquerade as Activation in Ligand-Gated Ion Channels. *Nat. Commun.* **2023**, *14* (1), 1907.

Therien, J. P. D.; Baenziger, J. E. Pentameric Ligand-Gated Ion Channels Exhibit Distinct Transmembrane Domain Archetypes for Folding/Expression and Function. *Sci. Rep.* **2017**, *7* (1), 450.

Thompson, M. J.; Baenziger, J. E. Ion Channels as Lipid Sensors: From Structures to Mechanisms. *Nat. Chem. Biol.* **2020a**, *16* (12), 1331–1342.

Thompson, M. J.; Baenziger, J. E. Structural Basis for the Modulation of Pentameric Ligand-Gated Ion Channel Function by Lipids. *Biochim. Biophys. Acta Biomembr.* **2020b**, *1862* (9), 183304.

Thompson, M. J.; Domville, J. A.; Baenziger, J. E. The Functional Role of the AM4 Transmembrane Helix in the Muscle Nicotinic Acetylcholine Receptor Probed through Mutagenesis and Co-Evolutionary Analyses. *J. Biol. Chem.* **2020**, *295* (32), 11056–11067.

Thompson, M. J.; Domville, J. A.; Edrington, C. H.; Venes, A.; Giguère, P. M.; Baenziger, J. E. Distinct Functional Roles for the M4 α-Helix from Each Homologous Subunit in the Hetero-Pentameric Ligand-Gated Ion Channel NAChR. *J. Biol. Chem.* **2022**, *297* (7), 102104.

Tol, M. B.; Deluz, C.; Hassaine, G.; Graff, A.; Stahlberg, H.; Vogel, H. Thermal Unfolding of a Mammalian Pentameric Ligand-Gated Ion Channel Proceeds at Consecutive, Distinct Steps. *J. Biol. Chem.* **2013**, *288* (8), 5756–5769.

Tong, A.; Petroff, J. T., 2nd; Hsu, F.-F.; Schmidpeter, P. A.; Nimigean, C. M.; Sharp, L.; Brannigan, G.; Cheng, W. W. Direct Binding of Phosphatidylglycerol at Specific Sites Modulates Desensitization of a Ligand-Gated Ion Channel. *Elife* **2019**, *8*.

Uchański, T.; Masiulis, S.; Fischer, B.; Kalichuk, V.; López-Sánchez, U.; Zarkadas, E.; Weckener, M.; Sente, A.; Ward, P.; Wohlkönig, A.; et al. Megabodies Expand the Nanobody Toolkit for Protein Structure Determination by Single-Particle Cryo-EM. *Nat. Methods* **2021**, *18* (1), 60–68.

Uhlén, M.; Fagerberg, L.; Hallström, B. M.; Lindskog, C.; Oksvold, P.; Mardinoglu, A.; Sivertsson, Å.; Kampf, C.; Sjöstedt, E.; Asplund, A.; et al. Proteomics. Tissue-Based Map of the Human Proteome. *Science* **2015**, *347* (6220), 1260419.

Unwin, N. Acetylcholine Receptor Channel Imaged in the Open State. *Nature* **1995**, *373* (6509), 37–43.

Unwin, N. Refined Structure of the Nicotinic Acetylcholine Receptor at 4 Å Resolution. *J. Mol. Biol.* **2005**, *346* (4), 967–989.

Unwin, N. Segregation of Lipids near Acetylcholine-Receptor Channels Imaged by Cryo-EM. *IUCrJ* **2017**, *4* (4), 393–399.

Unwin, N. Protein-Lipid Architecture of a Cholinergic Postsynaptic Membrane. *IUCrJ* **2020**, *7* (Pt 5), 852–859.

Unwin, N. Protein-Lipid Interplay at the Neuromuscular Junction. *Microscopy* **2022**, *71* (Supplement_1), I66–I71.

Unwin, N.; Fujiyoshi, Y. Gating Movement of Acetylcholine Receptor Caught by Plunge-Freezing. *J. Mol. Biol.* **2012**, *422* (5), 617–634.

Unwin, N.; Miyazawa, A.; Li, J.; Fujiyoshi, Y. Activation of the Nicotinic Acetylcholine Receptor Involves a Switch in Conformation of the Alpha Subunits. *J. Mol. Biol.* **2002**, *319* (5), 1165–1176.

Van Den Bogaart, G.; Meyenberg, K.; Risselada, H. J.; Amin, H.; Willig, K. I.; Hubrich, B. E.; Dier, M.; Hell, S. W.; Grubmüller, H.; Diederichsen, U.; et al. Membrane Protein Sequestering by Ionic Protein-Lipid Interactions. *Nature* **2011**, *479* (7374), 552–555.

Vanhaesebrouck, A. E.; Beeson, D. The Congenital Myasthenic Syndromes: Expanding Genetic and Phenotypic Spectrums and Refining Treatment Strategies. *Curr. Opin. Neurol.* **2019**, *32* (5), 696–703.

Velisetty, P.; Chakrapani, S. Desensitization Mechanism in Prokaryotic Ligand-Gated Ion Channel. *J. Biol. Chem.* **2012**, *287* (22), 18467–18477.

Velisetty, P.; Chalamalasetti, S. V.; Chakrapani, S. Conformational Transitions Underlying Pore Opening and Desensitization in Membrane-Embedded Gloeobacter Violaceus Ligand-Gated Ion Channel (GLIC). *J. Biol. Chem.* **2012**, *287* (44), 36864–36872.

Velisetty, P.; Chalamalasetti, S. V.; Chakrapani, S. Structural Basis for Allosteric Coupling at the Membrane-Protein Interface in Gloeobacter Violaceus Ligand-Gated Ion Channel (GLIC). *J. Biol. Chem.* **2014**, *289* (5), 3013–3025.

Verlet, L. Computer "Experiments" on Classical Fluids. I. Thermodynamical Properties of Lennard-Jones Molecules. *Physical Review* **1967**, *159* (1), 98–103.

Viel, G. T.; Yang, Q.; Lundahl, P.; Ensing, K.; de Zeeuw, R. A. Size-Exclusion Chromatographic Reconstitution of the Bovine Brain Benzodiazepine Receptor. Effects of Lipid Environment on the Binding Characteristics. *J. Chromatogr. A* **1997**, *776*, 101–107.

Wagner, T.; Merino, F.; Stabrin, M.; Moriya, T.; Antoni, C.; Apelbaum, A.; Hagel, P.; Sitsel, O.; Raisch, T.; Prumbaum, D.; et al. SPHIRE-CrYOLO Is a Fast and Accurate Fully Automated Particle Picker for Cryo-EM. *Commun Biol* **2019**, *2*, 218.

Wallace, T. L.; Bertrand, D. Neuronal A7 Nicotinic Receptors as a Target for the Treatment of Schizophrenia. *Int. Rev. Neurobiol.* **2015**, *124*, 79–111.

Walsh, R. M.; Roh, S.-H.; Gharpure, A.; Morales-Perez, C. L.; Teng, J.; Hibbs, R. E. Structural Principles of Distinct Assemblies of the Human A4β2 Nicotinic Receptor. *Nature* **2018**, *557* (7704), 261–265.

Wanamaker, C. P.; Christianson, J. C.; Green, W. N. Regulation of Nicotinic Acetylcholine Receptor Assembly. *Ann. N. Y. Acad. Sci.* **2003**, *998*, 66–80.

Wang, J.; Lester, H. A.; Dougherty, D. A. Establishing an Ion Pair Interaction in the Homomeric P1 γ-Aminobutyric Acid Type A Receptor That Contributes to the Gating Pathway. *J. Biol. Chem.* **2007**, *282* (36), 26210–26216.

Wang, J.; Kuryatov, A.; Jin, Z.; Norleans, J.; Kamenecka, T. M.; Kenny, P. J.; Lindstrom, J. A Novel A2/A4 Subtype-Selective Positive Allosteric Modulator of Nicotinic Acetylcholine Receptors Acting from the C-Tail of an α Subunit. *J. Biol. Chem.* **2015**, *290* (48), 28834–28846.

Wang, J.-M.; Zhang, L.; Yao, Y.; Viroonchatapan, N.; Rothe, E.; Wang, Z.-Z. A Transmembrane Motif Governs the Surface Trafficking of Nicotinic Acetylcholine Receptors. *Nat. Neurosci.* **2002**, *5* (10), 963–970.

Wang, L.; Zhou, H.; Zhang, M.; Liu, W.; Deng, T.; Zhao, Q.; Li, Y.; Lei, J.; Li, X.; Xiao, B. Structure and Mechanogating of the Mammalian Tactile Channel PIEZO2. *Nature* **2019**, *573* (7773), 225–229.

Wang, W.; MacKinnon, R. Cryo-EM Structure of the Open Human Ether-à-Go-Go-Related K+ Channel HERG. *Cell* **2017**, *169* (3), 422-430.e10.

Wang, X.; Zhang, X.; Dong, X. P.; Samie, M.; Li, X.; Cheng, X.; Goschka, A.; Shen, D.; Zhou, Y.; Harlow, J.; et al. TPC Proteins Are Phosphoinositide-Activated Sodium-Selective Ion Channels in Endosomes and Lysosomes. *Cell* **2012**, *151* (2), 372–383.

Wehrwein, E. A.; Orer, H. S.; Barman, S. M. Overview of the Anatomy, Physiology, and Pharmacology of the Autonomic Nervous System. *Compr. Physiol.* **2016**, *6* (3), 1239–1278.

Whorton, M. R.; MacKinnon, R. Crystal Structure of the Mammalian GIRK2 K+ Channel and Gating Regulation by G Proteins, PIP2, and Sodium. *Cell* **2011**, *147* (1), 199–208.

Whorton, M. R.; MacKinnon, R. X-Ray Structure of the Mammalian GIRK2-Bγ G-Protein Complex. *Nature* **2013**, *498* (7453), 190–197.

Williams, C. J.; Headd, J. J.; Moriarty, N. W.; Prisant, M. G.; Videau, L. L.; Deis, L. N.; Verma, V.; Keedy, D. A.; Hintze, B. J.; Chen, V. B.; et al. MolProbity: More and Better Reference Data for Improved All-Atom Structure Validation. *Protein Sci.* **2018**, *27* (1), 293–315.

Williamson, P. T. F.; Zandomeneghi, G.; Barrantes, F. J.; Watts, A.; Meier, B. H. Structural and Dynamic Studies of the γ-M4 Trans-Membrane Domain of the Nicotinic Acetylcholine Receptor. *Mol. Membr. Biol.* **2005**, *22* (6), 485–496.

Wittenberg, R. E.; Wolfman, S. L.; De Biasi, M.; Dani, J. A. Nicotinic Acetylcholine Receptors and Nicotine Addiction: A Brief Introduction. *Neuropharmacology* **2020**, *177*, 108256.

Woo, J.; Jeon, Y. K.; Zhang, Y. H.; Nam, J. H.; Shin, D. H.; Kim, S. J. Triple Arginine Residues in the Proximal C-Terminus of TREK K + Channels Are Critical for Biphasic Regulation by Phosphatidylinositol 4, 5-Bisphosphate. *American Journal of Physiology - Cell Physiology* **2019**, *316* (3), C312–C324.

Wootten, D.; Christopoulos, A.; Marti-Solano, M.; Babu, M. M.; Sexton, P. M. Mechanisms of Signalling and Biased Agonism in G Protein-Coupled Receptors. *Nat. Rev. Mol. Cell Biol.* **2018**, *19* (10), 638–653.

Wu, B.; Jayakar, S. S.; Zhou, X.; Titterton, K.; Chiara, D. C.; Szabo, A. L.; Savechenkov, P. Y.; Kent, D. E.; Cohen, J. B.; Forman, S. A.; et al. Inhibitable Photolabeling by Neurosteroid Diazirine Analog in the B3-Subunit of Human Hetereopentameric Type A GABA Receptors. *Eur. J. Med. Chem.* **2019**, *162*, 810–824.

Wulff, H.; Castle, N. A.; Pardo, L. A. Voltage-Gated Potassium Channels as Therapeutic Targets. *Nat. Rev. Drug Discov.* **2009**, *8* (12), 982–1001.

Xiong, W.; Cheng, K.; Cui, T.; Godlewski, G.; Rice, K. C.; Xu, Y.; Zhang, L. Cannabinoid Potentiation of Glycine Receptors Contributes to Cannabis-Induced Analgesia. *Nat. Chem. Biol.* **2011**, *7* (5), 296–303.

Xiong, W.; Cui, T.; Cheng, K.; Yang, F.; Chen, S.-R.; Willenbring, D.; Guan, Y.; Pan, H.-L.; Ren, K.; Xu, Y.; et al. Cannabinoids Suppress Inflammatory and Neuropathic Pain by Targeting A3 Glycine Receptors. *J. Exp. Med.* **2012**, *209* (6), 1121–1134.

Xiu, X.; Hanek, A. P.; Wang, J.; Lester, H. A.; Dougherty, D. A. A Unified View of the Role of Electrostatic Interactions in Modulating the Gating of Cys Loop Receptors. *J. Biol. Chem.* **2005**, *280* (50), 41655–41666.

Xu, Y.; Barrantes, F. J.; Luo, X.; Chen, K.; Shen, J.; Jiang, H. Conformational Dynamics of the Nicotinic Acetylcholine Receptor Channel: A 35-Ns Molecular Dynamics Simulation Study. *J. Am. Chem. Soc.* **2005**, *127*, 1291–1299.

Yakel, J. L. Cholinergic Receptors: Functional Role of Nicotinic ACh Receptors in Brain Circuits and Disease. *Pflugers Arch.* **2013**, *465* (4), 441–450.

Yin, Y.; Le, S. C.; Hsu, A. L.; Borgnia, M. J.; Yang, H.; Lee, S.-Y. Structural Basis of Cooling Agent and Lipid Sensing by the Cold-Activated TRPM8 Channel. *Science* **2019**, *363* (6430).

Yoder, N.; Jalali-Yazdi, F.; Noreng, S.; Houser, A.; Baconguis, I.; Gouaux, E. Light-Coupled Cryo-Plunger for Time-Resolved Cryo-EM. *J. Struct. Biol.* **2020**, *212* (3), 107624.

Yu, F. H.; Yarov-Yarov, V.; Gutman, G.; Catterall, W. A. Overview of Molecular Relationships in the Voltage-Gated Ion Channel Superfamily. *Pharmacol. Rev.* **2005**, *57* (4), 387–395.

Yu, J.; Zhu, H.; Lape, R.; Greiner, T.; Shahoei, R.; Wang, Y.; Du, J.; Lü, W.; Tajkhorshid, E.; Sivilotti, L.; et al. Mechanism of Gating and Partial Agonist Action in the Glycine Receptor. *Cell* **2021**, *184*, 1–12.

Yu, Z.; Cohen, J. B. Enantiomeric Barbiturates Bind Distinct Inter- and Intrasubunit Binding Sites in a Nicotinic Acetylcholine Receptor (NAChR). *J. Biol. Chem.* **2017**, *292* (42), 17258–17271.

Yu, Z.; Chiara, D. C.; Savechenkov, P. Y.; Bruzik, K. S.; Cohen, J. B. A Photoreactive Analog of Allopregnanolone Enables Identification of Steroid-Binding Sites in a Nicotinic Acetylcholine Receptor. *J. Biol. Chem.* **2019**, *294* (19), 7892–7903.

Yuan, B.; Hatchett-Walker, C.; Long, P.; Xu, Z.; Stephenson, F. A.; Haider, S.; Jovanovic, J. N. Control of Cell Surface Expression of GABAA Receptors by a Conserved Region at the End of the N-Terminal Extracellular Domain of Receptor Subunits. *J. Biol. Chem.* **2022**, *298* (12), 102590.

Zarkadas, E.; Zhang, H.; Cai, W.; Effantin, G.; Perot, J.; Neyton, J.; Chipot, C.; Schoehn, G.; Dehez, F.; Nury, H. The Binding of Palonosetron and Other Antiemetic Drugs to the Serotonin 5-HT3 Receptor. *Structure* **2020**, *28* (10), 1131-1140.e4.

Zarkadas, E.; Pebay-Peyroula, E.; Thompson, M. J.; Schoehn, G.; Uchański, T.; Steyaert, J.; Chipot, C.; Dehez, F.; Baenziger, J. E.; Nury, H. Conformational Transitions and Ligand-Binding to a Muscle-Type Nicotinic Acetylcholine Receptor. *Neuron* **2022**, *110* (8), 1358-1370.e5.

Zaydman, M. A.; Silva, J. R.; Delaloye, K.; Li, Y.; Liang, H.; Larsson, H. P.; Shi, J.; Cui, J. Kv7.1 Ion Channels Require a Lipid to Couple Voltage Sensing to Pore Opening. *Proc. Natl. Acad. Sci. U. S. A.* **2013**, *110* (32), 13180–13185.

Zeilhofer, H. U.; Acuña, M. A.; Gingras, J.; Yévenes, G. E. Glycine Receptors and Glycine Transporters: Targets for Novel Analgesics? *Cellular and Molecular Life Sciences* **2018**, *75* (3), 447–465.

Zhang, H.; Karlin, A. Contribution of the β Subunit M2 Segment to the Ion-Conducting Pathway of the Acetylcholine Receptor†. *Biochemistry* **1998**, *37* (22), 7952–7964.

Zhang, Y.; Chen, J.; Auerbach, A. Activation of Recombinant Mouse Acetylcholine Receptors by Acetylcholine, Carbamylcholine and Tetramethylammonium. *J. Physiol.* **1995**, *486 (Pt 1)* (Pt 1), 189–206.

Zhang, Y.; Dijkman, P. M.; Zou, R.; Zandl-Lang, M.; Sanchez, R. M.; Eckhardt-Strelau, L.; Köfeler, H.; Vogel, H.; Yuan, S.; Kudryashev, M. Asymmetric Opening of the Homopentameric 5-HT3A Serotonin Receptor in Lipid Bilayers. *Nat. Commun.* **2021**, *12* (1), 1074.

Zhang, Z.; Tóth, B.; Szollosi, A.; Chen, J.; Csanády, L. Structure of a TRPM2 Channel in Complex with Ca2+ Explains Unique Gating Regulation. *Elife* **2018**, *7*, e36409.

Zhao, Q.; Zhou, H.; Chi, S.; Wang, Y.; Wang, J.; Geng, J.; Wu, K.; Liu, W.; Zhang, T.; Dong, M.-Q.; et al. Structure and Mechanogating Mechanism of the Piezo1 Channel. *Nature* **2018**, *554* (7693), 487–492.

Zhao, Y.; Liu, S.; Zhou, Y.; Zhang, M.; Chen, H.; Eric Xu, H.; Sun, D.; Liu, L.; Tian, C. Structural Basis of Human A7 Nicotinic Acetylcholine Receptor Activation. *Cell Res.* **2021**, *31* (6), 713–716.

Zhu, D.; Xiong, W. C.; Mei, L. Lipid Rafts Serve as a Signaling Platform for Nicotinic Acetylcholine Receptor Clustering. *J. Neurosci.* **2006**, *26* (18), 4841–4851.

Zhu, F.; Hummer, G. Pore Opening and Closing of a Pentameric Ligand-Gated Ion Channel. *Proc. Natl. Acad. Sci. U. S. A.* **2010**, *107* (46), 19814–11981.

Zhu, H.; Gouaux, E. Architecture and Assembly Mechanism of Native Glycine Receptors. *Nature* **2021**, *599* (7885), 513–517.

Zhu, S.; Noviello, C. M.; Teng, J.; Walsh, R. M.; Kim, J. J.; Hibbs, R. E. Structure of a Human Synaptic GABAA Receptor. *Nature* **2018**, *559* (7712), 67–72.

Zhu, S.; Sridhar, A.; Teng, J.; Howard, R. J.; Lindahl, E.; Hibbs, R. E. Structural and Dynamic Mechanisms of GABAA Receptor Modulators with Opposing Activities. *Nat. Commun.* **2022**, *13* (1), 4582.

Zoli, M.; Pistillo, F.; Gotti, C. Diversity of Native Nicotinic Receptor Subtypes in Mammalian Brain. *Neuropharmacology* **2015**, *96* (Pt B), 302–311.

Zubcevic, L.; Herzik, M. A., Jr; Chung, B. C.; Liu, Z.; Lander, G. C.; Lee, S.-Y. Cryo-Electron Microscopy Structure of the TRPV2 Ion Channel. *Nat. Struct. Mol. Biol.* **2016**, *23* (2), 180–186.

Chapter 9. Appendix

9.1 Review Article 1: Ion channels as lipid sensors: from structures to mechanisms

Thompson, M.J., and Baenziger, J.E. (2020). Ion channels as lipid sensors: from structures to mechanisms. Nat. Chem. Biol. *16*, 1331–1342.
Adapted as a post-print from Nat. Chem Biol., https://doi.org/10.1038/s41589-020-00693-3.

9.1.1 Preface

Nature Chemical Biology asked Dr. Baenziger for an invited review article on the relationship between ion channels and lipids. The timing of this article happened to overlap with the COVID-19 pandemic when we did not have access to the lab. For several months during the pandemic, Dr. Baenziger and I worked on writing this review article, which we were addiment should not just be a regurgitation of the literature, but instead an insightful piece on how mechanisms of ion channel modulation by lipids has evolved in various ion channel families. We worked tirelessly toward this goal and the final product is one that I am very proud of. While we both contributed to all the sections in the article, my role was primarily in writing section 9.1.4 and 9.1.5, along with preparing the figures. Dr. Baenziger was originally going to be the first author on this paper, but in the end, he felt my contribution was significant enough for me to be the first author on the paper.

9.1.2 Abstract

Ion channels play critical roles in cellular function by facilitating the flow of ions across the membrane in response to chemical or mechanical stimuli. Ion channels operate in a lipid environment, which can modulate or define their function. Recent technical advancements have led to the solution of numerous ion channel structures solubilized in detergent and/or reconstituted into lipid bilayers, thus providing unprecedented insight into the mechanisms underlying ion channel-lipid interactions. Here, we describe how ion channel structures have evolved to respond to both lipid modulators and lipid activators to control the electrical activities of cells, highlighting diverse mechanisms and common themes.

9.1.3 Introduction

Ion channels have been central to research in molecular neuroscience since the early observation that the selective permeability of membranes to sodium, potassium and chloride ions underlies signaling in the nervous system. In fact, the membrane-imbedded ion channels of excitable cells establish resting membrane potentials, respond to synaptic stimuli, propagate action potentials and initiate the release of neurotransmitters into the synaptic cleft. Ion channels also control the flow of ions and other solutes across the membranes of non-excitable cells to stimulate exocytosis, regulate cell volume, etc., thus contributing more broadly to cellular homeostasis. Ion channels are central to human health and disease. They also represent the second largest target for existing drugs that treat human disorders (Overington et al., 2006).

Fundamental to understanding the diverse roles of ion channels in cellular biology and pharmacology is the elucidation of ion channel structures. The first near atomic resolution insight was achieved in 1998 with the solution of a crystal structure of KscA, a tetrameric K^+ channel housing both the permeation path across the membrane and the K^+ ion selectivity filter (Doyle et al., 1998). The KcsA structure was followed by crystal structures of a mechanosensitive (MS) ion channel (Chang et al., 1998), a Cl^- channel (Dutzler et al., 2002), a voltage gated K^+ channel (Jiang et al., 2003), trimeric, tetrameric and pentameric ligand-gated ion channels (pLGIC) (Hilf and Dutzler, 2008; Kawate et al., 2009; Sobolevsky et al., 2009) and a voltage-gated Na^+ channel (Payandeh et al., 2011), etc. These and many other structures have confirmed that some ion channels, referred to as "voltage-gated-like" (VGL) ion channels, have evolved from a common ancestor and thus share a core structural and functional architecture (Yu et al., 2005), albeit one that has evolved additional structural features that impart on different ion channels the ability to respond to a variety of signaling molecules. Others, such as the MS ion

channels, have evolved separately and thus exhibit diverse architectures with diverse mechanisms of action.

One theme common to all ion channels is that they function in a membrane environment, so their activities are influenced by lipids. While the functional sensitivities of ion channels to changes in membrane lipid composition have been documented for decades, more recent studies have focused on the complex roles played by signaling lipids, such phosphatidylinositol 4,5-bisphosphate (PIP_2), diacylglycerol (DAG), phosphatidylglycerol (PG), phosphatidic acid (PA), sterols, etc., in ion channel function and thus on the mechanisms by which the metabolic state of a cell is coupled to its electrical activity. Some ion channels are directly activated by signaling lipids, while the gating of others is dependent on or modulated by lipids (Poveda et al., 2017; Corradi et al., 2019; Duncan et al., 2020b). Further modulation of ion channel function by signaling lipids may also occur through complex mechanisms involving the formation of lipid microdomains (Dart, 2010; Comoglio et al., 2014).

The mechanisms by which lipids *directly* alter the activity of an ion channel are generally considered in either "molecular" or "physical" terms (Lee, 2004). Molecular refers to the binding of lipids to recognition sites where they act as activating ligands, cofactors or allosteric modulators, while physical typically refers to the coupling of bulk membrane properties, such as membrane hydrophobic thickness, curvature, tension, electrostatics, etc., to altered transmembrane (TM) helix-helix packing in a manner that influences function. Molecular recognition sites are often further described as annular or non-annular. Annular sites are located at the periphery of the transmembrane (TM) domain, with the lipids bound to these sites rapidly exchanging with others in the bulk membrane. Non-annular sites are located between the transmembrane α-helices in crevices or fenestrations/cavities where they are shielded from the

bulk membrane environment (Jost et al., 1973; Hesketh et al., 1976; Marsh and Barrantes, 1978; Narayanaswami and McNamee, 1993; Marsh, 2010). There is extensive evidence that lipids influence ion channel activity through both molecular and physical mechanisms, although in some cases the distinctions between the two have become blurred.

Recent developments in both x-ray crystallography and cryo-electron microscopy have led to an explosion of new ion channel structures leading to new understanding of the mechanisms underlying ion channel-lipid interactions. This review is centered on four representative ion channel families that each respond to lipids in a distinct manner: lipid-gated K^+ channels, lipid-dependent VGL channels, membrane tension-gated MS ion channels and lipid-modulated pLGICs (Fig. 9.1). We highlight diverse structures that impart on each family the ability to respond to lipids, while focusing on those structures that have led to detailed insight into the mechanisms underlying lipid-sensing. These select examples provide a basis for understanding the mechanisms by which all signaling lipids influence ion channel function to link the electrical activity of a cell to its metabolic state.

Figure 9.1 Role of lipids in ion channel function

Some ion channels are directly gated by lipids (lipid-gated and membrane tension-gated) while others either require lipids for gating (lipid-dependent voltage-gated) or are allosterically modulated by lipids (lipid-modulated ligand-gated). Lipids influence the activity of lipid-gated and lipid-dependent voltage-gated channels by binding to and thus enhancing the functional coupling between regulatory and pore domains. Many membrane tension-gated ion channels utilize a "slider-crank" mechanism to translate increased bilayer tension into channel gating, with an amphipathic helix acting as a horizontal force-coupling element that drag away the helices lining the TM pore, although tension may also influence lipid binding. Conserved binding sites on ligand-gated ion channels influence TM helix packing to alter channel function.

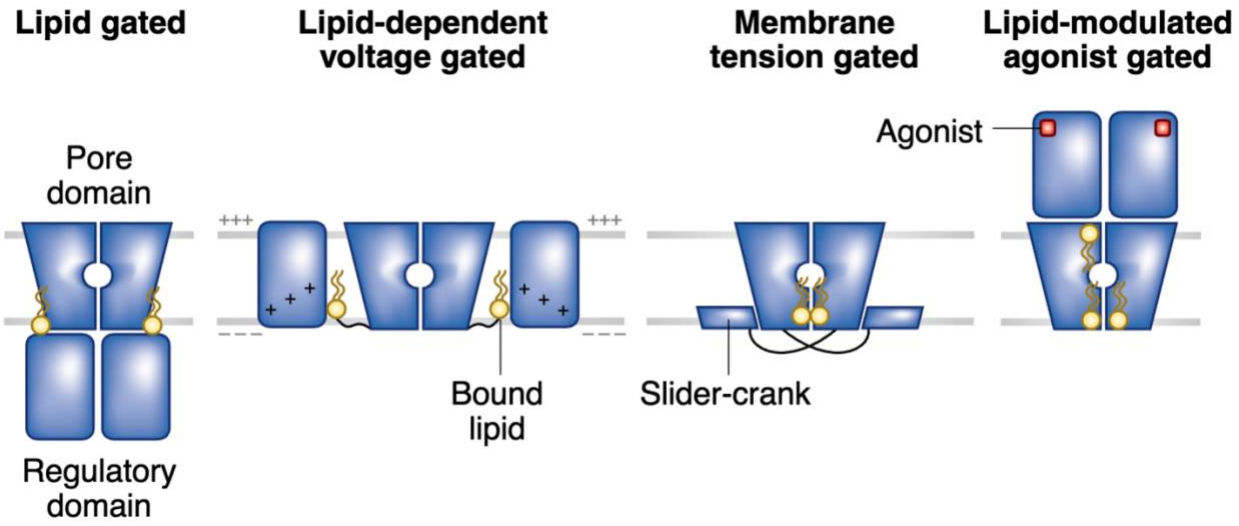
Lipid gated
Lipid-dependent voltage gated
Membrane tension gated
Lipid-modulated agonist gated
Pore domain
Regulatory domain
Bound lipid
Slider-crank
Agonist

9.1.4 Lipid-gated K^+ channels

Inward rectifying K^+ (Kir) channels are lipid-gated channels that help establish the resting membrane potentials of cells (Hibino et al., 2010). Direct gating of Kir channels by PIP_2 was first demonstrated in the late 1990s, with crystal structures of Kir2.2 in the presence and absence of bound PIP_2 providing the first structural insight into the underlying mechanisms (Huang et al., 1998; Kuo et al., 2003; Hansen et al., 2011). It is now known that Kir channels are sensitive to a variety of anionic signaling lipids, as well as cholesterol and metabolic factors. Kir channels thus couple the metabolic state of a cell to its electrical activity.

Kir2.2 is a tetrameric channel that consists of a classical K^+-selective TM pore domain and a large modulatory cytoplasmic domain, with the two domains connected by four flexible linkers (Fig. 9.2) (Kuo et al., 2003; Hansen et al., 2011). The TM pore domain is homologous to both KscA and the TM pore domains of voltage-gated ion channels (see below), with each subunit contributing two transmembrane helices, TM1 and TM2, a short pore helix and a highly conserved K^+ selectivity filter. In Kir channels, there are two in-tandem gates, an inner helix gate formed by hydrophobic residues on the inner TM2 helices of the TM pore domain and a G loop gate formed by a constriction at the apex of the cytoplasmic domain, although in Kir2.2 the latter appears to be constitutively open (Fig. 9.2a) (Hansen et al., 2011).

Direct PIP_2-gating of Kir channels results from a PIP_2-induced coupling of the regulatory cytoplasmic domain to the channel conducting TM pore domain. Specifically, PIP_2 binds to equivalent sites on each subunit of the tetramer with its acyl chains, glycerol backbone and 1' phosphate anchored to TM1, while its 4' and 5' phosphates are coordinated by Lys183 and Arg186 from M2 and Lys188 and Lys189 from the flexible linker (PDB:3SPI, 3.3Å resolution) (Hansen et al., 2011). The coordination of the 4' and 5' phosphate groups transitions the flexible

linker into a helical structure, which leads to a 6 Å translation of the cytoplasmic domain up towards the bilayer surface and a splaying and rotation of the pore-lining TM2 helices to move the hydrophobic gate residues away from the ion permeation pathway leading to a "pre-open" state (Fig. 9.3a), although it has been proposed that dynamic movements of pore-lining side chains may be sufficient for ion permeation (Sun and MacKinnon, 2020). Notably, PA, which lacks the 4',5'-phosphate-substituted inositol ring, binds to an overlapping site but fails to engage the helical linker and is therefore unable to produce the structural rearrangements observed with PIP_2 (PDB:3SPC, 2.5Å resolution).

The PIP_2-induced docking of the regulatory cytoplasmic and TM pore domains to induce channel gating is conserved in other Kir channels, with recent structures showing how this structural theme has evolved to allow the coupling of PIP_2-sensing to the sensing of other cellular metabolites (Fig. 9.2b). G-protein gated Kir3 (GIRK) channels, which have a domain structure similar to Kir2.2, require both PIP_2 and G-proteins for activation (Dascal, 1997). In GIRK2 channels, the cytoplasmic domain has evolved to bind the G protein βγ subunits, with binding to GIRK2 leading to a conformational change that propagates through the cytoplasmic domain to both open the G loop gate and elicit a partial splaying of the inner TM2 helices (PDB:4KFM, 3.5Å resolution) (Whorton and MacKinnon, 2013). Although crystal structures suggest that both PIP_2 and G-protein binding, the latter mimicked by the R201A mutation, are required to open the inner helix gate (PDB:3SYQ, 3.5Å resolution) (Whorton and MacKinnon, 2011), recent cryo-EM structures solved in lipid nanodiscs suggest that PIP_2 binding alone translates the cytoplasmic domain up towards the TM pore domain, as in Kir2.2 (Mathiharan et al., 2020).

Another example illustrating the evolved complexities of PIP_2-sensing is found in K_{ATP} channels, which are octamers consisting of four classical Kir channel subunits (in this case Kir6), each associated through its TM pore domain with a sulfonylurea receptor (SUR) subunit (Fig. 9.2b). K_{ATP} channels sense the metabolic state of the cell by responding to changes in ATP/ADP concentration. ATP directly inhibits K_{ATP} channel function through binding to the cytoplasmic domain, which leads to a rearrangement of the PIP_2 binding pockets to weaken PIP_2 binding (PDB:6C3O, 3.9Å resolution) (Hilgemann and Ball, 1996; Lee et al., 2017). In contrast, ADP+Mg^{2+} potentiates K_{ATP} function by binding to the catalytic site of each SUR1 subunit, which allosterically alters the ATP binding site to overcome ATP-induced inhibition. K_{ATP} channels have evolved a sensitivity to cell metabolites by coupling the core lipid sensing Kir channel domain to additional TM subunits.

Note that the PIP_2-induced gating of Kir channels is sensitive to other lipids, although the underlying mechanisms are less well-defined. For example, Kir2 channels are potentiated by anionic lipids, likely through binding to sites adjacent to the PIP_2 binding sites at the interface between the cytoplasmic and TM pore domains (Cheng et al., 2011; Lee et al., 2016; Duncan et al., 2020a), but are inhibited by cholesterol (Romanenko et al., 2004), although it is not yet clear whether cholesterol influences function via direct binding or by altering the physical properties of the surrounding membrane (Levitan et al., 2014; Barbera et al., 2018). In addition, the recent cryo-EM structures of GIRK2 reveal the binding of cholesterol to sites adjacent to the PIP_2 binding sites, with cholesterol likely potentiating function by stabilizing PIP_2-induced docking of the two domains (Mathiharan et al., 2020).

Figure 9.2 Structural diversity of lipid-gated and other VGL ion channels

(A) VGL channels consist of a TM pore domain (KcsA, left; PDB: 1BL8) that is linked either to a cytoplasmic regulatory domain (Kir2.2, center; PDB: 3SPJ) or to voltage sensors (Kv2.1-Kv1.2 chimera, right; PDB: 2R9R). For clarity, the side views show only two subunits with the regulatory and TM pore domains in red and blue, respectively. In the Kir2.2 structure, the TM pore domain and cytoplasmic domain from two subunits are rotated ~90^{o} relative to each other to highlight the inner helix (Ile177) and G loop (Met308/Thr309) gates, with the noted residues shown as tan spheres. (B) Side views of two subunits of the lipid-gated PIP_2 bound Kir2.2 (PDB: 3SPI), PIP_2 and Gβγ bound GIRK2 (PDB: 4KFM) and K_{ATP} with ADP/ ATP bound to the auxiliary SUR subunits (PDB: 6C3O). Gβγ and SUR are colored light orange, with lipids shown as predominantly yellow spheres. (C) Side views of two subunits of lipid-dependent VGL channels of PIP_2/KCNE3 bound Kv7.1 (PDB: 6V01), PIP_2 bound TRPV5 (PDB: 6DMU) and lipid bound TRPC3 (PDB: 6CUD). Accessory subunits/domains are coloured light orange. Note that PIP_2 is bound to the S4-S5 linker in Kv7.1 and TRPV5, as shown in more detail in Fig. 9.3, but is bound to both a different region of the S4-S5 linker and the TM pore domain in TRPC3. The structures in (B) and (C) highlight how increased structural complexity confers on Kir and VGL channels the ability to respond to both lipids and a variety of other cellular metabolites.

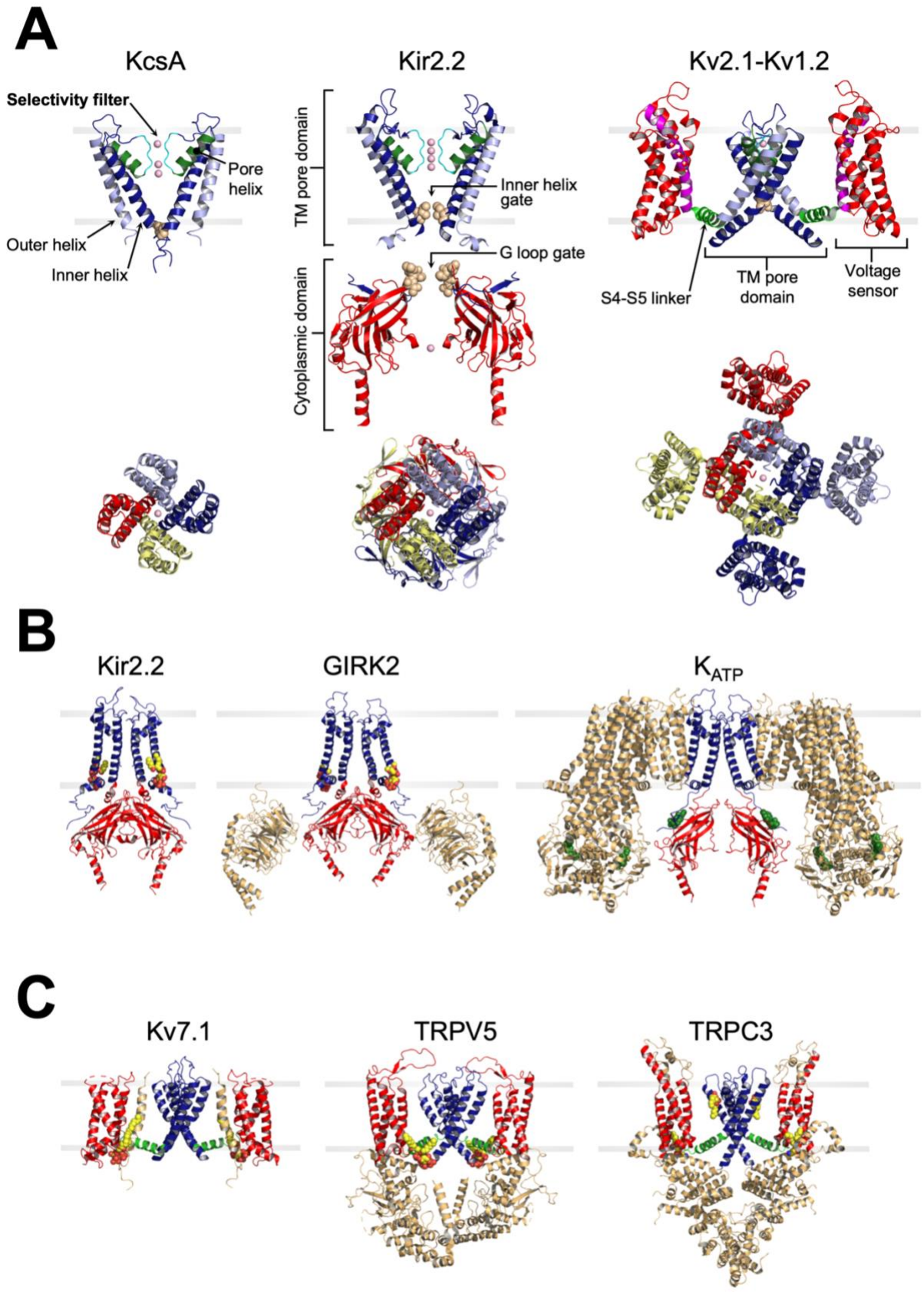
A
KcsA
Kir2.2
Kv2.1-Kv1.2
Selectivity filter
Pore helix
Outer helix
Inner helix
TM pore domain
Inner helix gate
G loop gate
Cytoplasmic domain
S4-S5 linker
TM pore domain
Voltage sensor
B
Kir2.2
GIRK2
K$_{ATP}$
C
Kv7.1
TRPV5
TRPC3

9.1.5 Lipid-dependent VGL channels

The basic theme of PIP_2-induced inter-domain coupling is also found in some voltage-gated K^+ (Kv) channels, but in these Kv channels the coupling is required for voltage-induced channel gating. Kv channels play a central role in electrical signaling by returning the depolarized cell to a resting state during an action potential (Wulff et al., 2009). As with Kir channels, Kv channels are tetramers, with each subunit containing a two TM helix (S5, S6) pore domain, although in this case the TM pore domain is linked via a helical S4-S5 linker to a four TM helix (S1-S4) voltage sensor that is physically positioned closer to an adjacent TM pore domain (i.e. the voltage sensor and TM pore domains adopt a domain swapped configuration, see Fig. 9.2a). The S4 helix contains basic residues that transition the voltage sensor from a down (inactive) conformation at resting membrane potentials to an up (active) conformation when the cell is depolarized, with movement of the voltage-sensor displacing the helical S4-S5 linker leading to a rotation and a splaying of the pore-lining inner S6 helices to open the channel gate (Long et al., 2005).

Kv7 channels are unique amongst Kv channels in that they require PIP_2 as a cofactor for voltage-induced gating (Zaydman et al., 2013). In the absence of PIP_2, the voltage-sensors of Kv7.1 still transition from down to up conformations in response to changes in voltage, but the movements of the voltage sensors are not relayed to the TM pore domain because there is a hinge loop inserted at the N terminus of each S4-S5 helical linker (PDB:5VMS, 3.7Å resolution) (Zaydman et al., 2013; Sun and MacKinnon, 2017). PIP_2 binds near the hinge loop of each subunit with its 4' and 5' phosphates interacting with Arg116, Arg181, Lys183 and Lys194 from the voltage sensor and the 1' phosphate and inositol ring directly coordinated by Gln244 and Arg249 from the S4-S5 linker (PDB:6V01, 3.2Å resolution). PIP2 binding leads to a more rigid

inter-helical linker, with binding required for effective coupling of voltage-induced movement of the voltage sensors to the gating of the TM channel pore (Fig. 9.3b) (Sun and MacKinnon, 2020). The introduction of a hinge loop into the S4-S5 linker thus converts Kv7 into a voltage-gated, but lipid-dependent channel.

Kv7 channels also interact with accessory subunits to create more complex mechanisms by which their function can be influenced by lipids. *In vivo*, each Kv7 subunit is associated with a KCNE (potassium channel subfamily E member) subunit, which is a single transmembrane spanning protein that regulates the voltage-dependence of channel gating (Fig. 9.2c). A recent cryo-EM structure of Kv7.1 (KCNQ1) complexed with both calmodulin and KCNE3 shows that KCNE3 binding to a shallow groove between the voltage sensor and the TM pore domains locks the voltage sensor in an active up conformation (PDB:6V00, 3.1Å resolution) (Sun and MacKinnon, 2020). Although KCNE3 alone does not stabilize an open conformation of the pore, KCNE3 binding allows PIP_2 to couple the activated voltage sensor to movement of the inner helix gate in the absence of a change in voltage. The accessory KCNE3 subunit thus converts Kv7.1 from a voltage-gated ion channel that requires PIP_2 for activation, into a PIP_2-activated ion channel that requires KCNE3.

Note that a small subset of VGL channels (hyperpolarization-activated cyclic nucleotide-gated (HCN) channels (Kv10-12)) have a non-domain swapped pore/voltage domain architecture that requires only a short S4-S5 loop rather than a helical S4-S5 linker (PDB:5U6O, 3.5Å resolution) (Lee and MacKinnon, 2017; Wang and MacKinnon, 2017). Intriguingly, a recent structure of the plant HCN channel, KAT1, shows that a phospholipid, likely PIP_2, intercalates between S4 of the voltage sensor and S5/S6 of the pore domain (PDB:6V1Y, 3.8Å resolution) (Clark et al., 2020). PIP_2 is known to affect the function of KAT1 (Liu et al., 2005). It will be

intriguing to characterize the mechanism by which the bound lipid influences the activity of a non-domain-swapped VGL channel.

Note also that the basic theme of PIP_2-dependent coupling of voltage-sensor and TM pore domains has evolved in other VGL channels to further elicit sensitivities to lipids. Na^+-conducting two-pore channels (TPCs) are dimers with each subunit consisting of two in-tandem voltage sensing/TM pore domains (Wang et al., 2012). TPC1 requires the endolysosomal specific binding of $PI(3,5)P_2$ to facilitate voltage-induced gating. Analogous to the role of PIP_2 in voltage-gating of Kv7, $PI(3,5)P_2$ must be bound to the S4-S5 linker for effective coupling between the voltage sensor and TM pore domain (PDB:6C9A, 3.2Å resolution) (She et al., 2018). In TPC2, however, cationic residues in S4 are substituted with neutral ones so that the voltage sensor is perpetually in an active conformation (PDB:6NQ0, 3.7Å resolution) (She et al., 2019). In this case, point mutations in S4 convert TPC2 from a voltage-gated channel that requires $PI(3,5)P_2$ for gating, to a voltage insensitive $PI(3,5)P_2$-gated channel.

Lipid action at transient receptor potential (TRP) channels, which respond to a variety of sensations including pain, temperature, tastes, pressure, etc., appears to be even more complex. TRP channels exhibit the classical tetrameric VGL channel architecture, with both voltage-sensing and TM pore domains, but bind auxiliary subunits (Fig. 9.2c). Similar to TPC2, the primary sequences of the S4 voltage sensors in TRPV5 (PDB:6DMU, 4.0Å resolution) and TRPV6 (PDB:6BO8, 3.6Å resolution) deviate substantially from that of traditional voltage-gated channels rendering these channels insensitive to changes in voltage, with PIP_2 binding to the S4-S5 linker leading to the movement of the pore lining S6 helices to open the ion pore (Hughes et al., 2018; McGoldrick et al., 2018). In other TRP channels, the binding of several lipids, including PIP_2, PA, DAG, phosphatidylcholine (PC) and cholesterol have been detected at a

plethora of sites including various sites at the interfaces between the voltage sensor and TM pore domains and on the pore domain itself (Fig. 9.2c). The functional effects of these bound lipids vary, with PIP_2 acting as a cofactor for Ca^{2+}-activated TRPM2 (PDB:6CO7, 3.1Å resolution) (Zhang et al., 2018), an allosteric potentiator for the cold-regulated TRPM8 (PDB:6NR3, 3.4Å resolution) (Yin et al., 2019) and an inhibitor of heat-activated TRPV1 (PDB:5IRZ, 3.2Å resolution), and possibly TRPV2 (PDB:5AN8, 4.0Å resolution) (Gao et al., 2016; Zubcevic et al., 2016). DAG directly activates TRPC3 (PDB:6CUD, 3.3Å resolution) and TRPC6 channels, likely through a pore domain binding site (PDB:6UZ8, 3.1Å resolution) (Fan et al., 2018; Lichtenegger et al., 2018; Bai et al., 2020). In other TRP channels, including the mechanosensitive NOMPC, the functional role of the bound lipids, including PIP_2, remains to be determined (PDB:5VKQ, 3.6Å resolution) (Rohács, 2014; Jin et al., 2017). Further structural and functional data are thus required to understand the potentially complex mechanisms by which lipid binding influences the activities of these important members of the VGL family.

Finally, as with Kir channels, lipids influence the activities of VGL channels through non-specific mechanisms. For example, movement of the voltage sensor, and thus voltage-dependent gating of Kv channels, is modulated by anionic lipids. Anionic lipids alter the electrostatic potential of the inner leaflet of the bilayer to stabilize the voltage sensor in the down conformation (Hite et al., 2014). Lipids thus influence Kv channel activity through both molecular and physical mechanisms.

Figure 9.3 Mechanisms of lipid action in VGL channels

(A) Side views of two subunits of apo (PDB: 3SPJ) and PIP_2 bound (PDB: 3SPI) Kir2.2 highlighting the PIP_2-induced ~6Å translation of the cytoplasmic domain towards the TM pore domain. The zoomed in view of the Kir2.2 PIP_2 recognition site highlights residues (tan sticks) that coordinate the phosphates of the inositol head group. (B) Side views of the voltage sensor, S4-S5 linker and TM pore domain of a single subunit (right) in the Kv1.2-Kv2.1 channel chimera (top; PDB: 2R9R), and the PIP_2/KCNE3 bound Kv7.1 channel (bottom; PDB: 6V01). Zoomed in views are of the hinge region (S4 and S4-S5 linker helix) in the Kv1.2-2.1 chimera and the PIP_2/KCNE3 bound Kv7.1. A helix links S4 (magenta) to S5 (green) in the Kv1.2-2.1 chimera. In Kv7.1, the helix is replaced by a flexible hinge loop. PIP_2 interacts with residues on the voltage sensor, the hinge loop and the S4-S5 helix to couple the voltage sensor effectively to the TM pore domain.

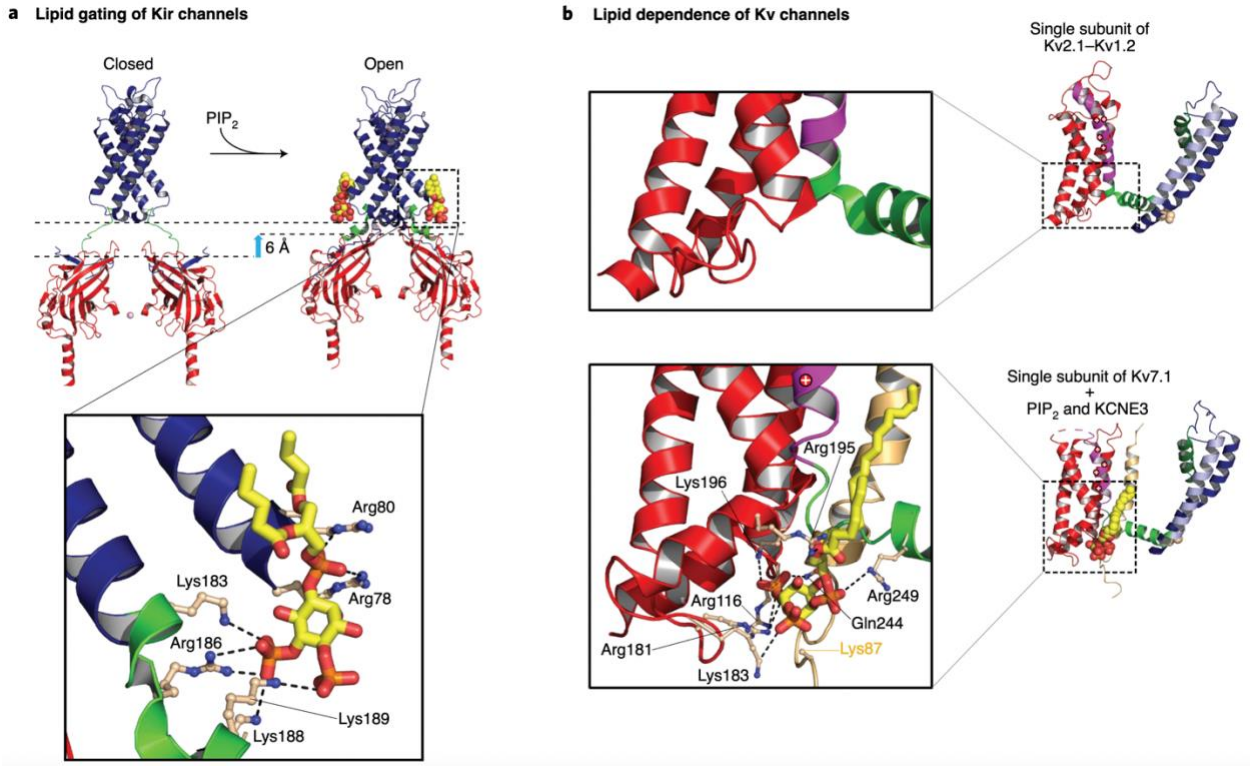
a Lipid gating of Kir channels
Closed
Open
PIP2
6 Å
Arg80
Lys183
Arg78
Arg186
Lys189
Lys188
b Lipid dependence of Kv channels
Single subunit of
Kv2.1–Kv1.2
Single subunit of Kv7.1
+
PIP2 and KCNE3
Arg195
Lys196
Arg116
Arg249
Gln244
Arg181
Lys87
Lys183

9.1.6 Force-from-lipids MS ion channels

Force-from-lipids MS channels are pore-forming membrane proteins that are directly gated by changes in bilayer tension, thus coupling force-sensing to the electrical activities of cells (Cox et al., 2018, 2019; Douguet and Honoré, 2019). Although the observation of mechanosensitive currents dates back to some of the earliest electrophysiological recordings, the existence of mechanosensitive channels was documented in a variety of cell types throughout the 1980s. The first structural insight into mechanosensation came with the solution of crystal structures of the bacterial large (MscL) (PDB:2OAR, 3.5Å resolution) and small (MscS) (PDB:2OAU, 3.9Å resolution) conductance MS channels (Chang et al., 1998; Bass et al., 2002). More recently, structures of eukaryotic MS channels, such as Piezo1/2, TRAAK, TREK1/2 and NOMPC, have led to major new insights into our understanding of mechanosensation (Brohawn et al., 2012; Guo and MacKinnon, 2017; Jin et al., 2017; Zhao et al., 2018; Wang et al., 2019) (Fig. 9.4). These new MS channel structures show that, unlike lipid-gated Kir channels/VGL channels where structural complexity has evolved from a common structural theme, MS channels have evolved independently to generate incredible structural diversity. These diverse structures lead to different mechanosensitivities and open-state ion selectivities (see below), as required by each MS channel's biological function.

MscL and MscS, the prototypic mechanosensitive ion channels, both function as pressure release valves to prevent lysis when cells swell upon exposure to hypo-osmotic shock (Levina et al., 1999). The best understood mechanosensitive channel, MscL, is formed from 5 identical subunits, each consisting of two TM helices, with TM1 lining the pore and TM2 interacting with lipids, an N-terminal amphipathic helix that is oriented parallel to the membrane at the bilayer-solvent interface and that connects to TM1 via a glycine hinge, and a C-terminal helix distal to

TM2 that bundles with helices from adjacent subunits and projects normal to the membrane into the cytoplasm (Chang et al., 1998). MscL utilizes a "slider-crank" mechanism to translate increased bilayer tension into channel gating. Specifically, the increase in membrane tension that occurs upon cell swelling leads to a flattening of the overall MscL structure, which is driven primarily by the membrane-imbedded N-terminal amphipathic helix (the slider) (Fig 9.5b) (Perozo et al., 2002). Thinning of the membrane in response to tension drags the N-terminal helix away from the central pore axis altering the glycine hinge to tilt and rotate TM1 (the crank) so that the N-terminal helix and TM1 become contiguous (Bavi et al., 2016). In effect, the N-terminal amphipathic helix acts as a horizontal force-coupling element dragging TM1 and TM2 away from the pore axis to create a large iris-like expansion of the pore to a diameter of ~30 Å, consistent with MscL's large unitary conductance (3 nS) and ability to conduct a variety of both ions and solutes across the membrane.

The large opening of MscL is significant because it accounts for two notable features in MscL's tensile response (Fig. 9.5a). First, MscL exhibits a high mechanosensitivity in that it fully transitions from fully closed to fully open conformations over a relatively small ~2 mN/m change in tension leading to a steep tension–response curve. In a simple two state models, the probability of MscL existing in closed versus open states depends on the free energy difference between the two conformations, $\Delta G = \Delta G_O - \gamma \Delta A$, where ΔG_O is the energy difference between closed and open states in the absence of membrane tension, γ is the membrane tension and ΔA is the change in cross-sectional area of the channel upon opening (Liang and Howard, 2018; Douguet and Honoré, 2019). Importantly, the energy that drives channel activation ($-\gamma \Delta A$) is proportional to the change in cross-sectional area expansion, ΔA, which for MscL is relatively

large (ΔA=~20 nm^2). It is this large change in cross-sectional area that confers upon MscL the ability to transition from closed to open states over a relatively small tensile range.

The second notable feature of MscL's tensile response is that the threshold for activation (~10mN/M) is close to the lytic tension of many membranes, higher than that of other mechanosensitive channels. The high activation threshold depends on both the protein and lipid deformations that occur upon channel gating (ΔG_O). The opening of MscL results from a large conformational change that leads to a large lipid deformation as the surrounding lipids adapt to the increase in channel circumference, the thinning of the open structure (which leads to hydrophobic mismatch between MscL and adjacent lipids) and the change from a more cylindrical to a more wedge-like shape. The high tensions required for MscL opening likely reflect the need to overcome both the large conformational change and the resulting bilayer deformation penalty that occur upon channel gating.

While these observations explain the tensile response of MscL, they raise questions regarding the mechanisms underlying mechanosensing in other channels that maintain ion-specific selectivity in the open state and have lower thresholds for activation. For example, Piezo1 undergoes a relatively steep tensile response suggestive of a large change in cross-sectional area upon gating, but in the open state exhibits a small unitary conductance (35 pS) with cation-selectivity (Fig. 9.5). Piezo 1 is also activated at very low thresholds (<1mN/m). On the other hand, TRAAK and TREK1/2 exhibit weak mechanosensitivities requiring a broad change in membrane tension to gate open, also with small open state unitary conductances (~100 pS) and cation-selectivity. In fact, patch clamp recordings show that TRAAK has a low, but measurable open probability at near-zero tensions, begins to activate over the 0.5 – 4 mN/m

range, and continues to transition to the open state over the entire tensile range until the patched membranes are lysed (Brohawn, 2015; Douguet and Honoré, 2019).

Piezo1 has overcome the apparently contradictory properties of high mechanosensitivity (steep tension-response curve) and low unitary channel conductance in the open state (small ΔA of the permeation pathway) through its large trimeric structure (PDB:6B3R, 3.7Å resolution) (Fig. 9.4b) (Guo and MacKinnon, 2017; Saotome et al., 2018; Zhao et al., 2018). Each subunit of the trimer consists of a large, curved and flexible blade, a domain-swapped central pore module and a long intracellular helical beam that extends out from the trimer center (near the central channel pore) to support the blade structure. Each blade acts as a mechanosensor and is formed from nine repeats of four TM helices that connect via a cuff to two pore-lining helices, with the inner helix lining the ion pore. Notably, the blades of the Piezo1 trimer curve up to form a dome shape that, when reconstituted into lipid vesicles, locally deforms the lipid bilayer into a similar dome shape (Guo and MacKinnon, 2017). Mechanical calculations predict that the dome shape extends well beyond the structure of Peizo1 leading to a large domed membrane footprint, with this malleable membrane footprint playing a key role in tension sensing (Haselwandter and Mackinnon, 2018). It is hypothesized that membrane tension translates through this membrane footprint leading to a flattening of the Piezo1 dome, primarily through movement of the large mechanosensitive blades. This flattening could increase the cross-sectional area (ΔA) of the entire trimer by up to ~120 nm^2, with this increase in ΔA upon flattening conferring a high mechanosensitivity (i.e. a steep tension-response curve) while maintaining a small change in the cross-sectional area of the permeation pathway (Fig 9.5c). The mechanical calculations further show that the mechanical properties of the extended membrane footprint renders Piezo1 exquisitely sensitive to membrane tension in the low-tensile

regime – i.e. the energetics of the membrane footprint are most sensitive to small perturbations around zero tension. Although the proposed gating mechanism of Piezo1 represents a more complex adaptation of the slider-crank mechanism used to rationalize the gating of MscL, Piezo1 has evolved the complex domed structure to sense tension via small changes in membrane curvature in order to exhibit the large change in cross-sectional area required for exquisite mechanosensitivity, while at the same time maintaining ion selectivity.

TRAAK and TREK1/2 are members of the two pore domain potassium (K_{2P}) channel family (Brohawn, 2015). These channels consist of a dimer of identical subunits, each subunit having two in-tandem TM pore domains, each pore domain with two TM helices and an extracellular helical cap (Brohawn et al., 2012, 2014; Dong et al., 2015). Together, the dimer of dimers forms a classical tetrameric helical K^+ ion selectivity filter and central ion cavity lined by four TM helices. Notably, TRAAK (PDBs:4WFF and 4WFE, both 2.5Å resolution) and TREK2 (PDBs:4KDK and 4BW5, 3.6 Å and 3.2Å resolution, respectively) have been crystallized in conformations referred to as "up" and "down" (Fig. 9.5d). In the up and presumably open conformation, the pore lining helices TM2 and TM4 are kinked upwards at a glycine hinge towards the extracellular surface of the bilayer thus opening the central cavity of the channel to the cytoplasm with a clear ion conduction pathway. In the down, and presumably closed configuration, TM2/TM4 are rotated down towards the cytoplasm leading to channel block (see below). Significantly, relative to the changes in structure proposed for MscL and Piezo1 on channel gating, the identified conformational changes attributed to gating in TRAAK and TREK1/2 are subtle. Estimated changes in the cross-sectional areas of TRAAK, TREK1 and TREK2 are 4.7, 1.8 and 2.7 nm^2, respectively (Honoré et al., 2006; Brohawn et al., 2014; Dong et al., 2015), thus accounting for the relatively broad tensile response – i.e. the driving force for

gating, $\gamma\Delta A$, requires a large increase in tension,γ, to compensate for the low change in cross sectional area, ΔA. The relatively small change in overall structure, which likely includes a small lipid deformation penalty, likely also leads to a relatively small ΔG_O and thus a low threshold for activation.

Lipids may also play a direct role in TRAAK and TREK1/2 activation through binding to distinct sites. Both TREK1 and TRAAK are directly activated by PA (Chemin et al., 2005; Comoglio et al., 2014). TREK1 displays a biphasic concentration dependent response to PIP_2 (Woo et al., 2019). Despite the lack of observed binding sites for the latter two lipids in structures of TRAAK and TREK1, mutagenesis has identified cationic residues post TM4 that are critical for channel modulation by anionic lipids (Soussia et al., 2018).

Furthermore, the movement of TM2 and TM4 to the closed down configuration of TRAAK opens lateral fenestrations between the channel pore and the lipid bilayer. The electron density in these fenestrations was modeled as acyl chains that extend into the ion channel cavity to block ion conductance. While the biological relevance of these lipid projections is still debated, fenestrations with bound lipid have similarly been observed in other mechanosensitive ion channels, including MscL, Piezo 1 and MscS, as well as in voltage-gated sodium channels where the fenestrations are proposed drug binding sites (PDB:6MVY, 3.0Å resolution) (Payandeh et al., 2011; Gamal El-Din et al., 2018). In fact, recent cryo-EM structures of MscS in lipid bilayers resolved a number of new features, including bound lipids, and led to a re-evaluation of MscS's mechanism of lipid sensing (PDB:6PWP, 3.1Å resolution) (Rasmussen et al., 2019; Reddy et al., 2019). MscS is a homo-heptamer, with each subunit containing three TM helices, as well as cytoplasmic projections contributing to a large C-terminal water-filled sphere (Fig. 9.6). The new structures show that TM1 extends further into the bilayer than previously

thought, and ends with a kink that links to a ring structure imbedded parallel to the membrane surface at the bilayer-solvent interface, reminiscent of the N-terminal amphipathic helix "slider" in MscL. These new bilayer-imbedded structures suggest a 14 Å shift in the placement of MscS within the bilayer relative to previous models. As noted, the new structures also identified lipids that interact tightly with the TM helices of each subunit (hook lipids) near conformationally-active regions of the protein, as well as lipids lining the permeation pathway (pore lipids) that block ion permeation in the closed state. Significantly, it was hypothesized that the binding of the hook lipids is altered by membrane tension, with the displacement of lipids contributing to the mechanisms underlying channel gating. The possibility that membrane tension displaces bound lipids to facilitate gating clearly blurs the distinction between "molecular" and "physical" mechanisms underlying mechanosensation.

Figure 9.4 MS channels have evolved diverse structures to respond to membrane tension
(A) Top (coloured by subunit) and side (TM and extramembranous domains colored blue and red, respectively) views of MscL (PDB: 2OAR), MscS (PDB: 6PWP), TRAAK2 (PDB: 4WFF), and AtOSCA1.2 (PDB: 6JIZ). (B) Top and side views of Piezo2 (PDB: 6KG7) coloured by subunit (left) and a side view of NOMPC (PDB: 5VKQ) coloured by domain (right). The Piezo 2 structures are scaled to 75% of the remaining structures the figure.

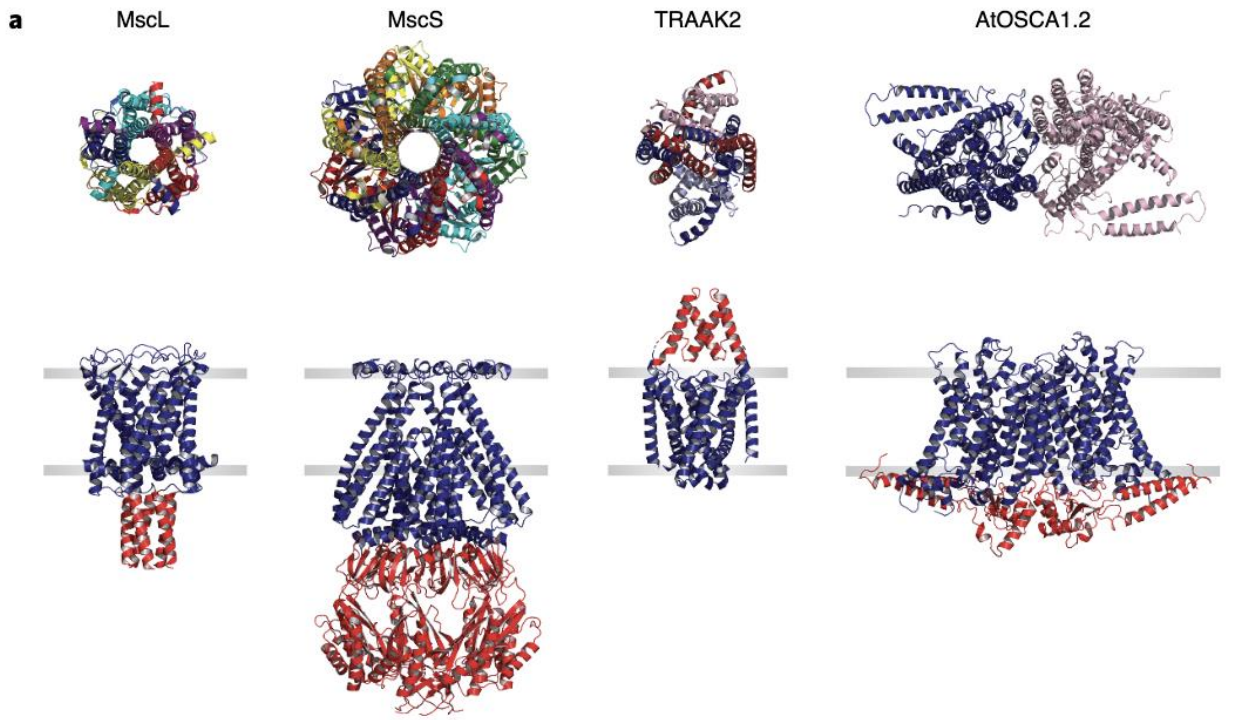
a
MscL
MscS
TRAAK2
AtOSCA1.2

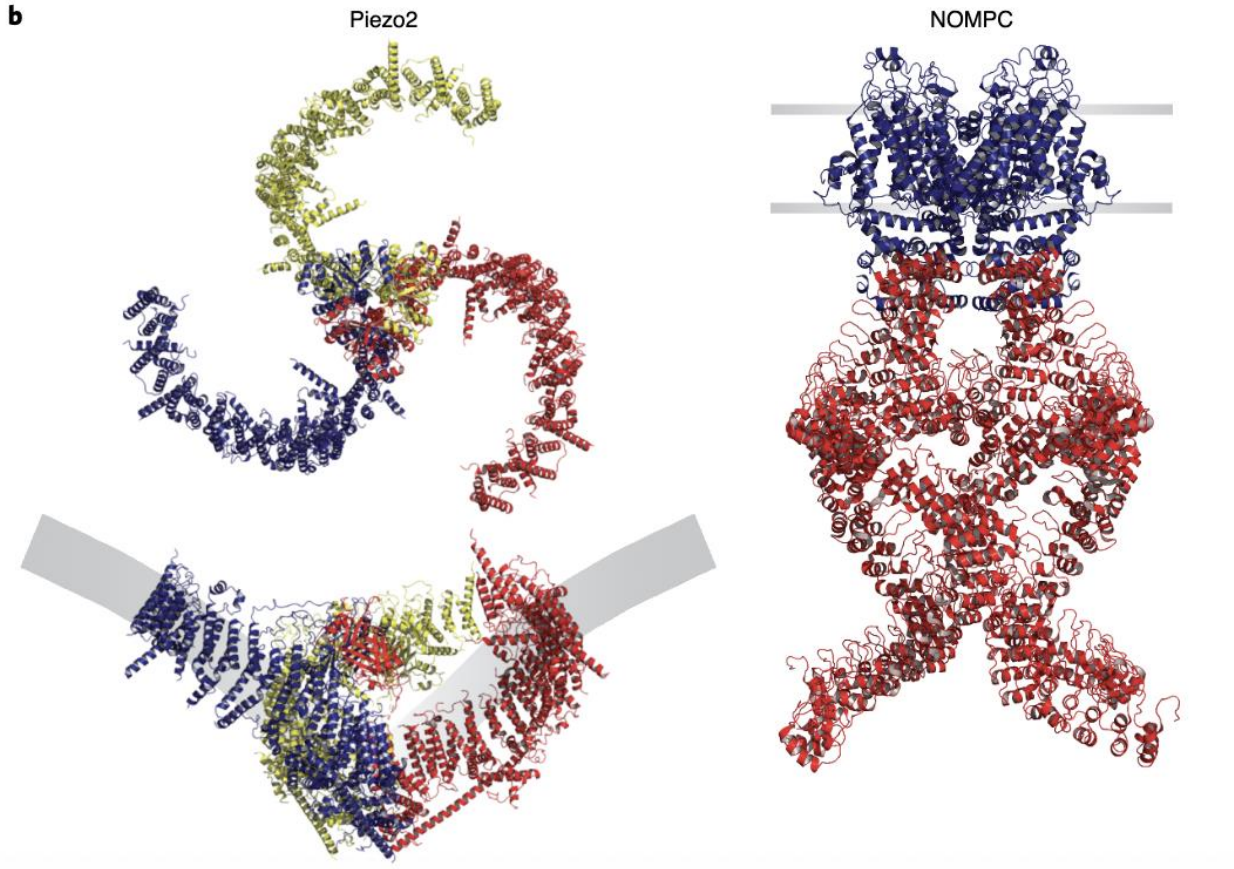
b
Piezo2
NOMPC

Figure 9.5 Mechanisms for sensing membrane tension

(A) Tensile response curves of MscL, Piezo1 and TRAAK modeled on Figure 2A from (Douguet and Honoré, 2019). (B) Schematic diagram showing the structural transition of MscL from closed to open conformations with increased tension leading to a thinning of the membrane, with the open structure determined using biophysical data (Perozo et al., 2002). Figure modeled on the structures presented in Fig. 4a of (Cox et al., 2018). (C) Schematic showing how the piezo channel is thought to respond to changes in membrane curvature leading to a large change in the surface area (ΔA) of the channel, while maintaining ion selectivity. (D) Side (top) and top (bottom) views of TRAAK2 in "down" closed (PDB:4WFF) and "up" open (PDB: 4WFE) conformations.

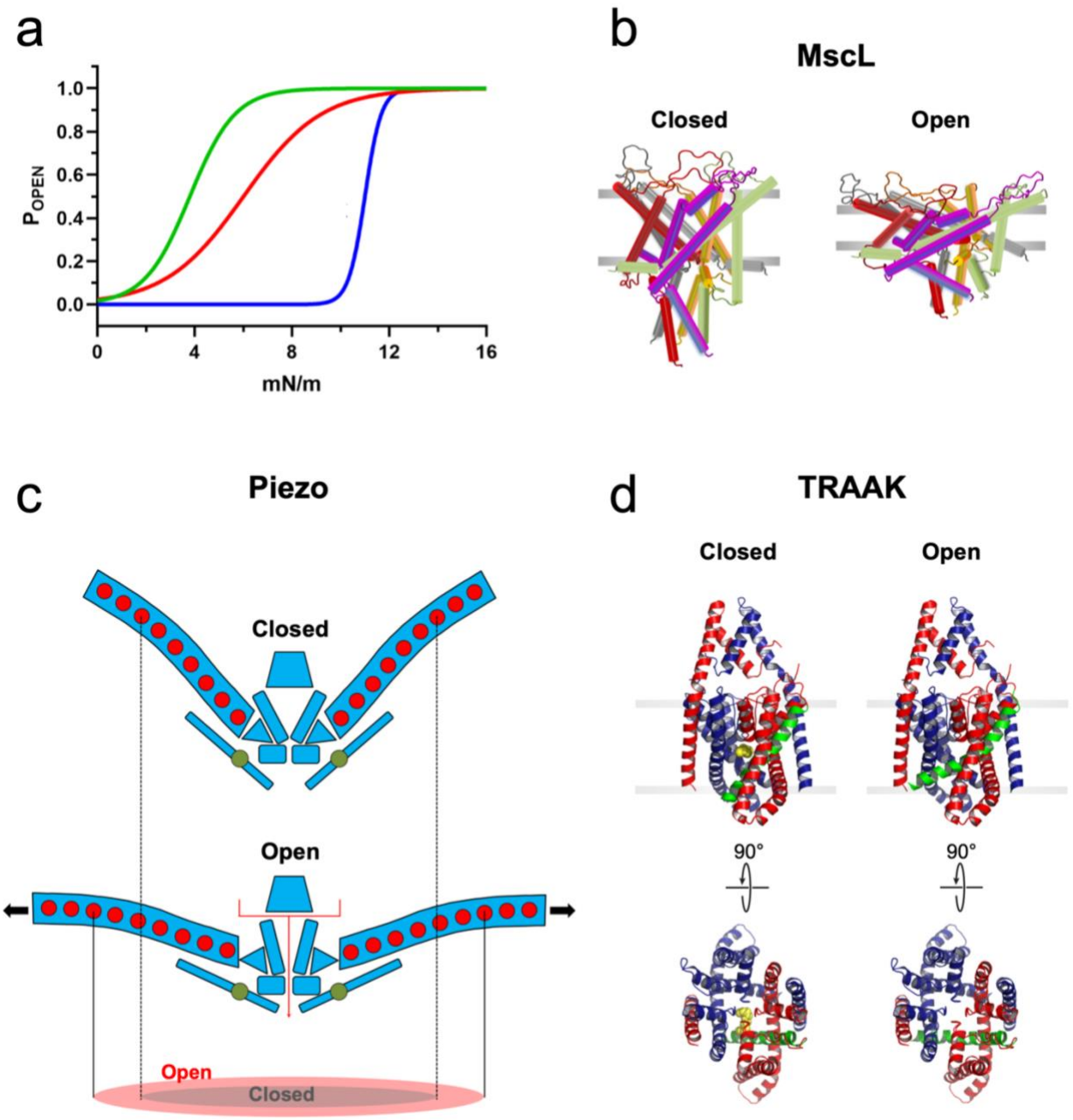
a
1.0
0.8
0.6
0.4
0.2
0.0
POPEN
0
4
8
12
16
mN/m
b
MscL
Closed
Open
c
Piezo
Closed
Open
Open
Closed
d
TRAAK
Closed
Open
90°
90°

Figure 9.6 New insight into MscS derived from structures solved in lipid membranes. (A) Side views of a lipid bilayer (PDB: 6PWN) and detergent-solubilized (right; PDB: 2OAU) structures of MscS. Regions of MscS that are disordered in the crystal structure are clearly seen in the lipid bilayer structure, thus establishing a new location for the lipid bilayer. (B) Side (left) and top (right) views of the TMD of MscS showing the bound hook and pore lipids as yellow spheres. Note that the head groups of each hook lipid extends through fenestrations into the permeation pathway, which is lined by pore lipids. (C) Zoomed in view of a hook lipid (primarily thick yellow sticks) bound at the interface between two subunits. The lipid appears to "hook" the TM2-TM3 linker with its head group extending into the permeation path. The pore lipids shown as thick yellow sticks establish the permeation path through the channel.

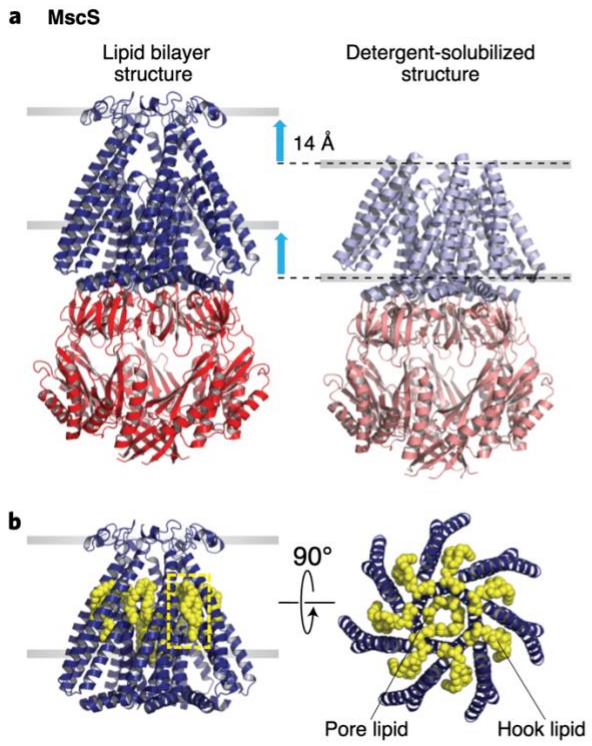
a MscS
Lipid bilayer structure
Detergent-solubilized structure
14 Å
b
90°
Pore lipid
Hook lipid

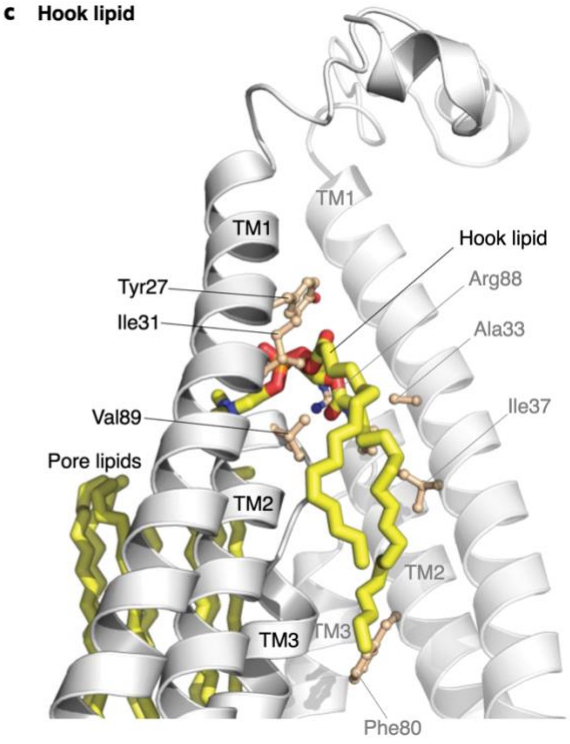
c Hook lipid
TM1
TM1
Hook lipid
Tyr27
Arg88
Ile31
Ala33
Ile37
Val89
Pore lipids
TM2
TM2
TM3
TM3
Phe80

9.1.7 Lipid-modulated pLGICs

pLGICs respond to the binding of a neurotransmitter by transiently opening an ion-selective channel across the membrane to elicit a post-synaptic response. Although different pLGICs respond to different neurotransmitters (acetylcholine, serotonin, glycine or GABA), all pLGICs share a common architecture with five identical or homologous subunits arranged either symmetrically (homomeric) or pseudo-symmetrically (heteromeric) around a central ion channel pore (Cecchini and Changeux, 2015) (Fig. 9.7a). Each subunit consists of an N-terminal extracellular domain, a TM domain and a cytoplasmic domain, although the latter is absent in prokaryotic homologs and some constructs used for crystallization. Each TM domain contains four helices, with TM2 lining the channel pore, TM1 and TM3 shielding TM2 from the surrounding lipids, and TM4 located at the periphery where it interacts extensively with lipids.

Although pLGICs are not gated directly and do not require specific lipids for ligand-induced gating, as is the case with the other ion channel families discussed in this review, the activity of the prototypic pLGIC, the nicotinic acetylcholine receptor (nAChR) from the electric fish, *Torpedo*, is exquisitely sensitive to lipids (Baenziger et al., 2015; Barrantes, 2015). When reconstituted into phosphatidylcholine (PC) membranes containing both cholesterol and anionic lipids, the *Torpedo* nAChR exhibits a robust agonist-induced response. In the absence of cholesterol and anionic lipids, the nAChR adopts an *uncoupled* conformation that binds agonist, but does not usually undergo agonist-induced conformational transitions (daCosta and Baenziger, 2009). Lipids modulate nAChR function via both conformational selection and kinetic mechanisms – i.e. they stabilize different proportions of activatable versus non-activatable states and facilitate the agonist-induced transitions between them (Baenziger et al., 2000; daCosta et al., 2009, 2013; Hénault et al., 2019; Tong et al., 2019) – and do so through

both molecular and physical mechanisms (daCosta et al., 2013; Hénault et al., 2019). Notably, recent pLGIC structures reveal electron density attributed to lipids in one or more of three broadly overlapping sites at the interfaces between TM4 and the adjacent TM1 and TM3 helices (Fig. 9.7a) (Thompson and Baenziger, 2020b). For the most part, the identities of the bound lipids remain speculative suggesting non-specific binding. In contrast, a recent structure of the $\alpha1\beta2\gamma2$ $GABA_A$ receptor unambiguously identified PIP_2 bound to each of the two $\alpha1$ subunits at the TM4-TM3 interface where the 4' and 5' phosphates are coordinated by Lys312 and Arg313 at the base of M3 and the backbone carbonyl of Ser388 from M4, while the 1' phosphate and inositol ring are coordinated by Arg249 from the M1-M2 loop and Ser390 and Lys391 from M4 (PDB:6I53, 3.2Å resolution). These specific interactions mimic those observed in the PIP_2 binding sites of VGL channels and thus suggest a regulatory role for PIP_2 (Fig. 9.7b) (Laverty et al., 2019). The functional effects of PIP_2 binding to the $GABA_A$ receptor, however, remain to be fully characterized.

While the mechanisms by which lipids influence the activities of pLGICs are not as well understood as in other channels, detailed insight has come from recent structures of the *Erwinia chrysanthemi* ligand-gated ion channel, ELIC. A relatively high resolution crystal structure of ELIC revealed electron density attributable to phosphatidylethanolamine (PE) (PG binds to the same site) bound in the cytoplasmic leaflet at the TM4-TM1 interface, with the lipid binding site framed by a proline-induced kink in TM4 (PDB:6HJX, 2.5Å resolution) (Hénault et al., 2019; Tong et al., 2019). Other ELIC structures show that TM4 is dynamic and adopts both kinked and unkinked conformations (Hénault et al., 2019). Significantly, PE/PG binding not only stabilizes exclusively the kinked conformation, but also leads to a *dramatic* slowing in the rates of ELIC desensitization (Fig. 9.7c). Conversely, mutations that weaken PE/PG binding and/or increase

TM4 dynamics lead to an increase in ELIC desensitization rates (Hénault et al., 2019). In the absence of bound lipid, increased TM4 conformational dynamics promotes an increase in the mobility at the cytoplasmic ends of all TM helices, including regions thought to form the desensitization gate. This increased mobility may facilitate the closing of the desensitization gate to enhance the rates of desensitization (Hénault et al., 2019).

Note that the bound PE was detected in only *one* of five subunits. In addition, bound lipids have not been detected in close to 30 other lower resolution structures. These observations suggest that crystal/cryo-EM structures may not always capture functionally critical lipid binding sites. Note also that cholesterol has been observed bound to the same site as PE in other pLGICs (Walsh et al., 2018; Gharpure et al., 2019). Cholesterol slows the rates of ELIC desensitization (Hénault et al., 2019). Cholesterol may influence desensitization through a similar mechanism as PE/PG, but its functional impact may be muted due to reduced affinity leading to reduced occupancy. Furthermore, other than PIP_2 binding to the $\alpha1\beta2\gamma2$ $GABA_A$ receptor, both lipid binding to pLGICs and the functional effects of lipids on the nAChR function to be relatively non-specific (Fig. 9.7b). It is possible that different lipids bind to the same sites on many pLGICs, but with distinct or muted functional consequences.

Finally, a recent cryo-EM structure of ELIC reconstituted into PC nanodiscs may provide insight into the uncoupled conformation adopted by the nAChR in similar PC membranes (PDB:6V03, 3.3Å resolution). Detergent-solubilized and PC membrane-reconstituted ELIC also adopts a conformation where agonist-binding does not lead to channel gating (Carswell et al., 2015a; Kumar et al., 2020b). The structure of ELIC in PC nanodisc shows that ELIC binds agonist and that the extracellular agonist-binding domain undergoes an agonist-induced conformational transition (Kumar et al., 2020b).

The structural changes in the extracellular domain, however, are not relayed across the coupling interface to the TM domain. These and other studies suggest that lipids alter TM helix-helix packing in a manner that facilitates interactions between the TM domain and the extracellular domain to promote agonist-induced conformational transitions (daCosta and Baenziger, 2009). Lipids may thus promote inter-domain coupling, as is observed in lipid-gated Kir channels and lipid-dependent VGL channels, although in pLGICs the enhanced inter-domain interactions likely occur via lipid binding to allosteric sites not located at the inter-domain interface. Inter-domain coupling may also be influenced by changes in bilayer physical properties (daCosta et al., 2013).

Figure 9.7 Lipid modulation of pLGICs

(A) A side view of the *Torpedo* nAChR (PDB: 6UWZ) is shown on the left coloured by domain, extracellular (ECD, red), TM (TMD, blue) and intracellular (ICD, green). A key residue in the agonist site (αTrp149) and residues that form the channel gate (Leu9' and Val13') are magenta and tan spheres, respectively. Top views of the ECD and TMD are shown on the right colored according to subunit. (B) Side views of lipid bound structures of GLIC (left; PDB: 3EAM), ELIC (center; PDB:6HJX), and the α1β2γ2 $GABA_AR$ (right; PDB: 6I53) with lipids shown as predominantly yellow spheres. Most bound lipids observed in pLGIC structures are at one of the three lipid sites observed in GLIC, which are located at the interfaces between either TM4 and TM1 or TM4 and TM3. Zoomed in views of PE binding to ELIC and PIP_2 binding to the α1β2γ2 $GABA_AR$. Note that the bound PIP_2 in $GABA_AR$ is coordinated by positively charged side residues, as is the case with PIP_2 binding to Kir and Kv channels. In contrast, there is a lack of headgroup specificity in PE binding to ELIC, as is the case with most of the observed lipids bound to pLGICs. (C) The TMDs of three of five subunits in ELIC are shown with the fourth TM helix of one subunit, TM4, highlighted in red. In the absence of bound lipid, some ELIC structures show that TM4 adopts either straight (PDB: 6HK0), kinked (PDB: 6HJX) or both conformations suggesting that TM4 is conformationally dynamic(Hénault et al., 2019). A dynamic TM4 leads promotes peptide backbone dynamics near the location of the desensitization gate (*) leading to rapid desensitization. PE/PG binding stabilizes TM4 in the kinked conformation, thus reducing peptide backbone motions and dramatically slowing desensitization rates.

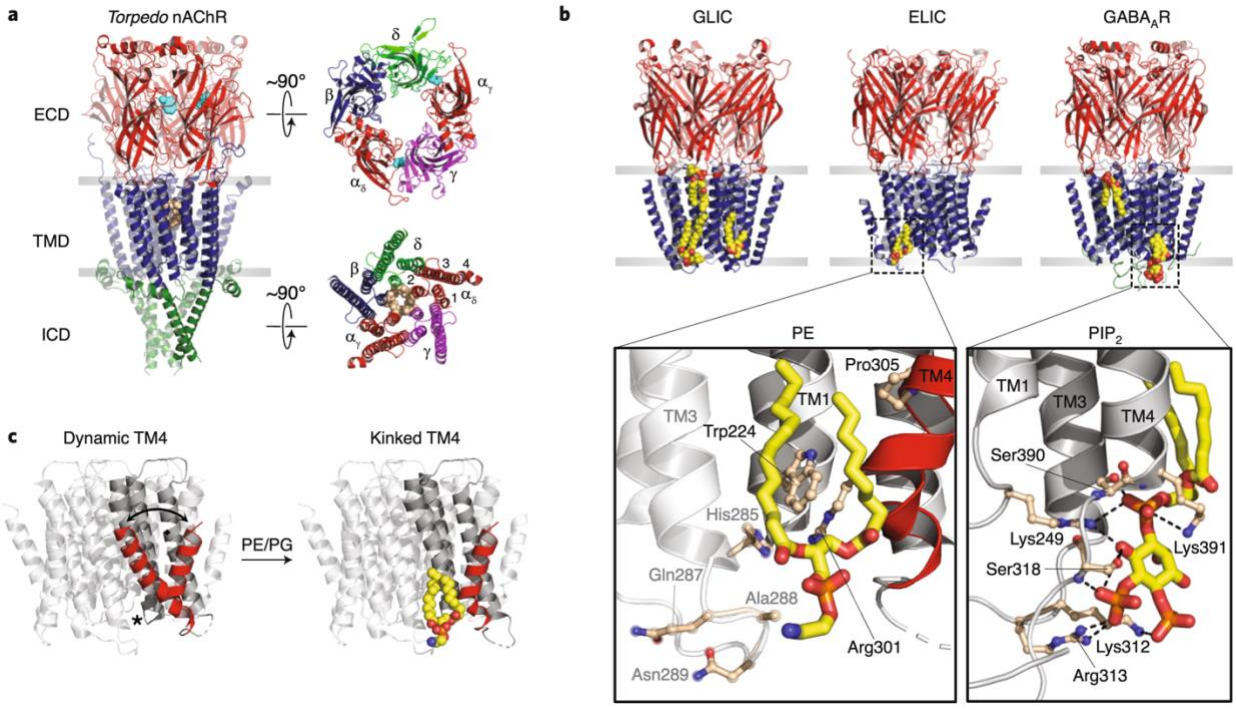
a
Torpedo nAChR
ECD
TMD
ICD
~90°
~90°
δ
β
α
γ
b
GLIC
ELIC
GABA$_A$R
PE
PIP$_2$
Pro305
TM4
TM1
TM3
Trp224
His285
Gln287
Ala288
Asn289
Arg301
Ser390
Lys249
Ser318
Lys391
Lys312
Arg313
c
Dynamic TM4
Kinked TM4
PE/PG

9.1.8 Conclusions

Ion channels have evolved complex structures that lead to diverse mechanisms by which they respond to the lipids in their surrounding membranes. These responses range from direct gating to lipid-dependent gating and the allosteric modulation of gating. These responses occur through both molecular (lipid binding) and/or physical (bulk membrane) mechanisms. While lipids likely influence the activities of every ion channel, and likely do so through complex mechanisms, recent structures show that each ion channel family has evolved distinct underlying mechanisms. Lipid binding to the interface between regulatory and TM pore domains is responsible for the gating of Kir channels and the lipid-dependence of VGL channels, although various members of both families have built on this theme and have evolved additional structural complexity that imparts additional gating requirements for other signaling molecules thus leading to complex mechanisms of regulation. In contrast, although MS channels likely use a variation of a similar slider-crank mechanism, with the help of bound lipids, to respond to membrane tension, the various MS channels have independently evolved incredibly diverse structures to implement this mechanism, which thus imparts on every MS channel unique mechanosensitive properties to suit its biological roles. Although the mechanisms by which lipids allosterically modulate the activities of pLGICs remain the least well-understood of the ion channels discussed here, pLGICs exhibit relatively conserved lipid binding sites and may thus share some common mechanisms for lipid-sensing.

Despite recent advances in x-ray crystallography and cryo-EM that have paved the way to new understanding of ion channel structures and thus lipid-ion channel interactions, much work remains to be performed to understand how lipids influence ion channel function. In many

cases, we still lack direct insight into the active conformations of lipid sensitive ion channels, thus precluding precise understandings of how lipids promote channel gating. Only recently has cryo-EM led to the solutions of ion channel structures imbedded in lipid bilayers, with some of these new structures leading to major revisions in our understanding of underlying mechanisms. Higher resolution structures are also increasingly detecting bound lipids that are not resolved in lower resolution structures, although in many cases the functional effects of these bound lipids remain to be fully characterized.

New technical advances over the coming years should fill in many of our gaps in knowledge of ion channel structure and should reveal how different lipids interact with ion channels to influence their function. In addition, advances in molecular dynamics simulations will also help us understand the dynamics of lipid binding and how such binding ultimately alters structure leading to altered function (Hedger and Sansom, 2016; Corradi et al., 2019; Enkavi et al., 2019; Manna et al., 2019; Duncan et al., 2020b). The application of these diverse biophysical methods should lead to a robust understanding of the molecular and physical mechanisms by which lipids both activate and modulate ion channel function to couple the electrical activities of cells to their metabolic states.

9.2 Review Article 2: Structural basis for the modulation of pentameric ligand-gated ion channel function by lipids.

Thompson, M.J., and Baenziger, J.E. (2020). Structural basis for the modulation of pentameric ligand-gated ion channel function by lipids. Biochim. Biophys. Acta - Biomembr. *1862*, 183304.
Adapted as a post-print from BBA Biomembranes, https://doi.org/10.1016/j.bbamem.2020.183304.

9.2.1 Preface

This was my first, first author publication. It was an invited review for BBA – Biomembranes who were looking for a review article for their special edition in honour of the late Dr. Michèle Auger, a friend and former colleague of Dr. Baenziger. We felt there was a need to revisit the wealth of biochemical data on pLGIC – lipid interactions in the context of new structural data which was beginning to emerge at an impressive rate. In fact, the structural data was moving so quickly I also contributed to another updated review two years later (Ananchenko et al., 2022). We used the combination of structural and functional data to proposed mechanisms for how lipids may modulate channel function, discussing both direct and indirect mechanisms. I once again contributed to the entire manuscript and created all the figures, but because this was my first publication, it took me a long time to complete, and I relied heavily on Dr. Baenziger's edits. It was an incredible learning experience and helped me immensely with all my future publications.

9.2.2 Abstract

Pentameric ligand-gated ion channels (pLGICs) play a central role in synaptic communication and are implicated in a plethora of neurological disorders leading to human disease. Membrane lipids are known to modulate pLGIC function, but the mechanisms underlying their effects are poorly understood. Recent structures reveal sites for the binding of membrane lipids to pLGICs, thus providing a structural basis for interpreting functional data on pLGIC-lipid interactions. Here, we review the literature describing the known functional effects of membrane lipids on different members of the pLGIC superfamily and highlight pLGIC structures that exhibit bound lipids. We discuss new insight into the mechanisms of pLGIC-lipid interactions that has been derived from these recent structures.

9.2.3 Introduction

Rapid synaptic communication is essential for signalling in both the central and peripheral nervous systems. Pentameric ligand-gated ion channels (pLGICs) both mediate and modulate fast synaptic communication, making them vital for many neurological processes, including memory, learning and motor coordination. The important roles played by pLGICs in the nervous system also make them important targets for the treatment of a variety of neurological and neuromuscular disorders, such as Alzheimer's disease, Parkinson's disease, schizophrenia, hyperekplexia, epilepsy, neuropathic pain and congenital myasthenic syndrome (Lemoine et al., 2012; Dineley et al., 2015; Rodriguez Cruz et al., 2018).

pLGICs respond to the binding of neurotransmitters by transiently opening ion channels across pre-, post-, and non-synaptic membranes. Neurotransmitter binding stabilizes a conductive open state, with prolonged exposure favoring non-conductive desensitized conformations. The relative stabilities of these and other states, as well as the rates of inter-conversation between them, shape the temporal nature of the agonist-induced ion flux across the membrane, and thus ultimately the physiological response that results from neurotransmitter binding. The agonist-induced response is also influenced by endogenous molecules, such as lipids, neurosteroids and endocannabinoids, etc. Lipids and other endogenous lipophilic molecules likely play an important biological role in signalling through pLGICs.

The functional sensitivity of pLGICs to membrane lipids has been known since the earliest attempts to isolate and reconstitute the prototypic pLGIC, the *Torpedo* nicotinic acetylcholine receptor (nAChR), into defined lipid bilayers. These pioneering studies suggested that for the nAChR to retain agonist-induced allosteric transitions, the detergent-solubilized nAChR must be purified in the presence of lipids and reconstituted into a bilayer with a

particular lipid composition (Heidmann et al., 1980; Criado et al., 1982; Fong and McNamee, 1986). The effects of lipids on *Torpedo* nAChR function have since been characterized extensively, as summarized in several reviews (Baenziger et al., 2015, 2017; Barrantes, 2015). More recently, studies of protein-lipid interactions have been extended to other members of the pLGIC super-family, including the prokaryotic *Gleobacter violaceus* ligand-gated ion channel, GLIC, and *Erwinia chrysanthemi* ligand gated ion channel, ELIC. Numerous pLGIC structures have also revealed the presence of lipid binding sites, thus providing a structural context for interpreting functional data on pLGIC-lipid interactions.

In this review, we focus on the role of lipid binding in the function of pLGICs. We first summarize the basic pLGIC structural architecture. We review the literature describing how membrane lipids influence the activity of different members of the pLGIC superfamily. We then highlight pLGIC structures that reveal the presence of bound lipids, including where mechanistically relevant, bound lipophilic modulators, such as neurosteroids and endocannabinoids. Finally, we discuss the new insight into the mechanisms of pLGIC-lipid interactions that has been derived from these recent structures. This review provides a roadmap for developing a more comprehensive understanding of the mechanisms by which lipids/membranes modulate pLGIC function to influence synaptic communication.

Figure 9.8 Structure of the *Torpedo* nAChR

A) A side view of the nAChR structure (PDB: 2BG9) is shown on the left with the ECD in red, the TMD in blue, and the intracellular domain (ICD) in green. Residues within the agonist binding sites (αTrp149) and the channel gate (Leu9' and Val13') are shown as yellow spheres. Top down views of the ECD and TMD are shown on the right. The top right view of the ECD highlights the agonist binding sites at the interfaces between principal (α_γ,α_δ) and complimentary (γ, δ) subunits. B) A side view of a single α-subunit highlighting the interfacial loops that mediate communication between the ECD and TMD.

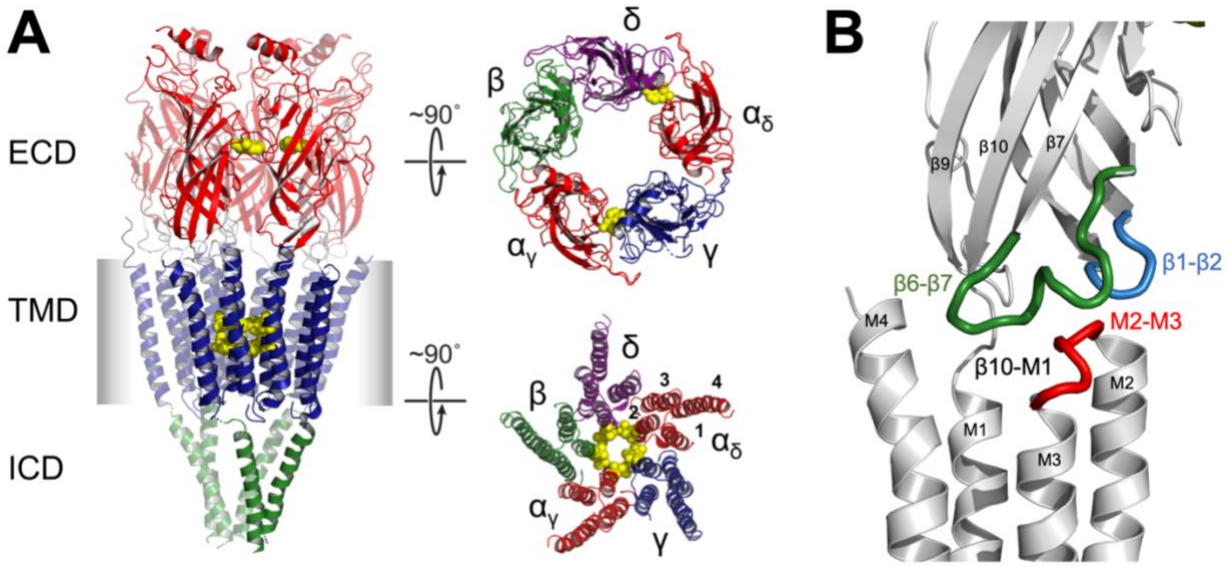
A
ECD
TMD
ICD
~90°
~90°
δ
β
αδ
αγ
γ
δ
β
3
4
2
1
αδ
αγ
γ
B
β9
β10
β7
β1-β2
β6-β7
M4
M2-M3
β10-M1
M2
M1
M3

9.2.4 pLGIC structure and diversity

The pLGIC super-family includes members from both eukaryotic and prokaryotic organisms. In humans, there are four families of pLGICs, including the excitatory cation-selective pLGICs that respond to the neurotransmitters acetylcholine (nicotinic acetylcholine receptor, nAChR) and serotonin (serotonin receptor, 5-HT_3R), and the inhibitory anion-selective pLGICs that respond to the neurotransmitters γ-aminobutyric acid (GABA receptor, $GABA_A$R) and glycine (glycine receptor, GlyR). Each of these four families includes a variety of both hetero- and homo-pentamers formed from combinations of different subunits - sixteen nAChR subunits (α1-α7, α9-α11, β1-β4, δ, γ, and ε), five 5-HT_3AR subunits (A, B, C, D, and E), nineteen $GABA_A$R subunits (α1-α6, β1-β3,γ1-γ3, ε, δ, π, θ, and ρ1-ρ3) and five GlyR subunits (α1-α4, and β). Each pLGIC formed from a different combination of subunits has unique physiological properties and is targeted to specific cell types and/or regions of the brain (Sparling and DiMauro, 2017).

Despite the subunit heterogeneity, all pLGICs share a common architecture with five subunits arranged either symmetrically (homomeric) or pseudo-symmetrically (heteromeric) around a central ion channel pore (Fig. 9.8). Each subunit adopts a common tertiary fold, with an N-terminal extracellular domain (ECD) that normally contributes to agonist binding, a transmembrane domain (TMD) that contributes to the ion-selective channel pore, and an intracellular domain (ICD) that contributes to interactions with the cytoskeleton, although the ICD is absent in prokaryotic pLGICs. Each ECD consists mainly of ten β-strands (β1-β10) that form two β-sheets folded together into a clamshell-like β-sandwich. Each TMD is formed from four transmembrane α-helices (M1 to M4), with M2 from each subunit lining the channel pore, M1 and M3 shielding M2 from the surrounding lipids, and M4 interacting extensively with the

lipid bilayer. Each ICD, located between M3 and M4, exhibits a disordered region typically followed by a long amphipathic α-helix, termed the MA α-helix. In some pLGICs, a short α-helix, referred to as the MX α-helix, is also located just after M3 where it is oriented parallel to the bilayer surface (see Fig. 9.10) (Hassaine et al., 2014).

Agonist sites in the ECD are formed from loops contributed by both the principal and complementary subunits (see Fig. 9.8a, top right panel). Neurotransmitter binding to these loops leads to concerted movements of the surrounding β-sheets, which are translated to the TMD in each subunit by the covalent link between the C-terminus of β10 in the ECD and the N-terminus of M1 in the TMD, as well as by non-covalent interactions between the β1-β2 and β6-β7 loops (in eukaryotes, the latter is referred to as the Cys-loop) of the ECD and the M2-M3 linker of the TMD (Fig. 9.8b) (Lee and Sine, 2005; Lee et al., 2008; Gupta et al., 2017). In the closed resting state, conserved hydrophobic residues midway along the M2 helices have been proposed to create an energetic barrier that prevents unsolvated ions from flowing into the cell (Unwin, 2005; Beckstein and Sansom, 2006), although cysteine accessibility experiments suggest the gate is closer to the intracellular end of the pore (Zhang and Karlin, 1998). Agonist binding ultimately leads to movement of the M2-M3 linker leading to a twisting and tilting of the M2 α-helices that widens and changes the chemical environment of the pore allowing the diffusion of hydrated ions down their electrochemical gradient into the cell (Unwin and Fujiyoshi, 2012; Du et al., 2015; Nemecz et al., 2016; Basak et al., 2018a; Polovinkin et al., 2018; Masiulis et al., 2019).

Prolonged agonist exposure leads to the formation of a desensitized state(s) that does not gate open in response to agonist binding, but that has a high affinity for agonist (Heidmann et al., 1978; Boyd and Cohen, 1980b). Desensitization is thought to arise from a constriction of the "desensitization gate" located near the intracellular end of the pore (Gielen and Corringer, 2018).

The rates of agonist-induced desensitization vary substantially from one pLGIC to another. In some pLGICs, loops at the interface between the ECD and TMD play a key role in determining the desensitization rates (Bouzat et al., 2008). A recent study also elucidated a role for the lipid exposed M4 α-helix in pLGIC desensitization (see below) (Hénault et al., 2019).

9.2.5 nAChRs

9.2.5.1 nAChR - lipid interactions

A wide range of biochemical and biophysical studies performed on the fetal muscle-type ($\alpha 1_2\beta 1\gamma\delta$) *Torpedo* nAChR affinity purified and reconstituted into defined lipid membranes show that the *Torpedo* nAChR exhibits an exquisite functional sensitivity to membrane lipids. Although similar membrane-reconstituted studies have not been performed for other nAChRs, it has been shown that methyl-β-cyclodextrin induced alterations in the lipid compositions of cells expressing mammalian muscle or neuronal nAChRs typically lead to a reduction in the whole-cell agonist-induced response, in some cases slowing desensitization (Santiago et al., 2001; Zhu et al., 2006; Borroni et al., 2007; Borroni and Barrantes, 2011; Colón-Sáez and Yakel, 2011; Almarza et al., 2014; Oyola-Cintrón et al., 2015; Báez-Pagán et al., 2016). Lowered cholesterol levels also lead to altered trafficking to and/or a redistribution of existing nAChRs in the cell membrane (Zhu et al., 2006; Borroni et al., 2007; Borroni and Barrantes, 2011; Almarza et al., 2014). In addition, mutations along the lipid-facing surface of M4 in the muscle nAChR, which alter M4-lipid interactions, modify channel function (Li et al., 1992; Lee et al., 1994; Lasalde et al., 1996; Guzmán et al., 2006), including one that leads to a congenital myasthenic syndrome (Shen et al., 2006). Collectively, these findings suggest that all nAChRs exhibit a functional sensitivity to lipids, and that this functional sensitivity plays a role in human biology.

9.2.5.2 The *Torpedo* nAChR

Studies performed in the early 1980s showed that the *Torpedo* nAChR reconstituted into vesicles composed of phosphatidylcholine (PC), cholesterol and anionic lipids at a molar ratio of

3:1:1 exhibits a robust agonist-induced cation influx, while the *Torpedo* nAChR reconstituted into vesicles lacking both cholesterol and anionic lipids does not (Fong and McNamee, 1986). Interestingly, membranes composed of 3:1 molar ratios of either PC:cholesterol or PC:anionic lipids were also deemed to lack an agonist-induced response. This led to the hypothesis that the occupancy of both cholesterol and anionic lipid binding sites is *required* for *Torpedo* nAChR channel activity, a view still common in the current literature (see (Baenziger et al., 2017) for a discussion of the nAChR's functional requirement for cholesterol).

These vesicle influx assays, however, were typically performed at a single PC to "lipid of interest" ratio and could not accurately quantify the relative magnitudes of the agonist-induced cation influx due to large lipid composition-dependent variations in the relative sizes of the reconstituted membranes. As a result, a cation influx threshold was arbitrarily established to define each membrane as either supporting channel function or not. More robust functional assays subsequently showed that increasing levels of *either* cholesterol or the anionic lipid, phosphatidic acid (PA), in a PC membrane led to an increasing proportion of agonist-responsive *Torpedo* nAChRs (Baenziger et al., 2000; Hamouda et al., 2006a). A variety of cholesterol analogs and other neutral lipids, including epicholesterol, cholestanol, coprostanol vitamin D_3 (cholecalciferol), α-tocopherol, androstanol, squalene, and diacylglycerol, were all found to substitute for cholesterol in supporting *Torpedo* nAChR function, (Sunshine and McNamee, 1992; Addona et al., 2003; Labriola et al., 2010). Although these later studies further confirmed that membranes composed of PC, PA and cholesterol are optimal for supporting nAChR function, they suggest that if allosteric sites for either lipid exist, then the lipid specificities of these sites is low and their occupancies not absolutely required.

Finally, while the addition of a variety of anionic lipids to membranes composed of both PC and cholesterol supports a robust agonist-induced response, only PA stabilizes a large proportion of agonist-responsive *Torpedo* nAChRs in PC membranes lacking cholesterol (daCosta et al., 2002, 2004, 2009). The unique ability of PA to stabilize a functional *Torpedo* nAChR may be due to its small headgroup, which gives the lipid a conical shape. The incorporation of this conical lipid into a PC bilayer leads to an ordering of the surrounding lipids, which may mimic some of the ordering effects observed when cholesterol is incorporated into a PC bilayer (daCosta et al., 2002). PA may be effective at stabilizing a functional *Torpedo* nAChR because it creates a bilayer with both the anionic charge and the bulk membrane physical properties required for optimal *Torpedo* nAChR function. The hypothesis that bulk membrane physical properties influence *Torpedo* nAChR function is further supported by the observation that membrane hydrophobic thickness influences *Torpedo* nAChR conformational transitions (see below) (daCosta et al., 2013).

9.2.5.3 Annular versus non-annular sites of lipid action

The intrinsic tryptophan fluorescence of the *Torpedo* nAChR is quenched to a greater extent by brominated cholesterol than by brominated PC. This and other observations were interpreted to suggest that cholesterol, and possibly other lipids, exhibit both annular and non-annular sites of lipid action (Fig. 9.9a) (Leibel et al., 1987; Jones and McNamee, 1988; Antollini and Barrantes, 1998; Fernández-Nievas et al., 2008). Annular sites are those located at the periphery of the TMD, while non-annular sites are those that exist between the transmembrane α-helices where they are shielded from the bulk membrane environment. Note that the term "annular" historically refers to a ring of motionally-restricted lipids that surrounds the nAChR at

the protein-lipid interface (Jost et al., 1973; Hesketh et al., 1976; Marsh and Barrantes, 1978; Narayanaswami and McNamee, 1993). At any given moment in time, lipids collide with and are bound to the nAChR surface, although bound annular lipids typically exchange rapidly with others in the bulk membrane environment (Marsh, 2010). Cholesterol and PA both show a preference over other lipids for the annulus of motionally restricted lipids surrounding the *Torpedo* nAChR (Marsh and Barrantes, 1978; Ellena et al., 1983). Here, we use the term annular to refer broadly to lipid binding sites located at the periphery of the TMD where they are in contact with the surrounding membrane environment.

Note that the M4 transmembrane α-helix in each subunit forms the predominant interface between the TMD and the surrounding lipids, and thus represent a main site for annular lipid binding. The location of M4 at the periphery of the TMD has led to the suggestion that it plays a central role in lipid-sensing (Barrantes, 2003; Antollini et al., 2005; Xu et al., 2005; Hénault et al., 2015b). Further supporting such a role, annular lipid binding sites have been detected in several pLGIC structures at the interfaces between M4 and the two adjacent TMD α-helices, M1 and M3 (see below). Also of significance, electrophysiology studies suggest that M4 moves during channel gating, which would thus provide the opportunity for lipids to interact differently with one conformation versus another to impact on channel function (Mitra et al., 2004). In this context, the entire lipid-exposed surface of the nAChR may serve as an annular "allosteric site" that is sensitive to both bound annular lipids and bulk membrane physical properties.

Note also that the 4 Å cryo-electron microscopy (cryo-EM) structure of the full length *Torpedo* nAChR exhibits "cavities" in the extracellular leaflet of the bilayer between transmembrane α-helices (Fig. 9.9b) (Unwin, 2005). The electron density in these cavities is similar to that of the surrounding lipid, consistent with the presence of non-annular bound lipids

(Brannigan et al., 2008). It has been proposed that cholesterol binds to three of these non-annular sites in each subunit, with two intra-subunit sites located at the M2-M1-M3 and the M1-M3-M4 interfaces and an inter-subunit site located between the M2/M3 helices of the principal subunit and the M2/M1 helices of the complimentary subunit (Brannigan et al., 2008). Further supporting a role for these non-annular sites in lipid action, the inhibitory neurosteroid, allopregnanolone, is thought to bind to the putative M2-M1-M3 cholesterol site (Yu et al., 2019), while the potentiating neurosteroid, β-estradiol, is thought to bind to the putative M2-M1-M3 cholesterol site on the neuronal α4β2 neuronal nAChR (Paradiso et al., 2001). General anesthetics and other synthetic lipophilic compounds also bind to these same non-annular sites on both *Torpedo* and neuronal nAChRs (Jayakar et al., 2013; Mowrey et al., 2013a; Wang et al., 2015). On the other hand, a photoactivatable cholesterol analog only labels lipid exposed surfaces of the *Torpedo* M1, M3, and M4 TMD α-helices (see below and Fig. 9.10) (Hamouda et al., 2006b). In addition, cholesteryl hemisuccinate covalently tethered to the glycerol backbone of PC is equally as effective as free cholesterol in supporting nAChR function in reconstituted PC/PA membranes (Addona et al., 1998). The presence of non-annular binding sites for cholesterol or other membrane lipids thus still requires experimental verification.

Finally, bioinformatics/computational studies highlight the existence of CRAC motifs (cholesterol recognition amino acid consensus: (L/V)-X_{1-5}-(Y)-X_{1-5}-(K/R)) within the nAChR, with this motif postulated to facilitate both cholesterol binding and the propensity of membrane proteins to incorporate into cholesterol-rich domains (Li and Papadopoulos, 1998). A CRAC motif is located just prior to the transmembrane α-helix, M1, in most subunits of the muscle type nAChR, proximal to the proposed M1-M2-M3 non-annular site noted above. An inverted or mirror image CRAC motif, termed CARC ((K/R)-X_{1-5}-(Y/F)-X_{1-5}-(L/V)), is also located on the

M4-facing surface of M1 adjacent to a proposed annular cholesterol site (Baier et al., 2011; Di Scala et al., 2017; Fantini et al., 2019), as well as on the γM4 α-helix adjacent to a site of ^{3}H-azicholesterol labeling (Hamouda et al., 2006b). Both docking studies and molecular dynamics simulations suggest that these CARC motifs, along with other regions of the TMD, interact with cholesterol (Baier et al., 2011). Furthermore, a peptide corresponding to the human nAChR γM4 interacts preferentially with cholesterol containing lipid membranes, with these interactions reduced or eliminated upon mutation of the central aromatic residue of the CARC motif to Ala (Fantini et al., 2016).

9.2.5.4 Bound lipids in nAChR structures.

Although bound lipids were not defined in the 2005 cryo-EM structure of the *Torpedo* nAChR, possibly due to the moderate 4 Å resolution of the structure, low-density patches of lipids attributed to cholesterol were visualized in the cryo-EM images in the region of the disulfide linkage between δ subunits of adjacent pentamers (Unwin, 2017). The functional significance of these cholesterol-rich patches located between disulfide linked dimers of pentamers remains unexplored.

Structures of the human $(\alpha4)_2(\beta2)_3$, $(\alpha4)_3(\beta2)_2$ and α3β4 nAChR have since been solved at resolutions ranging from 3.9 Å to 3.3 Å by x-ray crystallography and/or cryo-EM (Morales-Perez et al., 2016; Walsh et al., 2018; Gharpure et al., 2019), although structures of the α4β2 nAChR were solved using constructs where the majority of the ICD was truncated and structures of the α3β4 nAChR were solved using constructs where a fusion protein was inserted between the MX and MA helices thus replacing the disordered region of the ICD. The best diffracting crystals of the $(\alpha4)_2(\beta2)_3$ were formed in the presence of the water-soluble cholesterol analog,

cholesteryl hemisuccinate. Interestingly, the cryo-EM structures of the detergent solubilized and saposin nanodisc-reconstituted α4β2 and α3β4 nAChRs solved in the presence of cholesteryl hemisuccinate exhibit distinct regions of electron density in the cytoplasmic leaflet at the periphery of the TMD (Fig. 9.10). This electron density is located on both sides of M4 at the M4/M1 and M4/M3 interfaces of each subunit, with the binding sites adjacent to residues at positions analogous to those covalently labeled in the *Torpedo* nAChR by a photoactivatable cholesterol probe (Hamouda et al., 2006b). Significantly, these densities disappear from the α3β4 nAChR cryo-EM structures when cholesteryl hemisuccinate is not included during sample preparation.

The density attributed to cholesteryl hemisuccinate was modeled as cholesterol in both the α4β2 and α3β4 nAChR structures. In both cases, the cholesterol at the M4/M1 interface is located proximal to a CARC-like motif where the central Tyr/Phe is replaced by Trp, although the CARC-like motif plays little role in defining the cholesterol binding site (Figs. 9.10b and c). In fact, that majority of the interactions between the nAChR and cholesterol are mediated by aliphatic residues that form a relatively planar surface to which the rigid sterol ring binds, with aromatic residues wrapping around the sterol to form additional van der Waals contacts. A role for CRAC/CARC or CARC-like motifs in cholesterol binding to the nAChR or other pLGICs, thus remains to be validated.

It should also be noted that although cholesteryl hemisuccinate binding to the neuronal nAChRs provides the most compelling evidence to date for the existence of annular cholesterol binding sites on the nAChR, further experiments are required to test the functional significance of these cholesterol binding sites, particularly as two arginine residues located at the base of the binding sites (Figs. 9.10b and c) may facilitate cholesteryl hemisuccinate binding through

interactions with the carboxyl of the hemisuccinate group (the hemisuccinate group is not modeled in the structures). These putative electrostatic interactions may simply enhance cholesteryl hemisuccinate occupancy thus facilitating visualization of the electron density in the cryo-EM images. Alternatively, these electrostatic interactions may promote cholesteryl hemisuccinate binding to sites that are not physiologically important.

9.2.5.5 Mechanisms underlying nAChR-lipid interactions

Despite the wealth of functional data, and increasing structural data, our understanding of the mechanisms by which lipids modulate the activities of nAChRs remains incomplete. Although it is clear that both cholesterol (or more generally neutral lipids) and anionic lipids are required in a membrane for *optimal Torpedo* nAChR activity, it is still not clear whether either type of lipid influences function by binding to an allosteric site(s), by altering bulk membrane physical properties, or by a combination of these and/or other mechanisms. In the case of cholesterol, there is evidence supporting both specific binding sites and bulk membrane effects, but there is no definitive proof for either hypothesis – note that the two hypotheses are not mutually exclusive (see below for the $GABA_AR$). In the case of anionic lipids, there is no evidence supporting or refuting the existence of anionic lipid binding sites. An alternative is that the negative head group helps create a net negative electrostatic potential surrounding the nAChR at the membrane surface that impacts channel function through complex mechanisms (Sturgeon and Baenziger, 2010).

A consistent theme that has emerged from studies of the *Torpedo* nAChR in reconstituted membranes is that lipids modulate the agonist-induced cation flux primarily via a conformational selection mechanism. In other words, lipids and/or membranes influence function via a

mechanism similar to that used by ligands to alter channel function: ligands bind with higher affinity to one conformation versus another and use this extra binding energy to stabilize the high affinity state (Changeux, 2013). Similarly, lipids and/or membranes interact preferentially (either by binding with higher affinity to or via a bulk membrane interactions) with different conformations to stabilize different proportions of activatable versus non-activatable conformations (Baenziger et al., 2000). Although conformational selection was originally interpreted in terms of activatable resting versus non-activatable desensitized conformations (McCarthy and Moore, 1992; Ryan et al., 1996; Hamouda et al., 2006a), the *Torpedo* nAChR adopts a lipid-dependent uncoupled conformation that has a resting state-like affinity for agonist, but does not usually undergo agonist-induced transitions to "coupled" (resting, open or desensitized) conformations (daCosta and Baenziger, 2009; Sun et al., 2017). In reconstituted membranes, different lipids stabilize different proportions of resting, desensitized, uncoupled, and possibly other nAChR conformations (daCosta et al., 2009). In addition, although the *Torpedo* nAChR in PC bilayers with either 16 and/or 18 carbon acyl chains is locked in the uncoupled state, the nAChR in thicker PC membranes with 22 carbon acyl chains transitions from uncoupled to coupled conformations on the minutes to hours timescale (daCosta et al., 2013). The latter observation suggests that membranes/lipids interact with the transition states that occur between conformations to influence the rates of conformational transitions (i.e. via a "kinetic" mechanism). Lipids can thus influence function by both conformational selection and kinetic mechanisms (Fig. 9.11).

How precisely lipids or membrane physical properties interact with the TMD to preferentially stabilize one conformation over another, however, remains unclear. Lipids could compete directly with other lipophilic allosteric modulators for non-annular sites. Although no

high-resolution structures of nAChRs in active conformations are currently available, structures of GLIC and the 5-HT_{3A}R show the non-annular intrasubunit cavities expand upon activation suggesting the affinity of lipids or allosteric modulators for such sites could be state dependent, thus providing a mechanism for conformational selection (Velisetty et al., 2012; Polovinkin et al., 2018). Annular lipid binding or bulk membrane physical properties could also influence how the lipid exposed M4 α-helix packs against the adjacent TMD α-helices, M1 and M3. Altered M4 – M1/M3 interactions have long been thought to play a role in translating altered nAChR-lipid interactions into altered channel function, a hypothesis supported by the observation that mutations at the M4 - M1/M3 interface in the prokaryotic pLGIC, ELIC, alter its functional sensitivity to lipids (see below) (Barrantes, 2003; Carswell et al., 2015a, 2015b).

One potentially important experimental observation is that the lipid-dependent uncoupled *Torpedo* nAChR exhibits enhanced peptide backbone hydrogen exchange kinetics relative to the resting and desensitized conformations (Méthot et al., 1995; Baenziger et al., 1999; daCosta and Baenziger, 2009; Sun et al., 2017). The altered pattern of peptide hydrogen exchange suggests that a region(s) of the polypeptide backbone that is buried from the aqueous solvent in both the resting and desensitized states becomes exposed to solvent in the uncoupled state. Given the importance of the interface between the ECD and TMD in "coupling" agonist binding to channel gating, it was proposed that lipid dependent uncoupling results from weakened interactions and thus a physical separation between the ECD and TMD.

Consistent with the above hypothesis, molecular dynamics simulations suggest that the occupancy of cholesterol binding to both annular and non-annular sites stabilizes a structure of the TMD that supports contacts between the ECD and TMD that are likely essential for coupling of agonist binding to channel gating (Brannigan et al., 2008). It has also been proposed that

lipid-dependent alterations in the packing of M4 against M1/M3 ultimately modify interactions between the C terminus of M4 and the Cys-loop, a structure at the ECD - TMD interface that is important in channel gating (daCosta and Baenziger, 2009). Interactions between M4 and the Cys-loop (i.e. the β6 -β7 loop) are critical for folding and function in the prokaryotic pLGIC, GLIC (Hénault et al., 2015a). Such interactions may mediate neurosteroid-induced potentiation in the α4β2 nAChR. M4 – Cys-loop interactions are critical for maturation of the agonist site in an α7 nAChR - $5HT_3R$ chimera (Pons et al., 2004). On the other hand, M4 – Cys-loop interactions are not critical for function in the prokaryotic pLGIC, ELIC (see below) or in the α subunit of the adult muscle ($\alpha 1_2\beta 1\varepsilon\delta$) nAChR (Domville and Baenziger, 2018). A role for direct M4 – Cys-loop interactions in mediating lipid action may be present in some, but not other pLGICs.

Another possibility is that lipids modulate function by altering the energetic landscape of the nAChR in the resting, open and desensitized states, as illustrated by a recent mechanistic study focused on a congenital myasthenic syndrome causing mutation, αC418W. The αC418W mutation on the lipid facing surface of M4 in the human adult muscle ($\alpha 1_2\beta 1\varepsilon\delta$) nAChR potentiates channel function roughly 20-fold by altering M4 – lipid interactions. Mutant cycles suggest that the introduction of Trp418 leads to a reorientation of M4, which strengthens local interactions between Trp418/Thr422 on M4 and Ser226/Thr229 on M1 in the open state. By forming new interactions and by strengthening local interactions in the open state, the mutation energetically favors channel gating to potentiate function (Domville and Baenziger, 2018).

Finally, it is notable that lowered levels of cholesterol in cell membranes expressing mammalian nAChRs alters the rates of nAChR desensitization (Colón-Sáez and Yakel, 2011). Although the effects of lipids on nAChR desensitization rates have not been characterized in

detail, recent studies highlight a key role for lipids in shaping the desensitization kinetics of prokaryotic pLGICs (see below). Further studies are required to assess whether similar mechanisms contribute to nAChR - lipid interactions.

Figure 9.9 Annular and non-annular lipid binding sites on the *Torpedo* nAChR

A) Schematic top down view of the TMD showing putative cholesterol-binding sites at both annular (green circles, proposed in (Narayanaswami and McNamee, 1993)) and non-annular (yellow ovals, proposed in (Brannigan et al., 2008)) sites. Figure modified from (Brannigan et al., 2008). B) A slice through the TMD of the *Torpedo* nAChR structure (PDB:2BG9) shown from the extracellular side of the membrane. The slice highlights non-annular (i.e. inter-helical) cavities in the extracellular half of the TMD. The putative annular (green circles) and non-annular (yellow ovals) cholesterol sites from (A) are superimposed onto the *Torpedo* nAChR structure.

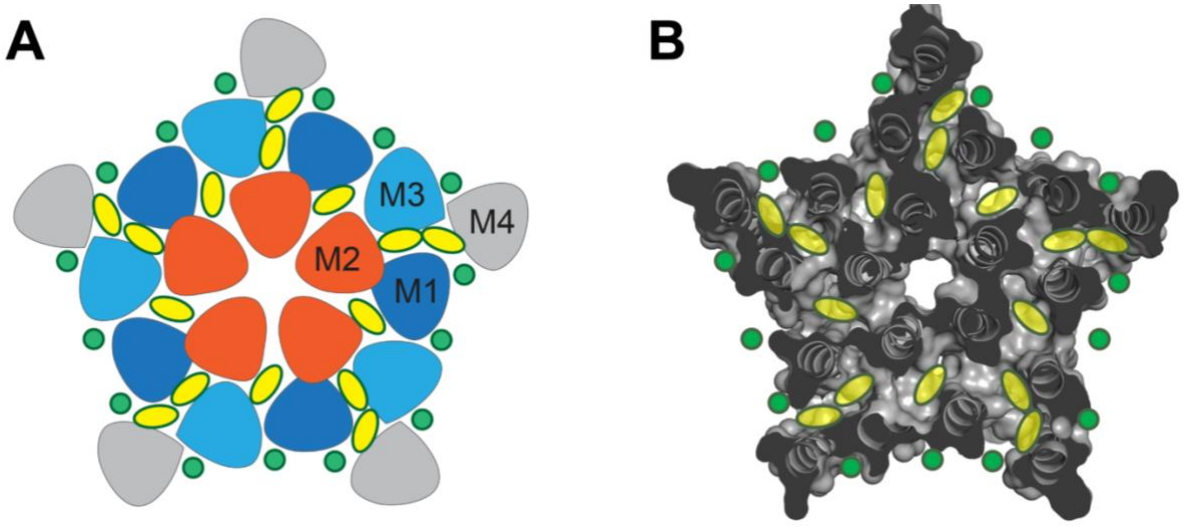
A
M3
M4
M2
M1
B

Figure 9.10 Cholesterol binding to the α3β4 and α4β2 nAChR

A) Structure of the α3β4 nAChR (PDB: 6PV7) with the principal (α3) and complimentary (β4) subunits colored salmon and light blue, respectively, and the modeled cholesterol shown as predominantly yellow spheres (carbon, yellow; oxygen, red; nitrogen, blue; and phosphorus/sulphur, orange). CARC and CARC-like motifs are shown as firebrick red spheres, although residues aligned with those labelled by a photoactivatable cholesterol analog in the *Torpedo* nAChR are shown as purple spheres. Zoomed in views of the cholesterol binding sites on the α3β4 and α4β2 (PDB:6CNK) nAChR structures are shown in B) and C), respectively. In both cases, a cartoon diagram on the left highlights residues contributing the binding pocket as sticks colored according to residue type: aromatic, yellow; aliphatic, tan; polar hydrogen bonding, green; and positively charged, blue, with the cholesterol as thicker yellow sticks. The surface contour of each cholesterol binding site is shown on the right.

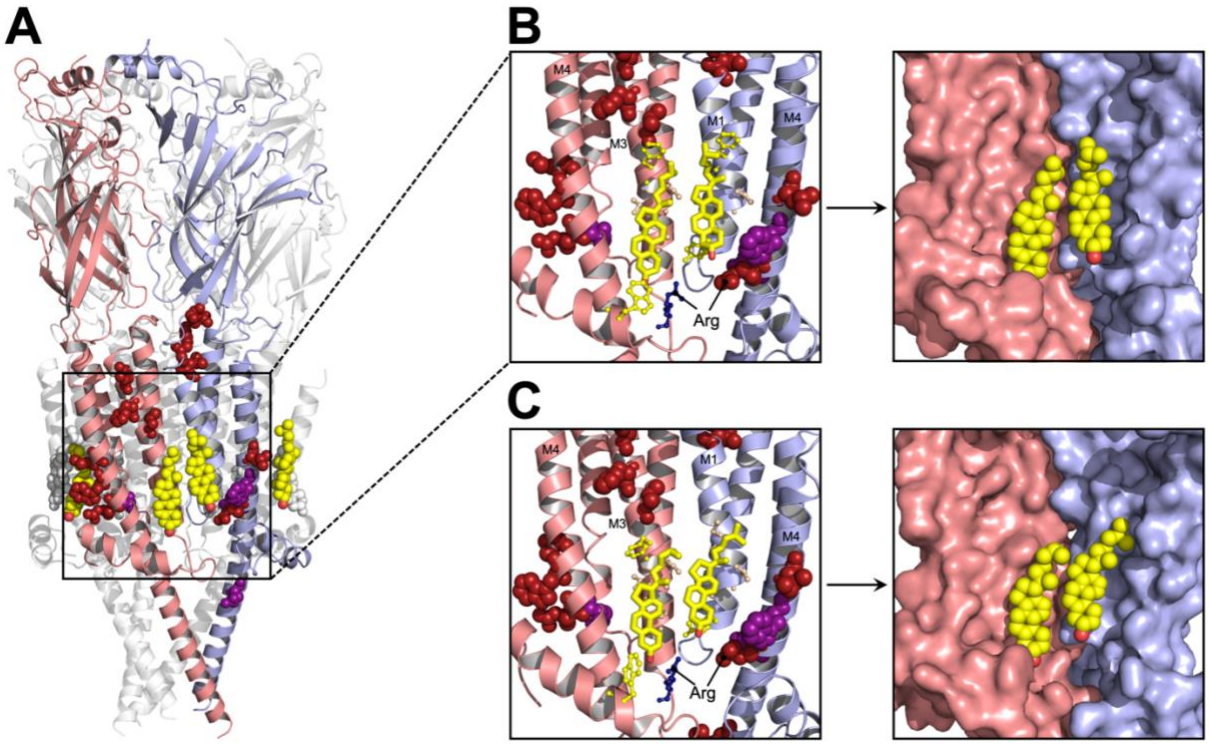
A
B
C
M4
M3
M1
M4
Arg
M4
M1
M3
M4
Arg

Figure 9.11 A thermodynamic framework for the mechanisms by which lipids modulate *Torpedo* nAChR function.

A) In the absence of agonist, the nAChR exists predominantly in a resting (R) conformation with a closed pore. Agonist leads to transient excursions into the open (O) state allowing cation flux across the membrane. Prolonged agonist exposure leads to the formation of a high agonist affinity desensitized (D) state with a closed pore. A lipid-dependent uncoupled (U) conformation exhibits R state like agonist binding affinity, but does not transition to O or D upon agonist binding. B) Lipids/membranes influence function by preferentially interacting with different states, lowering their relative energies to stabilize a greater proportion of activatable (R) versus non-activatable (D and U) states. Lipids/membranes can also interact preferentially with the transition states between conformations to influence the rates of conformational transitions. Structures of the *Torpedo* nAChR are available in both resting (PDB:2BG9) and open (PDB:4AQ9) conformations but only at a moderate to low resolution. Higher resolution structures of neuronal α4β2 (PDBs: 5KXI, 6CNK, 6CNJ) and α3β4 (6PV7, 6PV8) nAChRs have been solved each in a proposed desensitized conformation.

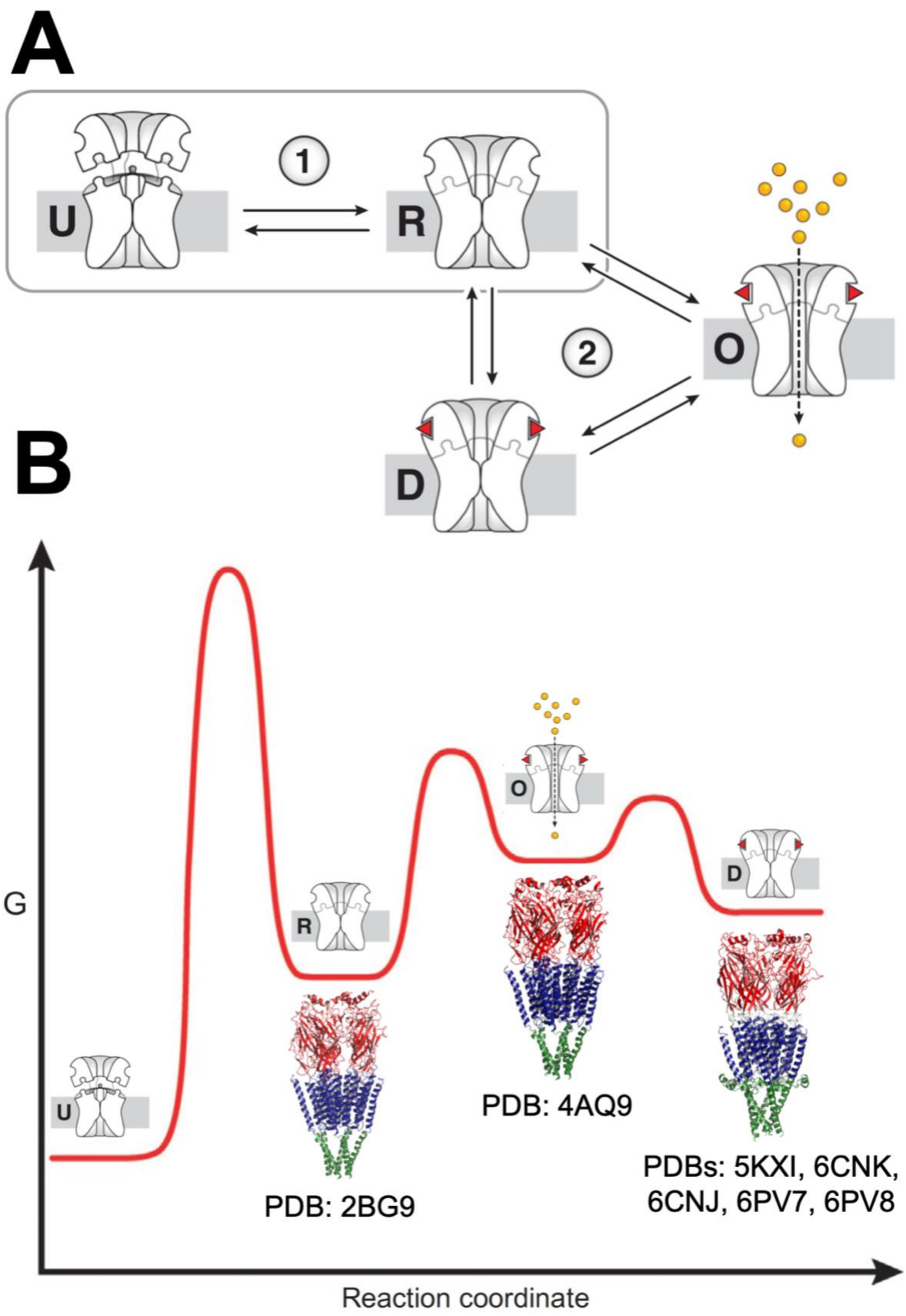
A
U
1
R
2
O
D
B
G
U
R
O
D
PDB: 2BG9
PDB: 4AQ9
PDBs: 5KXI, 6CNK,
6CNJ, 6PV7, 6PV8
Reaction coordinate

9.2.6 5-HT$_3$Rs

9.2.6.1 5-HT$_3$R - lipid interactions

Although not investigated directly, anecdotal evidence suggests that 5-HT$_3$R structure and function are sensitive to lipids. The thermal stability of the homomeric 5-HT$_{3A}$R is dependent upon the hydrophobic environment surrounding the TMD. Detergent solubilization followed by removal of native lipids leads to a loss in thermal stability, with this loss partially reversed by reconstitution into defined lipid membranes (Tol et al., 2013). Cholesterol depletion in the membranes of cells expressing the 5-HT$_{3A}$R through treatment with methyl-β-cyclodextrin or simvastatin reduces serotonin induced whole-cell current responses and slows the rates of 5-HT$_{3A}$R desensitization (Nothdurfter et al., 2010), consistent with what is observed for cells expressing α7 nAChRs (Colón-Sáez and Yakel, 2011). As with other pLGICs, cholesterol depletion alters the distribution of 5-HT$_{3A}$Rs on the cell surface. Interestingly, deletion or mutation of the C-terminal Ala residue (Ala455) leads to a massive decrease in expression of 5-HT$_{3A}$Rs, consistent with a role for the M4 C-terminus in folding/trafficking (Butler et al., 2009). On the other hand, a 12 Å resolution structure of the 5-HT$_{3A}$R reconstituted into lipid vesicles was found, within the limits of the obtained resolution, to be similar to that of detergent solubilized structures (Hassaine et al., 2014; Kudryashev et al., 2016; Polovinkin et al., 2018). Furthermore, Ala substitutions of residues on the lipid-exposed M4 α-helix of the mouse 5-HT$_{3A}$R are less impactful on channel function than analogous Ala mutations in the prokaryotic pLGICs, GLIC and ELIC (Mesoy et al., 2019).

9.2.6.2 Bound lipids in 5HT$_3$R structures

Several detergent-solubilized full-length mouse 5-HT$_{3A}$R structures have been solved by X-ray crystallography and cryo-EM. A cryo-EM structure of the apo 5HT$_{3A}$R, presumably in the

resting state, reveals densities in the cytoplasmic leaflet at the interface between the M4/M1 α-helices of the complimentary subunit and the M3 α-helix of the principle subunit (Basak et al., 2018b). Although the 4.3Å resolution of the structure was not sufficient to identify the nature of the bound lipids, the position of the observed density overlaps with one of the identified cholesteryl hemisuccinate sites on the neuronal nAChRs and with phospholipid binding sites on other pLGICs (see Fig. 9.15, below). Significantly, exogenous lipids were not added during purification, suggesting that the bound lipid is derived from the endogenous membranes in which the $5HT_{3A}R$ was expressed.

Seven additional cryo-EM structures of the $5HT_{3A}R$ have recently been solved in the presence of bound ligands and at higher resolutions, ranging from 2.92 Å to 4.2 Å (Basak et al., 2018a, 2019; Polovinkin et al., 2018). None of these structures have modeled lipid density at the protein-lipid interface. Although this could suggest that the lipid observed bound to the apo state of the $5HT_{3A}R$ has a higher affinity for, and thus stabilizes the resting conformation, electron density at the periphery of the TMD has, in fact, been observed in other structures but has not been of sufficient quality to warrant modeling as lipid (Hugues Nury, personal communications).

9.2.6.3 Mechanisms underlying 5-HT_3Rs – lipid interactions

There is currently insufficient data to begin to develop meaningful hypotheses surrounding 5-HT_3R – lipid interactions. Despite this, it is intriguing to note that both structural and simulation data suggest that the lipid-exposed M4 α-helix moves relative to M1/M3 during channel gating (Polovinkin et al., 2018). The gating motions of M4 change the shape and volume of the non-annular cavity at the M1-M4-M3 interface, which is one of the sites proposed for cholesterol and neurosteroid binding to nAChRs. The lipophilic allosteric potentiator trans-

3-(4-methoxyphenyl)-N-(pentan-3-yl)acrylamide is thought to bind to this cavity to potentiate 5-HT_3AR function (Polovinkin et al., 2018). This allosteric site may be conserved in all pLGICs.

9.2.7 $GABA_AR$s

9.2.7.1 $GABA_AR$ - lipid interactions

Early attempts to solubilize and reconstitute native $GABA_AR$s demonstrate a functional sensitivity to lipids. The solubilization of rat cerebral cortex $GABA_AR$s from synaptosomal membranes using different detergents is lipid dependent (Hammond and Martin, 1986). Endogenous rat cerebral cortex $GABA_AR$s reconstituted into membranes composed of a 4:1 molar mixture of asolectin:native bovine brain lipids retains the ability to bind ligands and undergo agonist-induced chloride flux, while $GABA_AR$s reconstituted into membranes composed of soybean asolectin alone do not, thus suggesting that a native brain lipid is important for function (Dunn et al., 1989). Incubating either native $GABA_AR$ synaptosomes or $GABA_AR$s solubilized in detergent with increasing concentrations of detergent-solubilized phosphatidylserine (PS) also leads to enhanced binding of the benzodiazepine, flunitrazepam, while incubation with other detergent-solubilized lipids has lessor effects (Hammond and Martin, 1987). As with the *Torpedo* nAChR, anionic lipids may play a role modulating $GABA_AR$ function.

Methyl-β-cyclodextrin-induced depletion of cholesterol levels in the cell membranes of rat hippocampal neurons expressing $GABA_AR$s diminish the magnitude of the agonist-induced response (Sooksawate and Simmonds, 2001a). Interestingly, subsequent enrichment with the cholesterol stereoisomer, epicholesterol, does not reverse the effects of cholesterol depletion, suggesting that cholesterol influences function by binding to enantiomer-specific sites. Further supporting the existence of such cholesterol sites, potentiating neurosteroids are more effective in cholesterol-depleted membranes, and less effective in cholesterol-enriched membranes.

Cholesterol and neurosteroids may have overlapping sites of action (Sooksawate and Simmonds, 2001b).

Note that the methyl-β-cyclodextrin-facilitated *enrichment* of cholesterol above its normal levels in the cytoplasmic membranes of cells expressing $GABA_AR$s also diminishes the magnitude of the agonist induced response. Optimal levels of cholesterol are thus required for optimal $GABA_AR$ function, as is observed with the *Torpedo* nAChR (Sooksawate and Simmonds, 2001a). In this case, however, epicholesterol enrichment *does* mimic the inhibition observed upon cholesterol enrichment, suggesting that the inhibitory effects at high cholesterol levels result from changes in the bulk membrane physical properties of the bilayers. Supporting a role for bulk membrane physical properties in $GABA_AR$ function, membrane vesicle size, which influences membrane curvature, also modulates flunitrazepam binding (Viel et al., 1997).

9.2.7.2 Bound lipids in $GABA_AR$ structures

The binding of lipids to a $GABA_AR$ was first observed in a 3.9 Å resolution cryo-EM structure of a detergent and cholesteryl hemisuccinate solubilized human α1β2γ2 $GABA_AR$, with a seven residue linker replacing the ICD in each subunit. Electron density at both annual and non-annular sites was modeled as cholesteryl hemisuccinate, with a total of 12 binding sites identified in the TMD (Zhu et al., 2018). The subsequent structure of a full-length agonist-responsive human α1β3γ2 $GABA_AR$ in MSP2N2/lipid nanodiscs, however, exhibited a different TMD structure, suggesting that the initial α1β2γ2 $GABA_AR$ structure may not represent a true physiological state (Laverty et al., 2019).

Although the MSP2N2/lipid nanodisc structure did not reveal the presence of bound cholesterol, PC molecules were modelled in the extracellular leaflet at the M4 – M1 interface of

the two α1 subunits and the intervening β3 subunit. More importantly, two phosphatidylinositol 4,5-bis phosphate (PIP_2) molecules were unambiguously identified in the intracellular leaflet at the interface between M4 and M3 in both α1 subunits, with the PIP2 headgroup bound through electrostatic interactions to polar and electro-positive residues (Fig. 9.12). Note that depletion of PIP_2 from the intracellular leaflet of the bilayer by the scavenger, poly-L-lysine, led to only a small change in the agonist-induced current. The lack of major changes led to the suggestion that PIP_2 plays a role in α1β2γ2 $GABA_AR$ trafficking, as opposed to α1β2γ2 $GABA_AR$ channel gating, although further studies are required to test a role for PIP_2 in both processes.

As noted, neurosteroids are known to affect the function of $GABA_ARs$ in a cholesterol dependent manner, suggesting that neurosteroids and cholesterol may have overlapping sites of action (Sooksawate and Simmonds, 2001b). Supporting this hypothesis, X-ray structures of homomeric chimeras containing the TMD of either the α1 or the α5 $GABA_AR$ subunits reveal both inhibiting and potentiating neurosteroid sites that overlap with those observed for cholesteryl hemisuccinate binding to the nAChR (Laverty et al., 2017) (Fig. 9.10). Specifically, potentiating neurosteroids are bound in the cytoplasmic leaflet at the interface between the M4 and M1 α-helices from the complimentary subunit and the M3 α-helix from the principal subunit (Laverty et al., 2017; Miller et al., 2017; Chen et al., 2018), while inhibiting neurosteroids are bound in the cytoplasmic leaflet on the opposite side of M4 at the interface with M3 (Laverty et al., 2017). Although the ICD for each these constructs was replaced by a three amino acid linker to facilitate crystallization – thus potentially impacting on neurosteroid binding - these sites of action have been verified through both mutagenesis and affinity labelling experiments in natural heteropentameric $GABA_ARs$ (Hosie et al., 2006; Wu et al., 2019).

Affinity-labelling and mutagenesis studies also suggest a site for potentiating neurosteroids in the extracellular leaflet at the interface between M4 and M1 of the α1-subunit (Cheng et al., 2018; Chen et al., 2019; Sugasawa et al., 2019). The absence of neurosteroids bound to this site in structures of the $GABA_AR$ chimeras is surprising, but could reflect the low resolution of the solved chimeric structures. Alternatively, detergent solubilisation may simply lead to displacement of the neurosteroids from this accessible potentiating site.

9.2.7.3 Mechanisms underlying $GABA_AR$-lipid interactions

Although the available biochemical data suggest that $GABA_AR$ function is sensitive to lipids, the underlying mechanisms remain unclear. Non-annular lipophilic binding sites may play a role in $GABA_AR$ function, as evidenced by the elucidated neurosteroid binding sites. The inability of epicholesterol to substitute for cholesterol in supporting $GABA_AR$ function provides evidence for the existence of specific cholesterol regulatory sites, a hypothesis supported by recent docking studies using cholesterol and epicholesterol (Barbera et al., 2019). Higher resolution structures may be necessary to verify the existence of these putative cholesterol binding sites. It will also be intriguing to explore further the potential role of PIP_2 in $GABA_AR$ function.

Figure 9.12 Phospholipid binding to the α1β3γ2 $GABA_AR$

A side view of the α1β3γ2 $GABA_AR$ structure (PDB: 6I53) is shown on the left with a single α-subunit highlighted in light blue. The extracellular leaflet lipid is modeled as PC, although the choline headgroup is not shown, while the intracellular leaflet lipid is PIP_2. Lipids are shown as predominately yellow spheres. An enlarged view of the PIP_2 binding site is shown on the right but rotated ~90° to highlight side chains interacting with the head group. Coloring is as in Fig. 9.8.

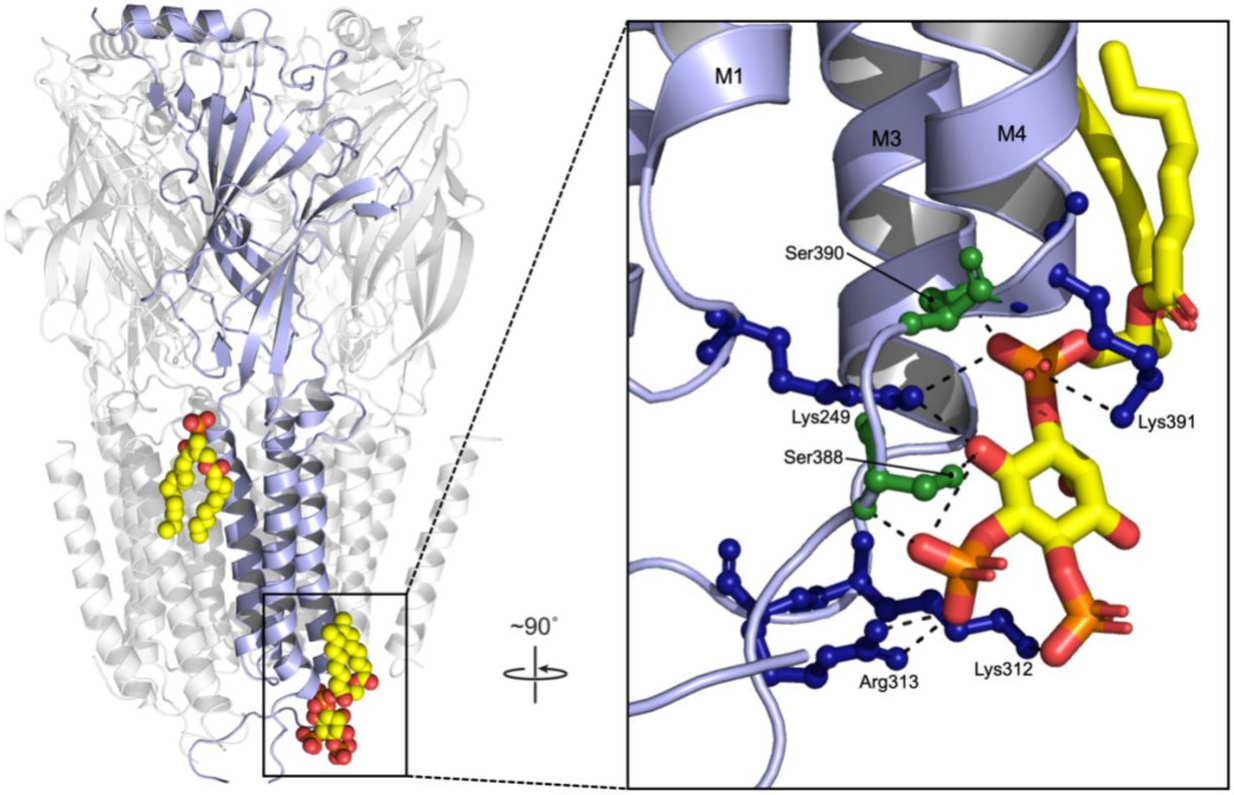
M1
M3
M4
Ser390
Lys249
Ser388
Lys391
Arg313
Lys312
~90°

9.2.8 GlyRs

9.2.8.1 GlyR - lipid interactions

Although GlyRs purified from rat spinal cord and reconstituted into soybean asolectin membranes are capable of undergoing agonist-induced anion flux (Riquelme et al., 1990), no studies to date have examined the effects of different lipids on GlyR function. Interestingly, M4-swapped chimeric constructs of the homologous glycine receptor α1 and α3 subunits demonstrate that subunit-specific agonist efficacy is driven in large part by M4 and residues at the M4-lipid interface (Chen et al., 2009). M4 is crucial for GlyR trafficking to the cell surface (Haeger et al., 2010). M4-M1/M3 interactions also appear to play a critical role in channel folding and function (Haeger et al., 2010; Tang and Lummis, 2018).

Despite the lack of functional data on lipid-GlyR interactions, recent structures provide compelling evidence that lipids play a significant role. Detergent-solubilization stabilizes the GlyR in the presence of glycine in a conformation with a "super-open" pore (Cerdan et al., 2018), although see (Dämgen and Biggin, 2020). In contrast, the GlyR in MSP1E3D1nanodisks containing brain total lipid extract adopts a glycine-induced desensitized state with a closed pore, while the GlyR in patches directly excised from cell membranes by styrene maleic acid copolymers exists in glycine-induced desensitized, open and super-open conformations. Significantly, the diameter of the pore in the open conformation is consistent with the experimentally measured channel conductance for the open state (Yu et al., 2021). These studies suggest that the membrane environment surrounding the GlyR alters function via a conformational selection mechanism.

9.2.8.2 Bound lipids in GlyR structures

A number of cryo-EM and x-ray crystallography structures are available for homomeric GlyRs with their ICD substituted by a tripeptide linker, but none of these structures exhibit the presence of bound lipids (Du et al., 2015; Huang et al., 2015, 2017a, 2017b; Yu et al., 2021). In fact, a crystal structure of the detergent-solubilized human α3 GlyR solved at 2.6 Å resolution, the highest resolution yet for a eukaryotic pLGIC, does not detect any bound lipid (Huang et al., 2017a). On the other hand, a recent mass spectrometry study identified sites for cholesterol action along M4 (Ferraro and Cascio, 2018). A nuclear magnetic resonance structure of the α3 GlyR TMD also modeled the binding of endo-cannabinoids in the middle of the bilayer at the interface between the M4 and M3 helices (Xiong et al., 2011, 2012).

9.2.8.3 Mechanisms of Lipid Action

Insufficient structural and functional data on GlyR – lipid interactions is available to speculate on putative mechanisms underlying lipid action. It is relevant to note that the GlyR exhibits an extensive network of aromatic residues at the M4 – M1/M3 interface. As noted below for the prokaryotic pLGIC, GLIC, a similar network of aromatic residues at this interface leads to relatively tight M4 - M1/M3 interactions and a relatively stable TMD structure that is relatively insensitive to its surrounding lipid environment. In addition, the introduction of a similar network of aromatic interactions reduces the functional sensitivity of ELIC to lipids (see below) (Carswell et al., 2015b). These findings, along with sequence comparisons, lead to the prediction that anion-selective pLGICs, GlyRs and $GABA_A$Rs, exhibit a weaker functional sensitivity to lipids than cation-selective pLGICs, nAChRs and $5HT_3$Rs (Therien and Baenziger, 2017).

9.2.9 Non-vertebrate pLGICs

9.2.9.1 Non-vertebrate pLGIC - lipid interactions

Since their discovery in the mid-2000s, the prokaryotic pLGICs, GLIC and ELIC, have increasingly been used as models for probing fundamental mechanisms underlying pLGIC-lipid interactions. Although the effects of lipids on GLIC and ELIC function in membranes of defined lipid composition have not yet been characterized, GLIC reconstituted in minimal PC membranes retains the ability to undergo agonist-induced cation flux while ELIC (the *Torpedo* nAChR) does not (Labriola et al., 2013; Carswell et al., 2015a). The ability of GLIC to couple agonist binding to channel gating in minimal PC bilayers has been attributed to the complex network of aromatic residues that exist at the M4 - M1/M3 interface. As noted above, these residues likely strengthen M4 – M1/M3 interactions making the TMD less malleable and thus less sensitive to surrounding lipids (Carswell et al., 2015a; Therien and Baenziger, 2017). In contrast, ELIC exhibits only a few aromatic residues at this interface, with these bulky residues likely preventing close M4 associations with M1/M3 thus creating a more malleable M4 – M1/M3 interface that renders ELIC more sensitive to its surrounding membrane environment. Further supporting this hypothesis, the introduction of a network of aromatic residues at the M4 – M1/M3 interface, similar to that observed in GLIC, restores the capacity of ELIC to undergo agonist-induced channel gating in minimal PC bilayers (Carswell et al., 2015a).

In addition to effects on channel gating, the rates of desensitization of both GLIC and ELIC are sensitive to membrane lipids. Interestingly, increasing levels of cholesterol in soybean asolectin membranes leads to increasing rates of GLIC desensitization (Velisetty and Chakrapani, 2012), while the addition of cholesterol to asolectin membranes has the opposite

effect slowing ELIC desensitization (Hénault et al., 2019). The rates of ELIC desensitization are slowed even further in PC membranes containing ether the anionic lipid, phosphatidylglycerol (PG), or mixtures of PG and phosphatidylethanolamine (PE) (Hénault et al., 2019; Tong et al., 2019).

9.2.9.2 Lipids and GLIC

An x-ray crystallographic structure of detergent solubilized GLIC solved in an apparently open conformation in 2009 was the first pLGIC structure to reveal the presence of bound lipids (Bocquet et al., 2009). Although the identities of the phospholipid headgroups were not unequivocally assigned, three PC molecules were modeled bound to each subunit, one in the extracellular leaflet of the bilayer and the other two in the intracellular leaflet. The lipid in the extracellular leaflet is located at the interface between M4 and M1 and overlaps with the site for PC binding to the α1β3γ2 $GABA_AR$ (see Fig. 9.12). This site is also close to a *proposed* neurosteroid potentiating site in both the α4β2 nAChR and the $GABA_AR$. The intracellular leaflet bound lipids are located at the M4/M1 and M4/M3 interfaces, although the M4/M1 bound lipid extending to contact the M3 α-helix from the adjacent principal subunit. These sites overlap with the binding of phospholipids to the $5HT_{3A}R$, α1β3γ2 $GABA_AR$, and ELIC, and to sterol/neurosteroid binding to the α4β2/α3β4 nAChRs and the α1/α5 $GABA_AR$. Note that GLIC was solubilized and crystallized in the absence of added lipids, so the lipids bound to the TMD were derived from the endogenous *E. coli* membranes in which GLIC was expressed. In addition, both cholesterol and neurosteroid photoaffinity probes label residues that broadly overlap with all the observed lipid binding sites on GLIC (Cheng et al., 2018; Budelier et al., 2019).

The lipid binding to GLIC in the extracellular leaflet is particularly intriguing as it is located near structures at the ECD/TMD interface that play an important role in channel gating. In this open conformation, the bound PC bridges interactions between Phe315 on M4 and Phe121 on the β6-β7 loop (the Cys-loop in eukaryotic pLGICs) while the choline head group projects towards Tyr194 on the pre-M1 loop (Fig. 9.13a). Arg117 and Arg118 from the β6-β7 loop form a cation-π interaction with Tyr251 on the M2-M3 linker and line the lipid binding pocket, respectively. Electron density for this lipid, however, is not observed in structures of GLIC solved in resting or locally closed conformations (Prevost et al., 2012; Sauguet et al., 2014a). In the absence of the bound lipid, density for the side chains of both Arg117 and Arg118 are no longer visible, likely due to high mobility (Fig. 9.13b). A speculative interpretation of these observations is that the lipid helps stabilize the open conformation by enhancing interactions between the β6-β7 loop and the M2-M3 linker. Consistent with this interpretation, deletion or Ala mutation of the lipid bridging residue, Phe315, leads to a reduction of GLIC expression and/or function (Hénault et al., 2015a).

Variable binding of the extracellular leaflet lipid is also observed in the presence of allosteric modulators. The binding of the inhibitory drugs, propofol and desflurane, both overlap with the lipid binding site, with propofol binding eliminating lipid binding and desflurane binding substantially altering the lipid binding pose so that the PC headgroup now extends toward Arg118 of the β6-β7 loop (Fig. 9.13d). In contrast, the fatty acid, docosahexaenoic acid (DHA), which enhances GLIC desensitization, binds to a site adjacent to the bound PC. DHA forms a salt bridge with Arg118 of the β6-β7 loop, with a consequent movement of Arg118 likely facilitating a subtle repositioning of both the PC headgroup and its fatty acyl chains (Fig. 9.13e) (Basak et al., 2017). Significantly, mutating Arg118 to Ala reduces the effects of DHA

on GLIC desensitization. In addition, electron paramagnetic resonance shows that the O_2 accessibility of residues in the lipid binding pocket is enhanced when GLIC transitions from the resting to desensitized states, suggesting a concomitant movement of the bound lipid (Velisetty et al., 2014; Basak et al., 2016). While further experiments are still required to establish a causative link between lipid binding and GLIC function, the altered lipid binding poses in different functional states implies a modulatory role.

9.2.9.3 Lipids and ELIC

Although close to 30 structures of ELIC have been solved, a recent 2019 crystal structure of ELIC at 2.5 Å resolution, the highest resolution yet for ELIC, was the first to reveal electron density for a bound lipid. This electron density is located in the intracellular leaflet at the M4/M1 interface, although the density extends towards M3 on the adjacent principal subunit (Fig. 9.14) (Hénault et al., 2019). The electron density was of sufficient quality to assign the bound lipid unequivocally to PE, consistent with the fact that ELIC was crystallized in the presence of an *E. coli* lipid extract that contains 58 mol% PE. A subsequent mass spectrometry/computer modeling study showed that ELIC binds both PE and PG, but PG with a higher affinity and likely to the same PE binding site observed in the ELIC crystal structure (Tong et al., 2019). The detected lipid binding pocket on ELIC is shaped by a M4 proline kink that positions Arg301 at the base of M4 to form a cation-π interaction with Trp224 on M1. This orients Trp224 so that it wedges between the hydrophobic tails of the bound lipid (Fig. 9.14). The WRP motif is strictly conserved in anionic pLGICs, suggesting that the binding pocket may also be conserved. Interestingly, the PE binding pocket overlaps with the previously identified

binding site for neurosteroids in α1- or α5-based $GABA_AR$ chimeras, as well as cholesteryl hemisuccinate binding sites in on both neuronal nAChRs and the α1β2γ2 $GABA_AR$ (Fig. 9.15).

Both structural and functional data suggest an intriguing mechanism by which lipid binding to ELIC influences channel gating (Carswell et al., 2015a). Mutations of residues that perturb the lipid binding site and that likely hinder or prevent PE/PG binding almost invariably lead to enhanced rates of ELIC desensitization - consistent with the above noted functional data suggesting that PE/PG binding slows desensitization rates. In particular, P305A, which eliminates the kink in M4 leads to a rapidly desensitizing phenotype. Although deletion of the final seven C terminal residues on M4 has little effect on ELIC function, deletion of the final eight C terminal residues or the entire M4 α-helix also leads to a rapidly desensitizing phenotype similar to that observed with the P305A. A crystal structure of the eight residue deletion mutant showed that density for the entire M4 α-helix is lacking, despite the deletion of only the final eight residues, and the bound lipid is absent. Deletion of the final eight residues also enhances the motions of the polypeptide backbone in the region of the putative desensitization gate located near the cytoplasmic side of the channel pore (Gielen et al., 2015). Furthermore, a survey of ELIC structures in the protein data bank reveals that many exhibit unreported electron density for M4 in both a straightened and a kinked conformation, with the former precluding lipid binding. These structures and other supporting biophysical studies highlight the dynamic nature of M4 and suggest that lipid binding stabilizes M4 in a less dynamic kinked conformation that likely reduces motions of the desensitization gate to slow the rates of ELIC desensitization.

Together, these data provide the most detailed insight yet into the mechanisms by which a bound lipid influences the function of a pLGIC. In this light, two observations are particularly important in the broader context of pLGIC-lipid interactions. First, only one lipid bound to one

subunit is observed in the ELIC crystal structure solved at 2.5 Å resolution, even though mass spectrometry suggests the existence of several binding sites. In fact, close to 30 other ELIC structures have been solved where no bound lipid is observed. This suggests that crystal and cryo-EM structures may not always reveal the presence of lipids bound to functionally important lipid binding sites. Second, it is prudent to note that cholesterol also slows ELIC desensitization, although not to the same extent as either PG or mixtures of PG and PE. In addition, the PE/PG binding site on ELIC overlaps with neurosteroid/cholesterol binding sites on both $GABA_A$Rs and nAChRs. A speculative interpretation of these two observations is that cholesterol binds to the same lipid binding site on ELIC as PE/PG to stabilize M4 in a less dynamic kinked conformation ultimately slowing the rates of desensitization (i.e. by the same mechanism as PE/PG), but that a weaker binding affinity for cholesterol to this modulatory site leads to reduced occupancy and thus a less pronounced functional effect on desensitization rates. This speculative interpretation suggests that different types of lipids may interact with overlapping modulatory sites on the same pLGIC to influence channel function.

Finally, cryo-EM structures of both apo and agonist-bound ELIC were recently solved in the minimal PC bilayers that are known to render ELIC insensitive to agonist (Carswell et al., 2015a; Kumar et al., 2020b). Consistent with the functional data, both the apo and agonist bound ELIC structures have similar pore diameters suggestive of a closed state. Close inspection, however, reveals that both the ECD and ECD-TMD interface of the agonist bound structure have partially transitioned to an active state, but these changes do not extend to the M2 helices - i.e. agonist binding fails to transition into channel gating. These new ELIC structures provide the first insight into a lipid-dependent uncoupled conformation.

9.2.9.4 Lipids and the glutamate-activated chloride channel (GluCl)

A 2014 crystal structure of GluCl from *C. elegans*, with the ICD replaced by a tripeptide, revealed the presence of bound PC – dc the first lipid binding site observed in a eukaryotic pLGIC (Althoff et al., 2014). The PC binding site on GluCl is unique in that it is wedged in between the M2/M3 α-helices of the principal subunit and the M1/M2 helices of the complimentary subunit, overlapping with a previously determined ivermectin binding site (Hibbs and Gouaux, 2011; Du et al., 2015; Huang et al., 2017b). The head group of the lipid is near the extracellular end of the TMD with the hydrophobic tails running between the subunits along the pore axis. PC was shown to potentiate the function of GluCl.

Figure 9.13 Phospholipid binding to GLIC

A) Side view of GLIC (PDB: 3EAM) in an open conformation with a single subunit colored light blue. Enlarged views of the extracellular lipid site are shown for B) the open conformation, C) the resting conformation (without bound lipid) (PDB: 4NPQ), D) an inhibited conformation with bound desflurane (PDB:3P50) and E) a DHA- desensitized conformation (PDB:5J0Z). Affected residues close to the lipid binding site are shown as sticks colored according to residues type as in Fig. 9.10. Lipids and bound allosteric modulators are shown in B) – E) as thick sticks colored predominantly yellow as in Fig. 9.8.

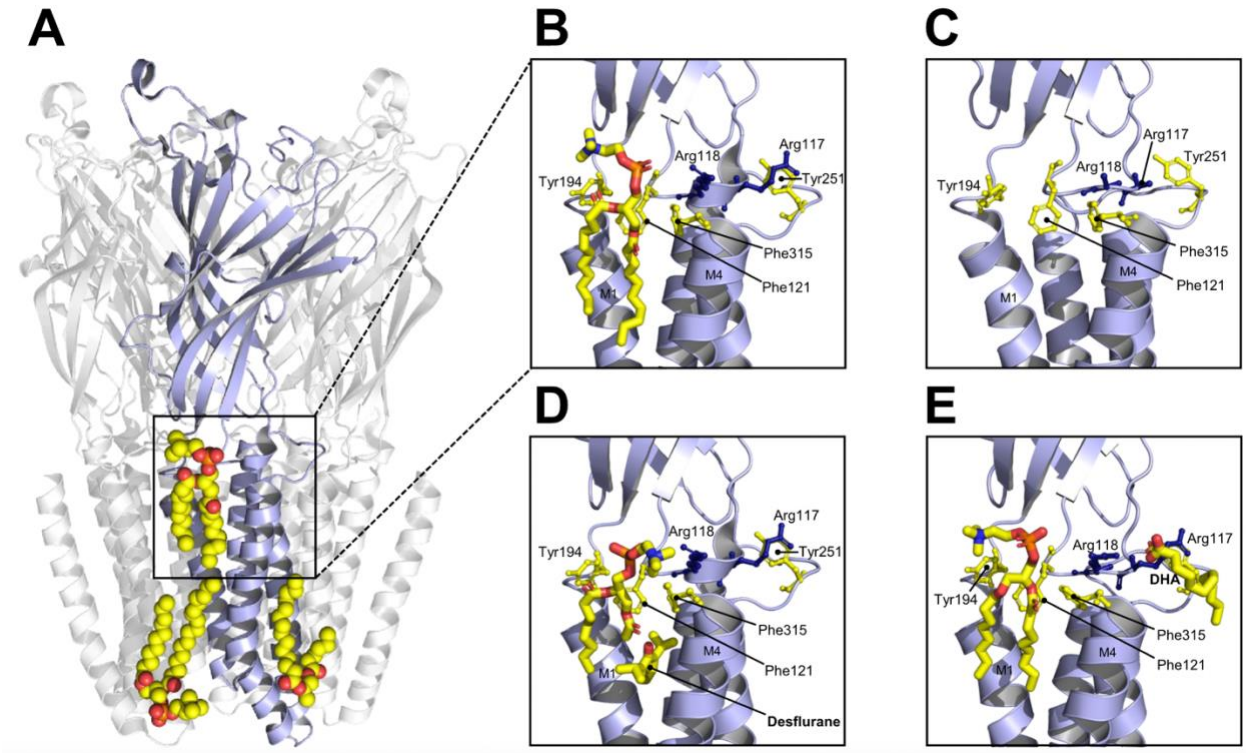
A
B
C
D
E
Arg118
Arg117
Tyr194
Tyr251
Phe315
M4
Phe121
M1
Desflurane
DHA

Figure 9.14 ELIC with bound PE

A) Side view of ELIC (PDB: 6HJX) with the principal subunit salmon, the complimentary subunit light blue, and the PE molecule shown as predominantly yellow spheres. The zoomed in view highlights residues involved in PE binding as sticks colored according to residues type (coloring as in Fig. 9.10). B) Comparison of the conformation of M4 in a lipid bound (left; PDB: 6HJX) and a lipid un-bound structure (right; PDB: 6HK0).

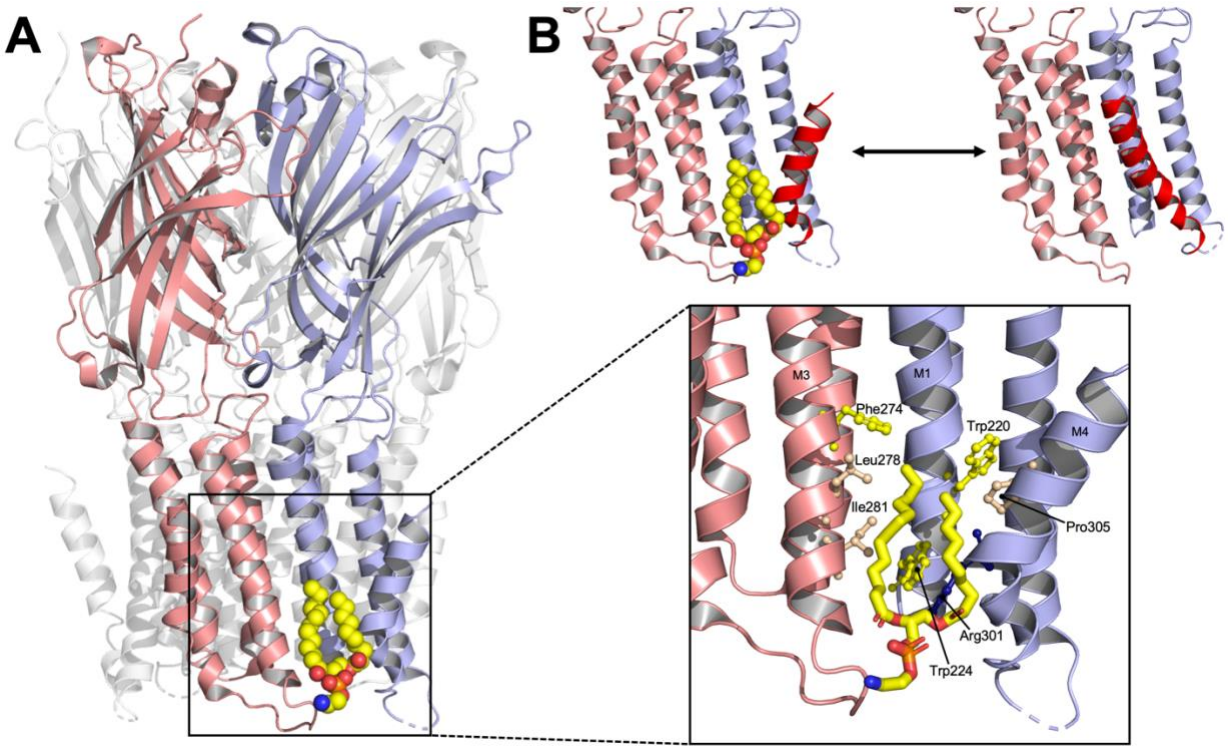
A
B
M3
M1
M4
Phe274
Trp220
Leu278
Ile281
Pro305
Arg301
Trp224

9.2.10 Summary and conclusions

Despite the increasing structural data, our understanding of pLGIC-lipid interactions continues to be shaped by studies performed using the *Torpedo* nAChR as a model system. These studies show that lipids influence the agonist-induced response by stabilizing different proportions of activatable (resting) versus non-activatable (desensitized and uncoupled) conformations, and by controlling the transitions between these states. A unique feature of the *Torpedo* nAChR is that it adopts a lipid – dependent uncoupled conformation. Although it remains to be determined whether other pLGICs adopt a similar uncoupled state, lipids likely influence the activities of other pLGICs through such conformational selection and kinetic mechanisms.

Biochemical and biophysical studies performed on the *Torpedo* nAChR originally highlighted the possibility of both annular and non-annular sites of lipid action. A common theme amongst the many pLGIC structures solved to date is the existence of overlapping annular lipid binding sites located primarily in the grooves between the outermost TMD α-helix, M4, and the adjacent α-helices, M1 and M3 of each subunit – although the poses of the bound lipids vary substantially from one pLGIC to another (Fig. 9.15). Moreover, these annular sites overlap with the sites of action for other lipophilic modulators, such as neurosteroids, cannabinoids, etc. In contrast, convincing structural evidence for the existence of non-annular bound membrane lipids is lacking.

In most cases, however, the mechanisms by which lipid binding to these sites to influence function remain unclear, although models are beginning to emerge. A prescient example is that of the prokaryotic pLGIC, ELIC, where the binding of PE/PG appears to dramatically slow ELIC desensitization by stabilizing the M4 α-helix in a relatively static kinked conformation. In this

one case, the data supporting a causality between lipid binding and altered function is relatively strong. This example is particularly instructive in the broader context of pLGIC-lipid interactions because the bound PE was only detected in one subunit of a relatively high 2.5 Å resolution structure of the ELIC homopentamer, while no bound lipids to this site were detected in close to 30 other solved structures, albeit at lower resolution. Also of interest, cholesterol was observed to have a similar, although muted, effect on ELIC desensitization. Structures of other pLGICs suggest that cholesterol may bind to the same modulatory site as PE/PG. In this case, cholesterol binding may exert its effects on ELIC desensitization through the same mechanism as PE/PG, but a weaker binding affinity leading to reduced occupancy of the modulatory site may lead to the less pronounced effect. Taken together, these observations highlight that crystal/cryo-EM structures may not always capture functionally critical lipid binding sites and that different lipids may bind to the same sites, albeit with distinct or reduced functional consequences.

Additional higher-resolution structures are clearly required to fully understand the nature of lipid binding to pLGICs. Such structural data along with increasingly sophisticated studies of the effects of lipids on pLGIC function should eventually lead to detailed insight into the mechanisms underlying pLGIC – lipid interactions and thus the roles of such interactions in human biology.

Figure 9.15 Overlapping lipid binding sites in pLGIC structures

A **s**ide view of GLIC (PDB:3EAM) with a single subunit colored light blue is shown in the middle highlighting the three main lipid binding sites observed in pLGICs, labelled as sites 1, 2, and 3. Lipids bound to these sites in GLIC and other pLGICs are shown on the left and right, with each lipid shown as a predominantly yellow spheres as in Fig. 9.10. Each pLGIC is shown with a surface representation. **Site 1:** i) PC bound to GLIC (PDB:3EAM) and ii) PC bound to the α1β3γ2 GABAAR (PDB:6I53). **Site 2:** i) cholesterol bound to the α3β4 nAChR (PDB:6PV7), ii) the potentiating neurosteroid tetrahydrodeoxycorticosterone bound to the α1 GABAAR (PDB:5OSB), iii) PC bound to GLIC (PDB:3EAM) and iv) PE bound to ELIC (PDB:6HJX). **Site 3:** i) cholesterol bound to the α3β4 nAChR (PDB:6PV7), ii) the inhibiting neurosteroid pregnanolone sulphate bound to the α1 GABAAR (PDB:5OSC), iii) PC bound to GLIC (PDB:3EAM) and iv) PIP2 bound to the α1β3γ2 GABAAR (PDB:6I53). Bound lipids in each site are shown as spheres colored according to atom as in figure 9.8 and the protein backbone shown in surface representation. For clarity, the ECD in the Site 1 diagrams has been made transparent, and the ICD, when present, has been removed from the diagrams for Sites 2 and 3.

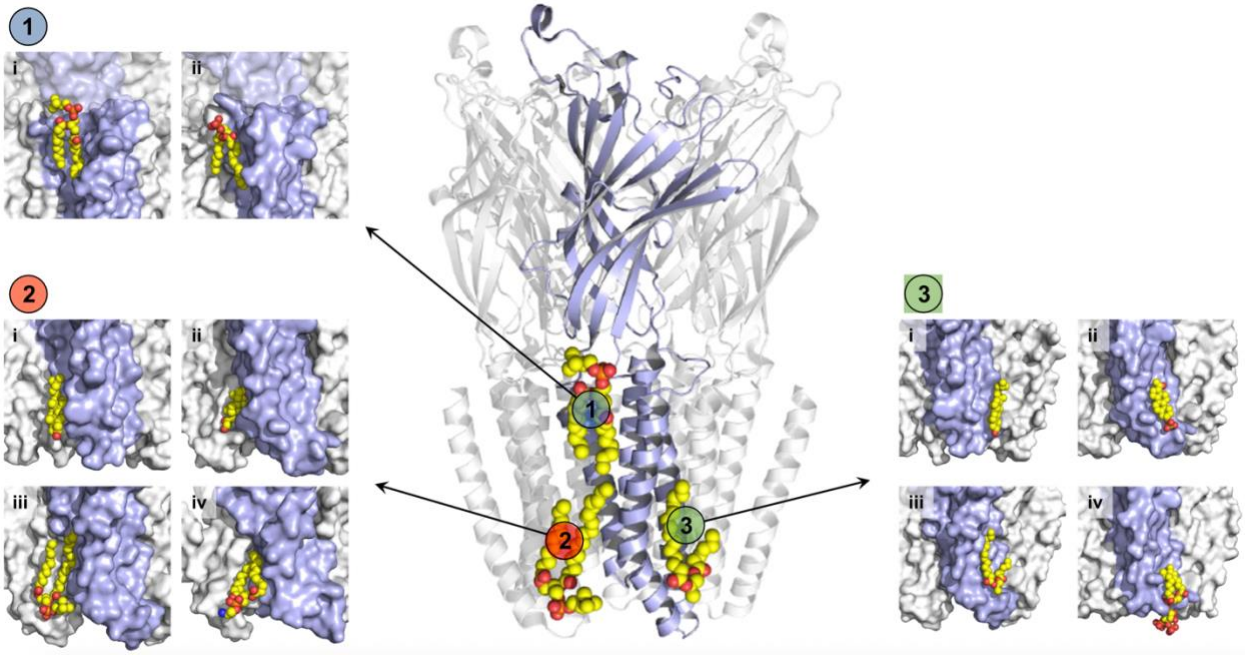
1
i
ii
2
i
ii
iii
iv
3
i
ii
iii
iv
1
2
3

Curriculum Vitae

Mackenzie Thompson

Education

PhD candidate Biochemistry
University of Ottawa, Ottawa, Ontario — Sept 2017 – Feb 2024

BSc Biochemistry & Biotechnology with Honours
Wilfrid Laurier University, Waterloo, Ontario — Sept 2012 – April 2017

Research Contributions

Articles published in peer-reviewed journals:

Thompson, M. J. and Baenziger, J. E. (2020) Structural basis for the modulation of pentameric ligand-gated ion channel function by lipids. BBA - Biomembranes. 1862: 183304 (PhD work).

Thompson, M. J., Domville, J. A. and Baenziger, J. E. (2020) The functional role of the αM4 transmembrane helix in the muscle nicotinic acetylcholine receptor probed through mutagenesis and co-evolutionary analyses. Journal of Biological Chemistry. 295: 11056–11067 (PhD work).

Thompson, M. J. and Baenziger, J. E. (2020) Ion channels as lipid sensors: from structures to mechanisms. Nature Chemical Biology. 16: 1331–1342 (PhD work).

Zarkadas, E., Pebay-Peyroula, E., **Thompson, M.J.**, Schoehn, G., Uchański, T., Steyaert, J., Chipot, C., Dehez, F., Baenziger. John E., and Nury, H. (2022). Conformational transitions and ligand-binding to a muscle-type acetylcholine receptor. Neuron 110: 1358–1370. (PhD work)

Thompson, M.J., Domville, J.A., Edrington, C.H., Venes, A., Giguère, P.M., and Baenziger, J.E. (2022). Distinct functional roles for the M4 α-helix from each homologous subunit in the hetero-pentameric ligand-gated ion channel nAChR. J. Biol. Chem. 297: 102104. (PhD work).

Ananchenko, A., Hussein, T.O.K., Mody, D., **Thompson, M.J.**, and Baenziger, J.E. (2022). Recent Insight into Lipid Binding and Lipid Modulation of Pentameric Ligand-Gated Ion Channels. Biomolecules 12: 814. (PhD work)

Slobodyanyuk, M., Banda-Vazquez, J. A., **Thompson, M. J.**, Baenziger, J. E., Chica, R. A., and daCosta C. J. B. (2022) Origins of acetylcholine antagonism in a bacterial pentameric ligand-gated ion channel. Communications Biology 5: 1264. (PhD work).

Thompson, M. J., Bekarkhanechi F. M., Ananchenko, A., Nury, H., Baenziger, J. E. (2023) A release of subunit heterogeneous conformational restraints underlies allosteric communication in a muscle nicotinic acetylcholine receptor. Accepted at Nat. Comm. (PhD work).

Thompson, M. J., Zarkadas, E., Nury, H., Baenziger, J. E. (2023) Asynchronous conformational transitions during nicotinic acetylcholine receptor activation. In preparation for Neuron. (PhD work).

Other peer-reviewed contributions:

Thompson, M. J. Farid Monsoub Bekarkhanechi, Hughes Nury and Baenziger, J. E. (2023) Asymmetric tense-to-relaxed subunit transitions drive gating of the heteromeric muscle nicotinic acetylcholine receptor. CNRS University of Illinois Urbana Champagne/Laboratoire International Associe annual meeting (international). Seminar (PhD work).

Thompson, M. J. Farid Monsoub Bekarkhanechi, Hughes Nury and Baenziger, J. E. (2022) The coupling of binding and gating in a muscle type nicotinic acetylcholine receptor. International Union of Pure and Applied Biophysics: Ion Channel Biophysics Meeting (international). Seminar (PhD work).

Thompson, M. J. Farid Monsoub Bekarkhanechi, Hughes Nury and Baenziger, J. E. (2022) The coupling of binding and gating in a muscle type nicotinic acetylcholine receptor. International Union of Pure and Applied Biophysics: Ion Channel Biophysics Meeting (international). Poster (PhD work).

Thompson, M. J. Farid Monsoub Bekarkhanechi, Hughes Nury and Baenziger, J. E. (2022) The coupling of binding and gating in a muscle type nicotinic acetylcholine receptor. Biophysical Society of Canada Annual Meeting (national). Poster (PhD work).

Thompson, M. J. and Baenziger, J. E. (2022) Probing the activation mechanisms of a muscle-type acetylcholine receptor using a combination of structural and functional measurements. Biophysical Society Annual Meeting (international). Poster (PhD work).

Thompson, M. J. Jamiee A. Domville and Baenziger, J. E. (2021) Functional role of the M4 lipid-sensor in muscle nicotinic acetylcholine receptor function. Biophysical Society of Canada Annual Meeting (national). Poster (PhD work).

Thompson, M. J. and Baenziger, J. E. (2019) The mechanisms underlying altered function of the nicotinic acetylcholine receptor by mutations leading to congenital myasthenic syndrome. Biophysical Society of Canada Annual Meeting (national). Poster (PhD work).

Thompson, M. J. and Jelokhani-Niaraki, M. (2017) Synthesis and purification of the analgesic neuropeptide neurotensin and three aromatically substituted analogues. Southern Ontario Undergraduate Student Chemistry Conference (regional). Seminar (Honours work).

Academic Awards

Alexander Graham Bell Scholarship – NSERC-CGSD $105,000 for 3 years 2021
Awarded to the top-ranking doctoral student researchers in the annual NSERC scholarship competition.

Ontario Graduate Scholarship (declined) $30,000 for 2 years 2021
Awarded to doctoral student researchers in the annual OGS scholarship competition.

Michael Smith Foreign Study Supplement $6,000 2022
Awarded to researchers holding a CGSD scholarship that are conducting international research.

Masters/PhD admission scholarship – University of Ottawa $9,000 per year 2017-2022
Awarded to any student with great than an A- average in their past two years of study

PhD excellence scholarship – University of Ottawa $9,000 per year. 2023
Awarded to students displaying academic excellence

University of Ottawa Biochemistry department award of excellence in graduate studies 2023
Awarded to a PhD student who has demonstrated academic excellence

PhD poster prize – Biophysical society of Canada annual meeting 2021

Best PhD seminar in the Biochemistry department – University of Ottawa 2021

Academic All-Canadian 2015-2016 academic year

Awarded to varsity athletes who obtained higher than an A- average during an academic year.
Dean's honor roll 2015-2016 and 2016-2017 academic years

Research Experiences

PhD research
University of Ottawa, Ottawa, Ontario Sept 2017 – Feb 2024
Supervisor: Dr. John Baenziger

Research focused on understanding mechanisms that dictate function in the muscle nicotinic acetylcholine receptor (nAChR). Specifically, to define mechanisms leading from congenital myasthenic syndrome causing mutations to altered nAChR function, provide a structural basis for how lipids modulate nAChR function, and uncover the mechanism by which agonist binding is coupled to channel gating in the nAChR. A combination of molecular biology techniques, including cloning, site-directed mutagenesis, and bacterial cell cultures, with biophysical techniques, including two-electrode voltage-clamp electrophysiology, radioligand-binding assays, and fluorescence-based assays were used for this research. Worked independently to perform experiments, analyze data, and critically assessing its meaning. Altogether, I generated over 1,000 mutants during my PhD and characterized their function by electrophysiology.

Spent the final eight months of at the Institut de Biologie Structurale (IBS) in Grenoble, France in the lab of Hugues Nury. Performed fluorescent assays to characterize the activation of the nAChR in lipid nanodiscs and performed cryo-EM of the nAChR at sub saturating concentrations of agonist to elucidate intermediate conformations. Made cryo-EM grids, screened grids on a 200 kV Glacios electron microscope and collected data. Processed this data on relion and cryosparc, resolved heterogeneity using 3D variability, 3D classification, and 3D flexibility analyses, built molecular models using Coot, Isolde and Phenix, and created new tools to characterized allosteric transitions in the nAChR.

Wrote two review articles and contributed to one other. Oversaw lab purchasing, technical support, training, and supervision for the lab on top of my own research. Performed all animal work in the lab, obtained quotes and navigated the purchasing of laboratory equipment, installed lab equipment and the corresponding software, and fixed every piece of the electrophysiology rig. Trained more than 15 students in laboratory techniques including one post-doc and five graduate students and have supervised 6 undergraduate research projects. Taught a six-week virtual course for third year undergraduate students on experimental techniques in the lab following the pandemic. Organized the "ion channel journal club" for three years, a monthly club for graduate students, post-docs, and professors who study ion channels at the University of Ottawa to discuss recent ion channel research.

Honors research
Wilfrid Laurier University, Waterloo, Ontario Sept 2016 – April 2017
Supervisor: Dr. Masoud Jelokhani-Niaraki

Studied the role of aromatic residues on the membrane association of the neuropeptide neurotensin. Performed solid-phase peptide synthesis, high-performance liquid chromatography, mass spectrometry, circular dichroism, and isothermal titration calorimetry. Learned how to effectively organize lab time, effectively communicate my research, and perform basic laboratory techniques.

Directed studies research

Wilfrid Laurier University, Waterloo, Ontario May 2016 – Aug 2016
Supervisor: Dr. Scott Smith

Studied the effect of dissolved organic matter composition on the concentration of free nickel from various water sources. Performed analytical immobilized metal affinity chromatography, titrations, and fluorescence spectroscopy. Learned the basics of being a laboratory scientist.

Other relevant experiences

Varsity Football Player
Wilfrid Laurier University, Waterloo, Ontario Sept 2012 – Jan 2016

Named 2015 academic All-Canadian for maintaining >A- average while committing >40 hours/week to football. Was named a team mentor in 2016 responsible for ensuring new members of the team succeeded both on and off the field. Helped forge my outstanding leadership, teamwork, and organization skills.

Brewmaster
The Garage Project Brewery, Wellington, New Zealand May 2015 – Aug 2015
Tatamagouche Brewing Company, Tatamagouche, Nova Scotia May 2017 – Aug 2017

Completed a summer internship at one of the world best breweries in Wellington, New Zealand. Went on to obtain a full-time brew master position before beginning my graduate studies. Was responsible for the use and maintenance of industrial bioreactors, quality control of yeast, and recipe design. Created a salt concentration calculator for brewers to accurately control the salt concentrations in their recipes.

Gender violence advocation
Not My Laurier: Combatting gender violence, Waterloo, ON September 2016 – May 2017

Male ally's coordinator for the Not My Laurier: Goldenhawks combating gender violence club, gender violence liaison for the Laurier captain's council, and founding member of the Laurier gender violence task force. Ran educational workshops, scheduled awareness events, and worked with the athletic director to increase gender violence education.